COMPREHENSIVE MEMBRANE SCIENCE AND ENGINEERING

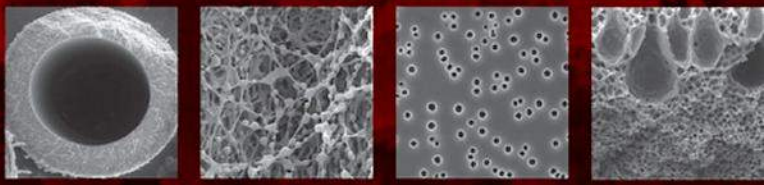

Edited by
Enrico Drioli • Lidietta Giorno

COMPREHENSIVE MEMBRANE SCIENCE AND ENGINEERING

This page intentionally left blank

COMPREHENSIVE MEMBRANE SCIENCE AND ENGINEERING

Editors

Enrico Drioli and Lidietta Giorno

Institute of Membrane Technology, ITM-CNR, University of Calabria, Rende (CS), Italy

Volume 1

BASIC ASPECTS OF MEMBRANE SCIENCE AND ENGINEERING

AMSTERDAM • BOSTON • HEIDELBERG • LONDON • NEW YORK • OXFORD
PARIS • SAN DIEGO • SAN FRANCISCO • SINGAPORE • SYDNEY • TOKYO
Academic Press is an imprint of Elsevier

Elsevier
The Boulevard, Langford Lane, Kidlington OX5 1GB, United Kingdom

First edition 2010

British Library Cataloging in Publication Data
A catalog record for this book is available from the British Library

Library of Congress Control Number
A catalog record for this book is available from the Library of Congress

ISBN: 978-0-444-53204-6

For information on all Elsevier publications
visit our website at elsevierdirect.com

Printed and bound in Italy

09 10 11 12 10 9 8 7 6 5 4 3 2 1

Contents of Volume 1

Contributors to Volume 1

P. Aimar
Université de Toulouse, Toulouse, France, CNRS, Toulouse, France

P. M. Ajayan
Rice University, Houston, TX, USA

V. Arcella
Solvay Solexis, Bollate (MI), Italy

M. Avataneo
Solvay Solexis, Bollate (MI), Italy

D. Bhattacharyya
University of Kentucky, Lexington, KY, USA

A. Buekenhoudt
Flemish Institute for Technological Research (VITO), Mol, Belgium

V. N. Burganos
Institute of Chemical Engineering and High Temperature Chemical Processes, Foundation for Research and Technology-Hellas, Patras, Greece

S. Cardea
University of Salerno, Fisciano, Italy

C. Causserand
Université de Toulouse, Toulouse, France, CNRS, Toulouse, France

E. Drioli
Institute of Membrane Technology, ITM-CNR, University of Calabria, Rende (CS), Italy

J. Durand
Université Montpellier, Montpellier, France

A. Ghielmi
Solvay Solexis, Bollate (MI), Italy

L. Giorno
Institute of Membrane Technology, ITM-CNR, University of Calabria, Rende (CS), Italy

N. Hilal
Swansea University, Swansea, UK

A. M. Hollman
University of Kentucky, Lexington, KY, USA

A. F. Ismail
Universiti Teknologi Malaysia, Johor, Malaysia

D. Johnson
Swansea University, Swansea, UK

A. Kovalevsky
Flemish Institute for Technological Research (VITO), Mol, Belgium

A. R. Ladhe
University of Kentucky, Lexington, KY, USA

K. Li
Imperial College London, London, UK

Ir. J. Luyten
Flemish Institute for Technological Research (VITO), Mol, Belgium

M. Majumder
Monash University, Clayton, VIC, Australia

G. Marchionni
Solvay Solexis, Bollate (MI), Italy

R. Mazzei
Institute of Membrane Technology, ITM-CNR, University of Calabria, Rende (CS), Italy

S. P. Nunes
King Abdullah University of Science and Technology, Thuwal, Saudi Arabia

D. R. Paul
University of Texas at Austin, Austin, TX, USA

K.-V. Peinemann
King Abdullah University of Science and Technology, Thuwal, Saudi Arabia

E. Reverchon
University of Salerno, Fisciano, Italy

S. Roualdes
Université Montpellier, Montpellier, France

V. Rouessac
Université Montpellier, Montpellier, France

V. Smuleac
University of Kentucky, Lexington, KY, USA

F. Snijkers
Flemish Institute for Technological Research (VITO), Mol, Belgium

H. Strathmann
Universitat Stuttgart, Stuttgart, Germany

P. Toniolo
Solvay Solexis, Bollate (MI), Italy

J. Xu
University of Kentucky, Lexington, KY, USA

Y. Yampolskii
A. V. Topchiev Institute of Petrochemical Synthesis, Moscow, Russia

Contents of All Volumes

Introduction

The last century has been characterized by a huge resource-intensive industrial development, particularly in some Asian countries, spurred by the growth in the global population level, by a significant elongation of life expectation, and by an overall increase in the standards characterizing the quality of life. These positive aspects of our recent history have been combined however with the emergence of related problems such as water stress, the environmental pollution, and the increase of CO_2 emissions into the atmosphere. These negative aspects of the transformations which have been characterizing our recent progress have been very much related to the momentum at which transformations themselves occurred and to the lack of innovations and introduction of new strategies capable of both controlling and minimizing the relatively obvious negative aspects of industrial development worldwide. A clear example is represented by the wastewater treatment strategy. As illustrated in **Figure 1**, from 1556 until today, the same concept is basically present in various wastewater-treatment systems.

The need to achieve a knowledge-intensive industrial development is nowadays well recognized. This will permit the transition from an industrial system based on quantity to one based on quality. Human capital is increasingly becoming the driving force behind this socio-economical transformation. The challenge of sustainable growth relies on the use of advanced technologies. Membrane technologies are in many fields already recognized as amongst the best-available technologies (BATs) able to contribute to this process (**Figure 2**).

Process engineering is one of the disciplines most involved in the technological innovations necessary to face the new problems characterizing the world today and in the future as well. Recently, the logic of process intensification has been suggested as the best process engineering answer to the situation. It consists of innovative equipment, design, and process development methods that are expected to bring substantial improvements in chemical and any other manufacturing and processing, such as decreasing production costs, equipment size, energy consumption, and waste generation, and improving remote control, information fluxes, and process flexibility (**Figure 3**).

How to implement this strategy is, however, not obvious. An interesting and important case is the continuous growth of modern membrane engineering whose basic aspects satisfy the requirements of process intensification. Membrane operations, with their intrinsic characteristics of efficiency and operational simplicity, high selectivity and permeability for the transport of specific components, compatibility between different membrane operations in integrated systems, low energetic requirement, good stability under operating conditions and environmental compatibility, easy control and scale-up, and large operational flexibility, represent an interesting answer for the rationalization of chemical and any other industrial productions. Many membrane operations are practically based on the same hardware (materials), only differing in their software (methods). The traditional membrane separation operations (reverse osmosis (RO), microfiltration (MF), ultrafiltration (UF), and nanofiltration (NF), electrodialysis, pervaporation, etc.), already largely used in many different applications, are today conducted with new membrane systems such as catalytic membrane reactors and membrane contactors. At present, redesigning important industrial production cycles by combining various membrane operations suitable for separation and conversion units, thus realizing highly integrated membrane processes, is an attractive opportunity because of the synergic effects that can be attained.

In various fields, membrane operations are already dominant technologies. Interesting examples are in seawater desalination (**Figure 4**); in wastewater treatment and reuse (**Figure 5**); and in artificial organs (**Figure 6**).

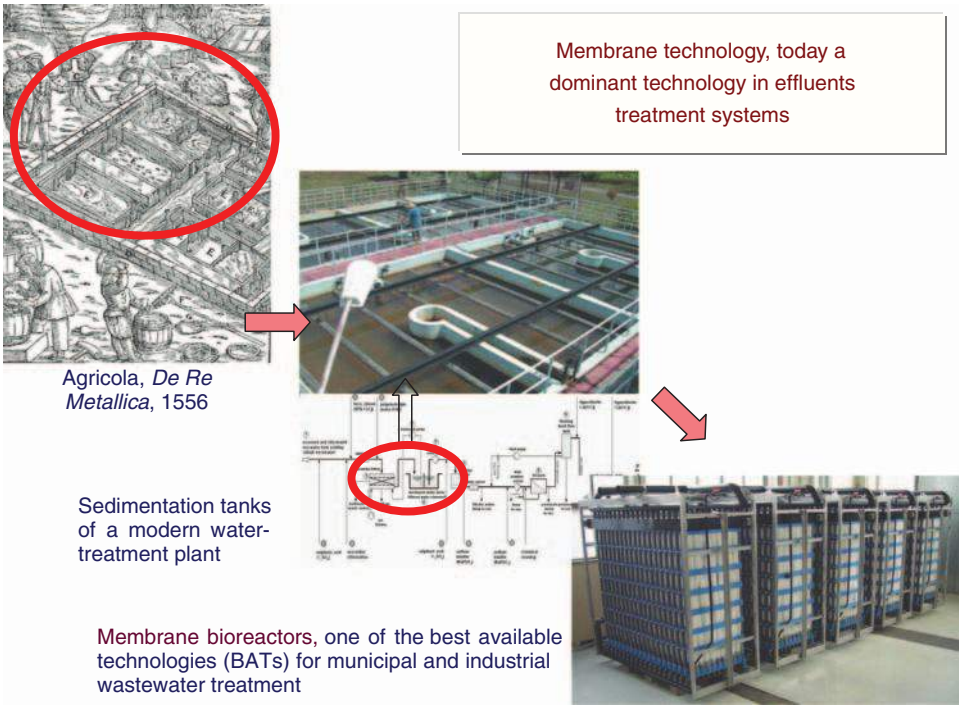

Figure 1 Wastewater-treatment technological approach in the past and today.

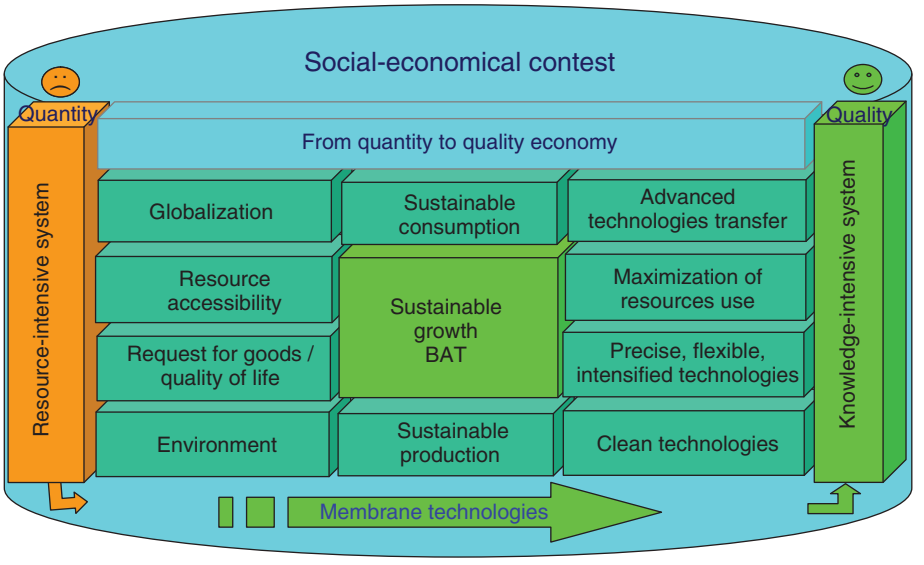

Figure 2 Current social-economical and technological contest driving the transition towards a knowledge-intensive system to guarantee sustainable growth.

It is interesting to consider that a large part of the membrane operations realized today at the industrial level has been in existence in the biological system and in nature ever since life came into being. A major part of biological systems is, in fact, well represented by membranes which operate molecular separations, chemical transformation, molecular recognition, energy, mass and information transfer, etc. (**Figure 7**).

Some of these functions have been transferred at the industrial level with success. We are, however, far away from being able to reproduce the complexity and efficiency of the biological membranes, to integrate the

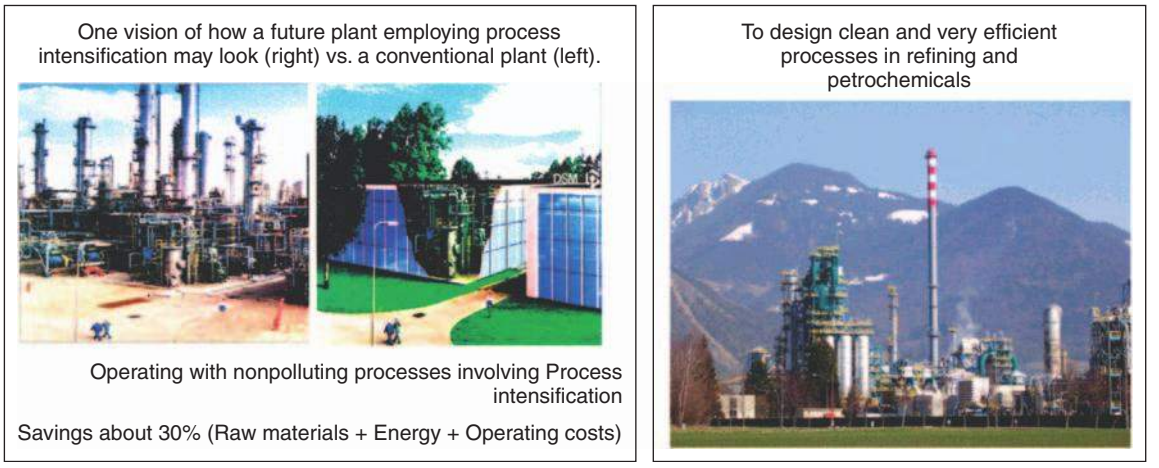

Figure 3 Process intensification strategy. Reproduced from Jean-Claude Charpentier, Modern Chemical Engineering in the Framework of Globalization, Sustainability, and Technical Innovation, Ind. Eng. Chem. Res., Vol. 46, No. 11, 2007.

Figure 4 Membrane desalination plant. RO membrane units from El Paso Desalintion Plant, Texas: the site of the word's largest inland desalination plant (104 000 $m^3\ d^{-1}$). Production costs for water are less than less than 0.36 \$ m^{-3}. From http://www.epwu.org/167080115.

various functionalities, the capability to repair damage, and to maintain for a very long time their specific activities, avoiding fouling problems, degradation of the various functions, and keeping the system alive. Therefore, future generations of membrane scientists and engineers will have to address their attention to understanding and reproducing the astonishing natural systems, which are at the basis of the life with which we are familiar.

In *Comprehensive Membrane Science and Engineering*, we have tried to present and discuss the most relevant results of membrane science and engineering reached during the last years.

Authors from all around the world, senior scientists, and PhD students have contributed to the four volumes covering fundamental aspects of membrane preparations and characterization, their applications in various unit

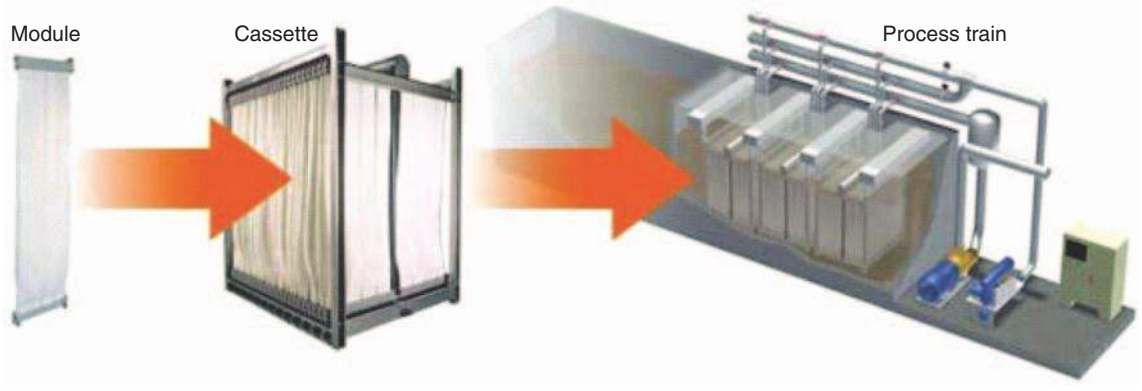

Figure 5 Submerged membrane module for wastewater treatment. From ZeeWeed® Submerged Membrane System, from http://www.gewater.com.

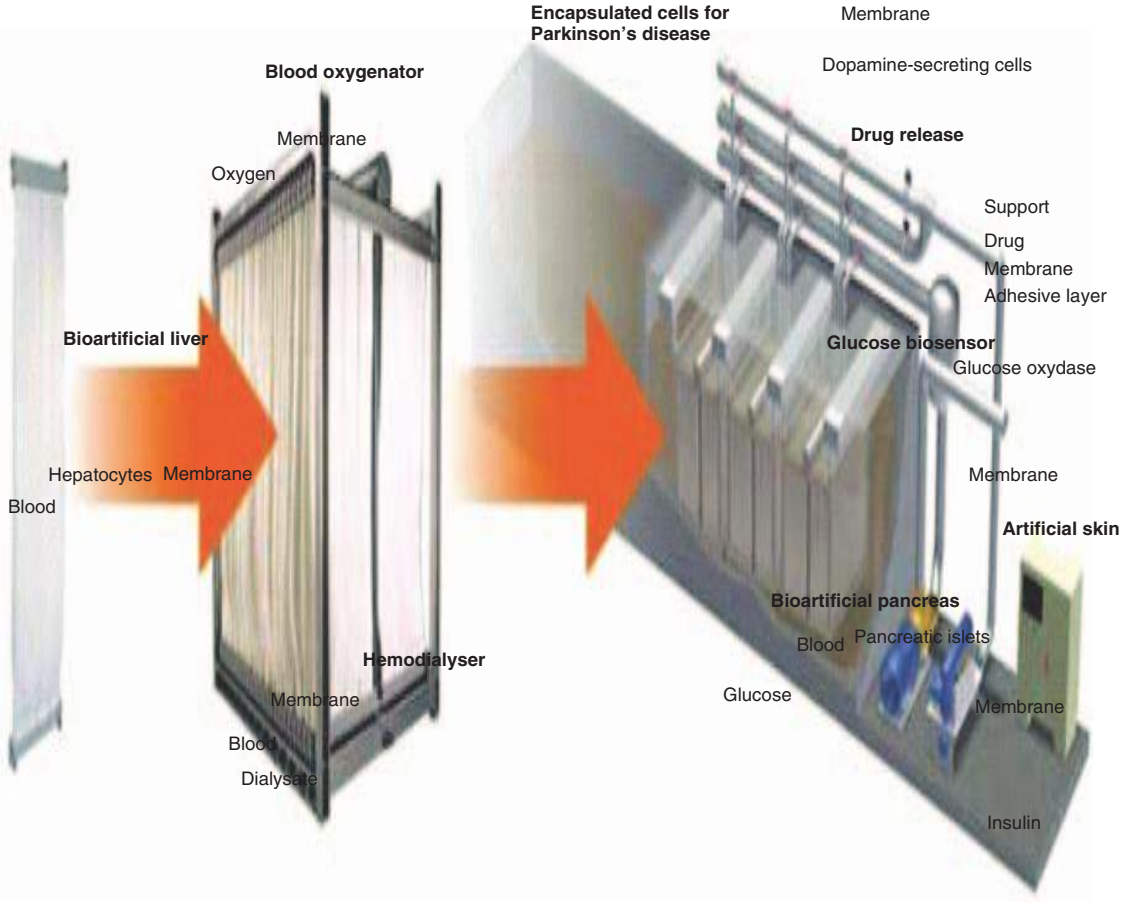

Figure 6 Membranes and membrane devices in biomedical applications. Modified from L. De Bartolo e E. Drioli. "Membranes in artificial organs" In Biomedical and Health Research vol. 16: New Biomedical Materials – Basic and Applied Studies Haris, P.I. and Chapman, D. (Eds.) IOS Press: Amsterdam/Berlin/Tokjo/Washington, (1998) pp. 167–181.

operations, from molecular separation to chemical transformations in membrane reactors, to the optimization of mass and energy transfer in membrane contactors. Their application in strategic fields, including energy, environment, biomedical, biotechnology, agro-food, and chemical manufacturing, has been highlighted.

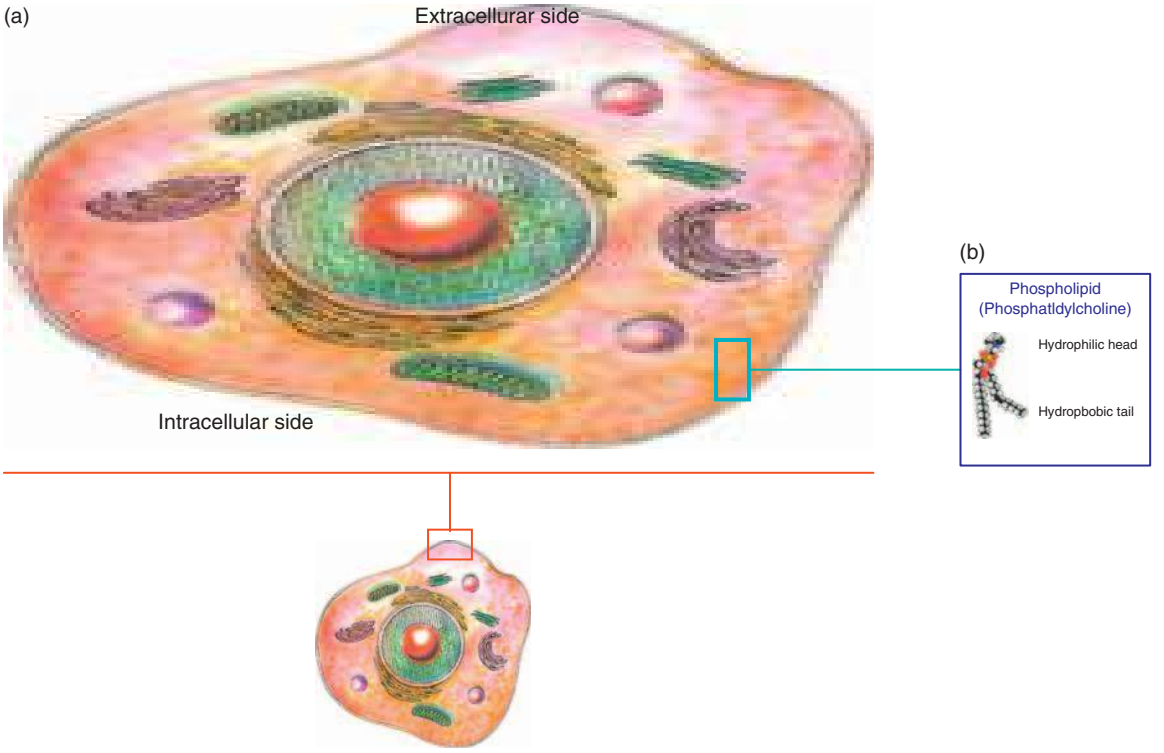

Figure 7 Biological membrane functions. From http://www.mcgraw-hill.it/.

Today, the possibility of redesigning a significant number of membrane operations, introduced via industrial production, is becoming more and more attractive and realistic.

Strong efforts are however necessary for spreading the available knowledge in membrane engineering to the public and for educating the younger generations more and more in the fundamentals and applications of these creative, dynamic, and important disciplines.

With this text we have tried to contribute to these efforts.

In Volume 1, fundamental aspects of the transport phenomena, which characterize permeability and selectivity in molecular separations based on polymeric, inorganic, and mixed-matrix membranes are discussed together with the basic principles for their preparation in various possible configurations (flat sheets, tubular fiber, microcapsules, etc.). The basic methodology generally utilized for their characterization is also discussed.

In Volume 2, the most relevant membrane operations such as the pressure-driven systems in liquid phase (MF, UF, NF, and RO) and in gas phase (gas separation and vapor permeation) together with other separation processes, such as dialysis, pervaporation, and electrochemical membrane systems, are analyzed and discussed in their basic principles and applications.

In Volume 3, the recent interest in the combination of molecular separations with chemical transformations largely present in biological systems is presented. It is important to recall that the industrial development of these membrane reactors and catalytic membrane systems is not yet at the level of the more well-known pressure-driven processes. However, the expectation of a significant fast growth of membrane reactors and membrane bioreactors is very significant. Interesting success, in fact, can already be indicated by the recognition of the submerged membrane reactors such as BAT in municipal wastewater treatment and reuse. The potentialities of this system in the area of bioengineering and biomedical applications are also very attractive, where bioartificial organs, such as bioartificial liver and pancreas, are in some case already at clinical trial level.

Volume 4 is addressed to the description of relatively new membrane operations, where membranes are not required to be selective. Their role is the optimization of the best mass and energy transfer between different phases, acting as membrane contactors. Membrane distillation, membrane crystallizers, membrane emulsifiers,

membrane strippers, and membrane scrubbers are typical examples of these important new unit operations in modern process engineering. New materials, for example, highly hydrophobic and nanostructured, and new complex configurations, will be developed for further exploitation of these systems.

The combination of all the different membrane operations described in the previous books in a single industrial productive cycle may permit the design of totally innovative industrial transformation, and integrated membrane operations where a process engineer could utilize the potentialities of the artificial membrane systems to realize a sustainable industrial development in the logic of the process intensification strategy.

It is also important to recall that not only the industrial world will benefit from this approach, but also the design of hybrid artificial organs and the development, in general, of regenerative medicine might benefit from the same strategy.

Acknowledgments

It has been really interesting and a pleasure working for these last two years for the preparation of the four volumes of *Comprehensive Membrane Science and Engineering*. We have been interacting and discussing with a large number of colleagues in reaching our objectives and we wish to thank all of them for the effective collaboration we have received.

We specially acknowledge our young colleague Dr. Enrica Fontananova, who has been helping from the beginning to coordinate our work, keeping in contact with all the contributors. Her excellent knowledge and experience of membrane science and membrane engineering has been quite necessary and fruitful in carrying out her work.

We hope these four volumes will help a large number of researchers, engineers, and technical people to increase their knowledge and interest in membranology.

Enrico Drioli and Lidietta Giorno

1.01 Biological Membranes and Biomimetic Artificial Membranes

L Giorno, R Mazzei, and E Drioli, Institute of Membrane Technology, ITM-CNR, University of Calabria, Rende (CS), Italy

Glossary

Aquaporin Protein system that permits the passage of water through the biological membrane.
Bioartificial synthetic membrane Artificial membrane system that simulates biological membrane.
Biological membrane A complex multifunctional and dynamically structured multicomponent system acting as an enclosing or separating barrier within or around a cell.
Biomembrane Biological membrane.
Biomimetic membrane system Artificial membrane system that biomimics biological membrane.
Integral protein Structural protein of biological membrane.
Phytoalexins Substances used from vegetal cells synthesized in response to pathogen attack.
Phytoanticipin Preformed substances, contained in vegetal cells used for defense against pathogens.

1.01.1 Introduction

The key feature that distinguishes a biological membrane from an artificial membrane is that the biological membrane is extremely selective, precise, and efficient in terms of: recognition properties; regulation of passage of diverse atoms and molecules having diverse physical and chemical properties; signaling and information transmission; response to external physical, chemical, and biochemical stimuli; and self-regulating, self-healing, and self-cleaning properties.

The biological membrane is able to recognize what the cell needs for its survival and accordingly promote the exchange of matter, information, and energy. The cell membrane is able to recognize harmful components and block their passage into the cell or even capture and eliminate them. The cell membrane performs these actions dynamically with the capacity to adapt to new events.

On the other hand, biological membranes would not be able to satisfy industrial production requirements in terms of mechanical stability and productivity, which must be much higher than the ones biomembranes can usually afford. On the contrary, artificial membranes can guarantee sustainable productivity and mechanical stability. In fact, unlike most biological membranes, artificial polymer membranes are very stable and can withstand considerable pressure, essential requirements for practical use, such as industrial production, water purification, and desalination processes. The challenges of man-made membranes are to achieve selective, recognition, and response properties similar to the ones biological membranes can exhibit while maintaining much higher mechanical and production properties.

The biological membrane has evolved through eons and, according to the evolution theory, it represents the most suitable system which adapted to the environment boundary conditions. It can be considered then, basically as the selected result of a long trial-and-error process, which most probably started with much simpler molecules and systems and evolved into the membranes we know today. The ambition is that by a rational approach, one may

dare to design and achieve such or better performance and even faster! The challenge is to know how. A holistic systems membrane engineering approach may represent an integrative strategy to advance the current knowledge achieved in the field.

It is worth considering that unlike biological membranes, which are formed on the basis of a very accurate and regulated bottom-up process (able to also correct eventually mistakes that occurred), artificial membranes have been initially developed by very far approach. Nowadays, bottom-up methodologies are being developed, including self-assembling of functional molecules. Still, most industrial applications rely on traditional polymer membranes. However, the advances in knowledge about individual element properties, their resulting functions when assembled in a complex system, as well as about how to prepare complex systems, will aid to move toward biomimetic artificial membranes with advanced efficiency. The term 'biomimetic' is used in the general sense of achieving performance, functions that mimic the biological ones (this can be achieved with the use of biological tools as well as with artificial tools used separately or as integrated hybrid systems).

1.01.2 Biological Membrane

A biological membrane or biomembrane is a complex multifunctional and dynamically structured multicomponent system acting as an enclosing or separating barrier within or around a cell (**Figure 1**). Such a barrier is a selectively permeable structure finely controlling the transport of substances in and out of it, needed for cell survival. The size, the charge, and other chemical properties of atoms and molecules will determine whether they will pass through it. Selective permeability is the essential key feature for effective separation of a cell or organelles from its surrounding. Biological membranes also have certain mechanical and elastic properties. If a particle is too large or otherwise unable to cross the membrane, but it is still needed by the cell, it could either go through one of the protein channels or be taken in by means of endocytosis..

The cell membrane contains a wide variety of biological molecules, primarily proteins and lipids, which are involved in a variety of cellular processes such as cell adhesion, ion channel conductance, cell signaling, and cell signal transduction.

The biological membrane also serves as the attachment point for the intracellular skeleton and,

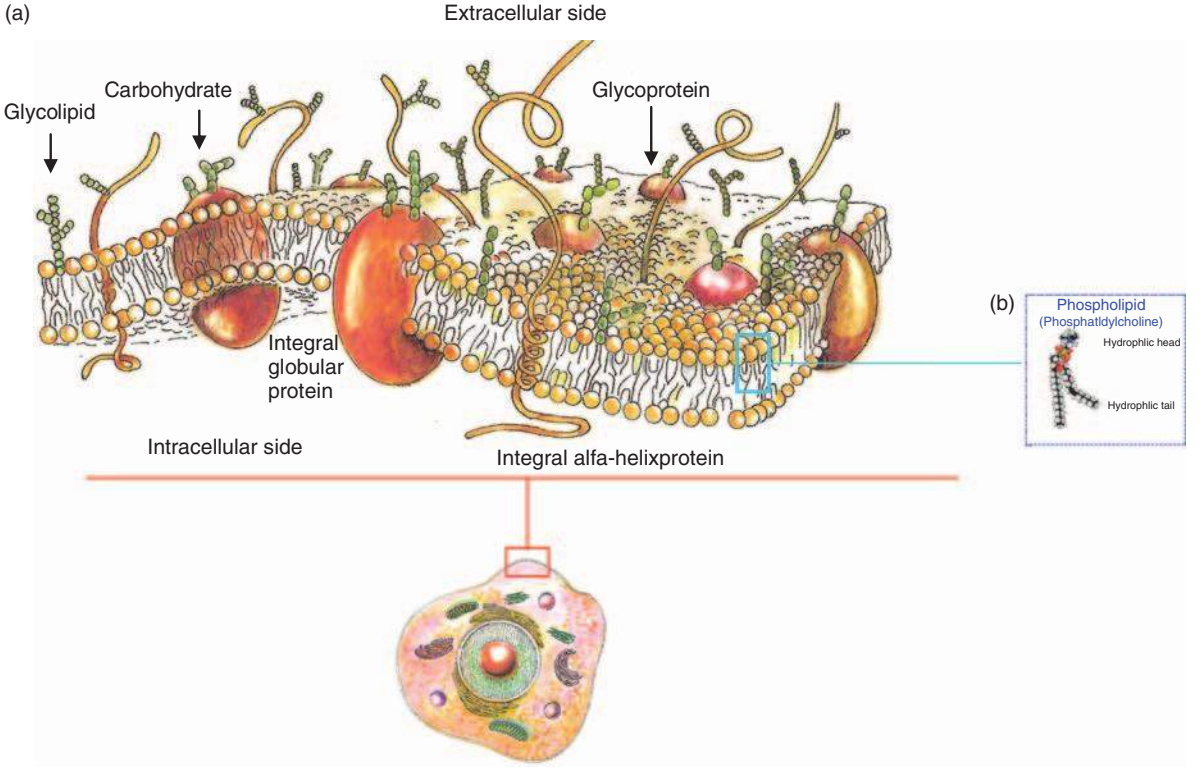

Figure 1 Biological membrane.

if present, the extracellular cell wall (such as in fungi, some bacteria, and plants).

The cell membrane is an amphipathic layer, composed by a double layer of lipid molecules (usually phospholipids) and proteins (**Figure 1(a)**). Amphipathic phospholipids (**Figure 1(b)**) spontaneously arrange so that the hydrophobic tail regions are shielded from the surrounding polar fluid, causing the more hydrophilic head regions to associate with the cytosolic and extracellular faces of the resulting bilayer. This is considered as a two-dimensional (2D) fluid phase (fluid mosaic model) where lipid and protein molecules composing it can move with a certain degree of freedom in the 2D plane (**Figure 1(a)**) [1]. This continuous lipid bilayer contains embedded specific proteins and various structures or domains, including integrins, cadherins, clathrin-coated pits, caveolaes, protein–protein complexes, lipid rafts, pickets, and fences formed by actin-based cytoskeleton, and large stable structures such as synapses or desmosomes. These proteins and structures afford the cell membrane the capability to execute a large variety of specific transactions and functions.

The cell membrane consists of three classes of amphipathic lipids: phospholipids, glycolipids, and steroids. The amount of each depends upon the type of cell, but, in general, phospholipids are the most abundant. Examples of the major membrane phospholipids include phosphatidylcholine (PtdCho) **1**, phosphatidylethanolamine (PtdEtn) **2**, phosphatidylinositol (PtdIns) **3**, and phosphatidylserine (PtdSer) **4**.

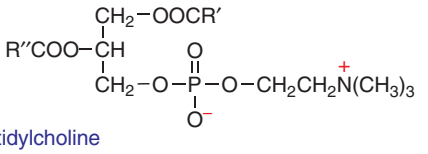

Phosphatidylcholine

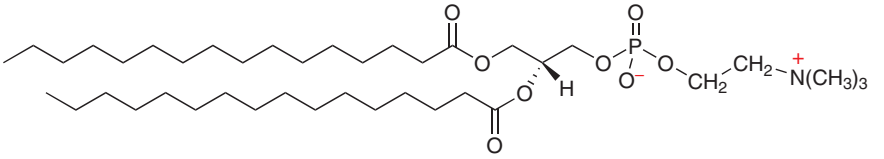

1,2-Dihexadecanoyl-*sn*-glycero-3-phosphocholine

1

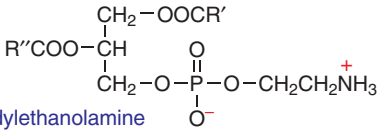

Phosphatidylethanolamine

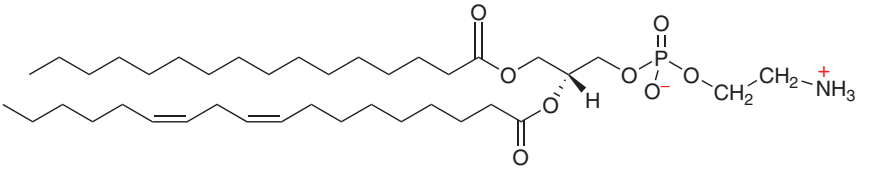

1-Hexadecanoyl, 2-(9Z,12Z-octadecadienoyl)-*sn*-glycero-3-phosphoethanolamine

2

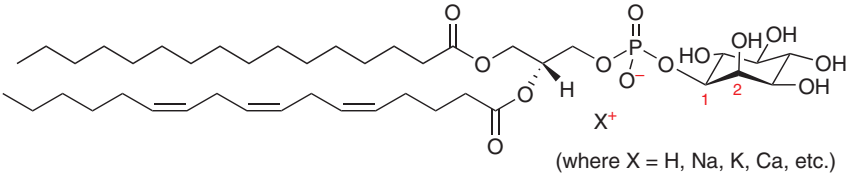

(where X = H, Na, K, Ca, etc.)

1-Octadecanoyl, 2-(5Z,8Z,11Z,14Z-elcosatetraenoyl)-*sn*-glycero-3-phospho-(1'-*myo*-inositol)

3

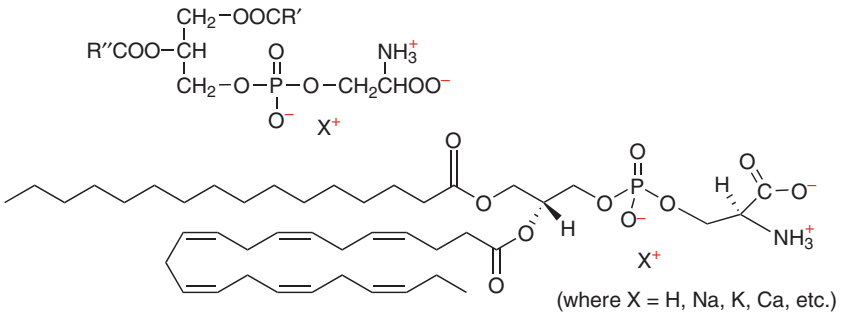

1-Octadecanoyl, 2-(4Z,7Z,10Z,13Z,16Z,19Z-docosahexaenoyl)-*sn*-glycero-3-phosphoserine

4

The fatty chains in phospholipids and glycolipids usually contain between 16 and 20 carbon atoms. The 16- and 18-carbon fatty acids are the most common. Fatty acids may be saturated or unsaturated, with the configuration of the double bonds nearly always *cis*. The length and the degree of unsaturation of fatty acid chains have important effect on membranes fluidity, as unsaturated lipids prevent the fatty acids from packing together tightly, thus increasing the fluidity of the membrane. The ability of some organisms to regulate the fluidity of their cell membranes by altering lipid composition is called homeoviscous adaptation. The entire membrane is held together via noncovalent interaction of hydrophobic tails. Under physiological conditions, phospholipid molecules in the cell membrane are in the liquid crystalline state. It means the lipid molecules are free to diffuse and exhibit rapid lateral diffusion along the layer in which they are present. However, the exchange of phospholipid molecules between intracellular and extracellular leaflets of the bilayer is a controlled process.

Plasma membranes also contain carbohydrates, predominantly glycoproteins, but with some glycolipids (cerebrosides and gangliosides). For the most part, no glycosylation occurs on membranes within the cell; rather, generally glycosylation occurs on the extracellular surface of the plasma membrane [2–4].

The glycocalyx is an important feature in all cells, especially epithelia with microvilli. Recent data suggest the glycocalyx participates in cell adhesion, lymphocyte homing, and in many others functions.

The penultimate sugar is galactose and the terminal sugar is sialic acid, as the sugar backbone is modified in the Golgi apparatus. Sialic acid derivatives, such as NANA or *N*-acetyl-neuraminic acid, carry negative charge, providing an external barrier to charged moieties. Sialic acids are found mostly in glycoproteins and gangliosides, important integral membrane proteins that play a role in cell–cell interactions.

Proteins in the cell membrane can be integral or peripheral (**Figure 1(b)**). Integral proteins span the entire membrane thickness; are constituted of a hydrophilic cytosolic domain, which interacts with internal molecules; a hydrophobic membrane-spanning domain consisting of one, multiple, or a combination of α-helices and β-sheet protein motifs – this domain anchors the protein within the cell membrane; and a hydrophilic extracellular domain that interacts with external molecules. They function as ion channels, proton pumps, and G-protein-coupled receptors. Peripheral proteins are present on only one side of the membrane. They are attached to integral membrane proteins, or associated with peripheral regions of the lipid bilayer. These proteins tend to have only temporary interactions with biological membranes, and, once having reacted, the molecules dissociate to carry out their role in the cytoplasm. They function as enzymes and hormones.

Lipid-anchored proteins that function as G proteins are covalently bound to single or multiple lipid molecules, hydrophobically insert into the cell membrane, and anchor the protein. The proteins themselves are not in contact with the membrane.

The amount of protein differs between species and according to function, however, the typical amount in a cell membrane is 50%. The cell membrane, being exposed to the outside environment, is an important site of cell–cell communication. Therefore, a large variety of protein receptors and identification

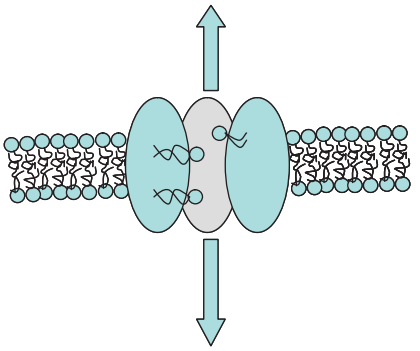

Figure 2 Scramblases.

proteins, such as antigens, are present on the surface of the membrane. Functions of membrane proteins can also include cell–cell contact, surface recognition, cytoskeleton contact, signaling, enzymatic activity, or transporting substances across the membrane.

The arrangement of hydrophilic polar heads and hydrophobic nonpolar tails of the lipid bilayer prevents polar solutes such as amino acids, nucleic acids, carbohydrates, proteins, and ions from diffusing across the membrane, but generally allows for passive diffusion of hydrophobic molecules. This affords the membrane the ability to control the transport of the polar substances via transmembrane protein complexes such as pores and gates. Membrane proteins working as transmembrane lipid transporter, such as flippases, permit the movement of phospholipid molecules between the two leaflets that compose the cell membrane (**Figure 2**).

As mentioned, membranes serve diverse functions in eukaryotic and prokaryotic cells. One of the most important roles is to regulate the movement of materials into and out of cells. The phospholipid bilayer structure with specific membrane proteins accounts for selective permeability and passive and active transport mechanisms. In addition, membranes in prokaryotes and in the mitochondria and chloroplast of eukaryotes facilitate the synthesis of adenosine triphosphate (ATP) through chemiosmosis.

When substances move across a membrane toward either chemical or electrical equilibrium, the movement typically requires no net input of energy. Passive transports, such as simple diffusion via gradients and facilitated diffusion via carriers, are instances of such movement (**Figure 3**).

Water crosses cell membranes by facilitated diffusion through the lipid bilayer, through water channel proteins called aquaporins (**Figure 4**). The presence of pores or channels in cell

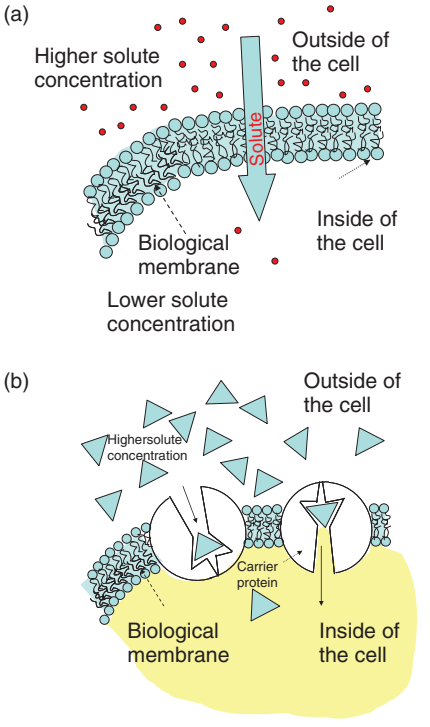

Figure 3 Passive transport: (a) simple diffusion via gradient (concentration); (b) facilitate diffusion via carrier (integral protein).

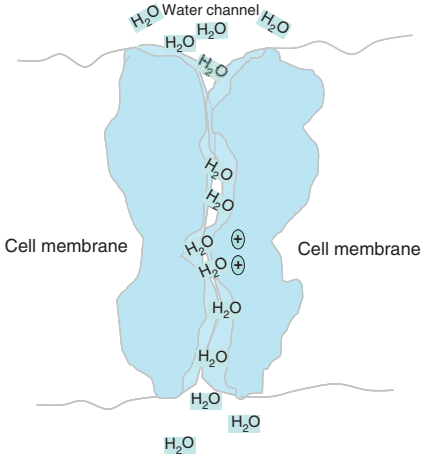

Figure 4 Aquaporin water channel facilitating passive transport of water.

membranes to permit a flow of water was thought to be because the osmotic permeability of some epithelial cells was much too large to be accounted for by simple diffusion through the plasma membrane. Aquaporins form tetramers in the cell membrane, which facilitate the transport

of water and, in some cases, other small solutes, such as glycerol. However, selectivity is a central property of such water pores, which are completely impermeable to charged species, such as hydronium ions, $H3O^+$, which are stopped on the way and rejected because of their positive charges. This is critical for the conservation of membrane's electrochemical potential.

Cells cannot rely solely on passive movement of substances across their membranes. In many instances, it is necessary to move substances against their electrical or chemical gradient to maintain the appropriate concentrations inside of the cell or organelle. Moving substances against their gradient requires energy, because they are being moved away from equilibrium. Cells use two different types of active transport, which directly or indirectly require chemical energy, such as from ATP, **5**, to move substances in this way.

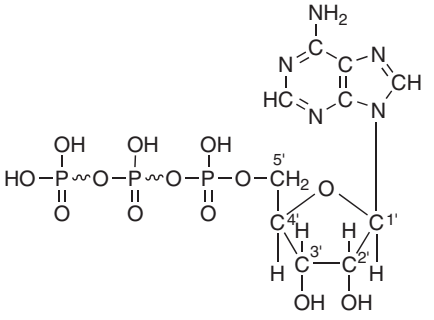

5

When the third phosphate group of ATP is removed by hydrolysis, a substantial amount of free energy is released (~7.3 kcal mol). The same can be said for the hydrolysis of the second phosphate of ADP. Actually, these weak bonds, with low bond energies, are able to release high amount of energy.

If the process uses directly ATP, it is termed primary active transport. If the transport also involves the use of an electrochemical gradient, it is termed secondary active transport. Both types of active transport require integral membrane proteins.

In the primary active transport, the molecule or ions binds to the carrier site; the binding promotes ATP hydrolysis; this causes carrier conformation change that moves molecule to the other side of the membrane. The sodium–potassium pump is an example of primary active transport, where energy

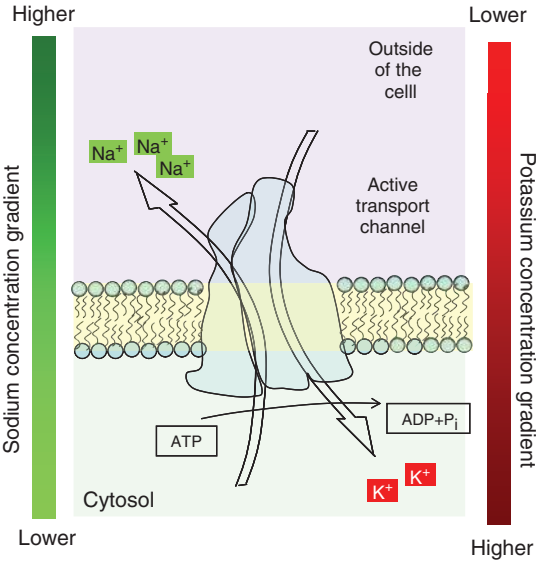

Figure 5 Scheme sodium–potassium pump, an example of active primary transport.

from hydrolysis of ATP is directly coupled to the movement of a specific substance across a membrane independent of any other species (**Figure 5**).

Secondary active transport uses the downhill flow of an ion to pump some other molecule or ion against its gradient. The driving ion is usually sodium (Na^+) with its gradient established by the Na^+/K^+ ATPase [4].

Sometimes, substances are cotransported in the same direction (symport). Example of this active indirect transport is the Na+/glucose pump. The Na^+/glucose transporter is the transmembrane protein that allows sodium ions and glucose to enter the cell together. The sodium ions flow down their concentration gradient while the glucose molecules are pumped up theirs. Later, the sodium is pumped back out of the cell by the Na^+/K^+ ATPase.

When one substance is transported in one direction at the same time as another substance is being transported in the other direction (countertransport), the transport is called antiport.

Cells must occasionally move very large particles, such as food particles or volumes of water, across their membranes. Cells do this by processes called endocytosis and exocytosis (bulk transport), where the substance to be transported is surrounded by an infolding of the cell membrane (**Figure 6**).

Specific proteins embedded in the cell membrane can act as molecular signals that allow cells to communicate with each other. Protein receptors are found ubiquitously and function to receive signals

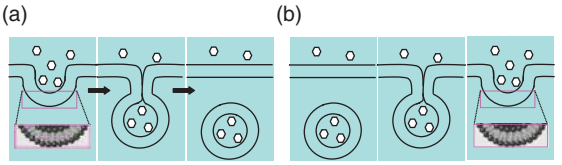

Figure 6 Bulk transport: (a) endocytosis; (b) exocytosis.

from both the environment and other cells. These signals are transduced and passed in a different form in the cell. For example, a hormone binding to a receptor may open an ion channel in the receptor and allow calcium ions to flow into the cell. Other proteins on the surface of the cell membrane serve as markers that identify a cell to other cells. The interaction of these markers with their respective receptors forms the basis of cell–cell interaction in the immune system.

The cell membrane also plays a role in anchoring the cytoskeleton to provide shape to the cell and in attaching to the extracellular matrix to help group cells together in the formation of tissues.

The cytoskeleton underlying the cell membrane in the cytoplasm provides a scaffolding for membrane proteins to anchor to, besides forming organelles that extend from the cell. Indeed, cytoskeletal elements interact extensively and intimately with the cell membrane. Anchoring proteins restricts them to a particular cell surface – for example, the apical surface of epithelial cells that line the vertebrate gut – and limits how far they may diffuse within the bilayer. The cytoskeleton is able to form appendage-like organelles, such as cilia, which are microtubule-based extensions covered by the cell membrane, and filopodia, which are actin-based extensions. These extensions are unsheathed in the membrane and project from the surface of the cell in order to sense the external environment and/or make contact with the substrate or other cells. The apical surfaces of epithelial cells are dense with actin-based finger-like projections known as microvilli, which increase cell surface area and thereby increase the rate of absorption of nutrients.

1.01.2.1 Examples of *In Vivo* Systems Compartimentalization

Living cells are divided into several compartments by a membrane unit. Each compartment has a specific structure and function and the interactions between compartments are regulated by specific signals. One important example of compartimentalization regulated by stimuli-responsive action is the defense against pathogens in plants.

The defense mechanism of plants is different in comparison to animals due to the fact that plants are sessile organisms that cannot flee their predators.

Through the course of evolution, plants have become nature's organic chemists par excellence, and collectively synthesize a plethora of secondary metabolites to defend themselves against herbivores and microorganisms and adapt to different types of abiotic environmental stresses.

The compounds used for defense are divided into two main categories: phytoanticipins and phytoalexins. Phytoanticipins are preformed substances and represent the first barrier to pathogens, while phytoalexins are synthesized in response to pathogen attack.

Many compounds used in plant defense are stored in a nonactive glucosylated form to chemically stabilize and increase the solubility of the defense compound, to render it suitable for storage in the vacuole, and to protect the plant from the toxic effects of its own defense system [5].

Upon cell disruption, caused, for example, by a chewing insect, the defense compounds are bioactivated via hydrolysis of the glucosidic linkage catalyzed by β-glucosidases. In intact plant tissue, the β-glucosidases are stored separately from the substrates (**Figure 7**).

This two-component system, of which each of the individual components is chemically inert, provides plants with an immediate chemical defense against attacking herbivores and pathogens. The catalytic mechanism of β-glucosidase is illustrated in **Figure 8**.

Two conserved glutamic acid residues serve as a catalytic nucleophile and a general acid/base catalyst, respectively. In retaining β-glucosidases, the catalytic glutamic acid residues are situated on opposite sides of the β-glucosidic bond of the docked substrate at a distance of 5.5 Å [6]. As the initial step in catalysis, the nucleophile performs a nucleophilic attack at the anomeric carbon, which results in the formation of a glucose–enzyme intermediate. In this process, aglicone departure is facilitated by protonation of the glucosidic oxygen by the acid catalyst. During the second catalytic step (deglucosylation), a water molecule is activated by the catalytic base to serve as a nucleophile for hydrolysis of the glucosidic bond and release of the glucose. Under suitable conditions, β-

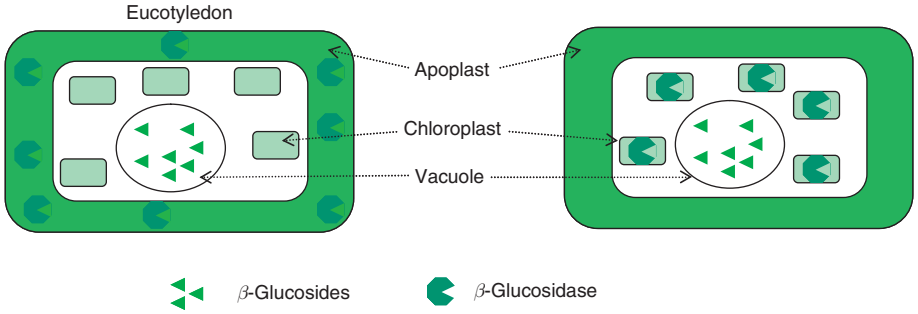

Figure 7 Schematic representation of the different compartmentalization of β-glucosidase and β-glucosides. From Morant, A.V., Jørgensen, K., Jørgensen, C., *et al*. *Phytochemistry* **2008**, *69*, 1795–1813.

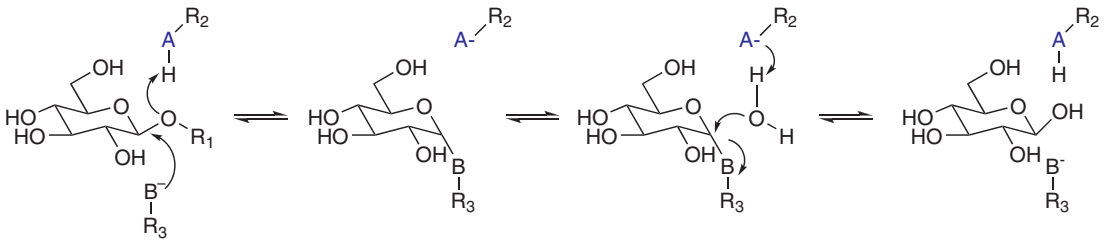

Figure 8 Schematic representation of catalytic action of β-glucosidase. From Morant, A.V. , Jørgensen, K., Jørgensen, C., *et al*. *Phytochemistry* **2008**, *69*, 1795–1813.

glucosidases can perform a transglucosylation in which the covalently bound glucose in the enzyme–glucose intermediate is transferred to an alcohol or a second sugar group. The biological activity of the defense compounds is attributed to their hydrolysis products, and therefore separation of glucosides and β-glucosidases into different (sub)cellular compartments in intact tissue is a critical feature of the two-component defense systems. As illustrated in **Figure 7**, the glucosides are stored in the vacuole [7] while the subcellular localization of the generally abundantly expressed β-glucosidases differs in monocotyledonous and eudicotyledenous plants. In some plants, the substrate and the bioactivator are additionally separated at the cellular level.

The separate compartmentalization provides the plant with a two-component defense system, in which each separate component is chemically inert. Upon tissue disruption, the glucosides come into contact with the degrading β-glucosidases resulting in an immediate release of toxic defense compounds. Often, the highest amount of the two components is found in seedlings and young plant parts in order to protect the plant from herbivore and pathogen attack at this fragile stage.

1.01.2.2 *In Vitro* Membrane Processes that Simulate *In Vivo* Systems

The ambition to mimic efficiency of biological membranes and create membrane-based separation and production systems/devices is among the visions and challenges of current technological development. In the development of biomimetic separation/transformation/sensor technology, individual elements, such as channels (ion and water channels), carriers (transporters), and so on and overall complex organization/function system are important aspects to be considered. The first aspect gives information on the individual blocks that contribute to the creation of high permselectivity. The second aspect provides information on how they are integrated in the whole system to achieve and maintain the given properties.

Generally, each class of transport proteins promotes the passage of specific molecular species in and out of the cell while preventing the passage of other components, a property critical for the overall conservation of the cell's internal physical-chemical environment and composition. As previously mentioned, aquaporin water channels are highly efficient

membrane pore proteins capable of transporting water molecules at very high rates, up to 10^9 molecules per second, while preventing hydronium ion passage. Carrier proteins generally have a lower turnover but are capable of transport against gradients by using the chemical energy of ATP. For both classes of proteins, their unique permeability and selective properties make them interesting as candidates in biomimetic membrane separation design and development. An ideal separation device requires use of such component properties and transport to be promoted only through them, while the supporting matrix must be virtually impermeable to anything but the solute in question. In practice, however, a biomimetic support matrix will generally have permeabilities to water, electrolytes, and nonelectrolytes. Therefore, the efficiency of a biomimetic system may depend on the relative contribution to the transport from biological components and artificial support. Further, the stability of the incorporated biological components must be addressed in order to achieve a sufficient lifetime and make it feasible for productive application.

A new generation of biomimetic membranes for water treatment and drug delivery was reported in 2007 by researchers at Illinois University [8]. The highly permeable and selective membranes are based on the incorporation of the functional water channel protein Aquaporin Z into a novel A–B–A triblock copolymer. The experimental membranes, in the form of vesicles, showed significantly higher water transport than common reverse-osmosis membranes used in water purification and desalination.

Aquaporin's biomimetic membrane with embedded aquaporins have been also reported in References 9–11. The system supported pressures up to 10 bar and allowed a water flux $>100\,l\,m^{-3}\,h^{-1}$. Therefore, the development of the Aquaporin membrane™ is closely linked to the simultaneous development of suitable porous support materials. The biomimetic membrane has been produced on a scale of few square centimeters and investigations to scale it up to square meters are currently in progress. The microfabrication method based on CO_2-laser ablation to generate support membranes with homogeneous apertures ranging from 300 down to 84 μm in diameter has been used. They are arranged in arrays with the densest packaging having a perforation level of up to 60%. The apertures are surrounded by a smooth bulge that is formed by melted material ejected from the aperture during laser ablation. Polydimethylsiloxane (PDMS) replicas were used to visualize and analyze these bulges.

Biocatalytic membranes containing enzyme immobilized in polymeric membranes represent another example of biomimetic membrane systems. Referring to the β-glucosidase/oleuropein system previously discussed, where the enzyme is compartmentalized in the wall and the oleuropein in the vacuole, a similar structure has been constructed by immobilizing the enzyme in a polymeric porous asymmetric membrane and feeding the substrate oleuropein by convective flow. The enzyme was anchored to the membrane while the oleuropein was converted while passing through it. The immobilized β-glucosidase enzyme maintained very high stability and selectivity, thanks to the protection offered by the polymeric membrane support. Immunochemical analyses showed the distribution of the enzyme within the membrane (**Figure 9**) [12]. The compartmentalization of β-glucosidase with oleuropein can be used for the production of bioactive molecules; in addition, it can be used as a model for bioactive packaging formulation. The combination of other membrane concepts, such as membrane emulsification, offers innovative possibilities in the preparation of functionalized microstructures able to

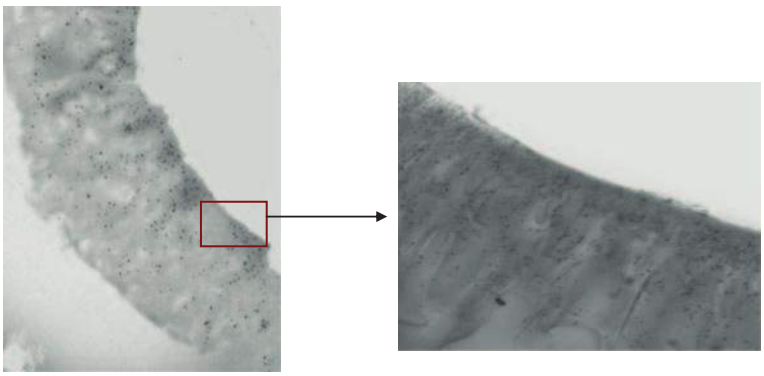

Figure 9 Black spot indicating the visualization *in situ* of immobilized protein.

compartmentalize bioactive molecules mimicking biological systems.

Enzyme immobilization in polymeric and inorganic membranes for the development of bioreactors is a well-developed strategy (for further information, see Chapter 3.08). [13, 14]

Biomimetic membrane properties are also developed in tissue engineering and regenerative medicine applications (for further information, see Chapter 3.10) [15, 16]. In this area, polymeric membranes are used as support for cell adhesion and at the same time as selective barrier to transport molecules in (metabolites) and out (catabolites) of the compartmentalized biohybrid system. The membrane may serve as a lung (to supply oxygen to cultured cells), as a glomerulus, as a vein, as skin, etc.

Biomimetic structures are attracting enormous interest. Bottom-up techniques, such as self-assembling [17] and layer by layer (LbL) [14], in addition to top-down techniques are assumed to play a key role in the development of controlled biomimicking artificial structures.

References

[1] Singer, S. J., Nicolson, G. L. *Science* **1972**, *175* (23), 720–731 (doi:10.1126/science.175.4023.720).
[2] Alberts, B., Johnson, A., Lewis, J., *et al. Molecular Biology of the Cell*, 4th edn.; Garland Science: New York, 2002 (ISBN 0-8153-3218-1).
[3] Gray, J., Groeschler, S., Le, T., Gonzalez, Z. *Membrane Structure* (SWF); Davidson College, 2002.
[4] Lodish, H., Berk, A., Zipursky, L. S., Matsudaira, P., Baltimore, D., Darnell, J. *Molecular Cell Biology*, 4th edn.; Scientific American Books: New York, 2004 (ISBN 0716731363).
[5] Jones, P., Vogt, T. *Planta* **2001**, *213*, 164–174.
[6] Davies, G., Henrissat, B. *Structure* **1995**, *3*, 853–859.
[7] Gruhnert, C., Biehl, B., Selmar, D. *Planta* **1994**, *195*, 36–42.
[8] Kumar, M., Grzelakowski, M., Zilles, J., Clark, M., Meier, W. *Proc. Natl. Acad. Sci. U.S.A.* **2007**, *104*, 201119–220424.
[9] Nielsen, C. H. J. *Anal. Bioanal. Chem.* **2009**, *395*, 697–718.
[10] Vogel, J., Perry, M., Hansen, J. S., Bolinger, P.-Y., Nielsen, C. H., Geschke, O. *J. Micromech. Microeng.* **2009**, *19*, 025026 (6pp) (doi: 10.1088/0960-1317/19/2/025026).
[11] Hansen, J. S., *et al. J. Micromech. Microeng.* **2009**, *19*, 025014 (11pp) (doi: 10.1088/0960-1317/19/2/025014).
[12] Mazzei, R., Giorno, L., Mazzuca, S., Drioli, E. *J. Membr. Sci.* **2009**, *339*, 215–223.
[13] Giorno, L., Drioli, E. *Trends Biotechnol.* **2000**, *18*, 339–348.
[14] Smuleac, V., Butterfield, D., Bhattacharyya, A. D. *Langmuir* **2006**, *22*, 10118–10124.
[15] Drioli, E., De Bartolo, L. *Artif. Organs* **2006**, *30*, 793–802.
[16] Stamatialis, D. F., Papenburg, B. J., Girones, M., *et al. J. Membr. Sci.* **2008**, *308*, 1–34.
[17] Barboiu, M., Cazacu, A., Michau, M., Caraballo, R., Arnal-Herault, C., Pasc-Banu, A. *Chem. Eng. Process.: Process Intensificat.* **2008**, *47*, 1044–1052.

Biographical Sketches

Lidietta Giorno is a membrane biotechnologist with background in biological science, chemical technologies, and new materials. Her research experiences include membrane bioengineering, biocatalytic membrane reactors, integrated membrane systems for bioseparations and bioconversions, downstream processing based on molecular separation, membrane chirotechnology, and membrane emulsifier. She has been involved in membrane science and engineering research and development for almost 20 years.

She is a director of the Institute on Membrane Technology of the National Research Council of Italy, ITM-CNR and is involved in research cooperations at European and international level. She worked abroad in the USA at Sepracor Inc. (1992); in The Netherlands at ATO-DLO (1994); and in France, at The University of Compiegne (1997 and 2000). She is a visiting professor at Tianjin University of Science and Technology, China, since 2008.

Lidietta Giorno is a co-author of three books and some 70 peer reviewed scientific papers in international journals. She is an editorial board member of scientific journals, a member of the referee pool of scientific journals and research agencies, and a member of international committees and several scientific societies.

She has served on the European Membrane Society Council for two mandates and is currently the president of the EMS Council and editor of the *EMS Membrane Newsletter*.

Rosalinda Mazzei is a researcher contractor at the Institute on Membrane Technology, ITM-CNR, Italy. She works in ITM-CNR since 2003. Her research experiences include membrane bioengineering, biocatalytic membrane reactors, membrane bioseparation and bioconversion and membrane emulsification.

Professor Enrico Drioli has been working in Membrane Science and Membrane Engineering for many years even when a student in chemistry at the University of Naples. He is a full professor at the Department of Chemical Engineering and Materials at the University of Calabria where he founded, in 1993, the Institute of Membrane Technology of the Italian Research Council. He served there as a director until December 2008. He also served as dean of the School of Engineering of the University of Calabria during the years 1982-85

He received various award and honors: Doctorate Honoris Causa from University of Paul Sabatier of Toulouse (France) (8 July 2009); International Cooperation Honor Award on September 2005 given by the Membrane Industry Association of China (MIAC) for his special dedication to the International Cooperation between China and Europe in the field of membrane and science technology; guest professor in the Environment and Safety Engineering Department at the Jiangsu Polytechnic University, China (since June 2005); Honorary Member of the A. V. Topchiev Institute of Petrochemical Synthesis at the Russian Academy of Sciences, Moscow (since 1999); Doctorate Honoris Causa in Chemistry and Chemical Technology from Russian Academy of Science (February 1992); Honorary Professor at the China Northwest University in Xi'an, Shaanxi, People's Republic of China (September 1991); President of the European Society of Membrane Science and Technology (known today as the European Membrane Society) (1982–98); Honorary President of the European Membrane Society (since 1999); Member of the International Scientific Advisory Committee of the Grand Water Research Institute at Technion – Israel Institute of Technology, Israel (since 2004); Member and Moderator of the Research Advisory Council of the Middle East Desalination Research Center Oman, Muscat (since May 1997); Member of the International Advisory Board of the State Key Laboratory of Catalysis, Dalian Institute of Chemical Physics, Chinese Academy of Sciences (since 2007); Founding member of the European Federation on Regenerative Medicine (since 2006); Expert in the panels of the OECD project 'Nanotechnology and clean water' (www.oecd.org/sti/nano).

His scientific activity has been mainly in: Membrane Science and Engineering; Membranes in Artificial Organs; Integrated Membrane Processes; Membrane Preparation and Transport Phenomena in Membranes; Membrane Distillation and Membrane Contactors; and Catalytic Membrane and Catalytic Membrane Reactors.

He is the author of more than 530 scientific papers, and 10 scientific books and holds 18 patents in the field of Membrane Science and Technology.

Drioli is the Member of the Advisory Boards of: *Journal of Membrane Science* - Elsevier, and *Polish Journal of Chemical Technology*. In addition, he is the member of the International Advisory Board of *Journal of Water Supply: Research and Technology* – AQUA. He is also the senior advisor to *Chinese Journal of Membrane Science and Technology* (China), and *Technology of Water Treatment Journal*.

Drioli is the member of the editorial boards for *Chemical Engineering and Processing* Elsevier: *Desalination* – Elsevier; *Chemical Engineering and Technology Journal* – Wiley-VCH; *Industrial* & *Engineering Chemistry Research* (from January 2002 to 2006) – American Chemical Society; *Separation Science and Technology* – M. Dekker; *Clean Technologies and Environmental Policy* – Springer-Verlag; *Water Treatment* – China Ocean Press (China); *Russian Journal of Physical Chemistry* – MAIK Nauka, Interperiodica Publ. (Russia); and *Journal of Separation and Purification Technology* – Childwall University Press (China).

1.02 Functionalized Membranes for Sorption, Separation, and Reaction: An Overview

A R Ladhe, J Xu, A M Hollman, V Smuleac, and D Bhattacharyya, University of Kentucky, Lexington, KY, USA

1.02.1 Introduction

The development of new-generation materials that extend the industrial applications of membrane processes will require a high level of control of both the characteristics of the base polymeric or inorganic support layer as well as its corresponding surface properties. Current research in membrane science is now focusing more on the modification of surface physical along with chemical properties to develop new membrane materials called functionalized membranes [1–3]. In addition to the size-based separations by conventional membrane processes, the functionalized membranes allow separations based on other driving forces like charge [4] and physical/chemical interactions [5, 6]. Functionalized membranes with appropriate functional groups can provide applications ranging from tunable water permeation and separations [4], toxic metal capture [7], toxic organic dechlorination [8–12], biocatalysis [13], and others (**Figure 1**).

The functionalized membranes also provide opportunities for process integration by achieving separation and reaction in single step [14]. Stimuli-responsive membranes have been developed by functionalization with materials which are sensitive to the surrounding environment. Such membranes are useful for developing biomimetic devices and controlled drug release applications. Membranes functionalized with polyelectrolytes are capable of charge-based ion separations or toxic metal capture. These microporous membranes allow nanofiltration (NF)-type separation at permeabilities much higher than conventional membranes [15, 16]. The chapter discusses various methods of preparation of functionalized membranes and their applications with reference to selected examples.

1.02.2 Preparation of Functionalized Membranes

The most common approach for the preparation of functionalized membranes is by surface modification of the existing membranes with desired functional groups. The desired functional groups can be introduced through either covalent or noncovalent attachment mechanism. Some of the commonly applied techniques for membrane functionalization include surface chemistry [1], polymer deposition [11, 17] alternate adsorption of oppositely charged polyelectrolytes [18–21], plasma or radiation

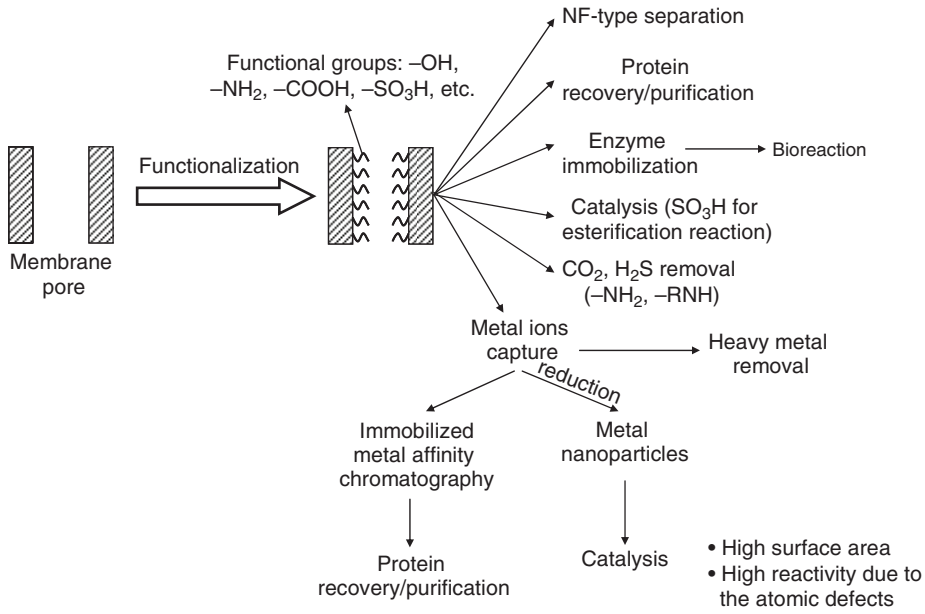

Figure 1 Applications of functionalized membranes.

induced grafting [22, 23], gold–thiol chemistry, [24–26] etc. The polymer deposition inside membrane pores can be achieved either by cross-linking the desired macromolecules or by *in situ* polymerization of corresponding monomers with simultaneous cross-linking. Surface chemistry allows covalent attachment of the desired molecules on the membrane surface. Polymer membrane supports, such as cellulose, cellulose acetate, alumina, polysulfone, and poly(vinylidine fluoride) (PVDF), can easily be functionalized through the surface activation of pores. Gold–thiol chemistry is studied for well-defined, polycarbonate track-etched (PCTE) membranes (after gold coating) for fundamental studies and precise quantification of membrane performance.

Another approach to introduce the functionalities in membranes is by preparation of hybrid or mixed matrix membranes [27–30]. Mixed matrix membranes consist of a continuous polymeric phase and a dispersed inorganic phase. In such membranes, the dispersed inorganic phase has the desired functional groups. Generally, the inorganic phase can be incorporated within polymer matrix during membrane preparation. Using silica as the dispersed phase in the membrane matrix allows the introduction of novel functionalities through the well-known silanization pathways. In this chapter, representative applications of the functionalized membranes prepared using some of the above mentioned techniques are described.

1.02.3 Classification of Functionalized Membrane Applications

Based on the role of membranes, the applications of the functionalized membranes can be classified into three different categories. The first category is the use of the functionalized membranes (including layer-by-layer (LbL) assembly) for separations, where the modified membranes allow selective permeation of one of the species and can be used in continuous mode.

The second category is the application of the functionalized membranes for sorption processes where the modified membranes act as adsorbents. In a way this also leads to separation and capture. A regeneration step is required in order to reuse the membranes. The third category is the use of functionalized membranes for catalytic applications where the functional groups, enzymes, or immobilized nanoparticles act as catalysts, and convert the reactants into products as they pass through the membrane pore. Some examples of each category are discussed with emphasis on membrane preparation and membrane performance.

1.02.4 Functionalized Membranes for Material Capture Applications

Membranes functionalized with polyfunctional molecules exhibit very high capture capacities. Ladhe *et al.* [17] studied poly(acrylic acid) functionalized membranes for nonionic surfactant capture which is important toward reuse solvents used in surfactant-based cleaning operations. Functionalized membranes with pore size 200–400 nm have also been studied as adsorbents in the area of toxic metal capture. It was demonstrated that membranes functionalized with covalently attached poly-L-glutamic acid (PLGA) [31] or polycysteine [32] show sorption of heavy metal ions with high capacity. **Figure 2** shows a schematic of a membrane functionalized with polyfunctional molecules.

The Pb capture with PLGA functionalized membrane was 23-fold higher than that with equimolar quantity of glutamic acid. With polyligand functionalized membranes, one can obtain metal sorption capacities as high as 1.2 g metal/g sorbent. Ritchie and Bhattacharyya [33] demonstrated up to 70% removal of chromium (Cr) from a stream containing multiple metal ions using two-stage PLGA functionalized membranes. Mixed matrix membranes provide another approach to obtain membrane-based sorbents. The inorganic dispersed phase like silica can be activated with desired functional groups with subsequent incorporation into membrane matrix. In the following part of this section, applications of functionalized membranes for nonionic surfactant capture and silver ion capture are discussed.

1.02.4.1 Poly(Acrylic Acid) Functionalized Membrane for Ethoxylated Nonionic Surfactant Capture

Ethoxylated nonionic surfactants are used in many industrial applications such as food processing, detergency, emulsifications, etc. Many of these applications involve the use of nonaqueous solvents, and a typical waste stream contains ethoxylated nonionic surfactants [17] dissolved in hydrophobic solvents along with other particulates. The separation of the surfactants is an important step for recycle and reuse of the solvents. In the light of this motivation, a poly(acrylic acid) (PAA) functionalized membrane process was developed for the capture of ethoxylated nonionic surfactants from a siloxane-based solvent (Decamethylcyclopentasiloxane or D5). Nontoxic D5 solvent is being increasingly used in surfactant-based cleaning operations.

PAA forms a complex with the ethoxylated nonionic surfactants through hydrogen bonding between carboxyl group of the PAA and ethylene oxide group

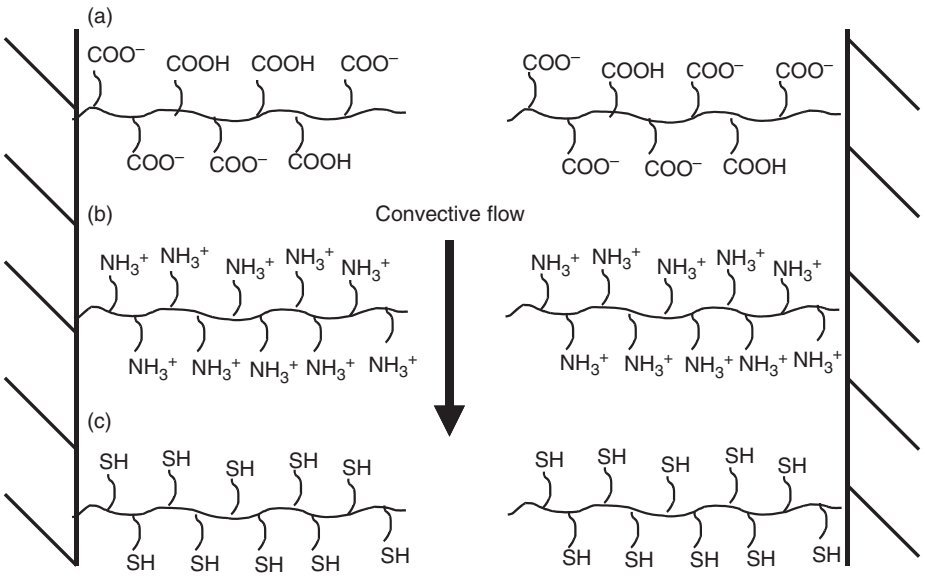

Figure 2 Schematic of membrane pore functionalized with polyfunctional molecules such as (a) COO^- (poly(glutamic acid)), (b) NH_3^+ (polylysine), and (c) SH (polycysteine). From Ritchie, S. M. C., Kissick, K. E., Bachas, L. G., Sikdar, S. K., Parikh, C., Bhattacharyya, D. *Environ. Sci. Technol.* **2001**, *35*, 3252–3258.

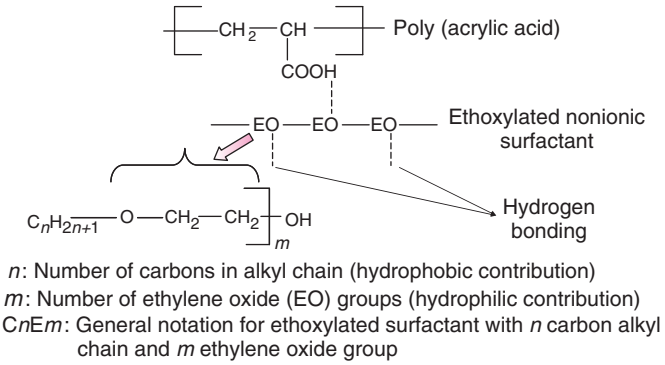

Figure 3 Ethoxylated nonionic surfactants and their interaction with poly(acrylic acid) (PAA). Modified from Ladhe, A. R., Radomyselski, A., Bhattacharyya, D. *Langmuir* **2006**, *22*, 615–621.

of the surfactant (**Figure 3**). This interaction is well studied in the aqueous environment [34–36].

The commercially available hydrophilized PVDF membrane (nominal pore size 650 nm, membrane thickness 125 μm) was used for functionalization. Aqueous solution of PAA (25 wt.%) containing ethylene glycol (4.3 wt.%) as a cross-linking agent was permeated through the membrane to coat the membrane pore with PAA layer. The membrane was heated in oven at 110 °C for 3 h to allow the cross-linking to occur. **Figure 4** shows the schematics of membrane functionalization with PAA. The process is repeated multiple times to increase the PAA loading in the membrane. Extent of functionalization for a typical membrane with three PAA coatings was 6 mg cm^{-2}.

The water permeance (A) of the membrane decreased from 0.2 $cm^3\,cm^{-2}\,s^{-1}\,bar^{-1}$ (bare membrane) to $1 \times 10^{-4}\,cm^3\,cm^{-2}\,s^{-1}\,bar^{-1}$ (PAA functionalized membrane). The permeance (A) can be represented by Hagen–Poiseuille relation as follows:

$$A_w = \frac{\mathcal{J}_w}{\Delta P} = \frac{\varepsilon_m r_p^2}{8\mu_w \tau L} \quad (1)$$

where $\mathcal{J}_w$ is the permeate flux, ε_m is the membrane porosity, r_p is the pore radius, μ_w is the viscosity of water, τ is the tortuosity of the membrane pores, and ΔP is the applied transmembrane pressure. Decrease in the permeance indicates decrease in the pore radius for the functionalized membrane due to functionalized PAA coating on the pore wall. Based on the membrane permeance data (pH 4–6) and using Hagen–Poiseuille equation, the estimated hydrodynamic pore size was about 100 nm down from 650 nm before functionalization. The PAA functionalized membrane was then studied for capture of

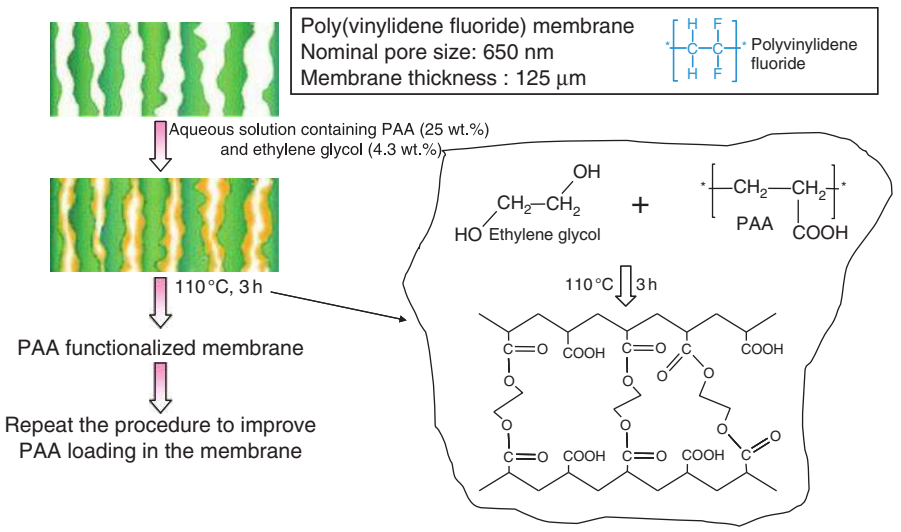

Figure 4 Schematics of membrane functionalization with PAA.

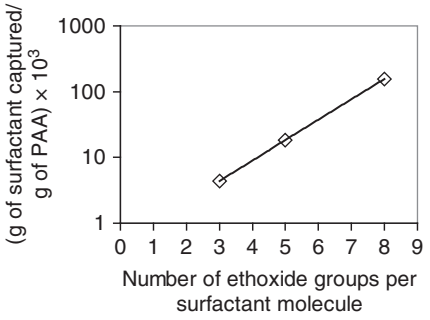

Figure 5 Surfactant capture by PAA functionalized membrane. From Ladhe, A. R., Radomyselski, A., Bhattacharyya, D. *Langmuir* **2006**, *22*, 615–621.

ethoxylated nonionic surfactants from their solutions in D5 and the results are shown in **Figure 5**.

The figure shows surfactant capture data for surfactants with varying ethylene oxide content (three, five, and eight ethylene oxide (EO) groups per surfactant molecule with a 12-carbon alkyl chain). It was observed that the membrane capture capacity increases exponentially with increasing ethylene oxide content of the surfactants (**Figure 4**). This was expected as the ethylene oxide groups contribute toward the PAA–surfactant interaction. The PAA–surfactant complex is sensitive to the pH of the surrounding environment and can be easily broken at alkaline conditions. Utilizing this fact, slightly alkaline water was permeated through the membrane containing captured surfactant, and approximately 70% of the captured surfactant was recovered and membrane is regenerated. The regenerated membrane was successfully applied for the surfactant capture process.

1.02.4.2 Functionalized Membrane for Silver Capture

Functionalized membranes containing thiol groups can selectively interact with metal ions such as silver and mercury which is important considering the high market value of silver ion and toxic nature of mercury. Ladhe *et al.* [37] studied thiol functionalized silica–polymer composite membrane for silver capture. **Figure 6** shows the schematics for the membrane preparation. Silica material (Huber 874-85-1, 3–5 μm) was functionalized with 3-mercaptopropyltrimethoxy silane through silane

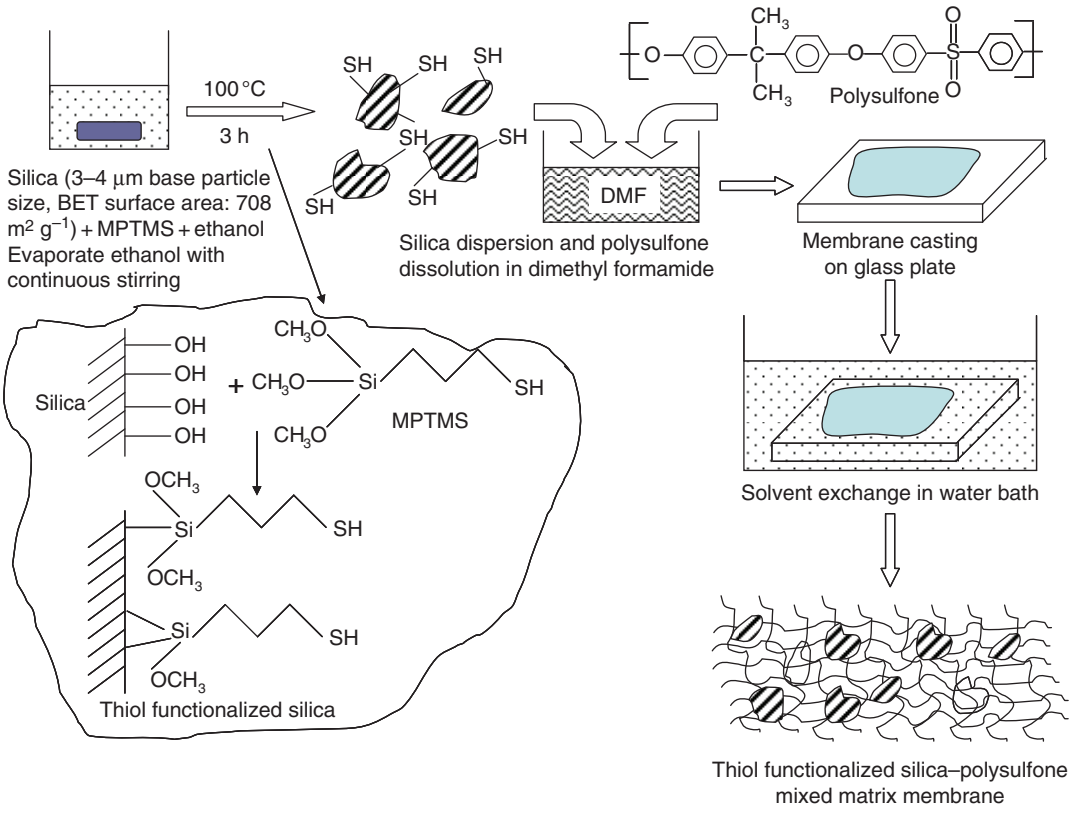

Figure 6 Schematics for synthesis of thiol functionalized silica–polysulfone mixed matrix membrane.

chemistry. This introduced free surface thiol groups (–SH) on the surface of the silica material. The thiol functionalized silica was then dispersed in the solution of polysulfone in dimethyl formamide (DMF) solvent. The mixture was then casted on a glass plate and the glass plate was immediately immersed into the water bath. The phase inversion process takes place and the DMF solvent is replaced by the water which occupies the pores of the membrane surface. The final membrane has the functionalized silica particles incorporated in the polysulfone matrix.

In order to determine the silver capture capacity and kinetics, silver nitrate solutions were permeated through the membrane and the permeate samples were analyzed using atomic absorption (AA) spectroscopy. **Figure 7** shows the silver capture data for varying membrane flux using the thiol functionalized composite membranes. The dotted line indicates maximum silver capture capacity of the silica material. It can be observed that with increasing membrane flux, rate of silver capture increased. This indicates that the thiol–silver interaction is very fast and the capture process is mass transport controlled under the experimental conditions. When exposed to equimolar concentration of silver and calcium, the membrane captured silver ions selectively (1.5 mmol g^{-1} of silica) with negligible calcium capture (<0.2 mmol g^{-1} of silica). This indicates the selectivity of the membrane toward silver capture. This is important toward practical applications where the feed stream may have high concentrations of Na and Ca ions.

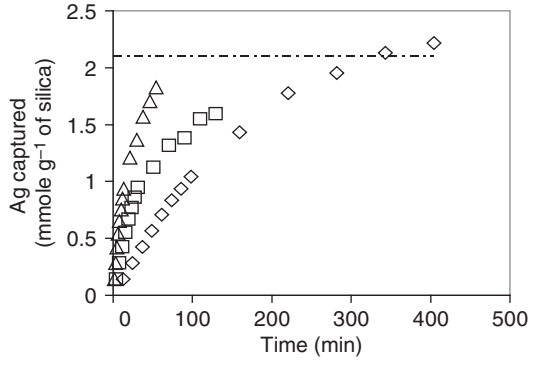

Figure 7 Silver capture using thiol functionalized silica–polysulfone mixed matrix membrane. Effect of membrane flux on silver capture capacity and rate of capture. Modified from Ladhe, A. R., Frailie, P., Hua, D., Darsillo, M., Bhattacharyya, D. *J. Membr. Sci.* **2009**, *326*, 460–471.

1.02.4.2.1 Modeling of silver ion transport through the functionalized membrane

The silver capture process using the mixed matrix membrane was modeled using unsteady-state one-dimensional model. As shown in **Figure 8**, the membrane was assumed to be composed of three phases: (1) active silica phase; (2) inert polymer phase; and (3) aqueous silver solution phase occupying the free volume fraction of the membrane.

The mass balances over the liquid and solid phase yield following equations:

$$\phi\frac{\partial C'}{\partial t'} + \mathcal{J}_w\frac{\partial C'}{\partial z'} + (1-\phi-\phi_p)\frac{\partial q'}{\partial t'} = 0 \qquad (2)$$

$$\frac{\partial q'}{\partial t'} = k(q_{eq} - q') \qquad (3)$$

with initial conditions as follows:

$$C'(0,t') = C_0$$
$$q'(z,0) = 0$$
$$C'(z',0) = 0$$

where ϕ is the free volume fraction; ϕ_p the polymer volume fraction; $(1-\phi-\phi_p)$ the fractional volume of silica particles; C' the concentration of Ag^+ in bulk liquid phase (moles of Ag^+/m^3 of liquid); q' the concentration of silver in silica phase (moles of Ag^+/m^3 of silica particles); q_{eq} the maximum concentration of silver in silica phase for C' (moles of Ag^+/m^3 of silica particles); k the volumetric mass transfer coefficient; $\mathcal{J}_w$ the membrane flux ($m\,s^{-1}$); t' the time (s); and z' the distance down the membrane thickness (m).

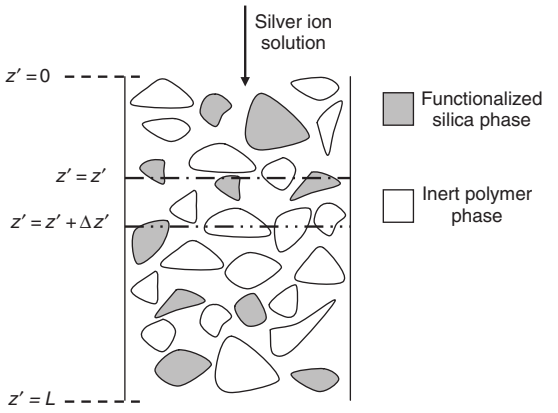

Figure 8 Schematic representation of the silica–polysulfone mixed matrix membrane for modeling purpose. Modified from Ladhe, A. R., Frailie, P., Hua, D., Darsillo, M., Bhattacharyya, D. *J. Membr. Sci.* **2009**, *326*, 460–471.

In this case, the axial diffusion is neglected as compared to axial convection. Assuming linear relationship between q_{eq} and C',

$$q_{eq} = \gamma C' \tag{4}$$

where γ is the silver–thiol affinity constant.

Equations (2)–(4) were solved using COMSOL. The comparisons of the predicted data (dotted lines) with the experimental data are shown in **Figure 9**.

All the required parameters were obtained from experimental values or correlations. Considering the fact that no adjustable parameter was used, the reasonable prediction of the experimental data demonstrates applicability of the model under varying operating conditions. The model is an efficient way to predict the effect of various parameters on the silver capture process. With appropriate changes, the model can be applied for other processes that involve mixed matrix membranes for liquid-phase applications including metal capture.

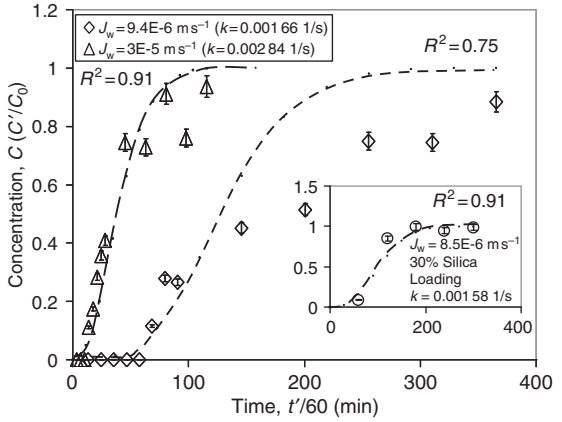

Figure 9 Comparison of the experimental and predicted data for varying operating conditions. Dotted lines represent predicted data. From Ladhe, A. R., Frailie, P., Hua, D., Darsillo, M., Bhattacharyya, D. *J. Membr. Sci.* **2009**, *326*, 460–471.

1.02.5 Functionalized Membranes for Separations

Modification of membranes with immobilized functional polyelectrolytes has gained interest due to its potential for development of high capacity ion-exchange materials [31, 38, 39] and tunable membrane separations [40–44]. Some of the commonly used polyelectrolytes (polypeptides) for such applications are shown in **Figure 10**. The macromolecules can be incorporated within the membrane pore structure by single-point covalent attachment through the reactive groups on the membrane surface [41].

Once functionalized, the presence of these charged macromolecules inside the pores leads to the establishment of an electric potential field far removed from the pore wall. This allows ion exclusions in the highly open geometries at high membrane permeabilities as opposed to the low permeabilities encountered in the conventional nanofiltration applications. Thus, one can obtain NF-type separations at very low pressures. External stimulants such as pH, ionic strength, and surfactants can cause change in the degree of ionization of the polyelectrolytes leading to the well-known

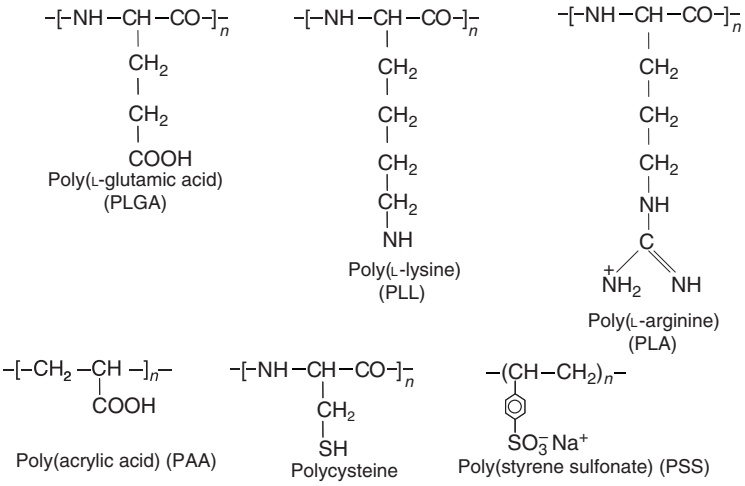

Figure 10 Commonly used polyelectrolytes to develop high-capacity ion-exchange membrane materials.

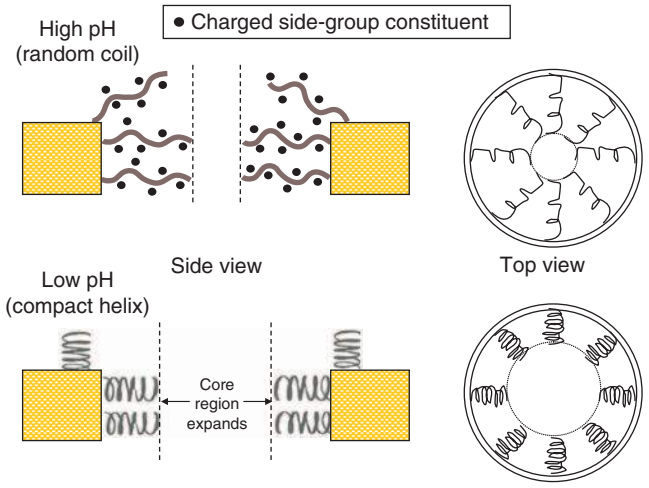

Figure 11 Schematics for helix–coil transition of a polyelectrolyte functionalized inside membrane pore. From Onda, M., Lvov, Y., Ariga, K., Kunitake, T. *J. Ferment. Bioeng.* **1996**, *82*, 502–506.

helix–coil transitions [42], thus facilitating tunable separation applications. The helix–coil transition phenomenon is schematically represented in **Figure 11**. At pH > 6 (for PLGA, pH < 4, 100% helix) conditions the repulsion between the adjacent ionized groups of the polyelectrolyte leads to extended random coil conformation which decreases membrane permeability due to added flow resistance. The concept of single-layer polyelectrolyte immobilization can be easily extended to nonstoichiometric multilayer immobilization (LbL assembly) [15], enhancing the density of the ionizable groups in the membrane phase. This section deals with separation characteristics of the membranes functionalized with either single-layer or LbL assembly of charged polyelectrolytes.

1.02.5.1 Single-Layer Polyelectrolyte Functionalized Membranes for Ionic Solute Rejections

Among the various polyelectrolytes used for membrane functionalization, poly(amino acid) are the most common as the amine group chemistry provides various options for functionalization. Poly(amino acid) functionalized microporous membranes were studied for the separation of dilute electrolytes such as As(V), Cr(III), and Cr(VI) from aqueous solutions [41]. Arsenic and chromium fall under the category of toxic metals in water, and stringent government regulations on their concentrations demand separation process designed for dilute systems. Arsenic and chromium are typically present in the form of divalent oxyanions ($HAsO_4^{2-}$, CrO_4^{2-}, or $Cr_2O_7^{2-}$) in water, and the charge-based membrane separation process is desirable for the same.

In order to achieve the covalent attachment of the amine-terminated poly-amino acids, reactive groups on the membrane pore surface are required. The membrane supports can be derivatized to achieve required reactive groups. For example, in the case of cellulosic supports, ozone oxidation creates aldehyde groups on the surface. In the case of silica membranes, the support can be silanized with epoxy-terminated silanes to achieve highly reactive epoxy groups on the silica surface. PCTE can be first gold-coated [43] and then subjected to thiol-terminated organic monolayer adsorption [24, 44] with subsequent oxidation to obtain surface aldehyde groups [26]. Schematics of the derivatized membranes are shown in **Figure 12**. Under appropriate pH conditions, the nonprotonated terminal amine group of the poly(amino acid) reacts with surface aldehyde/epoxy groups to form the covalent linkage [41].

Table 1 summarizes the solute rejection data for these membranes. The rejection (R) is calculated by following equation:

$$R = \left(1 - \frac{C_p}{C_f}\right) \times 100 \qquad (5)$$

where C_p and C_f are concentrations of the solute in permeate and feed solutions.

It is interesting to note that the neutral molecules (dextran and PEG) showed significantly lower rejections (1.5% and 30%, respectively) despite the bigger size of their molecules (20 and 3.5 nm, respectively)

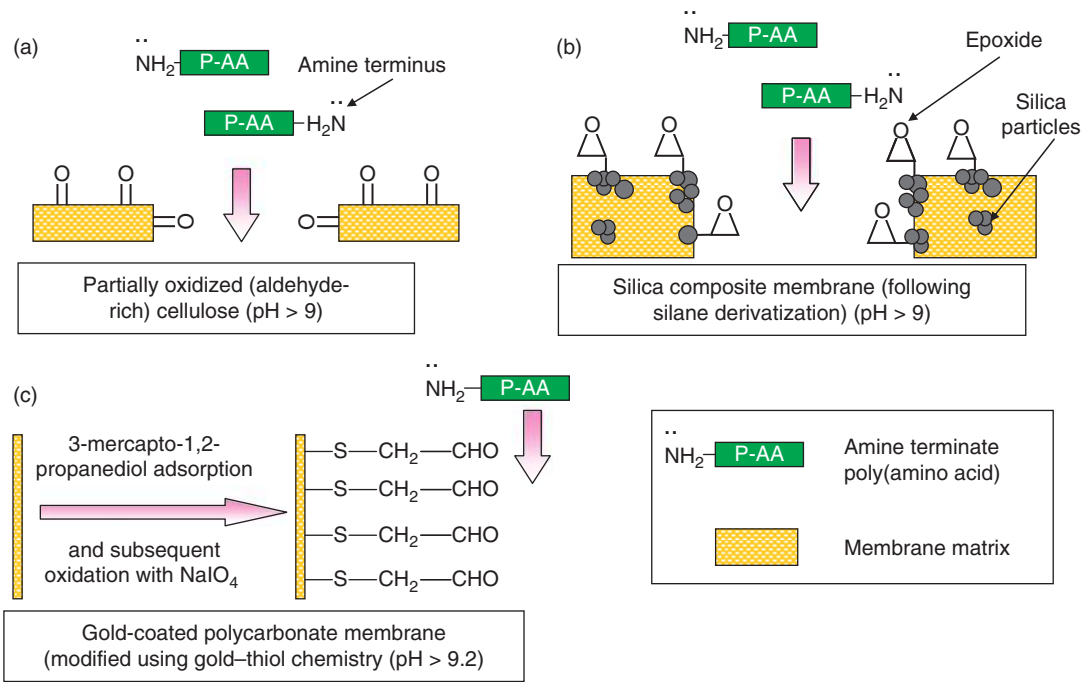

Figure 12 Schematics for single-point covalent attachment of amine-terminated PAA on; (a) cellulose membranes; (b) silica–polyethylene composite (Daramic, Inc) membranes; and (c) gold-coated polycarbonate membrane.

Table 1 Solute rejection for various polyelectrolyte functionalized membranes

Membrane type	*Solute studied*	*Size of the hydrated ion/molecule (nm)*	*Observed rejection* $R = (1 - C_p/C_f) \times 100$ *(%)*
PLGA-silica[a]	Na_2SO_4	0.4	88.6
($n = 356$, $d_p = 96$ nm)	Na_2HAsO_4, i.e., (As(V))		88.7
	Na_2CrO_4, i.e., (Cr(VI))	0.4	80.0
	Dextran (neutral)	20	1.5
PLL-cellulose[a]	$CaCl_2$		97 (Ca^{2+} rejection)
($n = 461$, $d_p = 100$–200 nm)			
PLGA-PCTE[b]	Polyethylene glycol	3.5	30
($n = 116$, $d_p = 30$ nm)	Na_2SO_4	0.4	89

[a] Modified from Hollman, A. M., Scherrer, N. T., Cammers-Goodwin, A., Bhattacharyya, D. *J. Membr. Sci.* **2004**, *239*, 65–79.
[b] Modified from Smuleac, V., Butterfield, D. A., Bhattacharyya, D. *Chem. Mater.* **2004**, *16*, 2762–2771.
n, Number of repeat units in the polyelectrolyte; d_p, pore diameter of the unmodified membrane.

as compared to the hydrated anions SO_4^{2-} and CrO_4^{2-} (0.4 nm) which showed rejections higher than 80%. It is clear that the observed solute rejections are not based on physical or steric interactions but it is a result of charged domain (Donnan exclusion) influencing the transport of the ionic species.

The transport of ionic species through the charged media is generally described by the extended Nernst–Planck (N–P) equation

$$\mathcal{J}_{x,i} = -D_i \frac{dC_i}{dx} + v_m C_i - \frac{D_i z_i C_i F}{RT} \frac{d\Phi}{dx} \qquad (6)$$

where $\mathcal{J}_{x,i}$ is the flux of the ionic solute i in x-direction, D_i the diffusivity of the ionic solute, C_i the ion concentration, v_m the velocity across the membrane, z_i the ion valency, F the Faraday constant, R the gas constant, T the temperature, and Φ the net electrostatic potential inside the membrane pore. The first, the middle, and the last term of the equation accounts

for diffusional, convective, and electrostatic transport of the ionic solute, respectively.

The ionic rejections by traditional RO and NF membranes increase with applied transmembrane pressure. However for the functionalized microporous membranes, R may decrease at higher permeate flux values owing to the core leakage through the membrane pores. This could be advantageous for selective separations (e.g., Na_2SO_4 from NaCl).

1.02.5.2 Multilayer Polyelectrolyte Functionalized Membranes Using LbL Assembly in Pores

LbL assembly offers an easy and inexpensive way to create functionalized membranes with multilayers (using nonstoichiometric amounts) of charged polyelectrolytes. It was first suggested by Iler [21] and established by Decher and coworkers [19, 20]. An excellent review from Ariga *et al.* [18] summarizes various physicochemical fundamentals and possibilities for practical applications of the LbL assembly.

Functionalization of the membranes using LbL technique allows flexibility in terms of number layers and the layering sequence. A typical schematic of membrane functionalization using LbL technique is shown in **Figure 13**. Depending on the desired applications of the LbL modified membranes, the multilayers can be deposited either on the membrane surface [45–47] or inside the membrane pores by using convective flow [15]. By varying the deposition conditions such as pH and supporting electrolyte concentration, the adsorbed layer properties can be optimized.

Liu and Bruening [47] functionalized the external surface of porous alumina membranes with multiple bilayers of poly(styrene sulfonate) (PSS) and poly(allylamine hydrochloride) (PAH). The membranes were studied by diffusion dialysis and by NF-type separations of neutral molecules such as methanol, glucose, sucrose, and glycerol. The membrane performance was evaluated in terms of selectivity of permeation between the two solutes. The selectivity was defined as follows:

$$\text{Selectivity} = (100 - R_1)/(100 - R_2) \qquad (7)$$

where R_1 and R_2 are the rejections of solutes 1 and 2, respectively. The findings of the study are listed in **Table 2**. It is clear that the LbL modification of the membrane increases the glucose/sucrose selectivity significantly. It was also interesting to note that by changing the surface properties of the LbL assembly by capping it with 1.5 bilayer of [PAA/PAH], the separation selectivity was enhanced drastically as indicated by their diffusion dialysis experiments. The lower selectivity values in the case of methanol/glycerol imply that the pores in the LbL-modified membranes are still too large to separate small molecules such as methanol.

Hollman and Bhattacharyya [15] prepared highly permeable ion-selective membranes through immobilization of polyelectrolyte multilayer within the

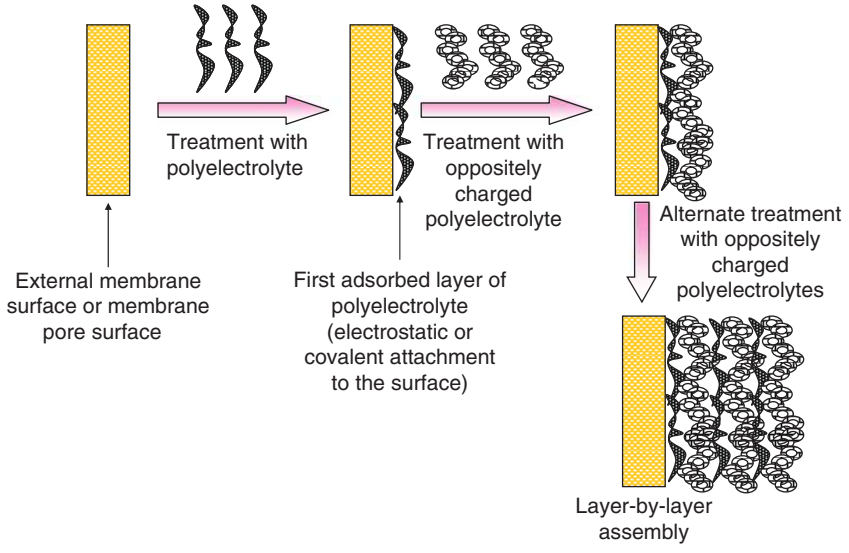

Figure 13 Schematics for membrane functionalization with LbL assembly technique.

Table 2 Selectivity values for neutral solutes using layer-by-layer surface-modified alumina membrane

Film composition	*Methanol/glycerol*[a]	*Glycerol/glucose*[b]	*Glucose/sucrose*[b]
$[PSS/PAH]_6PSS$	1.96	3.7	68
$[PSS/PAH]_7$	2.0	7.7	>100

[a] Diffusion dialysis experiments.
[b] NF experiments.
Modified from Liu, X., Bruening, M. L. *Chem. Mater.* **2004**, *16*, 351–357.

pores of microporous membranes. The polyelectrolytes used were PLGA and poly(L-lysine) (PLL). The first layer was covalently attached to the membrane support through surface chemistry and the rest of the layers were assembled through electrostatic interactions. Unlike stratified surface deposition, the film growth in this case proceeds perpendicular to the direction of solvent flux. The role of NaCl concentration in the carrier solvent on polyelectrolyte adsorption was studied. It was observed that as the NaCl concentration was increased from 0 to 0.1 to 0.5 M, the polyelectrolyte attachment density increased from 0.1×10^{-4} to 0.15×10^{-4} to 0.22×10^{-4} mmol cm^{-2}, respectively. This can be attributed to a reduction in number of ionic site interactions per adsorbed chain during deposition with increasing salt solution. The membranes show As(V) rejection greater than 95% at membrane permeances (pressure < 2 bar) that exceed commercially available NF membranes.

1.02.6 Functionalized Membranes for Catalytic Applications

Functionalized membranes have the potential to contribute significantly toward the improvement of catalytic applications by providing alternative support for catalyst immobilization. Membrane-supported catalytic applications not only mitigate the need for dispersion of the catalyst and its subsequent removal from reaction mixture, but also provide very high mass transport conditions. For example, sulfonated polystyrene graft functionalized membranes have been studied as heterogeneous, solid-phase flow through catalyst for esterification reaction between ethanol and acetic acid [48]. A residence time of 20 s in the flow through studies gave the same conversion as obtained in 11 h for batch reactions with either membrane or commercial ion-exchange resin. This emphasizes the significant improvement in reaction kinetics using membrane-supported catalyst.

An important area of catalytic applications involves the use of metal nanoparticles. In addition to the large surface area to volume ratios, the different electronic properties of the nanoparticles (as compared to bulk materials) contribute toward the significant enhancements in catalytic activities. In the next section, application of membrane-immobilized metal nanoparticles for catalytic dechlorination of chloro-organics are discussed.

1.02.6.1 Membrane-Immobilized Nanoparticles for Chloro-Organic Dechlorination

Zero-valent iron-based bimetallic nanoparticles are known for the degradation of toxic-chlorinated organic compounds which is important for groundwater remediation. Nanoparticle synthesis in aqueous phase for dechlorination studies has been reported [49–51]. However, in the absence of polymers or surfactants, the nanoparticles can easily aggregate into large particles with wide size distribution. Xu and Bhattacharyya [10–12] reported a novel *in situ* synthesis method of bimetallic nanoparticles embedded in PAA functionalized microfiltration membranes by chemical reduction of metal ions bound to the carboxylic acid groups. Along with high mass transfer rate, reduction of particle loss and prevention of particle aggregation are the added advantages of membrane-based nanoparticle synthesis. The procedure for the synthesis of membrane-immobilized bimetallic nanoparticles is schematically shown in **Figure 14**.

PVDF membrane was functionalized either by dip coating with PAA solution or by *in situ* polymerization of acrylic acid monomers inside membrane pores. The PAA was converted into sodium form by soaking the membrane in sodium hydroxide solution. The ferrous ions (Fe^{2+}) were loaded into membranes by ion exchange between Na^+ ions in the membrane and Fe^{2+} ions from aqueous ferrous chloride solution. The membrane was then immersed in the sodium borohydrate solution to reduce the Fe^{2+}

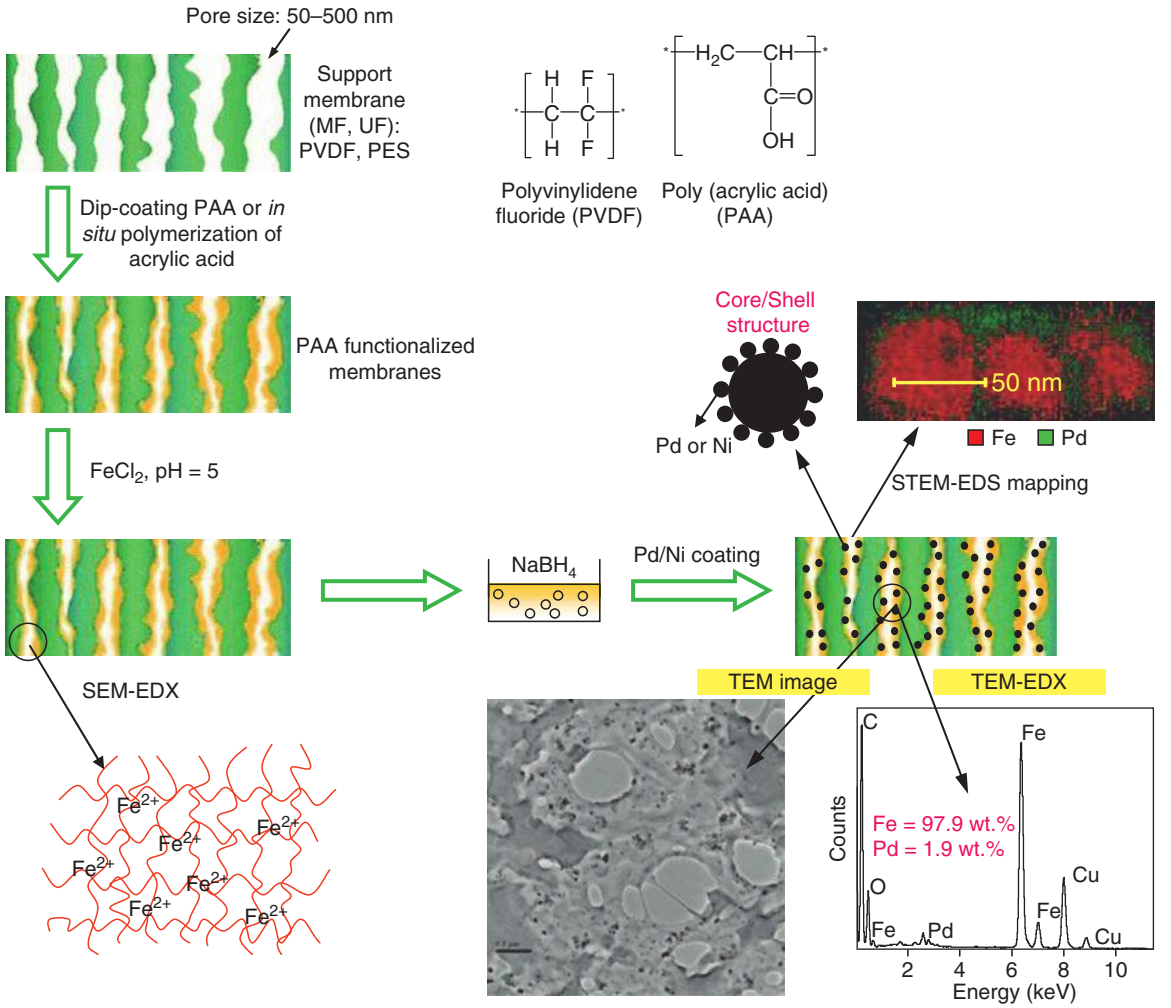

Figure 14 Synthesis of bimetallic nanoparticles in functionalized membranes. Modified from Xu, J., Bhattacharyya, D. *Ind. Eng. Chem. Res.* **2007**, *46*, 2348–2359.

ions to form Fe^0 nanoparticles embedded in the PAA/PVDF matrix. Bimetallic (core/shell) nanoparticles were formed by postdeposition of other metals such as Pd or Ni ($Pd^{2+} + Fe^0 \rightarrow Fe^{2+} + Pd^0$). **Figure 14** also shows the TEM image of the membrane-immobilized Fe/Pd nanoparticles. According to the TEM-EDS spectra, the Fe/Pd nanoparticles contain 1.9 wt.% Pd. The STEM-EDS mapping images of the nanoparticles demonstrate a core–shell structure with Fe in the core region and Pd in the shell region. The membrane was studied for dechlorination of 2,2′-dichlorobiphenyl (DiCB) in convective mode.

The dechlorination experiments were carried out at four different residence times and the DiCB concentration profiles as shown in **Figure 15**. The figure also shows the concentrations of the intermediate 2-chlorobiphenyl and the final product biphenyl; for 40 s residence time, complete dechlorination of DiCB takes place at room temperature.

The dechlorination process can be described by a two-dimensional model. **Figure 16** shows the schematics of the membrane pore with two regions: (1) membrane pore region and (2) PAA layer containing Fe/Pd nanoparticles. The system can be described by the following equations:

For the membrane pore region,

$$U_z \frac{\partial C}{\partial z} = D_s \frac{1}{r} \frac{\partial C}{\partial r} \left(r \frac{\partial C}{\partial r} \right) + D_s \frac{\partial^2 C}{\partial z^2} \qquad (8)$$

For the PAA layer region containing Fe/Pd nanoparticles,

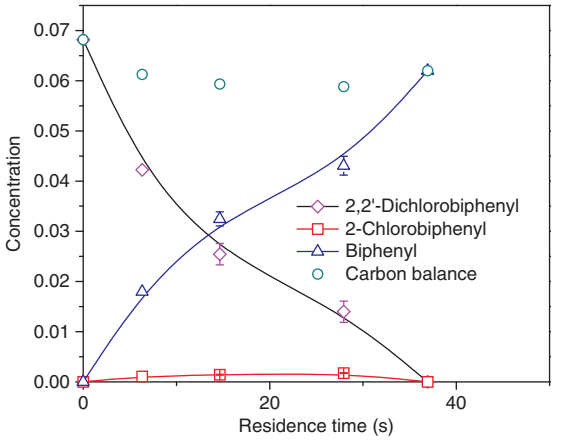

Figure 15 Dechlorination results for 2,2′-dichlorobiphenyl using membrane-immobilized Fe/Pd nanoparticles. Modified from Xu, J., Bhattacharyya, D. *Ind. Eng. Chem. Res.* **2007**, *46*, 2348–2359.

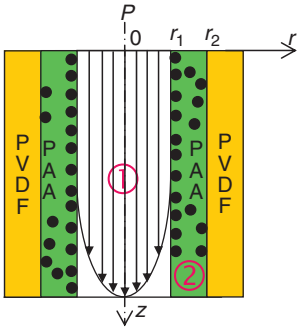

Figure 16 Schematic representation of the membrane pore for modeling purpose. Modified from Xu, J., Bhattacharyya, D. *J. Phys. Chem. C* **2008**, *112*, 9133–9144.

$$D_m \frac{1}{r}\frac{\partial C}{\partial r}\left(r\frac{\partial C}{\partial r}\right) + D_m \frac{\partial^2 C}{\partial z^2} + (-k_{in}\rho S_a C) = 0 \qquad (9)$$

where C is the PCB concentration; D_s the diffusivity of DiCB in pore fluid; D_m the diffusivity of DiCB in membrane; k_{in} the reaction rate constant in convective flow; ρ the Fe/Pd density in PAA layer; S_a the surface area per unit mass; U_z the fluid velocity in z-axis, $U_z = 2U_0(1 - (r/r_1)^2)$, for a fully developed laminar flow, with U_0 being the average velocity.

The equations were solved [12] with appropriate initial/boundary conditions with k_{in} as the fitting parameter to fit the model data to the experimental data. The model was successfully able to predict the experimental data for varying operating conditions such as residence time, wt.% of Pd in the bimetallic nanoparticles, and membrane pore size. This model is a useful tool for the prediction and evaluation of chloro-organic degradation at various conditions, and for the optimization of nanoparticles loading in membranes.

Acknowledgments

The authors would like to acknowledge the research grant supports from the NIEHS-SBRP program (P42ES007380) and Huber Corporation.

References

[1] Klein, E. *Affinity Membranes: Their Chemistry and Performance in Adsorptive Separation Processes*; Wiley: New York, 1991.
[2] Butterfield, D. A., Ed. *Biofuncitonal Membrances*; Proceedings of the International Conference on Biofunctional Membranes, University of Kentucky, Lexington, KY, 9–11 April 1995; Plenum: New York, 1996.
[3] Roper, D. K., Lightfoot, E. N. *J. Chromatogr. A* **1995**, *702*, 3–26.
[4] Hollman, A. M., Bhattacharyya, D. *Membr. Sci. Technol. Ser.* **2003**, *8*, 329–352.
[5] Datta, S., Bhattacharyya, D., Ray, P. D., Nath, A., Toborek, M. *Sep. Sci. Technol.* **2007**, *42*, 2451–2471.
[6] Datta, S., Ray, P. D., Nath, A., Bhattacharyya, D. *J. Membr. Sci.* **2006**, *280*, 298–310.
[7] Smuleac, V., Butterfield, D. A., Sikdar, S. K., Varma, R. S., Bhattacharyya, D. *J. Membr. Sci.* **2005**, *251*, 169–178.
[8] Xu, J. Doctoral Dissertation, University of Kentucky, 2007.
[9] Tee, Y.-H., Grulke, E., Bhattacharyya, D. *Ind. Eng. Chem. Res.* **2005**, *44*, 7062–7070.
[10] Xu, J., Bhattacharyya, D. *Environ. Prog.* **2005**, *24*, 358–366.
[11] Xu, J., Bhattacharyya, D. *Ind. Eng. Chem. Res.* **2007**, *46*, 2348–2359.
[12] Xu, J., Bhattacharyya, D. *J. Phys. Chem. C* **2008**, *112*, 9133–9144.
[13] Datta, S., Cecil, C., Bhattacharyya, D. *Ind. Eng. Chem. Res.* **2008**, *47*, 4586–4597.
[14] Onda, M., Lvov, Y., Ariga, K., Kunitake, T. *J. Ferment. Bioeng.* **1996**, *82*, 502–506.
[15] Hollman, A. M., Bhattacharyya, D. *Langmuir* **2004**, *20*, 5418–5424.
[16] Malaisamy, R., Bruening, M. L. *Langmuir* **2005**, *21*, 10587–10592.
[17] Ladhe, A. R., Radomyselski, A., Bhattacharyya, D. *Langmuir* **2006**, *22*, 615–621.
[18] Ariga, K., Hill, J. P., Ji, Q. *Phys. Chem. Chem. Phys.* **2007**, *9*, 2319–2340.
[19] Decher, G. *Science* **1997**, *277*, 1232–1237.
[20] Decher, G., Schmitt, J. *Prog. Colloid Polym. Sci.* **1992**, *89*, 160–164.
[21] Iler, R. K. *J. Colloid Interface Sci.* **1966**, *21*, 569–594.
[22] Hautojarvi, J., Kontturi, K., Nasman, J. H., Svarfvar, B. L., Viinikka, P., Vuoristo, M. *Ind. Eng. Chem. Res.* **1996**, *35*, 450–457.
[23] Yamaguchi, T., Nakao, S., Kimura, S. *Macromolecules* **1991**, *24*, 5522–5527.
[24] Chun, K.-Y., Stroeve, P. *Langmuir* **2001**, *17*, 5271–5275.
[25] Lee, S. B., Martin, C. R. *Chem. Mater.* **2001**, *13*, 3236–3244.
[26] Smuleac, V., Butterfield, D. A., Bhattacharyya, D. *Chem. Mater.* **2004**, *16*, 2762–2771.

[27] Avramescu, M.-E., Girones, M., Borneman, Z., Wessling, M. *J. Membr. Sci.* **2003**, *218*, 219–233.
[28] Lin, Y.-F., Ma, C.-C. M., Lin, Y.-Y., Yen, C.-Y., Hung, C.-H. *Key Eng. Mater.* **2007**, *334–335*, 945–948.
[29] Sambandam, S., Ramani, V. *J. Power Sources* **2007**, *170*, 259–267.
[30] Yen, C.-Y., Lee, C.-H., Lin, Y.-F., *et al. J. Power Sources* **2007**, *173*, 36–44.
[31] Bhattacharyya, D., Hestekin, J. A., Brushaber, P., Cullen, L., Bachas, L. G., Sikdar, S. K. *J. Membr. Sci.* **1998**, *141*, 121–135.
[32] Ritchie, S. M. C., Kissick, K. E., Bachas, L. G., Sikdar, S. K., Parikh, C., Bhattacharyya, D. *Environ. Sci. Technol.* **2001**, *35*, 3252–3258.
[33] Ritchie, S. M. C., Bhattacharyya, D. *Ion Exch. Solvent Extr.* **2001**, *14*, 81–118.
[34] Anghel, D. F., Saito, S., Baran, A., Iovescu, A. *Langmuir* **1998**, *14*, 5342–5346.
[35] Nagarajan, R. *J. Chem. Phys.* **1989**, *90*, 1980–1994.
[36] Robb, I. D., Stevenson, P. *Langmuir* **2000**, *16*, 7168–7172.
[37] Ladhe, A. R., Frailie, P., Hua, D., Darsillo, M., Bhattacharyya, D. *J. Membr. Sci.* **2009**, *326*, 460–471.
[38] Hestekin, J. A., Bachas, L. G., Bhattacharyya, D. *Ind. Eng. Chem. Res.* **2001**, *40*, 2668–2678.
[39] Ritchie, S. M. C., Bachas, L. G., Olin, T., Sikdar, S. K., Bhattacharyya, D. *Langmuir* **1999**, *15*, 6346–6357.
[40] Hollman, A. M., Bhattacharyya, D. *Langmuir* **2002**, *18*, 5946–5952.
[41] Hollman, A. M., Scherrer, N. T., Cammers-Goodwin, A., Bhattacharyya, D. *J. Membr. Sci.* **2004**, *239*, 65–79.
[42] Zhang, W., Nilsson, S. *Macromolecules* **1993**, *26*, 2866–2870.
[43] Nishizawa, M., Menon, V. P., Martin, C. R. *Science* **1995**, *268*, 700–702.
[44] Ito, Y., Park, Y. S., Imanishi, Y. *Langmuir* **2000**, *16*, 5376–5381.
[45] Hong, S. U., Miller, M. D., Bruening, M. L. *Ind. Eng. Chem. Res.* **2006**, *45*, 6284–6288.
[46] Krasemann, L., Tieke, B. *J. Membr. Sci.* **1998**, *150*, 23–30.
[47] Liu, X., Bruening, M. L. *Chem. Mater.* **2004**, *16*, 351–357.
[48] Shah, T. N., Ritchie, S. M. C. *Appl. Catal. A: Gen.* **2005**, *296*, 12–20.
[49] Feng, J., Lim, T.-T. *Chemosphere* **2005**, *59*, 1267–1277.
[50] Lowry, G. V., Johnson K. M. *Environ. Sci. Technol.* **2004**, *38*, 5208–5216.
[51] Zhang, W.-X., Wang, C.-B., Lien, H.-L. *Catal. Today* **1998**, *40*, 387–395.

Biographical Sketches

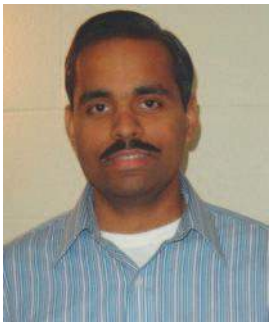

Dr. Abhay R Ladhe received his bachelor of chemical engineering degree from the University of Mumbai, Institute of Chemical Technology in 2003. Subsequently, in December 2008, he received his PhD degree from the Department of Chemical Engineering, University of Kentucky. Professor Bhattacharyya was his research advisor. Dr. Ladhe has published five articles and has made six presentations in various meetings. He was the recipient of Elias Klien Founders' travel award for International Congress on Membranes and Membrane Processes (ICOM) 2008, Honolulu, Hawaii. At the University of Kentucky, he also received the Research Challenge Trust Fund (RCTF) Fellowship. Dr. Ladhe joined Cargill Corporation in 2009 as a research chemical engineer.

Professor Dibakar Bhattacharyya (DB) is the University of Kentucky alumni professor of chemical engineering and a fellow of the American Institute of Chemical Engineers. He received his PhD from the Illinois Institute of Technology, MS from Northwestern University, and BS from Jadavpur University. He is the co-founder of the Center for Membrane Sciences at the University of Kentucky. He has published over 175 refereed journal articles and 20 book chapters, and has recently received four US patents (three on functionalized membranes, and one on hazardous waste destruction technology). He and his group developed a highly novel platform for the detoxification of organics by membrane-based nanoparticles. He and his graduate students have pioneered the development of functionalized membranes for enzyme catalysis, ultrahigh capacity metal capture, and nanostructured metal synthesis for environmental and bioapplications. Dr. Bhattacharyya has received a number of awards for his research and educational accomplishments, including the 2004 Kirwan Prize for Outstanding Research, Larry K. Cecil AIChE Environmental Division Award, the Kentucky Academy of Sciences Distinguished Scientist Award, Henry M. Lutes Award for Outstanding Undergraduate Engineering Educator, AIChE Outstanding Student Chapter Counselor Awards, and the University of Kentucky Great Teacher (1984, 1996, and 2008) Awards. He was the editor (with Butterfield as a coeditor) of a recently published (Elsevier) book *New Insights into Membrane Science and Technology: Polymeric and Biofunctional Membranes*. At the 2007 Annual Meeting of the North American Membrane Society, Dr. Bhattacharyya was honored for his contributions in the area of membranes and environmental applications.

This page intentionally left blank

1.03 Modeling and Simulation of Membrane Structure and Transport Properties

V N Burganos, Institute of Chemical Engineering and High Temperature Chemical Processes, Foundation for Research and Technology-Hellas, Patras, Greece

Nomenclature

B_o	hydraulic permeability of the membrane	c_s	speed of sound
c_i	concentration of species i	c_t	total concentration of a mixture
C_s	Cunningham correction factor	D_B	Brownian diffusivity

D_e	orientationally averaged effective diffusivity
D_i	transport diffusivity of species *i* within the pore structure
d_l	interface thickness
D_{ij}	binary ordinary diffusivity of component *i* in component *j*
$D_{ij,e}$	effective ordinary diffusivity of the (*ij*) pair
D_{im}	diffusion coefficient of component *i* in the membrane
D_K	Knudsen diffusivity
D_{Ke}	effective Knudsen diffusion coefficient
$D_{Ki,e}$	effective Knudsen diffusivity of component *i*
D_m	molecular diffusivity
d_m	molecular size
d_p	characteristic pore size
d_{par}	effective particle diameter
$D_{s,i}$	self-diffusivity of species *i* within the pore structure
$D_{x,y,ze}$	effective diffusivity in *x*-, *y*-, *z*-direction, respectively
E	potential energy
$\underset{\sim}{e}_i$	velocity in the *i*-direction in the lattice-Boltzmann method
F	Faraday constant
$\underset{\sim}{F}_i$	force acting on particle *i* in molecular dynamics
f_i	fugacity of species *i*
$f_i(\underset{\sim}{x},t)$	particle distribution
$f_i^{eq}(\underset{\sim}{x},t)$	equilibrium distribution function in the lattice-Boltzmann method
$f_i^{eq}(\underset{\sim}{x},t)$	solute distribution function in the lattice-Boltzmann method
f_T	transmission probability
$\underset{\sim}{g}_i$	force that accounts for all types of constraints
H	Hurst exponent
H_{st}	isosteric heat of adsorption
k_B	Boltzmann constant
K_H	Henry constant
Kn	Knudsen number, ratio of the mean free path to the mean pore size
m_i	mass of particle *i* in molecular dynamics
M_s	molecular weight of the sorbate
M_w	molecular weight
N_i	transport flux of species *i*
$\dot{N}_i$	transport rate in capillary *i*
p	pressure
Pe	Peclet number
P_i	membrane permeability
p_i	partial pressure of component *i*
p_0	vapor pressure for planar interfaces
q	scattering vector
q_{sat}	saturation concentration
R	ideal gas constant
R_f	random number in the interval (0, 1)
$R_Z(\underset{\sim}{u})$	normalized autocorrelation function
$\bar{r}$	hydraulic radius of the accessible pore space of the membrane
r_i	radius of capillary *i*
$\underset{\sim}{r}_i$	position vector of particle *i* in molecular dynamics
r_p	pore radius
S_α	accessible specific surface area
S_i	solubility
T	temperature
$T_{desired}$	desired temperature
T_{system}	temperature of the system
$\bar{u}$	mean thermal speed
u_i	species mobility
V_i	partial molar volume of species *i*
$\underset{\sim}{x}$	position vector
x_i	mole fraction of species *i*
Z	configurational integral
Z^{ig}	configurational integral for a sorbate molecule in an ideal gas phase
z_i	species charge number
$z(\underset{\sim}{x})$	phase function
α_i'	viscous selectivity parameter
β	$= (k_B T)^{-1}$
Γ_{ij}	thermodynamic correction factor for the (*ij*) pair
γ_i	activity coefficient of species *i*
$\gamma(r)$	density fluctuation autocorrelation function
Δc_i	concentration difference between exit and entrance faces
δ	thickness of the adsorbed layer
ε_α	accessible porosity
η_B	tortuosity factor for bulk diffusion
η_K	tortuosity factor
θ	contact angle
θ_i	fractional occupancy of the sorption sites by component *i*
θ_{n+1}	fraction of unoccupied sites
κ	fluid parameter in the nonideal lattice-Boltzmann model
λ	mean free path

μ	dynamic viscosity	ρ_s	solute density
μ_i	chemical potential of species *i*	σ	interfacial tension
ν	kinematic viscosity	σ_n	variance of random additions at stage *n* of the fBm process
ξ	displacement of a test molecule from its initial position	τ	relaxation time
ξ_x	displacement of a molecule in the *x*-direction	τ_s	solute relaxation time
ρ	density of the condensate	Φ	electrostatic potential
ρ_0	mass density of the solid	Ψ	free energy density functional
ρ_p	fluid density	ψ	bulk free energy density

1.03.1 Introduction

The design and preparation of membranes for the efficient separation of gas mixtures and fluid–solid systems relies heavily on the understanding of the effects of the internal structure of the membrane material on the transport and sorption during the separation process. Although such an interrelation is significant in numerous other applications of porous materials or more general transport systems, its role in membrane separations becomes truly crucial. It is straightforward to realize that the interaction of the mixture compounds with the membrane material is responsible, to a large extent, for the rate of their transport through the membrane or for their differential ability to percolate across the membrane or even for the accessibility of the interior of the membrane by the particular mixture species.

In fact, demanding separation processes nowadays call for materials that can offer a sieving operation at the molecular scale, thus excluding the passage of certain mixture species and selectively allow the transmission of others. A significant amount of research work has already been devoted to the in-depth understanding and quantification of the structure-to-separation interrelation using a multitude of experimental and theoretical techniques. Modeling and simulation techniques in membrane science have traditionally relied on similar efforts in the context of porous materials and have adapted appropriately structure approximations and flux relations. As a result, pore/grain/fiber models of the internal structure of membranes and their supports have appeared, followed by the application of single, binary, and multicomponent transport equations, usually involving some tortuosity factors. A significant improvement in the modeling of the pore structure was noted when computer-aided reconstruction techniques started to find extensive use in the literature of porous materials and, later, in that of membrane science. Such techniques have the clear advantage over earlier pore models that the description of the structure is in digital form and, as such, can lend itself directly to transport calculations, thus avoiding the assumption of specific geometry of the pores, grains, or any other structural element of the material. Progressively, the need to assume some value for the tortuosity factor was removed, thanks to the incorporation of molecular trajectories in the calculation of the diffusion coefficient in pore structures.

However, the need for detailed description of penetrant–membrane interactions cannot be removed as microporous materials become gradually the target material-type, at least for efficient gas separation. To this end, molecular simulations have enjoyed tremendous development in the field of membrane science in the recent years, addressing both the membrane material itself and the transport and sorption phenomena that take place during the separation process. Needless to say, substantial progress toward the accurate prediction of transport and structural properties would not be possible without the direct linking of molecular simulations with experimental data at the atomic level and also with quantum mechanical calculations. Among other pieces of information, the latter can deliver molecular geometry and electronic properties as well as accurate data on the molecular interaction potentials that can be introduced into the force field models of Monte Carlo and molecular dynamics techniques.

Nevertheless, despite the significant progress that has been made at the level of molecular simulations and the tremendous evolvement of computer

technology that allowed outstanding improvements in computer performance regarding memory, code compilation, and computational time, the length and time scales of molecular simulations remain several orders of magnitude below the macroscopic scale that is related to process design and process calculations. Hence, the design, preparation, and application of membrane materials have to rely on an appropriate bridging of the molecular scale results to the scale that would allow actual material engineering. To this end, it was recently realized that some kind of hierarchical modeling could provide the required leverage for the scale-up with minimal loss at each scale-transition of the accuracy that was offered by the computations at the previous scale. Although useful for all types of materials, such an approach is recognized nowadays as a necessity in the field of polymers, and consequently in that of polymeric membranes, where several levels of the so-called coarse-graining process are frequently required to fill the gap of about 10 orders of magnitude in the length-scale spectrum and 20 orders of magnitude in the time-scale spectrum [1]. Despite the rapid improvement of computer hardware, which on average doubles its efficiency every 2 years (Moore's law) [2] and, recently, does so almost every 18 months, essential progress in this respect requires faster algorithms and in-depth understanding of the underlying phenomena that will allow reliable filtering of the truly needed parameters in the simulations across scales.

More specifically, modeling of membrane materials and membrane processes is of indisputable significance not only for the understanding and description of material structure and penetrant transport but also for the reliable screening of material and module candidates based on performance and end-property predictions that they can offer. Consequently, membrane modeling and simulation can drastically alleviate the experimental workload by recommending suitable material structures and separation process conditions and, equally importantly, excluding whole ranges of poor candidates.

A separate but well-accepted contribution of modeling and simulation techniques in the field of membrane science and technology is that toward testing and validation of several theories that have been developed for the prediction of transport properties, usually within the general framework of effective medium approximation, volume averaging approaches, smooth field approximation, etc. Their attractiveness mainly stems from their simplicity and wide applicability to entire classes of materials, typically porous materials or blends of various components. However, the strong assumption that such theories usually invoke limits their accuracy to levels that may not be adequate for fine design or accurate process calculations. Therefore, one must resort to more advanced modeling and simulation techniques for testing these theories or even for modification of the working equations that usually quantify the underlying phenomena. Although the review of these theories is beyond the scope of this chapter, some reference to them is made in the context of assessment of the usefulness and performance of the various simulators.

The rest of this chapter is organized as follows. An overview of the main transport mechanisms during membrane-based gas mixture and fluid–solid separation is followed by a presentation of additional phenomena that take place during gas–liquid and liquid–liquid processing. Emphasis is placed on the treatment of nanoscale fluid transport, which becomes increasingly important and interesting in the field of microporous membrane separations. Although numerous publications in simulating diffusion at the nanoscale have appeared in the literature, the same is not true for the simulation of pressure-driven flow of mixtures at the nanoscale with or without simultaneous diffusive transport. Then, recent developments in the computer-aided reconstruction of the internal structure of porous membranes are discussed, followed by some fresh ideas on the adaptation of multiphase flow approaches to the digital representation of composite membranes. Once such digitized representations are available, a variety of transport phenomena can be simulated, and transport properties can be calculated without having to resort to tortuosity factors or any other structure-related geometrical or topological correction factor. Subsequently, the molecular scale is considered and the atomic scale reconstruction of inorganic and polymeric membrane materials is discussed. The concept of coarse graining in the context of hierarchical modeling is then presented and the interface with macroscopic flux formulations is discussed.

1.03.2 Mechanisms of Transport in Membranes

Depending on the nature of penetrants and their physical state, various transport mechanisms are possible, each of which requiring usually its own modeling approach. The overview that is presented here aims to provide the reader with the necessary

understanding of the transport mechanisms to the degree that will allow, in a later section, the adoption of the suitable modeling and simulation alternatives. This presentation will also serve as an introduction to the identification of the different scales that are encountered in membrane modeling.

1.03.2.1 Mechanisms of Gas Transport

Transport of gases through membranes and their supports may involve a large variety of mechanisms, separate or combined. Although different types of mechanism classification can be envisaged, it appears very convenient to employ two indices to identify the various transport regimes. The first one is the Knudsen number, Kn, which is defined as the ratio of the mean free path, λ, to some characteristic or average pore size, d_p, that is,

$$Kn = \frac{\lambda}{d_p} \tag{1}$$

The second index is the ratio of the molecule size (usually the equivalent sphere diameter), d_m, to the pore size:

$$b_m = \frac{d_m}{d_p} \tag{2}$$

1.03.2.1.1 Knudsen flow and diffusion

The so-called Knudsen transport (flow or diffusion) refers to the transport of gases through a pore or a porous material under conditions that correspond to very high Kn values. These conditions usually involve low pressure (large λ) or sufficiently small pores (small d_p), the latter being obviously critical in membrane separations. In this case, penetrant molecules exchange momentum almost exclusively with the pore walls due to the much higher frequency of molecule–wall collisions than that of gas phase molecular collisions (see **Figure 1(a)**). Practically, this mechanism dominates transport for $Kn > \sim 100$. Upon collision with the wall, the gas molecule

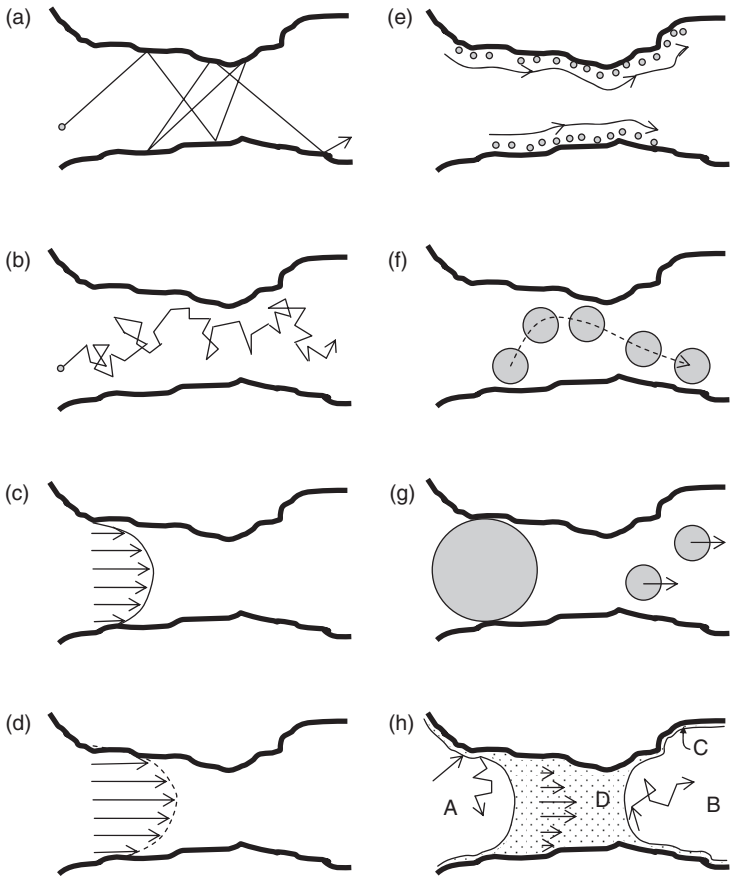

Figure 1 Schematic representation of fluid transport mechanisms in porous membranes.

undergoes a change in the direction of its motion, departing, typically, at a direction that is unrelated to the direction of the molecular path prior to collision. Such a diffuse reflection process is consistent with the assumption that the colliding molecule is momentarily adsorbed on the surface and is subsequently reemitted from it. The time that elapses during this adsorption stage is assumed to be sufficient for the molecule to lose completely its memory and, hence, to leave eventually the surface into a totally random direction. Experimental evidence has provided considerable support to this assumption, which is customarily used in the simulations within this transport regime, as discussed later.

Although both terms, namely, Knudsen flow and Knudsen diffusion, are usually employed interchangeably, strictly speaking the former term must be used for free-molecule transport under the action of a pressure gradient, whereas the latter under the action of a concentration gradient. Put in the form of a driving force formula, Knudsen transport follows the action of the driving force $\nabla p_i/RT$, where p_i is the partial pressure of component i, R the ideal gas constant, and T the temperature. Considering that $p_i = x_i p$, where p is the total pressure, it follows that

$$\nabla p_i = x_i \nabla p + p \nabla x_i \tag{3}$$

where x_i is the mole fraction of species i. It is, hence, apparent that both a pressure gradient and a composition gradient can give rise to gas transport [3].

The effective Knudsen diffusion coefficient $D_{K,e}$ is usually related to the tortuosity factor, η_K, that provides a measure of the resistance to gas transport owing to the presence of the pore walls along the tortuous pathways across the membrane itself or across the porous support structure, through the expression

$$D_{K,e} = \frac{\varepsilon_\alpha D_K(\bar{r})}{\eta_K} \tag{4}$$

In Equation (4), ε_α is the accessible porosity (the isolated void space does not contribute to transport) and $D_K(\bar{r})$ is the Knudsen diffusivity in an infinitely long cylindrical pore having radius equal to the hydraulic radius of the accessible pore space of the material, that is,

$$\bar{r} = \frac{2\varepsilon_\alpha}{S_\alpha} \tag{5}$$

where S_α is the accessible specific surface area.

The relation

$$D_K(\bar{r}) = \frac{2}{3}\bar{r}\,\bar{u} \tag{6}$$

where

$$\bar{u} = \sqrt{\frac{8RT}{\pi M_w}} \tag{7}$$

is the mean thermal speed of the gas molecules and M_w, the molecular weight, implies that $D_K(\bar{r})$ and, hence, $D_{K,e}$ are directly proportional to the quantity $(T/M_w)^{1/2}$. Hence, the separation factor for binary gas mixtures can be estimated from the square root of the inverse ratio of the molecular weights.

It is shown in a later section that the evaluation of the tortuosity factor, η_K, which is traditionally determined upon fitting to experimental data, can be actually calculated directly, under certain conditions, from modeling and simulation techniques.

1.03.2.1.2 Molecular or ordinary or bulk diffusion

In the small Kn regime, which is relevant at ambient or elevated pressures (small λ) or for relatively large pores (large d_p), gas molecules collide mainly with each other in the gas phase, the molecule–wall collisions being quite rare (see **Figure 1(b)**). This is the regime of molecular, ordinary, or bulk diffusion and, in practice, it is achieved for $Kn < \sim 0.01$. The effective bulk diffusion coefficient is usually expressed as

$$D_{B,e} = \frac{\varepsilon_\alpha D_m}{\eta_B} \tag{8}$$

where D_m is the molecular diffusivity in the absence of pore walls and η_B is the tortuosity factor for bulk diffusion. In general, $\eta_B \neq \eta_K$ due to the different level of resistance to transport that the gas molecules encounter in the interior of the porous material in the bulk and Knudsen diffusion regimes. Again, modeling and simulation techniques can, in principle, provide good estimates of η_B, thus avoiding resorting to fitting experimental data. In addition, as it is also the case in the Knudsen transport regime, models and simulators can elucidate the effect of the pore structure geometry and topology on the resistance to bulk diffusion in a membrane or in its support layer. However, it must be mentioned that the conditions (operating pressure, temperature, or structural features) that favor this transport mechanism are not of much interest in the gas mixture separation field due to the poor separation factors that can be achieved in

this case. However, it may well be one of the dominant mechanisms of transport in one of the support layers, yet, usually of limited importance to the overall process of gas separation.

1.03.2.1.3 Viscous flow

Under the action of a total pressure gradient, convective flow takes place and the exact driving force becomes $x_i \nabla p/RT$. That is, each mixture component is transported through the membrane at a rate which is proportional to its mole fraction and to the pressure gradient. For $Kn \ll 1$, the continuum assumption is valid and the classical Stokes, Navier–Stokes, or compressible momentum conservation equations can be used in the void space (see **Figure 1(c)**). However, integration over the entire membrane structure is far from straightforward due to the presence of the pore structure that is usually quite complicated. Hence, the Darcy equation or some other phenomenological equation is typically used, depending mainly on the porosity level and also on the degree of the equations that describe the boundary conditions. In general, the transport coefficient is, in this case, proportional to p/μ, where μ is the dynamic viscosity of the fluid. The proportionality constant is the viscous permeability, the value of which is characteristic of the particular membrane or support structure. Viscous flow in a porous membrane is not by itself very efficient regarding selectivity in a mixture separation, since the main hydraulic mechanism of separating the species is the differential driving of the species molecules toward the center or the edges of the pores. Usually, viscous flow is present as a consequence of a pressure drop across the two sides of the membrane but it occurs in combination with some diffusion mechanism that undertakes the main separation task.

1.03.2.1.4 Rarefied gas flow

In the event that the condition $Kn \ll 1$ is not met and the total pressure gradient is not zero, rarefied flow develops within the pore structure (see **Figure 1(d)**). Such a condition is frequently present in gas separations owing to the small size of the membrane pores. Although the two extremes ($Kn \ll 1$, continuum limit flow, and $Kn \gg 1$, Knudsen flow) have been addressed in a great number of publications and several books, the same is not true for moderate Kn values. The compressibility of the fluid and the position-dependent viscosity are among the complications that have probably hindered the extensive modeling treatment of this regime. Typically, in membrane separations, convective flow in the form of either continuum limit flow or rarefied fluid flow is accompanied by concentration gradient-driven diffusion of the mixture components, thus complicating further the modeling and simulation attempts. However, given the significance of the rarefied flow regime within the areas of micro- and nanofluidics, some special discussion on relevant modeling approaches is provided later in this chapter.

1.03.2.1.5 Surface diffusion

It is well known that all gases, to a greater or less extent, may get adsorbed on solid surfaces along which they may be transported, subject to some surface concentration gradient, before they are desorbed back into the gas phase (see **Figure 1(e)**). This mechanism of gas transport may become significant under certain conditions of pressure, temperature, and for a specific pore size range. Because of the practical difficulty in measuring or theoretically monitoring surface concentrations, it is preferred to resort to the adsorption isotherm when expressing surface diffusion fluxes and, thus, to employ the local concentration in the bulk phase instead. In the particular case of sufficiently small bulk concentrations to assume linearity in the adsorption isotherm, one may write that the surface flux of species i is proportional to the gradient of the bulk concentration gradient of this species, the proportionality constant being the product of the linearity constant of the adsorption isotherm (a function of temperature) and an effective surface diffusivity. The latter is the product of the surface diffusivity and the specific surface area of the membrane, multiplied by the porosity and divided by a tortuosity factor, η_s [4]. Although molecular simulations are the obvious choice for the description of surface diffusion, the straightforward additivity of the surface diffusion flux to the gas-phase diffusion flux has been customarily employed in phenomenological approaches.

1.03.2.1.6 Activated or configurational diffusion

Even though surface diffusion is itself an activated transport process in the sense that it requires some activation energy to take place, namely, the energy that is needed for hopping of adsorbed molecules from site to site on the pore surface, the term activated or configurational diffusion is typically reserved for the process of transport in micropores (<2 nm), the size of which is comparable to that of the penetrant molecules (see **Figure 1(f)**). Therefore,

many similarities between the phenomenology of surface diffusion and configurational diffusion exist. The practical difference relates to the fact that the pore size in the case of configurational diffusion is too small to allow any bulk motion and the entire process is controlled by the interactions of the gas molecules with the pore walls.

At least two different transport coefficients are relevant in this case. The self-diffusivity, $D_{s,i}$, is a measure of the translational mobility of the gas molecules of species i within the pore structure and is usually obtained from the calculation of the mean-square displacement per unit of time. The transport diffusivity, D_i, is defined as the proportionality constant between the species flux and the negative of the concentration gradient of the same species. The two diffusivities are usually related through the Darken equation [5]

$$D_i = D_{s,i}\left(\frac{\partial \ln f_i}{\partial \ln c_i}\right) \tag{9}$$

where f_i is the fugacity of species i and c_i the concentration of species i in the adsorbed phase per unit volume of the porous medium. This is an approximation and, strictly, one should use the so-called corrected diffusivity in place of the self-diffusivity in Equation (9) (corrected for the thermodynamic nonidealities).

In membrane-based separation of gas mixtures, the configurational and Knudsen diffusion mechanisms are the most significant ones. The latter leads to fluxes that are inversely proportional to the square root of the molecular weights of the species. The former provides permselectivities that depend on the shape and size of the gas molecules, the pore size, and the interactions between gas molecules and pore walls.

1.03.2.1.7 Molecular sieving

If the size of the membrane pores is between the size of the smaller and the larger molecules in a binary mixture, a sieving mechanism develops that can lead to very high separation factors (see **Figure 1(g)**). The same applies to multicomponent mixtures but further sieving will then be required to separate the components with molecule size below or above the mean pore size of the membrane. Separation factors greater than 10 could be achieved for membrane pore sizes below 0.5 nm. However, in practice, there is a distribution of pore sizes in the membrane and more moderate separation factors are usually reached. Significant research efforts are made to produce membranes with very narrow pore-size distribution in the molecular size range, without, however, sacrificing porosity and losing, therefore, valuable throughput. An additional feature in molecular sieving operation is that of reduced rigidity of the membrane structure (or increased deformability), which may influence drastically the relative ability of the penetrant molecules to pass through the pore space. This feature is encountered especially not only in polymeric membranes but also in inorganic ones, and is discussed later.

1.03.2.1.8 Condensation and capillary flow

As the relative pressure p/p_0 of the gas species is increased, where p_0 is the vapor pressure for planar interfaces, the amount of adsorbed gas on the pore walls increases and, progressively, the sorption site occupancy increases until saturation. Further increase of the relative pressure gives rise to the formation of adsorbed (liquid) layers, which, in turn, grow gradually in thickness and eventually coalesce, initially in small pores and progressively in larger ones (see **Figure 1(h)**). For a cylindrical pore, the capillary condensation pressure, p_c, is related to the pore radius, r_p, through the Kelvin equation

$$\frac{\rho RT}{M_w}\ln\frac{p_c}{p_0} = -\frac{2\sigma\cos\theta}{r_p - \delta} \tag{10}$$

where ρ is the density of the condensate, σ the interfacial tension, θ the contact angle, and δ the thickness of the adsorbed layer. Depending on the level of adsorption, different mechanisms of transport may occur simultaneously. For instance, in the situation depicted in **Figure 1(h)**, ordinary diffusion takes place in the gas-phase regions A and B, pressure-drop-driven hydrodynamic flow develops along the adsorbed (liquid) layers C, and capillary pressure-driven flow in area D.

Such situations develop very often in the interior of porous membranes, not only during operation (for instance, separation of mixtures of condensable gases) but also during certain pore-structure characterization procedures that involve condensable gases, as is the N_2 sorption/desorption technique. In both cases, one needs to have reliable models that will be able to describe and monitor the condensation and capillary flow phenomena, which, in turn, necessitate

the availability of simulators of two-phase flow equipped with the phase transition feature.

It must have become obvious from the above that several different mechanisms of gas transport in membranes may develop and become dominant depending on the nature of the gas–membrane interactions, the membrane pore size, the prevailing conditions, and the nature of the gaseous penetrants (permanent gases or condensable vapors, etc.). In practice, one expects that more than one mechanisms are likely to occur simultaneously because, typically, the membrane pore size follows a certain distribution across the structure. A usual combination of transport mechanisms in the support layers is that of Knudsen and ordinary diffusion in the so-called transition diffusion regime, in which case both gas-phase and gas-surface collisions are responsible for the momentum transfer. Other typical examples are the combination of surface and configurational diffusion in the active membrane layer, the combination of convective and diffusive transport in the support layers, and the combination of liquid- and gas-phase transport with or without phase transition in all layers.

1.03.2.2 Mechanisms of Transport in Fluid–Solid Separations

In the presence of solid particles or solutes in the fluid stream, additional transport mechanisms need to be considered, which usually pertain not only to the interaction of the particles with the external membrane surfaces and internal pore walls but also with the carrying fluid or with the solvent.

1.03.2.2.1 Fluid transport

The mechanisms of fluid transport in fluid–solid separations are mainly viscous flow in the case of liquid suspensions and flow with or without diffusion in the case of aerosols. Usually, the flow field in the interior of the membrane is calculated as the result of the action of an externally applied pressure drop across the two sides of the membrane. However, depending on the pore size, features of transport that are related to the existence of very narrow pathways may become significant, as is the case of the flow in nanofiltration (NF) membranes. The validity of the continuum assumption is the main issue that is raised in these cases.

1.03.2.2.2 Transport of suspended particles

Depending on the relative size of suspended particles and membrane pores but also on particle–wall interactions, various mechanisms of permeation through or rejection from the membrane structure can be distinguished. The main types are summarized below.

Hydrodynamic convection. Particles are, in general, carried along by hydrodynamic drag that originates from the flow field that develops in the interior of the membrane. As the particles approach the pore walls, some significant hydrodynamic resistance comes to hinder their collision with the solid surface, which increases rapidly with decreasing clearance and tends to infinity upon contact if both the particle and the wall are nonporous. If at least one of the two bodies is permeable, then the hydrodynamic resistance remains finite as the stress that is applied to the fluid is dissipated into the porous body. Because of the great significance of these phenomena, intensive analytical and numerical efforts have been made for the calculation of correction factors to the classical Stokes hydrodynamic force expression for both porous and nonporous bodies, during normal or tangential motion of the particles relative to the pore wall (see, for instance, References 6–12). It is also interesting to note that in the vicinity of the wall, hydrodynamic torque becomes considerable giving rise to particle rotation prior to potential capture.

Sedimentation and flotation. Gravitational effects are usually significant for particles larger than about 1 μm. Depending on the relative density of particles to that of the carrying fluid, sedimentation or flotation may arise. Nevertheless, in most cases gravitational effects act in combination with other migration mechanisms, like hydrodynamically driven migration, as mentioned above.

Particle–wall interactions. In the vicinity of the pore walls, particle–surface interactions become significant and as the particle approaches the wall, they become dominant. Usually, London van der Waals and electrokinetic double-layer interactions determine the motion of particles in the close vicinity of the pore walls. The attraction that is caused by the former and, usually, also by the latter changes in most cases – depending, of course, on the sign of surface and solution charges – to a net repulsion at clearances smaller than a critical value due to the switch of the double-layer forces to rapidly increasing repulsive ones.

Despite the obvious need for estimates of the physicochemical constants to describe quantitatively these interactions, it has been shown that once these constants are below or above some critical values, the particle retention rate is not sensitive to the precise value of these constants [13]. It must be stressed that in NF membranes, where the pore size is usually smaller than 10 nm, such electrokinetic phenomena may become dominant and extend over the entire membrane domain resulting, in many cases, in quite high rejection rates.

Sieving. Size exclusion-based separation is theoretically the simplest mechanism of retention of suspended particles that can also lead to very high filtration efficiencies. However, small pore size usually implies unacceptably low permeation, which decreases further during filter operation due to the creation of a cake on the feed side of the membrane requiring some special treatment for its removal, typically backwashing.

Particle diffusion. In liquid filtration, Brownian diffusion may become a significant transport mechanism for submicron particles. For sufficiently small values of the ratio d_{par}/d_p, where d_{par} is the effective particle diameter, the process can be assumed to occur in the continuum limit and, consequently, it can be treated as a mass diffusion process that can be described by the classical diffusion equation. In this case, the ordinary diffusion coefficient is replaced by the Brownian diffusivity, given by

$$D_B = \frac{C_s k_B T}{3\pi\mu d_{par}} \tag{11}$$

where C_s is the Cunningham correction factor and k_B the Boltzmann constant. If both hydrodynamic drag and Brownian forces are significant, the particle displacement results from the combination of a convective step (determined solely by the local fluid velocity and the time step) and a Brownian step (of random direction and with magnitude that is determined by the Brownian diffusivity and the time step). In the case of aerosols, a similar description of particulate transport applies except that the diffusivity of the submicron particles is used in place of the ordinary diffusion coefficient in the classical mass diffusion formulation.

1.03.2.3 Mechanisms of Transport in Nonporous Membranes

In nonporous (dense) membranes, transport of species can take place only through the membrane material itself, usually in the general sequence of solution, diffusion, and eventual discharge. That is, the species is first dissolved into the entrance face of the membrane, travels in the interior of the membrane material through some diffusion or conduction process, and eventually exits from the other side into the effluent stream. Consequently, the separation efficiency of the membrane is a function of the solubility ratio and diffusivity ratio for a binary separation.

Depending on the nature of the transported species and that of the membrane material, different types of dissolution and diffusion are encountered in dense membranes. Of particular interest are the ionic conducting membranes, including most notably solid oxides and proton exchange membranes. Among other applications, these materials have a central role in fuel cells and, thus, have attracted tremendous attention from investigators in basic and applied material science and material engineering.

Solid oxides conduct oxygen and mixed ionic electronic conductors conduct both oxygen ions and electrons. The oxygen permeation process involves usually the following steps: electrochemical surface reaction at the entrance face of the membrane to create oxygen ions, transport of oxygen ions through the bulk oxide via a sequence of oxygen vacancies, and surface oxidation reaction at the exit face forming molecular oxygen. The exceptional selectivity of these membranes and the relatively high fluxes that are achieved compared to the polymeric membranes are the main attractive features of these materials. However, there are still some technical problems that must be overcome before large modules of them become operational, like thermal gradient-induced cracking, sealing issues, etc.

Proton exchange membranes can be either polymeric or inorganic and can be used in power-generation devices as they conduct protons. Although several types of proton exchange membranes have already been synthesized, Nafion® appears to be the most studied one. In sulfonated polymers such as Nafion®, the hydrogen ions in the SO_3H groups become mobilized upon addition of water. A possible mechanism of hydrogen ion transport through the membrane is that of proton addition into a water molecule, hopping across the water molecule and then onto another water molecule, and so on. An alternative or simultaneous transport mechanism might involve proton combination with a water molecule into a complex molecule followed by diffusion of this complex molecule through the membrane material.

It is speculated that water becomes less bound as hydration progresses giving rise to the creation of a network of pathways through the membrane. In turn, this implies the development of additional mechanisms of transport, from simple percolation to hydrodynamic flow of water and convective diffusion of ions [14]. The Nernst–Planck equation is relevant in this case, which in the single-phase approximation of the membrane reads

$$N_i = -z_i u_i F c_i \nabla \Phi - D_i \nabla c_i + c_i u \qquad (12)$$

where N_i is the transport flux of species i, z_i is the species charge number, u_i is the species mobility, c_i is the species concentration, F is the Faraday constant, Φ is the potential, D_i is the species diffusivity, and u is the solvent velocity. The first term represents the species migration due to a potential gradient; the second term stands for the purely diffusive contribution to the species flux, and the third term represents the convective flux of the species, which results from the flow field of the solvent. The latter becomes meaningful at sufficiently high hydration levels so that individual pore segments have the opportunity to develop in the interior of the membrane. In fact, such a bulk pathway formation is held responsible for undesirable crossover of fuel during fuel-cell operation. Hindrance effects can be included in this equation through the introduction of correction factors to the convection and diffusion/mobility terms.

In membrane-based ionic separations, as are the cases of NF and reverse osmosis (RO) for water desalination, steric hindrances combined with the Donnan and polarization layer effects come to add themselves to the mechanisms of ion transport through the membrane. In these cases, one has to take into account the corresponding terms in the calculation of the overall transport potential across the membrane and address the phenomena such as exclusion-enrichment and partitioning at the membrane–bulk interface. An excellent review of transport phenomena in nanofluidics with emphasis on electrokinetic phenomena was recently provided by Schoch *et al.* [15].

1.03.3 Modeling Approaches

The variety of transport mechanisms that may control transport in the interior of membranes and of their porous supports complicates accurate modeling and simulation of the separation or reactive process. This complication becomes far more severe if the interplay of these mechanisms with the usually tortuous structure of the membrane is taken into account. In fact, the interrelation between structural features and end properties is the main target of modeling efforts not only in the membrane sector but in the more general class of functional materials. In the particular case of membranes, however, this becomes a truly multiple scale task for two reasons: first, the separation of two or more species is usually controlled at the microscopic scale (molecular or finest pore scale) and second, membranes are typically very thin and require various layers of support to improve their mechanical and functional properties. In order to address this complexity, modeling not only at individual scales but also across scales is needed. The analysis that follows borrows concepts and ideas from the more general class of porous materials taking into account, wherever needed, the peculiarities of the membrane materials. The goal is to provide a framework of transport modeling and simulation in membranes in a top-bottom approach so that key measurable quantities can be identified on the one hand, and the main modeling pathways are presented on the other as the internal membrane features are gradually zoomed in.

1.03.3.1 Flux Relations – Phenomenology

The simplest and most convenient description of transport phenomena in membranes that provides also a quantitative relationship between driving force and resulting flux is the one that transport phenomenology has to offer. In fact, this is also a very useful approach for the organization and compilation of experimental data (flux measurements under conditions of pressure or composition gradients). In the general case of multicomponent diffusion of ideal gases in the absence of pore walls, the Stefan Maxwell equations apply:

$$-\frac{1}{RT}\nabla p_i = \sum_{\substack{j=1 \\ j\neq i}}^{n} \frac{x_j N_i - x_i N_j}{D_{ij}}, \; i = 1, \ldots, n \qquad (13)$$

where p_i is the partial pressure of component i, x_i, N_i are the mole fraction and molar flux of component i, respectively, and D_{ij} is the binary ordinary diffusivity of component i in component j. In the presence of pore walls (case of porous membranes), Equations (13) take the form of the so-called dusty-gas

equations (see, for instance, Reference 4 for further discussion):

$$-\frac{1}{RT}\nabla p_i = \sum_{\substack{j=1 \\ j\neq i}}^{n} \frac{x_j N_i - x_i N_j}{D_{ij,\mathrm{e}}} + \frac{N_i}{D_{Ki,\mathrm{e}}}, \; i = 1, \ldots, n \quad (14)$$

where $D_{ij,\mathrm{e}}$ is the effective ordinary or bulk diffusivity of the (ij) pair and $D_{Ki,\mathrm{e}}$ is the effective Knudsen diffusivity of component i. A common way to express the effective diffusivities is through

$$D_{ij,\mathrm{e}} = \frac{\varepsilon_\alpha}{\eta_\mathrm{B}} D_{ij} \quad (15)$$

and

$$D_{Ki,\mathrm{e}} = \frac{\varepsilon_\alpha}{\eta_\mathrm{K}} D_\mathrm{K}\left(\bar{r}_\mathrm{p}\right) \quad (16)$$

with $\bar{r}_\mathrm{P}$ given by Equation (5). In Equations (15) and (16), ε_α is the accessible porosity whereas the tortuosity factors, η_B and η_K, are the same as those used in Equations (4) and (8). In fact, the statement that the tortuosity factor for self-diffusion in the bulk diffusion regime is the same with that for binary diffusion is not of obvious validity. However, this has been verified experimentally and confirmed theoretically by Sotirchos and Burganos [16] following a rigorous spectral analysis treatment of multicomponent diffusion in pore networks combined with the effective medium theory and the smooth field approximation. More specifically, it was proved by Burganos and Sotirchos [17] that the diffusional resistance of a network of pores of nonuniform size is, to an excellent approximation, practically identical to that of a network of uniformly sized pores with the same topology as that of the original network, provided that the effective pore diffusivity is calculated from the effective medium theory equation. Once homogenized, the overall effective diffusivity can be obtained in a straightforward fashion; for instance, the smooth field approximation can be used as it becomes exact for regular networks of pores. If this methodology is applied to multicomponent mixtures [16], similar expressions and conclusions can be extracted using a spectral analysis and it turns out that not only the Knudsen tortuosity factor but also the bulk tortuosity factor is the same for each component. This is a very convenient observation that simplifies tremendously the measurement or computation of tortuosity factors as they need to be determined only once, for any species, and can then be applied to the rest of the mixture components as well.

For nonideal mixtures, the multicomponent diffusion equations must be modified to include the chemical potential gradients in place of the partial pressure ones. The flux equations can then be recast in the form

$$-\frac{x_i}{RT}\nabla_T \mu_i = \sum_{j\neq i} \frac{x_j N_i - x_i N_j}{c_t D_{ij,\mathrm{e}}} \quad (17)$$

in the absence of pore walls, with c_t the total concentration of the mixture [18]. The Gibbs–Duhem equation implies that only $n - 1$ of Equations (17) are independent, since

$$\sum_{i=1}^{n} c_i \nabla_T \mu_i = \nabla p \quad (18)$$

In the presence of pore walls and under the action of external forces (here, electrostatic force), the flux equations take the form

$$-\frac{x_i}{RT}\nabla_{T,p}\mu_i - \frac{x_i}{RT}V_i\nabla p - \frac{x_i}{RT}z_i F\nabla\Phi = \sum_{j+i}\frac{x_j N_i - x_i N_j}{c_t D_{ij,\mathrm{e}}} + \frac{N_i}{c_t D_{Ki,\mathrm{e}}} \quad (19)$$

where V_i is the partial molar volume of species i, F is the Faraday constant, and Φ is the electrostatic potential (see [18] for a discussion). The total pressure gradient that applies in addition to the composition gradient gives rise to viscous flow of the mixture and, hence, to convective fluxes for each component that are additive to the diffusive fluxes. For ideal gases, it has been shown following a similar spectral analysis for multicomponent convective diffusion in pore networks as the one mentioned above and applying the effective medium theory followed by the smooth field approximation, that a single tortuosity factor is required for the convective part of the fluxes, which is the same for all components [19]. For nonideal gases, in the presence of viscous flow the flux equations become

$$-\frac{c_i}{RT}\nabla_{T,p}\mu_i - \frac{c_i}{RT}V_i\nabla p - \alpha_i' c_i \frac{B_0}{\eta_\mathrm{B} D_{Ki,\mathrm{e}}}\nabla p - c_i z_i \frac{F}{RT}\nabla\Phi = \sum_{j=1}^{n}\frac{x_j N_i - x_i N_j}{D_{ij,\mathrm{e}}} + \frac{N_i}{D_{Ki,\mathrm{e}}} \quad (20)$$

where c_i is the molar concentration of component i, α_i' is a viscous selectivity parameter, B_0 is the permeability of the membrane, and D_{im} is the diffusion coefficient of component i in the interior of the membrane [18, 20]. It is accepted that viscous flow has some separative effect on the mixture transport

through the membrane: larger molecules will tend to move close to the center of the pore, whereas smaller molecules may more easily stay closer to the walls and attach to them depending on their size and on physicochemical interactions. Needless to say, flow may also induce a straining or sieving effect on the mixture transport since larger molecules may be driven to stationary regions of flow due to inertia, where they may get trapped, whereas smaller molecules are more likely to follow the streamlines (in the absence of diffusion) and be transmitted over to the permeate side.

The case of micropore diffusion is of particular interest in the context of membrane-based gas separations. Given the very small size of the pores (< 2 nm), which in this case is similar to that of penetrant molecules, the gas–wall interactions become dominant (configurational diffusion) and hopping from sorption site to sorption site becomes the main mechanism of transport. This surface diffusion mechanism is obviously affected by the availability of vacant or occupied sites and the dusty gas equations now assume the form [18]

$$-\nabla\mu_i = RT\sum_{j=1}^{n}\theta_j\frac{u_i-u_j}{D_{ij,S}} + RT\theta_{n+1}\frac{u_i-u_{n+1}}{D_{i,n+1,S}},\ i=1,\ldots,n \tag{21}$$

where $-\nabla\mu_i$ is the surface chemical potential gradient, u_i is the velocity of species i, θ_i is the fractional occupancy of the sorption sites by component i, and θ_{n+1} is the fraction of unoccupied sites

$$\theta_{n+1} = 1-\sum_{i=1}^{n}\theta_i \tag{22}$$

The relation of the chemical potential gradients to those of the surface occupancies is usually cast in the form [18]

$$\frac{\theta_i}{RT}\nabla\mu_i = \sum_{j=1}^{n}\Gamma_{ij}\nabla\theta_j \tag{23}$$

where Γ_{ij} is a thermodynamic factor defined as

$$\Gamma_{ij} = \theta_i\frac{\partial\ln p_i}{\partial\theta_j},\quad i,j=1,\ldots,n. \tag{24}$$

The missing link between occupancies and partial pressures of the various components is provided by the adsorption isotherm for the particular mixture.

In terms of the surface fluxes, $N_{i,s}$, the dusty gas equations for micropore diffusion of multicomponent mixtures become

$$-\frac{\theta_i}{RT}\nabla\mu_i = \sum_{\substack{j=1\\ j\neq i}}^{n}\frac{\theta_j N_{i,s}-\theta_i N_{j,s}}{\rho_p\varepsilon_\alpha q_{sat}D_{ij,S}} + \frac{N_{i,S}}{\rho_p\varepsilon_\alpha q_{sat}D_{i,S}},\ i=1,\ldots,n \tag{25}$$

where ρ_p is the fluid density, q_{sat} is the saturation concentration, and subscript S denotes surface terms. An excellent review of the Maxwell-Stefan approach to mass transfer along with a detailed presentation and discussion of the aforementioned equations are given in [18].

Membrane structure connectivity and pore-blocking effects have also attracted the interest of investigators in microporous membrane separations [21]. These flux relations find extensive use in applications that involve gas sorption and diffusion in zeolites. However, it must be stressed that this phenomenological approach, although quite useful in guiding experimentalists, provides no information on the magnitudes of the diffusion coefficients much less on their dependence on the membrane material and structure or on the externally applied conditions of separation. Any progress on this issue would require investigation of the internal pore structure of a membrane and switching scale of observation down to the pore or grain scale, as described next.

1.03.3.2 Pore-Scale Modeling

The need to have quantitative estimates of the transport coefficients in porous materials inspired a large variety of simplified descriptions of their internal structure.

1.03.3.2.1 Pore models

The simplest and earliest attempts involved the assumption of straight, uniform, parallel capillaries spanning the interior of the material in the direction of macroscopic transport. Although overly simplistic in concept, this model has been adopted by numerous investigators, who had to invoke a correction factor in their calculations that would account for the usually complex structure in actual porous media. This is also a very attractive model for experimentalists, as they only need to measure this tortuosity factor once for each material sample and, thus, achieve a simple transformation from the transport property in the absence of walls to the effective one that reflects the interactions of the penetrant species with the pore walls. Despite the criticism that such an oversimplification has

experienced, it appears that in certain cases of modern membrane technology and applications, its employment offers a quite realistic representation of the actual situation. More specifically, several production routes in the food and pharmaceutical industries demand narrow droplet or particle-size distributions that can be provided by membranes with almost uniform, parallel pores of constant cross section. The manufacturing of such idealistic membranes is already in the market and, obviously, among all other practical advantages that they offer, they also allow a relatively straightforward physical description and mathematical modeling of the transport phenomena that underlie the membrane operation (typically, emulsification in a wider sense of the term). It is interesting to note that this is the only, practically, case in which the tortuosity factor becomes approximately equal to 1, provided of course that the transport coefficient is not dependent upon the pore size or the species concentration. A typical example is that of ordinary diffusion of a trace component in pores with sufficiently large diameter to exclude activated or configurational diffusion phenomena. Then, the transport rate, $\dot{N}_k$, through any capillary i would be given from

$$\dot{N}_k = -D_k \pi r_k^2 \frac{\Delta c_k}{L} \tag{26}$$

where r_k is the radius of capillary k, D_k is the diffusivity of this species in capillary k, Δc_k is the concentration difference between exit and entrance faces, and L is the length of the capillary in the direction of transport. The transport flux is then given by

$$\begin{aligned} N_D &= \frac{\sum_k \dot{N}_{ik}}{A} \\ &= -\pi \frac{\sum D_k r_k^2}{A} \frac{\Delta c}{L} \end{aligned} \tag{27}$$

where the concentration drop is assumed to be the same for all capillaries (uniform concentration across the entrance and across the exit face). If the diffusivity is independent of the pore size, then Equation (27) becomes

$$N_D = -\varepsilon D \frac{\Delta c}{L} \tag{28}$$

which by comparison with Equation (8) implies that $\eta_B = 1$. This result is valid not only for uniform capillaries but for distributed sizes also provided that all capillaries are parallel to the macroscopic transport direction and do not overlap.

Similar results can be obtained for other transport mechanisms in parallel, nonoverlapping pores, provided that the transport coefficient does not depend on the pore size or the local pressure or concentration. This is, for instance, the case of viscous, incompressible flow of liquids in membranes. For an ideal gas flowing in a cylindrical capillary under the action of a pressure gradient in the z-direction, the flux expression reads

$$N_v = -\frac{r^2 p}{8\mu RT} \frac{\mathrm{d}p}{\mathrm{d}z} \tag{29}$$

The overall flux can then be found in a fashion similar to that used above for the diffusion case. To become more realistic, pore models evolved into models of multidimensional arrays of parallel pores, overlapping or nonoverlapping. In the latter case, the tortuosity factor was shown to equal 2 for two-dimensional sets of pores provided that the concentration gradient vector lies on the plane that is defined by the pore axes, and 3 for three-dimensional sets of pores, provided that the transport coefficient is orientationally averaged [17]. This simple and convenient result is valid not only for single or binary diffusion but also for multicomponent diffusion as it was shown by a spectral analysis method that employed the effective medium theory followed by the rigorous application of the smooth field approximation [16].

However, if the pores are allowed to overlap, then the simple flux expressions for individual capillaries become invalid and a different technique must be employed. More specifically, if the ratio of the molecular size to the size of the pores or, in general, to some characteristic size of the interstitial space in the interior of the membrane is sufficiently small to justify treatment of the traveling molecule as a mathematical point and neglecting interactions with the pore walls other than diffuse reflection from them, random molecular trajectories can be computed, subject to the prevailing conditions of transport. This is an effort that attracted the strong interest of investigators in the area of porous media in the 1980s and elucidated strongly the effects of pore structural features on the transport (mainly diffusion) coefficients. This technique, along with other techniques that can be used for the simulation of flow and dispersion in porous membranes, is discussed in the next section.

The addition of spherical chambers to a network of capillaries introduces a rich variety of pore geometries and interfaces into the pore-type representation of the

structure of porous membranes. This can be done in a well-defined and ordered manner, like the introduction of spherical chambers at the junctions of regular networks of capillaries [22, 23], or in a random, orderless fashion [24]. In both cases, one may assume entirely random sampling of sphere and cylinder sizes to decorate the network or prescribe some spatial correlation of sizes among chambers, among capillaries, or among chambers and capillaries. Obviously, the prediction of transport coefficients in such pore structures has to resort to trajectory computations or numerical techniques due to the inevitable appearance of considerable overlapping among pore segments. Despite the increased complexity in the construction of such pore space representations and in the prediction of their transport properties, they have found extensive use in a wide variety of porous materials, including porous rocks, catalysts, membranes, etc. The main supporting argument of their use is that they appear to represent the pore space of a variety of porous materials better than capillary networks do. In fact, optical or electron microscopy analysis of consolidated materials indicate the existence of large pore spaces that are interconnected through narrow pore necks. In addition, it is often convenient to represent the nonsolid space of granular materials by a collection of large cavities and narrow interconnectors. Alternatively, these domains can also be represented by networks of pore necks with converging–diverging geometry (for instance, sinusoidally shaped ends). The former is more suitable for unconsolidated materials, whereas the latter is usually employed for the description of the interstitial space in low porosity, consolidated materials. Thanks to the limited pore overlap in low porosity materials, the technique of the equivalent resistor network approximation can be used for the determination of the overall flow permeability or gas diffusivity [23].

Briefly, the resistor network approach proceeds as follows. Suppose that the pore space of a membrane can be represented by a regular network of capillaries with sinusoidally shaped ends [25]. The decoration of the network bonds with cylindrical segments is achieved through appropriate sampling from the pore-size distribution that results, for instance, from the intrusion part of the mercury porosimetry curve [22]. The chamber sites that define the sizes of the sinusoidal openings at the two capillary ends can be sampled from the size distribution of large cavities as they are recognized and quantified from optical or electron microscopy analyses. The review of efforts for the determination of the detailed pore topology is beyond the scope of this chapter. It is noteworthy, however, that elimination of the diameter of a capillary renders the particular bond nontransmitting, thus reducing the local coordination number (i.e., the number of bonds that meet at an intersection) by 1. Application of this pore-eliminating concept to the entire network with a certain probability at each neck allows easily the adjustment of the average coordination number to the desired value. Subsequently, the flow or diffusion rate in each individual pore is calculated with some numerical or analytical technique. The application of the mass conservation condition (Kirchoff's law in the electrical resistor analog) gives rise to a set of linear algebraic equations in terms of the pressure or concentration value at each node of the network. These equations are complemented by the appropriate boundary conditions (usually fixed pressure or composition at the entrance and exit faces, and periodicity at the lateral faces) and solved numerically using some conjugate gradient or Gauss–Seidel with relaxation technique. Once the nodal values for the pressure or the concentration are determined, the overall transport property can be calculated in a straightforward manner from the definition of the effective transport coefficient and taking into account the local pressure or composition differences across, usually, the array of those pores that are connected to the exit face or across the entire network [23]. However, care must be exercised before this technique is applied to membranes with micro- or mesopores since the continuum assumption may no longer be valid and some discrete simulation technique may be more appropriate to use, as discussed in the next section.

1.03.3.2.2 Grain models

The representation of the solid part of porous membranes by grain packings is a rather realistic approach in several cases, particularly when micro- or nanopowders are used as precursors of the final membrane. The construction of the grain model of a membrane can proceed as follows. Initially, transmission electron microscopy analysis of the powder is performed and digital images are obtained. Image processing and image analysis are nowadays possible through appropriate software and allow the direct or algorithmic counting of grains per unit projected area or the measurement of the equivalent sphere diameters of the grains. Mercury porosimetry or gas adsorption–desorption can be used for the determination of the accessible porosity and the specific

surface area of the powder. Once these quantities, along with the grain size distribution, are known, a packing simulator can lead to the three-dimensional reconstruction of the powder that will reproduce all the aforementioned measurable properties.

Different packing models and simulators have been suggested in the literature (see, for instance, References 26–28). A typical one, using the ballistic packing concept, would proceed as follows. First, spherical grain diameters can be sampled from the original (prior to compaction and heating) powder size distribution, which is obtained using image-processing software as described above.

Subsequently, gravity-driven packing can be applied to simulate powder packing prior to compression. In fact, any body force into a fixed direction would give the same result for sufficiently large systems, since gravity itself may not be the dominant external force for the nanopowder at hand. The diameters that have been sampled are assigned to spherical grains that are allowed to move in the direction of the external force one at a time. Typically, a rectangular vessel can be used as a physical container of the nanopowder, and periodicity is applied in directions that are normal to the direction of the external force. Once contact of the sphere with the bottom side of the vessel is made, the sphere is immobilized and a new sphere is allowed to move along the direction of the external force. If the sphere touches another sphere that has already been immobilized, a decision must be made as to whether it will stay there or will continue its trajectory. The criterion is certainly related to the desired value of the porosity of the nanopowder, which is determined experimentally as described above. Immediate immobilization upon first contact will lead to relatively high porosity values. If more dense packings are sought, then the sphere is allowed to roll over the surface of the sphere that it has encountered until it comes in contact with a second sphere. At this position (two contact points) a decision has to be made as above. Depending on the actual packing density, the sphere may get immobilized or roll over both spheres until it acquires a third contact point [29]. The sticking probability is common for all spheres and is chosen in a way that allows eventually the desired porosity value to be approached. In the aforementioned procedure, sorting of the spheres to be dropped with respect to their size is expected to affect significantly the outcome of the simulation regarding the maximum density that can be achieved but also the homogeneity of the porosity across the reconstructed nanopowder. More specifically, if the large spheres are dropped first, a relatively high value of porosity will be initially obtained, which will be gradually lowered as smaller spheres are dropped and allowed to penetrate into the void space among the larger ones. On the other hand, if the small spheres are dropped first, a relatively dense packing will be formulated that will remain practically unaltered by the subsequent dropping of the larger spheres. In this case, density gradient packings will be generated which may or may not be realistic depending on the actual physical process of generating the nanopowder. Alternatively, a Monte Carlo procedure can be employed to generate random packings [27]: at each step, a set of N spheres is dropped simultaneously and only the one that reaches the lowest position is retained as the new member of the stack. This procedure was found to perform satisfactorily for sufficiently large N ($>10^5$).

To simulate sintering of the nanopowder, which is usually required to improve the mechanical properties of the material, mass transfer between touching grains must be allowed. Different algorithms have been presented in the literature for the construction of sintered materials with increased grain sizes (see, for instance, the work by Roberts and Schwartz [28]). If electron microscope images of the actual sintered sample are available, the grain size distribution can be determined using an image-analysis technique and the number density of grains per unit area can also be counted. This information can be used in the following way [29]. Rather than developing simulators of the mass transfer at the microscopic scale, a shortcut can be devised, that allows partial or complete mass transfer from smaller grains to larger grains provided they are in contact with each other. The decision as to whether complete, partial, or no mass transfer will be assumed is based on the selection of a critical ratio of sizes of the touching grains, which ensures that eventually the desired grain size distribution and number density of grains are recovered. The smaller the critical size ratio (smaller to larger grain size) for mass transfer to occur, the more limited the extent of sintering and, hence, the smaller the effect on the porosity and the grain size distribution. In order to capture also intermediate stages of the sintering process for two or more touching grains, incomplete mass transfer can be assumed to occur in cases where the size ratios are within a specific interval of ratio values. To increase the accuracy of the simulations and to render the whole process more realistic, the characteristic times of partial or complete mass transfer can be employed either from experiments or from independent sintering models for

touching grains. It has been observed that both the sintering temperature and the heating ramp can affect the mass transfer process and its kinetics [30]. Such a shortcut approach circumvents the need to get into the details of the sintering process, as it is guided by direct electron microscope images of the sintered material through a two-parameter procedure. Obviously, several variants of this methodology can be formulated but it is noteworthy that the outcome is in any case a three-dimensional granular structure with features that are consistent with the actual ones and can directly lend itself to flow, mass transport, or sorption computations without having to resort to any arbitrary geometrical or topological assumptions.

However, the lack of topologically ordered, straight conduits of transport in grain models excludes the employment of the convenient resistor network technique for the calculation of effective transport properties. Numerical techniques must be used for the solution of the differential equations that describe diffusion, flow, or convective diffusion subject to the impermeable grain condition that is usually invoked. If the grains themselves are porous, then a separate treatment of the transport through them is required (for instance, Darcy or Brinkman equation) and the impermeable grain condition is replaced by the continuity of flux at the grain surface. In addition to the numerical techniques that discretize the differential equation (finite differences, for instance), other techniques can also be used to solve the diffusion and flow problems in the space among the solid grains, like the lattice-Boltzmann technique, the Direct Simulation Monte Carlo (DSMC) technique, and the transmission probability or mean-square displacement techniques. The advantage of these methods over the more conventional numerical techniques is that they can be used also in the case of elevated Knudsen number, which is of strong interest in separation applications involving porous membranes. These techniques are discussed in the next section.

1.03.3.2.3 Fiber models

The use of fibrous materials for the construction of filters, membranes, and electrodes for diverse applications is quite common. Reconstruction of such materials on the computer can be implemented using either finite-length fibers or infinite length fibers of distributed diameter in the sense that the fibers extend across the entire control volume. Image-analysis techniques can also be used just as in the grain model case above for the determination of the fiber length and diameter distributions. Of particular interest here is the possible correlation of length to diameter for the same fiber, which may obviously affect not only the porosity value but also the transport properties. An additional parameter in the fiber models is the orientation of the fibers, which is obviously not an issue in the spherical grain models. Bundles of parallel fibers in one, two, or three dimensions can be assumed with the same or different number density per unit volume in each direction. Alternatively, systems of randomly oriented fibers can be employed with structural characteristics that are similar to those of the corresponding randomly oriented capillaries. In fact, it is straightforward to transfer structural properties from the pore model to the corresponding fiber model, considering that each of them is the negative of the other. Porosity in the former is equal to the solid fraction in the latter; specific surface area is the same, and so on. Of course, the transport properties of the two classes of models are quite different since the fluid will use the pores as conduits of transport in the pore models and the void space among the fibers in the fiber models. As a result, the resistor network approach cannot be applied in the case of fibrous structures due to the lack of straight conduits of transport as is the case in the pore models. Diffusion and flow in fiber models can be described by the corresponding differential equations in the continuum limit, which can be solved using some numerical method (finite differences, finite elements, etc.). The lattice-Boltzmann technique can also be employed to this end and can deal with both flow and convective diffusion problems as mentioned in the previous section. As the Knudsen number increases, the continuum approaches can no longer be used as rarefaction effects must be taken into account. The molecular trajectory technique is very convenient to describe diffusion at elevated Kn values and will be detailed below to a degree that it can be useful for applications in porous membranes. The same holds for the lattice-Boltzmann technique, which can also be modified to account for rarefaction effects. All these transport phenomena, namely, diffusion of multicomponent mixtures, flow, and convective diffusion at elevated Kn values, can also be treated by the DSMC method. These mesoscopic techniques are discussed in the next section.

1.03.3.2.4 Digitized structure models

If the geometry of the structural features of the membrane does not resemble that of some classical shape (cylinder, sphere, ellipsoid, etc.) or if the

history of the membrane synthesis route (for instance, preparation of nanopowder, compaction, thermal sintering etc.) is not known, then a different class of structure representation techniques can be used that produce three-dimensional digital arrays of solid and void voxels. If the actual porous membrane sample can be mapped onto a discrete array of 1 (for void) and 0 (for solid), a very convenient representation of the internal structure can be obtained, that can be subsequently used directly for the numerical solution of the transport equations or for the application of various transport simulation methods. Another advantage of such reconstruction procedure is that no explicit assumption regarding the shape or connectivity of the structural features is required. In addition, in the case of asymmetric membranes, these techniques can offer distinct digital representation of each layer separately as it has been already demonstrated in the literature [31].

A variety of reconstruction techniques have appeared over the last decade, most of which are based on much older reconstruction concepts. However, because of the clear advantage that they offer compared to pore or grain models on the one hand and their significance for the accurate representation of microstructural features in membrane science on the other, a tremendous growth of interest in this direction was noted recently. The serial sectioning or serial tomography technique could theoretically offer a direct description of the internal structure of a porous or, in general, biphasic material, provided that the characteristic size of the structural features is larger than the distance between successive sections and than the pixel size that is used to discretize the image of each section. Although this technique has been applied successfully to geological materials (e.g., References 32 and 33) and in diagnostic medicine, resolution issues arise in the case of membranes. In addition, the need to perform repeated, physical sectioning (or, rather, polishing) of the material at equidistant depth levels renders the technique impractical. A serious additional difficulty is associated with the need to align the various physical sections with sufficient precision and with tolerance that should be only a small fraction of the pixel size.

The stochastic reconstruction of porous structures from single images is free of the aforementioned drawbacks and, therefore, has attracted the strong interest of investigators in the area. In general, the procedure involves the following steps. First, an optical or electron microscope image of some section of the material is obtained. Obviously, in the case of membranes, electron microscope images of sufficient resolution are needed to ensure capture of the smallest relevant size scale. A second requirement is that this section be representative of the membrane structure, which, in turn, implies sufficiently large size of the section and care to avoid nontypical segments of the material. If the material is suspected to be inhomogeneous or anisotropic, as is the case of asymmetric membranes, then multiple images are needed with different orientation and within each distinct layer. The second step involves some image processing and analysis. Specifically, the images are scanned and saved in electronic form if not directly done so by the electron microscope software. The image files are then passed through convolution filters and through filters that enhance the contrast at the boundaries between the two phases. The color values in each pixel are then replaced by the binary values, 1 or 0, that indicate majority occupation of the pixel by void or by solid matter, respectively. The phase function of the material is then defined as follows:

$$z(\underline{x}) = \begin{cases} 1 \text{ if } \underline{x} \text{ belongs to the void space} \\ 0 \text{ otherwise} \end{cases} \tag{30}$$

where $\underline{x}$ is the position vector. Obviously, the porosity of the material section can be obtained in a straightforward manner through the expression

$$\varepsilon = \langle z(\underline{x}) \rangle$$

where the averaging process involves all pixels on the image. Note that the porosity that is obtained in this way involves both the accessible and the inaccessible void volumes. Further structural properties of the binarized structure can be obtained from the calculation of the n-point correlation function. The 2-point or autocorrelation function contains already a significant amount of information concerning the phase distribution on the particular section as it maps the distance between two pixels on the probability of these pixels to share the same value of the phase function (i.e., to lie in the same domain, void or solid).

The normalized autocorrelation function is given by

$$R_z(\underline{u}) = \frac{\langle (z(\underline{x}) - \varepsilon) z(\underline{x} + \underline{u}) - \varepsilon) \rangle}{\varepsilon - \varepsilon^2} \tag{31}$$

and for isotropic structures it becomes one-dimensional as it is a function of the distance $u = |\underline{u}|$ only.

Needless to say, higher order correlation functions contain further structural information regarding the particular material but at the same time they complicate the stochastic reconstruction process.

The next step is the generation of three-dimensional binary arrays that represent in a discretized form the biphasic material. The elements of this array must be such that the porosity and any desired moment of correlation function are satisfied. The early efforts in this direction employed conditioning and truncation of random Gaussian fields [33–35] with encouraging results regarding both the visual resemblance of the reconstructed materials to the actual ones and the agreement of the calculated transport properties with the measured ones. However, this method lacks the flexibility to satisfy further moments of the correlation function beyond the first two (porosity and autocorrelation function). As a result, biphasic materials with some ordering or correlation in their interface shape, like granular or fibrous media, cannot be successfully reconstructed with this method. A more complicated option would be to include several moments of the correlation function, or, alternatively, other distribution functions that can be measured or computed on the original actual image like linear path, chord size etc., in the objective energy function that is to be minimized. Such a simulated annealing procedure – in the sense that a minimum energy configuration is pursued [36] – can lead to quite satisfactory reconstructions of the material at the heavy expense, of course, of computational time.

An alternative stochastic reconstruction technique that exploits only porosity and autocorrelation data but appears to satisfy implicitly more structural properties than does the Gaussian field method is a technique that generates three-dimensional binary arrays that follow fractional Brownian motion (fBm) statistics. This method has been applied with considerable success not only to geological media but also to multilayered ceramic membranes, as discussed below. Briefly, the main concept is based on the definition of fBm [37] as a process that satisfies

$$\langle B_H(\underset{\sim}{x}) - B_H(\underset{\sim}{x}_0)\rangle = 0$$

$$\langle [B_H(\underset{\sim}{x}) - B_H(\underset{\sim}{x}_0)]^2\rangle = |\underset{\sim}{x} - \underset{\sim}{x}_0|^{2H}$$

where H is the Hurst exponent. The term fBm is indeed relevant if one notes that for $H = 1/2$, the classical Brownian process is recovered. Depending on the H value, uncorrelated or correlated structures can be generated, the degree of correlation being a monotonic function of the H value. In the context of transport in porous media, this technique was first employed to reproduce correlated permeability maps for large-scale geological media but following Kikkinides and Burganos [38, 39], it can be applied also to the structure itself replacing the local permeability value with the binary index of the corresponding pixel (or voxel) in digitized porous materials. One first assigns random numbers from a Gaussian distribution with average 0 and standard deviation 1 to the corners of a cubical domain that is meant to contain the sample to be reconstructed. An algorithm that assigns sequential averages to internal positions of this cube is used, thus increasing progressively the space discretization. The value of the Hurst exponent, H, is selected such that the autocorrelation function that is determined on the image of the actual, physical section is recovered to a satisfactory degree. However, such a reconstruction would contain a limited number of pores in each realization since their characteristic size is of the same order of magnitude as the correlation length. To circumvent this problem, the working domain can be divided into a number of smaller cubes, each of which becomes the starting cube for the application of the fBm process. To ensure smooth interweaving, the lattice nodes that lie at the boundaries between these cubes receive contribution from all immediately neighboring cubes. More details on this procedure can be found in the articles by Kikkinides and Burganos [38, 39]. Typical examples of a reconstructed porous material using the fBm procedure are shown in **Figure 2** for various values of the Hurst exponent. This technique has been applied to asymmetric alumina membranes with very satisfactory results [31]. More specifically, all the three layers of the membrane have been reconstructed in three dimensions using only one image per layer. The generated structures were found to resemble closely the actual ones and the calculated permeability values were very similar to the measured ones. It is expected that the method can be applied to several other types of membrane materials, not only porous ones, but also, more generally, biphasic ones, such as crystalline–amorphous polymer blends.

The aforementioned reconstruction techniques can be applied to membrane materials with characteristic pore sizes that can be visible on electron

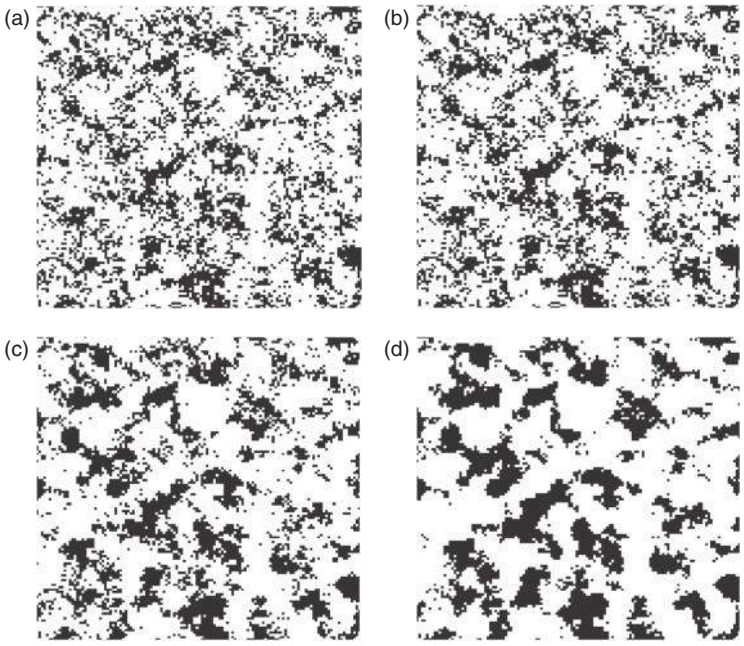

Figure 2 Reconstructions of a porous material using the fractional Brownian motion method: (a) $H = 0$; (b) $H = 0.1$; (c) $H = 0.5$; and (d) $H = 0.99$.

microscope images. If the characteristic size is in the nanoscale range, then an alternative technique can be used to extract the autocorrelation function. Specifically, for isotropic materials, small angle neutron scattering experiments can provide in an implicit manner the autocorrelation function, according to the equation [40]

$$I(q) = 4\pi\rho^2 V \int_0^\infty r^2 \gamma(r) \frac{\sin\, qr}{qr} \mathrm{d}r \qquad (32)$$

where V is the volume of the material sample, ρ is the scattering length density, $\gamma(r)$ is the density fluctuation autocorrelation function, and q is the scattering vector, given by

$$q = \frac{4\pi \sin\theta}{\lambda}$$

for isotropic scattering. Applying the inverse Fourier transform to Equation (32), the density fluctuation autocorrelation function can be obtained, which, in turn, can lead to the determination of the two-point correlation function from [40]

$$R_z(u) = \gamma(u) + \varepsilon^2$$

Once the autocorrelation function is known, the rest of the reconstruction procedure can be applied as described above, provided of course that the porosity of the membrane is experimentally available.

1.03.3.3 Mesoscopic Transport Simulation

With the exception of some simplified representations of the internal structure, such as the regular networks of cylindrical pores, for instance, which can be treated with continuum flux models, the majority of membrane reconstructions or structural models require the employment of some computational technique for the treatment of the transport phenomena that take place during separation. This intermediate scale of study is of key importance for the understanding and the quantification of the relationship between the structural features of the membrane with its end properties. These techniques can also yield useful estimates of the transport or sorption properties within finite regions inside the membrane, which can then be included in local flux expressions prior to integration toward the macroscopic scale. The presentation of the various transport models and simulation techniques that follows is focused on the features that are of particular relevance to porous membranes. These models assume that the atomic-scale fluid–membrane interactions are lumped into interaction factors that enter the simulation as boundary conditions, thus avoiding the need to rescale the window of observation into and out of the atomic description of the solid phase. In a later section, such hybrid techniques are also

discussed in the context of multiscale modeling and simulation.

1.03.3.3.1 Trajectory techniques

If the molecular size is much smaller than the pore size, one can treat the gas molecule as a mathematical point (dimension 0) that travels in the pore space of the membrane. In fact, since as it was mentioned above the solid surface effects are assumed to be lumped into effective parameters of reflection only and affect negligibly the molecular motion in the bulk, these trajectories proceed in straight paths between successive collisions in the gas phase or with the solid walls. The relative frequency of the two types of collision is a function of the Knudsen number. Such techniques were first used for the calculation of the diffusion coefficient in the bulk phase in the absence of solid surfaces, whereas their employment in the estimation of effective diffusion coefficients in porous materials started in the 1980s. Thanks to their generic character, these techniques can be directly applicable to porous membranes to provide tortuosity factor values that can then be used in the flux models as explained above. In practice, they can be simplified to account only for gas–wall collisions given that the pore size in actual membranes corresponds to large Knudsen number (free molecule flow regime) or to the configurational diffusion regime, which is known to yield sufficiently high separation factors. One can proceed in two different ways to calculate the tortuosity factor in a porous membrane with this type of techniques: calculate the transmission probability using molecular trajectories or calculate the mean square displacement of a large number of test molecules per unit of travel time.

Transmission probability method. Let F_1 and F_2 be the two opposite faces of the working domain that represents a portion of a porous membrane sample (**Figure 3**) and assume that the concentration of a gas species is maintained constant at values c_1 and c_2, respectively. The concentration drop that is, thus, created gives rise to diffusion in the x-direction, which is normal to the two faces. Suppose that a number of gas molecules are released from the void part of face F_1 per unit of time into the void space of the working domain. At equilibrium, this rate is obviously proportional to the concentration c_1 according to the kinetic theory. These molecules will travel in the void space of the sample colliding with each other and with the pore walls until they either reach the opposite face F_2 (and exit the sample) or return after some travel to the entrance face F_1 and exit through it. The fraction of molecules that exit through face F_2 will provide a measure of the transmission probability, f_T. The effective diffusivity in the x-direction will then be given by [41–43]

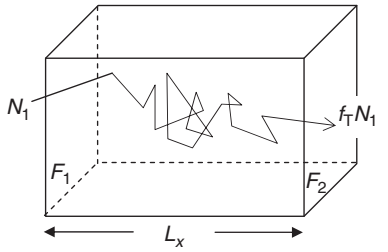

Figure 3 Schematic representation of trajectory approach for the calculation of effective diffusivities in porous materials.

$$D_{x,e} = \frac{f_T L_x \bar{u}}{4}$$

where L_x is the length of the working domain in the x-direction and $\bar{u}$ is the mean thermal speed of the gas molecules. More rigorously, one should consider the limit of $L_x \to \infty$ in the above equation to ensure that the effective diffusivity value is not a function of the size of the working domain. In practice, this limit is attained when L_x becomes a few times larger than the correlation length of the structure. The precise value of required L_x depends strongly on the Kn value: if the Kn value increases, the molecules take longer paths between successive collisions and reach the exit faces increasingly fast having increasingly smaller opportunities to explore the interior of the structure and, thus, to furnish information about the tortuosity of the available pathways; as a result, longer samples in the x-direction are required.

Some interesting features of the molecular trajectories in the pore space are presented next. The distance, λ', between successive collisions in the gas phase is sampled randomly from a Poisson distribution with mean that is equal to the actual mean free path, λ, of the gas at the actual pressure and temperature of the process. This is accomplished with the help of the expression

$$\lambda' = -\lambda \ln R_f \tag{33}$$

where R_f is a random number in the interval (0,1). At the new position, the molecule is assumed to

suffer a collision with another molecule and continues its trajectory into a randomly selected direction. A new free path λ' is calculated from Equation (33), and the procedure is repeated until eventual exit of the molecule through any of the two opposite faces, F_1 or F_2. A new test molecule is injected into the working domain; its trajectory is computed as described above, and so on, until a sufficiently large of test molecules has been used to eliminate statistical errors in the calculation of the transmission probability, f_T, with an acceptable tolerance. If it happens that the molecule encounters some solid wall prior to reaching the end of the path λ', then its path is interrupted and a molecule–wall collision is allowed to occur. Typically, a random reflection is assumed in these simulations, which is compatible with the cosine law of reflection (diffuse reflection law). In fact, it has been shown [23] that if a different reflection law is used, then the effective diffusivity in the positive x-direction is different from the one in the negative x-direction, thus inducing sense anisotropy in the diffusion process. If the molecule hits any of the faces of the working domain that are parallel to the mean diffusion direction, then the molecule is allowed to reenter the domain from the opposite face retaining its direction (periodic boundary conditions).

If the same procedure is repeated in the y- and z-direction, the values of the effective diffusivity in these directions are obtained, D_{ye} and D_{ze}, respectively. To overcome possible anisotropy difficulties that may arise artificially due to the finite size of the working domain, the orientationally averaged effective diffusivity is calculated from

$$D_e = \frac{1}{3}\left(D_{xe} + D_{ye} + D_{ze}\right)$$

However, although this is quite meaningful for porous materials in general, in the particular case of porous membranes that are used for, say, a specific gas separation, structural anisotropy is far from rare and one should confine the computation of the effective diffusivity in the direction of the concentration gradient, provided that the membrane thickness is much smaller than its width, which is typically the case in practical applications.

Mean-square displacement method. The transmission probability method bases the calculation of the effective diffusivity on the final outcome of the simulated trajectories of a number of test molecules without any reference to the time that is required by each molecule to reach any of the opposite faces, either the entrance (F_1) or the exit (F_2). Consequently, surface roughness effects are of no importance in this method provided that the characteristic roughness scale is sufficiently small to exclude alteration of the trajectory and to limit its role to the time delay of the molecular motion only. The mean-square displacement method does account for the time that elapses during the motion of the test molecules in the interior of the membrane structure [44–46]. The molecules are released in this case at randomly selected positions in the interior of the working domain and not on some of the external faces. The trajectory computations are performed in a similar manner to that in the transmission probability method except that periodicity is applied to all faces of the working domain. Thus, the trajectories are not terminated when crossing any of the external faces but only when a fixed travel time, t_0, has elapsed, which is common for all the test molecules. The effective diffusivity in, say, the x-direction is then calculated from

$$D_{xe} = \lim_{t_0 \to \infty} \frac{\langle \xi_x^2 \rangle}{2t_0} \tag{34}$$

where ξ_x is the displacement of a molecule in the x-direction from its initial position after the time t_0 has elapsed and the average is taken over the entire ensemble of test molecules used in the simulation. Time is easily tracked through the speed of the traveling molecules, which is usually assumed to be constant and equal to the thermal speed. In fact, it has been shown that the incorporation of the Maxwell–Boltzmann distribution of molecular speeds in this type of simulation has a negligible effect on the value of the effective diffusivity [47–50]. To ensure that the effective diffusivity estimate is not a function of travel time, sufficiently large travel times must be allowed in the simulation according to Equation (34). For short travel times, traveling molecules do not have the opportunity to explore statistically adequate regions of the membrane structure and the mean-square displacement is not proportional to the travel time no matter how many test molecules are used. This has given rise to some confusion in the literature as certain investigators have included this phenomenon of nonlinearity in the more general notion of anomalous diffusion, which, however, is

not the case here. The orientationally averaged effective diffusivity is obtained from

$$D_e = \lim_{t_0 \to \infty} \frac{\langle \xi^2 \rangle}{6t_0}$$

where ξ is the displacement of a test molecule from its initial position after time t_0.

Coding of this algorithm is not complicated and the resulting software can be parallelized to reduce significantly the computational time, thanks to the fact that each test molecule is treated independently of the others. This is not to imply that molecular interactions are neglected since, as it was mentioned above, the molecular collision frequency is taken into account through the fact that the molecular motion is interrupted at distances that are randomly sampled from the Poisson distribution of free paths with mean equal to the mean free path. This technique is also applicable to, practically, any type of pore structure that can be generated either with the help of some geometrical feature (grain, fiber, pore, etc.) model or through the application of some reconstruction technique [51]. In the former case, some analytical function is used to describe piecewise the solid–void interface and the intersection of the molecular pathway with it is obtained as the (x, y, z) point that belongs to both the interface and the line of the molecular path and is closest to the starting position for this step. In the latter case, the medium is discretized into unit cubes (or volume elements, voxels) and the molecule–wall collision sites are found in a similar manner. Thanks to the straightforward applicability of this technique to any pore structure, it has become possible to study the effects of various structural features on the tortuosity factor of the membrane material, including most notably those of the spatial correlation among pore or grain sizes. In fact, it has been shown that size correlation leads to increased diffusion coefficients, the precise degree of this increase being a function of the degree of correlation, the type of the structural elements, their ordering and topology and so on [24].

1.03.3.3.2 Direct simulation Monte Carlo method

The DSMC method is a stochastic process that is suitable for the simulation of flow and convective diffusion of gases even at nonzero Knudsen number values, where the continuum limit is not fully validated. In essence, it can be considered as smart and very efficient molecular dynamics with stochastic Monte Carlo ingredients. It avoids the need to solve the equation of motion at the atomic scale or construct equilibrium configurations using microscopic flow fields. It also sidesteps the meaningless integration of the straight portions of molecular trajectories. DSMC is an off-lattice pseudoparticle simulation method, originally suggested and developed by Bird [52]. The main concept is that instead of attempting to follow the evolution of the actual number of molecules in a control volume, to monitor the trajectories of only hundreds of thousands or millions of pseudoparticles that mimic the trajectories of actual molecules using some lumped parameters.

The state of the system is defined by the positions and velocities of a set of such pseudo-particles that travel and collide with each other in a fixed working domain, which is discretized using a certain number of cells. The average cell size is of the order of $\lambda/3$, where λ is the mean free path of the molecules at the prevailing conditions of pressure and temperature. This is required in order to be able to resolve large gradients of pressure in flow problems with realistic viscosity values. The system evolution is decomposed into two relatively uncorrelated subprocesses, namely, that of molecular translation and that of intermolecular collisions. Implementation of these subprocesses involves four distinct steps in the course of the simulation:

1. *Collisionless convection of particles during the time interval* Δt. Initially, the particles are assigned velocities with random orientation and magnitudes sampled from the Maxwell–Boltzmann distribution. The time Δt is chosen to be smaller than the collision time for the particular gas under the particular pressure and temperature conditions. Since some of the particles will find themselves outside their own cells or even outside the working domain, it is required at this point to impose boundary conditions and also define the way of calculating macroscopic quantities. This is also dictated by the fact that some of the particles will experience a wall collision within this time interval. The molecule–surface interactions are modeled through the employment of some accommodation coefficient.
2. *Indexing and tracking of the particles*. This is an important step in the DSMC simulations since a significant portion of the particles may have switched cells during the convection step.
3. *Intermolecular collisions using a stochastic approach*. During this step, a fraction of the particles will

suffer collisions with other particles. In contrast to the molecular dynamics technique, pairs of particles are chosen randomly and the collision probability is calculated for each pair. If this probability, which among others is a function of the velocities of the two particles, is greater than a threshold value, the collision is allowed to occur; otherwise, the two particles assume their convection-defined positions. To expedite calculations, the no-time-counter approach is usually adopted according to which a preselected number of collisions will be allowed to take place, thus avoiding the tracking of time along the sequence of intermolecular collisions. To increase the accuracy of the computations, the collision frequency is defined at the cell level but the colliding pairs are selected within subdivisions of the cells, called subcells. In this way, pairs of molecules that are in close vicinity to each other are preferentially selected to produce a collision.

4. *Calculation of macroscopic quantities.* During this step all macroscopic properties of interest are calculated within the various cells, hence producing a map of these quantities across the working domain. These averages can be taken spatially or temporally depending on the application and on the role of the corresponding quantities in the particular process.

Following molecule–surface collisions, the typical choices for the selection of the new direction are diffuse (random) and elastic (specular) reflections. The former results in no-slip flow for dense gases ($Kn \simeq 0$) but produces some finite slip velocity for rarefied gases. Other accommodation coefficients can also be used but their detailed discussion is beyond the scope of this chapter. Instead, it is worth noting that DSMC is a very useful tool for the simulation of viscous flow of rarefied gases, the application of which to porous membranes would add significantly to our understanding and quantification of rarefied flows in the presence of pore walls. In fact, although other numerical techniques can also be used in this context, DSMC is particularly attractive as it can be easily combined with pixelized media and digital reconstructions in contrast to certain other numerical techniques that become quite complicated when it comes to treat complex boundaries. In addition, depending on the boundary conditions (pressure and/or concentration differences) at the two faces of the membrane, DSMC yields local pressure and concentration fields, velocity fields, permeabilities, and diffusivities for sufficiently narrow-pore structures that correspond to elevated *Kn* values.

An example of the application of the DSMC method to the flow of N_2 in a porous membrane that is reconstructed using the fBm stochastic reconstruction technique ($H = 0.99$) is shown in **Figure 4(a)**. The Knudsen number at the exit is set to 2.5. For the sake of comparison, the flow field for the same gas under the same conditions and the same porosity but $H = 0$ (uncorrelated structure) is shown in **Figure 4(b)**. The ratio of the permeabilities in these two cases is equal to 6.23. Note that the permeability ratio at the continuum limit is 9.87. Thus, it appears that flow simulation techniques, such as DSMC, that can treat rarefied gases in tight pore structures may prove extremely useful in the prediction of the actual permeability of porous membranes and guide the design of new or modified materials with increased separation factors.

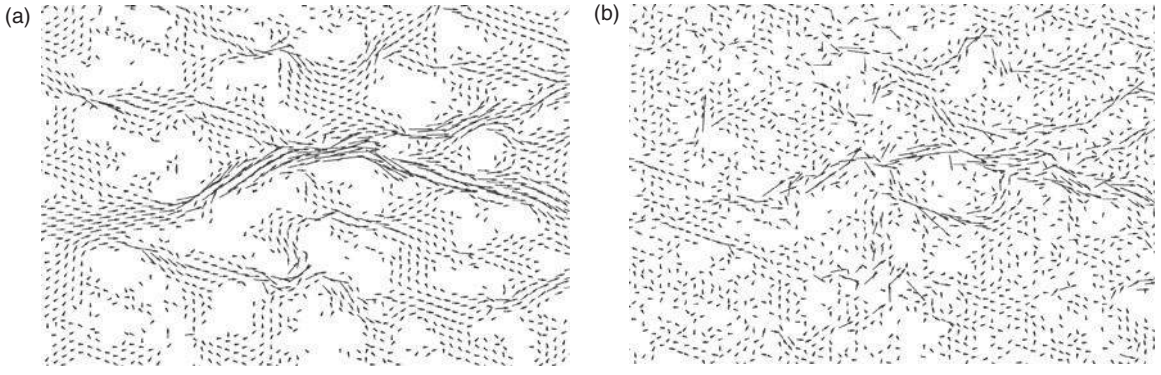

Figure 4 Flow field in a reconstructed porous material (fBm) using the direct simulation Monte Carlo method. (a) $H = 0.99$ and (b) $H = 0$.

1.03.3.3.3 Lattice-Boltzmann simulation of flow in porous membranes

The lattice-Boltzmann technique has historically evolved from the lattice gas model originally suggested by Frisch *et al.* [53] and Wolfram [54]. In the lattice gas, a set of identical particles is assumed to represent the actual fluid. These particles are equipped with the appropriate momenta that will take them from one site of a regular lattice that spans the working domain to a neighboring site within a unit time interval. Each site is either occupied by a single particle or is not occupied at all. The evolution of the particles in time and space involves two steps: direction and collision. The lattice-Boltzmann model is based on an ensemble average of the evolution equation of the lattice gas particles so that occupation probabilities or population densities are considered in place of individual particles. Depending on the dimensionality of the working domain, two-dimensional (square, triangular, etc.) or three-dimensional (usually cubic) lattices are employed to discretize space.

The evolution of the particle distribution function $f_i(\underset{\sim}{x}, t)$ is computed from the equation

$$f_i(\underset{\sim}{x} + \underset{\sim}{e}_i, t+1) - f_i(\underset{\sim}{x}, t) = -\frac{1}{\tau}\left[f_i(\underset{\sim}{x}, t) - f_i^{\mathrm{eq}}(\underset{\sim}{x}, t)\right]$$

where $\underset{\sim}{e}_i$ is the velocity in the i-direction, $\underset{\sim}{x}$ is the position vector, τ is the relaxation time parameter, and $f_i^{\mathrm{eq}}(\underset{\sim}{x}, t)$is the equilibrium distribution function. In this equation, the Bhatnagar–Gross–Krook (BGK) approximation [55] has been introduced to simplify the otherwise quite complicated collision operator. The local density and velocity can be determined from the expressions

$$\rho = \sum_i f_i$$

$$\rho \underset{\sim}{u} = \sum_i f_i \underset{\sim}{e}_i$$

It can be shown that in the limits of $Kn \to 0$ and vanishingly small discretization elements in space and time, the Navier–Stokes equation

$$\rho \frac{\partial \underset{\sim}{u}}{\partial t} + \rho \underset{\sim}{u} \cdot \nabla u = -\nabla p + \rho \nu \nabla^2 \underset{\sim}{u}$$

can be derived from the lattice-Boltzmann equation, where ν is the kinematic viscosity and p is the pressure. The corresponding isothermal equation of state is given by

$$p = c_s^2 \rho$$

where c_s is the speed of sound, the precise expression for which is a function of the discrete velocity set and, hence, of the choice of lattice used in the particular application. The kinematic viscosity is related to the sound speed and to the relaxation time through the expression

$$\nu = c_s^2 \left(\tau - \frac{1}{2}\right)$$

The equilibrium density function can be expanded in the following form:

$$f_i^{\mathrm{eq}} = A + B \underset{\sim}{e}_i \cdot \underset{\sim}{u} + C(\underset{\sim}{e}_i \cdot \underset{\sim}{u})^2 + D \underset{\sim}{u} \cdot \underset{\sim}{u}$$

where *A, B, C,* and *D* are numerical coefficients that are specific to the lattice-type that is used in the simulation.

The lattice-Boltzmann model offers significant advantages over the lattice gas model and, consequently, it enjoys increasing use in flow problems. Technically, it is practically free of the numerical fluctuations that appear in the lattice gas model. Galilean invariance is restored in the lattice-Boltzmann model up to a certain order in wave number. If one also considers that the viscosity is easy to adjust and the application to complex geometries, like those encountered in the interior of porous materials, is rather straightforward, it can be recognized as an approach with strong potential to simulate flow in practically arbitrary domains.

Upon collision with the pore walls, which in the lattice-Boltzmann model corresponds to the propagation of a population density to a site that resides at the solid–void interface, several options are available concerning the reflected population. Typically, the bounce-back condition is adopted which, practically, results in the inversion of the direction of the local f_i that arrived at the solid site. In the limit $Kn \to 0$, this reproduces the no-slip condition. Alternatively, the population that arrives at a solid site may be redirected into a different direction, satisfying either the specular reflection law (inversion of the normal to the wall component of the momentum only) or an intermediate reflection condition (random selection of any of the directions from the wall into the main stream). If some slip velocity is prescribed, the values of the reflected f_i's can be selected so that the prescribed slip velocity is recovered.

Different choices are also available for the generation of flow in a certain domain. Specifically, one can either impose a body force on the population densities in the direction of macroscopic flow or fix the pressure at the two ends of the domain, thus maintaining a constant driving force for flow. In practice, some round off error

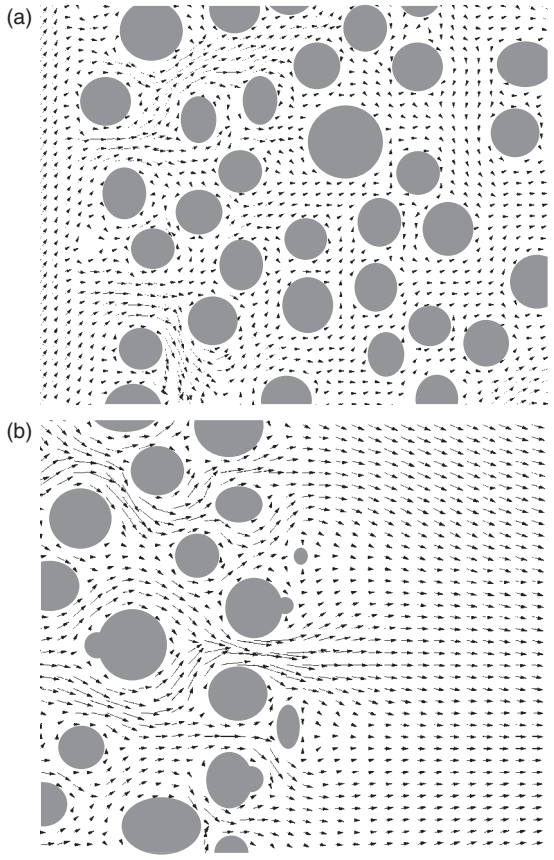

Figure 5 Flow field at the inlet (a) and outlet (b) of a porous membrane, as calculated by the lattice-Boltzmann method.

may develop and cause instabilities in the computations that can usually be prevented through the appropriate selection of the parameters of the simulation. A typical example of the application of the lattice-Boltzmann technique to the simulation of flow in a network of pores with distributed size is shown in **Figure 5**. It is noteworthy that the mean superficial velocity that is calculated using the lattice-Boltzmann method is found to be proportional to the pressure gradient for the same fluid and the same pore structure for relatively small porosity, thus satisfying the Darcy law for flow in porous media.

In the case of porous membranes that have sufficiently small pores to make the Knudsen number finite (larger than 0), this type of lattice-Boltzmann model is inappropriate to describe the flow in the porous microstructure. The Knudsen number becomes a function of position and some modification to the model formulation is required. Various attempts have been made in this direction that incorporate the mean-free-path concept in the model and arrive at expressions that include the relaxation time $\tau(\underset{\sim}{x})$ as a function of position. This is, of course, a direct consequence of the fact that the density acquires a nonnegligible dependence on position and so does the kinematic viscosity. Hence, the application of the lattice-Boltzmann model to such porous membranes necessitates the calculation of a local relaxation time parameter, which is a function of time as well. The dynamic viscosity also changes with the Knudsen number and can be approximated by the harmonic mean of the viscosity in the bulk (away from solid surfaces) and that in the free molecule flow regime just like in the diffusion case (Bosanquet expression [56, 57]). Interesting and encouraging comparisons of the prediction of the pressure variation during flow in a straight slit-shaped pore as provided by modified lattice-Boltzmann simulators to the corresponding predictions of the DSMC method have been made [58] that, in general, reveal the need for more accurate expressions for the viscosity in terms of the Knudsen number. A second major issue in this context is certainly the boundary condition at the pore surface and the appropriate definition and incorporation in the model of gas accommodation coefficients on the wall. It is also interesting to note that the use of the continuum approach to describe flow at elevated Kn values would necessitate the incorporation of an arbitrary slip velocity to complement the Navier–Stokes equation. However, such an approach suffers from the usually unsafe employment of first- or higher order slip boundary conditions that involve parameters which, in general, cannot be estimated or expressed in any general form. Even if such slip parameters are properly adjusted to reproduce some desired slip velocities, the rest of the flow field ceases to remain comparable, qualitatively or quantitatively, to that predicted by the DSMC or the lattice-Boltzmann method. Therefore, one appears to have no choice but abandon the continuum description and the corresponding numerical techniques and resort to mesoscopic methods such as the ones that are presented in this section. The areas of micro- and nanofluidics are of particular interest to membrane science and it is expected that an increasing amount of research efforts will be devoted to this type of models and simulators within the membrane field.

1.03.3.3.4 Pore-scale simulation of dispersion in porous membranes

The complexity of the pore structure that is usually encountered in the interior of porous membranes (except for particular cases that involve straight-

through pores for specific applications) gives rise to a strong heterogeneity of the flow field across the porous domain. In turn, this gives rise to dispersion of the solute particles or of the gas species, depending on the nature of the separation. Additional dispersion factors that take it away from a given streamline include the Brownian force, gravity, electrostatic forces, etc. The result is the dispersion of the species across some portion or over the entire region of the membrane structure, depending on the scale of heterogeneity, magnitude of the forces on the various species molecules or particles, and the time scale of the particular separation process. The mesoscopic equation that describes dispersion in a porous structure has the same form as that of convection–diffusion equation and this fact has repeatedly caused some confusion regarding the nature of each process and the differences between them. Except for the hydrodynamic heterogeneity issue that was mentioned above, one also needs to make the distinction between the scale of strict application of the convection–diffusion equation that uses the molecular diffusivity (typically, the pore scale) and the application of the dispersion equation, which involves the local macroscopic velocity and the dispersion coefficient in place of the molecular diffusivity (scale of a porous region or of a pore provided that some flow nonuniformity develops, for instance, Taylor dispersion in a tube). Thus, an obvious approach to treat dispersion in pore networks would be to solve the convection–diffusion equation in each pore segment and then integrate the flux expression over the scale of the working domain using the resistor network technique. This would still provide a local dispersion coefficient at the mesoscopic scale and further integration would be needed to upscale to the macroscopic level.

In the event that a pore network cannot reliably represent the void space of the membrane, a reconstruction technique can be employed that will yield either a geometric approximation of the structure (granular, fibrous, etc.) or a stochastic, three-dimensional representation of the structure as a binary array of 0 and 1. In any case, the lattice-Boltzmann or some other method can be employed to determine the local flow field. To incorporate convective diffusion or dispersion also, a modified lattice-Boltzmann method can be used, that contains two evolution equations, one for the carrier fluid and one for the solute or, in the gas mixture case, one for the mixture as an entity on its own and one for each component of the mixture. The first equation describes the main flow of the carrier fluid or of the mixture and the second equation describes the stochastic motion of the solute or of the mixture component, which travels at the mean mixture velocity but also diffuses at a rate that is proportional to a diffusive mobility parameter. Such models have been developed by Dawson *et al.* [59], Kumar *et al.* [60], and other investigators who adapted them to the specific needs of the application of interest. The species evolution equation reads

$$f_{s,i}(\underset{\sim}{x}+\underset{\sim}{e}_i,t+1)-f_{s,i}(\underset{\sim}{x},t)=-\frac{1}{\tau_s}\left(f_{s,i}-f_{s,i}^{eq}\right)$$

where subscript s denotes the solute or the individual species and all other terms have the same physical meaning as those used in the classical lattice-Boltzmann evolution equation. The solute or species density is now given from

$$\rho_s(\underset{\sim}{x},t)=\sum_i f_{s,i}(\underset{\sim}{x},t)$$

and the velocity from

$$\rho_s u_s(\underset{\sim}{x},t)=\sum_i f_{s,i}(\underset{\sim}{x},t)\underset{\sim}{e}_i$$

The fact that each species or solute shares the same mean velocity u, which is the velocity of the carrier fluid or of the mixture, is reflected on the constraint

$$\rho_s u(\underset{\sim}{x},t)=\sum_i f_{s,i}^{eq}(\underset{\sim}{x},t)\underset{\sim}{x}_i$$

The following form of the convection-diffusion equation is recovered using the Chapman–Enskog procedure

$$\frac{\partial\rho_s}{\partial t}+\nabla\cdot(\rho_s u)-D_s\nabla^2\rho_s=0$$

where the diffusion coefficient, D_s, is related to the relaxation time of this species through

$$D_s=c_s^2\left(\tau_s-\frac{1}{2}\right)$$

This model has been successfully applied to pore or fracture intersections for various values of the Peclet number (Pe), which is a measure of the relative importance of convection and diffusion in a transport process [64]. More specifically, Pe is defined in this context as

$$Pe=\frac{uL}{D_s}$$

where L is some characteristic length of the system, for instance, the pore length between successive intersections with other pores or the pore width. It has been shown that this lattice-Boltzmann convection–diffusion technique is relatively fast compared to other techniques for simple pore intersections for low *Pe* values. However, it still remains to be seen how efficient it can prove if applied to complex pore structures of sufficient size to justify definition of a dispersion coefficient.

1.03.3.3.5 Particle-tracking method for dispersion simulation

Once the flow field inside a porous membrane is made available through the lattice-Boltzmann method or any other numerical technique, solute transport can be simulated by a random walk type of approach. In the absence of any other force but the hydrodynamic drag and the stochastic Brownian force, the motion of each particle can be monitored through the vectorial summation of the displacement that is caused by these two forces [61–63]. Within a short time interval, δt, the total vectorial displacement is given by

$$\delta \underset{\sim}{r} = \underset{\sim}{u}(\underset{\sim}{r})\delta t + \delta \underset{\sim}{\xi} \tag{35}$$

where $\delta \underset{\sim}{\xi}$ is the random vectorial displacement due to the stochastic thermal motion. The velocity $\underset{\sim}{u}$ is the local velocity of the carrier fluid, which is assumed to remain unaffected by the motion of the solute. This is usually justified in the cases of dilute dispersions of nanoparticles. In all other cases, the distortion of the flow field by the moving solute must be taken into account.

The lattice-Boltzmann or other space-discretization numerical technique that can be used to compute the main flow field will provide the local velocity components at lattice or grid nodes. However, the stochastic nature of the particle motion will clearly necessitate the knowledge of the values of the velocity components at off-lattice positions. Various interpolation algorithms can be employed to this end, the presentation or review of which is beyond the scope of this chapter. The magnitude of the random displacement, $\delta\xi$, can be calculated from the equation

$$D_s = \frac{\delta \xi^2}{6\delta t} \tag{36}$$

The physical meaning of the use of this equation is the following. During the time δt, the solute particle will have the opportunity to experience a statistically adequate number of unit steps for a meaningful diffusive process to develop. This, in practice, implies that the value of δt is much larger than the mean time between successive free paths. On the other hand, δt must be sufficiently short to prevent excessively long steps that would dislocate the particle to a region of different fluid velocity. That is, the value of δt must be limited to time intervals that allow very small steps of the particle to ensure smooth, controlled variation of the local flow field. According to Salles *et al.* [61], a compromise between these two constants is to use a δt value that allows a total displacement of the particle of the order of a fraction (say 1/2) of the pixel size in binarized pore structures. Once the value of δt is fixed, the value of $\delta\xi$ is calculated from Equation (36) and a hypothetical sphere is generated with center at the current particle position and radius equal to $\delta\xi$. Since the assumption is made that the stochastic part of the process is diffusive and a large number of intermediate steps is taken before the displacement $\delta\xi$ is achieved, it can be safely assumed that at the end of the δt interval the particle has lost its memory from the previous position. Consequently, a point on the surface of this sphere can be selected randomly (usually by selecting random direction cosines in spherical coordinates) and identified as the position that the traveling particle would reach if only the diffusion process were taken into account and the main fluid flow were neglected. Then, the vectorial summation of Equation (35) is performed to determine the next position of the particle as the result of both convection and diffusion. Obviously, if a prescribed *Pe* value is used, the relative importance of convective and diffusive displacement is precisely defined: for small *Pe* values, the diffusive term is the one that dictates the motion of the particle in a stochastic manner whereas for large *Pe* values, particles follow closely the streamlines because of the limited role of diffusion. However, it must be stressed that even at large *Pe* values (e.g., 100 or more) where diffusion is limited, some small stochastic displacement of the particle may take it to a different streamline, from this one to a different one and so on, eventually leading it to extensive deviation from the original streamline, especially in the interior of porous membranes with locally heterogeneous pore structure. This, in turn, may lead to dispersion coefficients that are quite sensitive to the precise value of the Peclet number. It may also have some profound effect on the

efficiency of the separation of various solutes or dissolved species and the conditions under which such efficiency can be maximized.

Some care is needed to avoid confusion of this dispersion algorithm with the implementation of the diffusion simulation that was presented earlier and consisted in the computation of molecular trajectories. In that case, each and every individual step of the molecule is considered following sampling from the Poisson distribution of paths with mean value that is equal to the mean free path. The time that elapses during such individual steps is quite small and, certainly, much smaller than the time interval δt that is used in the dispersion simulation. Superposition of the convective and diffusive motions in the latter case is made possible if the δt value is sufficiently large for Equation (36) to be valid. Another basic difference is that the stochastic displacement, $\delta\xi$, is constant during the simulation (i.e., of fixed length) in contrast to the individual molecular paths which are of distributed length with mean equal to the mean free path.

Snapshots of the evolution of a set of solute particles that travel in a simulated porous membrane under the action of a mainstream flow field and a Brownian field are shown in **Figure 6**. Note that for the lower *Pe* value, the mixing time is of the order of the flow-through time whereas for the higher *Pe* value, the solute particles follow the streamlines rather closely. However, as it was mentioned above, even a small random displacement off the streamline may carry gradually the particle to a different flow region and eventually lead it to a different pore segment from the one that was initially selected by the particle. It is straightforward to envisage much wider dispersion of solute particles at larger scales due to the heterogeneity of the fluid flow. These phenomena can be studied in depth using the particle tracking or the lattice-Boltzmann convection–diffusion technique. Recent studies [64] revealed a satisfactory agreement between the predictions of these two methods at the scale of a pore intersection. The interesting difference between the two is that the particle tracking method is much slower than the lattice-Boltzmann convection–diffusion method for low *Pe* values where diffusion is important but becomes faster than it in the high *Pe* range where flow dominates transport. Thus, depending on the conditions, one may select one or the other method to follow the dispersion process and calculate the dispersion coefficients. In the case of porous filters, it appears that the longitudinal dispersion coefficient is of more direct significance than that of the

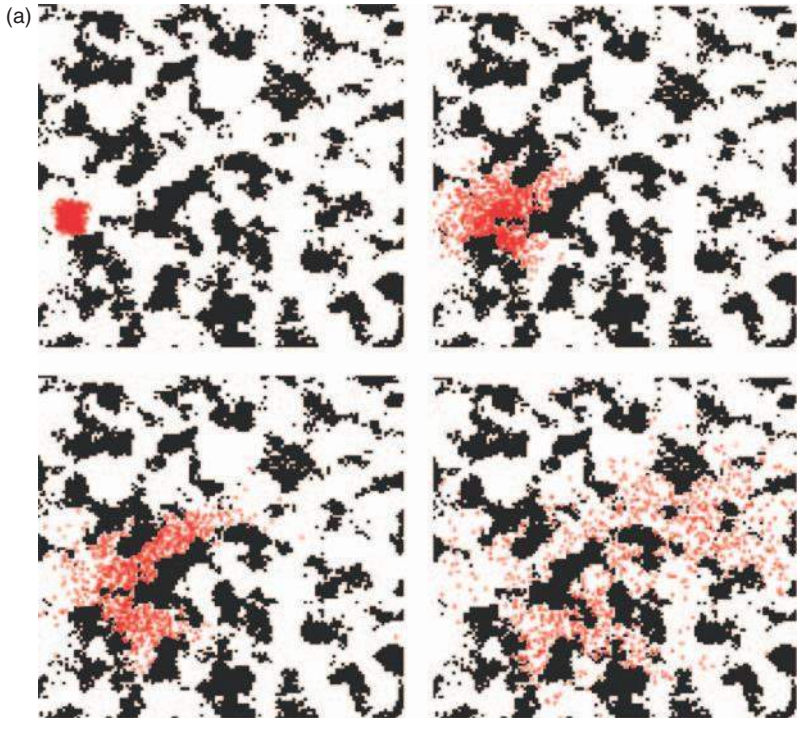

Figure 6 (a) Dispersion of a pulse in a reconstructed membrane at $Pe = 0.1$. Time sequence: right and down.

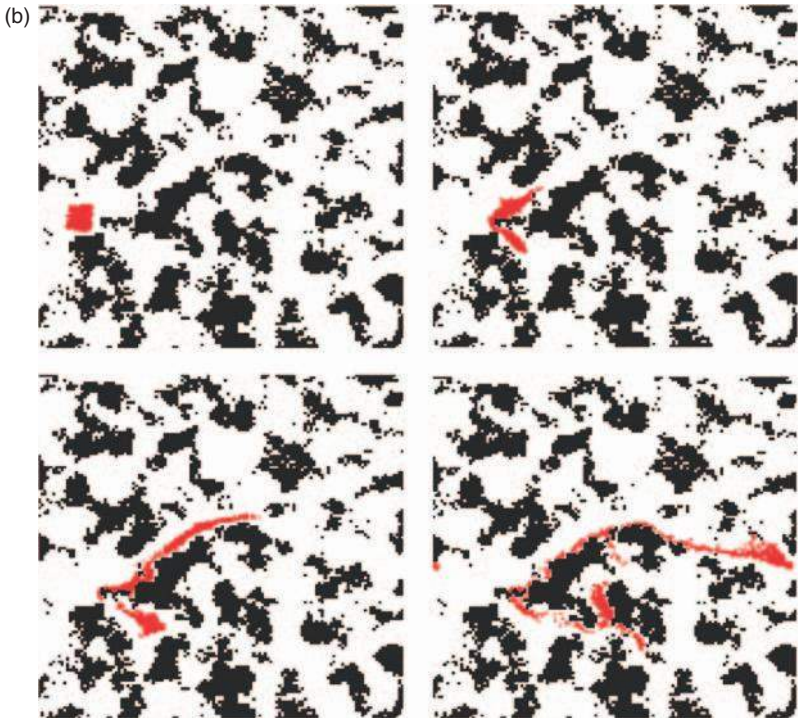

Figure 6 (b) Dispersion of a pulse in a reconstructed membrane at $Pe = 100$. Time sequence: right and down.

transverse one since all measurable quantities of interest are along the mean direction. However, in the case of cross-flow operation using porous membranes, both longitudinal and transverse dispersion processes become important and retain their increased significance along the course of the separation process due to the gradual entrapment of particles within the pore space and the concomitant alteration of the structural features of the membrane in an asymmetric fashion.

If the pore space of the membrane can be simulated by a network of individual pores, a resistor-type of approach can be used to evaluate the flow field in the interior of the membrane and the pressure at pore junctions. Once the flow solution is available, dispersion at each pore segment can be modeled using the convection–diffusion equation that will yield the solute concentration difference across each pore. Using the resistor analog again, this time for the solute mass balance, one can obtain the concentration profile across the entire membrane and from that one can extract the longitudinal and transverse dispersion coefficients [65, 66]. Alternatively, a random walk technique can be used to simulate the motion of test particles through the pore network using the pore velocities as the main criterion of selecting the exit-pore from each junction [67]. Within each pore, the particles can either simply follow the mean pore velocity or allowed to switch streamlines, thanks to the stochastic diffusion process. A more refined algorithm was recently developed [67a] that accounts also for upstream particle transport at low *Pe* values.

1.03.3.3.6 Pore-scale simulation of membrane fouling

In the previous sections, solute particles were assumed to travel in the interior of a porous membrane under the action of the hydrodynamic and Brownian forces. If a particle approaches the pore wall, particle–surface interactions become significant and are, eventually, responsible for the capture and deposition of the particle at the site or its repulsion back to the main stream. Typical forces of this nature are the London van der Waals force and the electrokinetic (double layer) force. For particles larger than about 1 μm in size, the gravitational force is usually too significant to neglect, in contrast to the Brownian force that becomes negligible at room temperature. In addition, as the particle approaches the wall, a correction factor must be introduced to the hydrodynamic drag expression due to the additional hydraulic resistance that is exerted by the liquid body that lies between the particle and the surface on the traveling particle. Such correction factors have been calculated

both analytically and numerically for porous and nonporous particles and surfaces as discussed earlier in this chapter (Michalopoulou *et al.* [10, 11] and references therein). If both the particle and the wall are nonporous, the drag force increases rapidly to infinity as the clearance decreases to zero and it is only due to the strongly attractive van der Waals force that the particle may get captured by the surface. If either the particle (e.g., an aggregate) or the wall (e.g., a porous substrate or a particulate deposit in the context of fouling) is porous, the drag force remains finite even at contact thanks to the flow that develops in the interior of the porous body. Obviously, this is also the case when both bodies are porous. If the particle approaches the wall in any other direction but the normal one to it, the drag force gives rise to a hydrodynamic torque that is responsible for particle rotation, which may affect (usually to a small extent) the precise position of capture. As it was mentioned above, all these factors have already been taken into account in simulations of particle deposition in porous filters and membranes resulting in estimates of the particle removal efficiency and its dependence on the magnitude of several parameters (for instance, Burganos *et al.* [13]), including most notably fluid velocity, particle surface interaction constants, pore shape particle size and density, and flow orientation for larger particles.

Regarding the algorithm that can be followed to implement these calculations, one can distinguish two main types of approach: integration of the particle trajectory across the entire domain of the membrane sample or resorting to the resistor network method. The former can be applied to any structure type and depending on the quantities that are pursued, the initial positions of the traveling particles can be at the entrance face (calculation of removal efficiency, monitoring of fouling) or at random positions in the interior of the membrane (calculations of transport properties such as the longitudinal and transverse dispersion coefficients). The resistor network method can be applied to porous structures that can be approximated by networks of individual pore segments. In this case, particle trajectories are confined within each pore segment, the deposition rate is calculated in each and every pore in the network, and the population balances written at each pore intersection are solved for the local pressure profile and particle fluxes. Then, the overall deposition rate can be calculated and the filtration efficiency along the course of the filtration process can be determined. Recently, some concrete progress on the gradual deposit built up has been made through the dynamic simulation of suspension flow in filters [68–70]. More specifically, the particle trajectories are calculated leading to estimates of the distribution of the local deposition rate inside the filter. This information can be used for the stepwise update of the deposit profile across the medium and of the concomitant decrease of the hydraulic permeability, which necessitates the recalculation of the local pressure profile and local flow field. At some critical value of shear stress, portions of the deposited material may get reentrained into the main stream, travel downstream, and redeposit elsewhere, altering inevitably the flow field and, quite often, even the available pathways for transport, leading progressively to fouling. However, it is interesting to note that the deposit plugs are porous and act as exceptional filters themselves though increasing considerably the hydraulic resistance. This type of approach can also be applied to porous membranes under certain conditions regarding the relative size of solute particles and pores, the concentration of the flowing suspensions, the agglomeration tendency, etc. Note that dense suspensions require a different treatment inasmuch as the assumption of independent particle trajectories, that is, trajectories that remain unaffected by the presence of neighboring particles, becomes invalid just like the assumption of uniform physicochemical properties throughout the suspension.

1.03.3.3.7 Lattice-Boltzmann simulation of two-phase flow with phase change

Two-phase flow and phase change processes are frequently encountered during a variety of membrane-related processes, including membrane preparation, membrane characterization, and membrane module operation. Notable examples are the infiltration and sintering processes, mercury and gas porosimetry, separation through membrane contactors or pervaporators, membrane emulsification etc. As modern technologies require the design of increasingly finer architectures in the nanosize range and efficient control of the end properties and of the actual operation, reliable simulators and fast codes are needed that will allow better understanding of the phenomena at the pore scale and provide valuable data to material and technology developers.

Lattice-gas and lattice-Boltzmann models can be very useful in the simulation of two-phase flow with or without phase change, especially if they are to be applied to porous domains. This is because they are self-adjusting in complex geometries, such as the pore structures in the discretized form of binarized

media or other types of membrane reconstruction. Thus, if a certain lattice is selected for the application of the lattice-Boltzmann model, mapping of the lattice onto the porous sample will result in a straightforward labeling of a number of lattice sites as solid sites, which obviously do not participate in the process of evolution of the fluid particle population. If, in addition, the fluid is assumed to be nonideal, obeying thus a certain nonlinear equation of state, some (p,T) region can be found within which phase transition may occur. Phase coexistence implies the existence of an interfacial region, the shape and width of which are functions of the pressure and temperature for the particular fluid. Such a two-phase system was modeled by Swift *et al.* [71] using a lattice-Boltzmann model that employed a Cahn–Hilliard type of approach for phase transition. More specifically, the free energy functional

$$\psi = \int \left[\frac{\kappa}{2}|\nabla\rho|^2 + \psi(\rho)\right] \mathrm{d}x$$

is used to determine the diagonal term of the pressure tensor, which for a nonideal fluid reads

$$\underline{\underline{p}} = p\underline{\underline{\delta}} + \kappa\nabla\rho\nabla\rho$$

where κ is a fluid parameter and ψ is the bulk free energy density. The diagonal term, p, is given by

$$p = p_{\mathrm{f}} - \kappa\rho\nabla^2\rho - \frac{\kappa}{2}|\nabla\rho|^2$$

where p_{f} is the fluid pressure and is connected to the temperature through the equation of state.

In this model, the equilibrium density function can be expanded in a slightly different form from that in the ideal case, and reads

$$f_i^{\mathrm{eq}} = A + B\left(\underset{\sim}{e}_i \cdot \underset{\sim}{u}\right) + c\left(\underset{\sim}{e}_i \cdot \underset{\sim}{u}\right)^2 + D\underset{\sim}{u}\underset{\sim}{u} + \underline{\underline{G}} : \underset{\sim}{e}_i\underset{\sim}{e}_i$$

for the moving populations and

$$f_0^{\mathrm{eq}} = A_0 + D_0 u^2$$

for the nonmobile population. It is interesting to note that the thickness, d_{I}, of the interface is related to the gas and liquid densities, ρ_{g} and ρ_{l}, respectively, through the equation [72]

$$\kappa = \frac{3d_{\mathrm{I}}\sigma}{2\left(\rho_{\mathrm{l}} - \rho_{\mathrm{g}}\right)^2}$$

where σ is the interfacial tension, expressed as

$$\sigma = \kappa \int_{-\infty}^{\infty} \left(\frac{\partial\rho}{\partial z}\right)^2 \mathrm{d}z$$

The kinematic viscosity of the gas and liquid phases, ν_{g} and ν_{l}, respectively, are related to the corresponding relaxation times through simple equations of the form

$$\nu_j = \frac{2\tau_j - 1}{8}$$

for the 7-bit hexatriangular lattice and

$$\nu_j = \frac{2\tau_j - 1}{6}$$

for the 15-bit cubic lattice. Using a mean-field approach, it can be shown that the fluid density across a flat interface satisfies the equation

$$\kappa\rho''(z) = \mu(\rho, T) - \mu_{\mathrm{eq}}(T) \tag{37}$$

in which the local chemical potential excess acts as an external force. The expression [72]

$$\rho(z) = \rho_{\mathrm{c}} + \frac{1}{2}\left(\rho_{\mathrm{l}} - \rho_{\mathrm{g}}\right)\tanh\left(\frac{z}{2d_{\mathrm{I}}}\right)$$

satisfies Equation (37) with good accuracy. **Figure 7** shows the variation of the fluid density across the interface for three values of the liquid to gas density. It is easy to see that the density profile is quite smooth and free of jump discontinuities that are typically encountered in other types of numerical approaches. This model was incorporated by Angelopoulos *et al.* [73] in two-phase flow simulations of immiscible flow in pore networks.

When the recovery of the mass and momentum conservation equation was attempted from these starting equations, it was noticed that the lattice-

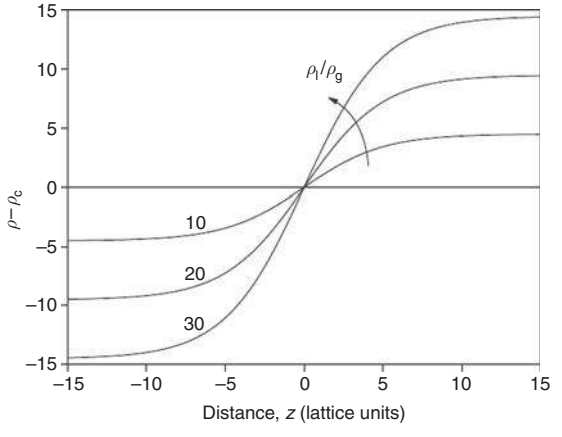

Figure 7 Density profile across a liquid–gas interface in the nonideal lattice-Boltzmann model.

Boltzmann derived momentum equation resembles closely the Navier–Stokes equation except for two terms that contain density gradients and imply lack of Galilean invariance. Although such terms may be negligibly small in the bulk regions of uniform fluids, they become quite large in the interface region due to the usually large difference in the densities of the two phases. To rectify this, a reformulation of the motion equation and the pressure expression was devised [74–76] that eventually restored the Galilean invariance. A similar result was obtained by Inamuro *et al.* [77] using an asymptotic analysis. Kalarakis *et al.* [75] demonstrated the success of the modified model through simulations of jet break-up and droplet shearing. The fact that droplet generation can be simulated with the help of this lattice-Boltzmann model in a direct manner that allows evolution of the interface and snap-off upon exit from the orifice is very encouraging for the employment of this technique for the simulation of emulsification processes. It must be mentioned, however, that since this method pays attention also to the interior of the interface in order to ensure continuous description of the density variation from one phase over to the other, some finite number of lattice sites are inevitably required within the interface itself. This necessitates the use of relatively thick interfaces if the overall size of the lattice is to remain reasonably small for computational reasons. In turn, this corresponds to elevated temperature and, to allow phase coexistence, to elevated pressure, the exact ranges of which depend of course on the state equation and the parameter values that are used. A way to get around this problem, which is not only confined to the free energy-based lattice-Boltzmann model but to other multiphase flow lattice-Boltzmann models also, is to use adaptive meshes for the discretization of space in the vicinity of the interface [78].

In addition to the advantages of direct applicability to digitized pore structures and automatic propagation of interfaces, another interesting feature of this lattice-Boltzmann model must be stressed, namely, the straightforward incorporation of controlled wettability conditions on the solid surfaces. This can be done in several ways, the easiest one involving the local assignment of chemical potential or density [75] to the solid sites, thus essentially assigning hydrophilicity, hydrophobicity, or any intermediate situation to each site at the solid–void interface.

The employment of a nonideal fluid in the model and, consequently, of a nonlinear state equation allows spontaneous condensation or evaporation, depending on the prevailing static and flow conditions. This phase transition feature can prove to be very useful in membrane applications that involve condensable vapors or volatile liquids. It is also a valuable tool for the simulation of pore structure characterization processes like the nitrogen adsorption/desorption process. **Figure 8** shows various snapshots of such a simulation for a granular medium, for example, alumina powder prior to compaction and sintering. As the partial pressure, p, of nitrogen increases, progressive thickening of the surface film (sorbed fluid) is noticed leading to condensation in the narrowest interstitial spacing first, followed by condensation in gradually larger openings according to Kelvin equation, Equation (10). Thus, for a given value of the ratio p_c/p_0, the pore radius, r_p, above which all pores will be empty of capillary condensate can be calculated. Adsorption and desorption snapshots are shown in this figure and the well-known hysteresis can be inferred easily. It is obvious that such a tool can greatly facilitate the interpretation of gas adsorption/desoprtion curves and elucidate the role of the various structural features of the membrane or its precursors in obtaining the desired transport and separation properties of the membrane material. In addition, the permeability and diffusivity values can be determined at intermediate stages of the adsorption/desorption process by hypothetically freezing the sorption process and applying the corresponding lattice-Boltzmann flow simulator or the molecular trajectory approach.

Application of this two-phase lattice-Boltzmann model to the simulation of membrane-based emulsification can proceed in the following manner [79]. A straight-through pore is drilled in an otherwise solid domain (lattice of solid sites) by changing the labeling of a set of lattice sites from solid to void. In the lattice-Boltzmann model this simply means that these sites are allowed to participate in the loop that updates the local density functions according to the lattice-Boltzmann equation. Then, the liquid density and liquid kinematic viscosity values are assigned to the liquid sites inside the pore, whereas the corresponding gas values are assigned to the sites outside the membrane domain. The surface tension and interface thickness values are also selected and some body force is applied to each liquid site by enhancing the f_i values in the direction of the flow. Gradually, a liquid meniscus is formed which propagates into the gas region where it is

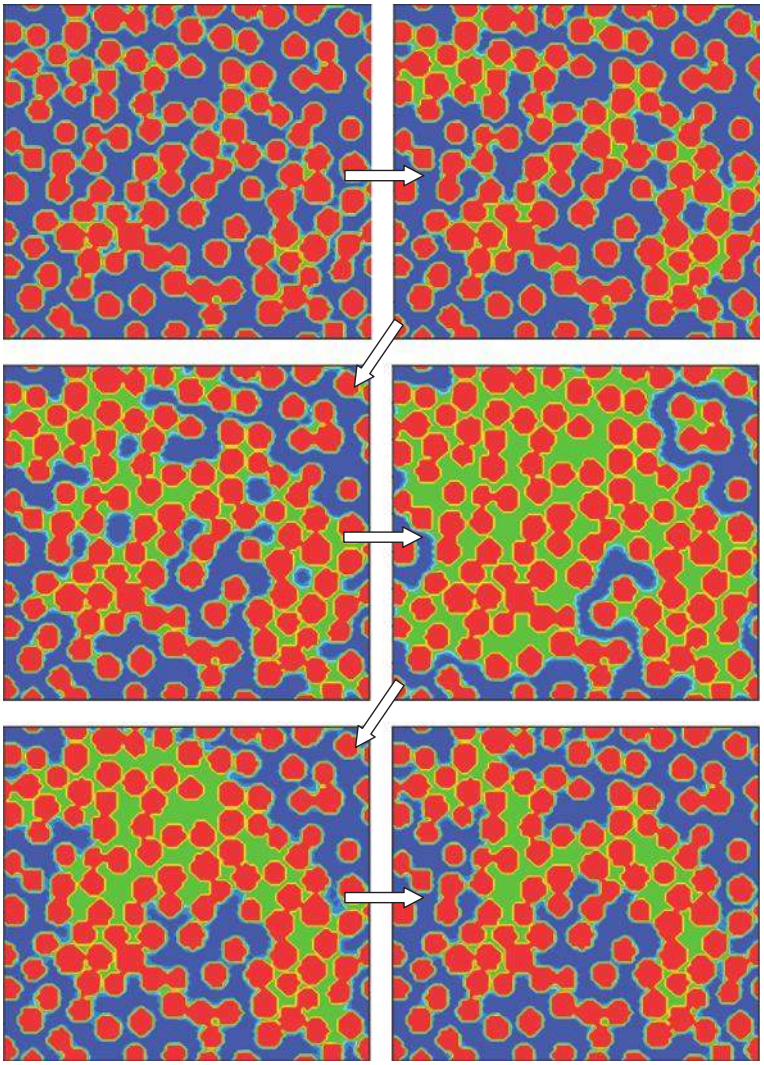

Figure 8 Snapshots of gas adsorption, condensation, and evaporation in a simulated granular material using the two-phase lattice-Boltzmann model that allows phase transition. Time sequence: right and down.

subjected to a shear flow, the effect of which on the liquid can be simulated by the effect of a body force in the direction perpendicular to the pores. The time of break-up and the size of the droplet that is thus generated are functions of several parameters, including the pore size, the relative magnitudes of the main and cross-flow velocities, the surface tension, and the liquid viscosity. **Figure 9** shows a set of snapshots taken during such a simulation using the free energy-based two-phase lattice-Boltzmann technique.

In the event that the pores in the interior of the membrane are nanosized, a modification of the lattice-Boltzmann method is needed to account for

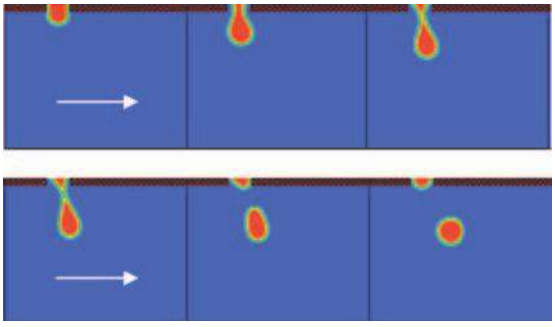

Figure 9 Snapshots of membrane-based emulsification using the two-phase flow lattice-Boltzmann simulator. Mainstream flow is in the direction of the arrows. Time sequence: right and down.

rarefaction effects. To this end, the models that were presented in the previous section can be invoked to describe flow in the elevated Knudsen number regime within the bulk of the phases. Development of a two-phase flow lattice-Boltzmann model away from the continuum limit is currently in progress and is expected to find extensive use in membrane applications involving gas and liquid phases, with or without phase change, with pores in the submicron range.

It is well known that liquid droplets at both the nano- and micron-size scale are subject to coalescence with each other forming larger droplets. This is usually an undesirable event inasmuch as it shifts the mean droplet size to larger sizes that do not happen to share the properties of the original emulsion. For instance, if microemulsions are pursued for cosmetic or food applications, coalescence into larger droplets will have a strongly negative effect on the end properties of the final product. In addition, if liposomes of specific mean size and standard deviation are produced by some membrane emulsification or membrane screening technique, coalescence will lead to larger sizes with larger deviation. Both of these changes will reduce the efficiency of the adsorption of the active ingredient in the pathological tissue and increase its adsorption in healthy tissues thus intensifying side effects of drug administration to the patient. Although several techniques are considered to mediate these effects, droplet coalescence is certainly a phenomenon that requires reliable simulators with the ability to predict the correct dynamics of the process within reasonable computational time.

The two-phase flow lattice-Boltzmann method can also be employed to study droplet coalescence and its dynamics. Among its advantages over more traditional techniques is its ability to simulate coalescence of multiple droplets simultaneously and not only of droplets in an isolated pair. Another significant advantage is its direct applicability to droplet coalescence in the interior of any structural configuration including digitally reconstructed materials, as described above. Application of the aforementioned simulator is straightforward and coalescence is driven mainly by the action of the interfacial tension that tends to minimize the surface area of the liquid bodies. In fact, not only viscous sintering but also controlled particle sintering can be simulated with this method, leading to structures that are more connected than the original ones, with less surface area and less porosity. **Figure 10** shows the evolution of a granular material during viscous sintering

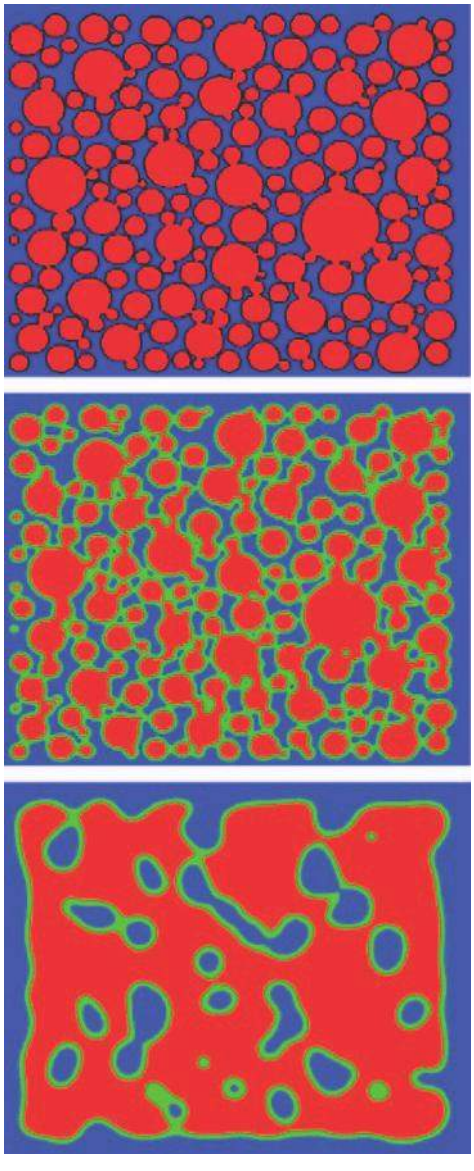

Figure 10 Simulated sintering of a granular material using the two-phase flow lattice-Boltzmann method.

using the lattice-Boltzmann method. If the particles are assumed to have a solid core that does not participate in the mass transfer process, surface controlled sintering can be simulated and the kinetics of the process can be delayed at an adjustable rate. The degree of sintering can be easily controlled if microscope images of the final product are available. Otherwise, this method can be employed to produce several structural configurations at intermediate levels of sintering, which can then be used as input to transport simulators for the prediction of diffusivities and permeabilities. In this way, one can have a set of data on the transport properties of the

membrane or support material at different sintering levels. Obviously, this type of information can be very useful in the design of improved materials and for guiding the experimentalists to the optimal set of preparation conditions.

1.03.3.4 Simulations at the Atomic Scale

The need to resort to microscopic- or atomic-scale simulations originates from at least two main issues, namely, the control of the separation process by nanoscale phenomena and the major role that fluid–solid interfaces play during fluid transport. In both cases, it is self-evident that sufficient knowledge of the interactions among atoms and their reliable simulation are of paramount importance for the design of improved membrane materials and for the identification of the optimal conditions of operation. In general, one can first reconstruct on the computer the configuration of interest at the atomic scale using some force field description of the interactions among the various constituents of the system. The parameters and data that are needed are usually obtained from measurements and *ab initio* computations. The next step involves specific attempts to identify stable versions of the configuration and suggest modifications at the atomic scale (ion exchange, hydroxylation, and functionalization in the general sense) that promise improvements in the end properties of the material and its eventual performance during application in some specific separation process. Sorption and transport in these structures can also be simulated at the atomic scale where needed or at the mesoscopic scale, paying particular attention to the fluid interaction with the solid surfaces. Although rather limited in terms of the time and space scale ($\sim$10 ns and $\sim$10 nm, respectively) which they can span, atomistic simulations can provide a vast amount of information and valuable insight into the competitive transport of species in microporous membranes and bridge the gap between quantum mechanical calculations on the one hand and mean field theories and mesoscopic simulations on the other. Although several common features underline the molecular simulation of inorganic and polymeric membrane materials, it is more convenient to give separate presentations of these two types of material and stress the differences where needed.

1.03.3.4.1 Atomistic reconstruction of inorganic membrane materials

The structure of various inorganic materials that have the potential to be used in membrane systems has been repeatedly studied at the atomic scale using Monte Carlo techniques or molecular dynamics. The reconstruction procedure involves, usually, the following intermediate stages. First, positioning of the atoms of the structure takes place at reference bulk lattice sites using literature data. A force field is selected to describe the atomic interactions and calculate the potential energy of the configuration. Various force fields are available in the literature, ranging from quick and simple to highly sophisticated ones that, however, pose more severe computational demands. Such force fields contain a number of parameters that are usually estimated from experimental data or *ab initio* calculations. A typical example is the general purpose universal force field (UFF, Rappé *et al.* [80]), which has been parametrized for the entire periodic table. It is a purely diagonal, harmonic force field, the parameters of which are generated from rules based on the atom type, hybridization, and connectivity. Both intramolecular (bonded) and intermolecular (nonbonded) interactions are taken into account in the formulation of the expression for the potential energy. Among intramolecular interactions, most notable contributions are: bond stretching, which is described by a harmonic term; angle bonding, which is given in terms of a three-term cosine Fourier expansion; torsion, which is expressed using cosine Fourier expansion terms with the dihedral angle between the two phases defined by an atom quadruplet in their arguments; inversion, which is expressed in a similar way as torsion is, but using the angle that is formed by the off-plane bond and the plane that is defined by the other three atoms in the arguments of the cosine Fourier terms. The van der Waals interactions are described by the 12-6 Lennard–Jones potential or the exponential-6 (Buckingham) potential. Electrostatic interactions are also taken into account using atomic monopoles and a screened (distance-dependent) Coulombic term. The next step involves the setting of boundary conditions, which can be periodic or of the free surface type. The final stage is the one that involves the minimization of the potential energy of the structure, using Newton–Raphson, steepest descent, or conjugate gradient techniques. Modifications of the structure are also possible at this stage, for instance, cation addition or ion exchange (particularly useful in

designing zeolites, introduction of structural defects, for example, removal of oxygen atoms from the surface of oxides) and any other hypothetical or actual alteration that appears promising or interesting from the scientific or technological viewpoints.

In addition to direct literature data for the various spatial characteristics of a material at the atomic scale, valuable input can be provided by X-ray diffraction (XRD) patterns, which can be utilized in an effort to solve the inverse patterning problem, that is, to find the structural details that reproduce the experimentally obtained diffraction patterns. More specifically, indexing of the X-ray patterns can be first implemented using a trial reciprocal lattice construction technique (for instance, the ITO method [81]). Subsequently, refinement methods can be employed for the optimum determination of the structure, like Pawley [82] and Rietveld [83] refinements. Initial guesses for such a procedure can be constructed from the data reported in the literature followed by an energy minimization step using the UFF or some other force field that, however, must be optimized for the particular material under investigation (see also, Navascues *et al.* [84] for details).

1.03.3.4.2 Simulated annealing

A method to overcome local energy minima and, thus, maximize the efficiency of the energy minimization procedure is using the simulated annealing technique. First, energy minimization of the structure under consideration takes place using some force field description of the atom-to-atom interactions and a conjugate gradient technique for the minimization process. Molecular dynamics is subsequently used under conditions of constant number of atoms, constant volume, and constant temperature (N, V, and T) until a configuration of atoms moving with the desired velocity distribution at the specific temperature is obtained. Then, the temperature is increased to a different value and the steps of minimization and molecular dynamics are repeated as mentioned above. This procedure is repeated at several temperature levels until a predefined upper limit is reached, which is usually safely below the melting point. Then, the same procedure is repeated in the reverse order, cooling down the system to the initial temperature. This method can be applied, practically, to any atomic-scale structure to yield equilibrated configurations with a global energy minimum, avoiding entrapment within local energy minima (see, for instance, Deem and Newsam [85]). Recent experience with zeolite reconstruction, namely, NaX faujasite (FAU) crystals [86] revealed that simulated annealing can also offer much reduced statistical deviation in energy calculations by almost two orders of magnitude compared to those in calculations with the nonannealed structure.

1.03.3.4.3 Simulation of sorption – Monte Carlo technique

Sorption at the atomic scale inside a microporous material is known to control the relative permeation and, eventually, the separation efficiency in numerous membrane-based applications. In fact, selective sorption of one or more species in cavities may either facilitate or obstruct selectively the transport of these species or of the nonsorbed species, depending on whether pore blocking or pathway clearing takes place. In the presence of electrostatic interactions, it is obvious that sorption at the different sites inside the structure may affect strongly the interaction of the rest of the species with both the surface ions and the adsorbed ions.

The thermodynamics of sorption can be calculated using different techniques. The details of the dependence of the partition function on the spatial extent of the system under consideration are incorporated in the configurational integral, which for an N-dimensional vector of coordinates reads

$$Z = \int \exp[-\beta E(r_1, r_2, \ldots, r_N)]\mathrm{d}^3 r_1 \mathrm{d}^3 r_2 \ldots \mathrm{d}^3 r_N$$

where E is the potential energy, $\beta = (k_B T)^{-1}$, and T is the temperature at the simulation conditions (see, for instance, Hecht [87]). Monte Carlo integration is an attractive method to calculate this integral, which in practice is estimated from

$$Z = \frac{V}{N_0} \sum_{i=1}^{N_0} \exp[-\beta E(r_i)]$$

where V is the volume of the system and N_0 is the number of random configurations that are constructed.

Although Monte Carlo integration is considerably more efficient than conventional numerical integration techniques, it can be further improved to reduce the generation of configurations that have high probability of overlapping with the solid structure. This is increasingly important as the number of degrees of freedom increases, as is the case, for instance, with alkane chains [88]. The energy-bias technique is found to improve drastically the evaluation of the configurational integral in such cases.

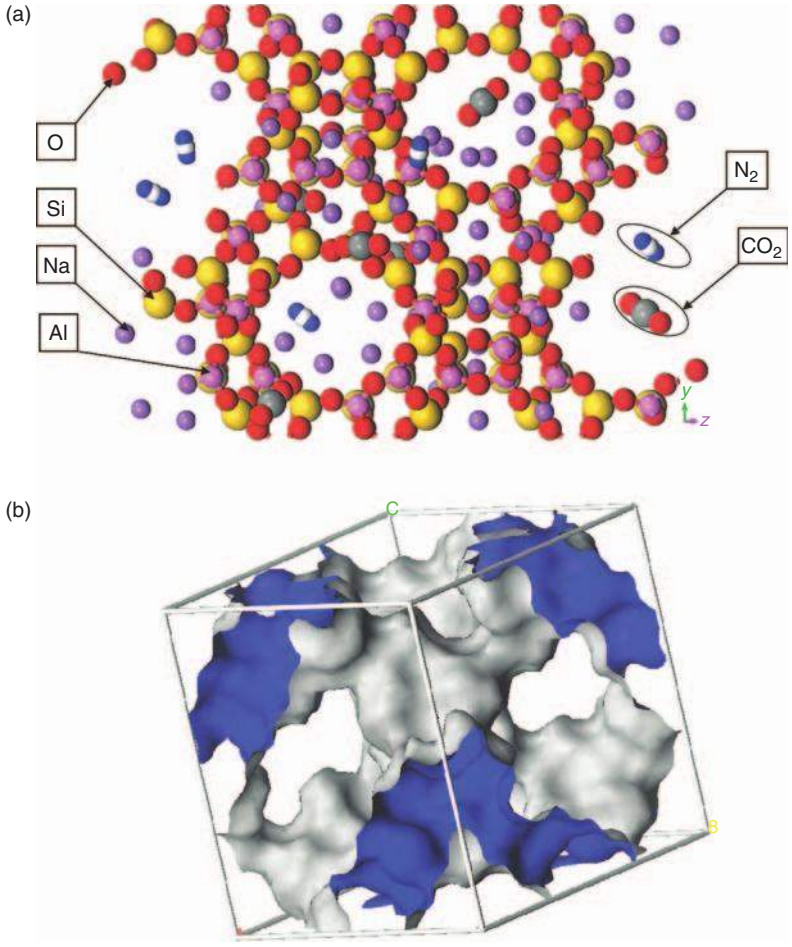

Figure 11 (a) Ball-and-stick representation of CO_2 and N_2 molecules sorbed inside the NaX faujasite framework. (b) Solid-free volume in NaX faujasite. Penetrant molecules can use the gray domain only for their sorption and transport, the interior of which is shown here in blue for easier identification of the internal morphology. The figure was created with the help of the Materials Visualizer module of the Materials Studio suite by Accelrys Inc.

Properties such as the Henry constant and the isosteric heat of adsorption can be calculated using postprocessing of the sorption simulation. The latter is typically performed under conditions of constant chemical potential, constant volume, and constant temperature (μVT), thus allowing fluctuation in the number of sorbate molecules that are contained within a fixed control volume. The Henry constant (K_H) is the ratio of the loading of sorbate molecules (N) to the pressure (p) of the system in the limit of low pressure:

$$K_H = \lim_{p \to 0} \frac{<N>}{p}$$

Equivalently, it is the slope of the sorption isotherm as $p \to 0$ and can be calculated from

$$K_H = \frac{M_s}{RT\rho_0} \frac{Z}{Z^{ig}}$$

where M_s is the molecular weight of the sorbate, ρ_0 is the mass density of the solid, and Z^{ig} is the configurational integral for a sorbate molecule in an ideal gas phase [89]. As pressure is reduced, sorbate–sorbate interactions become less frequent and at the limit of $p \to 0$, sorbate–surface interactions become dominant and control fully the value of the Henry constant.

The isosteric heat of adsorption (H_{st}) is a measure of the change of the internal energy that is caused by sorption and is given by

$$H_{st} = R\left[\frac{\partial \ln P}{\partial(1/T)}\right]_N = RT - \left[\frac{\partial < U >}{\partial < N >}\right]_{T,V}$$

A limited dependence of H_{st} on pressure is indicative of sorbate–surface interaction through dispersion–repulsion forces. On the other hand, nonnegligible dependence of H_{st} on pressure indicates preferential adsorption near charged surface atoms. As sorption progresses, additional sorbate molecules reside far from charged surface atoms at positions of lower potential energy. Obviously, the precise location of sorption sites is very significant in the case of molecular separations as they are known to affect the pathways of the rest of the species and, hence, the separation efficiency. **Figure 11(a)** shows a snapshot of CO_2 and N_2 molecules sorbed in the 12-member ring of the NaX form of faujasite with $Si/Al = 1$ (see Krokidas *et al.* [86] for details). Calculation of the void volume that is available for sorption and transport through the main cage of this framework is shown in **Figure 11(b)**: gray color is used to indicate the external boundary of this solid-free volume and blue is used to indicate the interior of the free volume (obtained with the help of Materials Studio®).

The interaction of the sorbed molecules with the internal structure of the microporous membrane can, to some extent, distort the solid configuration and, consequently, have some effect on the sorption capacity and transport dynamics. Although the solid structure is, typically, assumed rigid in Monte Carlo simulations of sorption, relaxation of this assumption is computationally feasible and can offer interesting results concerning the accommodation of sorbate molecules at different loadings and temperature levels. This is particularly interesting in the case of zeolites, which are known to have, among others, exceptional molecular-sieving properties and find applications in diverse processes over a wide range of temperature values. This phenomenon is complicated by the fact that zeolite framework distortion can also be due to temperature changes in addition to the distortion caused by sorbate–structure interactions and by the fact that these two sources are, usually, affected by each other. For instance, some frameworks have been observed to exhibit negative thermal expansion coefficient and, hence, contract upon heating with obvious consequences on their sorption and selective sorption capacity, on their sieving performance, and on the mechanical stability of the membrane-support system (for a recent review, see Caro *et al.* [90]). Such effects are already tractable by molecular dynamics techniques, an overview of which is given next.

1.03.3.4.4 Simulation of diffusion – Molecular dynamics

The evolution of a microscopic description in time can be simulated by equilibrium or nonequilibrium molecular dynamics. In the absence of external forces that would lead to measurable fluxes, equilibrium molecular dynamics can be very efficient in monitoring the motion of the fluid and structure atoms (or particles) through the integration of Newton's equation of motion for each and every individual particle. The self-diffusion coefficient can be calculated with the help of molecular dynamics and compared directly with pulsed field gradient nuclear magnetic resonance (NMR) measurements as both methods refer to equilibrated systems. If, on the other hand, macroscopic mass transport fluxes are generated under the action of externally applied composition gradients, nonequilibrium molecular dynamics can be employed to yield transport coefficients.

Just like in the case of Monte Carlo simulation of sorption that was described above, the application of the molecular dynamics technique to the calculation of the self-diffusion coefficient requires an equilibrated structure and a reliable force field for modeling the interatomic interactions. Considerable savings in computational time are achieved if short-range interactions, like dispersive and repulsive ones, are truncated at a cut-off radius, the precise definition of which is based on a tradeoff between accuracy and computational time constraints. In zeolite structures, cut-off radius between 1.2 and 1.8 nm are typically used. Energy discontinuities and truncation errors using cutoffs in periodic systems are usually treated with dumping functions or Ewald summation techniques [91, 92]; cutoffs can even be avoided (occasionally) using hierarchical approaches (multipole expansion methods [93]). If the structure atoms are held fixed in space, then the computational time can be severely decreased by constructing look-up tables for the sorbate–structure interaction data using the results of interaction calculations for a certain type of sorbate atoms that need to be obtained only once.

In the classical limit, the equation of motion

$$m\frac{d^2 \underset{\sim}{r}_i}{dt^2} = \underset{\sim}{F}_i$$

must be integrated, where m_i, $\underset{\sim}{r}_i$, and $\underset{\sim}{F}_i$ are the mass, position vector, and force acting on particle i, respectively. The force $\underset{\sim}{F}_i$ is given by the expression

$$\underset{\sim}{F}_i = -\nabla_{r_i} E + \underset{\sim}{g}_i$$

where E is the potential energy of the particle configuration and $\underset{\sim}{g}_i$ is a force that accounts for all types of constraints that develop between the site coordinates (e.g., fixed bond lengths) [94].

Once some initial condition is specified in the form of an initial configuration of particles, the equation of motion can be integrated using some finite difference scheme. Thus, if the particle positions, momenta, and interaction data are available at time t, updating of these quantities is achieved at time $t+\delta t$, where δt is small enough to ensure conservation of the total energy of the system with sufficient accuracy, yet large enough to allow completion of the computation within reasonable time. Although several integration techniques have been reported in the context of molecular dynamics, the Verlet algorithm

$$\underset{\sim}{r}(t+\delta t) = 2\underset{\sim}{r}(t) - \underset{\sim}{r}(t-\delta t) + \delta t^2 \underset{\sim}{\alpha}(t) + O(\delta t^4)$$

where $\underset{\sim}{\alpha}$ is the local acceleration vector, is probably the most popular one since it sidesteps the need for explicit evaluation of the velocities at each time step. However, these can be obtained easily from

$$\underset{\sim}{v}(t) = \frac{\underset{\sim}{r}(t+\delta t) - \underset{\sim}{r}(t-\delta t)}{2\delta t} + O(\delta t^2)$$

if needed, for instance, for the estimation of the kinetic energy. The self-diffusion coefficient can be calculated from the large travel time limit of the ratio of the mean-square displacement to $6t$:

$$D_{s,i} = \lim_{t\to\infty} \frac{\langle [\underset{\sim}{r}_i(t) - \underset{\sim}{r}_i(0)]^2 \rangle}{6t}$$

The transport diffusivity, D_i, is related to the self-diffusivity through Equation (9).

Another useful quantity that can be provided by molecular dynamics is the mean residence time (MRT) of the sorbate molecules, which is defined as the time that the molecules spend within a specified region. MRT is usually rendered dimensionless through division by the total time allowed for the simulation. This is a particularly interesting quantity for gas molecules near sensitive layers (e.g., gas sensors [95, 96]) and also for membranes as this sorbate–surface interaction is the precursor stage to sorption. The dimensionless MRT is given by

$$\mathrm{MRT} = \frac{\int_0^\infty \rho_{NVT}^{\text{transition}}(\underset{\sim}{r}^N(t)/\delta z)\mathrm{d}t}{\int_0^\infty \rho_{NVT}^{\text{transition}}(\underset{\sim}{r}^N(t))\mathrm{d}t}$$

where $\underset{\sim}{r}$ is the position vector, N is the number of particles in the canonical ensemble (NVT), and the vicinity extends to a distance δz from the surface. This quantity can be calculated at any time step during the molecular dynamics procedure as a post-processing calculation and characterizes the transition of fluid particles from the bulk into the boundary layer. It can also be associated with a steady-state adsorption rate constant [97].

Assigning the desired temperature and maintaining it constant during the simulation are not straightforward procedures and some interesting features can be presented here that can be involved in their implementation. At the first stage of the simulation, the particles are assigned velocities that are sampled from the Maxwell–Boltzmann distribution for the prescribed temperature. This distribution is subject to change during the evolution of the simulation and such a deviation may become significant for systems that have started from a configuration that was far from the equilibrated state. Restoring the desired temperature requires diminishing of such a deviation and production of configurations that fulfill the constraints of statistical mechanics. This can be achieved through the use of the so-called thermostats, like the direct velocity scaling procedure. Specifically, each time a nonnegligible deviation is noted during the simulation, the particle velocities are readjusted according to the relation

$$\left(\frac{v_i'}{v_i}\right)^2 = \frac{T_{\text{desired}}}{T_{\text{system}}}$$

where v_i and v_i' are the velocities of particle i prior and after correction, respectively, T_{system} is the temperature of the system as it has been calculated at the particular time step, and T_{desired} is the desired temperature value [97a]. This thermostat is usually employed in cases where considerable deviations are obtained and rapid restoring of the correct temperature is needed. Finer, yet, slower adjustments can be made if this thermostat is followed by a less aggressive thermostat, like the one suggested by Berendsen *et al.* [98] according to which each particle velocity is corrected by the factor

$$\frac{v_i'}{v_i} = \left[1 - \frac{\delta t}{\tau}\left(\frac{T_{\text{system}} - T_{\text{desired}}}{T_{\text{system}}}\right)\right]^{1/2}$$

where τ is some characteristic relaxation time. Such thermostats can be employed to the simulation of the membrane structure or of the sorbate molecules or even of the entire sorbate–structure system.

Finally, it must be mentioned that the technique of molecular dynamics can be employed in sorption studies as well, not only at the stage of reconstruction (thermal effects in the atomic-scale configuration) but also during the sorption process itself. More specifically, it has been realized that Monte Carlo simulations of sorption cannot always capture steric phenomena associated with the accessibility of the sorption cages from the ambient. This is easy to visualize in materials like zeolites, where large cavities that can accommodate a significant amount of sorbate molecules are not always connected to the rest of the material, and eventually to the ambient, through equally wide avenues. On the contrary, it is well known that narrow pathways must be used by sorbate molecules to gain access to the larger cages. In the case of faujasite, for instance, which has the potential to perform efficient separation of CO_2 and light hydrocarbons, the sodalite cage has an effective diameter of about 1.25 nm, whereas the access pathways are only 0.74 nm wide. Therefore, the use in Monte Carlo simulation of sorption of an initial configuration that involves a certain number of sorbate molecules within the soladite cages is based on the arbitrary assumption that these, or further added molecules during the simulation, have found a way to penetrate into the cage through pathways that are narrower than the sorbate molecule size. If the sorption process is simulated in a dynamic way using molecular dynamics, then the initial configuration can be an empty framework that is exposed to a reservoir of a prespecified concentration of sorbate molecules. In this way, not only the accessibility issue but also the concomitant distortion of the framework can be taken into account and the sorption capacity can be evaluated in a more realistic manner.

1.03.3.4.5 Structure and transport simulation in polymers

Polymeric membranes of relatively large porosity can, in general, be treated in the way described above in the context of mesoscopic and macroscopic techniques. In dense polymeric membranes, the following expression is typically used for the flux, N_i, of gas species i:

$$N_i = D_{ei} S_i \Delta p_i / L$$

where Δp_i is the partial pressure drop across the membrane thickness L, the diffusion coefficient D_{ei} reflects the mobility of the gas molecules in the membrane, and the gas sorption coefficient, S_i, reflects the number of gas molecules that are dissolved in the membrane. The quantity $D_{ei}S_i$ is also called the permeability, P_i, of the membrane as it is a measure of the capability of the membrane to allow permeation of the gas.

For a binary mixture, the membrane selectivity can be written as

$$\frac{D_{ei}}{D_{ej}}\frac{S_i}{S_j}$$

where the first ratio is the contribution to the selectivity of the relative mobility of the two species, which is strongly effected by the relative size of the two types of molecules, and the second ratio is the sorption or solubility selectivity. The two contributions act, typically, in opposite directions thus making their study very interesting and useful, since large polymer molecules typically imply lower diffusion coefficient and higher solubility.

The diffusivities and solubilities in polymer membranes can be calculated using atomistic simulations and concepts similar to the ones mentioned above for inorganic materials. Expressions for the potential energy that involve bonded and nonbonded interaction terms are used both for the atomistic reconstruction of the polymer structure and for the calculation of transport and sorption properties. Atomistic packing of polymers usually follows the methodology that was suggested by Theodorou and Suter [99] and defines the configuration through the specification of the tacticity of the parent chain, of three Eulerian angles describing its orientation, and of the rotation angles of the skeletal bonds. The motion of united atoms is extensively used in packing and transport simulations of polymers thus lumping the behavior of individual atoms of the same polymer part or penetrant molecule and saving considerable computational time. An interesting method to predict the infinite dilution solubility or Henry's constant is the Widom's test particle approach [100] according to which a ghost molecule is injected at a randomly selected position inside the polymer structure. Subsequently, the interaction energy of this molecule with the surrounding atoms of the polymer matrix is computed and the excess chemical potential is calculated in the *NPT* ensemble. Henry's constant can

then be calculated as a function of temperature and of the excess chemical potential through the equation

$$K_H = \frac{V_0}{RT}\exp(-\beta\mu_{ex})$$

as was recently done by Tsolou *et al.* [101] for the sorption of light gases in polyisobutylene, where V_0 is the molar volume of ideal gases at standard conditions of pressure and temperature.

Alternatively to the atomistic simulations, the transition state theory (TST) after Gusev and Suter [102] can be used for the calculation of the diffusivities and solubilities that are required for the prediction of the separation factor of mixtures. Briefly, the free energy that is needed for a penetrant molecule to be inserted in the polymer packing is calculated at fixed grid positions. These values are used for the generation of a map of holes that can accommodate sorbate molecules and for the calculation of the probability of sorbate transition from one hole to another. For sufficiently low loading, the solubility approaches Henry's constant, whereas at higher loadings both liquid-like sorption and gas sorption are expected to take place.

An alternative technique to calculate structural features and diffusivities in polymers is the one that is based on the free volume theory and its variants. Following Cohen and Turnbull [103], diffusion takes place thanks to the continuous redistribution of the free volume that creates instantaneous openings for the dislocation of the penetrant molecules. In this original chapter, each individual jump was considered as part of the diffusion process of a single hard sphere molecule. This theory was generalized later to binary mixtures by Vrentas and coworkers [104, 105] in a series of relevant publications (see Duda and Zielinski [106] for a comprehensive presentation and discussion) and furnished expressions for the self-diffusion coefficient in terms of the specific hole free volumes of the two components that are required for a jump to occur. Experimentally, the free volume of a polymer can be characterized using positron annihilation lifetime spectroscopy (PALS) [107] whereas, computationally, it can be determined using grid-based techniques or variants of the small sphere probing method. Satisfactory agreement between TST and molecular dynamics calculations has been observed in a number of polymer studies (see also the recent work by Heuchel *et al.* [108] for polymers with intrinsic microporosity) as much as between molecular dynamics and free-volume theories [109]. The visualization of free volume elements in polymer membranes offers a valuable and direct means for the elucidation of the topological and geometrical features of the material.

1.03.4 Concluding Remarks – Multiscale Modeling

Technical demands of increased performance of membranes in separation applications have necessitated the development of a variety of theoretical and experimental techniques that will allow more accurate determination of material and process details as well as in-depth understanding of the structure-to-transport interrelationship. Phenomenological approaches remain certainly of unique usefulness for the quantification of the intermediate and end properties of the membranes as they offer convenient working equations with measurable macroscopic parameters or coefficients. However, any progress on the design of improved membrane materials with tailored properties relies inevitably on the detailed study and probing of the structure at the atomic or mesoscopic scale, depending on the nature of the material and the requirements of the specific application that is targeted. Passing from the atomic scale to the macroscopic scale or vice versa involves several transition steps as described in this chapter. In fact, the top-down approach that is depicted in **Figure 12** is indicative of a typical framework of analysis that refocuses itself onto progressively finer details of the membrane structure. On the other hand, computation of transport properties starting from the fundamentals follows a bottom-up procedure and is the natural way to proceed if sufficient information at the atomic level is available. Such a multilevel modeling has stimulated the development of coarse-graining techniques, which are nowadays among the major challenges of material science and engineering and have, consequently, attracted the attention of a great variety of scientific disciplines. At every coarsening stage, details of the lower scale are blurred and some lumping of properties is invoked without losing valuable information. Matching of the modeling approaches at the interface of these scales is of critical importance in this process, requiring, in turn, consistent descriptions of the material properties and behavior across scales. The united or super atom approach is the most popular tool for such coarse-graining as it lumps the properties of individual constituents into effective properties of the system at the upper level. More sophisticated approaches pursue a mapping of the system onto a number of variables

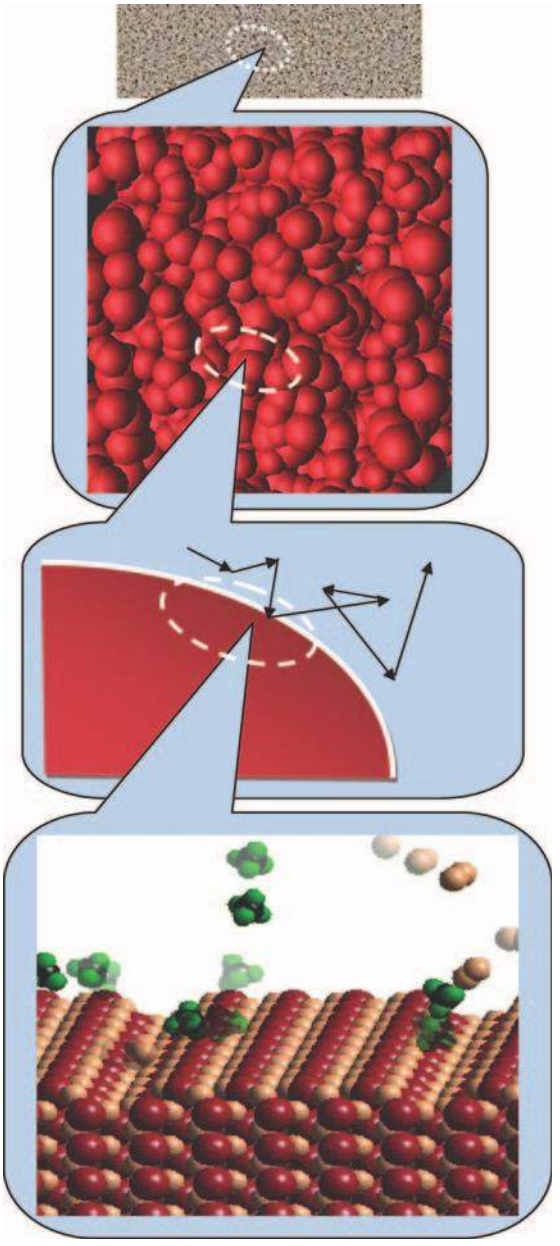

Figure 12 Modeling across scales from the macroscopic down to the atomistic one: granular crystalline material with active surface.

that can characterize the behavior of the system over sufficiently large length and time scales.

The aforementioned issue of multiscale modeling becomes a true challenge in the case of membrane nanomaterials for a multitude of reasons. Commercially viable separations require sufficiently high separation factors that are favored by sieving at the molecular or individual particle level. As a result, atomic-scale design of new or improved materials becomes a major, direct task that creates tremendous opportunities for envisaging radical structures with, however, tractable synthesis routes. Because of the usually strong requirement for thin membrane materials (to ensure reasonable throughput), improved sieving properties must be accompanied by adequate mechanical stability. Additional requirements are frequently posed by demanding operating conditions that may involve high pressure or high temperature or both. Chemically resistant materials may be also needed depending on the nature of the fluids that will be handled. This is obviously a heavily complicated problem that necessitates a combination of different techniques and an algorithm of design and implementation routing. Computational techniques can truly guide investigations in this direction and are nowadays recognized as indispensable – in combination with sufficiently accurate experimental techniques – in a number of design and synthesis challenges, including zeolite framework modifications, dense polymers for selective ionic conduction, pore networking within otherwise dense materials for controlled two-phase flow operation etc.

Acknowledgments

The author is indebted to Alexandros Kalarakis, Panagiotis Krokidas, and Vasilis Michalis for some indicative calculations and illustrations that are included in this chapter and to Eugene Skouras and Vlasis Mavrantzas for discussions and review of selected portions of the chapter.

References

[1] Theodorou, D. N. *Chem. Eng. Sci.* **2007**, *62*, 5697–5714.
[2] Moore, G. E. *Electronics* **1965**, *38*, 114–117.
[3] Sotirchos, S. V., Burganos, V. N. *Mater. Res. Soc. Bull.* **1999**, *24* (3), 41–45.
[4] Jackson, R. *Transport in Porous Catalysts*; Elsevier: New York, 1977.
[5] Darken, L. S. *Trans. AIME* **1948**, *174*, 184.
[6] Goren, S. L. *J. Colloid Interface Sci.* **1979**, *69*, 78–85.
[7] Nir, A. *J. Eng. Math.* **1981**, *15*, 65–75.
[8] Sherwood, J. D. *Physicochem. Hydrod.* **1988**, *10*, 3–12.
[9] Payatakes, D. *Chem. Eng. Comm.* **1987**, *58*, 119–138.
[10] Michalopoulou, A. C., Burganos, V. N., Payatakes, A. C. *AIChE J.* **1992**, *38*, 1213–1228.
[11] Michalopoulou, A. C., Burganos, V. N., Payatakes, A. C. *Chem. Eng. Sci.* **1993**, *48*, 2889–2900.
[12] Babler, M. U., Sefcik, J., Morbidelli, M., Baldyga, J. *Phys. Fluids* **2006**, *18*, 013302.
[13] Burganos, V. N., Paraskeva, C. A., Payatakes, A. C. *J. Colloid Interface Sci.* **1993**, *158*, 466–475.
[14] Weber, A. Z., Newman, J. *Chem. Rev.* **2004**, *104*, 4679–4726.

[15] Schoch, R. B., Jongyoon, H., Renaud, P. *Rev. Mod. Phys.* **2008**, *80*, 839–883.
[16] Sotirchos, S. V., Burganos, V. N. *AIChE J.* **1988**, *34*, 1106–1118.
[17] Burganos, V. N., Sotirchos, S. V. *AIChE J.* **1987**, *33*, 1678–1689.
[18] Krishna, R., Wesselingh, J. A. *Chem. Eng. Sci.* **1997**, *52*, 861–911.
[19] Sotirchos, S. V. *AIChE J.* **1989**, *35*, 1953–1961.
[20] Mason, E. A., Lonsdale, H. K. *J. Membr. Sci.* **1990**, *51*, 1–81.
[21] Chen, Y. D., Yang, R. T. *AIChE J.* **1991**, *37*, 1579–1582.
[22] Tsakiroglou, C. D., Payatakes, A. C. *J. Colloid Interface Sci.* **1991**, *146*, 479–494.
[23] Burganos, V. N., Payatakes, A. C. *Chem. Eng. Sci.* **1992**, *47*, 1383–1400.
[24] Burganos, V. N. *J. Chem. Phys.* **1993**, *98*, 2268–2278.
[25] Constantinides, G. N., Payatakes, A. C. *Chem. Eng. Comm.* **1989**, *81*, 55–81.
[26] Coelho, D., Thovert, J.-F., Adler, P. M. *Phys. Rev. E* **1997**, *55*, 1959–1978.
[27] Kainourgiakis, M. E., Kikkinides, E. S., Galani, A., Charalambopoulou, G. C., Stubos, A. K. *Transp. Porous Med.* **2005**, *58*, 43–62.
[28] Roberts, J. N., Schwartz, L. M. *Phys. Rev. B* **1985**, *31*, 5990–5997.
[29] Skouras E. D. Diffusion and Sorption in Gas Sensors Made of Semiconducting Nanoceramics. PhD Dissertation, University of Patras,2000.
[30] Willett, M. J., Burganos, V. N., Tsakiroglou, C. D., Payatakes, A. C. *Sens. Actuators B* **1998**, *53*, 76–90.
[31] Kikkinides, E. S., Stoitsas, K. A., Zaspalis, V. T., Burganos, V. N. *J. Membr. Sci.* **2004**, *243*, 133–141.
[32] Yao, J., Thovert, J. F., Adler, P. M., *et al. Revue de l' IFP,* **1997**, *52*, 3–21.
[33] Adler, P. M., Jacquin, C. J., Quiblier, J. A. *Int. J. Mult. Flow* **1990**, *16*, 691–712.
[34] Joshi, M. Y. A Class of Stochastic Models for Porous Materials PhD Dissertation, University of Kansas, 1974.
[35] Quiblier, J. A. *J. Colloid Interface Sci.* **1984**, *98*, 84–102.
[36] Yeong, C. L. Y., Torquato, S. *Phys. Rev. E* **1998**, *57*, 495–506.
[37] Mandelbrot, B. B., van Ness, J. W. *SIAM Rev.* **1968**, *10*, 422.
[38] Kikkinides, E. S., Burganos, V. N. *Phys. Rev. E* **1999**, *59*, 7185–7194.
[39] Kikkinides, E. S., Burganos, V. N. *Phys. Rev. E* **2000**, *62*, 6906–6915.
[40] Kikkinides, E. S., Kainourgiakis, M. E., Stefanopoulos, K. L., Mitropoulos, A. C., Stubos, A. K., Kanellopoulos, N. K. *J. Chem. Phys.* **2000**, *112*, 9881–9887.
[41] Burganos, V. N., Sotirchos, S. V. *Chem. Eng. Sci.* **1998**, *43*, 1685–1694.
[42] Abbasi, M. H. A Monte Carlo Simulation of the Diffusion of Gases and Radiant Heat Transfer in Porous Solids or Packed Beds. PhD Dissertation, University of California, Berkeley, CA, 1981.
[43] Evans, J. W., Abbasi, M. H., Sarin, A. *J. Chem. Phys.* **1980**, *72*, 2967–2973.
[44] Akanni, K. A., Evans, J. W., Abramson, I. S. *Chem. Eng. Sci.* **1987**, *42*, 1945–1954.
[45] Burganos, V. N., Sotirchos, S. V. *Chem. Eng. Sci.* **1989**, *44*, 2451–2462.
[46] Burganos, V. N., Sotirchos, S. V. *Chem. Eng. Sci.* **1989**, *44*, 2629–2637.
[47] Tomadakis, M. M., Sotirchos, S. V. *AIChE J.* **1993**, *39*, 397–412.
[48] Melkote, R. R., Jensen, K. F. *AIChE J.* **1992**, *38*, 56–66.
[49] Levitz, P. *Europhys. Lett.* **1997**, *39*, 593–598.
[50] Jeans, J. H. *The Dynamical Theory of Gases*; Cambridge University Press: London, 1925.
[51] Burganos, V. N. *J. Chem. Phys.* **1998**, *109*, 6772–6779.
[52] Bird, G. A. *Molecular Gas Dynamics and the Direct Simulation of Gas Flows*; Clarendon: Oxford, 1994.
[53] Frisch, U., Hasslacher, B., Pomeau, Y. *Phys. Rev. Lett.* **1986**, *56*, 1505–1508.
[54] Wolfram, S. *J. Stat. Phys.* **1986**, *45* (3/4), 471–526.
[55] Bhatnagar, P. L., Gross, E. P., Krook, M. *Phys. Rev.* **1954**, *94*, 511–525.
[56] Beskok, A., Karniadakis, G. E. *Microscale Thermophys. Eng.* **1999**, *3*, 43–77.
[57] Pollard, W. G., Present, R. D. *Phys. Rev. E* **1948**, *73*, 762–774.
[58] Shen, C., Tian, L. B., Xie, C., Fan, J. *Microscale Thermophys. Eng.* **2004**, *8*, 423–432.
[59] Dawson, S. P., Chen, S., Doolen, G. D. *J. Chem. Phys.* **1993**, *98*, 1514–1523.
[60] Kumar, R., Nivarthi, S. S., Davis, H. T., Kroll, D. M., Maier, R. S. *Int. J. Numer. Methods Fluids* **1999**, *31*, 801–819.
[61] Salles, J., Thovert, J. F., Prevors, L., Auriault, J. L., Adler, P. M. *Phys. Fluids A* **1993**, *5*, 2348–2376.
[62] Maier, R. S., Kroll, D. M., Bernard, R. S., Howington, S. E., Peters, J. F., Davis, H. T. *Phys. Fluids* **2000**, *12*, 2065–2079.
[63] Salamon, P., Fernàndez-Garcia, D., Gómez-Hernández, J. J. *J. Contam. Hydrol.* **2006**, *87*, 277–305.
[64] Michalis, V. K., Kalarakis, A. N., Skouras, E. D., Burganos, V. N. *Comp. Math. Appl.* **2008**, *55*, 1525–1540.
[65] Koplik, J., Redner, S., Wilkinson, D. *Phys. Rev. A* **1988**, *37*, 2619–2636.
[66] De Arcangelis, L., Koplik, J., Redner, S., Wilkinson, D. *Phys. Rev. Lett.* **1986**, *57*, 996–999.
[67] Sahimi, M., Imdakm, A. O. *J. Phys. A: Math. Gen.* **1988**, *21*, 3833–3870.
[67a] Michalis, V. K., Kalarakis, A. N., Skouras, E. D., Burganos, V. N. *Water Resour. Res.* **2009**, *45*, W08429 doi:10.1029/2008WR007659.
[68] Skouras, E. D., Burganos, V. N., Paraskeva, C. A., Payatakes, A. C. *Sep. Purif. Technol.* **2007**, *56*, 325–339.
[69] Skouras, E. D., Burganos, V. N., Paraskeva, C. A., Payatakes, A. C. *J. Chin. Inst. Chem. Eng.* **2004**, *35*, 87–100.
[70] Burganos, V. N., Skouras, E. D., Paraskeva, C. A., Payatakes, A. C. *AIChE J.* **2001**, *47*, 880–894.
[71] Swift, M. R., Osborn, W. R., Yeomans, J. M. *Phys. Rev. Lett.* **1995**, *75*, 830–833.
[72] Rowlinson, J. S., Widom, B. *Molecular Theory of Capillarity*; Clarendon: Oxford, 1982.
[73] Angelopoulos, A. D., Paunov, V. N., Burganos, V. N., Payatakes, A. C. *Phys. Rev. E* **1998**, *57*, 3237–3245.
[74] Holdych, D. J., Rovas, D., Georgiadis, J. G., Buckius, R. O. *Int. J. Mod. Phys. C* **1998**, *9*, 1393–1404.
[75] Kalarakis, A. N., Burganos, V. N., Payatakes, A. C. *Phys. Rev. E* **2002**, *65*, 56702-1/13.
[76] Kalarakis, A. N., Burganos, V. N., Payatakes, A. C. *Phys. Rev. E* **2003**, *67*, 016702-1/8.
[77] Inamuro, T., Konishi, N., Ogino, F. *Comput. Phys. Commun.* **2000**, *129*, 32–45.
[78] Toolke, J., Freudiger, S., Krafczyk, M. *Comput. Fluids* **2006**, *35*, 820–830.
[79] Kalarakis, A. N., Burganos, V. N. (in preparation).
[80] Rappé, A. K., Casewit, C. J., Colwell, K. S., Goddard, W. A., III, Skiff, W. M. *J. Am. Chem. Soc.* **1992**, *114*, 10024–10035.
[81] Visser, J. W. *J. Appl. Crystallogr.* **1969**, *2*, 89–95.
[82] Pawley, G. S. *J. Appl. Crystallogr.* **1981**, *14*, 357–361.
[83] Rietveld, H. M. *J. Appl. Crystallogr.* **1969**, *2*, 65–71.

[84] Navascues, N., Skouras, E. D., Nikolakis, V., Burganos, V. N., Tellez, C., Coronas, J. *Chem. Eng. Proc.* **2008**, *47*, 1139–1149.
[85] Deem, M. W., Newsam, J. M. *J. Am. Chem. Soc.* **1992**, *114*, 7198–7207.
[86] Krokidas, P., Skouras, E. D., Nikolakis, V., Burganos, V. N. *Mol. Simul.* **2008**, *34*, 1299–1309.
[87] Hecht, C. E. *Statistical Thermodynamics and Kinetic Theory*; Freeman: New York, 1990.
[88] Maginn, E. J., Bell, A. T., Theodorou, D. N. *J. Phys. Chem.* **1995**, *99*, 2057–2079.
[89] June, R. L., Bell, A. T., Theodorou, D. N. *J. Phys. Chem.* **1990**, *94*, 1508–1516.
[90] Caro, J., Noack, M., Kolsch, P., Schafer, R. *Microporous Mesoporous Mater.* **2000**, *38*, 3–24.
[91] Ewald, P. P. *Ann. Phys.* **1921**, *369*, 253–287.
[92] Karasawa, N., Goddard, W. A. *Macromolecules* **1992**, *25*, 7268.
[93] Greengard, L., Rokhlin, V. I. *J. Comput. Phys.* **1987**, *73*, 325.
[94] Allen, M. P., Tildesley, D. J. *Computer Simulation of Liquids*; Clarendon: Oxford, 1987.
[95] Skouras, E. D., Burganos, V. N., Payatakes, A. C. *J. Chem. Phys.* **1999**, *110*, 9244–9253.
[96] Skouras, E. D., Burganos, V. N., Payatakes, A. C. *J. Chem. Phys.* **2001**, *114*, 545–552.
[97] Agmon, N. *J. Chem. Phys.* **1984**, *81*, 3644–3647.
[97a] Hu, Y., Sinnott, S. B. *J. Comp. Phys.* **2004**, *200*, 251–266.
[98] Berendsen, H. J. C., Postma, J. P. M., van Gunsteren, W. F., DiNola, A., Haak, J. R. *J. Chem. Phys.* **1984**, *81*, 3684–3690.
[99] Theodorou, D. N., Suter, U. W. *Macromolecules* **1985**, *18*, 1467–1478.
[100] Widom, B. *J. Chem. Phys.* **1963**, *39*, 2808.
[101] Tsolou, G., Mavrantzas, V. G., Makrodimitri, Z. A., Economou, I. G., Gani, R. *Macromolecules* **2008**, *41*, 6228–6238.
[102] Gusev, A. A., Suter, U. W. *J. Chem. Phys.* **1993**, *99*, 2228–2234.
[103] Cohen, M. H., Turnbull, D. *J. Chem. Phys.* **1954**, *31*, 1164–1169.
[104] Vrentas, J. S., Duda, J. L. *J. Polym. Sci. Part B: Polym. Phys.* **1977**, *15*, 403–416.
[105] Vrentas, J. C., Vrentas, C. M., Faridi, N. *Macromolecules* **1996**, *29*, 3272–3276.
[106] Duda, J. L., Zielinski, J. M. Free-Volume Theory. In *Diffusion in Polymers*; Neogi, P., Ed.; Marcel Dekker: New York, 1996; pp 143–171.
[107] Finkelshtein, E. S., Makovetskii, K. L., Gringolts, M. L., *et al. Macromolecules* **2006**, *39*, 7022–7029.
[108] Heuchel, M., Fritsch, D., Budd, P. M., McKeown, N. B., Hofmann, D. *J. Membr. Sci.* **2008**, *318*, 84–99.
[109] Harmandaris, V. A., Angelopoulou, D., Mavrantzas, V. G., Theodorou, D. N. *J. Chem. Phys.* **2002**, *116*, 7656–7665.

Biographical Sketch

Vasilis N. Burganos is research director at the Institute of Chemical Engineering and High Temperature Chemical Processes, one of the seven institutes that comprise the Foundation for Research and Technology, Hellas. He received his diploma in chemical engineering from the National Technical University of Athens, Greece, and his MSc and PhD from the University of Rochester, USA. His research activities are focused in the general areas of transport phenomena and porous materials, with emphasis on diffusion and sorption, separation processes, semiconductive sensors, single and multiphase flow in porous media, capillarity, and pore structural analysis. He has also developed computer-aided simulators of jet-break-up and atomization for the preparation of microelectronic circuits, and of land contamination by organic mixtures for the purposes of risk assessment. He has coordinated research in several research and development (R&D) projects, funded by the European Commission, the General Secretariat for Research and Technology, and the industry. He has authored or coauthored more than 80 publications in scientific journals and international conference proceedings, edited a Materials Research Society (MRS) bulletin on membranes and membrane processes, organized an MRS symposium on membranes, and organized or co-organized various international scientific and educational events on nanomaterials and porous media

1.04 Fundamentals of Transport Phenomena in Polymer Membranes

D R Paul, University of Texas at Austin, Austin, TX, USA

1.04.1 Introduction

The objective of this chapter is to provide the beginning researcher or practitioner a comprehensive introduction to mass transport in polymeric membranes that will help in digesting and perhaps extending the vast literature that has developed over the past half-century and continues to grow rapidly. The scope is limited to systems where transport occurs by a solution-diffusion mechanism; this implies that the membrane has no pores or is fully dense. Of course, useful membranes are generally complex structures, but the type of interest here has at least a dense skin that controls the transport at a molecular level.

A common feature of all membranes processes is the transfer of one or more species from an upstream fluid phase through the membrane to a downstream fluid phase; the fluid phases may be gases, vapors, or liquids. In the solution-diffusion process, the species being transported molecularly dissolve in the polymer membrane, diffuse through the polymer segments, and then leave the membrane at the downstream surface to enter the fluid phase there. The polymer is an active participant in both the solution and diffusion processes. The sorption is a thermodynamic process while the transport is a kinetic process, and in each the polymer comprising the membrane has to be considered one of the components. In many porous membranes, the membrane material is not an active participant and only its pore structure matters, not its molecular structure. In the following sections the relationships that describe penetrant diffusion in polymers will be described; these can vary from very simple to complex depending on levels of approximation that are permissible. Then the various sorption or solution relationships that can be operative will be described for the different polymeric states that find use as membranes. The solution and diffusion relationships are then combined in various forms for describing the permeation and permselectivity of species through membranes. These relationships are first developed for binary systems, that is, the membrane and one penetrant. In most membrane processes, there are two or more penetrants since the purpose is to separate these species. In some cases, the simple binary relationships give an adequate description even for multiple penetrants if the penetrants permeate more or less independently. However, penetrant–penetrant interactions in both sorption and diffusion

can occur; thus, the reader is introduced to the considerably more complex ternary relationships.

There are a number of books [1–8] and review articles [9–16] that the interested reader can consult for more details and a further introduction to the literature on membrane processes.

1.04.2 Diffusion in Polymers

Quite often discussion of diffusion in polymers begins with the following simple relation between the flux of penetrant and the gradient of its concentration:

$$\text{Flux} = -D\frac{\mathrm{d}C}{\mathrm{d}z} \tag{1}$$

where D is the diffusion coefficient. This version of Fick's law seems intuitive in its similarity to Fourier's law for heat conduction or Ohm's law for electrical current flow. In may cases, this is an entirely appropriate description of mass transport, but there are cases where the inherent assumptions implicit in Equation (1) are not met so it is useful to go back to more rigorous beginnings and understand when the simple version is adequate and when it is not.

1.04.2.1 Binary Systems: Fick's Law

The diffusive flux of a species in a mixture must be expressed relative to some frame of reference. There are several ways to deal with this but an easily understandable one is to use a fixed frame of reference or stationary coordinates; this is particularly appropriate for membranes since this means relative to the membrane itself. The following are two fully equivalent forms of Fick's law of binary diffusion in three-dimensional (vector) form [17]:

$$\boldsymbol{n}_1 = w_1(\boldsymbol{n}_1 + \boldsymbol{n}_2) - \rho\mathcal{D}_{12}\nabla w_1 \tag{2}$$

$$\boldsymbol{N}_1 = x_1(\boldsymbol{N}_1 + \boldsymbol{N}_2) - C\mathcal{D}_{12}\nabla x_1 \tag{3}$$

where $\boldsymbol{n_i}$ is the mass flux of species i relative to stationary coordinates, $\boldsymbol{N_i}$ the molar flux, w_i the mass fraction of i, x_i the mole fraction, ρ the mass density of the mixture, C its molar density, and $\mathcal{D}_{12}$ the binary diffusion coefficient. Either version can be converted to the other by simple definitions. Corresponding relations can be written for component 2 by interchanging the subscripts realizing that $D_{12} = D_{21}$. These forms look similar to Equation (1) except for the terms $w_1(\boldsymbol{n}_1 + \boldsymbol{n}_2)$ or $x_1(\boldsymbol{N}_1 + \boldsymbol{N}_2)$ that are necessary to express what the diffusion fluxes are relative to as will become clearer below. Equation (3) turns out to be more convenient for mixtures of gases since at constant pressure and temperature, the total molar density, C, is a constant; for ideal gases $C = RT/p$, where p is the total pressure. Equation (2) is more convenient for liquids since the mass density, ρ, of such a mixture is more likely to be nearly constant than C. So how are these relations adapted to diffusion of a penetrant in a membrane?

First, it is useful to let the membrane component be identified with the subscript m and the penetrant with the subscript 1; this is particularly useful for the cases when there are other penetrants as we can identify them as 2, 3, etc. In some cases, the binary form of Fick's law can be used when there are more than two components but not always. Second, since diffusion through membranes is almost always unidirectional (e.g., the z-direction), Equations (2) and (3) can be written without vector notation as done for Equation (1). Third, for all practical cases in steady state, the membrane itself is stationary so the flux of this component is zero. Finally, it is important to recognize that for polymeric membranes, molar concentrations and terms like x_i or C in Equation (3) are at best ill-defined and at worst not meaningful since the molecular weight of the polymer may not be unique or may even be infinite. The earliest thermodynamic treatments of polymer mixtures revealed that mole fractions were not an appropriate way to express compositions in such systems [18]. Thus, Equation (2) provides a more useful form of Fick's first law for membrane systems. With the simplifications noted above, it becomes

$$n_1 = -\frac{\rho\mathcal{D}_{1\mathrm{m}}}{1-w_1}\frac{\mathrm{d}w_1}{\mathrm{d}z} = -\frac{\rho\mathcal{D}_{1\mathrm{m}}}{w_\mathrm{m}}\frac{\mathrm{d}w_1}{\mathrm{d}z} \tag{4}$$

This still does not quite look like the simple form of Equation (1). First, there is the $(1 - w_1) = w_\mathrm{m}$ term which arises because of frame of reference considerations or a convection term. As shown later, it is necessary to include this term in some cases; however, when the content of penetrant in the membrane is very small, $w_1 \ll 1$, then $w_\mathrm{m} \cong 1$. In addition, when the mass density of the membrane–penetrant mixture, ρ, is constant (this will surely be the case when $w_1 \ll 1$), then Equation (4) reduces to

$$n_1 = -\mathcal{D}_{1\mathrm{m}}\frac{\mathrm{d}\rho_1}{\mathrm{d}z} \tag{5}$$

where ρ_1 is the mass concentration of species 1 and n_1 is the mass flux. Dividing both sides by the molecular weight of 1 leads to

$$N_1 = -\mathcal{D}_{1m}\frac{dC_1}{dz} \tag{6}$$

where C_1 is the molar concentration of 1 and N_1 is its molar flux; in this simple form the flux and concentration can be written in any units so long as they are consistent. Equation (6) is identical to the familiar Equation (1) noting that $D = \mathcal{D}_{1m}$. It is clear what assumptions are behind Equations (1) and (6) and why it is necessary to be careful about these details in order to have $\mathcal{D}_{1m}$ be the same quantity through all these different forms.

Of course, for all membrane separations there is always more than one penetrant so the question is how to formulate a proper diffusion law for a ternary or multicomponent mixture. Fortunately, in many cases it is adequate to use a version of Equations (5) or (6) applied to each component *i*. This amounts to assuming that each component diffuses as if the other were not present; however, there are several ways such a simplification can fail. A most common situation is when the presence of component *j* affects the diffusion coefficient for component *i*, that is, $\mathcal{D}_{1m} = f(C_j)$ or plasticization occurs. Another complication is when the penetrant concentrations are not small enough to use the approximation $w_m \cong 1$. A further complication is when the flux of one species is dependent on the gradient of concentration of other species. It is truly difficult to correctly and accurately sort out all these potential interactions. The next section gives a logical starting framework to deal with these effects.

1.04.2.2 Ternary Systems: Maxwell–Stefan Equations

In some simple cases, *ad hoc* generalizations of Equations (2) or (3) to multicomponent mixtures have been suggested [17]; however, in general, this approach is not sufficient and leads to obvious problems [16]. A more sound approach is to begin with the Maxwell–Stefan equations that were originally developed to describe multicomponent diffusion in gas mixtures at low density and can be derived from kinetic theory [17, 19]. These equations have been extended with good success to dense gases, liquids, and polymers [17]; many review papers and books have discussed uses of these equations [17, 20]. A general form of the one-dimensional Maxwell–Stefan equations for isothermal multicomponent mixtures can be written as

$$d_i = -\sum_{j\neq i}\frac{x_i x_j}{\mathcal{D}_{ij}}(v_i - v_j) \tag{7}$$

where the $\mathcal{D}_{ij}$ are multicomponent diffusion coefficients [17], x_i is the mole fraction of *i* in the mixture, and v_i is the velocity of *i* in the *z*-direction relative to stationary coordinates. The term d_i is a generalized force (in the *z*-direction) for component *i* that causes it to diffuse relative to other species. Its general form is

$$CRT\, d_i = C_i\, d\mu_i^m/dz - w_i dp_m/dz \tag{8}$$

where

$$\frac{d\mu_i^m}{dz} = RT\frac{d\ln a_i^m}{dz} + \bar{V}_i\frac{dp_m}{dz} \tag{9}$$

where C is the molar density of the mixture, C_i is the molar concentration of *i* (note $x_i = C_i/C$), μ_i^m is the chemical potential of *i* in the membrane, a_i^m in the activity of *i* in the membrane, and p_m is the pressure in the membrane. For nonporous-supported membranes, the pressure throughout the membrane is constant (see References 14, 16, and 21–30) so for the cases of interest here, $dp_m/dz = 0$. As a result, Equation (7) simplifies to

$$-\sum_{j\neq i}\frac{x_i x_j}{\mathcal{D}_{ij}}(v_i - v_j) = x_i\frac{d\ln a_i^m}{dz} \tag{10}$$

The pressure that drives many membrane transport processes does not enter the picture by the flux law but comes in via the boundary conditions used in the integration of these equations.

Equation (10) can be expressed in forms more useful for describing diffusion in membranes. In steady state, the velocity or flux of the membrane material is zero relative to stationary coordinates, that is, $v_m = n_m = 0$. Penetrant velocities can be converted to fluxes via

$$n_i = w_i\rho v_1 \tag{11}$$

where ρ is the mass density of the membrane-penetrants mixture. As noted earlier, use of mole fractions is not useful for membrane systems; this issue can be resolved by converting to volume or mass fractions as discussed in recent papers [16, 31, 32]. Mass fractions and fluxes will be used here, and the conversion can be accomplished by the following:

$$x_i = \frac{M}{M_i}w_i, \quad M = \left[\sum\frac{w_j}{M_j}\right]^{-1} \tag{12}$$

where M_i is the molecular weight of *i* and M is the number average molecular weight of the mixture. It could be said that M is ill-defined because of the

ambiguity of the molecular weight of the membrane material; however, this potential complication appears to be resolved by redefining the diffusion coefficients. In the end, these diffusion coefficients must be determined experimentally. For a ternary system, Equation (10) requires three independent coefficients: $Đ_{1m}$, $Đ_{2m}$, and $Đ_{12}$. With the conversion to mass fractions, it becomes useful to redefine the diffusion coefficients in the following way:

$$D_{ij} = D_{ij}\frac{M_j}{M} \tag{13}$$

since they always appear in these combinations [16, 31]; similar redefinitions in terms involving molar volumes are needed when expressing Equation (10) in terms of volume fractions [32]. With the above simplifications, the Maxwell–Stefan equations for the 1–2-m ternary can be reduced to the following equations (after considerable algebra):

$$n_1 + \left(\frac{w_2 n_1 - w_1 n_2}{w_m}\right)\left(\frac{\mathcal{D}_{1m}}{\mathcal{D}_{12}}\right) = -\frac{\rho w_1 \mathcal{D}_{1m}}{w_m}\frac{d\ln a_1}{dz} \tag{14}$$

$$n_2 + \left(\frac{w_1 n_2 - w_2 n_1}{w_m}\right)\left(\frac{M_2}{M_1}\frac{\mathcal{D}_{2m}}{\mathcal{D}_{12}}\right) = -\frac{\rho w_2 \mathcal{D}_{2m}}{w_m}\frac{d\ln a_2}{dz} \tag{15}$$

The $w_m(= 1 - w_1 - w_2)$ in the denominator of the right-hand terms in each of the two equations reflects convection or frame of reference considerations inherently included in the Maxwell–Stefan equations. Alternate forms of Equations (14) and (15) can be written in terms of gradients of concentration or weight fractions by making use of the definition

$$\mathcal{D}_{im} = \mathcal{D}_{im}\left(\frac{\partial \ln a_i}{\partial \ln w_i}\right)_{T,p} \tag{16}$$

to get

$$n_1 + \left(\frac{w_2 n_1 - w_1 n_2}{w_m}\right) = -\frac{\rho \mathcal{D}_{1m}}{w_m}\frac{dw_1}{dz} \tag{17}$$

$$n_2 + \left(\frac{w_1 n_2 - w_2 n_1}{w_m}\right)\left(\frac{M_2}{M_1}\frac{\mathcal{D}_{2m}}{\mathcal{D}_{12}}\right) = -\frac{\rho \mathcal{D}_{2m}}{w_m}\frac{dw_1}{dz} \tag{18}$$

Equations (17) and (18) can be solved simultaneously to get independent equations for n_1 and n_2, but this adds great complexity [9]. Indeed, this complexity is why the more rigorous Maxwell–Stefan formulation is used so infrequently in the membrane literature. Importantly, Equations (17) and (18) reduce to Fick's law, Equation (4), where there is component 2 present and likewise, in some cases, where w_2 and n_2 are small.

1.04.3 Sorption of Gases and Vapors in Polymers

Knowledge about the equilibrium sorption of gases or vapors in polymers is essential for understanding the process of permeation by the solution-diffusion mechanism. Thus, considerable effort has been devoted to measuring and interpreting the sorption isotherms for small molecules in rubbery, glassy, and semi-crystalline polymers [4–9, 33–38]. The limiting cases described below are useful for understanding the possibilities. In a subsequent section these models are used to set the boundary conditions for permeation of gas and vapors in polymers.

1.04.3.1 Rubbery Polymers

Consider an amorphous polymer membrane above its glass transition temperature, T_g, surrounded by a vapor of component 1 at a partial pressure p_1. If the saturation vapor pressure of 1 is p_1^*, then its activity in the vapor phase is $a_1 = p_1/p_1^*$. The Flory–Huggins thermodynamic model for mixing small molecules of molar volume $\bar{V}_1$ with large polymer molecules of molar volume $\bar{V}_m$ combines an estimate for the entropy of mixing with a measure of the enthalpy of mixing, expressed in terms of an interaction parameter χ_1, to give the following expression for the equilibrium sorption [18]:

$$\ln a_1 = \ln \phi_1 + (1 - \bar{V}_1/\bar{V}_m)\phi_m + \chi_1 \phi_m^2 \tag{19}$$

where the ϕ_i are volume fractions. **Figure 1** shows example calculations, using Equation (19), of the amount of sorption of penetrant 1, expressed as ϕ_1, in the membrane at equilibrium versus its activity in the vapor phase for several values of the dimensionless interaction parameter, χ_1. At low activity, the extent of sorption is proportional to p_1; however, the isotherm shows upward curvature at higher activities. The degree of curvature increases with the extent of sorption as the interaction parameter decreases or becomes more favorable for mixing. If the interaction parameter depends on the amount of vapor sorbed, the shape will be altered somewhat but the upward curvature remains a generally expected shape for simple systems where sorption can be modeled as a nearly random mixing process.

In the limit of low activities or small extents of sorption, a linear approximation to the sorption

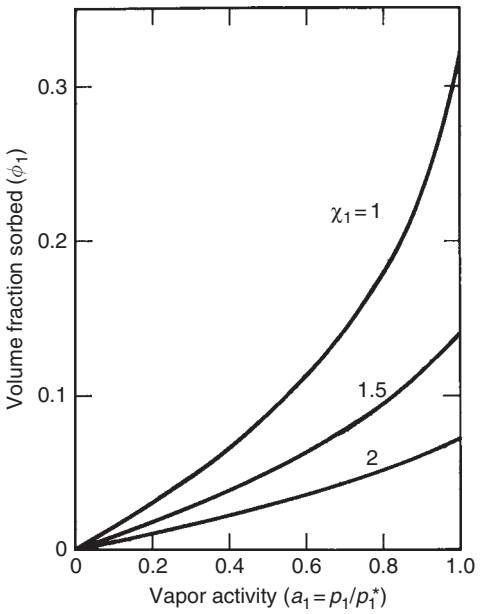

Figure 1 Predictions of sorption isotherms by the Flory–Huggins theory, Equation (19) with $\bar{V}_1/\bar{V}_m = 0$, for a vapor in an amorphous, rubbery polymer using the interaction parameters indicated [33].

isotherm provides an adequate description; that is, Henry's law applies,

$$C = Sp_1 \tag{20}$$

where C is the concentration of gas or vapor in the membrane in equilibrium with the gas phase at partial pressure p_1, and S is a solubility coefficient. This limiting case of the Flory–Huggins type of isotherm is normally used to analyze the behavior of gases in polymers above their glass transition temperatures.

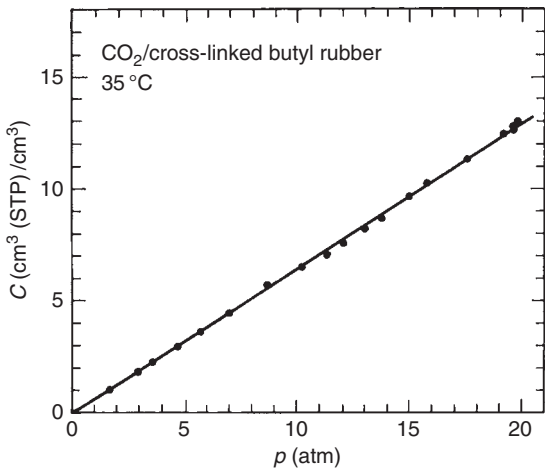

Figure 2 Sorption isotherm for CO_2 in a lightly crosslinked butyl rubber at 35 °C [33].

Figure 2 shows that sorption of CO_2 gas at 35 °C in crosslinked butyl rubber [33] is well described by Henry's law up to at least 20 atm. Since the critical temperature of CO_2 is about 31 °C, it is not possible to define an activity relative to the liquid state, but simple extrapolation of the vapor pressure curve to 35 °C allows one to see that CO_2 at 20 atm has an effective activity of less than 0.3. If the measurements in **Figure 2** were extended to pressures two to three times this level, curvature similar to that in **Figure 1** would probably be seen. For less soluble gases, such as O_2, N_2, and argon, Henry's law behavior is assured over a very wide range of pressures. Consequently, it may be said that linear isotherms are characteristic of gas sorption in rubbery polymers.

The solubility coefficient S increases with the condensability of the gas and generally can be correlated with the boiling point, the critical temperature, or other measures of the cohesive forces between the gas molecules [8, 9].

1.04.3.2 Glassy Polymers

It is well established that the shape of gas sorption isotherms in glassy polymers, that is, polymers below their T_g values, stands in marked contrast to the forms described above for rubbery polymers. The sorption of CO_2 in poly(phenylene oxide) (PPO) at 35 °C shown in **Figure 3** clearly illustrates this [39]. The isotherms for glassy polymers are far from linear, and the curvature has the opposite sense to that seen in **Figure 1**. Such isotherms can be well

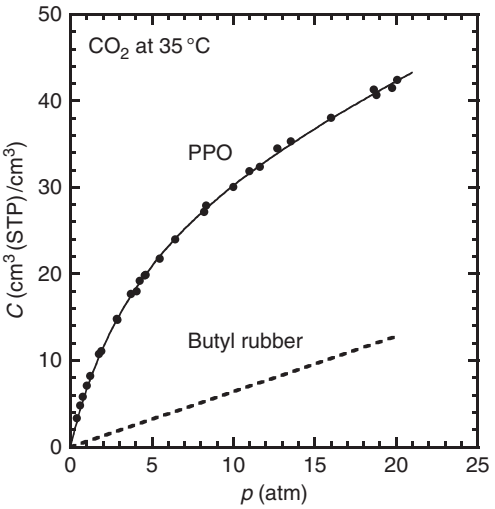

Figure 3 Sorption isotherm for CO_2 in poly(phenylene oxide) at 35 °C [39]. Dotted line represents data for butyl rubber from **Figure 2**.

described by a model that is an additive combination of Henry's law and a Langmuir isotherm, that is,

$$C = k_d p + \frac{C'_H b p}{1 + b p} \tag{21}$$

where k_d, C'_H, and b are parameters of the model. This form implies that there are two mechanisms of sorption in glassy polymers [9, 36–41]. Many alternatives to this model and its implied mechanistic aspects have been suggested over the years [40–55]; however, this so-called dual sorption model continues to be widely used for describing sorption in glassy polymers.

Generally, gases are more soluble in glassy polymers than rubbery ones [9] as may be seen in **Figure 3** by comparing the sorption of CO_2 in PPO versus that in butyl rubber; the dashed line is reproduced from **Figure 2**. Studies have shown that the k_D parameter from the dual sorption model, obtained from sorption data below T_g, varies smoothly with temperature through the glass transition forming a continuous connection with data above T_g, where simple Henry's law behavior, that is, Equation (20), is observed [38]. This, plus other observations, provide strong evidence that the Henry's law term in Equation (21) is physically a manifestation of the same solubility mechanism operative for gases in rubbery polymers or organic liquids. Thus, it follows that the Langmuir term in Equation (21) stems from the nonequilibrium character of the glassy state, and this is supported by considerable evidence [9, 55–61]. Additional evidence for this can be seen by examining the Langmuir capacity term C'_H for one gas, CO_2, measured at a single temperature, 35 °C, in a wide range of glassy polymers; **Figure 4** shows that C'_H plotted versus the polymer glass transition temperature provides a remarkable correlation [56]. It has been suggested [55] that the Langmuir term arises from packing of gases like CO_2 into the unrelaxed volume of the glass $(V_g - V_l)$ with a liquid-like density. The unrelaxed volume at any temperature T may be estimated from thermal expansion coefficients above and below T_g; that is,

$$\frac{V_g - V_l}{V_g} = (\alpha_l - \alpha_g)(T_g - T) \tag{22}$$

Since $(\alpha_l - \alpha_g)$ values are quite similar for most polymers, it follows from this picture that C'_H should be proportional to $(T_g - T)$, as seen in **Figure 4**. The support for this interpretation of the Langmuir mode

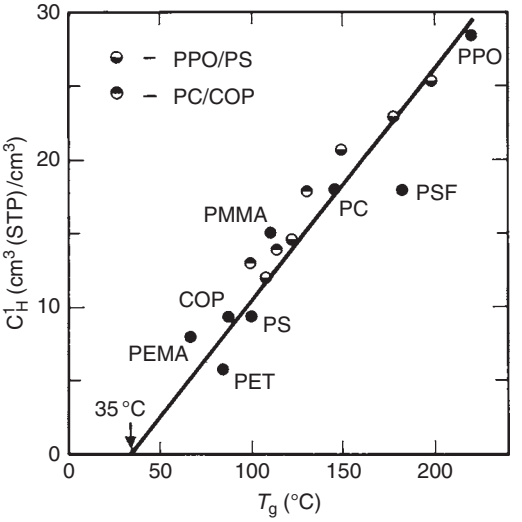

Figure 4 Correlation of measured values of the Langmuir sorption capacity at 35 °C with the glass transition temperature of the polymer [34]. PPO, poly(phenylene oxide); PSF, polysulfone; PC, polycarbonate; PMMA, poly(methyl methacrylate); PS, polystyrene; COP, copolyester; PEMA, poly(ethyl methacrylate); and PET, poly(ethylene terephthalate). Miscible blends of polymer pairs shown: (◡) PPO/PS; (◠) PC/COP.

is the quantitative agreement shown by numerous sets of experimental observations, including **Figure 4** [57]. From the above, it should be clear that sorption in glassy polymers will depend on the material's prior history as supported by many observations [60, 61]. The unrelaxed volume of the glass may decrease with aging time, especially at temperatures just below T_g, leading to decreased sorption [60]. On the other hand, sorption of gases or vapors in the polymer may lead to an increased unrelaxed volume upon desorption that in turn leads to increased sorption in subsequent experiments [61]. These effects of conditioning are sometimes manifested as hysteresis between sorption and desorption observations [4].

Sorption of large enough amounts of gases and vapors in any polymer causes plasticization; one manifestation of this is a reduction in the glass transition temperature. Because of this, the sorption isotherm under certain conditions may exhibit the characteristic glassy-type shape (see PPO data in **Figure 3**) at low pressures and then revert to the characteristic rubbery-type shape (shown by butyl rubber in **Figures 2** and **3**) at high pressures [62]. This can be seen for glassy polymers whose T_g values are not much higher than the temperature of sorption

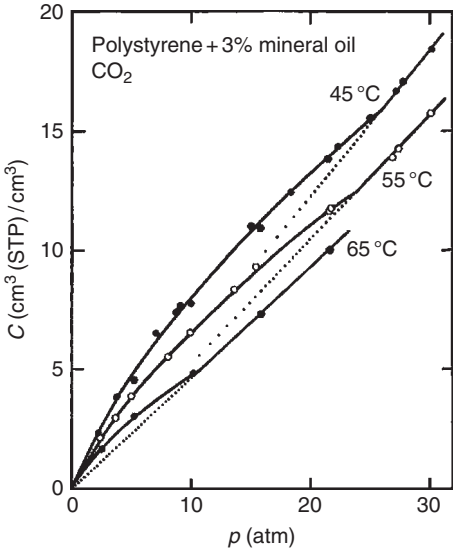

Figure 5 Effect of temperature on sorption isotherms for CO_2 in polystyrene containing mineral oil [33].

and whose T_g values are lowered by plasticization as gas or vapor is sorbed such that the original glass becomes a rubber within the range of pressure over which the isotherm is measured. **Figure 5** shows an example of this for sorption of CO_2 in a polystyrene containing 3 wt.% of the lubricant, mineral oil [62].

1.04.3.3 Semi-Crystalline Polymers

In most cases, penetrants do not dissolve in the crystalline regions of semi-crystalline polymers [63]. The reason for this is that usually the crystal is significantly more dense than the amorphous phase; thus, there is much less free volume to accommodate insertion of penetrants. However, there are some exceptions where the crystals are similar in density as the amorphous phase in which case there is evidence for solubility in the crystal phase [64–66]. If there is no solubility in the crystalline regions, then sorption is modulated by the extent of crystallinity [63]. The shape of the sorption isotherm is dictated by whether the amorphous phase is above or below its T_g.

1.04.3.4 Sorption of Gas or Vapor Mixtures

For membrane separation processes the feed contains two or more types of gases. In the simplest of cases when the extent of sorption by all species is quite small, the individual components sorb as if the others are not present. However, there can be interactions between the penetrants or between one or more of the penetrants and the membrane polymer that cause more complex behavior; in these cases, mixed gas sorption data may be needed [67, 68]. The most typical case is where one component is sorbed to a rather considerable extent plasticizing the polymer and, thereby, altering the sorption behavior of other components. In glassy polymers, there may be competitive sorption effects that can be described by an extension of the dual sorption model [69].

1.04.4 Permeation of Gases and Vapors in Polymers

To understand or describe the permeation of small molecules through polymer membranes by the solution-diffusion mechanisms requires combining the results in Sections 1.04.3 and 1.04.4 using only appropriate assumptions so that the details of interest can be captured. Permeation involves transferring components from an upstream fluid phase into the membrane, diffusion through the membrane, and then transferring these components to a downstream fluid phase. Basically, the sorption behavior discussed in Section 1.04.3 defines the boundary conditions for the diffusion in the membrane discussed in Section 1.04.2. In nearly all cases the surfaces of the membrane are in equilibrium with the fluid phase to which they are adjacent. Permeability coefficients are based on the driving force difference between the upstream and downstream fluid phases while diffusion coefficients are based on the driving force difference between the two surfaces but within the membrane phase.

1.04.4.1 Rubbery Polymers

First, we consider the steady-state permeation of simple gases in rubbery polymers where Equations (20) and (6) adequately describe the sorption and diffusion processes. Assuming $\mathcal{D}_{1m}$ is not concentration dependent, Equation (6) can be integrated across the membrane to get

$$N_1 = \mathcal{D}_{1m}\frac{C_{10} - C_{1\ell}}{\ell} \tag{23}$$

where ℓ is the membrane thickness, C_{10} and $C_{1\ell}$ are the concentrations of 1 in the membrane at the upstream ($z = 0$) and downstream ($z = \ell$) surfaces, respectively. From Equation (20), $C_{10} = S_1 p_{10}$ and $C_{1\ell} = S_1 p_{1\ell}$, where p_{10} and $p_{1\ell}$ are the partial pressures of 1 in the upstream and downstream fluid phases, respectively. Thus, Equation (23) becomes

$$N_1 = \mathcal{D}_{1m}\frac{S_1 p_{10} - S_1 p_{1\ell}}{\ell} = \mathcal{D}_{1m} S_1 \frac{\Delta p_1}{\ell} \qquad (24)$$

where $\Delta p_1 = p_{10} = p_{1\ell}$. The permeability coefficient P_1, in general, is defined by

$$P_1 \equiv \frac{\ell N_1}{\Delta p_1} \qquad (25)$$

but is given by the product $\mathcal{D}_{1m} S_1$ in this case.

If a second gas 2 is also permeating but the concentrations of both 1 and 2 are small enough that $\mathcal{D}_{im}$ and S_i are the same as if the other gas were not present, then the permeation in the mixed gas case can be described by the pure gas coefficients. An often-used measure of the selectivity of this permeation process is the ratio of the permeability coefficients:

$$\frac{P_1}{P_2} = \left(\frac{\mathcal{D}_{1m}}{\mathcal{D}_{2m}}\right)\left(\frac{S_1}{S_2}\right) \qquad (26)$$

that is the product of diffusion and solubility selectivity components.

Transient permeation experiments are often used to obtain the P, $\mathcal{D}$, and S coefficients. In this experiment, the membrane is degassed from both sides until no sorbed gas remains. At time $t = 0$, a certain fixed pressure is imposed at the upstream surface of the membrane while the total amount of gas that has exited the downstream membrane surface until time t, Q_t, is measured. The result will look like the graph of Q_t versus t shown in **Figure 6**. Eventually, a steady state is reached where the flux is given by $(1/A)(dQ/dt)_{ss}$, where A is the membrane area.

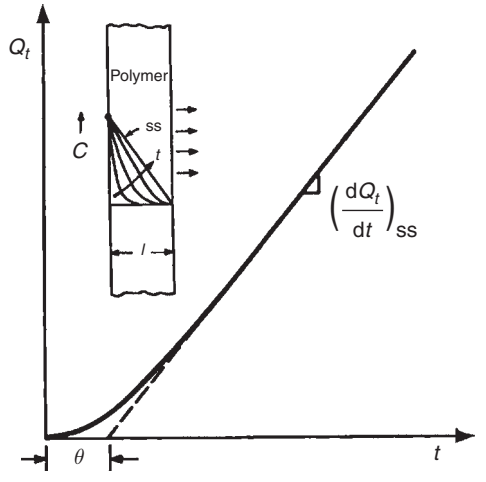

Figure 6 Amount of gas that has permeated through a membrane in time t illustrating a transient permeation experiment. Inset shows how the concentration profile develops over time.

Extrapolation of the linear region of Q_t versus t intercepts the time axis at $t = \theta$. This time lag, θ, reflects the time it takes for a steady-state concentration profile to build inside the membrane (see inset in **Figure 6**). To describe this unsteady-state situation requires combining Equation (6) with a differential mass balance to get Fick's second law:

$$\frac{\partial C_1}{\partial t} = -\frac{\partial N_1}{\partial z} = \frac{\partial}{\partial z}\left(\mathcal{D}_{1m}\frac{\partial C_1}{\partial z}\right) = \mathcal{D}_{1m}\frac{\partial^2 C_1}{\partial z^2} \qquad (27)$$

The last step is only justified when the diffusion coefficient does not depend on concentration. Equation (27) can be solved [70] using the conditions at the membrane surface described earlier, that is, $C_1 = 0$ for all z at $t < 0$, then for $t \geq 0$ $C_{10} =$ constant and $C_{1\ell} = 0$. From such a solution, the following important result can be deduced [70]:

$$\theta = \frac{\ell^2}{6\mathcal{D}_{1m}} \qquad (28)$$

Thus, by the transient permeation experiment one measures θ and P from which $\mathcal{D}_{1m}$ is obtained from Equation (28) and S_1 from $P_1 = \mathcal{D}_{1m} S_1$. Of course, S_1 can also be measured directly using sorption experiments. Often, diffusion and solubility coefficients are deduced from transient experiments when the assumptions implicit in the above are not strictly met, for example, a concentration-dependent diffusion coefficient, in which case these coefficients should be considered apparent values; they may still have some utility, however.

For rubbery polymers, highly condensable gases or vapors may no longer follow Henry's law but follow relations more similar to those in **Figure 1**. In principle, the same methodology described above can be followed, but certain caveats apply. First, the solubility coefficient is no longer a constant. Second, the diffusion coefficient is most likely not constant due to plasticization. Finally, at high penetrant concentrations, the convective terms seen in Equations (2)–(4) may not be negligible as assumed in Equations (5) and (6). When there is only a single penetrant, these problems can be dealt with using somewhat more complicated mathematical analyses and more detailed experimental measurements. For example, Equation (4) can be integrated as follows for a steady-state analysis:

$$\int_0^\ell n_1 dz = n_1 \ell = \int_{w_{1\ell}}^{w_{10}} \left(\frac{\rho \mathcal{D}_{1m}}{1 - w_1}\right) dw_1 \qquad (29)$$

If one knows $\mathcal{D}_{1m}$ as a function of w_1, then the integration can be carried out, at least numerically, to calculate the flux as a function of the boundary conditions or the external fluid phase partial pressures, or activities, assuming the sorption isotherm has been measured. More often than not, the situation is that n_1 has been measured as a function of the external fluid phase conditions and the issue is to deduce $\mathcal{D}_{1m}$ (w_1) from this information. Often one assumes a mathematical form for $\mathcal{D}_{1m}$ (w_1) such as

$$\mathcal{D}_{1m} = (\mathcal{D}_{1m})_0 e^{-Aw_1} \tag{30}$$

and performs the integration in Equation (29), perhaps with some simplifications, and fits the resulting mathematical form to the experimental data to get the model parameters.

However, when there are two or more penetrants, as there always is for separations, this problem grows more complex in several respects. In general, the various components do not sorb or diffuse as if the others were not there as in the case for very slightly soluble gases (e.g., see Equation (26)). Rather, the permeation of the species may be coupled in various ways. At the very least, the diffusion coefficient for one species may depend not only on its own concentration but on the concentration of all the other species as well. In the simplest of these cases, all the diffusion coefficients depend on the total penetrant concentration, that is, $w = w_1 + w_2$ for the case of two penetrants. Such an approach has recently been described, and the reader is referred to Reference 68 for the details.

Coupling at a more subtle level may occur by the flux of one species depending on the gradient of the concentration of another species. These issues, plus the frame of reference terms, are formally considered in the Maxwell–Stefan equations discussed in Section 1.04.2.2. This level of complexity has rarely been used in analyzing membrane processes for understandable reasons. However, a recent paper provides an in-depth experimental study with the results analyzed by the Maxwell–Stefan equations as well as Fick's law [68]. In this case, the contribution of the extra effects included by the Maxwell–Stefan approach versus Fick's law was of similar order as the experimental uncertainty. It is premature to judge if this conclusion is general or not.

1.04.4.2 Glassy Polymers

Steady-state permeation of a gas through a glassy polymer raises the questions of whether there are two populations of sorbed gas as implied by Equation (21) and, if there are, do they have different levels of mobility. A vast body of literature too numerous to list here has dealt with these questions [9, 57, 72–77]. Within the context of the dual sorption idea, the following model for the flux of a pure gas has been widely used [9, 57, 72, 73]:

$$\text{Flux} = -D_D \frac{\partial C_D}{\partial z} - D_H \frac{\partial C_H}{\partial z} \tag{31}$$

where two diffusion coefficients and concentrations corresponding to the Henry's law population (D = dissolved) and the Langmuir population (H = holes) in Equation (21) are used. At first glance, Equation (31) would appear to suggest two parallel and independent pathways of diffusion; however, Barrer [73] has shown that this model is more general. A steady-state analysis of Equations (21) and (31) shows the permeability coefficient, P, to be given by [72]

$$P = k_D D_D \left[1 + \frac{FK}{1 + bp_0}\right] \tag{32}$$

where $F = D_H/D_D$, $K = C'_H b/k_D$, and p_0 = upstream pressure of the permeating gas; the downstream pressure has been assumed to be zero. For clarity, subscripts denoting the component have been omitted. Equation (32) indicates that the permeability decreases slightly as p_0 increases as has been observed repeatedly for glassy polymers [9, 57, 58]. **Figure 7** shows data for CO_2 permeation in PPO [39] plotted as suggested by Equation (32); clearly, the experimental

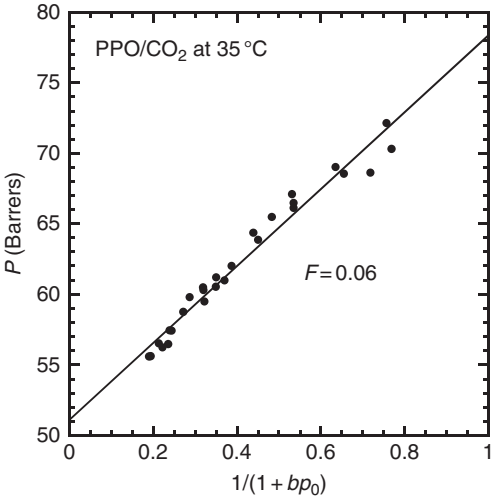

Figure 7 Permeability of CO_2 in poly(phenylene oxide) as a function of upstream pressure, p_0, plotted as suggested by Equation (32). From Maeda, Y. PhD Dissertation, University of Texas at Austin, 1985.

results conform quite well to this theoretical prediction as has been shown repeatedly for glassy polymers when complicating factors like plasticization are not important [9, 57, 58, 74–77]. The parameters of Equation (21) can be deduced by fitting of sorption data while the parameters D_D and F can be obtained by fitting of permeation data to Equation (32); the data in **Figure 7** give a value of $F = 0.06$ which is typical of most glassy polymers. The implications are that the Langmuir part of the sorption processes in glassy polymers tends to partially trap gas molecules, that is, their mobility is about an order of magnitude less than the gas molecules sorbed by the equilibrium or Henry's law mode.

An analysis of transient permeation has been made for the case when Equations (21) and (31) apply [9, 72] and predicts the time lag θ to be a complex relation of the form

$$\theta = \frac{\ell^2}{6D_D}[1 + f(K, F, bp_0)] \tag{33}$$

where the function f is quite involved [72]. This relation predicts that θ is a decreasing function of p_0 as observed experimentally [9, 58]; this is in contrast to the simple equation (28) where θ is independent of the upstream pressure. Clearly, values of the solubility, diffusion and permeability coefficients for glassy polymers computed by the methods outlined in Section 1.04.4.1 are only apparent values and are pressure dependent. Nevertheless, such quantities are useful and widely used in the literature, for example, Equation (26) continues to be used to assess what part of the permselectivity (i.e., P_1/P_2) is due to solubility versus diffusive selectivity [4, 8].

The above results assume that effects due to plasticization by the sorbed gas are not significant; however, as the concentration of the gas in the polymer increases to high enough levels due to very high pressures or high intrinsic solubility (e.g., highly condensable gases like CO_2 or vapors), plasticization inevitably occurs and the above analyses no longer describe the observations. A particularly important example of this involves separation of CO_2 or light hydrocarbons from high pressure natural gas [4, 7, 8]. Typically, the permeability of glassy polymers to CO_2 will first decrease as the driving pressure increases as expected from Equation (32) and then go through a minimum and rise with further increases in upstream pressure owing to plasticization [14–82]. Formally, one can describe such effects by assigning concentration dependence to the parameters in Equations (21) and (31) [78]; however, this increases the number of parameters and the resulting analyses become very complex and can be devoid of physical meaning as a result. Since glassy polymers are not in equilibrium, the observations also become time dependent [79, 80] and may show hysteresis as the pressure is moved up and down [43].

For gas separations by glassy polymers, pure gas permeation behavior is not always a reliable indicator of mixed gas behavior. As a result, mixed gas measurements for both sorption and permeation may be needed [82]. Even in the absence of plasticization, competitive sorption effects can occur such that the presence of one component affects the transport of the other as shown by theoretical analyses and experiment [83, 84]. These effects can become quite severe in very high free volume polymers [85]. Of course, plasticization complicates the behavior even further [83, 85–87]. An active area of research is the development of membrane materials that are more resistant to plasticization [82, 86–89].

1.04.4.3 Semi-Crystalline Polymers

As described in Section 1.04.3.3, the presence of crystallinity in a polymer generally reduces the sorption of penetrants since usually these molecules do not enter the crystals. The effects on permeation can be even more dramatic since the shape of the crystals, in addition to their amount, affects the diffusion process owing to the tortuosity effect. In addition, the presence of crystals may alter the mobility of the penetrant in the amorphous phase. Further discussion of this complex, but important, behavior will not be given here since generally semi-crystalline polymers are not used for membranes owing to their usually lower permeability and issues of processing. The reader can consult a few key references to begin exploring this subject [90–92].

1.04.5 Liquid Permeation in Membranes

There are at least two important membrane processes (reverse osmosis [1, 16] and pervaporation [2]) that operate by a solution-diffusion mechanism where the feed is a liquid. Here, the latter is dealt with briefly while the former is analyzed more extensively.

1.04.5.1 Pervaporation

In this process, a mixture of liquids, for example, ethanol and water or aromatic and aliphatic hydrocarbons, are fed to the upstream side of a dense membrane while the permeate leaves as vapor; thus, the term stems from **per**meation + **e**v**aporation**. This is a very complex process to describe mathematically since interactions of the permeating species with the polymer and with each other clearly require the consideration of plasticization, convective terms, and possibly coupling as treated by the Maxwell–Stefan equations. There is a vast experimental and theoretical literature on the topic; it is beyond the scope here to review this.

Here, we treat the problem in its simplest possible form where all of the complications mentioned above are ignored. We assume that the equilibrium uptake of component 1 by the membrane is w_1^* and that the activity of 1 in the polymer is given by $a_1^{\mathrm{m}} = w_1/w_1^*$. Ignoring convective terms, plasticization or interaction issues, the flux of 1 would then be given by [9]

$$n_1 = -\frac{\rho\mathcal{D}_{1\mathrm{m}}}{\ell}(w_{10} - w_{1\ell}) = \frac{\rho w_1^*\mathcal{D}_{1\mathrm{m}}}{\ell}\left[1 - p_1/p_1^*\right] \qquad (34)$$

since by our assumptions $a_{1\ell}^{\mathrm{m}} = w_1/w_1^* = p_1/p_1^*$. In the limit of a high vacuum on the downstream side, the maximum possible flux becomes [9]

$$n_1 = \frac{\rho w_1^*\mathcal{D}_{1\mathrm{m}}}{\ell} \qquad (35)$$

We will return to this result later. Clearly, the permselectivity of species 1 relative to 2 is given by the product of solubility and diffusivity parts as in Equation (26). Of course, in practice the flux and permselectivity are described by much more complex relations [2, 71].

1.04.5.2 Reverse Osmosis

Reverse osmosis refers to a process where a solvent (species 1) and solute (species 2) are fed to the upstream of the membrane at a high pressure p_0 while the permeate stream exits the downstream at a lower pressure p_ℓ (typically atmospheric) as a liquid with a lower content of solute. The most common application of this process is desalination of water (1); however, this technique may be applied to situations where solvents and solutes other than water and salt are involved. The main purpose here is to show how the driving force $\Delta p = (p_0 - p_\ell)$ leads to the transport of solvent across the membrane by a solution-diffusion mechanism [16].

We begin with the binary form of Fick's law given in Equation (4); a similar result comes from Equation (17) when w_2 and n_2 are small as assumed here. The convective term in the denominator, $(1 - w_1)$, can be ignored when w_1 is small but doing so results in a redefinition of the binary diffusion coefficient when w_1 is significant compared to unity. Equation (4) is written in either of the following differential or integrated forms when ρ and $\mathcal{D}_{1\mathrm{m}}$ are independent of concentration:

$$n_1 = -\frac{\rho\mathcal{D}_{1\mathrm{m}}}{1-w_1}\frac{\mathrm{d}w_1}{\mathrm{d}z} = \frac{\rho\mathcal{D}_{1\mathrm{m}}}{\ell\langle w_{\mathrm{m}}\rangle}(w_{10} - w_{1\ell}) \qquad (36)$$

The convective term in the denominator of the differential form means that the concentration profile, or w_1 versus z, is not strictly linear which complicates the integration. To retain the expected form of the integration and its associated physical meaning, it is convenient to define an average value of $1 - w_1 = w_{\mathrm{m}}$ designated as $\langle w_{\mathrm{m}}\rangle$. The thickness in Equation (36) is the actual thickness of the membrane with a solvent gradient which may differ from the dry thickness when there is no solvent in the membrane or the uniformly swollen thickness. The details of computing $\langle w_{\mathrm{m}}\rangle$ and ℓ are given elsewhere [9] and are not repeated here as it detracts from our main purpose.

The value of $w_{10} - w_{1\ell}$ to be inserted in Equation (36) stems from the thermodynamic equilibrium the two membrane interfaces have with the upstream and downstream external phases (see schematic in **Figure 8**). Paul *et al.* described an explicit procedure for handling this thermodynamic analysis in reverse osmosis or the so-called hydraulic permeation

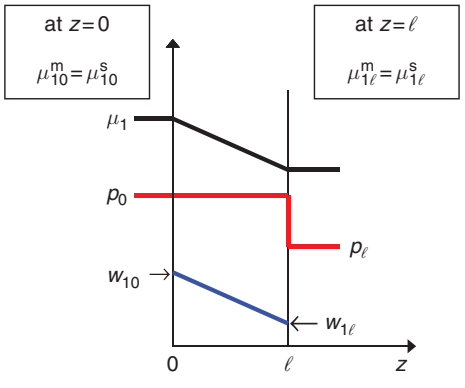

Figure 8 Chemical potential, pressure, and concentration profiles in a reverse osmosis membrane.

[21–30]. The fundamental premise of this approach is to realize that the conditions of mechanical equilibrium require the pressure in a homogeneous, supported membrane to be constant throughout its thickness at the value imposed upstream, p_0, as schematically illustrated in **Figure 8**. This point, which was somewhat controversial when first introduced, now seems to be well recognized [14–16]. For any species i, or component 1 as shown in **Figure 8**, the chemical potentials in the phases on each side of either membrane-solution interface are equal as stipulated by thermodynamics. Inside either the solution or the membrane phases, we can write the following expression for the chemical potential of i in terms of activity (or concentration) and pressure as follows:

$$\mu_i = \mu_i^{\circ} + RT \ \ln a_i + \bar{V}_i(p - p_r) \tag{37}$$

where p_r is an arbitrary reference pressure (we will take this to be p_ℓ) and μ_i° is a corresponding integration constant that depends on the reference pressure chosen. Equation (37) assumes the membrane or solution phases are effectively incompressible; and if this is not the case, the last term can be replaced by $\int_{p_r}^{p} \bar{V}_i \mathrm{d}p$. At the upstream interface ($z = 0$) where the pressure is p_0 in both the solution and membrane phases, thermodynamics connects the activity in the two phases as follows:

$$a_{i0}^{\mathrm{m}} = a_{i0}^{\mathrm{s}} \mathrm{e}^{-\left(\bar{V}_{i0}^{\mathrm{m}} - \bar{V}_{i0}^{\mathrm{s}}\right)(p_0 - p_\ell)/RT} \tag{38}$$

From this point on, superscripts s and m refer to the solution and membrane phase. At the downstream surface ($z = \ell$), the pressure in the membrane phase is p_0 while that in the solution phase is p_ℓ so there is a pressure discontinuity and the activities on either side are related by

$$a_{i\ell}^{\mathrm{m}} = a_{i\ell}^{\mathrm{s}} \mathrm{e}^{-\bar{V}_{i\ell}^{\mathrm{m}}(p_0 - p_\ell)/RT} \tag{39}$$

In general, the partial molar volume of i will be different in the two phases and will depend on the concentration in these phases; thus, we need to designate $\bar{V}_i$ by both a superscript (phase) and a subscript for location ($z = 0$). In many cases, we may regard $\bar{V}_i$ as a constant independent of composition which is the same in both phases. In this case, Equations (38) and (39) reduce to the following more simple forms:

$$a_{i0}^{\mathrm{m}} = a_{i0}^{\mathrm{s}} \tag{40}$$

$$a_{i\ell}^{\mathrm{m}} = a_{i\ell}^{\mathrm{s}} \mathrm{e}^{-\bar{V}_i(p_0 - p_\ell)/RT} \tag{41}$$

By a suitable theory or by experiment, the relationship between the concentration of i and its activity in a given phase can be established. For example, the Flory–Huggins theory gives a convenient framework for polymer systems.

We see from Equation (40) that the concentration of solvent in the membrane at its upstream surface in hydraulic permeation is the equilibrium swelling, w_{10}, of the polymer in the pure solvent $\left(a_{i0}^{\mathrm{s}} = 1\right)$ or the upstream solution for the general case. On the other hand, Equation (41) shows that the pressure discontinuity decreases the activity of solvent (hence, its concentration) in the membrane at the downstream surface, that is, solvent is squeezed out leading to a concentration gradient within the membrane. This is the origin of the diffusional flux induced by the pressure applied upstream.

The general results above can be expressed in some commonly used forms by using the definition of osmotic pressure in the external liquid phases, $\pi = -RT\ell \mathrm{n} a_1^{\mathrm{s}}/\bar{V}_1$, and an assumption of ideality in the membrane phase, that is, $a_1^{\mathrm{m}} = w_1/w_1^*$, where w_1^* is the equilibrium swelling of the membrane in the solvent 1; when no solute is present, that is, $a_1^{\mathrm{s}} = 1$. With these, Equations (40) and (41) become

$$w_{10} = w_1^* \mathrm{e}^{-\bar{V}_1 \pi_0/RT} \tag{42}$$

$$w_{1\ell} = w_1^* \left(\mathrm{e}^{-\bar{V}_1 \pi_\ell/RT}\right)\left(\mathrm{e}^{-\bar{V}_1 \Delta p/RT}\right) \tag{43}$$

Thus, we get

$$\begin{aligned}(w_{10} - w_{1\ell}) &= w_1^* \mathrm{e}^{-\bar{V}_1 \pi_\ell/RT}\left[1 - \mathrm{e}^{-\bar{V}_1(\Delta p - \Delta\pi)RT}\right] \\ &= w_{10}\left[1 - \mathrm{e}^{-\bar{V}_1(\Delta p - \Delta\pi)RT}\right]\end{aligned} \tag{44}$$

where $\Delta\pi = \pi_0 - \pi_\ell$. When the exponent is small enough, a series expansion of the exponential term is justified such that

$$(w_{10} - w_{1\ell}) \cong \frac{w_{10}\,\bar{V}_1\,(\Delta p - \Delta\pi)}{RT} \tag{45}$$

Equations (36) and (45) can be combined to get

$$n_1 = \frac{\mathcal{D}_{1\mathrm{m}} C_{10}^{\mathrm{m}} \bar{V}_1 (\Delta p - \Delta\pi)}{\ell RT} \tag{46}$$

which is the classical result for solvent flux in reverse osmosis when $<w_{\mathrm{m}}> \sim 1$ and $C_1^{\mathrm{m}} = \rho w_1$ [1, 9].

To develop a relation for solute (salt) flux from Fick's law, it has been correctly argued for desalination purposes that the pressure should have a negligible effect on salt partitioning into the membrane; thus, we can write

$$n_2 = -\mathcal{D}_{2m}\frac{dC_2^m}{dz} \cong \mathcal{D}_{2m}\frac{\Delta C_2^m}{\ell} = \mathcal{D}_{2m}\ K_2\left(\frac{C_{20}^s - C_{2\ell}^s}{\ell}\right) \tag{47}$$

where K_2 is the distribution coefficient for salt (or solute) between the solution and membrane phases. Using the definition of solute rejection

$$R = 1 - C_{2\ell}^s/C_{20}^s \tag{48}$$

and a mass balance, Equations (46) and (47) can be combined to obtain the familiar result [1, 16]

$$R = \left[1 + \frac{\mathcal{D}_{2m}\,K_2\,RT\,C_{1\ell}^s}{\mathcal{D}_{1m}\,C_1^m\bar{V}_1(\Delta p - \Delta\pi)}\right]^{-1} \tag{49}$$

For our purposes here, it will prove useful to recast these results in another form by defining permeability coefficients as follows:

$$P_2 = K_2\mathcal{D}_{2m} \quad \text{where} \quad K_2 = C_2^m/C_2^s \tag{50}$$

$$P_1 = K_1\mathcal{D}_{1m} \ \text{where} \quad K_1 = C_1^m/C_1^s \cong C_1^m/\rho_1 \tag{51}$$

where in the latter the solvent concentration in the external phase is taken to be the pure solvent density ρ_1 which is valid for relatively dilute solutions. We now define a selectivity factor α for solute over solvent in analogy with other membrane terminology:

$$\alpha = P_2/P_1 = \alpha_S\alpha_D = \left(\frac{\rho_1 K_2}{C_1^m}\right)\left(\frac{\mathcal{D}_{2m}}{\mathcal{D}_{1m}}\right) \tag{52}$$

where α_S and α_D represent the solubility and diffusivity components.

The limitations of the simple theory embodied in Equations (46) and (49) have been described previously [9]. One of these is that the simple linear relation between $\left(C_{10}^m - C_{1\ell}^m\right)$ and the net pressure driving force given in Equation (46) only holds for small driving forces. Clearly $C_{1\ell}^m$, or $w_{1\ell}$, can, at most, only go to zero and this occurs at infinite pressure. Thus, the relation between solvent flux and the pressure driving force must be nonlinear in the general case. The upper limit on flux, when $\Delta p \to \infty$, is given by

$$n_1 \to \frac{C_{10}^m\mathcal{D}_{1m}}{\ell\langle w_m\rangle} \tag{53}$$

or the result of Equation (35) when $\langle w_m\rangle \sim 1$. Thus, the limit on solvent flux in reverse osmosis is the same as that in pervaporation; these connections are reviewed more extensively elsewhere [14, 16].

For reverse osmosis or hydraulic permeation, one might ask when do nonlinearities in flux–pressure relationship become important. First, it is important to recognize three separate causes for nonlinearities. The simplest arises when the argument of the exponential term in Equation (44) is too large to use the truncated series expansion introduced to obtain Equation (45). The difference between Equations (44) and (45) is 5% (typical of the level of experimental sensitivity) when $\bar{V}_1(\Delta p - \Delta\pi)/RT = 0.1$. For water where $\bar{V}_1 \cong 18$ $cm^3\,mol^{-1}$, this requires pressures of the order of 136 atm or 2000 psi; such pressures are usually not reached in reverse osmosis applications so nonlinearity from this source would never be expected. However, for an organic solvent with $\bar{V}_1 \cong 100\,cm^3\,mol^{-1}$, this 5% discrepancy occurs at the much lower pressure of 24.5 atm or 360 psi; such pressures might easily be required in such a membrane operation. At $\bar{V}_1 \cong 300\,cm^3\,mol^{-1}$, the pressure is correspondingly lower at 8.2 atm or 120 psi. Thus, high partial molar volumes bring these effects into a range where they may not be negligible; water is a special case because of its low molecular weight. For highly swollen membranes, the term $\langle w_m\rangle$ cannot be approximated as unity and will depend on pressure adding another potential source of nonlinearity. The final source of nonlinearity can be the concentration dependence of the diffusion coefficient.

References

[1] Merten, U., Ed. *Desalination by Reverse Osmosis*; MIT Press: Cambridge, 1966.

[2] Ho, W. S. W., Sirkar, K. K., Eds. *Membrane Handbook*; van Nostrand Reinhold: New York, 1992.

[3] Kesting, R. E., Fritzsche, A. K. *Polymeric Gas Separation Membranes*; Wiley: New York, 1993.

[4] Paul, D. R., Yampol'skii, Y. P., Eds. *Polymeric Gas Separation Membranes*; CRC Press: Boca Raton, FL, 1994.

[5] Freeman, B. D., Pinnau, I., Eds. *Polymeric Membranes for Gas and Vapor Separations: Chemistry and Materials; ACS Symposium Series 733*; American Chemical Society: Washington, DC, 1999.

[6] Pinnau, I., Freeman, B. D., Eds. *Advanced Materials for Membrane Separation; ACS Symposium Series 876*; American Chemical Society: Washington, DC, 2004.

[7] Baker, R. W. *Membrane Technology and Applications*, 2nd edn.; Wiley: Chichester, 2004.

[8] Yampol'skii, Y., Pinnau, I., Freeman, B. D., Eds. *Materials Science of Membranes for Gas and Vapor Separation.* Wiley: Chichester, 2006.

[9] Paul, D. R. *Ber. Bunsenges. Phys. Chem.* **1979**, *83*, 294–302.

[10] Soltanieh, M., Gill, W. N. *Chem. Eng. Commun.* **1981**, *12*, 279–363.

[11] Paul, D. R., Morel, G. Membrane Technology. In *Kirk–Othmer Encyclopedia of Chemical Technology,* 3rd edn.; Mark, H. F., Othmer, D. O., Eds.; Wiley: New York, 1981; Vol. 15, pp 92–131.

[12] Koros, W. J., Fleming, G. K., Jordan, S. M., Kim, T. H., Hoehn, H. H. *Prog. Polym. Sci.* **1988**, *13*, 339–401.

[13] Koros, W. J., Hellums, M. W. Transport Properties. In *Encyclopedia of Polymer Science and Engineering*, 2nd edn.; Mark, H. F., Bikales, N. M., Overberger, C. G., Menges, G., Kroschwitz, J. I., Eds.; Wiley: New York, 1989; Supplement volume, pp 724–802.
[14] Wijmans, J. E., Baker, R. W. *J. Membr. Sci.* **1995**, *107*, 1–21.
[15] Bhattacharyya, D., Mangum, W. C., Williams, M. E. Reverse Osmosis. In *Kirk–Othmer Encyclopedia of Chemical Technology*, 4th edn.; Wiley: New York, 1997; Vol. 21, pp 303–333.
[16] Paul, D. R. *J. Membr. Sci.* **2004**, *241*, 371–386.
[17] Bird, R. B., Stewart, W. E., Lightfoot, E. N. *Transport Phenomena*, 2nd edn.; Wiley: New York, 2002.
[18] Flory, P. J. *Principles of Polymer Chemistry*; Cornell University Press: Ithaca, NY, 1955.
[19] Curtiss, C. F., Bird, R. B. *Ind. Eng. Chem. Res.* **1999**, *38*, 2515–2522.
[20] Zielinski, J. M., Hanley, B. F. *AIChE J.* **1999**, *45*, 1–12.
[21] Paul, D. R., Ebra-Lima, O. M. *J. Appl. Polym. Sci.* **1970**, *14*, 2201–2224.
[22] Paul, D. R., Ebra-Lima, O. M. *J. Appl. Polym. Sci.* **1971**, *15*, 2199–2210.
[23] Paul, D. R. *J. Appl. Polym. Sci.* **1972**, *16*, 771–782.
[24] Paul, D. R. *J. Polym. Sci. A-2* **1973**, *11*, 289–296.
[25] Paul, D. R. Diffusive Transport in Swollen Polymer Membranes. In *Permeability of Plastic Films and Coatings to Gases, Vapors, and Liquids*; Hopfenberg, H. B., Ed.; Plenum: New York, 1974; pp 35–48.
[26] Paul, D. R. *J. Polym. Sci.: Polym. Phys. Ed.* **1974**, *12*, 1221–1230.
[27] Paul, D. R., Paciotti, J. D., Ebra-Lima, O. M. *J. Appl. Polym. Sci.* **1975**, *19*, 1837–1845.
[28] Paul, D. R., Ebra-Lima, O. M. *J. Appl. Polym. Sci.* **1975**, *19*, 2759–2771.
[29] Paul, D. R., Paciotti, J. D. *J. Polym. Sci.: Polym. Phys. Ed.* **1975**, *13*, 1201–1214.
[30] Paul, D. R. *Sep. Purif. Methods* **1976**, *5*, 33–50.
[31] Bausa, J., Marquardt, W. *AIChE J.* **2001**, *47*, 1318–1332.
[32] Fornasiero, F., Prausnitz, J. M., Radke, C. J. *Macromolecules* **2005**, *38*, 1364–1370.
[33] Chiou, J. S., Maeda, Y., Paul, D. R. *J. Appl. Polym. Sci.* **1985**, *30*, 4019–4029.
[34] Toi, K., Morel, G., Paul, D. R. *J. Appl. Polym. Sci.* **1982**, *29*, 2997–3005.
[35] Suwandi, M. S., Stern, S. A. *J. Polym. Sci.: Polym. Phys. Ed.* **1973**, *11*, 663–681.
[36] Vieth, W. R., Howell, J. M., Hsieh, J. H. *J. Membr. Sci.* **1976**, *1*, 177.
[37] Koros, W. J., Chan, A. H., Paul, D. R. *J. Membr. Sci.* **1977**, *2*, 165–190.
[38] Koros, W. J., Paul, D. R. *J. Polym. Sci.: Polym. Phys. Ed.* **1978**, *16*, 1947–1963.
[39] Maeda, Y. PhD Dissertation, University of Texas at Austin, 1985.
[40] Barrer, R. M., Barrie, J. A., Slater, J. *J. Polym. Sci.* **1958**, *27*, 177–197.
[41] Michaels, A. S., Wieth, W. R., Barrie, J. A. *J. Appl. Phys.* **1963**, *34*, 1–12; 13–20.
[42] Weiss, G. H., Bendler, J. T., Shlesinger, M. F. *Macromolecules* **1992**, *25*, 990–992.
[43] Raucher, D., Sefcik, M. D. Gas Transport and Cooperative Main-Chain Motions in Glassy Polymers. In *Industrial Gas Separations;* Whyte, T. E., Yon, C. M., Wagener, E. H., Eds.; ACS Symposium Series 223; American Chemical Society: Washington, DC, 1983; pp 89–124.
[44] Mi, Y., Zhou, S., Stern, S. A. *Macromolecules* **1991**, *24*, 2361–2367.
[45] Lipscomb, G. G. *AIChE J.* **1990**, *36*, 1505–1516.
[46] Wissinger, R. G., Paulaitis, M. E. *Ind. Eng. Chem. Res.* **1991**, *29*, 842–851.
[47] Barbari, T. A., Conforti, R. M. *Polym. Adv. Technol.* **1994**, *5*, 698.
[48] Barbari, T. A., Conforti, R. M. *J. Polym. Sci. Part B: Polym. Phys.* **1992**, *30*, 1261–1271.
[49] Silverman, B. D. *J. Appl. Polym. Sci.* **1993**, *47*, 1013–1018.
[50] Horas, J. A., Nieto, F. J. *J. Polym. Sci. Part B: Polym. Phys.* **1992**, *30*, 1889–1898.
[51] Kirchheim, R. *Macromolecules* **1992**, *25*, 6952–6960.
[52] Doghieri, F., Sarti, G. C. *Macromolecules* **1996**, *29*, 7885–7896.
[53] Sarti, G. C., Doghieri, F. *Chem. Eng. Sci.* **1998**, *53*, 3435–3447.
[54] Baschetti, M. G., Doghieri, F., Sarti, G. C. *Ind. Eng. Chem. Res.* **2001**, *40*, 3027–3037.
[55] De Angelis, M. G., Sarti, G. C., Doghieri, F. *J. Membr. Sci.* **2007**, *289*, 106–122.
[56] Toi, K., Paul, D. R. *J. Appl. Polym. Sci.* **1982**, *27*, 2997–3005.
[57] Kanehashi, S., Nagai, K. *J. Membr. Sci.* **2005**, *253*, 117–138.
[58] Chan, A. H., Koros, W. J., Paul, D. R. *J. Membr. Sci.* **1978**, *3*, 117–130.
[59] Koros, W. J., Paul, D. R. *J. Polym. Sci.: Polym. Phys. Ed.* **1978**, *16*, 2171–2187.
[60] Chan, A. H., Paul, D. R. *Polym. Eng. Sci.* **1980**, *20*, 87–94.
[61] Wonders, A. G., Paul, D. R. *J. Membr. Sci.* **1979**, *5*, 63–75.
[62] Chiou, J. S., Maeda, Y., Paul, D. R. *J. Appl. Polym. Sci.* **1985**, *30*, 4019–4029.
[63] Michaels, A. S., Bixler, H. J. *J. Appl. Polym. Sci.* **1961**, *50*, 393–412.
[64] Puleo, A. C., Paul, D. R., Wong, P. K. *Polymer* **1989**, *30*, 1357–1366.
[65] Larobina, D., Sanguigno, L., Vindetto, V., Guerra, G., Mensitieri, G. *Polymer* **2004**, *45*, 429–436.
[66] Müller-Plathe, F. *J. Chem. Phys.* **1995**, *103*, 4346–4351.
[67] O'Brien, K. C., Koros, W. J., Barbari, T. A., Sanders, E. S. *J. Membr. Sci.* **1986**, *29*, 229–238.
[68] Raharjo, R. D., Freeman, B. D., Paul, D. R., Sarti, G. C., Sanders, E. S. *J. Membr. Sci.* **2007**, *306*, 75–92.
[69] Koros, W. J. *J. Polym. Sci.: Polym. Phys. Ed.* **1980**, *18*, 981–992.
[70] Crank, J. *The Mathematics of Diffusion*, 2nd edn.; Oxford University Press: London, 1975.
[71] Matsui, S., Paul, D. R. *J. Membr. Sci.* **2004**, *235*, 25–30.
[72] Paul, D. R., Koros, W. J. *J. Polym. Sci.: Polym. Phys. Ed.* **1976**, *14*, 687–702.
[73] Barrer, R. M. *J. Membr. Sci.* **1984**, *18*, 25–35.
[74] Wang, J.-S., Kamiya, Y. *J. Polym. Sci. Part B: Polym. Phys.* **2000**, *38*, 883–888.
[75] Wang, J.-S., Kamiya, Y., Naito, Y. *J. Polym. Sci. Part B: Polym. Phys.* **1998**, *36*, 1695–1702.
[76] Wang, J.-S., Naito, Y., Kamiya, Y. *J. Polym. Sci. Part B: Polym. Phys.* **1996**, *34*, 2027–2033.
[77] Kamiya, Y., Hirose, T., Mizoguchi, K., Naito, Y. *J. Polym. Sci. Part B: Polym. Phys.* **1986**, *24*, 1525–1539.
[78] Chiou, J. S., Paul, D. R. *J. Appl. Polym. Sci.* **1986**, *32*, 2897–2918.
[79] Chiou, J. S., Paul, D. R. *J. Polym. Sci. Part B: Polym. Phys.* **1987**, *25*, 1699–1707.
[80] Puleo, A. C., Paul, D. R., Kelley, S. S. *J. Membr. Sci.* **1989**, *47*, 301–332.
[81] Bos, A., Pünt, I. G. M., Wessling, M., Strathmann, H. *J. Membr. Sci.* **1999**, *155*, 67–78.
[82] Wind, J. D., Paul, D. R., Koros, W. J. *J. Membr. Sci.* **2004**, *228*, 227–236.
[83] Koros, W. J., Chern, R. T., Stannett, V. T., Hopfenberg, H. B. *J. Polym. Sci. Part B: Polym. Phys.* **1981**, *19*, 1513–1530.

[84] Chern, R. T., Koros, W. J., Yui, B., Hopfenberg, H. B., Stannett, V. T. *J. Polym. Sci. Part B: Polym. Phys.* **1984**, *22*, 1061–1084.
[85] Raharjo, R. D., Freeman, B. D., Paul, D. R., Sanders, E. S., *Polymer* **2007**, *48*, 7329–7344.
[86] Wind, J. D., Staudt-Bickel, C., Paul, D. R., Koros, W. J. *Ind. Eng. Chem. Res.* **2002**, *41*, 6139–6148.
[87] Wind, J. D., Staudt-Bickel, C., Paul, D. R., Koros, W. J. *Macromolecules* **2003**, *36*, 1882–1888.
[88] Hillock, A. M., Koros, W. J. *Macromolecules* **2007**, *40*, 583–587.
[89] Bos, A., Pünt, I. G. M., Wessling, M., Strathmann, H. *Sep. Purif. Technol.* **1998**, *14*, 27–39.
[90] Michaels, A. S., Bixler, H. J. *J. Polym. Sci.* **1961**, *50*, 27–39.
[91] Mogri, Z., Paul, D. R. *Polymer* **2001**, *4*, 7765–7780; 7781–7789.
[92] Laguna, M. F., Cerrada, M. L., Benevente, R., Perez, E., Quijoda, R. *J. Polym. Sci. Part B: Polym. Phys.* **2003**, *41*, 2174–2184.

Biographical Sketch

D. R. Paul holds the Ernest Cockrell, Sr. Chair in engineering at the University of Texas at Austin and is also the director of the Texas Materials Institute. He received degrees in chemical engineering from North Carolina State University (BS) and the University of Wisconsin (MS. and PhD) and then worked at the Chemstrand Research Center for 2 years. He joined the Department of Chemical Engineering at the University of Texas at Austin in 1967, where he served as the department chairman during 1977–85. His research has involved various aspects of polymer blends, membranes for separation, drug delivery, packaging, processing, and nanocomposites. He has edited numerous books on polymer blends and membranes and has published more than 570 research papers. He has received awards for teaching, research, and leadership from the University of Texas, ACS, AIChE, SPE, and the Council for Chemical Research. He has been designated a distinguished graduate of North Carolina State University and of the University of Wisconsin. He was elected to the National Academy of Engineering in 1988 and to the Mexican Academy of Sciences in 2000. He has served as an editor of *Industrial and Engineering Chemistry Research*, published by ACS, since 1986.

1.05 Basic Aspects in Polymeric Membrane Preparation

H Strathmann, Universitat Stuttgart, Stuttgart, Germany

L Giorno and E Drioli, Institute of Membrane Technology, ITM-CNR, University of Calabria, Rende (CS), Italy

1.05.1 Materials and Structures of Synthetic Membranes

Synthetic membranes show a large variety in their physical structure and the materials they are made from. Based on their structure, they can be classified into four groups:

1. porous membranes,
2. homogeneous solid membranes,
3. solid membranes carrying electrical charges, and
4. liquid or solid films containing selective carriers.

Furthermore, the structure of membranes may be symmetric, that is, the structure is identical over the entire cross section of the membrane, or it may be asymmetric, that is, the structure varies over the cross section of the membrane.

The materials used for the preparation of membranes include polymers, ceramics, glass, metals, or liquids; and the materials may be neutral or carry electrical charges, that is, fixed ions. The membrane conformation can be flat, tubular, or a hollow fiber. The schematic drawing of **Figure 1** illustrates the

The chapter is based on a series of lectures Prof. Strathmann has given at ITM-CNR during advanced courses for Ph.D Students and published in the book "An introduction to membrane science and technology", Strathmann H., Giorno L., Drioli E., CNR, Rome, 2006.

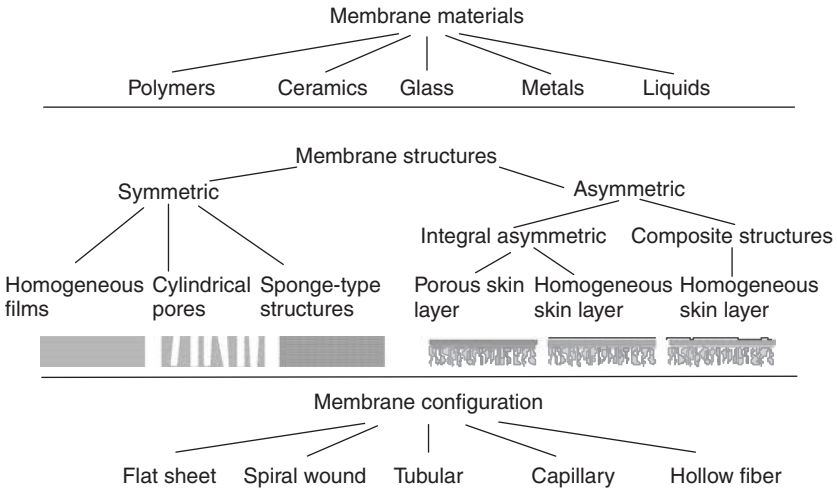

Figure 1 Schematic drawing illustrating the various materials, structures, and configuration of technically relevant synthetic membranes.

morphology, materials, and configuration of some technically relevant synthetic membranes.

1.05.1.1 Symmetric and Asymmetric Membranes

As indicated earlier, synthetic membranes may have a symmetric or an asymmetric structure. In a symmetric membrane, the structure and the transport properties are identical over the entire cross section and the thickness of the entire membrane determines the flux. Today, symmetric membranes are mainly used in dialysis and electrodialysis. In asymmetric membranes, structural as well as transport properties vary over the cross section of the membrane. An asymmetric membrane consists of a 0.1–1-μm-thick skin layer on a highly porous 100–200-μm-thick substructure. The skin represents the actual selective barrier of the asymmetric membrane. Its separation characteristics are determined by the nature of the material or the size of pores in the skin layer. The mass flux is determined mainly by the thickness of the skin. The porous sublayer serves only as a support for the mostly thin and fragile skin and has little effect on the separation characteristics or the mass transfer rate of the membrane. Asymmetric membranes are primarily used in pressure-driven membrane processes such as reverse osmosis, ultrafiltration, or gas and vapor separation, since here the unique properties of asymmetric membranes, that is, high fluxes and good mechanical stability, can be best utilized. Two techniques are used to prepare asymmetric membranes: one utilizes the phase-inversion process, which leads to an integral structure with the skin and the support structure made from the same material in a single process [1], and the other resembles a composite structure where a thin barrier layer is deposited on a porous substructure in a two-step process [2]. In this case, barrier and support structures are generally made from different materials.

1.05.1.2 Porous Membranes

A porous structure represents a very simple form of a membrane, which closely resembles the conventional fiber filter as far as the mode of separation is concerned. These membranes consist of a solid matrix with defined holes or pores which have diameters ranging from less than 1 nm to more than 10 μm. The macromolecular size of the species to be separated plays an important role in determining the pore size of the membrane to be utilized and the related membrane process. Porous membranes with average pore diameters larger than 50 nm are classified as macroporous; those with average pore diameters in the intermediate range between 2 and 50 nm are classified as mesoporous; and membranes with average pore diameters between 0.1 and 2 nm are classified as microporous. Dense membranes have no individual permanent pores, but the separation occurs through fluctuating free volumes. The schematic representation of such classification is illustrated in **Figure 2**.

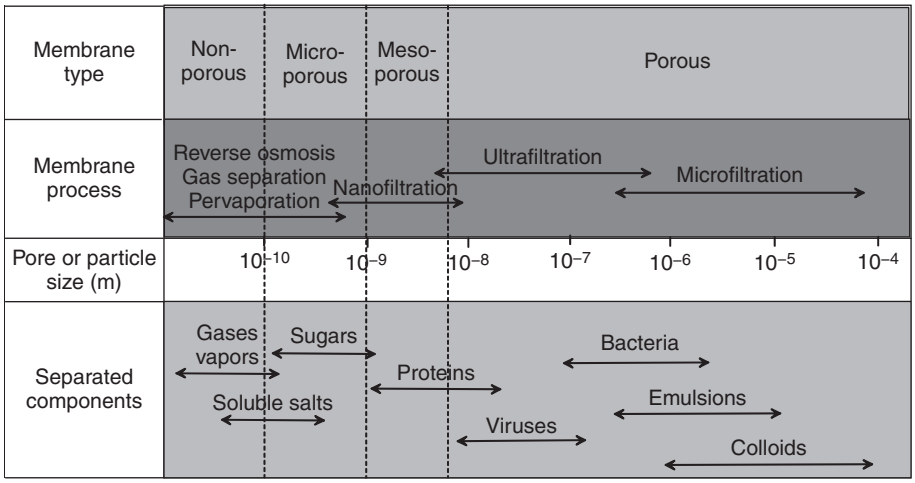

Figure 2 Schematic classification of membranes, related processes, and separated components.

In pressure-driven membrane processes, the separation of the various components is achieved by a sieving mechanism with the pore diameters and the particle sizes being the determining parameters. In thermally driven membrane processes, the separation is based on the principle of phase equilibrium where the non-wetability of membrane pores is the determining parameter. Porous membranes can be made from various materials such as ceramics, graphite, metal or metal oxides, and various polymers. Their structure may be symmetric, that is, the pore diameters do not vary over the membrane cross section, or they can be asymmetric, that is, the pore diameters increase from one side of the membrane to the other typically by a factor of 10–1000. The techniques for the preparation of porous membranes can be rather different and include simple pressing and sintering of polymer or ceramic powders, irradiation and leaching of templates, as well as phase-inversion and polymer precipitation procedures or sol–gel conversion techniques. Porous membranes are used to separate components that differ markedly in size or molecular weight in processes such as micro- and ultrafiltration or dialysis [3].

1.05.1.3 Homogeneous Dense Membranes

A homogeneous membrane is merely a dense film through which a mixture of molecules is transported by a pressure, a concentration, or an electrical potential gradient. The separation of the various components of a mixture is directly related to their transport rates within the membrane phase, which is determined by their diffusivities and concentrations in the membrane matrix. Therefore, homogeneous membranes are referred to as solution–diffusion-type membranes [4]. They can be prepared from polymers, metals, metal alloys, or, in some cases, ceramics, which may also carry positive or negative electrical charges. Since the mass transport in homogeneous membranes is based on diffusion, their permeabilities are rather low. Homogeneous membranes are used mainly to separate components which are similar in size but have different chemical nature in processes such as reverse osmosis, gas and vapor separation, and pervaporation [5]. In these processes, asymmetric membrane structures are used, which consist of a thin homogeneous skin supported by a porous substructure.

1.05.1.4 Ion-Exchange Membranes

Films carrying charged groups are referred to as ion-exchange membranes. They consist of highly swollen gels carrying fixed positive or negative charges. The properties and preparation procedures of ion-exchange membranes are closely related to those of ion-exchange resins [6]. There are two different types of ion-exchange membranes:

1. cation-exchange membranes, which contain negatively charged groups fixed to the polymer matrix and
2. anion-exchange membranes, which contain positively charged groups fixed to the polymer matrix.

In a cation-exchange membrane, the fixed anions are in electrical equilibrium with mobile cations in the interstices of the polymer. In contrast, the mobile anions are more or less completely excluded from the cation-exchange membrane because of their electrical charge, which is identical to that of the fixed ions. Due to this exclusion of the anions, a cation-exchange membrane permits transfer of cations only. Anion-exchange membranes carry positive charges fixed on the polymer matrix; therefore, they exclude all cations and are permeable to anions only. Although there are a number of inorganic ion-exchange materials, most of them based on zeolites and bentonites, these materials are rather unimportant in ion-exchange membranes compared to polymer materials [7]. The main applications of ion-exchange membranes are in electrodialysis or electrolysis [8]. They are also used as ion-conducting separators in batteries and fuel cells.

1.05.1.5 Liquid Membranes

Liquid membranes are mainly used in combination with the so-called facilitated transport, which is based on carriers that transport certain components such as metal ions selectively across the liquid membrane interphase.

Generally, it is no problem to form a thin fluid film. It is difficult, however, to maintain and control this film and its properties during a mass separation process. In order to avoid a breakup of the film, some type of reinforcement is necessary to support such a weak membrane structure. Two different techniques are used today for the preparation of liquid membranes. In the first case, the selective liquid barrier material is stabilized as a thin film by a surfactant in an emulsion-type mixture [9]. In the second technique, a porous structure is filled with the liquid membrane phase. Both types of membranes are used today on a pilot-plant stage for the selective removal of heavy metal ions or certain organic solvents from industrial waste streams [10]. They have also been used rather effectively for the separation of oxygen and nitrogen.

1.05.1.6 Fixed Carrier Membranes

Fixed carrier membranes consist of a homogeneous or porous structure with functional groups, which selectively transport certain chemical compounds. These membranes can have a symmetric or an asymmetric structure depending on their application. Fixed carriers may be not only ion-exchange groups but also complexing or chelating agents. They are used today, for example, in co- and counter-current transport and in the separation of alkane/alkene mixtures.

1.05.1.7 Other Membranes

Inorganic membranes prepared from zeolites [11, 12] and from perovskites [13] have been studied and also applied at the industrial level. The interesting adsorption and catalytic properties of zeolites can be well utilized when realized in a membrane configuration.

1.05.1.7.1 Perovskites

The perovskite systems with their high selectivity for O_2 and H_2, related to vacancies in the crystalline structures, introduce a new transport mechanism which makes them very promising materials for potential use as dense ceramic membranes in gas separation, high-temperature fuel cells, and membrane reactors. Perovskite-type oxides have also received attention because they combine a high electronic and ionic conductivity. They have been already studied as high-temperature superconductors, ferro- and piezoelectric materials, magneto-resistive materials, and oxygen ion and proton conductors. For practical applications, these membranes must possess sufficiently high oxygen permeability and sustainable structural stability to harsh conditions such as elevated temperature and high oxygen or carbon dioxide concentrations. Perovskite membranes can be made as disks or sheets or tubes by pressing the perovskite powder into the appropriate form and sintering at temperatures between 1100 and 1500 °C.

1.05.1.7.2 Zeolite membranes

Zeolites with their interesting molecular sieving functions, large surface areas, controlled host–substrate interactions, and catalytic properties have always been considered of interest for being utilized in membrane configurations and operations [14]. Zeolites are three-dimensional, microporous crystalline materials with well-defined structures of voids and channels of discrete size, which is accessible through pores of well-defined molecular dimensions that contain aluminum, silicon, and oxygen in their regular framework. They can be classified into small, medium, large, and ultra-large pore materials [15]. They can be processed into symmetric self-supported membranes or asymmetric

supported membranes [16]. The first type is constituted by pure zeolitic phase, while the second one consists of the zeolite thin layer formed on a support. Zeolites can separate molecules based on size, shape, polarity, and degree of unsaturation. The combination of many properties, such as the uniform pore dimensions, the ion-exchange properties, the ability to develop internal acidity, high thermal stability, and large internal surface area, makes them unique among inorganic oxides and also leads to unique selectivity.

1.05.2 Membrane Preparation

The most important part in any membrane separation process is the membrane itself. Membranes are very different as far as their structure, function, transport properties, their transport mechanism, and the material they are made from is concerned. Just as diverse as the different membranes are, so also are the methods of making them. Some membranes are manufactured by simple sinter techniques of fine powders, others are prepared by irradiation and track etching of thin films or by inversion of homogeneous liquid mixtures or melts into heterogeneous solid phases. Composite membranes are prepared by dip-coating techniques, interfacial polymerization, and plasma polymerization. Inorganic membranes are prepared as composite structures using powder sintering techniques and the sol–gel method. Liquid membranes with mobile selective carriers are prepared as emulsions or supported in porous structures. Fixed carrier and ion-exchange membranes are prepared by introducing positively or negatively charged groups into suited polymer structures.

The selection of a suitable base material and preparation technique depends on the type of application the membrane is to be used in. In some applications, such as in gas separation or pervaporation, the membrane material used as the barrier layer is of prime importance for the performance of the membrane. In other applications, such as in micro- or ultrafiltration, the membrane material is not quite as important as the membrane structure.

The most important characteristic of a membrane is its selective transport properties, selectivity, and permeability, that is, permselectivity.

The selectivity, combined with a significant permeability, results from the intrinsic chemical properties of the material forming the membrane and its physical properties.

The choice of a given polymer as a membrane material is not arbitrary, but based on specific properties, originating from structural factors, such as molecular weight, chain flexibility, and chain interaction.

The structural factors determine the thermal, chemical, and mechanical properties of polymers. Such factors also determine the permeability.

The molecular weight distribution is an important property relative to membrane chain flexibility. Chain flexibility is determined by two factors:

- the character of the main chain

Flexible	*Less flexible*	
[–C–C–]	[–C═C]	[–C–C═C–C–] (organic)
[–Si–O–]	[–P═N–]	(inorganic)

- the presence and nature of the side chains or side groups

R = [–H]	no influence on rotational freedom
R = [–C_6H_5]	reduces rotational freedom.

Primary covalent bonds occur in network polymers. Secondary intermolecular forces (dipole forces (Debye forces); dispersion forces (or London forces); and hydrogen bonding forces) occur in linear and branched polymers.

The permeability of porous membranes is not very much influenced by the choice of the polymer, but chemical and thermal stability and also surface effects such as adsorption and wettability are affected. On the contrary, for dense nonporous membranes, polymeric material directly influences the membrane performance; in particular, the glass transition temperature and the crystallinity are very important parameters. The permeability is in general much lower in the glassy state than in the rubbery state. Transport takes place through amorphous rather than crystalline regions. The mobility of the polymeric chain is very restricted in the glassy state, since the segments cannot freely rotate around the main chain bonds. In the rubbery state, the segments can freely rotate along the main chain, implying a high degree of chain mobility.

Thermal and chemical stability are favored by rigid chain, aromatic ring, chain interactions, high T_g, etc.

As the stability of a polymer increases, it generally becomes more difficult to process. The two effects of stability and processability oppose each other.

Mechanical behavior involves the deformation of a material under the influence of an applied force. The mechanical properties of a polymeric membrane can be improved by suitable supports, although hollow-fiber and capillary membranes must be self-supporting.

Membrane preparation procedures are often developed empirically and described in the literature often as detailed recipes [17, 18, 19, 20].

1.05.3 Preparation of Porous Membranes

Porous membranes consist of a solid matrix with defined pores, which have diameters ranging from less than 1 nm to more than 10 μm. They can be made from various materials, such as ceramics, graphite, metal or metal oxides, and polymers. Their structure may be symmetric, or asymmetric. Porous membranes are mainly used in microfiltration and ultrafiltration. They can be classified according to

- the material they are made of, that is, ceramic or polymer;
- their structure, that is, symmetric or asymmetric; and
- their pore size and pore-size distribution.

The membrane material determines the mechanical properties and the chemical stability of the membrane. The chemical properties of the material such as its hydrophilicity or hydrophobicity affect its performance in a practical application due to specific adsorption of feed mixture constituents.

The methods used most widely today for making porous membranes are sintering of powders, stretching of films, irradiation and etching of films, and phase-inversion or sol–gel processes. The different structures, the material they are made from, their preparation, and their typical applications are summarized in **Table 1**.

1.05.3.1 Symmetric Porous Membranes Prepared by Sintering, Track Etching, and Leaching Techniques

Sintering is a rather simple technique to obtain porous structures from organic as well as from inorganic materials (**Table 2**).

A powder consisting of certain size particles is pressed into a film or plate and sintered just below the melting point of the material. The structure of a typical sintered membrane is shown in the scanning electron micrograph of **Figure 3(a)**. This photograph shows the surface of a porous membrane made by pressing and sintering a plate of fine polytetrafluoroethylene powder. The process yields a porous structure of relatively low porosity in the range of 10–40%, and a rather irregular pore structure with a very wide pore-size distribution. The material selection for the preparation of sintered membranes is determined mainly by the required mechanical properties and the chemical and thermal

Table 1 Porous membranes, their preparation and application

Membrane type	*Membrane material*	*Pore Size (μm)*	*Preparation process*	*Application*
Symmetric porous structures	Ceramic, metal, polymer, graphite	0.1–20	Powder pressing and sintering	Microfiltration, gas separation
Symmetric porous structures	Polymer of partial crystallinity	0.2–10	Extruding and stretching of films	Microfiltration, battery separator
Symmetric porous structures	Polymer, mica	0.05–15	Irradiation and etching of films	Microfiltration, point-of-use filter
Symmetric porous structures	Polymer, metal, ceramic	0.5–20	Template leaching of films	Microfiltration
Symmetric porous structures	Polymer	0.5–10	Temperature-induced phase inversion	Microfiltration
Asymmetric porous structures	Polymer	<0.01	Diffusion-induced phase inversion	Ultrafiltration
Asymmetric porous structures	Ceramic	<0.01	Composite membrane gel–sol process	Ultrafiltration

Table 2 Sintering method

Schematic of the Process	*Materials used*	
	Powders of polymers	Polyethylene, PTFE, polypropylene
Membrane pore size distribution 0.1–10 μm Porosity: 10–20% with polymers 80% with metals	Powder of metals Powder of ceramics Powder of graphite Powder of glass	Stinless steel, tungsten Aluminium oxide, zirconium oxide Carbon Silicalite

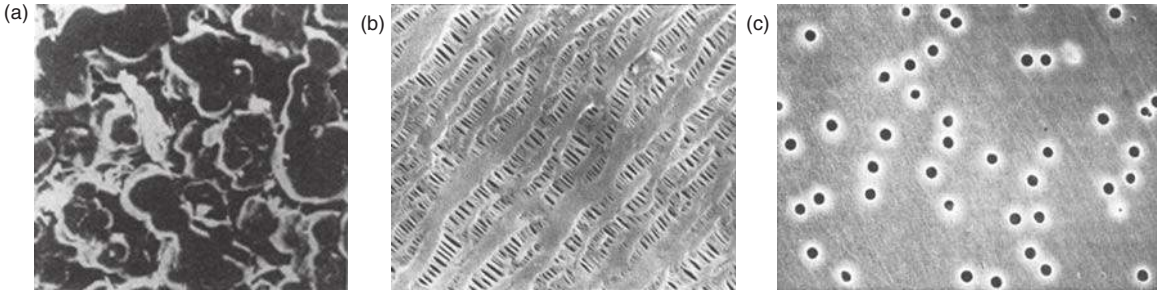

Figure 3 Scanning electron micrographs of (a) a sintered membrane prepared from a polymer powder, (b) a membrane prepared by stretching an extruded polytetrafluoroethylene film perpendicular to the direction of extrusion, and (c) a capillary pore polycarbonate membrane made by track etching.

stability of the material in the application of the final membrane. Sintered membranes are made on a large scale from ceramic materials such as aluminum oxides, graphite, and metal powders such as stainless steel and tungsten. The particle size of the powder is the main parameter determining the pore sizes of the final membrane, typically ranging from 0.2 to 20 μm. The lower limit of the pore diameter is determined by the particle size of the powder. Sintered membranes can be made in the form of disks, cartridges, or fine-bore tubes. They are used for the filtration of colloidal solutions and suspensions. They are also suitable for gas separation and widely used for the separation of radioactive isotopes.

Porous carbon membranes are also prepared by pyrolizing preformed polyacrylonitrile membranes in an inert atmosphere at 600–800 °C. The membranes are generally coated on a porous ceramic support or prepared as hollow fibers. Their pore size is 1–4 nm. The membranes are used for both ultrafiltration and gas separation. However, they are very brittle and, thus, difficult to handle in large-scale practical applications.

Another relatively simple procedure for preparing porous membranes is the stretching of a homogeneous polymer film of partial crystallinity. This technique is mainly employed with films of polyethylene or polytetrafluoroethylene, which have been extruded from a polymer powder at temperatures close to its melting temperature coupled with a rapid drawdown. The crystallites in the semi-crystalline polymer are aligned in the direction of drawing. After annealing and cooling, the extruded film is stretched perpendicular to the direction of drawing. This leads to a partial fracture of the film, and relatively uniform pores with diameters of 0.2–20 μm are obtained. A typical stretched membrane prepared from polytetrafluoroethylene is shown in the scanning electron micrograph of **Figure 3**(**b**). The membranes can be produced as flat sheets as well as tubes and capillaries. Because of the hydrophobic nature of the basic polymer, these membranes are highly permeable for gases and vapors but impermeable for aqueous solutions. They are used in sterile filtration, blood oxygenation, and membrane distillation. The stretched membranes made out of polytetrafluoroethylene are also used as water

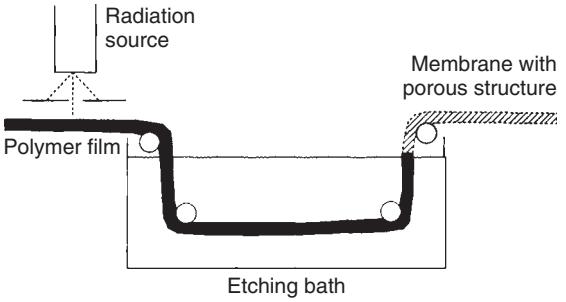

Figure 4 Track-etching method.

repellent textile. Because of its high porosity, this membrane has a high gas and vapor permeability, but it is, up to a certain hydrostatic pressure, completely impermeable to aqueous solutions.

Porous membranes with very uniform, almost perfectly round cylindrical pores are obtained by a process referred to as track etching [21]. The membranes are made in a two-step process, as shown in **Figure 4**. A film or foil (polycarbonate) is subjected to high-energy particle radiation applied perpendicular to the film. The particles damage the polymer matrix and create tracks. The film is then immersed in an acid (or alkaline) bath and the polymeric material is etched away along the tracks to form uniform cylindrical pores with narrow pore distribution – pore size 0.2–10 mm and porosity 10%.

During the first step, a homogeneous 6–15-μm-thick polymer film is exposed to collimated charged particles in a nuclear reactor. As particles pass through the film, they leave sensitized tracks where the chemical bonds in the polymer backbone are damaged. In the second step, the irradiated film is placed in an etching bath. In this bath, the damaged material along the tracks is preferentially etched forming uniform cylindrical pores. The pore density of a track-etched membrane is determined by the residence time in the irradiator, while the pore diameter is controlled by the residence time in the etching bath. The minimum pore diameter of these membranes is approximately 0.01 μm. The maximum pore size that can be achieved in track-etched membranes is determined by the etching procedure and is ~5 μm. The scanning electron micrograph in **Figure 3(c)** shows a typical track-etched polycarbonate membrane. Capillary porous membranes are prepared mainly from polycarbonate and polyester films. The advantage of these polymers is that they are commercially available in very uniform films of 10–15-μm thickness, which is the maximum penetration depth of collimated particles obtained from a nuclear reactor. Because of their narrow pore-size distribution and low tendency to plug, capillary porous membranes made from polycarbonate and polyester have found applications on a large scale in analytical chemistry and microbiological laboratories, and in medical diagnostic procedures. Capillary porous membranes are used on an industrial scale for the production of ultrapure water for the electronic industry. Here, they show certain advantages over other membrane products because of their short rinse-down time and good long-term flux stability. Because of their surface filter characteristics, particles retained by the membranes can be further monitored by optical or scanning electron microscopy.

Other techniques to produce porous microfiltration membranes are based on micro-lithography and template leaching. These membranes often have a narrow pore-size distribution and high fluxes. The template leaching technique is also applied to prepare membranes from glass, metal alloys, or ceramics [22]. The preparation procedure for porous glass and metal membranes is relatively simple: two different types of glass or metals are homogeneously mixed; then, one type is dissolved and a network with well-defined pore sizes of the undissolved material is obtained. For example, for porous glass membranes, a homogeneous melt (1000–1500 °C) of a three-component system (e.g., Na_2O–Ba_2O_3–SiO_2) is cooled and the system separates in two phases, one consisting mainly of SiO_2, which is not soluble, while the other is soluble. This second phase is leached out by an acid or base and a wide range of pore diameter can be obtained. The minimum pore size achievable is 0.05 μm.

1.05.3.2 Symmetric Porous Polymer Membranes Made by Phase-Inversion Techniques

The so-called phase-inversion process, in which a polymer is dissolved in an appropriate solvent and spread as a 20–200-μm-thick film on a plate, a belt, or a fabric support, prepares most commercially available symmetric microporous membranes. A precipitant such as water is added to this liquid film, causing separation of the homogeneous polymer solution into two phases, that is, a polymer-rich solid phase and a solvent-rich liquid phase. The precipitated polymer forms a porous structure containing a network of nearly uniform pores. A microporous

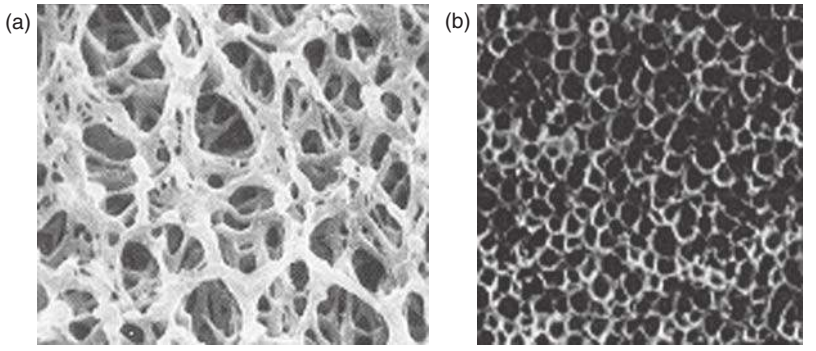

Figure 5 Scanning electron micrograph of the surface of (a) a porous cellulose nitrate membrane prepared from a homogeneous polymer solution by water vapor precipitation and (b) a porous polypropylene membrane precipitated by thermal gelation from a hot polymer solution.

cellulosic membrane made by phase inversion is shown in the scanning electron micrograph of **Figure 5**(**a**).

Porous phase-inversion-type membranes can be made from almost any polymer, which is soluble in an appropriate solvent and can be precipitated in a nonsolvent. By varying the polymer, the polymer concentration, the precipitation medium, and the precipitation temperature, porous phase-inversion membranes can be made with a very large variety of pore sizes, from less than 0.1 to more than 20 μm, and with varying chemical and mechanical properties. These membranes were originally prepared from cellulosic polymers by precipitation at room temperature in an atmosphere of approximately 100% relative humidity. Recently, symmetric microporous membranes are also prepared from various polyamides, polysulfone, and polyvinylidene difluoride by precipitation of a cast polymer solution in water. The phase-inversion process is today the most important technique for obtaining porous structures. Polypropylene or polyethylene can also be used for the preparation of porous membranes. However, since these polymers are not readily dissolved at room temperature, the preparation technique must be slightly varied. Polypropylene, for example, is dissolved in an appropriate amine at elevated temperatures. A solution of 20–30% polymer is spread at elevated temperature into a film. The precipitation of the polymer, however, is not induced by the addition of a nonsolvent but merely by cooling the solution to a point where a two-phase system forms. The resulting open foam structure is shown in **Figure 5**(**b**). The pore size of membranes depends on the polymer concentration, the solvent system, the solution temperature, and the cooling rate. This membrane preparation technique is usually referred to as thermal gelation.

The symmetric, porous polymer membranes made by phase inversion are widely used for separations on a laboratory and industrial scale. Typical applications range from the clarification of turbid solutions to the removal of bacteria or viruses, the detection of pathological components, and the detoxification of blood in an artificial kidney. The separation mechanism is that of a typical depth filter which traps the particles somewhere within the structure. In addition to the simple sieving effect, porous phase-inversion membranes often show a high tendency of adsorption because of their extremely large internal surface. They are, therefore, particularly well suited when a complete removal of components, such as viruses or bacteria, is desired. They are suited for immobilization of enzymes to be used in modern biotechnology. They are also widely used for culturing of microorganisms in water quality control tests.

1.05.4 Preparation of Asymmetric Membranes

Most membranes used today in large-scale separation processes have an asymmetric structure, which consists of a very thin, that is, 0.1–1 μm selective skin layer on a highly porous ~100–200-μm-thick substructure, as indicated in the scanning electron micrographs of **Figure 6**, which shows the cross section of an asymmetric membrane with a so-called graded pore structure (**Figure 6**(**a**)) and an asymmetric membrane with a finger-type structure

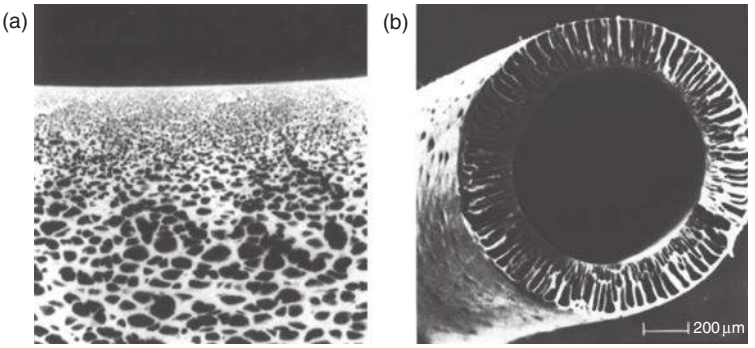

Figure 6 Scanning electron micrographs showing the cross section of (a) an asymmetric reverse osmosis membrane with a graded pore structure and (b) an asymmetric ultrafiltration capillary membrane with a finger-type structure.

(**Figure 6**(**b**)). The very thin skin represents the actual membrane. It may consist of homogeneous polymer or may contain pores. Its separation characteristics are determined by the nature of the polymer or the pore size in the skin, while the mass transport rate is determined by the thickness of the skin. The porous substructure serves only as a support for the thin and sometimes fragile skin and has little effect on separation characteristics or the mass transfer rate of the membrane.

Figure 7 shows the schematic of the equipment to prepare capillary membrane. A polymer solution is pumped through the spinneret, where the nonsolvent flowing along the bore forms the lumen of the capillary (or hollow fiber) membrane as it is formed in the cogulation bath by phase inversion.

Asymmetric membranes are used primarily in pressure-driven membrane processes such as reverse osmosis, ultrafiltration, or gas separation, as it is here that the unique properties in terms of high mass transfer rates combined with good mechanical stability can be best utilized. In addition to high filtration rates, asymmetric membranes are very resistant to fouling. Conventional symmetric structures act as depth filters and retain particles within their internal structure. These trapped particles plug the membrane and so the flux declines during use. Asymmetric membranes are surface filters and retain all rejected materials at the surface where they can be removed by shear forces applied by the feed solution moving parallel to the membrane surface.

Two techniques are used to prepare asymmetric membranes. The first technique utilizes the phase-inversion process and leads to a membrane where the skin and the substructure consist of the same polymer. This membrane is referred to as integral asymmetric. In the second technique, an extremely

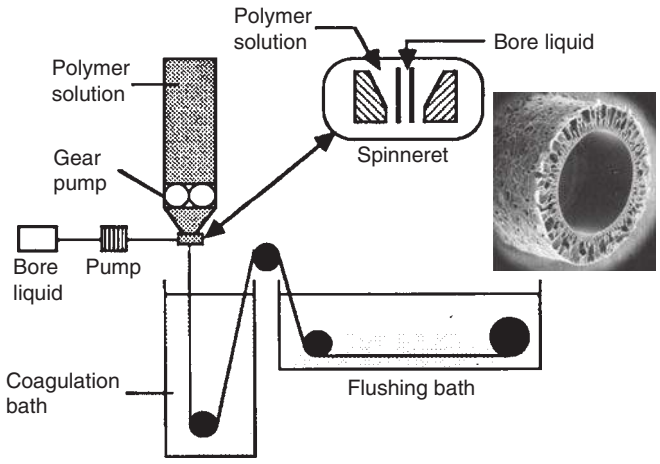

Figure 7 Preparation of capillary membranes by immersion precipitation.

thin polymer film is deposited on a preformed porous substructure, leading to the so-called composite membranes.

The development of the first integral asymmetric membranes by phase inversion was a major breakthrough in the development of ultrafiltration and reverse osmosis. These membranes were made from cellulose acetate and yielded fluxes 10–100 times higher than symmetric structures with comparable separation characteristics. Today, however, most reverse osmosis membranes are composite structures.

1.05.4.1 The Preparation of Integral Asymmetric Membranes by Phase Inversion

Asymmetric phase-inversion membranes can be prepared from virtually all polymers that are soluble at a certain temperature in an appropriate solvent or solvent mixture and can be precipitated as a continuous solid phase by either changing the temperature or the composition of the system by the following general procedures [23, 24, 25, 26]:

- cooling of a homogeneous polymer solution, which separates at a certain temperature in two phases;
- evaporation of a volatile solvent from a homogeneous polymer solution with two or more solvents of different dissolution capacity; and
- addition of a nonsolvent or nonsolvent mixture to a homogeneous solution.

All the three procedures result in the formation of two phases, that is, a liquid phase forming the membrane pores and a solid phase forming the membrane structure, which may be either symmetric and porous or asymmetric with a more or less dense skin at one or both surfaces of a porous bulk phase. The only thermodynamic presumption for all the three preparation procedures is that the system has a miscibility gap over a defined concentration and temperature range.

A phase separation caused by a temperature change is called temperature-induced phase separation and a phase separation caused by the addition of a nonsolvent or nonsolvent mixture to a homogeneous solution is referred to as diffusion-induced phase separation. In the practical membrane preparation, combination and certain variations of the basic processes are used to produce membranes with tailor-made structures and properties.

1.05.4.2 The Practical Membrane Preparation by the Diffusion-Induced Phase Separation Process

The diffusion-induced phase-separation process consists of the following consecutive steps:

- a polymer is dissolved in an appropriate solvent to form a solution,
- the solution is cast into a film of the order of 100–500-μm thickness, and
- the film is quenched in a nonsolvent, typically water or an aqueous solution.

During the quenching process, the polymer solution separates into two phases: a polymer-rich solid phase that forms the membrane structure, and a solvent-rich liquid phase that forms the liquid-filled membrane pores. Generally, the pores at the film surface, where precipitation occurs first and most rapidly, are much smaller than in the interior or at the bottom side of the film. This leads to the asymmetric membrane structure.

There are different variations to this general preparation procedure described in the literature, for example, sometimes an evaporation step prior to the precipitation is used to change the composition in the surface of the cast film and an annealing step is applied to change the structure of the precipitated membrane [27, 28].

The original recipes and subsequent modifications for preparing asymmetric membranes are deeply rooted in empiricism. Detailed descriptions of membrane preparation techniques are given in the literature [1, 25, 29, 30, 31]. Only after extensive use of the scanning electron microscope, which provided the necessary structural information, was it possible to rationalize the various parameters responsible for the membrane structure forming processes. It then became evident that both symmetric and asymmetric porous structures can be prepared by the diffusion-induced phase-separation process from a large number of polymers when the preparation parameters are chosen correspondingly. The actual phase separation or phase inversion cannot only be induced by the addition of nonsolvent but also be induced by the controlled evaporation of a volatile solvent from a three-component mixture of solvent/precipitant/polymer, causing precipitation as the system becomes enriched in precipitant [24]. Alternatively,

precipitation of a simple two-component polymer-solvent casting solution can be brought about by imbibing precipitant from the vapor phase [20]. This technique was the basis of the original porous membranes and is still used commercially today by several companies.

1.05.4.3 The Practical Membrane Preparation by the Temperature-Induced Phase-Separation Process

In the temperature-induced phase-separation process, the precipitation of a casting solution is achieved by cooling a polymer solution which forms a homogeneous solution only at elevated temperature, for example, polypropylene dissolved in *N*,*N*-bis-(2-hydroxyethyl)tallow amine [23]. The temperature-induced phase-separation process generally results in a symmetric porous structure. Under certain experimental conditions, it can also result in asymmetric structures [32]. The temperature-induced phase separation is not only applicable to polymers, but it is also used for the preparation of porous membranes from glass mixtures and metal alloys in combination with a leaching procedure, as indicated earlier.

1.05.5 Rationalization of the Phase-Inversion Membrane Preparation Process

Although the recipes given in the literature for the preparation of porous structures from polymers, metals, or glasses by phase inversion are very different, they are all based on similar thermodynamic and kinetic parameters, such as the chemical potentials and diffusivities of the individual components and Gibb's free energy of mixing of the entire system. Identification of the various process parameters is the key to understanding the membrane formation mechanism – a necessity for optimizing membrane properties and structures.

1.05.5.1 Phenomenological Description of the Phase-Separation Process

A quantitative treatment considering all thermodynamic and kinetic parameters involved in the phase-inversion process is difficult. However, a phenomenological description of the process with the aid of the phase diagram of a mixture consisting of a polymer, one or more solvents, and nonsolvents at constant or different temperatures is very useful for a better understanding of the relation between membrane structure and the different preparation parameters. It must, however, be realized that the phase diagram is the thermodynamic description of an equilibrium state. In the membrane formation process, the phase separation is also determined by kinetic parameters, and thermodynamic equilibrium is generally not obtained on a macroscopic scale. The quantitative description of the kinetics is difficult. However, just a general thermodynamic description of the phase separation based on the phase diagram of the polymer/solvent/nonsolvent system provides valuable information concerning the membrane structures obtained by the phase-inversion process.

The temperature-induced phase separation of a two-component polymer mixture is illustrated in **Figure 8(a)**, which shows a phase diagram of a two-component mixture of a polymer and a solvent as a function of temperature. The diagram indicates a miscibility gap over a wide range of composition at low temperature. Above a certain temperature, the polymer and solvent form a homogeneous solution at all compositions. At other temperatures, the system is not stable at certain compositions and will separate into two phases. This region is referred to as the miscibility gap, which is surrounded by the binodale curve. If a homogeneous polymer–solvent mixture of a certain composition at a temperature T_1, as indicated by point A in **Figure 8(a)**, is cooled to the temperature T_2, as indicated by point B, it will separate into two different phases, the composition of which is indicated by the points B′ and B″. The point B″ represents the polymer-rich phase and the point B′ the solvent-rich polymer-lean liquid phase. The lines B′–B and B″–B represent the ratio of the amounts of the two phases in the mixture, that is, the overall porosity of the obtained porous system. If the polymer concentration in the polymer-rich phase has reached a certain value, its viscosity is increased to such an extent that it can be considered as solid. The polymer-rich phase forms the solid membrane structure and the polymer-lean phase the liquid-filled pores.

The phase separation induced by the addition of a nonsolvent to a homogeneous polymer solution is illustrated in **Figure 8(b)**, which shows a three-component isothermal phase diagram. The three-component mixture exhibits a miscibility gap over a wide range of compositions. If a nonsolvent is added to a solution consisting of polymer and solvent, the composition of

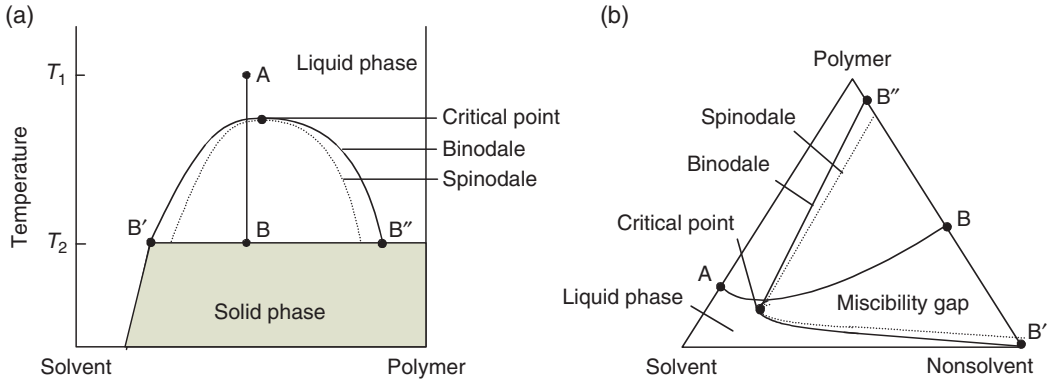

Figure 8 Schematic diagram showing the formation of a microporous system by (a) thermal precipitation of a two-component mixture and (b) addition of a nonsolvent to a homogeneous polymer solution in a three-component mixture exhibiting a miscibility gap at certain conditions of temperature and composition. A, casting solution; B, membrane porosity; B′, polymer-lean phase; B″, polymer-rich phase.

which is indicated by the point A on the solvent–polymer line, and, if the solvent is removed from the mixture at about the same rate as the nonsolvent enters, the composition of the mixture will change following the line A–B. When the composition of the system reaches the miscibility gap it will separate into two phases forming a polymer-rich phase represented by the upper boundary of the miscibility gap, which is determined by the binodale and a polymer-lean phase represented by the lower boundary of the miscibility gap. When the solvent is replaced completely by the nonsolvent, the mixture has reached the composition represented by point B. The point B represents a mixture of the solid polymer-rich phase and a liquid polymer lean phase of compositions B′ and B′′, respectively. Instead of adding a nonsolvent to a polymer–solvent mixture, phase separation can also be achieved by evaporation of a solvent from a solvent/polymer/nonsolvent mixture, which is used as casting solution for the membrane [24].

The description of the formation of porous systems by means of the phase diagrams, as illustrated in **Figure 8**, is based on the assumption of thermodynamic equilibrium. It predicts under which conditions of temperature and composition a system will separate into two phases. However, it will not provide any information concerning the size of the domains of the two phases and their shapes, that is, the pore size, the pore shape, that is, finger- or sponge-like, and the pore-size distribution of the membrane. These parameters are determined by kinetic parameters such as the diffusivities of the various components in the mixture, the viscosity of the solution, and the chemical potential gradients, which act as driving forces for the diffusion of the various components in the mixture. As these parameters change continuously during the phase separation, which constitutes the actual membrane formation process, no transient states of equilibrium will be achieved. Therefore, the kinetic parameters are difficult to determine by independent experiments and, thus, they are not readily available. This makes a quantitative description of the membrane formation mechanism very difficult.

The phase-inversion process can make both symmetric and asymmetric membranes with rather different structures from a variety of polymers, as indicated before in the scanning electron micrographs of **Figures 5** and **6**. Polymers that are used today on a commercial basis to prepare membranes by the phase-inversion process for various applications and processes are listed in **Table 3**. The resistance of some of the polymers to organic solvents is reported in **Table 4**.

1.05.6 Preparation of Composite Membranes

In processes such as reverse osmosis, gas separation, and pervaporation, the actual mass separation is achieved by a solution–diffusion mechanism in a homogeneous polymer layer. Since the diffusion process in a homogeneous polymer matrix is relatively slow, these membranes should be as thin as possible, as indicated before. Therefore, an asymmetric membrane structure is mandatory for these processes. Unfortunately, many polymers with satisfactory

Table 3 Polymers of commercial membranes prepared by phase inversion and their applications

Membrane material	*Membrane process*
Cellulose acetate	EP, MF, UF, RO
Cellulose esters (mixed)	MF, D
Polyacrylonitrile (PAN)	UF
Polyamide (aromatic, aliphatic)	MF, UF, RO, MC
Polyimide	UF, RO, GS
Polypropylene	MF, MD, MC
Polyethersulfone	UF, MF, GS, D
Polysulfone	UF, MF, GS, D
Sulfonated polysulfone	UF, RO, NF
Polyvinylidenefluoride	UF

EP, elctrophoresis; MF, microfiltration; UF, ultrafiltration; RO, reverse osmosis; GS, gasseparation; NF, nanofiltration; D, dialysis; MD, membrane distillation; MC, membrane contactore.

selectivity and permeability for the various components in gas mixtures or liquid solutions are not well suited for the phase-inversion membrane preparation process. This has led to the development of the so-called composite membranes. A typical composite membrane is shown schematically and as scanning electron micrograph in **Figures 9(a)** and **9(b)**. It is composed of a 20–1000-nm-thin dense polymer barrier layer formed over an approximately 50–100-μm-thick porous film.

The advantages of composite membranes over integral asymmetric structures are that different polymers may be used for the porous support and the selective barrier layer. This means that polymers, which show the desired selectivity for a certain separation problem, but are not suited for preparation into integral asymmetric membranes because of poor mechanical strength or poor film-forming properties, may well be utilized as the selective barrier in composite membranes. On the other hand, polymers suited for the preparation of porous structures but without the required properties for a certain separation task can be used as support structure. This expands the variety of available materials for the preparation of membranes with properties required in a given separation task considerably.

The preparation of composite membranes involves two steps: the first is the preparation of a suitable porous support and the second is the preparation of the actual barrier layer on the surface of the support structure. The performance of a composite membrane is not only determined by the properties of the selective barrier layer, but it is also significantly affected by properties of the porous support.

Although, almost exclusively, the actual barrier layer determines the selectivity of a composite membrane, its flux rate is also to some extent determined by the pore size and overall porosity of the substructure. The effect of pore size and overall porosity is illustrated in **Figure 10** that shows an idealized homogeneous barrier layer on a porous support.

The actual diffusion pathway of the component through the barrier layer into a pore of the support structure is always longer than the thickness of the barrier layer z_o but shorter than the longest path z_{max}.

If it is assumed that the transport in the support structure is exclusively through the pores, the effective path length can be expressed as a function of the overall membrane porosity, the thickness of the barrier layer, and the radius of the pores in the support structure by

$$z_{eff} = \omega z_o + (1-\omega)\frac{1}{2}\left(\sqrt{r^2\left(\frac{1-\omega}{\omega}\right) + z_o^2} + z_o\right) \quad (1)$$

Here, z_{eff} and z_o are the effective diffusion path length and the thickness of the barrier layer, respectively, r is the radius of the pores in the support structure, and ω is the surface porosity of the support structure.

This relationship, which can be obtained by simple geometric considerations [33], indicates that the effective diffusion path length z_{eff} is strongly affected by the surface porosity of the substructure. According to Equation (1), the effective diffusion length is approximately equal to the thickness of the barrier layer at relatively high surface porosity (>50%). However, it increases by an order of magnitude when the porosity is less than 1% if the barrier layer thickness is assumed to be approximately the same as the pore radius. Accordingly, the flux decreases by the same magnitude. The geometrical consideration expressed in Equation (1) indicates that the surface porosity of the support layer significantly affects the membrane flux. The porosity should always be as high as possible to achieve optimal flux rates with thin-film composite membranes. To ensure adequate mechanical strength, the pore diameter should not be significantly greater than the film thickness.

Table 4 Most common polymers used to prepare membrane and resistance to organic solvents

Polymer / Solvent	*Methanol*	*Amyl alcohol*	*Tetra-hydrofuran*	*Hexane*	*Xylene*	*Toluene*	*Acetone*	*Ethyl ether*
Aliphatic polyamide (PA) (nylon-6)	SC	LC	NC	LC	-	-	LC	LC
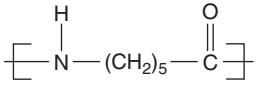								
Aromatic polyamide (PA) (nomex)	SC	LC	NC	LC	-	-	LC	LC
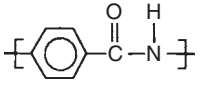								
Polyimide (PI)	LC	-	NC	-	-	NC	-	-
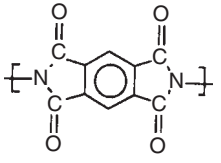								
Polypropylene (PP)	LC	LC	SC	NC	SC	LC	LC	LC
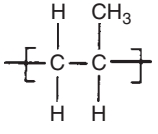								
Polyvinylfluoride (PVDF)	LC	LC	LC	LC	LC	LC	NC	LC
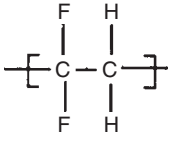								

(*Continued*)

Table 4 (Continued)

Polymer / Solvent	*Methanol*	*Amyl alcohol*	*Tetra-hydrofuran*	*Hexane*	*Xylene*	*Toluene*	*Acetone*	*Ethyl ether*
Polysulfone (PS)	LC	LC	NC	LC	NC	NC	NC	LC
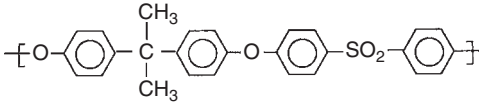								
Polyetheretherketone (PEEK)	-	-	-	LC	-	LC	NC	-
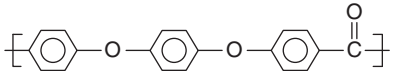								

LC, long compatibility; SC, short compatibility; NC, noncompatible.

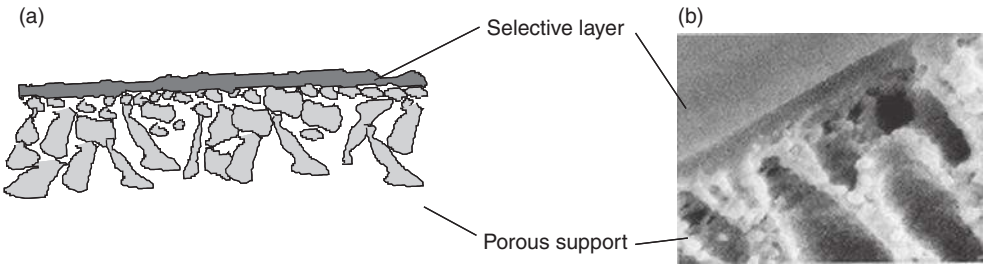

Figure 9 (a) Schematic diagram of a composite membrane showing the porous support structure and the selective skin layer, and (b) scanning electron micrograph of a composite membrane with polydimethylsiloxane as the selective layer on a polysulfone support structure.

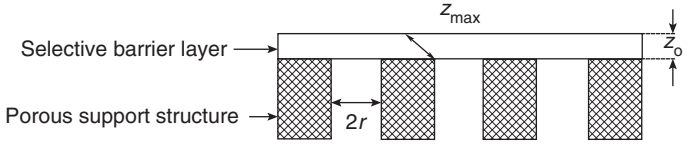

Figure 10 Schematic drawing illustrating the diffusion path of a component through a selective barrier layer of a composite membrane (z_o represents the shortest and z_{max} the longest path).

1.05.6.1 Techniques Used for the Preparation of Polymeric Composite Membranes

The techniques used for the preparation of composite membranes may be grouped into four general procedures:

- casting of the barrier layer, for example, on the surface of a water bath and then laminating it on the porous support film;
- coating of the porous support film by a polymer, a reactive monomer, or pre-polymer solution, followed by drying or curing with heat or radiation;
- gas-phase deposition of the barrier layer on the porous support film from a glow discharge plasma; and
- interfacial polymerization of reactive monomers on the surface of the porous support film.

Casting an ultrathin film of cellulose acetate on a water surface and transferring the film on a porous support constitute one of the earliest techniques used for preparing composite reverse osmosis membranes. However, this technique is no longer used today [34].

Coating a porous support structure by dipping it into a polymer or pre-polymer solution is today applied mainly for the preparation of composite membranes to be used in gas separation and pervaporation. Particularly, polymers such as polydimethylsiloxane, which are available as soluble pre-polymers and which can easily be crosslinked by a heat treatment procedure, thus becoming insoluble in most solvents, are suited for the preparation of this type of composite membrane. If the pore dimension in the support membrane is selected properly, the pre-polymer is unable to penetrate the support, and a rather thin uniform barrier layer of 0.05–1-μm thickness can easily be prepared. A typical composite membrane prepared by dip coating is shown in **Figure 9(b)**, which is the scanning electron micrograph of an asymmetric polysulfone ultrafiltration membrane that was coated by a 1 wt.% solution of polydimethylsiloxane in an appropriate solvent followed by thermal crosslinking [33].

Gas-phase deposition of the barrier layer on a dry porous support membrane by plasma polymerization was also successfully used for the preparation of reverse osmosis membranes. Although reverse osmosis membranes with excellent desalination properties showing salt rejection in excess of 99%, and fluxes of 1.2 $m^3\ m^{-1}\ d^{-1}$ when tested with seawater, have been prepared on a laboratory scale by plasma polarization, it is not used on a large-scale industrial production of composite membranes [35].

Today, by far the most important technique for preparing composite membranes is the interfacial polymerization of reactive monomers on the surface of a porous support film. The first membrane produced on a large scale with excellent reverse osmosis desalination properties was developed in the early 1970s in the North Star Research Institute under the code name NS 100 [36, 37]. The procedure for the

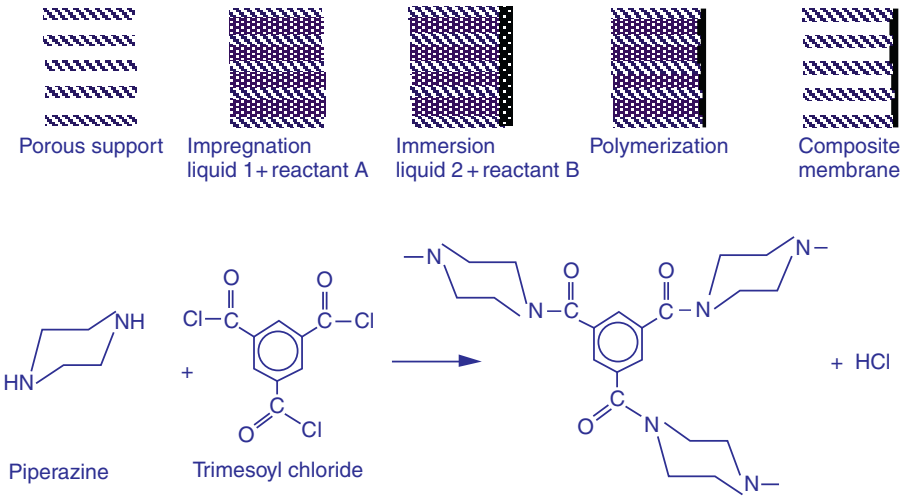

Figure 11 Schematic diagram showing the formation of a composite membrane by interfacial polymerization of piperazine with trimesoyl chloride.

preparation of this membrane, which exhibited water fluxes of about $1\,m^3\,m^2\,d^{-1}$ and salt rejections in excess of 99% when tested with seawater at 6 MPa pressure, was rather simple [38]. A polysulfone support membrane was soaked in an aqueous solution of 0.5–1% polyethyleneimine, which was reacted interfacially at the membrane surface with a 0.2–1% solution of toluene diisocyanate in hexane. A heat-curing step at 110 °C leads to further crosslinking of the polyethyleneimine. The preparation of composite membranes based on piperazine and trimesoyl chloride is shown schematically in **Figure 11**.

The process seems to involve two types of reactions. In a first step, the piperazine reacts rapidly at the interface with the trimesoyl chloride to form a polyamide surface skin while amine groups below this surface remain unreacted. In the second heat treatment step, internal crosslinking of these amine groups takes place. Thus, the final membrane has three distinct layers of increasing porosity: (1) the dense polyamide surface skin, (2) a thin crosslinked piperazine layer, which extends into the pores of the support film, and (3) the actual polysulfone support membrane.

1.05.7 Preparation of Homogeneous Solid Membranes

The selective barriers of many composite membranes may be considered as homogeneous solid membranes as discussed earlier. In homogeneous solid membranes, the entire membrane consists of a dense, solid, and pore-free structure. They are made from polymers as well as inorganic materials such as glass or metal. Because of their high selectivity for different chemical components, homogeneous membranes are used in various applications, which generally involve the separation of low-molecular-mass components with identical or nearly identical molecular dimensions. The most important applications are in gas separation.

One of the more important homogeneous solid metal membranes is the palladium or palladium alloy membrane used for the separation and purification of hydrogen [39]. The permeability of hydrogen in palladium, palladium alloys, and several other metals such as platinum, silver, and nickel is several orders of magnitude higher than that of any other gas. The permeability of hydrogen in palladium alloy membranes is highly temperature dependent and separation is carried out at elevated temperature of about 300 °C. Membranes generally consist of 10–50-μm-thick metal foils. Because of their high selectivity, these membranes are used to produce high purity in excess of 99.99% hydrogen.

Homogeneous silica glass membranes are homogeneous structures that show promise as selective barriers for the separation of helium. Like metal membranes, glass membranes are employed at elevated temperature. Homogeneous glass membranes also have a high selectivity for hydrogen ions and are used as the selective barrier in pH electrodes.

1.05.8 Preparation of Liquid Membranes

Liquid membranes are important in combination with facilitated and coupled transport, which utilizes selective carriers, as discussed earlier, to transport certain components such as metal-ions selectively and at a relatively high rate across the liquid membrane. Liquid membranes generally consist of a thin film separating two phases, which may be aqueous solutions or gas mixtures. The material used for the liquid membrane should be immiscible with water and should have a low vapor pressure to guarantee long-term stability of the membrane. It is relatively easy to form a thin oil film between two aqueous or gas phases. It is difficult, however, to maintain and control this film and its properties during a mass separation process. Two different techniques are used today for the preparation of liquid membranes. In the first preparation technique, leading to the so-called supported membranes, the pores of a porous membrane are filled with the selective liquid barrier material as shown in **Figure 12(a)**. In the second technique, the liquid membrane is stabilized as a thin oil film by a surfactant in an emulsion-type mixture as illustrated in **Figure 12(b)**. In the supported liquid membranes, the porous structure provides the mechanical strength and the liquid-filled pores the selective separation barrier. Both types of membranes can be used for the selective removal of heavy metal-ions or certain organic components from industrial effluents [40–43]. They have also been used rather effectively for the separation of oxygen and nitrogen [44].

The preparation of supported liquid membranes is extremely simple. To maximize the useful lifetime of a membrane, the liquid membrane material should have low viscosity, low vapor pressure (i.e., high boiling point), and when used in aqueous solutions, low water solubility. The porous substructure should have a high porosity and a pore size small enough to support the liquid membrane phase under hydrostatic pressure; the polymer of the substructure should be hydrophobic because most liquid membranes are used with aqueous feed solutions. In practice, liquid membranes are prepared by soaking a hydrophobic porous membrane made from polytetrafluorethylene such as Gore-Tex® or from polyethylene such as Cellgard® [45], in a hydrophobic liquid. The liquid may be a selective carrier such as an oxime or a tertiary or quaternary amine dissolved in kerosene. The disadvantage of supported membranes is their thickness, which is determined by the thickness of the porous support structure. The latter is in the range of 10–50 μm, and therefore about 100 times thicker than the selective barrier of an asymmetric polymer membrane. Thus, the fluxes of supported liquid membranes can be low even when their permeabilities are high.

The preparation of the unsupported liquid membrane is more complex [9]. Here, two immiscible phases, that is, the hydrophobic oil-type membrane phase and a water phase, often referred to as stripping solution, are mixed to form an emulsion of water droplets in a continuous oil phase, which is stabilized by the addition of a surfactant. This emulsion is then added to the second aqueous phase, the feed solution with the first emulsion forming droplets in the second aqueous phase. The overall result is the separation of two aqueous phases by an oil phase forming the liquid membrane. Ideally, droplets form in this process, in which the aqueous phase is surrounded by a relatively thin hydrophobic phase, the membrane, which is surrounded by a second continuous aqueous phase. In reality, several aqueous droplets are found in a single hydrophobic droplet as shown in **Figure 12(b)** and the diffusion pathways become longer. With another aqueous solution, the

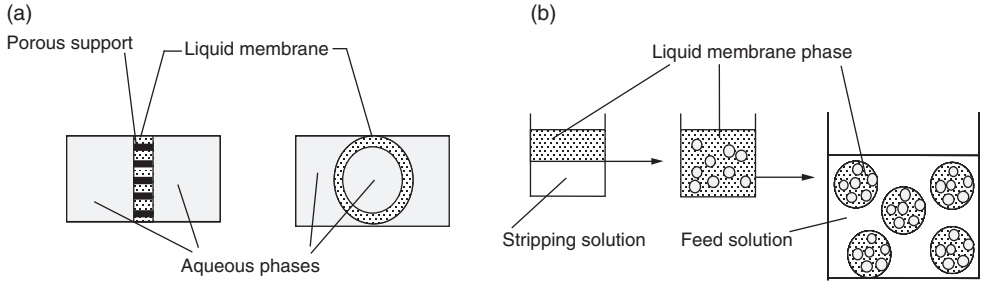

Figure 12 Schematic drawing of (a) supported hollow-fiber liquid membrane and (b) the preparation of an emulsion-type liquid membrane.

component to be eliminated is supplied to the original emulsion and passes through the membrane into the internal solution.

1.05.9 Preparation of Ion-Exchange Membranes

Ion-exchange membranes consist of highly swollen gels carrying fixed positive or negative charges. The properties and preparation procedures of ion-exchange membranes are closely related to those of ion-exchange resins. As with resins, there are many possible types with different polymer matrixes and different functional groups to confer ion-exchange properties on the product. Although there are a number of inorganic ion-exchange materials, most of them based on zeolites and bentonites, these materials are rather unimportant in ion-exchange membranes and will not be discussed further.

The types of ion-exchange membranes include (1) cation-exchange membranes, which contain negatively charged groups fixed to the polymer matrix, and (2) anion-exchange membranes, which contain positively charged groups fixed to the polymer matrix. Moreover, it is possible to laminate cation- and anion-exchange layers to obtain a bipolar membrane.

In a cation-exchange membrane, the fixed anions are in equilibrium with mobile cations in the interstices of the polymer.

The matrix of a cation-exchange membrane contains fixed anions. Mobile cations are referred to as counterions. In contrast, the mobile anions, called co-ions, are more or less completely excluded from the polymer matrix because of their electrical charge, which is identical to that of the fixed ions. Due to the exclusion of the co-ions, a cation-exchange membrane permits transfer of cations only. Anion-exchange membranes carry positive charges fixed on the polymer matrix; therefore, they exclude all cations and are permeable to anions only.

For the practical preparation of ion-exchange membranes two rather different procedures are used. A quite simple technique is based on mixing an ion-exchange resin and a binder polymer, such as polyvinylchloride and extruding the mixture as a film at a temperature above the melting point of the polymer. The result is a heterogeneous membrane with relatively large domains of ion-exchange material and no conductive regions of the binder polymer. To obtain ion-exchange membranes with satisfactory conductivity the fraction of ion-exchange resin must be in excess of 50–70 wt.%. This often leads to rather high swelling and to poor mechanical stability of the membrane. Furthermore, the size of the ion-exchange particles should be as small as possible, that is, <2–$20\,\mu m$ in diameter to be able to make thin membranes with low electrical resistance and high permselectivity. Nevertheless, the method is still used today on a large scale for the preparation of ion-exchange membranes.

More recently homogeneous ion-exchange membranes are produced either by a polymerization of monomers that carry anionic or cationic moieties or by introducing these moieties into a polymer which may be in an appropriate solution or a preformed film.

References

[1] Kesting, R. E. *J. Appl. Polym. Sci.* **1973**, *17*, 1771.
[2] Cadotte, J. E., Petersen, R. I. Thin Film Reverse Osmosis Membranes: Origin, Development, and Recent Advances. In *Synthetic Membranes*; Turbak, A. F., Ed.; ACS Symposium Series 153, Vol. I, Desalination; American Chemical Society: Washington, DC 1981, pp 305–325.
[3] Cheryan, M. *Ultrafiltration and Microfiltration Handbook*; Technomic Publishing: Lancaster, PA, 1998.
[4] Merten, U. Transport Properties of Osmotic Membranes. In *Desalination by Reverse Osmosis*; Merten, U., Ed.; MIT Press: Cambridge, MA, 1966; pp 15–54.
[5] Raymond, Z. R., Flemming, G. K. Gas Permeation. In *Membrane Handbook*; Ho, W. S., Sirkar, K. K., Eds.; Van Nostrand Reinhold: New York, 1992.
[6] Strathmann, H. *Ion-Exchange Membrane Separation Processes*; Elsevier: Amsterdam, 2004.
[7] Helfferich, F. *Ion-Exchange*; McGraw-Hill: London, 1962.
[8] Spiegler, K. S. *Electrochemical operations. In Ion-Exchange Technology*; Nachod, F. C., Schubert, J., Eds.; Academic Press: New York, 1957.
[9] Li, N. N. *AIChE J.* **1971**, *17*, 459.
[10] Kemperman, A. J. B., Rolevink, H. H. M., Bargeman, D., van den Boomgaard, T., Strathmann, H. *J. Membr. Sci.* **1998**, *138*, 43.
[11] Dessau, R. M., Grasselli, R. K., Lago, R. M., Tsikoyiannis, J. G. Processes for converting feedstock organic compounds. US Pat. 5316661, 1994.
[12] Haag, W. O., Tsikoyiannis, J. G. Membrane Composed of a Pure Molecular Sieve. US Pat. 5019263, 1991.
[13] Tsai, C. Y., Dixon, A. G., Ma, Y. H., Moser, W. R., Pascessi, M. R. *J. Am. Ceram. Soc.* **1998**, *81*(6), 1437.
[14] Tavolaro, A., Drioli, E. *Adv. Mater.* **1999**, *11* (12), 975–996.
[15] Nagy, B., Bodart, P., Hannus, I., Kiricsi, I. In *Synthesis, Characterization and Use of Zeolitic Microporous Materials*; Konya, Z., Tubak, V., Eds. DecaGen: Szeged-Szoreg, Hungary, 1998.
[16] Bein, T. *Chem. Mater.* **1996**, *8* (8), 1636–1653.
[17] Hood, H. P., Nordberg, M. E. Treated Borosilicate Glass. US Pat. 2106744, 1938.
[18] Loeb, S., Sourirajan, S. High Flow Porous Membranes for Separating Water from Saline Solutions. US Pat. 3133132, 1964.

[19] Pall, D. B. Process for Preparing Hydrophilic Polyamide Membrane Filter Media and Product. US Pat. 4340479, 1982.
[20] Zsigmondy, R. Filter and Method of Producing Same. US Pat. 1421341, 1922.
[21] Fleischer, R. L., Price, P. B., Walker, R. M. *Sci. Am.* **1969**, *220*, 30.
[22] van Rijn, C. J. M. *Nano and Micro Engineered Membrane Technology*; Elsevier: Amsterdam, 2004.
[23] Hiatt, W. C., Vitzthum, G. H., Wagner, K. B., Gerlach, K., Josefiak, C. *Microporous Membranes Via Upper Critical Temperature Phase Separation in Material Science of Synthetic Membranes*; Lloyd, D. R., Ed.; ACS Symposium Series 269; 1985; pp 229 –244.
[24] Kesting, R. E. Phase Inversion Membranes. In *Material Science of Synthetic Membranes*; Lloyd, D. R., Ed.; ACS Symposium Series 269; 1985; Vol. 131.
[25] Manjikian, S. *Ind. Eng. Chem. Prod. Res. Dev.* **1967**, *6*, 23.
[26] Strathmann, H., Production of Microporous Media by Phase Inversion Processes. In *Material Science of Synthetic Membranes*; Lloyd, D. R., Ed.; ACS Symposium Series 269; 1985; Vol. 165.
[27] Strathmann, H., Scheible, P., Baker, R. W. *J. Appl. Polym. Sci.* **1971**, *15*, 811.
[28] Wijmans, J. G., Baaij, J. P. B., Smolders, C. A. *J. Membr. Sci.* **1983**, *14*, 263.
[29] Broens, L., Altena, F. W., Smolders, C. A. *Desalination* **1980**, *32*, 33.
[30] Frommer, M. A., Feiner, I., Kedem, O., Block, R. *Desalination* **1970**, *7*, 393.
[31] Sourirajan, S., Kunst, B. Cellulose Acetate and Other Cellulose Ester Membranes. In *Reverse Osmosis and Synthetic Membranes*; Sourirajan, S., Ed.; National Research Council Canada: Ottawa, 1977.
[32] Kamide, K., Manabe, S. Role of Microphase Separation Phenomena in the Formation of Porous Polymeric Membranes. In *Material Science of Synthetic Membranes*; Lloyd, D. R., Ed.; ACS Symposium Series 269; 1985; Vol. 197.
[33] Strathmann, H., Gudernatsch, W., Bell, C.-M., Kimmerle, K. *Chem. Ing. Technol.* **1988**, *60*, 590.
[34] Riley, R. L., Lonsdale, H. K., Lyons, C. R., Merten, U. *J. Appl. Polym. Sci.* **1967**, *11*, 2143.
[35] Yasuda, H. Composite Reverse Osmosis Membranes Prepared by Plasma Polymerization. In *Reverse Osmosis Synthetic Membranes*; Sourirajan, S., Ed.; National Research Council Canada: Ottawa, 1977.
[36] Cadotte, J. E. Reverse Osmosis Membrane. US Pat. 4277,344, 1981.
[37] Rozelle, L. T., Cadotte, J. E., Cobian, K. E., Kopp, C. V. Nonpolysaccharide Membranes for Reverse Osmosis: NS 100 Membranes for Reverse Osmosis and Synthetic Membranes. In *Reverse Osmosis Synthetic Membranes*; Sourirajan, S., Ed.; National Research Council Canada: Ottawa, 1977.
[38] Cadotte, J. E. Evolution of Composite Reverse Osmosis Membranes. In *Material Science of Synthetic Membranes*; Lloyd, D. R., Ed.; ACS Symposium Series 269; 1985; Vol. 229.
[39] Kammermeyer, K. Gas and Vapor Separation by Means of Membranes. In *Progress in Separation and Purification*; Perry, S., Ed.; Wiley-Interscience: New York, 1972.
[40] Cussler, E. L. *Diffusion*; Academic Press: Cambridge, MA, 1984.
[41] Kimura, S. G., Matson, S. L., Ward, W. J., III Industrial Applications of Facilitated Transport. In *Recent Developments in Separation Science*; Li, N. N., Ed.; CRC Press: Boca Raton, FL, 1979 Vol. V.
[42] Schultz, J. S., Goddard, J. D., Suchdeo, S. R. *AIChE J.* **1974**, *20*, 417.
[43] Ward, W. J., III *AIChE J.* **1970**, *16*, 405.
[44] Baker, R. W., Roman, J. C., Lonsdale, H. K. *J. Membr. Sci.* **1987**, *31*, 15.
[45] Babcock, W. C., Baker, R. W., Lachapelle, E. D., Smith, K. L. *J. Membr. Sci.* **1980**, *7*, 71–87.

Biographical Sketch

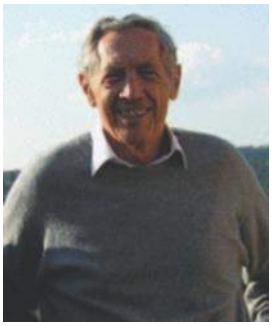

Heinrich Strathmann was born in Detmold, Germany in 1934. He received his *Diplôme d'Ingénieur* (Dipl.-Ing.) in chemistry from the University of Darmstadt, Germany in 1961. In 1965, he was awarded a doctorate degree in chemistry by the University of Darmstadt, Germany. In 1982, he was awarded the habilitation degree, by the University of Tübingen, Germany. Since 1988, he has been a professor at the University of Stuttgart, Germany.

From 1962 to 1966, he worked as a research assistant at the University of Aachen, Germany. Between 1966 and 1971, he was associated with Amicon Corp., Lexington, MA, USA. From 1971 to 1982, he was associated with Forschungsinstitut Berghof GmbH, Germany. Between 1982 and 1992, he worked with the Fraunhofer Institute for Bioengineering, Stuttgart, Germany. From 1988 to 1992, he was a professor at the University of Stuttgart, Germany. Between 1992 and 1999, he was a professor at the University of Twente, the Netherlands. From 1999 to 2000, he was a professor at the University of Colorado, Boulder, USA. He has been professor emeritus at the University of Stuttgart, Germany since 2000.

He was with the editorial board of the *Journal of Membrane Science* in 1976. He was an editor of *Separation and Purification Technology* (1997–2002). He worked in the fields of desalination (1978), filtration and separation (1987–2002), and gas separation and purification (1982–96).

Apart from being a member of the scientific advisory board of various companies, he holds membership in various scientific organizations such as DECHEMA, Frankfurt, Germany and European Membrane Society. He is also a member of the board of scientific organizations such as the European Membrane Society (1984–98) (vice-president), UNESCO Center for Membrane Technology, Sydney, Australia (1993–98), and the UN-University, Environmental Science, Gwangju, Korea (2003–06).

He has authored three textbooks on *Membrane Science and Technology*, coauthored eight reference books, and has more than 200 scientific publications and 36 patents to his credit.

His responsibilities include teaching chemical engineering and supervising PhD students.

He is a recipient of various awards including the 1994 Honorary Professor at the Dalian Institute Chemical Physics, 1998 Willy Hager Price and gold medal, 2005 Honorary Professor at the South China Central University, and 2007 R. Barrer Price of the European Membrane Society.

1.06 Advanced Polymeric and Organic–Inorganic Membranes for Pressure-Driven Processes

S P Nunes and K-V Peinemann, King Abdullah University of Science and Technology, Thuwal, Saudi Arabia

1.06.1 Membranes for Pressure-Driven Processes

A more detailed review of membranes and membrane materials has been published before [1]. In this chapter, first the state of the art of conventional membranes for pressure-driven processes (reverse osmosis (RO), nanofiltration, ultrafiltration, and gas separation) will be summarized, taking into account the most representative examples currently in application. Thereafter, the emphasis is placed on recent developments of advanced polymeric and organic–inorganic materials for membranes.

Certainly, the most used method for polymer porous membrane preparation is the so-called phase inversion, which consists of the induction of phase separation in a previously homogeneous polymer solution either by temperature change, by immersing the casting solution in a nonsolvent bath (wet process) or by exposing it to a nonsolvent atmosphere (dry process). The wet process is the most common and is at least part of the industrial production of ultrafiltration, RO, and gas separation (GS), giving a high permeable and selective asymmetric structure. Additional thin coating steps can be further performed to give the needed selectivity for RO or GS. The preparation of asymmetric membranes by phase inversion and the influence of parameters such as casting solution composition and temperature have been topics of many reviews [1–6] and will not be detailed here.

1.06.1.1 RO Membranes

RO is long established as a large-scale industrial membrane process. The large desalination plants around the world are running with RO technology. One of the early materials used for membrane production is cellulose acetate (CA), easily prepared by phase inversion with a solution cast on a nonwoven and immersed in water. The characteristic structure of an integral asymmetric membrane is formed with a selective top layer and pores of increasing size across the membrane. CA is still being successfully used,

especially in water treatment (in spiral wound modules) with relatively high chlorine tolerance and stability in applications where the feed water has a high fouling potential, such as in municipal effluents and surface water supplies. The handicap of CA membranes is evident for applications in chemical and pharmaceutical industries when organic solvents are part of the feed or in processes operating at temperatures higher than 50 °C or pH lower than 3 or higher than 7. For these conditions aromatic polyamides have a much higher solvent resistance and may be used in a wider pH range (pH 4–11). The main application is the treatment of brackish water and seawater. They can be produced in very thin hollow fibers with large surface area/volume. The main disadvantage is the very low chlorine tolerance. Desalination and wastewater treatment need membranes with large flows. A very successful class of membranes for this application is that of thin film composites (TFCs), prepared by interfacial polymerization on the surface of a porous support. A very good review of composite membranes was published by Petersen and coworkers [7, 8]. TFC membranes usually allow quite high water flows with low salt solubility. They consist of an ultrathin layer, usually of polyamide or polyetherurea, which is polymerized *in situ* and cross-linked on an asymmetric porous support, usually polysulfone. Since the dense selective layer is very thin, the membranes can operate at higher flux and lower pressure. The chemical stability is very good, although the chlorine tolerance is low. They can operate in a pH range of between 2 and 11. The membrane preparation consists of immersing the porous support in an aqueous solution containing a water-soluble monomer. After that the support is immersed in a solution of the second monomer in a nonpolar solvent. Both monomers are only allowed to react at the interface between organic and aqueous solution, forming a thin polymer layer at the surface of the porous support. As soon as the polymer layer is formed, it acts as a barrier for the monomer transport and avoids the continuity of the polycondensation. On the other hand, any defect on the polymer layer is immediately repaired with a kind of self-healing mechanism, since monomer transport and polycondensation is allowed at that point (**Figure 1**).

One of the most successful TFC membranes is the FilmTec FT-30, developed by Cadotte *et al.* [7, 8] and now commercialized by Dow Water Solutions. The reaction involved in the preparation of the FT-30 is as follows:

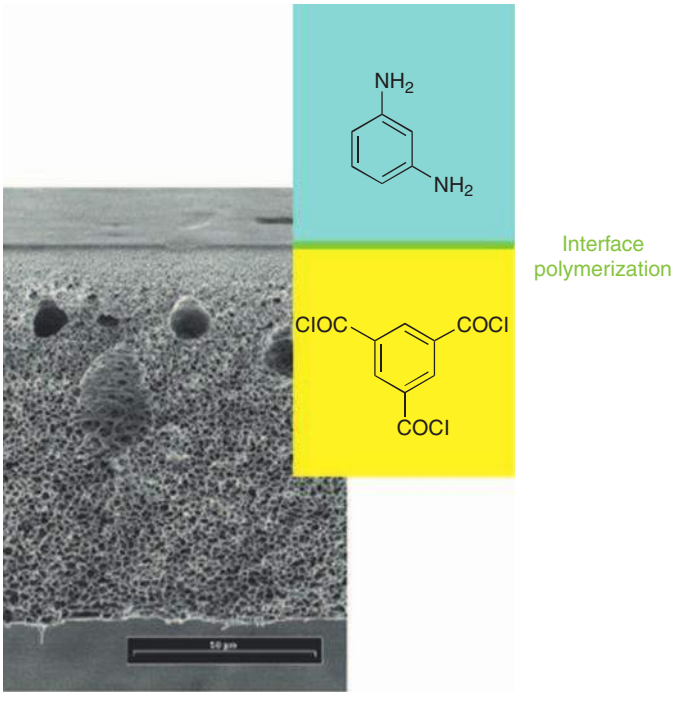

Figure 1 Thin film-coating membrane preparation.

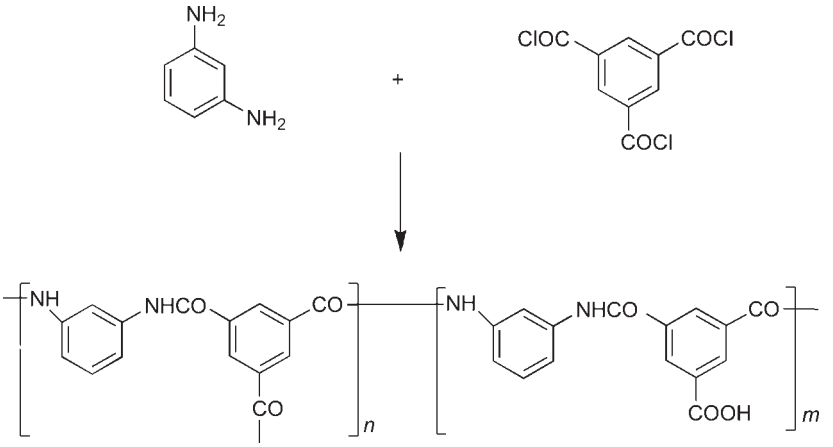

The polyamide layer is formed on an asymmetric microporous polysulfone support cast on a polyester support web. The polyester web gives the major structural support, and the polysulfone support with small surface pores with diameter of ~15 nm is the proper substrate for the formation of a 0.2-μm polyamide top layer. The maximum operating pressure of the FT-30 is ~7 MPa with free chlorine tolerance <0.1 ppm.

Although the membranes for RO are well established in the market, new membranes are required for related emerging fields. This is the case of osmotic power or pressure retarded osmosis plants, a concept, which has been independently proposed in the 1970s by Norman [9], Jellinek [10], and Loeb [11] and is now becoming a reality in Norway. An introduction on this technology is given in Reference [12]. The technology takes advantage of the high osmotic pressure which is built when salt water from the sea meets water from fjords and rivers (**Figure 2**).

The pressure is about 29 bar at 20 °C for 35 g salt l^{-1} (seawater). The pressure is enough to move turbines and provide 2.2 MW of energy, working with water flow rate of 1 $m^3 s^{-1}$. In typically large rivers, water flows at about 10 000 $m^3 s^{-1}$. For each MW 200 000 m^2 of membrane would be required, signifying a huge market for membranes. The requirements for these membranes are high salt rejection like in RO, however with much higher water fluxes, as well as much thinner and opener porous supports (**Figure 3**).

Membrane performance ~5 W m^{-2} is needed to make the process economically competitive. Currently, the best commercial cellulose derivative membranes have around one-tenth of the needed performance. The best commercial TFC membranes for RO would give 0.1 W m^{-2}. Membranes developed at the laboratory are available for 3.7 W m^{-2}.

1.06.1.2 NF Membranes

While RO and ultrafiltration are long implemented in several applications, the lack of available membranes with cutoffs between 400 and 4000 g mol^{-1} has been effectively filled much later with the development of nanofiltration membranes. Nanofiltration is important for water softening, removal of organic contaminants, concentration and demineralization of

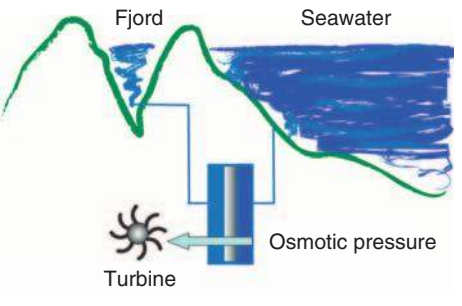

Figure 2 Principles of osmotic power.

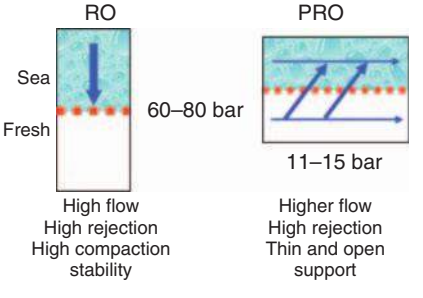

Figure 3 Membrane requirements for reverse osmosis (RO) and for osmotic power.

whey, concentration of sugar and juice, etc. An extensive review on principles and applications of nanofiltration has been published recently [13].

Analogously to the RO membranes, interfacial polycondensation has been used for the development of NF membranes. Dow Water Solutions offers a series of FILMTEC membranes: NF55, NF70, and NF90 (water flow of NF55 > NF70 > NF90) with rejection of at least 95% magnesium sulfate. The top layer is a fully aromatic cross-linked polyamide. NF270 is composed of a semi-aromatic piperazine-based polyamide layer on top of a polysulfone microporous support reinforced with a polyester nonwoven [14]. The membrane is very hydrophilic and its surface is negatively charged leading to the repulsion of also negatively charged solutes. Hydranautics commercializes the ESNA membrane series, also a TFC with an aromatic polyamide layer.

GE-Osmonics (part of GE Water Technologies) commercializes the Desal™ five nanofiltration membranes. The membrane has 4 layers, a polyester nonwoven, an asymmetric microporous polysulfone, and two proprietary thin films, which might be based on sulfonated polysulfone and polypiperazineamide [7]. Desal™ nanofiltration membranes work also at very low pH levels.

Another way to obtain nanofiltration membranes is the modification of RO membrane [15–17], by treatment with acid, triethanolamine or the coating of ultrafiltration membranes with different polymer solutions [18, 19] like hydroxyalkyl derivatives of cellulose. A new approach was proposed by Lu *et al.* [20]. They deposited six-arm rigid star amphiphiles on a methanol/PVA-conditioned polysulfone membrane and stabilized the resulting film by stitching the building blocks. These stars are shape-persistent molecules with hydrophilic arms and a hydrophobic core, which could anchor to the support membrane through noncovalent supramolecular interactions. Rejection of organic contaminants such as rhodamine and As(III) was confirmed.

A key issue for nanofiltration today is the improvement of solvent stability of the available membranes, since it would open a wide range of potential applications in the chemical and pharmaceutical industries.

SelRO® nanofiltration membranes, later commercialized by Koch Membrane Systems, are examples of excellent solvent-resistant membranes on the market. New material developments will be reviewed. The MPS-44 and -50 membranes are stable in alkanes, alcohols, acetates, ketones, and aprotic solvents. The MPS-44 is a hydrophilic membrane suitable, for instance, for separation processes in solvent mixtures containing water and organics. Solutes with molecular weights around 250 g ml^{-1} can then be separated or concentrated, while the composition of the solvent mixture does not change through the membrane. The hydrophilic MPS-50 is a nanofiltration membrane for use in a pure organic medium. The membrane composition is not completely disclosed. Patents of the same company, which introduced them [21, 22], describes the cross-linking of porous polyacrylonitrile (PAN) membranes by immersion in metal alkoxide solutions and heating, leading to insolubility in dimethylformamide (DMF), *N*-methyl-2-pyrrolidone (NMP), or dimethyl sulfoxide (DMSO). Cross-linked PAN membranes coated with polydimethylsiloxane have been tested for filtration of oligomers in organic solvents [23]. Coating with a hydrophilic polymer (e.g., polyethylenimine), which is later cross-linked, brings the membrane cut-off to the NF range. Vanherck *et al.* [24] reported asymmetric Matrimid®-based polyimide membranes for nanofiltration, both unfilled and filled with nanosized zeolite precursors and cross-linked with aromatic *p*-xylylenediamine. Membranes were then stable in the aprotic solvents DMF, NMP, dimethylacetamide (DMAc), and DMSO.

1.06.1.2.1 Antifouling

One of the most common issues in pressure-driven membrane separation processes applied to liquids is fouling. Most of the polymers used for preparation of porous membranes have a rather hydrophobic character, which make them susceptible to adsorption of organics. Many strategies have been proposed in the last decades to overcome this problem, varying from chemical grafting to plasma surface modification [1]. The use of plasma for surface modification of membranes has been reviewed by Kramer *et al.* [25]. Grafting using plasma has been explored for instance by Belfort and Ulbricht [26, 27]. Grafting promoted by ultraviolet (UV)-irradiation [28] is a common alternative to add quaternary ammonium groups to the membrane surface, increasing the positive charge and control fouling. Some new developments on technologies for water treatment have been recently summarized by Shannon *et al.* [29], including membranes with reduced fouling susceptibility. Reducing operation prices in membrane processes can be achieved if less cleaning is necessary. Furthermore multistep production of membranes increases price. Taking this into account, an interesting approach is

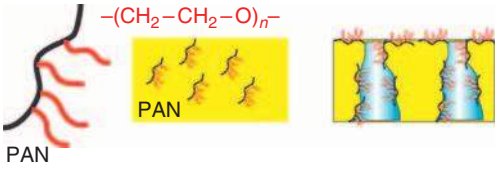

Figure 4 Membrane preparation with antifouling characteristics. (Adapted from Ref. [29]).

the use of additives such as comb copolymers with hydrophobic backbones and hydrophilic side chains, which can be automatically positioned in the membrane surface and pore walls during the membrane formation (**Figure 4**) [30–33].

1.06.1.3 Membranes for GS

Compared to other fields of membrane application, such as water treatment, food processing, and dialysis, GS still has a limited market. However with the development of new membranes and with the increasing need for clean industrial processes and low emission plants, the importance of GS is constantly increasing. A motivation is the need for modernization of the energy sector leading to clean refineries and coal power plants. Although many processes in this field require high temperature and therefore favor inorganic membranes, polymeric membranes can potentially be applied for the treatment of platformer off-gases (H_2/hydrocarbon separation) in refineries and for CO_2 separation from other gases in coal plants. Membranes stable till 250 °C would also allow the application in water-gas shift reactors. Developments on membranes for CO_2 separation are being reported in the literature with increasing frequency.

A special class of polymers is constituted by polymers with very high-free volumes, like some functionalized polyacetylenes, which bridge the gap between microporous and dense polymeric materials. The best-known examples for these polymers are poly(1-trimethylsilyl-1-propyne) (PTMSP) and poly(4-methyl-2-pentyne) (PMP). Although the PMP was already synthesized in 1982 [34], its high gas permeabilities were first published in 1996 by Morisato and Pinnau [35] at MTR, Menlo Park. MTR is currently evaluating the performance of PMP membranes for hydrocarbon separation. An attractive application of membranes in this field is natural gas hydrocarbon dew pointing, the separation of higher hydrocarbons like butane present in natural gas from methane. The performance of PTMSP and PMP for hydrocarbon separation is superior to all other known polymers. The main reason why these membranes have not been applied in large scale is their capability to strongly absorb low-vapor-pressure components, leading to a drastically reduced permeability. Recently, it has been reported that the flux and even the selectivity of PMP and PTMSP can be enhanced by the addition of nanoparticles [36, 37]. Merkel *et al.* [36] added fumed silica to PMP and observed a simultaneous increase of butane flux and butane/methane selectivity. This unusual behavior was explained by fumed-silica-induced disruption of polymer chain packing and an accompanying increase in the size of free volume elements through which molecular transport occurs. Gomes *et al.* [37] incorporated nano-sized silica particles by sol–gel technique into PTMSP and found also for this polymer a simultaneous increase in flux and selectivity. It has to be studied if physical aging of the polyacetylenes is reduced by the addition of nanoparticles.

A new class of polymers with high-free volumes has been introduced recently by Budd *et al.* [38]. The molecular structure of these polymers contains sites of contortion (e.g. spiro-centers) within a rigid backbone (e.g., ladder polymer). The inventors call this polymer class polymers of intrinsic microporosity (PIMs), because their porosity arises as consequence of the molecular structure and is not generated solely through processing. Recently, the tertiary structure of these polymers has been confirmed by molecular modeling [39, 40]. The gas permeation properties of membranes formed from PIM-1 were investigated at the GKSS Research Center [41]. With an oxygen permeability of 370 Barrer and an O_2/N_2 selectivity of 4.0, the PIM-1 shows an extraordinary behavior as GS polymer. However, long-term measurements revealed a physical aging of PIM-1 analogous to PTMSP, which resulted in reduced permeabilities. When the aging problems can be solved, the PIMs will be a highly interesting polymer class for fabrication of GS membranes. The research in high-free volume polymers with intrinsic microporosity will remain very attractive. Large-scale membrane applications for gas and vapor separation will emerge.

Membrane separation is an emerging technology for CO_2 capture. With increasing energy costs, methane purification from biogas becomes more and more attractive. Large international projects evaluate the possibility to capture carbon dioxide from flue gas by membrane separation.

Recently, Lin and Freeman [42] have reported an overview on material selection for membrane preparation to remove CO_2 from gas mixtures. CO_2 solubility and CO_2/gas solubility selectivity in solvents and polymers containing different polar groups were discussed. It was concluded that ethylene oxide (EO) units in the polymer appear to be the most useful groups to achieve high CO_2 permeability and high CO_2/light gas selectivity. Homo-poly(ethylene oxide) (PEO) consists of EO monomeric units, but its disadvantage is the strong tendency to crystallize and consequently it presents low gas permeability [43].

Block copolymers containing EO units as poly(amide-*b*-ether) have been shown as alternative material for this purpose. Copolymers of this type are produced under the trade name Pebax® ARKEMA. The PA blocks provide the mechanical strength, and gas transport occurs through the PEO phase. Block copolymers with immiscible soft and rigid blocks like Pebax® can form various microphase-separated structures. Varying the polyamide and polyether segment, molecular weight, and the content of each block, the mechanical, chemical, and physical properties can be conventionally modeled. Pebax® has been demonstrated as promising membrane materials for acid gas treatment [44]. Bondar *et al.* [44] have studied CO_2/N_2 and CO_2/H_2 separation using different grade of Pebax® membranes. They have reported high CO_2/N_2 and CO_2/H_2 selectivity, which were attributed to high CO_2 solubility due to the strong affinity of the polar ether linkages for CO_2. Kim *et al.* [45] have also reported high permeability and high selectivity for CO_2 over N_2 as well as SO_2 over N_2, and these properties were attributed to polarizability of gases due to PEO segments. Mesoblends of polyether block copolymers and poly(ethylene glycol) (PEG) were generated by Patel and Spontak [46] and it was found that CO_2/H_2 selectivity can be improved by incorporation of PEG. The effect of PEG in the polymer chain to CO_2 transport properties in different polymer systems was also described by other researchers [47–51] and it was proven that EO units influence CO_2 transport in glassy and rubbery polymers. It was shown recently that blends of low molecular weight with Pebax® exhibit exceptional properties for carbon dioxide separation [52, 53].

1.06.1.3.1 Mixed-matrix membranes

Many of the more recent membranes are not only polymeric but contain an inorganic phase. The advantage of organic–inorganic materials for membranes is the possibility of achieving synergetic effects on permeability and selectivity, as well as introducing new functionalizations and improving mechanical and thermal stability. Tailoring innovative materials with organic and inorganic phases coexisting in a nanoscale with multifunctionalization is an appealing approach to control at the same time free volume and gas solubility.

The most representative examples of introducing permeable inorganic fillers in a polymeric matrix for separation purposes are the so-called mixed-matrix membranes. Not only rather passive particles are included, but molecular sieves such as zeolites and also functionalized fillers, which might be much more active in the separation process. The term mixed-matrix membrane has been introduced by Kulprathipanja *et al.* [54], who performed pioneering work in the field of polymer/zeolite hybrid membranes. Kulprathipanja showed that the CO_2/H_2 selectivity of CA could be reversed by the addition of silicalite. The silicalite-CA membrane had a CO_2/H_2 selectivity of 5.1, whereas the pure CA membrane exhibited a selectivity of 0.77.

te Hennepe *et al.* [55], from the university of Twente, proved for the first time that the incorporation of silicalite in PDMS increased the ethanol/water selectivity significantly under steady-state conditions in pervaporation experiments. Later it was shown by Jia *et al.* [56] that using the same approach (silicalite in PDMS), the gas selectivity could also be changed due to a molecular sieving effect. However, the effects were too small to be of any interest for practical applications. One problem of these membranes was that the permeability ratio $P_{PDMS}/P_{zeolite}$ was too high (see Equation (2)).

The formation of polymer chains or networks with organic and inorganic segments has been used by different membrane groups. Molecular sieves such as zeolites have a much higher selectivity for many gas mixtures than polymeric membranes due to their well-defined pore sizes. The preparation of defect-free zeolite layers on a large scale is extremely difficult. The possibility of incorporating zeolites into a flexible organic polymer matrix enables the combination of the superior gas selectivities of these molecular sieves with the processibility of polymeric membranes [57].

The estimation of the permeability and selectivity of membranes with permeable fillers can be done using the equation derived by Maxwell [58] to calculate the electric conductivity of a metal in which small spheres of a second metal are dispersed. The

permeability of the membrane to a defined gas is as follows:

$$P = P_c[P_d + 2P_c - 2\phi_d(P_c - P_d)]/[P_d + 2P_c + \phi_d(P_c - P_d)] \quad (1)$$

The selectivity for gases 1 and 2 of a membrane prepared with a continuous phase of permeabilities P_{c1} and P_{c2} and a dispersed phase with permeabilities P_{d1} and P_{d2} can be calculated therefore by

$$\alpha_{eff} = \alpha_c \frac{1 + 2P_{rel} - 2\phi(P_{rel} - 1)\frac{1}{\alpha_d} + \frac{2P_{rel}}{\alpha_c} + \phi\left(\frac{P_{rel}}{\alpha_c} - \frac{1}{\alpha_d}\right)}{1 + 2P_{rel} + \phi(P_{rel} - 1)\frac{1}{\alpha_d} + \frac{2P_{rel}}{\alpha_c} - 2\phi\left(\frac{P_{rel}}{\alpha_c} - \frac{1}{\alpha_d}\right)} \quad (2)$$

where α_c and α_d are the selectivity of the continuous and dispersed phases for the gas pair 1 and 2, and P_{rel} is the permeability ratio between continuous and dispersed phase.

From this equation, it can be seen that the selectivity highly depends on the permeability of the filler and of the matrix. When the polymer permeability is too high, the selectivity of the mixed-matrix membrane approaches the polymer selectivity. However, if the permeability of the filler and the matrix is not too far apart, the properties of the membrane will have a large contribution from the highly selective filler. The compatibility between inorganic molecular sieves and polymers is very important in order to eliminate gas diffusion pathways at the interface between them, as discussed by Moore and Koros [59].

1.06.2 Next Generation of Membrane Materials

The phase inversion membrane manufacture process is responsible for the breakthrough of the membrane technology and its implementation in numerous industrial applications. New advanced filtration processes are now conceivable but they require membranes with much narrower pore-size distribution and better chemical resistance. A sharp pore-size distribution can only be obtained with the implementation of new materials and new manufacture technologies. Approaches under investigation to tailor pore size include block and graft/comb copolymers, which self-assemble to form regular nanopores.

Furthermore, new separation tasks could be fulfilled if the membrane pores would specifically respond to different stimuli and act analogously to biological gates. It is also possible to imagine membranes which are self-cleaning with fouling-resistant surfaces, as well as self-healing membranes. The most inspiring source for new developments is nature itself, which is full of supramolecular chemistry, self-assemblies, controlled textures, sophisticated architectures, and functional systems. The following sections discuss as to how to tailor pores using self-assembly approaches, how to produce hierarchical structures using organic–inorganic materials, how to promote a jump in the current membrane properties by using nanotubes, and how to manufacture a new generation of membranes, which react to external stimuli.

1.06.2.1 Next Generation of Mixed-Matrix Membranes

There are still manufacturing problems to be solved, before mixed-matrix membranes are introduced in commercial GS. We see an increasing number of patents filed by big companies active in GS [60–63], and it can be concluded that mixed-matrix membranes are on the brink of practical application. The development of new mixed-matrix materials for GS will remain an attractive research field. Besides classical zeolites and carbon molecular sieves (CMSs), new selective adsorbants have to be considered. One candidate, for example, might be metal-organic frameworks (MOFs), three-dimensional (3D) nanoporous networks of transition metal complexes. MOFs have been reviewed by Kitagawa *et al.* [64] and Rowsell and Yaghi [65]. A huge number of architectures have been published in the last years. The possibility of tailoring the structures and choosing the right linkers to build networks with sieve dimensions able to discriminate gas permeants is particularly attractive for membrane development. Issues such as stability and reproducibility must however be controlled. Recent findings suggest that MOFs can revolutionize GS and storage [66]. MOFs are nanoporous metal-organic soft materials analogous to zeolites, but with all the chemical diversity of polymeric compounds. MOFs exhibit a very high porosity with exactly tailorable pore sizes. One example is an MOF with manganese atoms, which has been reported recently [67]. This material, which features permanent porosity with pore aperture diameters of ~0.45 nm, sorbs carbon dioxide but essentially completely excludes methane and nitrogen. Won *et al.* [68] recently reported

membranes made of polysulfone and $[Cu_2(PF_6)(NO_3)(4,4'bpy)_4]\ 2PF_6{\cdot}2H_2O]_n$ and tested them for hydrogen/methane separation. Atomically detailed simulations were used to predict the performance of MOFs as membranes for GSs, using the separation of CO_2/CH_4 mixtures by MOF-5 as an example [69]. A particularly interesting hybrid framework has been reported by Serre *et al.* [70], which is able to swell under external stimuli such as pressure, temperature, light, gas or solvent adsorption. The highest reported swelling or breathing is 40%. Hence, mixed-matrix membranes containing this MOF might be very attractive for natural gas and biogas purification. This is just one example for potential future developments of mixed-matrix membranes.

1.06.2.2 Molecular Imprinted Membranes

One elegant and very specific way to control pore sizes is the concept of molecular imprinted membranes. This approach has been explored by different groups [71, 72]. A nice review on that and other functional membranes has been published by Ulbricht [71]. One procedure to prepare imprinted membranes is the polymerization of a functional monomer in the presence of an analyte (template), which will be imprinted in the polymer and later extracted [72]. The extraction gives a specific recognition site able to selectively bind analogous molecules. Other procedure is the preparation of membranes from polymer blends via phase separation. One polymer has the function of building the membrane structure and is chosen among those well investigated for phase inversion asymmetric membranes (e.g., CA, polysulfone, and PAN). The second polymer is added to provide strong interaction with the small molecules, which are included as templates. The small template molecules are added to the casting solution and, after a fast membrane formation by phase inversion in a coagulation bath, are extracted, leaving sites which are particularly favored for accommodating other analogous molecules in a filtration process. Since the sites are expected to have a certain chemical affinity for the original molecule, the functional mechanism is similar to antibodies or enzymes.

1.06.2.3 Block Copolymers

Block copolymers have been proposed for pore formation in membranes for a long time [73–79]. Ishizu and Amemiya [75] used block copolymers to develop charge mosaic membranes, polymeric films with microphase separation containing both negatively and positively charged phases. Pebax®, a commercial block copolymer of polyamide and PEO, has been used for nanofiltration [18] and gas separation [44]. Lee *et al.* [74] synthesized copolymers with one block containing isoprene and the second functional silyl groups. The immiscibility between the two different blocks led to microphase separation. The dense films were cross-linked by promoting the hydrolysis and condensation of the silyl-containing blocks. The isoprene blocks were decomposed with ozone and further leached with solvent, creating pores in a polysiloxane matrix. The pore size could be controlled by using copolymers with bocks of different sizes. Phillip *et al.* [76] prepared membranes based on triblock copolymer of polylactide–poly(dimethylacrylamide)–polystyrene (PLA–PDMA–PS). By controlling the relative block length, spherical domains, lamellae, and cylinders of PLA coated with PDMA in a continuum of PS could be obtained. The PLA blocks were then removed by etching with aqueous base to form regular pores with diameter 13.7 nm. One of the main problems is however to establish a method to vertically orient micro-domains and ensure pore connectivity from one side to the other. One possibility is the application of external fields [77, 78]. Peinemann *et al.* [79] prepared integral asymmetric membranes from diblock copolymer poly (styrene-*b*-4-vinylpyridine), PS-*b*-P4VP in a mixture of high and low boiling point solvents, observing the formation of cylindrical porous structure of 40 nm diameter, perpendicular to the membrane surface. A follow-up of this work with new forms of self-assembly for membranes is continuing at KAUST (**Figure 5**).

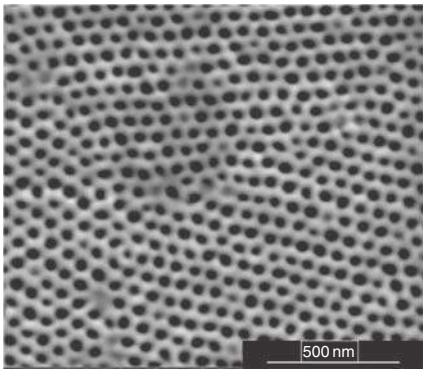

Figure 5 Membranes prepared from self-assemblies of PS-b-P4VP block copolymer. From Peinemann, K.-V., Abetz, V., Simon, P. F. W. *Nat. Mater.* **2007**, *6*, 992–996.

The volatile solvent starts to evaporate, leading to a concentration gradient between one side of the membrane to another. By increasing the copolymer concentration, conditions for phase separation are reached, forming the domains, which will later give rise to the pores, spreading along the gradient and guiding the growth of the cylindrical domains. Ikkala and ten Brinke [80] summarized the potential application of self-assembly of polymeric supramolecules as basis for tunable nanoporous materials and smart membranes. They proposed the use of flow, electric or magnetic field to align comb-shaped copolymers, which self-organize in cylinders, aiming the application for membranes.

1.06.2.4 Organic–Inorganic Self-Assembly

The concept of molecular self-organization and self-assembly first from small molecules to supramolecular structures using a bottom-up strategy has been explored by Lehn [81]. Barboiu *et al.* [82] have been using the self-organization of organic–inorganic molecules to prepare hybrid membranes by the sol–gel process. The membranes can function for instance as an ion-powered adenosine triphosphate pump. For the membrane formation, molecules containing macrocyclic groups (e.g., crown ether) are self-organized in solution forming a superstructure with strong H-bonds, which is later polymerized by sol–gel, forming a hybrid heteropolysiloxane material.

Nature can be the best inspiration for new organic–inorganic materials [83]. Silicic skeletons of unicellular organisms Radiolaria and diatoms have a regular complex and finely porous morphology. A big challenge is to manufacture membranes with similar pores. In the last years, some approaches have been made, bringing some possibility in this direction. The group of Wiesner [84, 85] uses block copolymers and inorganic precursors to create regular organic–inorganic structures. An example is the use of an amphiphilic poly(isoprene-*block*-EO) block copolymer (PI-*b*-PEO) in combination with 3-(gycidyloxypropyl)trimethoxysilane, GLYMO, and aluminum *sec*-butoxide, which by sol–gel synthesis generates an organically modified aluminosilicate network. A regular porous structure results after calcination.

Another interesting organic–inorganic nanoporous materials with potential use for membranes are periodic mesoporous organosilicas with domain functionality [86, 87]. Organic groups embedded into pore walls brought a new direction in the research of mesoporous molecular sieves. These materials are synthesized using bridged organosilica precursors ((EtO)3Si-R-Si(OEt)3) in conditions analogous to those for the preparation of mesoporous silicas. Compared to pure mesoporous silica, the organic modification allows tuning hydrophobicity and hydrophilicity of the porous network. In comparison with microporous zeolites, they feature increased pore dimensions and the ability to control the molecular recognition properties of the porous network by altering organic functionalities. Mesoporous silica with $-CH_2-CH_2-$/$-CH{=}CH-$ bridges and with benzene rings have been reported, which can be used for further functionalization.

1.06.2.5 Organically Modified Inorganic Membranes

In this chapter emphasis is given to polymeric membranes and polymeric membranes with inorganic components. On the other hand, inorganic porous sieves can be functionalized with organic segments. The early efforts to graft organic groups into the micropores of zeolites generally failed, resulting in the modification of primarily the external surface of the crystals. The first microporous, crystalline silicates with organic groups covalently bound within the micropores [88] were made by adding organosilanes [$(CH_3O)_3SiR$] to the silicate synthesis gel and incorporating into the zeolites during synthesis, yielding organic-functionalized molecular sieves with potential application for catalysis.

Ordered anodized alumina substrates are available with very regular pores, which can be functionalized by using silanes. They can work then as scaffolds with selective gates on the pores if surface-bound molecules that change conformation with pH are further attached to the silanes functionalities [89, 90].

1.06.2.6 Membranes with Carbon Fillers

The preparation of carbon membranes has the motivation of high thermal stability (in nonoxidative environment) and the possibility of operation in the presence of organic solvents. CMS membranes are usually obtained by pyrolysis of organic polymers like cellulose [91] and polyimide [92]. The porous structure can be tailored by choosing the right polymer precursor, the pyrolysis temperature and environment, and the time spent at this temperature. A detailed review of CMS membranes is beyond the

scope of this chapter. Exotemplating is an alternative method for the preparation of hierarchically structured meso-macroporous carbon materials. In this approach suitable templates such as alumina membranes, zeolites, zirconia, and mesoporous silica are impregnated with carbon precursors such as sucrose and carbonized under nonoxidizing conditions. The templates are then washed out with fluoridric acid. Carbon porous structures with aligned macrochannels were reported by Su *et al.* [93].

However, carbon membranes have drawbacks, which have still hindered their successful industrial application. They are brittle and the production process in large scale is much more expensive and complex than that of polymeric membranes. Promising approaches for polymeric membrane development are being reported in the last years using different geometries of carbon fillers: CMSs, fullerenes, and carbon nanotubes (CNTs).

The dispersion of CMSs as filler for Matrimid® 5218 and Ultem® 1000 has been successfully explored by the group of Koros in mixed-matrix membranes [94]. It was shown that the CMS particles produced a membrane having significantly enhanced effective permselectivities (CO_2/CH_4 and O_2/N_2) and fast-gas permeabilities (CO_2 and O_2) over the intrinsic properties of the pure polymer matrix phase alone. For the CO_2/CH_4 separation, enhancements by as much as 45% in CO_2/CH_4 permselectivity and 200% in CO_2 permeability over the corresponding intrinsic permeation properties of the pure polymer matrix phases were observed.

Homogeneously fullerene-dispersed membranes for GS were first prepared using a matrix of poly(1-trimethylsilyl-1-propyne) [95]. The fullerene in that case was just physically dispersed. Sterescu *et al.* [96] prepared poly(2,6-dimethyl-1,4-phenylene oxide) (PPO) membranes with covalently attached fullerenes (C_{60}). The idea was that their hard-sphere properties may inhibit molecular polymer-chain packing possibly resulting in a high-free volume. The PPO-bonded C_{60} membranes exhibit significantly higher gas permeability (up to 80%) in comparison to pure PPO, without compromise in selectivity.

CNTs offer a unique combination of properties: high aspect ratio/high surface area, electron conductivity, superhydrophobicity, and frictionless surfaces to lead to fast fluid flow, simple functionalization, and dispersion in organic polymers, capability to enhance mechanical strength with small filler content as well as the potentially close control of pore dimension at the nanometer scale [97, 98]. Furthermore, the functionalization can be directed to the entrance of the CNT, giving an excellent opportunity for developing gates for separation.

During the CNT growth process, the nanotube size is set by the diameter of the catalyst particle [99, 100], offering a practical route for pore diameter control through well-determined catalyst synthesis. Aiming membrane application, introducing nanotubes with well-defined inner core sizes into polymer films shall enable a fine control of pore dimension at the nanometer scale. These characteristics started to be explored in membrane applications for gas and liquid separation [101–105]. Hinds *et al.* [101] made a pioneering contribution, reporting on the preparation of an aligned CNT membrane for gas permeation and for transport of $Ru(NH3)_6^{3+}$ ions in aqueous solution. He followed theoretical predictions [101], which suggest that the diffusivity of light gases inside CNTs with diameter around 1 nm to be orders of magnitude higher than in other porous structures like zeolites, due to the inherent molecular smoothness. After the first simulations [104] of water transport in nanotubes, experimental results also demonstrated higher than expected flow rates, making CNT membranes promising candidates for water desalination with the possibility of tailoring the tube diameters to retain salt [106]. Salt rejection coefficients that match or exceed those of commercially available nanofiltration membranes, while exceeding their flux by up to 4 times [107].

CNTs have also been proposed for manufacturing electrodes for water desalination promoting flow through capacitor [99]. Furthermore, they are considered as mechanical support for catalysts [100] and could therefore be an attractive additive in the design of a new generation of catalytic membranes.

Furthermore by choosing nanotubes with suitable electron conductivity and controlling their distribution in the polymer electrolyte, an optimum catalyst–electrode–electrolyte interphase layer could be tailored [98].

However although the idea of using nanotubes for membranes is fascinating, there are many challenges involved. The first challenge is to prepare the polymer composite with aligned CNTs and free of defects. Another possible issue is the propensity for fouling given the hydrophobic nature of CNTs. CNT alignment has been claimed to be advantageous in different membrane applications. Some authors [108] predicted higher gas permeability when the CNTs are aligned. Furthermore for the

aligned tubes, superhydrophobicity might be much more evident. Different alignment strategies have been reported in literature [103, 109–111]. Nednoor *et al.* [109] obtained a vertically aligned array of multiwalled CNTs grown on quartz by chemical vapor deposition (CVD). The space between the tubes was filled with polystyrene and the membrane was removed from the quartz by treatment with fluoridic acid. Prehn pressed a carpet of CNTs grown on silicon wafers against a thin layer of melted polystyrene, detached it from the silicon substrate, and further coated the nanotubes with ionic polymer aiming the use as fuel cell membrane-electrode assemblies. The styrene was then dissolved making the CNT tips free for catalyst deposition. Mi *et al.* [111] grew vertically aligned CNTs directly on a porous alumina support and filled the space between the CNTs with polystyrene as well. Kim *et al.* [103] fabricated the membrane by orienting functionalized single-wall CNTs with a filtration method [112].

A very interesting property of CNTs is the superhydrophobicity. Once water is inside the pores, an exceptional flux is observed, exceeding all the initial predictions. The high flux may be due to the CNTs' atomically smooth, hydrophobic walls allowing considerable slip of water through the pores [29]. However, for water to wet the nanotube membranes, some work is required. Modifying the surfaces of the membrane, as discussed for nanofiltration membranes, can alter the surface properties, and thus potentially decrease the energy barrier to enter the tubes. Wang *et al.* [113] studied the effect of the application of external potential on the droplet stability and wetting behavior of water on CNTs and demonstrated that water can be efficiently wet and pumped through superhydrophobic aligned multiwalled nanotube membranes by application of a small positive direct current (DC) bias.

Membranes containing CNTs are therefore considered to have a great potential for water desalination [105]. As mentioned before, the water desalination with membranes is an established process and some of the currently used membranes have been developed for decades. According to recent papers, a new generation of membranes could be feasible with nanotubes, inspired by biological water pores, known as aquaporins [114, 115]. The flow rates of water through nanotubes have been reported to be exceptionally high and independent of the tube length. The use of nanotubes in membranes might make real the dream of mimicking protein ion channels by precisely gated with selective and reversible chemical interactions. With this idea Nednoor *et al.* [109] prepared membranes with aligned CNTs, after activating the CNT tips to have carboxylic groups, and further derivatized them with a molecule that binds to a bulky receptor. The receptor can open/close the pore entrance. Successful results were demonstrated by functionalizing nanotubes with a desthiobiotin derivative that binds reversibly to streptavidin.

Majumder *et al.* [116] proposed the use of CNTs for voltage-gated membranes, taking advantage of the fact that CNTs are conductors inside an insulating matrix allowing for the concentration of electric field at the tips. Modest voltages (100 mV) could then be applied to control the steric environment of the channel entrance. Besides the functionalization, technological challenges for CNT membranes will be the scaling up, increasing the pore density per area of the active layer and decreasing the cost of membrane fabrication. However, the synthesis of CNTs is becoming less expensive and at least multiwalled CNTs are already available now in large scale.

1.06.2.7 Responsive Membranes

A concept which leads to new generation of advanced membranes is that of switchable surfaces. A review on intelligent surfaces was recently published by Gras *et al.* [117].

1.06.2.7.1 Response to temperature

The response of polymers to stimuli has been known for a long time. Probably, the most-reported and well-investigated effect of this kind is the contraction and expansion of polymer chains in solution by simply changing the temperature. Heskins and Guillet [118] published in 1968 their investigation on poly(*N*-isopropylacrylamide) reporting that the system has a lower critical solution temperature (LCST) at 32 °C. Polymer–solvent interactions in general can improve or deteriorate as the temperature increases. Numerous systems are known for which the thermodynamic conditions for polymer dissolution improve with the temperature. In this case, the thermodynamic phase diagram is determined by upper critical solution temperatures, below which demixing occurs. This is the case for many polymers in organic solvents. On the opposite, the solubility of poly(*N*-isopropylacrylamide) increases when the temperature decreases. Above

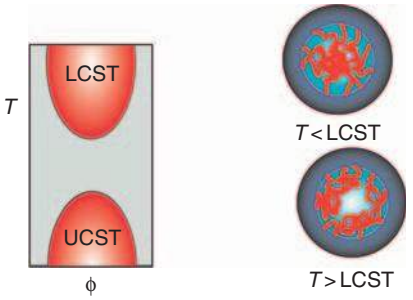

Figure 6 Lower critical solution temperature (LCST) and thermal-responsive membranes.

LCST water becomes a bad solvent for this polymer (**Figures 6** and **7**).

The polymer chains react then by contracting themselves above the LCST and expanding below it. In the particular case of this polymer, the expansion is due to strong hydrogen bonds between the amide groups in the polymer chains and the surrounding water molecules. Water is in this form retained in the polymer gel. As the temperature increases above the LCST, the polymer hydrophobic groups are exposed and the hydrogen bonds with water are interrupted. The water molecules are squeezed out of the gel while the polymer chains shrink [119].

With an LCST near the body temperature, this system was predestinated for biomedical applications, being the object of investigation for drug delivery [120], bioseparation [121], enzyme immobilization [122], and cell culture for tissue engineering [123].

Another very interesting aspect of analogous systems is that the LCST can be shifted if additional factors such as pH or ionic strength are changed. However, although thermo-responsible gels have found applications for instance in chromatography, their application in the membrane manufacture came much later, since as a film they are not self-supportable. Different approaches have been used to overcome this disadvantage, mainly the copolymerization and preparation of phase inversion porous membranes [124, 125] and the manufacture of

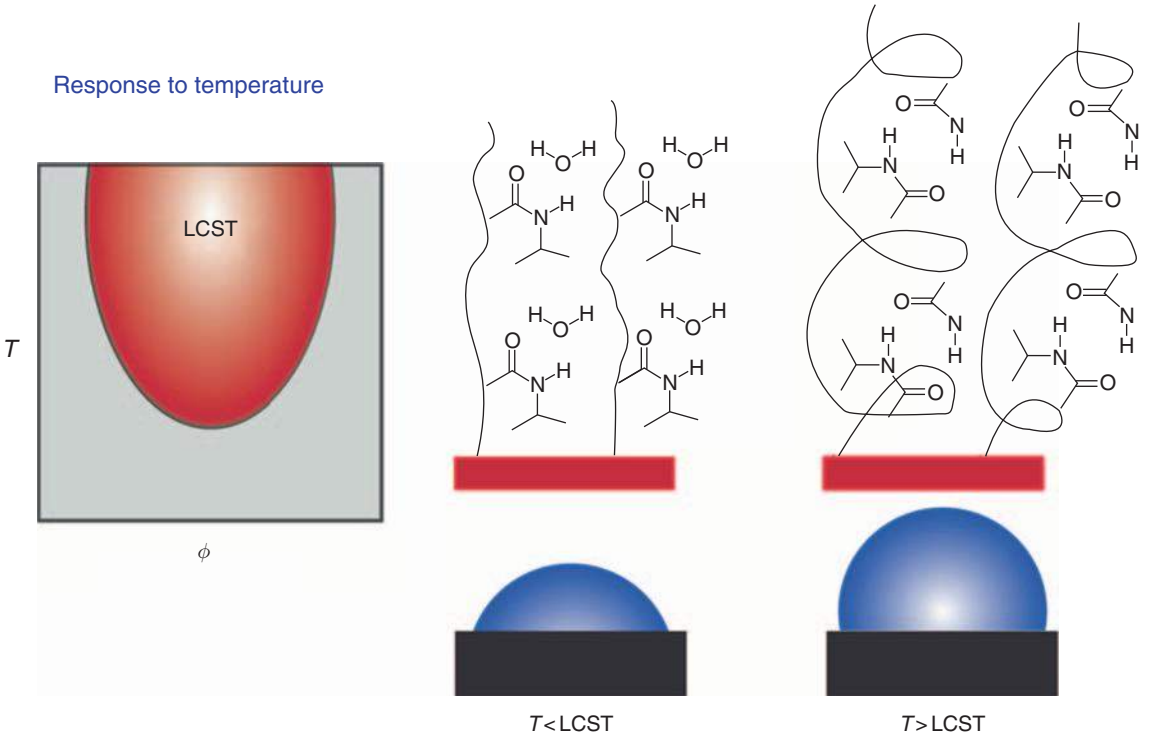

Figure 7 Change of conformation of poly(*N*-isopropylacrylamide) in thermal-responsive Membranes. Modified from Gras, S. L., Mahmud, T., Rosengarten, G., Mitchell, A., Kalantar-Zadeh, K. *ChemPhysChem* **2007**, *8*, 2036–2050.

composite membranes by grafting onto high-strength polymeric micro-porous films such as track-etched polycarbonate [119] or PET membrane [126].

Besides temperature there is a large variety of external stimuli, which can trigger changes in surface hydrophobicity, including electrical, electrochemical, and photonic effects.

1.06.2.7.2 Electric and electrochemical response

By applying voltage to a surface, electric charge is generated and wettability and even chemical properties can change [127–136]. Change on wettability when voltage is applied is illustrated in **Figure 8**.

This effect is achieved for instance by changing the redox state. A conceivable membrane could have redox-active groups attached to its pore walls. The groups could be oxidized by the electric charge, forming cations and making the membrane hydrophilic, analogously to what is observed for surfactants. After withdrawing the voltage, the membranes would become hydrophobic again. Bulky molecules such as rotaxanes can respond to electrochemical impulses or to changes in proton concentration nearby by changing their conformation. They are being considered for potential application as artificial molecular muscles, but could also be useful if attached to membrane surfaces [137].

Electrochemically responsive surfaces, which could be useful for membranes, could be prepared by attaching hydrophobic chains with negatively charged tips. This was demonstrated by Lahann *et al.* [138] for mercaptohexadecanoic acid molecules on gold surface. If electrical potential is applied, the negatively charged tips (carboxylic groups) are bended to the surface exposing the hydrophobic part of the chain.

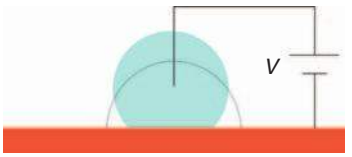

Figure 8 Electric-responsive surfaces.

1.06.2.7.3 Photo-response

It has been reported that molecules such as azobenzene suffer reversible isomeric changes of conformation by illumination with UV light (**Figure 9**) [139].

The *cis* form is more hydrophobic and less expanded than the *trans*. The grafting of similar segments onto membrane pore surfaces would also selectively change their flow rates. Isomerization under UV light is also observed for pyrimidine [140] and spiropyran [141].

1.06.3 Final Remarks

The research on nanotechnology is dramatically growing in the last years. Many of the innovative approaches reported for other applications can be adapted to tailor membrane surface and pore size. Micro-patterning of membranes has been successfully used to increase their surface and flow [142]. Taking into account the different approaches mentioned in this chapter and combining other nanofabrication methods such as photolithography,

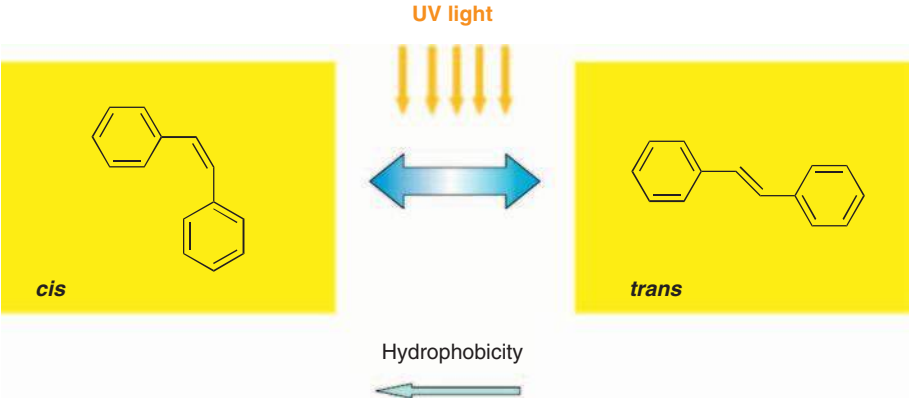

Figure 9 Photoresponsive materials.

layer-by-layer assembling [143], and conventional methods of membrane preparation, it will be possible to tune pores and surface functionalities. Some years ago, the membrane field seemed to be stagnated, after testing a large range of available homopolymers for manufacture, which in many cases was upscaled and brought to successful implementation in industrial separation processes. With the application of recent achievements of nanoscience, new challenges for membrane development are now becoming reality and it is clear that innumerous possibilities are still open for exploration.

References

[1] Nunes, S. P., Peinemann, K.-V. *Membrane Technology in the Chemical Industry*, 2nd edn.; Wiley-VCH: Weinheim, 2006.
[2] Kesting, R. E. *Synthetic Polymeric Membranes. A Structural Perspective*; Wiley: New York, 1985.
[3] Strathmann, H. *J. Membr. Sci.* **1981**, *9*, 121–189.
[4] Baker, R. W., Cussler, E. L., Eykamp, W., Koros, W. J., Riley, R. L., Strathmann, H. *Membrane Separation Systems: Recent Developments and Future Directions*; Noyes Publishing: Park Ridge, NJ, 1991.
[5] Mulder, M. *Basic Principles of Membrane Technology*; Kluwer: Dordrecht, 1991.
[6] Nunes, S. P. *Trends Polym. Sci.* **1997**, *5*, 187–191.
[7] Petersen, R. J. *J. Membr. Sci.* **1993**, *83*, 81–150.
[8] Cadotte, J. E., Petersen, R. J., Larson, R. E., Erickson, E. E. *Desalination* **1980**, *32*, 31.
[9] Norman, R. W. *Science* **1974**, *186*, 350.
[10] Jellinek, H. H. G. (Potsdam, NY), Osmosis Process for Producing Energy. US Pat. 3,978,344, November 1974.
[11] Loeb, S. *Science* **1975**, *189*, 654–655.
[12] Peinemann, K.-V., Gerstandt, K., Skilhagen, S. E., Thorsen, T., Holt, T. Membranes for Power Generation by Pressure Related Osmosis. In *Membranes for Energy Conversion;* Peinemann, K.-V., Nunes, S. P., Eds.; Wiley-VCH: Weinheim, Germany, 2008; pp 263–274.
[13] Schäfer, A. I., Fane, A. G., Waite, T. D., Eds. *Nanofiltration – Principles and Applications*; Elsevier: Oxford, UK, 2005.
[14] Mänttäri, M., Pekuri, T., Nyström, M. *J. Membr. Sci.* **2004**, *242*, 107–116.
[15] Cadotte, J. E., Walker, D. R. (Filmtec). Novel Water Softening Membranes. US Pat. 4,812,270, March 1989.
[16] Wheeler, J. W. (Du Pont). Process for Opening Reverse Osmosis Membranes. US Pat. 5,262,054, November 1993.
[17] Mickols, W. E. (Dow Chemical). Method of Treating Polyamide Membranes to Increase Flux. US Pat. 5,755,964, May 1998.
[18] Nunes, S. P., Sforca, M. L., Peinemann, K. V. *J. Membr. Sci.* **1995**, *106*, 49–56.
[19] Schmidt, M., Peinemann, K. V., Paul, D., Rödicker, H. *Angew. Makromol. Chem.* **1997**, *249*, 11–32.
[20] Lu, Y., Suzuki, T., Zhang, W., Moore, J. S., Marinas, B. J. *Chem. Mater.* **2007**, *19*, 3194–3204.
[21] Linder, C., Perry, M., Nemas, M., Katraro, R. (Aligena). Solvent Stable Membranes. US Pat. 5,039,421, August 1991.
[22] Perry, M., Yacubowicz, H., Linder, C., Nemas, M., Katraro, R. (Membrane Products Kiryat Weizmann). Polyphenylene Oxide-Derived Membranes for Separation in Organic Solvents. US Pat. 5,151,182, September 1992.
[23] Ebert, K., Koll, J., Dijkstra, M. F. J., Eggers, M. *J. Membr. Sci.* **2006**, *285*, 75–80.
[24] Vanherck, K., Vandezande, P., Aldea, S. O., Vankelecom, I. F. J. *J. Membr. Sci.* **2008**, *313*, 135–157.
[25] Kramer, P. W., Yeh, Y.-S., Yasuda, H. *J. Membr. Sci.* **1989**, *46*, 1–28.
[26] Belfort, G., Ulbricht, M., *J. Appl. Polym. Sci.* **1995**, *56*, 325–343.
[27] Ulbricht, M., Belfort, G. *J. Membr. Sci.* **1996**, *111*, 193–215.
[28] Wang, D. (Millipore). Hydrophobic Membrane Having Hydrophilic and Charged Surface and Process. US Pat. 5,137,633, August 1992.
[29] Shannon, M. A., Bohn, P. W., Elimelech, M., Georgiadis, J. G., Marinas, B. J., Mayes, A. M. *Nature* **2008**, *452*, 301–310.
[30] Deratani, A., Li, C. L., Wang, D. M., Lai, J. Y. *Ann. Chim. Sci. Mat.* **2007**, *32*, 107–118.
[31] Hester, J. F., Banerjee, P., Mayes, A. M. *Macromolecules* **1999**, *32*, 1643–1650.
[32] Hester, J. F., Mayes, A. M. *J. Membr. Sci.* **2002**, *202*, 119–135.
[33] Wang, Y. Q., Wang, T., Su, Y., Peng, F., Wu, H., Jiang, Z. *Langmuir* **2005**, *21*, 11856–11862.
[34] Masuda, T., Kawasaki, M., Okano, Y., Higashimura, T. *Polym. J.* **1982**, *14*, 371.
[35] Morisato, A., Pinnau, I. *J. Membr. Sci.* **1996**, *121*, 243–250.
[36] Merkel, T. C., Freeman, B. D., Spontak, R. J., *et al. Science* **2002**, *296*, 519–522.
[37] Gomes, D., Nunes, S. P., Peinemann, K. V. *J. Membr. Sci.* **2005**, *246*, 13–25.
[38] Budd, P. M., Ghanem, B. S., Makhseed, S., McKeown, N. B., Msayib, K. J., Tattershall, C. E. *Chem. Commun.* **2004**, *2*, 230–231.
[39] Heuchel, M., Fritsch, D., Budd, P. M., McKeown, N. B., Hofmann, D. *J. Membr. Sci.* **2008**, *318*, 84–99.
[40] Ghanem, B. S., McKeown, N. B., Budd, P. M., Fritsch, D. *Macromolecules* **2008**, *41*, 1640–1646.
[41] Budd, P. M., Msayib, K. J., Tattershall, C. E. *et al. J. Membr. Sci.* **2005**, *251*, 263–269.
[42] Lin, H., Freeman, B. D. *J. Mol. Struct.* **2005**, *739*, 57–74.
[43] Lin, H., Freeman, B. D. *J. Membr. Sci.* **2004**, *239*, 105–117.
[44] Bondar, V., Freeman, B. D., Pinnau, I. *J. Polym. Sci., Part B: Polym. Phys.* **1999**, *37*, 2463–2475.
[45] Kim, J. H., Ha, S. Y., Lee, Y. M. *J. Membr. Sci.* **2001**, *190*, 179–193.
[46] Patel, N. P., Spontak, R. J. *Macromolecules* **2004**, *37*, 1394–1402.
[47] Okamoto, K., Fujii, M., Okamyo, S., Suzuki, H., Tanaka, K., Kita, H. *Macromolecules* **1995**, *28*, 6950–6959.
[48] Patel, N. P., Hunt, M. A., Lin-Gibson, S., Bencherif, S., Spontak, R. J. *J. Membr. Sci.* **2005**, *251*, 51–57.
[49] Kawakami, M., Iwanaga, H., Hara, Y., Iwamoto, M., Kagawa, S. *J. Appl. Polym. Sci.* **1982**, *27*, 2387–2393.
[50] Li, J., Wang, S., Nagai, K., Nakagawa, T., Mau, A. W.-H. *J. Membr. Sci.* **1998**, *138*, 143–152.
[51] Kim, J. H., Ha, S. Y., Nam, S. Y., Rhim, J. W., Baek, K. H., Lee, Y. M. *J. Membr. Sci.,* **2001**, *186*, 97–107.
[52] Car, A., Stropnik, C., Yave, W., Peinemann, K.-V. *J. Membr. Sci.* **2008**, *307*, 88–95.
[53] Car, A., Stropnik, C., Yave, W., Peinemann, K.-V. *Sep. Purif. Technol.* **2008**, *62*, 110–117.

[54] Kulprathipanja, S., Neuzil, R. W., Li, N. N. Separation of Fluids by Means of Mixed Matrix Membranes. US Pat. 4,740,219, 26 April 1988.
[55] te Hennepe, H. J. C., Bargeman, D., Mulder, M. H. V., Smolders, C. A., *J. Membr. Sci.* **1987**, *35*, 39–55.
[56] Jia, M., Peinemann, K.-V., Behling, R.-D. *J. Membr. Sci.* **1991**, *57*, 289–292.
[57] Nunes, S. P. Organic–Inorganic Membranes. In *Inorganic Membranes: Synthesis, Characterization and Applications*; Mallada, R., Menendez, M., Eds.; Elsevier, 2008; pp 121–134.
[58] Maxwell, J. C. *A Treatise on Electricity and Magnetism*; Dover: New York, 1873; Vol. 1, p 440.
[59] Moore, T. T., Koros, W. J. *J. Mol. Struct.* **2005**, *739*, 87–98.
[60] Miller, J., Kuperman, A., De Vu, Q. Mixed Matrix Membranes with Small Pore Molecular Sieves and Methods for Making and Using Membranes. US Pat. 20,050,139,066, 30 June 2005.
[61] Koros, W. J., Wallace, D., Wind, J. D., Miller, S. J., Staudt-Bickel, C., Vu, De Q. Crosslinked and Crosslinkable Hollow Fiber Mixed Matrix Membranes and Method of Making Them. US Pat. 6,755,900, 29 June 2004.
[62] Kulprathipanja, S., Charoenphol, J. Mixed Matrix Membrane for Separation of Gases. US Pat. 6,726,744, October 2002.
[63] Ekiner, O. M., Kulkarni, S. S. Process for Making Hollow Fiber Mixed Matrix Membrane. US Pat. 6,663,805, September 2002.
[64] Kitagawa, S., Kitaura, R., Noro, S. *Angew. Chem. Int. Ed.* **2004**, *43*, 2334–2375.
[65] Rowsell, J. L. C., Yaghi, O. M. *Microporous Mesoporous Mater.* **2004**, *73*, 3–14.
[66] Snurr, R., Hupp, J. T., Nguyen, S. T. *AIChE J.* **2004**, *50*, 1090–1095.
[67] Dybtsev, D. N., Chun, H., Yoon, S. H., Kim, D., Kim, K. *J. Am. Chem. Soc.* **2004**, *126*, 32–33.
[68] Won, J., Seo, J. S., Kim, J. H., *et al. Adv. Mater.* **2005**, *17*, 80.
[69] Keskin, S., Sholl, D. S. *J. Phys. Chem. C* **2007**, *111*, 14055–14059.
[70] Serre, C., Mellot-Draznieks, C., Surblé, S., Audebrand, N., Filinchuk, Y., Férey, G. *Science* **2007**, *315*, 1828–1831.
[71] Ulbricht, M. *Polymer* **2006**, *47*, 2217–2262.
[72] Tasselli, F., Donato, L., Drioli, E. *J. Membr. Sci.* **2008**, *323*, 235–240.
[73] Brooks, T. W., Daffin, C. L. *Polym. Prepr.* **1969**, *10*, 1174–1181.
[74] Lee, J.-S., Hirao, A., Nakahama, S. *Macromolecules* **1989**, *22*, 2602–2606.
[75] Ishizu, K., Amemiya, M. *J. Membr. Sci.* **1990**, *54*, 75–87.
[76] Phillip, W. A., Rzayev, J., Hillmyer, M. A., Cussler, E. L. *J. Membr. Sci.* **2006**, *286*, 144–152.
[77] Morkved, T. L., Lu, M., Urbas, A. M. *et al. Science* **1996**, *273*, 931–933.
[78] Schmidt, K., Schoberth, H. G., Ruppel, M., *et al. Nat. Mater.* **2008**, *7*, 142–145.
[79] Peinemann, K.-V., Abetz, V., Simon, P. F. W. *Nat. Mater.* **2007**, *6*, 992–996.
[80] Ikkala, O., ten Brinke, G. *Science* **2002**, *295*, 2407–2409.
[81] Lehn, J. M. *Supramolecular Chemistry: Concepts and Perspectives*; Wiley-VCH: Germany, 1995.
[82] Barboiu, M., Cerneaux, S., van der Lee, A., Vaughan, G. *J. Am. Chem. Soc.* **2004**, *126*, 3545–3550.
[83] Sanchez, C., Arribart, H., Guille, M. M. G. *Nat. Mater.* **2005**, *4*, 277–288.
[84] Toombes, G. E. S., Mahajan, S., Thomas, M., *et al. Chem. Mater.* **2008**, *20*, 3278–3287.
[85] Simon, P. F. W., Ulrich, R., Spiess, H. W., Wiesner, U. *Chem. Mater.* **2001**, *13*, 3464–3486.
[86] Jones, J. T. A., Wood, C. D., Dickinson, C., Khimyak, Y. Z. *Chem. Mater.* **2008**, *20*, 3385–3397.
[87] Inagaki, S., Guan, S., Ohsuna, T., Terasaki, O. *Nature* **2002**, *416*, 304–305.
[88] Jones, C. W. *Science* **2003**, *300*, 439–440.
[89] Jirage, K. B., Hulteen, J. C., Martin, C. R. *Science* **1997**, *278*, 655–658.
[90] Hollman, A. M., Bhattacharyya, D. *Langmuir* **2004**, *20*, 5418–5424.
[91] Grainger, D., Hägg, M.-B. *J. Membr. Sci.* **2007**, *306*, 307–317.
[92] Steel, K. M., Koros, W. J. *Carbon* **2003**, *41*, 253–266.
[93] Su, B.-L., Vantomme, A., Surahy, L., Pirard, R., Pirard, J.-P. *Chem. Mater.* **2007**, *19*, 3325–3333.
[94] Vu, D. Q., Koros, W. J., Miller, S. J. *J. Membr. Sci.* **2003**, *221*, 233–239.
[95] Higuchi, A., Yoshida, T., Imizu, T., *et al. J. Polym. Sci., Part B: Polym. Phys.* **2000**, *38*, 1749–1755.
[96] Sterescu, D. M., Bolhuis-Versteeg, L., van der Vegt, N. F. A., Stamatialis, D. F., Wessling, M. *Macromol. Rapid Commun.* **2004**, *25*, 1674–1678.
[97] Reich, S., Thomsen, C., Maultzsch, J. *Carbon Nanotubes: Basic Concepts and Physical Properties*; Wiley-VCH: Weinheim, 2004.
[98] Prehn, K., Adelung, R., Heinen, M., Nunes, S. P., Schulte, K. *J. Membr. Sci.* **2008**, *321*, 123–130.
[99] Zhang, D., Shi, L., Fang, J., Dai, K. *J. Mater. Sci.* **2007**, *42*, 2471–2475.
[100] Planeix, J. M., Coustel, N., Coq, B., *et al. J. Am. Chem. Soc.* **1994**, *116*, 7935–7936.
[101] Hinds, B. J., Chopra, N., Rantell, R., Andrew, R., Gavalas, V., Bachas, L. G. *Science* **2004**, *303*, 62–65.
[102] Skoulidas, A. I., Ackerman, D. M., Johnson, J. K., Sholl, D. S. *Phys. Rev. Lett.* **2002**, *89*, 185901.
[103] Kim, S., Jinschek, J. R., Chen, H., Sholl, D. S., Marand, E. *Nano Lett.* **2007**, *7*, 2806–2811.
[104] Hummer, G., Rasaiah, J., Noworyta, J. *Nature* **2001**, *414*, 188–190.
[105] Corry, B. *J. Phys. Chem. B* **2008**, *112*, 1427–1434.
[106] Holt, J. K., Park, H. G., Wang, Y., *et al. Science* **2006**, *312*, 1034–1037.
[107] Fornasiero, F., Park, H. G., Holt, J. K., *et al. Proc. Natl. Acad. Sci. U.S.A.* **2008**, *105*, 17250.
[108] Li, W., Wang, X., Chen, Z., Waje, M., Yan, Y. *Langmuir* **2005**, *21*, 9386–9389.
[109] Nednoor, P., Chopra, N., Gavalas, V., Bachas, L. G., Hinds, B. J. *Chem. Mater.* **2005**, *17*, 3595–3599.
[110] Liu, Z., Lin, X., Lee, J. Y., Zhang, W., Han, M., Gan, L. M. *Langmuir* **2002**, *18*, 4054–4060.
[111] Mi, W., Lin, Y. S., Li, Y. *J. Membr. Sci.* **2007**, *304*, 1–7.
[112] Yang, D. J., Wang, S. G., Zhang, Q., Sellin, P. J., Chen, G. *Phys. Lett. A* **2004**, *329*, 207–213.
[113] Wang, Z., Ci, L., Chen, L., Nayak, S., Ajayan, P. M., Koratkar, N. *Nano Lett.* **2007**, *7*, 697–702.
[114] Walz, T., Smith, B. L., Zeidel, M. L., Engel, A., Agre, P. *J. Biol. Chem.* **1994**, *269*, 1583–1586.
[115] Qiao, R., Georgiadis, J. G., Aluru, N. R. *Nano Lett.* **2006**, *6*, 995–999.
[116] Majumder, M., Zhan, X., Andrews, R., Hinds, B. J. *Langmuir* **2007**, *23*, 8624–8631.
[117] Gras, S. L., Mahmud, T., Rosengarten, G., Mitchell, A., Kalantar-Zadeh, K. *ChemPhysChem* **2007**, *8*, 2036–2050.
[118] Heskins, M., Guillet, J. E. *J. Macromol. Sci. Chem.* **1968**, *2*, 1441–1455.
[119] Lue, S. J., Hsu, J.-J., Wei, T.-C. *J. Membr. Sci.* **2008**, *321*, 146–154.

[120] Chilkoti, A., Dreher, M. R., Meyer, D. E., Raucher, D. *Adv. Drug Delivery Rev.* **2002**, *54*, 613–630.
[121] Pişkin, E. *Int. J. Pharm.* **2004**, *277*, 105–118.
[122] Kim, H. K., Park, T. G. *Enzyme Microb. Technol.* **1999**, *25*, 31–37.
[123] Kikuchi, A., Okano, T. *J. Control. Release* **2005**, *101*, 69–84.
[124] Ying, L., Kang, E. T., Neoh, K. G. *Langmuir* **2002**, *18*, 6416–6423.
[125] Ying, L., Kang, E. T., Neoh, K. G., Kato, K., Iwata, H. *J. Membr. Sci.* **2004**, *243*, 253–262.
[126] Spohr, R., Reber, N., Wolf, A., *et al. J. Control. Release* **1998**, *50*, 1–11.
[127] Feng, L., Li, S., Li, Y., *et al. Adv. Mater.* **2002**, *14*, 1857–1860.
[128] Lau, K. K. S., Bico, J., Teo, K. B. K., *et al. Nano Lett.* **2003**, *3*, 1701–1705.
[129] Verplanck, N., Galopin, E., Camart, J.-C., Thomy, V. *Nano Lett.* **2007**, *7*, 813–817.
[130] Sondag-Huethorst, J. A. M., Fokkink, L. G. J. *Langmuir* **1994**, *10*, 4380–4387.
[131] Gallardo, B. S., Gupta, V. K., Eagerton, F. D., *et al. Science* **1999**, *283*, 57–60.
[132] Tajima, K., Huxur, T., Imai, Y,. Motoyama, I., Nakamura, A., Koshinuma, M. *Colloids Surf. A* **1995**, *94*, 243–251.
[133] Gallardo, B. S., Metcalfe, K. L., Abbott, N. L. *Langmuir* **1996**, *12*, 4116–4124.
[134] Aydogan, N., Gallardo, B. S., Abbott, N. L. *Langmuir* **1999**, *15*, 722–730.
[135] Gallardo, B. S., Abbott, N. L. *Langmuir* **1997**, *13*, 203–208.
[136] Riskin, M., Basnar, B., Chegel, V. I., *et al. J. Am. Chem. Soc.* **2006**, *128*, 1253–1260.
[137] Balzani, V., Credi, A., Silvi, S., Venturi, M. *Chem. Soc. Rev.* **2006**, *35*, 1135–1149.
[138] Lahann, J., Mitragotri, S., Tran, T.-N., *et al. Science* **2003**, *299*, 371–374.
[139] Ichimura, K., Oh, S.-K., Nakagawa, M. *Science* **2000**, *288*, 1624–1626.
[140] Abbott, S., Ralston, J., Reynolds, G., Hayes, R. *Langmuir* **1999**, *15*, 8923–8928.
[141] Bunker, B. C., Kim, B. I., Houston, J. E., *et al. Nano Lett.* **2003**, *3*, 1723–1727.
[142] Peters, A. M., Lammertink, R. G. H., Wessling, M. *J. Membr. Sci.* **2008**, *320*, 173–178.
[143] Ariga, K., Hill, J. P., Ji, Q. *Phys. Chem. Chem. Phys.* **2007**, *9*, 2319–2340.

Biographical Sketches

S. P. Nunes is a principal reserch scientist at the Advanced Membranes and Porous Materials Center at KAUST, Saudi Arabia. She was the head of Department of Membranes for Sustainable Energy at GKSS, Germany. She has been working in the membrane field for more than 25 years and is the author of more than 10 patents, 120 papers in scientific journals, and is the co-editor of five books. Her main research topics have been membranes for fuel cell, CO_2, and hydrogen separation for energy application. She received her PhD in chemistry in 1985 at the University of Campinas, Brazil, where shelater worked as an assistant and associate professor from 1987 to 1997, after being a Humboldt fellow at the University of Mainz, Germany and working at Pirelli ResearchCenter in Brazil. She has coordinated European projects and co-organized several workshops and congresses in the field of membranes and polymer science.

Klaus-Viktor Peinemann is a co-founder of the GMT Membrantechnik GmbH, honorary professor at the University of Hannover, Germany, and principal reserch scientist at the Advanced Membranes and Porous Materials Center of KAUST, Saudi Arabia. He is the author of more than 20 patents, 85 papers in scientific journals, and is the co-editor of five books. He has been the president of the European Membrane Society and has more than 25 years of experience in membrane development and application, coordinating projects and co-organizing several workshops and congresses in the field of membranes. He received his PhD in chemistry in 1985 at the University of Kiel, Germany, worked at Membrane Technolgy Research, USA in 1986, and was head of the Department of Membrane Development at GKSS, Germany for several years. His main research topics have been membranes for gas separation, nanofiltration, reverse osmosis and osmotic power.

This page intentionally left blank

1.07 Norbornene Polymers as Materials for Membrane Gas Separation

Y Yampolskii, A.V. Topchiev Institute of Petrochemical Synthesis, Moscow, Russia

Glossary

Addition polymerization Process of polymerization of norbornene and norbornadiene monomers by opening of double bonds and formation of completely saturated products with retaining bicycling fragments in the main chain.

Diffusion coefficient or diffusivity *D* ($m^2\ s^{-1}$) Proportionality constant between the molar flux due to molecular diffusion and the gradient in the concentration of the species (or the driving force for diffusion).

Fractional free volume (FFV) The method that characterizes free volume in polymers; it is based on calculation of occupied volume found via van der Waals volume and determination of specific volume (reciprocal density) of polymers.

Inverse gas chromatography The method for investigation of physicochemical (thermodynamic) properties of polymers; it is based on measurements of specific retention volumes of certain solutes in the polymers dispersed in a chromatographic column.

Permeability coefficient *P* (Barrer or mol $m^{-1}\ s^{-1}\ Pa^{-1}$) Parameter defined as a transport flux per unit transmembrane driving force per unit membrane thickness.

Permselectivity Dimensionless parameter defined as the ratio of the permeability coefficient of component A to that of component B.

Positron annihilation lifetime spectroscopy (PALS) The method based on measuring lifetimes of positrons in polymers and other condensed phases; it allows an estimation of size and concentration of free volume elements.

Ring opening metathesis polymerization Process of polymerization of strained norbornene and norbornadiene monomers with formation of unsaturated cyclo-linear products.

Robeson diagram The correlation of permeability coefficients Pi and permselectivity Pi/Pj for different gas pairs in polymers.

Solubility coefficient *S* (mol $cm^{-3}\ Pa^{-1}$ or cm^3 (STP) $cm^{-3}\ atm^{-1}$; STP means at standard temperature 273.2 K and 1 atm) Parameter which indicates how much gas is taken up by the membrane when equilibrated with a given gas pressure.

Sorption isotherm Dependence of the concentration of gas dissolved in the membrane on gas pressure.

1.07.1 Introduction

Norbornene (bicyclo[2.2.1]hept-2-ene) and its derivatives present an unusually interesting group of monomers. Depending on the choice of catalysts they can produce a wealth of polymeric materials with variations of both chemical and spatial structures, as well as physicochemical and membrane properties.

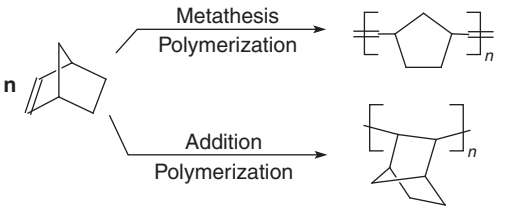

Scheme 1

In the presence of the catalysts on the basis of WCl_6, $RuCl_3$, and Re_2O_7/Al_2O_3, as well as Grubbs Ru complexes, strained structure of these bicycles is prone to ring-opening metathesis polymerization (ROMP), which leads to formation of cyclolinear, unsaturated polymers, as shown in **Scheme 1**.

Polymers of norbornene itself and its various derivatives with side groups, such as CN, $Si(CH_3)_3$, $Ge(CH_3)_3$, CF_3, and Cl, have been prepared and investigated as potential membrane materials. Because of the presence of double bonds in the main chain, different *cis–trans* configurations of the polymer units can be obtained depending on the choice of the catalysts. It was shown that the properties of the polymers prepared (such as gas permeability, free volume, and solubility coefficients) strongly depend on the nature of the side groups and the *cis*-content in the main chains. All the metathesis polynorbornenes (MPNBs) have relatively flexible chains; however, the structure of the side groups results in strong variation of the glass transition temperatures, which can be above 200 °C.

However, since norbornenes are cyclo-olefins, they can also be polymerized via the opening of double bonds in the presence of Ni and Pd catalysts. This reaction, addition-type polymerization, leads to bulky bicyclic repeat units that do not contain unsaturated bonds (**Scheme 1**). Properties of addition-polymerized polynorbornenes (APNBs) are entirely different from those of the MPNBs: APNBs, nonsubstituted or with small side groups, have extremely high glass transition temperatures.

The chapter presents a survey of the gas permeation properties of various norbornene polymers of both types, as well as a discussion of their structure based on the application of computer modeling, and the studies of free volume in these polymers.

1.07.2 Norbornene Polymers Obtained via ROMP

Since the 1980s various polynorbornenes (PNBs) of this type with different side groups were prepared mainly in the presence of WCl_6-based catalysts. Their gas permeation parameters were characterized, and a summary of the results is given in **Table 1**. It is known that the glass transition temperatures, T_g, which can serve as a measure of the stiffness of polymer chains, can affect the gas permeation parameters [6]. The relationship among chemical structure of MPNB, their T_g, and permeability coefficients allows an analysis of this trend for a big group of polymers having similar structure.

Appearance of bulky ($SiMe_3$) or small polar (CN) groups as substituents leads to strong increase in T_g. However, polymers with longer substituents due to self-plasticization show much lower T_g: thus, the polymer with $SiMe_2CH_2SiMe_3$ side group has T_g as low as 24 °C, that is, lower than T_g of unsubstituted PNB (polymer 1 of Table 1). So low is its T_g that in many respects this polymer behaves as a rubber: its sorption isotherms are convex to the pressure axis (in contrast to those of other, glassy MPNBs) [2] and the permeability coefficient of ethane is larger than that of methane [1], which is typical for rubbers. Similar trends in the variations of T_g can be noted for CN-containing polymers 6–8 as well as the polymers 10–12 that include alkyl side groups. The growth of the *P* values caused by the appearance of $SiMe_3$ group is approximately the same independently of other substituents R_2 (cf. the pairs of polymers 1–2 and 5–6).

Although the effects of $SiMe_3$ groups as structural modifiers are well known for various classes of polymers [6], **Table 1** gives interesting information on the effects of the introduction of a small and polar CN group, which behaves in an opposite manner as compared with $SiMe_3$. For example, a

Table 1 The effects of the side groups of substituted MPNB with the general structure on their properties. (catalyst: WCl_6 with different cocatalysts; transport parameters reported at room temperature)

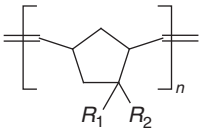

No	R_1	R_2	T_g (°C)	$P(O_2)$ (Barrer)	$D(O_2)\ 10^7$ ($cm^2\ s^{-1}$)	$S(O_2)\ 10^2$ (cm^3(STP) $cm^{-3}\ cm^{-1}\ Hg^{-1}$)	$\alpha(O_2/N_2)$	Ref.
1	H	H	31; 42	2.8	1.5	0.19	1.9	[1–3]
2	H	$SiMe_3$	113	30	4.2	0.71	4.2	[1–3]
3	H	$SiMe_2CH_2SiMe_3$	24	16	2.1	0.76	4.3	[1–3]
4	H	CH_2GeMe_3	-	7.7	-	-	4.3	[4]
5	CN	H	140	0.53	0.70	0.075	6.3	[5]
6	CN	$SiMe_3$	211	7.6	1.7	0.15	4.6	[5]
7	CN	CH_2SiMe_3	128	11	1.7	0.65	4.2	[5]
8	CN	$SiMe_2SiMe_3$	120	4.4	1.2	0.36	4.6	[5]
9	CN	$SiMe_2OSiMe_3$	88	15.3	6.5	0.23	4.4	[5]
10	CN	Et	134	1.7	1.5	0.11	5.2	[5]
11	CN	Pr	108	2.0	1.0	0.19	5.0	[5]
12	CN	n-Bu	87	2.4	1.8	0.13	4.6	[5]
13	H	Cl	-	2.3	-	-	2.6	[1]
14	H	CH_2Cl	-	0.46	-	-	1.9	[1]

comparison of the polymers 2 and 6 indicates that replacement of H atom by CN group results in significant decreases in the *P*, *D*, and *S* values, which are accompanied by relatively small traditional tradeoff increase in selectivity. Much stronger growth in selectivity is observed for the pair of the polymers 1–5: CN-containing polymer is much less permeable but has substantially greater selectivity.

Returning to the question of the effects of chain stiffness on permeability, it can be concluded that there is no unified trend for MPNB presented. Although in certain cases, an increase in chain stiffness is accompanied by noticeable growth of permeability, some polymers with relatively flexible side groups (e.g., polymers 3 and 9) are characterized by low T_g and relatively large $P(O_2)$ values. In spite of some variations in permeability (by one order) and permselectivity, these parameters of the considered group of MPNB do not reach the range of values attractive for practical application.

Another bicyclic unsaturated compound, norbornadien, is also capable of giving high-molecular-mass products via ROMP. Polynorbornadienes differ from PNBs by the presence of an additional double bond in the five-member cycle. This hardly affects chain structure and packing, so the gas permeation parameters of both groups of polymers are rather similar, as **Table 2** illustrates.

Much more interesting results were obtained for disubstituted PNBs having hydrogen atoms replaced by larger groups in positions 5 and 6:

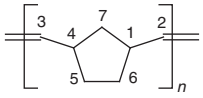

It is seen from **Table 3** that such polymers have permeability coefficients larger at least by an order than those of nonsubstituted PNB. It is also obvious

Table 2 Permeability coefficients of poly(trimethylsilylnorbornene) (PTMSNB) and poly(trimethylsilylnorbornadiene) PTMSNBD: catalyst WCl_6/1,1,3,3-tetramethyl-1,3-disilacyclobutane) [7]

		P (Barrer)				
No	Polymer	H_2	O_2	N_2	CO_2	CH_4
2	PTMSN	77	21	6.2	79	17
15	PTMSNBD	81	20	4.9	64	8.5

Table 3 Transport properties of disubstituted polynorbornenes and poly(norbornene spirocyclopropane)

			P (Barrer)						
No	*Polymer*	T_g (°C)	H_2	O_2	N_2	CO_2	CH_4	C_2H_6	*Ref.*
1	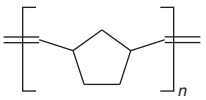	31	21	2.8	1.5	15.4	2.5	1.4	[1]
16	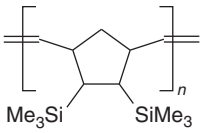	167	375	95	25	445	45	30	[7]
17	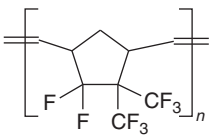	169	166	50	17	200	13	6.6	[8]
18	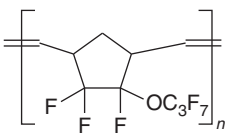	77	130	55	17	200	18	14	[8]
19	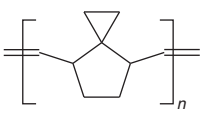	-	7.0	1.0	0.3	2.0	0.4	0.2	[1]

that an introduction of two bulky substituents renders polymers much more permeable than those that include only one bulky group (see **Table 1**). It should also be noted that increases in permeability are not accompanied by decreases in permselectivity as it often takes place (**Table 4**).

Gas sorption in MPNB was also studied extensively [2, 8, 9]. Sorption isotherms in all glassy PNBs at room temperature (25–30 °C) have the form consistent with the dual-mode sorption model, that is, concave to the pressure axis. The only exception is nonsubstituted PNB, whose low T_g (31 °C) is the reason for transition to the rubbery state induced by very small concentration of solute: this results in sorption isotherms concave to the concentration axis (**Figure 1**).

The order of isotherms of various gases is usually governed by condensability. So the common order of the sorption isotherms is as follows: $He < N_2 < Ar < CH_4 < CO_2 < C_2H_6$ (see, e.g., [2, 9]). An unexpected result was obtained in studies of fluorine-containing polymers 17 and 18 of **Table 3** and **4**: in these cases, the sorption isotherm of ethane is located below that of carbon dioxide (**Figure 2**).

This was, apparently, a first evidence of reduced solubility of hydrocarbons in fluorine-containing polymers due to unfavorable interactions between C–H and C–F bonds of solutes and polymers extensively studied and discussed eventually [10–12].

Free volume in MPNB was experimentally evaluated using different probe methods – positron annihilation lifetime spectroscopy (PALS), spin probe method (SPM), and inverse gas chromatography (IGC).

The simplest and a common way to estimate free volume in polymers is to use the Bondi method [13] for the determination of the fractional free volume (FFV): $FFV = 1 - V_{occ}/V_{sp}$, where V_{occ} is the

Table 4 Separation factors $\alpha_{ij} = P_i/P_j$ of several disubstituted polynorbornenes [1, 7, 8]

Polymer	O_2/N_2	H_2/N_2	CO_2/CH_4
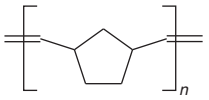	1.9	14.4	6.3
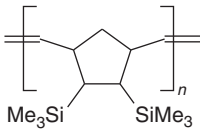	3.8	15	9.9
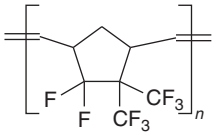	2.9	9.8	15.4
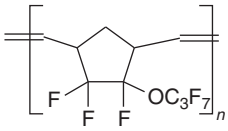	3.2	7.6	11

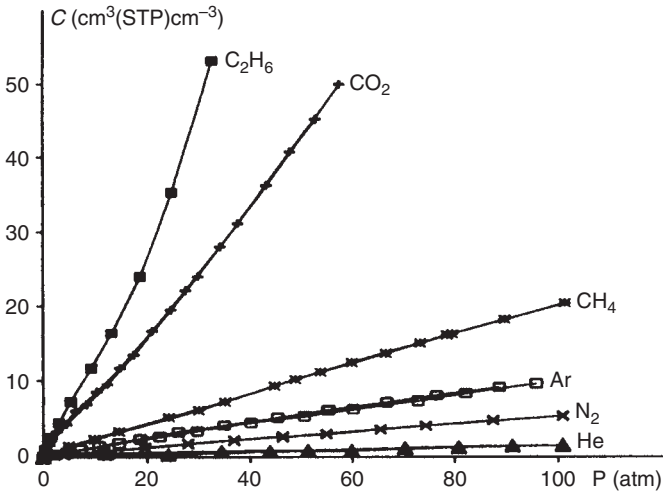

Figure 1 Sorption isotherms in metathesis polynorbornene at 25 °C [8]. From Yampolskii, Yu. P., Bespalova, N. B., Finkelshtein, E. Sh., Bondar, V. I., Popov, A. V. *Macromolecules* **1994**, *27*, 2872–2878.

occupied volume that can be calculated via van der Waals volume of the repeat units and V_{sp} is the specific volume or the reciprocal density of the polymers. In MPNB the values of FFV are in the range 0.16–0.20 and do not strongly depend on the structure of the polymers. The studies of MPNB using the PALS method indicated that size distribution of free volume in these polymer is monomodal and the radii of microcavities R calculated using the Tao–Eldrup equation [14, 15] are in the range 2.9–4.1 Å, which corresponds to the volumes of microcavities V_f of 100–290 Å^3. A rough correlation is observed between the R and V_f values and the permeability and diffusivity of these polymers [8].

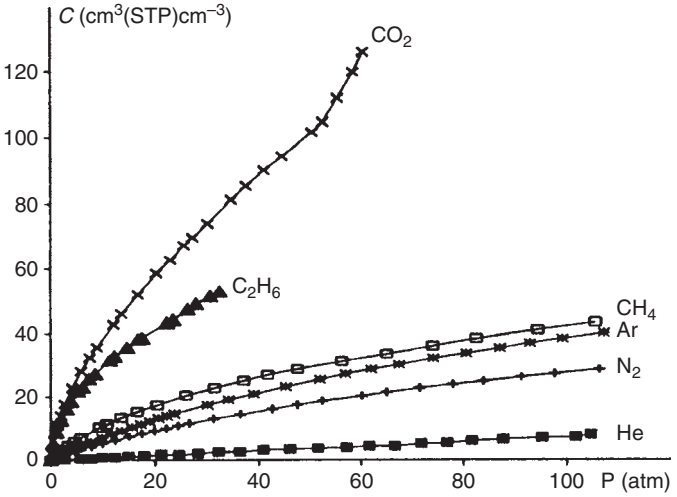

Figure 2 Sorption isotherms in poly[5,5-difluoro-6,6-bis(trifluoromethyl)norbornene] at 25 °C [8]. From Yampolskii, Yu. P., Bespalova, N. B., Finkelshtein, E. Sh., Bondar, V. I., Popov, A. V. *Macromolecules* **1994**, *27*, 2872–2878.

It is known that the frequency of rotation of stable free radical 2,2,6,6-tetramethylpiperidine-1-oxyl (TEMPO) can serve as a measure of the size of microcavity in polymers [16] (so-called spin probe method (SPM)). The frequencies of rotation ν of TEMPO in MPNB presented in **Tables 1** and **3** were found to be 0.1 $10^{-9}\,s^{-1}$ for 1, 0.5 $10^{-9}\,s^{-1}$ for 2, and $10^{-9}\,s^{-1}$ for 17. For the two latter polymers the ν values are indicative of fast rotation and, hence, of relatively large size of microcavity, which is consistent with the results of the PALS method [17].

The IGC method has been used successfully for characterization of free volume in high-permeability polymers (see Reference 6, p 191). It was shown [18] that the volume of microcavity in poly[5,6-bis(trimethylsilyl)norbornene] (polymer 16 of **Table 3**) is about 820 $Å^3$, which is in agreement with its relatively high gas permeability.

It is known that the microstructure of polymer main chains such as tacticity of polyolefins and *cis–trans* configuration of the chains of dienes can influence many physicochemical properties, including their gas permeability. Since the microstructure of the polymers is a result of the polymerization conditions and nature of the catalysts used, one can control stereochemistry, for example, by varying temperature, and the type of solvents and catalysts employed during polymerization. Ivin *et al.* [19] studied the *cis/trans*-double bond distribution in ROMP PNBs. They used a variety of catalysts (WCl_6, $MoCl_5$, $ReCl_5$, etc.) and a number of cocatalysts and additives. Strong effects of the *cis/trans* ratio in a polyacetylene on its diffusivity were demonstrated by Morisato *et al.* [20]. A study of similar effects in PNB and poly(trimethylsilyl norbornene) (PTMSNB) were undertaken using three catalytic systems: Re_2O_7/Al_2O_3 promoted with tetrabutiltin, WCl_6-phenylacetylene, and $RuCl_3\ 3H_2O$ [21, 22]. The Re catalyst induced the formation of the prevailing concentration of a *cis*-configuration (70–75%), while the Ru catalyst led to the formation of a *trans*-configuration (*cis*-content of 20–31%). The W catalyst had the poorest stereoselectivity: *cis*-content 55–67%.

Table 5 summarizes the effects of the microstructure of the two MPNBs. The *cis*-content was determined using infrared (IR) spectroscopy. The intensities of the 750 and 970 cm^{-1} bands were used for finding the content of *cis*- and *trans*-units, respectively, in the case of PNB; for PTMSNB, the content of *trans*-units was calculated via the intensity of the band at 970 cm^{-1}, while the band at 1250 cm^{-1} (δ-Si-CH_3) was used as an inner standard. Somewhat different trends were observed for the two chemical structures of MPNBs. For PNB, the *cis*-content weakly affected the glass transition temperature, but the permeability coefficients of the polymers with the smallest *cis*-content were markedly lower. An opposite observation can be made for PTMSNB: a noticeable sensitivity of T_g to the *cis*-content and very weak variations of the P values. Qualitatively similar conclusions can be made based on the results of Steinhauser and

Table 5 Gas permeability coefficients P, Barrer of polynorbornenes (PNBs) and poly(trimethylsilyl norbornenes) (PTMSNBs) with different microstructure [21, 22]

Catalyst	Cis-content (%)	T_g (°C)	H_2	He	O_2	N_2	CO_2	CH_4
PNB								
Re	70	43	17.7	12.9	3.2	0.80	14.4	1.4
W	55	42	19.4	13.0	2.6	0.75	13.9	1.9
Ru	20	35	7.3	6.0	-	0.20	3.1	0.26
PTMSNB								
Re	75	59	51	56	18	4.4	72	9.2
W	67	101	77	58	21	6.2	79	17
Ru	31	85	67	51	16	4.8	66	4.8

Koros [23], who used more stereoselective catalysts: $ReCl_5/EtAlCl_2$/ethyl acrylate catalyst allowed obtaining PNB with *cis*-content >98% ($T_g = 67\,°C$) and $IrCl_3\ xH_2O/EtAlCl_3$ catalyst that produced PNB ($T_g = 36\,°C$) with *cis*-content of 12%. It was shown that the polymer obtained in the presence of the Re catalyst was more permeable by a factor of 1.5–3. Some difference between the results of the works in References 21 and 23 can be explained by tacticity of the polymers prepared in the presence of different catalytic systems: racemic dyads that correspond to head–head and tail–tail sequences in one case and atactic (tail–head and head–tail connections) in other cases. In this situation, the *trans*- and *cis*-double bonds are not statistically distributed but instead form microblocks. There is no sufficient information in the literature to confirm or discard these statements.

Another interesting group of MPNB was studied by Mexican researchers [9, 24–26]. These authors prepared MPNB by polymerization of N-substituted exo-norbornene-5,6-dicarboximides. As radicals, 1-adamantyl, cyclohexyl, and phenyl were chosen. In addition, copolymers with norbornene and the product of hydrogenation of double bonds in the main chain were prepared and tested. The incentives for these studies were hopes to obtain polymers with more rigid chains that would have higher permeability and permselectivity. The results presented in **Table 6** show that indeed these polymers have much more rigid chains: their glass transition temperatures are in the range 129–233 °C.

Table 6 Transport properties of MPNB with dicarboximide moiety substituted by various groups [24–26]

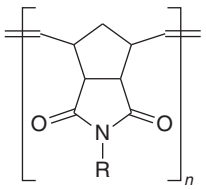

R	T_g (°C)	P (Barrer) H_2	O_2	N_2	CO	CO_2	CH_4	C_2H_6
Adamantyl	271	12.8	1.59	0.50	0.51	8.39	0.58	0.07
Cyclohexyl	129	16.1	2.13	0.61	1.04	18.11	1.12	0.13
Cyclopentyl	174	-	1.95	0.45	-	8.8	0.54	-
Phenyl	233	11.0	1.44	0.31	0.52	11.44	0.54	0.09
Phenyl[a]	197	7.22	0.66	0.12	0.21	4.51	0.15	-

[a] The double bonds of the main chains were hydrogenated.

Table 7 Separation factors $\alpha_{ij} = P_i/P_j$ of MPNB with dicarboximide moiety substituted by various groups [24–26]

R	O_2/N_2	H_2/N_2	CO_2/CH_4
Adamantyl	3.2	25.6	14.5
Hexyl	3.5	26.4	16.2
Phenyl	4.6	35.5	21.2
Phenyl[a]	5.5	60.2	30.0

[a] The double bonds of the main chains were hydrogenated.

However, apparently due to strong interchain interactions caused by polar dicarboximide groups, permeability is reduced by one to two orders as compared with other MPNBs (see, e.g., **Table 3**). Permselectivity of this new group of MPNB is, indeed, somewhat higher than those of other MPNBs characterized so far (see **Table 4**), although the actual values of separation factors reported in **Table 7** are not very attractive if being compared with polymers of other classes (e.g., polyimides) [27]. This subject is discussed in a more detailed manner subsequently in this chapter.

So far, main attention was directed to gas permeation parameters of MPNB. However, recently, pervaporation behavior of hydrogenated poly[5-(*N*-carbozoyl methylene)-2-norbornene] was reported [28]. Polymerization of such derivatives of norbornene in the presence of Ru catalysts was described earlier [29, 30]. It was shown that this polymer behaves as a material of highly selective hydrophilic membrane. In separation of 90 wt.% aqueous ethanol mixtures, high degree of enrichment of permeate with water was achieved. The separation factors of water/ethanol are in the range 350–600 at 25–55 °C, and it puts this polymer among the most selective in hydrophilic pervaporation. However, the observed permeation rates of 300–400 g m^{-2} h indicate that the membranes made of this polymer are not very permeable. The permeation rates decrease in the series of alcohols C_1–C_4, which shows that the process is diffusivity controlled.

1.07.3 Addition-Type Norbornene Polymers

A possibility of polymerization of norbornene polymers via the opening of double bonds in the presence of Ni and Pd catalysts has been demonstrated by several authors [31–33]. These polymers have entirely different properties: much higher glass transition temperatures, greater thermal stability, and, in some cases, larger free volume, which are determined by bulky, bicyclic structure of their repeat unit (see **Scheme 1**).

1.07.3.1 Structure and Free Volume

Three structural features determine the unusual transport properties of APNB:

- bulky repeat units that are the cause for very rigid main chains;
- possibility of formation of stereoisomers in the process of polymerization in the presence of different catalysts; and
- effects of the side groups: the effects here are stronger that those in the polymers with more flexible main chains.

It has been shown using the Monte Carlo simulation [34] that the polymers produced in the presence of Pd and Ni catalysts have different microstructures. In the presence of the Pd catalysts, highly stereoregular 2,3-erythro diisotactic structure is formed. In this configuration, the bridgehead carbons point in alternative directions (Stereoarchitecture A). Such stereochemical assignment was confirmed by nuclear magnetic resonance (NMR) spectroscopy [35]. The polymers produced in the presence of the Ni catalyst are atactic materials, which supposedly includes 2,3-erythro diisotactic units (75%) and 2,3-erythro disyndiotactic units (25%), randomly distributed throughout the polymer main chain (Stereoarchitecture B). In the latter configuration, the bridgehead carbons point in the same direction. Further modeling work [36] suggested that the polymers with stereoarchitecture A have large gaps between polymer chains as a consequence of the long persistence length of helical chains. By contrast, the polymers with stereoarchitecture B have more disruption and form more compact clusters. These assumptions were consistent with the results of the study of the methyl-substituted APNB using wide-angle X-ray diffraction (WAXD) and the PALS method [37]. In particular, it was shown that the polymer with stereoarchitecture A is characterized by somewhat larger size of microcavity and, hence, larger diffusion coefficients.

APNBs were studied in detail using WAXD [37–40]. In all the cases, completely amorphous structures were demonstrated with two peaks of amorphous halo observed in WAXD pattern. This is typical for high free volume, high-permeability polymers such as polyacetylenes [41–43] and amorphous Teflons AF

Table 8 X-ray scattering data of APNB with different side groups

Catalyst	R	$2\theta_1$ (deg)	$2\theta_2$ (deg)	d spacing[a] (Å) d_{B1}	d spacing[a] (Å) d_{B2}	Ref.
$Ni(acac)_2$	H	10	18.5	8.8	4.7	[39]
Pd	Me	9.5	18.2	9.3	4.9	[38]
Pd	Bu	7.2	18.8	12.3	4.7	[38]
Pd	C_6H_{13}	6.6	19.2	13.5	4.6	[38]
$[(Nph)_2Ni]$-methylaluminoxane	$SiMe_3$	6.5	15.5	13.6	5.7	[40]

[a] The *d* spacing is found as the Bragg's distance $d_B = \lambda/(2\sin\theta)$, where λ is the wavelength of Cu-K_α radiation (1.54 Å).

[42]. For low-permeability polymers, such as polyimides, one peak of amorphous halo is characteristic. Different interpretations for this behavior can be found in the literature. Wilks *et al.* [38] assumed that low 2θ peaks can be attributed to intermolecular interactions (or intersegmental *d* spacing), while the high 2θ peaks are predominantly due to intramolecular interactions. The summary of WAXD data is given in **Table 8**.

The results obtained for substituted APNB with different side groups allow one to note a distinct effect of chemical structure onto the observed *d* spacing (d_{B1}). The smallest d_{B1} value is observed for nonsubstituted APNB [39]. There is an evident trend in the d_{B1} values for alkyl substituents of increasing size: the largest value is observed for the polymer with hexyl side chain. It means that larger side groups tend to push the polymer backbones apart. The largest value of d_{B1} is observed for the bulky substituent – $SiMe_3$. A study of two methyl-substituted PNBs with different stereoarchitecture did not reveal any difference in the observed *d* spacing [37]. It can be added that computer simulation (molecular dynamics method) provided a nice agreement with the experimental WAXD data [38]. All the APNBs are characterized by larger *d* spacing than that of conventional glassy polymers, such as polycarbonates and polysulfones, where the corresponding values of *d* spacing (4–6 Å) indicate more densely packed chains.

The most reliable experimental tool for probing free volume in polymers is PALS. This method is based on the measurement of lifetime spectra of positrons in polymers – lifetimes τ_i (ns) and corresponding intensities I_i (%). Longer lifetimes τ_3 (or τ_3 and τ_4) (the so-called ortho-positronium (o-Ps) lifetimes) can be related to the mean size of free volume elements (FVEs) in polymers using the universally accepted Tao–Eldrup equation [14, 15]. A single o-Ps lifetime gives a monomodal size distribution of free volume. In highly permeable polymers, usually two o-Ps lifetimes (τ_3 and τ_4) give better statistical fit, so bimodal size distribution of free volume results. **Table 9** summarizes the results of the application of this method to APNB.

The largest size of FVEs (microcavities) found by this method is observed in $SiMe_3$-substituted APNB. It can also be noted that here bimodal size distribution of free volume is observed, which is typical of other highly permeable polymers [44, 45]. In alkyl-substituted APNB, an increase in the length of the

Table 9 PALS data of APNB

R	Catalyst	τ_3 (ns)	I_3 (%)	τ_4 (ns)	I_4 (%)	R_3/R_4 (Å)	V_f (Å^3)	Ref.
H	Ni(acac)	2.87	36.4	-	-	3.58 (R_3)	192	[39]
Me	Pd	3.49	32.2	-	-	3.95 (R_3)	258	[38]
	Ni	3.15	33.3	-	-	3.74 (R_3)	219	[37]
Bu	Pd	2.95	32.5	-	-	3.60 (R_3)	195	[38]
C_6H_{13}	Pd	2.77	31.6	-	-	3.48 (R_3)	176	[38]
$SiMe_3$	*a*	3	10	7	30	3.7/5.7	212/775	[40]

[a] $[(Nph)_2Ni]$-methylaluminoxane.

side group is accompanied by certain decreases in the size of FVEs. Apparently, larger substituents partly fill microcavities that are located along main chains. It indicates that the WAXD and PALS methods give independent information: the chains are pushed apart by larger side groups, but this effect is overridden by partial filling of FVEs. The values of o-Ps lifetimes and corresponding radii of FVEs in alkyl-substituted APNB are of the same order as those in MPNB.

Free volume in the $SiMe_3$-substituted APNB was also studied using IGC [46]. In this method, the partial molar enthalpies of mixing ΔH_s are determined for a series of molecular probes – *n*-alkanes of different size. For glassy polymers, the correlations of ΔH_s versus the size of the probes (e.g., the critical volume V_c or molecular volume V_b at boiling point) pass through a minimum. It was assumed (see Reference 6, p 191) that the coordinates of these minima ($V_{c(min)}$) correspond to the average size of FVEs in the polymer. The values of $V_{c(min)}$ increase when gas permeability and diffusivity of the polymers increase. **Figure 3** shows such correlation for the $SiMe_3$-substituted APNB and, for comparison, for some other silicon-containing polymers.

It is seen that the addition-type polymer is characterized by (1) very large size of FVEs and (2) by bimodal size distribution of free volume. This type of size distribution is common in the PALS studies of high-permeability polymers, so finding it by using an independent technique confirms those results. The size of larger FVEs can be estimated as 1260 $Å^3$ if one assumes that the sorbed phase has the critical density (V_c as the scaling parameter) and 500 $Å^3$ for the assumption of liquid density (V_b as the scaling parameter). Hence, the observed value of the size of free volume is qualitatively consistent with the results of the PALS method. For two other polymers presented in this figure, the coordinates of the minima correspond to smaller sizes of FVEs, which is in agreement with their lower gas permeability.

It can be added that the results of the application of SPM to the investigation of APNB are in agreement with the data obtained using other probe methods. It was shown that the rotation frequency of the spin probe TEMPO was $1 \times 10^9\ s^{-1}$ in $SiMe_3$-containing APNB and $0.6 \times 10^9\ s^{-1}$ for nonsubstituted PNB [17].

The changes of the FFV as determined using the Bondi method [13] for APNB with different side groups are in line with the results of more refined methods for evaluation of free volume: thus, in nonsubstituted APNB, FFV = 0.115–0.15 [39, 40]; in Me-substituted APNB, FFV = 0.17–0.18 [37, 48]; and for the polymer having $SiMe_3$ group as a substituent, FFV = 0.275 [40].

It is interesting that APNB can be used for obtaining nanoporous materials not only because of intrinsic, loose packing of their chains but also by means of chemical transformations. These polymers are distinguished by good thermal stability (decomposition temperatures in inert atmosphere are above 350–40 0 °C) [37, 40]. However, graft copolymers with thermally labile compounds (e.g., polylactide) allow obtaining, after

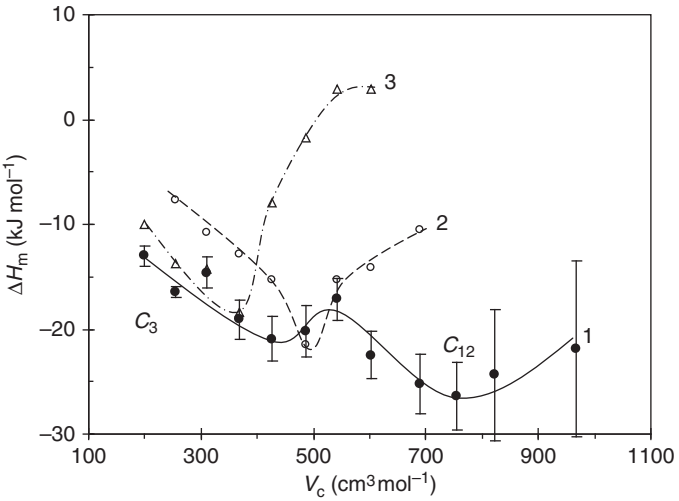

Figure 3 Correlation of ΔH_m vs. the critical volume of solutes for different polymers [18, 46, 47]. (1) $SiMe_3$-substituted APNB; (2) bis-$SiMe_3$-substituted MPNB (polymer 16 of **Table 3**); and (3) polyvinyltrimethylsilane. From Starannikova, L., Pilipenko, M., Belov, N., Yampolskii, Yu., Gringolts, M., Finkelshtein, E. *J. Membr. Sci*. **2008**, *323*, 134–143.

performing subsequent pyrolysis at 250 °C, nanoporous thin films, where thermally stable PNB forms a matrix (porosity up to 18%) [49].

1.07.3.2 Transport and Thermodynamic Properties

Table 10 presents permeability coefficients of APNB that differ by chemical structure and stereoarchitecture.

The strong effects of the chemical structure on the observed *P* values are obvious. Thus, a replacement of H atoms by Me group results in a drastic (by a factor of 8–10) increase in permeability. An even more dramatic increase is observed due to the appearance of the bulky $SiMe_3$ group: here the permeability increases by two orders. The increases in the length of the alkyl substituents in the series Me, *n*-Bu, and *n*-C_6H_{13} result in a reduction of gas permeability. Apparently, it is caused by the self-plasticization effect (decreases in T_g to 280 °C for the Bu-derivative and even to 150 °C for the polymer containing $C_{10}H_{21}$ group [48]). Such more flexible chains can be packed better, so a decrease in free volume is observed. The differences in the stereoarchitecture of the polymers having the same chemical structure, but obtained in the presence of different catalysts (e.g., Ni and Pd), are also manifested in permeability coefficients: Me-substituted polymers, including 2,3-erythro diisotactic sequences, are characterized by greater permeability coefficients for all the gases.

The most permeable among the considered group of polymers is $SiMe_3$-substituted APNB. It is well known that the introduction of bulky $Si(CH_3)_3$ group in various main chains results in a noticeable increase in gas permeability [6]. However, the quantitative effects can be different for various polymer classes. Thus, in the case of relatively flexible main chain (vinylic-type polymers such as polyethylene or polystyrene) the increases in the *P* values amount to usually one order. The same is true for MPNB. For APNB, the effect is much stronger – *P* increases by nearly two orders of magnitude. It can be related to much more rigid main chains in APNB. However, the largest separation factors $\alpha_{ij} = P_i/P_j$ are observed for nonsubstituted APNB, so the well-known tradeoff behavior is also observed for this group of norbornene polymers. (We return to this subject later in this chapter.)

An important shortcoming of some high free-volume, high-permeable polymers (e.g., poly(1-trimethylsilyl-1-propyne) (PTMSP)) is their tendency to reduce permeability in time (the so-called aging). Therefore, all the polymers that have high gas permeation parameters should be tested on time stability of their *P* values. Corresponding experiments carried out with the films of $SiMe_3$-substituted APNB showed that a very weak decrease (<4%) in permeability is observed during 50 days when the film was subjected to tests at 20–60 °C. For comparison, permeability of PTMSP decreased for the same period by a factor of 2–3 [50].

Since the $SiMe_3$-substituted APNB showed such a high gas permeability, its transport properties were studied in more detail [40, 46]. An interesting feature that can be potentially important from the practical viewpoint is solubility-controlled

Table 10 Permeability coefficients *P*, barrer of APNB (at 22–35 °C)[a]

R	*Cat*	*He*	H_2	O_2	N_2	CO_2	CH_4	*Ref.*
H	$Ni(acac)_2$	-	-	10.8	2.7	49.1	-	[39]
	Ni[b]	29.4	41.5	6.9	1.5	33.6	2.6	[40]
CH_3	Pd	309.4	502.1	89.2	24.1	396.3	30.3	[48]
	Pd	174.4	-	-	12.6	202.1	16.9	[37]
	Ni	88.8	-	-	4.3	81.1	5.6	[37]
n-C_4H_9	Pd	66.7	110.7	33.3	11.2	141.9	28.4	[48]
		70	-	-	9.9	139.7	23.0	[38]
n-C_6H_{13}	Pd	36.8	57.2	19.8	6.9	83.8	18.7	[48]
		53.4	-	-	8.2	109.8	23.1	[38]
n-$C_{10}H_{21}$	Pd	38.9	62.4	25.3	8.7	111.1	28.1	[48]
$Si(CH_3)_3$	Ni[b]	790	1680	780	297	4350	790	[40]
		840	1800	980	390	4480	993	

[a] No detailed information on the nature of the catalysts used if not stated otherwise.
[b] $[(Nph)_2Ni]$-methylaluminoxane; the variation in the values of *P* corresponds to differences in molecular mass.

selectivity of this and other high-permeability, high free-volume polymers revealed in separation of hydrocarbons according to their molecular mass. As permeability coefficients can be presented as the product $P = DS$, where D is the diffusion coefficient and S is the solubility coefficient, the variations of the P values for the series penetrants can be ascribed to corresponding trends of the D and S values [51]. In conventional glassy polymers, size sieving or mobility selectivity, which is determined by the variations of the diffusion coefficients, prevails; therefore, the separation factors reveal higher permeation rates of lighter components, for example, $\alpha(C_4H_{10}/CH_4) < 1$. By contrast, in rubbers, the diffusion coefficients only weakly depend on the penetrant size, so the opposite inequality $\alpha(C_4H_{10}/CH_4) > 1$ is valid, because the solubility coefficient becomes a parameter more sensitive to penetrant size and properties. It is important that in some high free-volume glassy polymers (first and foremost, PTMSP) solubility-controlled permeation behavior is observed as well [52].

In this regard, it was interesting to compare permeability coefficients of APNB with $SiMe_3$ side group and other polymers for *n*-alkanes C_1–C_4 at 1 atm (**Table 11**). It can be concluded that this polymer reveals the solubility-controlled selectivity of separation: permeability coefficient of *n*-butane is much greater than that of methane. This is a common type of behavior of several high free-volume polymers as the data for some polyacetylenes also show (**Table 11**). It can be ascribed to open porosity type of free volume typical for these polymers.

It can be mentioned that another polymer with bulky units in the main chain has been described – exo-polybicyclopentadiene (PBCPD).

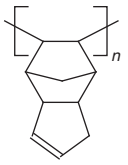

It has also very high glass transition temperature, above 400 °C. Its transport parameters are shown in **Table 12**. The values of the permeability and solubility coefficients of this polymer are similar to those of alkyl-substituted APNB, whereas the diffusion coefficients are somewhat lower.

The diffusion coefficients of several gases in substituted APNB are presented in **Table 13**. For substituted polymers, the diffusion coefficients increase with increasing intersegmental d spacing. The largest D values are observed for the polymer containing bulky $SiMe_3$ group. By contrast, for alkyl-substituted polymers, there is no positive correlation with the free volume as sensed by PALS: the larger D values are observed for the polymer with C_6H_{13} side groups, which is characterized by smaller radius of FVEs [37, 38]. It is worth noting that for the polymer with $SiMe_3$ group both WAXD and PALS data are in agreement with the observed high D values for all the gases [40, 46].

The second, thermodynamic contribution of permeability is the solubility coefficient S. **Table 14**

Table 11 Permeability of high free volume polymers in respect of hydrocarbons[a]

	P (Barrer)				
Polymer	CH_4	C_2H_6	C_3H_8	C_4H_{10}	*Ref.*
APNSi	790	1430	1740	17 500	[40]
PTMSP	15 000	31 000	38 000	-	[52]
PMP	2900	3700	7300	26 000	[53]
AF2400	435	252	97	-	[45]

[a] PTMSP, polytrimethylsilylpropyne; PMP, polymethylpentyne; AF2400, random copolymer of 13% tetrafluoroethylene and of 87% 2,2-bis(trifluoromethyl)-4,5-difluoro-1,3-dioxole.

Table 12 Transport properties of exo-PBCPD [54]

Gas	*P* (Barrer)	*D* 10^8 ($cm^2\,s^{-1}$)	*S* (cm^3(STP)/cm^{-3} atm^{-1})
H_2	81.8	-	-
He	49.5	-	-
O_2	20.9	44	0.36
N_2	5.8	19	0.23
CO_2	131	21	4.7
CH_4	10.4	8.2	0.96

Table 13 Diffusion coefficients D 10^8 $cm^2\,s^{-1}$ of APNB at 35 °C [37, 38, 46]

Side group	*Catalyst*	*Ar*	CH_4	N_2	CO_2	O_2
Me	Ni	12.3	3.2	7.5	23.2	-
	Pd	26	8	24	48	-
Bu	Pd	69	27	55	75	-
C_6H_{13}	Pd	150	62	201	118	-
$SiMe_3$	Ni[a]	-	180	270	320	500

[a] $[(Nph)_2Ni]$-methylaluminoxane; at 22 °C.

Table 14 Solubility coefficients S cm^3(STP)cm^{-3} atm^{-3} of APNB at 35 °C [37, 38, 46]

Side group	*Catalyst*	*Ar*	*CH_4*	*N_2*	*CO_2*	*O_2*
Me	Ni	0.76	1.56	0.41	3.21	-
	Pd	0.67	1.30	0.44	2.66	-
Bu	Pd	0.27	0.64	0.14	1.42	-
C_6H_{13}	Pd	0.11	0.29	0.03	0.70	-
$SiMe_3$	Ni[a]	-	3.6	0.91	9.8	1.3

[a] $[(Nph)_2Ni]$-methylaluminoxane; at 22 °C.

shows the *S* values for substituted addition-type PNBs. Joint consideration of **Tables 10**, **13**, and **14** indicates that the increases in the diffusion rate is not the determining factor for the permeability coefficients for all gases in alkyl-substituted APNB. The decrease in the *P* values for methyl- to hexyl-substituted polymers is a result of a decrease in the solubility coefficients. The situation is quite different for the polymer with $SiMe_3$ group: it is distinguished by the largest values of both *S* and *D* (in agreement with its large free volume). An unusual result obtained for alkyl-substituted APNB can imply that solubility-controlled permeation should be characteristic for these polymers (and not only for the polymer with $SiMe_3$ group). Hence, further studies of permeation of hydrocarbons C_1–C_4 in these polymers are highly desirable, as well as more detailed atomistic modeling of their structure.

1.07.4 Membrane Properties of Different Types of Norbornene Polymers

In assessment membrane applicability of different polymers, it is common to consider the so-called Robeson diagrams [55] (correlations of the permeability coefficients P_i and separation factors P_i/P_j) and the position of the data points of certain polymers in those diagrams. Norbornene polymers are now among the most explored groups of polymers.

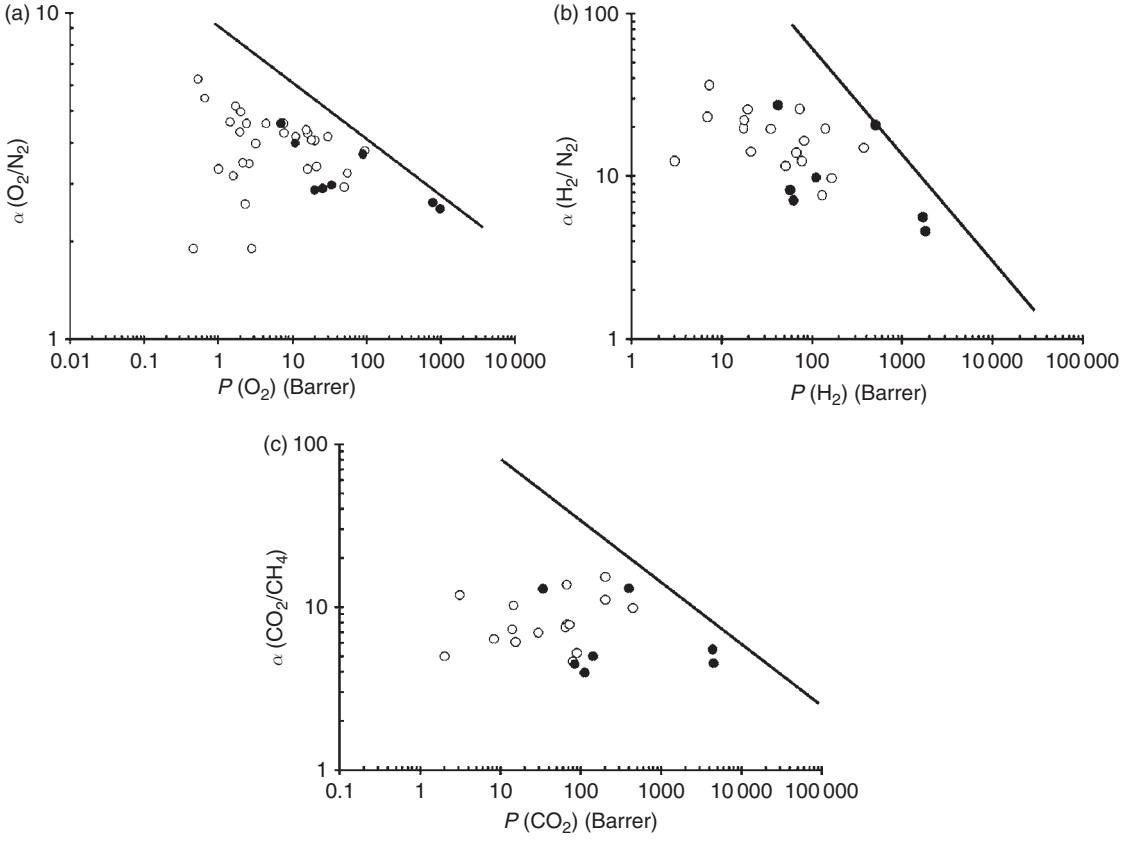

Figure 4 Robeson diagrams of MPNB and APNB for (a) O_2/N_2 pair; (b) H_2/N_2 pair; (c) CO_2/CH_4 pair. MPNB open points, APNB closed points.

On the one hand, this permitted elucidation of various effects of chemical structure of polymers onto their transport parameters and free volume, which was the subject of the previous section. On the other hand, an analysis of their permeability and permselectivity seems also to be meaningful. The Robeson diagrams for MPNB and APNB for several gas pairs are shown in **Figure 4**.

It is seen that the cloud of the data points of APNB is shifted to greater permeability as compared with that of MPNB. Interestingly, in the diagram for the CO_2/CH_4, no obvious tradeoff can be discerned: the increases in the *P* values are not accompanied by a reduction in selectivity. By contrast, an evident tradeoff can be observed for the O_2/N_2 gas pair. The data points for both types of norbornene polymers are located below the upper bound of Robeson, although in some cases they are rather close to this.

Bearing in mind the high permeability of $SiMe_3$-substituted APNB for *n*-butane and large selectivity of this polymer in separation of *n*-butane/methane pair as well as strong effects of the solubility coefficients on *P* of other APNBs, as has been mentioned earlier, it is of interest to consider the corresponding Robeson diagram for this gas pair. Although selectivity of separation of *n*-butane/methane was not reported for other norbornene polymers, some data are available for polymers of other classes of membrane materials: silicon-containing rubbers [56, 57], polyacetylenes [58], and high free-volume polymers charged with nanoparticles [59]. Analysis of such data indicates that APNB belongs to the most attractive materials, as can be judged by the combination of its $P(C_4)$ and $P(C_4)/P(C_1)$ values obtained in pure gas permeation experiments. If these results will be confirmed in mixed gas runs, this polymer can be considered as a material for separation of natural and associated petroleum gas.

1.07.5 Conclusions

Norbornene polymers now form one of the most explored groups of glassy polymers, potential materials for gas-separation membranes. An analysis of the structure–properties relationships provides much information on the effects of side groups, structure, and stiffness of the main chains that can be used in directed search for advanced membrane materials of other classes. Much more interesting results have been obtained for addition-type norbornene polymers. Here, significantly smaller number of the structures has been examined so far, so much is yet to be done. From the synthetic viewpoint, these polymers pose a bigger challenge: in contrast to easy and fast polymerization with ring opening due to high strain of norbornene ring, here the process of cyclo-olefin polymerization is often slow and sensitive to impurities in the monomers. By contrast, the already estimated transport parameters of some of the polymers of this group are very attractive. They indicate solubility-controlled permeation rather unusual in glassy polymers, so addition-type polymers of norbornene derivatives are promising candidates for separation of hydrocarbon gas mixtures. Further studies are needed to evaluate their value as actual materials for gas- and vapor-separation membranes.

References

[1] Finkelshtein, E., Bespalova, N., Portnykh, E., *et al. Polym. Sci.* **1993**, *35*, 589–593.
[2] Bondar, V., Kukharskii, Yu., Yampolskii, Yu., Finkelshtein, E., Makovetskii, K. *J. Polym. Sci. Part B: Polym. Phys.* **1993**, *31*, 1273–1283.
[3] Finkelshtein, E. Sh., Portnykh, E. B., Makovetskii, K. L., Ostrovskaya, I. Ya., Bespalova, N. B., Yampolskii, Yu. P. Synthesis of Membrane Materials by ROMP of Norbornenes. In *Metathesis Polymerization of Olefins and Polymerization of Alkynes*; Imamoglu, Y., Ed.; NATO ASI Series C; Kluwer: Dordrecht, 1998; Vol. 506, pp 189–199.
[4] Finkelshtein, E., Portnykh, E., Ushakov, N., Gringolts, M., Yampolskii, Yu. *Macromol. Chem. Phys.* **1997**, *198*, 1085–1090.
[5] Kawakami, Y., Toda, H., Higashino, M., Yamashita, Y. *Polym. J.* **1988**, *20*, 285–292.
[6] Yampolskii, Yu., Pinnau, I., Freeman, B. D., Eds. *Materials Science of Membranes for Gas and Vapor Separation*; Wiley: Chichester, 2006.
[7] Finkelshtein, E. Sh., Gringolts, M. L., Ushakov, N. V., Lakhtin, V. G., Soloviev, S. A., Yampol'skii, Yu. P. *Polymer* **2003**, *44*, 2843–2851.
[8] Yampolskii, Yu. P., Bespalova, N. B., Finkelshtein, E. Sh., Bondar, V. I., Popov, A. V. *Macromolecules* **1994**, *27*, 2872–2878.
[9] Tlenkopachev, M., Vargas, J., Almareaz-Giron, M. A., Lopez-Gonzales, M., Riande, E. *Macromolecules* **2005**, *38*, 2696–2703.
[10] Merkel, T. C., Bondar, V., Nagai, K., Freeman, B. D. *Macromolecules* **1999**, *32*, 370–374.
[11] Bondar, V. I., Freeman, B. D., Yampolskii, Yu. *Macromolecules* **1999**, *32*, 6163–6171.
[12] Song, W., Rossky, P. J., Maroncelly, M. *J. Chem. Phys.* **2003**, *119*, 9145–9162.
[13] Bondi, A. *Physical Properties of Molecular Crystals, Liquids, and Glasses*; Wiley: New York, 1968.
[14] Tao, J. *J. Chem. Phys.* **1972**, *56*, 5499–5510.
[15] Eldrup, M., Lightbody, D., Sherwood, J. N. *Chem. Phys.* **1981**, *63*, 51–58.
[16] Wasserman, A. M., Kovarsii, A. L. *Spin Probes and Labels in Physical Chemistry of Polymers*; Nauka: Moscow, 1986 (in Russian).
[17] Yampolskii, Y., Motyakin, M., Wasserman, A., *et al. Polymer* **1999**, *40*, 1745–1752.

[18] Yampolkii, Yu., Soloviev, S., Gringolts, M. *Polymer* **2004**, *45*, 6945–6952.
[19] Ivin, K. J., Laverty, D. T., O'Donnell, J. H., Rooney, J. J., Steward, C. *Macromol. Chem.* **1979**, *180*, 1989.
[20] Morisato, A., Miranda, N. R., Freeman, B. D., *et al. J. Appl. Polym. Sci.* **1993**, *49*, 2065–2074.
[21] Yampolskii, Yu., Finkelshtein, E., Makovetskii, K., *et al. Polym. Sci. A* **1996**, *38*, 959–963.
[22] Yampolskii, Yu., Finkelshtein, E., Makovetskii, K., Bondar, V., Shantarovich, V. *J. Appl. Polym. Sci.* **1996**, *62*, 349–357.
[23] Steinhauser, T., Koros, W. J. *J. Polym. Sci. Part B: Polym. Phys.* **1997**, *35*, 91–99.
[24] Diaz, K., Vargas, J., Del Castillo, L. F., Tlenkopatchev, M. A., Aguilar-Vega, M. *Macromol. Chem. Phys.* **2005**, *206*, 2316–2322.
[25] Contreras, A. P., Tlenkopatchev, M. A., del Mar Lopez-Gonzales, M., Riande, E. *Macromolecules* **2002**, *35*, 4677–4684.
[26] Vargas, J., Santiago, A. A., Tlenkopatchev, M. A. *Macromolecules* **2007**, *40*, 563–570.
[27] *Gas Permeation Parameters of Glassy Polymers.* Database, No. 3585, Informregistr RF, Moscow, 1998.
[28] Wang, Y.-C., Li, C.-L., Lee, K.-R., Liaw, D.-J. *J. Membr. Sci.* **2005**, *246*, 59–65.
[29] Lee, J. H., Park, J. W., Ko, J. M., Chang, Y. H., Cjoi, S. K. *Polym. Bull.* **1993**, *31*, 339.
[30] Finkelshtein, E., Portnykh, E., Ushakov, N., Greengolts, M., Fedorova, G., Plate, N. *Macromol.Chem. Rapid Commun.* **1994**, *15*, 2039.
[31] Kaminsky, W. *Macromol. Chem. Phys.* **1996**, *197*, 3907.
[32] Makovetskii, K. L. *Vysokomol. Soed. B* **1999**, *41*, 1525–1543.
[33] Janiak, Ch., Lassahn, P. *J. Mol. Catal. A: Chem.* **2001**, *166*, 193.
[34] Ahmed, S. PhD *Dissertation*, Georgia Institute of Technology, Atlanta, 1998.
[35] Barnes, D. A., Benedikt, G. M., Goddall, B. L., *et al. Macromolecules* **2003**, *36*, 2623–2632.
[36] Chung, W. J. PhD *Dissertation*, Georgia Technological Institute, Atlanta, 2003.
[37] Wilks, B. R., Chung, W. J., Ludovice, P. J., Rezac, M. R., Meakin, P., Hill, A. J. *J. Polym. Sci. Part B: Polym. Phys.* **2003**, *41*, 2185–2199.
[38] Wilks, B. R., Chung, W. J., Ludovice, P. J., Rezac, M. E., Meakin, P., Hill, A. J. *J. Polym. Sci. Part B: Polym. Phys.* **2006**, *44*, 215–233.
[39] Zhao, C., do Rosario Ribeiro, M., de Pinho, M. N., Subrahmanyam, V. S., Gil, C. L., de Lima, A. P. *Polymer* **2001**, *42*, 2455–2462.
[40] Finkelshtein, E., Makovetskii, K., Gringolts, M., *et al. Macromolecules* **2006**, *39*, 7022–7029.
[41] Yampolskii, Yu., Shishatskii, S., Shantorovich, V., *et al. J. Appl. Polym. Sci.* **1993**, *48*, 1935–1944.
[42] Korikov, A. PhD Thesis, TIPS, Moscow, 2001.
[43] Masuda, T., Isobe, E., Higashimura, T. *Macromolecules* **1985**, *18*, 841–845.
[44] Consolati, G., Genco, I., Pegoraro, M., Zanderighi, L. *J. Polym. Sci. Part B: Polym. Phys.* **1996**, *34*, 357–367.
[45] Alentiev, A., Yampolskii, Yu., Shantarovich, V., Nemser, S. M., Plate, N. *J. Membr. Sci.* **1997**, *126*, 123–132.
[46] Starannikova, L., Pilipenko, M., Belov, N., Yampolskii, Yu., Gringolts, M., Finkelshtein, E. *J. Membr. Sci.* **2008**, *323*, 134–143.
[47] Yampolskii, Yu., Kaliuzhnyi, N., Durgaryan, S. *Macromolecules* **1986**, *19*, 846–850.
[48] Dorkenoo, K. D., Pfromm, P. H., Rezac, M. E. *J. Polym. Sci. Part B: Polym. Phys.* **1998**, *36*, 797–803.
[49] Oh, S., Char, K. *Polym. Prepr.* **2007**, *97*, 803–804.
[50] Robeson, L. M., Burgoyne, W. F., Langsam, M., Savoca, A. C., Tien, C. F. *Polymer* **1994**, *35*, 4970–4978.
[51] Freeman, B., Pinnau, I. *Trends Polym. Sci.* **1997**, *5*, 167–173.
[52] Merkel, T. C., Bondar, V., Nagai, K., Freeman, B. D. *J. Polym. Sci. Part B: Polym. Phys.* **2000**, *38*, 273–296.
[53] Morisato, A., Pinnau, I. *J. Membr. Sci.* **1996**, *121*, 243–250.
[54] Makovetskii, K., Yampolskii, Yu. (unpublished results).
[55] Robeson, L. M. *J. Membr. Sci.* **1991**, *62*, 165–185.
[56] Robb, W. L. *Ann. N.Y. Acad. Sci.* **1968**, *146*, 119–137.
[57] Alentiev, A., Economou, I. G., Finkelshtein, E., *et al. Polymer* **2004**, *45*, 6933–6944.
[58] Pinnau, I., Morisato, A., He, Zh. *Macromolecules* **2004**, *37*, 2823–2828.
[59] Merkel, T. C., He, Zh., Pinnau, I., Freeman, B. D., Meakin, P., Hill, A. J. *Macromolecules* **2003**, *36*, 8406–8414.

Biographical Sketch

Yuri Yampolskii, professor, doctor of science (chemistry), and head of laboratory of membrane gas separation, A. V. Topchiev Institute of Petrochemical Synthesis (TIPS), Russian Academy of Sciences, graduated from the M. V. Lomonosov Moscow State University, Chemical Faculty, in 1961. Since 1961, he has been a staff member of TIPS. His first period of research (1961–75) focused on kinetics of hydrocarbon pyrolysis and free radical reactions. The results of these years are summarized in a monograph, Yu.P. Yampolskii 'Elementary processes and mechanism of hydrocarbon pyrolysis', Moscow, Khimia, 1990.

His current field of expertise and scientific interests include membrane science and technology, material science, physical chemistry of polymers, and thermodynamics of sorption.

He has authored/co-authored about 300 peer-reviewed publications including six books. He won the award of the government of Russian Federation in 1995 for research in membrane science and technology.

He is currently a member of the scientific councils in the Institute of Petrochemical Synthesis, an associated member of IUPAC; and a member of the editorial board of the journal *Separation and Purification Technology*, a Russian journal *Membrany*. He has presented plenary lectures on invitation at many international symposia, congresses, and conferences, including IUPAC, ICOM, Euromembranes, ACS meetings, NAMS, and IMSTEC.

1.08 Amorphous Perfluoropolymer Membranes

V Arcella, P Toniolo, M Avataneo, A Ghielmi, and G Marchionni, Solvay Solexis, Bollate (MI), Italy

Glossary

Cytop® Homopolymer of perfluorobutenylvinylether (Asahi glass).
Galden® Low-boiling perfluoropolyether fluids (Solvay Solexis).
Hyflon® AD Amorphous copolymer of tetrafluoroethylene and 2,2,4-trifluoro-5-trifluoromethoxy-1,3-dioxole (Solvay Solexis).
Hyflon® ion Copolymer of tetrafluoroethylene and short-side-chain sulfonyl vinyl ether (Solvay Solexis).
Nafion® Copolymer of tetrafluoroethylene and sulfonyl vinyl ether (Du Pont).
Teflon® AF Copolymer of tetrafluoroethylene and 2,2-bistrifluoromethyl-4,5-difluoro-1,3-dioxole (Du Pont).

Nomenclature

Polymers

PFA	copolymer of tetrafluoroethylene and perfluoropropyl vinyl ether
FEP	copolymer of tetrafluoroethylene and perfluoropropene

1.08.1 Introduction

Membranes based on fluoropolymer materials are of increasingly greater interest in industrial applications due to a remarkable combination of outstanding properties. In addition, amorphous perfluoropolymers, having a high solubility in fluorinated solvents, can be advantageously used for the preparation of membranes both by solution and by melt processing. The extremely high thermal and chemical resistance, associated with other unique physical properties (low dielectric constant, optical transparency, water and oil repellence, etc.), justifies their use in not only highly extreme but also profitable areas. With the sustained price rise of crude oil in the international market, fluorine products, that previously had a high cost, have started to show a satisfactory performance/price ratio and this explains why the demand for fluorinated products in the market is growing so drastically.

A recent study, published by the US National Academy of Sciences [1], indicates that carbon dioxide emissions from fossil-fuel burning and industrial processes have been accelerating at a global scale, with their growth rate increasing from 1% for the 1990–99 period to more than 3% for the 2000–04 period. The growth rate of CO_2 emissions is highest in rapidly developing economies, such as China; however, developed countries, with less than a sixth of the world's population, still contribute more than two-thirds of the total emissions of the greenhouse gas.

The complexity of this problem requires different actions in different areas, for example, the development of new sources and systems for energy supply, including the clean use of coal, advanced nuclear systems, and renewable energy systems. From an industrial point of view, the major contribution will probably be from the introduction of new

technological processes that can guarantee lower power consumption. Industrial separation of liquids and gases is a typical example of a high energy consuming process since traditional technologies are based on condensation, distillation, evaporation, and drying operations. On the contrary, membrane-separation processes are much more economical in terms of energy necessary for the operation, since they require only less energy consumption pressure systems. The simplicity of the membrane technology and the possibility of production of different membranes with different selectivity make them very promising for a wide range of applications. An important process in the topic of clean energy sources, a way for the production of hydrogen, is the steam reforming of carbon; however, this process requires the separation of a mixture of hydrogen and carbon dioxide and other gases. The membrane technology represents, in this case, a suitable and economical alternative to obtain pure hydrogen.

In the market, different types of membranes are available: ceramic (zeolite), metal (palladium, platinum, and nickel), glass, and organic polymeric membranes. Regarding organic polymeric membranes, the possibility to not only modify the separation mechanism (adsorption, diffusion, or a combination of both) but also regulate the selectivity by varying the porosity and the character of the membrane (hydrophilic or hydrophobic) makes them useful for a wide variety of potential applications. In highly extreme conditions, for example, reactive chemicals and high temperatures, fluorinated membranes are definitely the most valuable choice. In this chapter, a review of the developments in the field of amorphous perfluoropolymer membranes, with both hydrophobic and hydrophilic character, is presented and discussed. Hydrophobic membranes are often used in the filtration and separation of gases, since they allow gases and vapors, which have a low surface tension, to pass while excluding liquids, such as water, which have a higher surface tension. They are also finding application in emerging water treatment membrane processes, such as membrane distillation. Hydrophilic perfluoropolymer membranes are permeable to water and, for this reason, they can find application in electrochemical electrolyzers (chloro-alkali [2] and HCl electrolysis [3]), fuel cells (proton exchange membrane fuel cells [2] and direct methanol fuel cells [4]), energy storage and delivery devices, microfiltration [5], reverse osmosis and ultrafiltration [5], pervaporation [5], electrodialysis, diffusion dialysis [6], and membrane catalytic reactors [7].

1.08.2 Hydrophobic Perfluoropolymer Membranes

Hydrophobic amorphous perfluoropolymers can be obtained by the incorporation of bulky groups, for example, dioxolenic units, into perfluorinated chains with the aim of avoiding the crystallization and increasing the glass transition temperature (T_g) of the material. Amorphous perfluoropolymers have exceptional properties such as very good mechanical strength, high thermal and chemical resistance, low surface energies, low dielectric constant, low refractive indexes, and high optical transmission across a broad wavelength from ultraviolet (UV) to near infrared. As they are soluble in fluorinated solvents, amorphous perfluoropolymers can be easily processed both by melt (extrusion, compression, and injection molding) and by solution, such as diffusion-induced phase separation (DIPS), casting, spin coating, and dip coating. Spin coating is used to obtain an ultrathin, uniform thickness coating on a flat surface, whereas nonplanar surfaces can be coated by dipping.

A commercial hydrophobic amorphous perfluoropolymer is represented by Hyflon® AD (**Figure 1**),

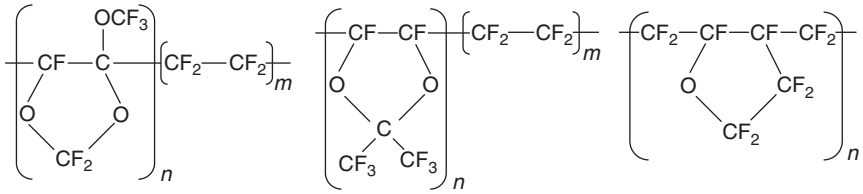

(a) Hyflon® AD (b) Teflon® AF (c) Cytop®

Figure 1 Structure of three commercial perfluorinated amorphous glassy polymers: (a) Hyflon® AD, (b) Teflon® AF, and (c) Cytop®.

which is produced by Solvay Solexis by microemulsion free radical polymerization of tetrafluoroethylene (TFE) and 2,2,4-trifluoro-5-trifluoromethoxy-1,3-dioxole (TTD).

Unlike other fluoropolymers such as polytetrafluoroethylene (PTFE), copolymer of tetrafluoroethylene and perfluoropropyl vinyl ether (PFA), and copolymer of tetrafluoroethylene and perfluoropropene (FEP) which are semicrystalline, Hyflon® AD is completely amorphous when the TTD molar content is in the range of 25–100%. Independent from the composition, Hyflon® AD grades show high glass transition temperatures (T_g), which are always above room temperature [8]; this can be explained by considering the presence of the cyclic units and their steric hindrance which severely limits chain motion. Increasing the TTD content of the copolymer concomitantly increases its T_g up 192 °C which corresponds to the T_g of the TTD homopolymer. **Table 1** shows the T_g values for Hyflon® AD grades with different TTD contents. In the same table, T_g values for two other amorphous glassy polymers commercially available from Du Pont (Teflon® AF) and Asahi Glass (Cytop®) are shown for comparison [9, 10]. The structures of these two polymers are also shown in **Figure 1**. In addition, for Teflon® AF, the permeability to gases increases with the T_g of the copolymer.

Table 1 Glass transition temperature (T_g) of amorphous perfluoropolymers at different compositions

	TFE	*TTD*	*PDD*	*BVE*	
Polymer	*(% mol)*				*T_g (°C)*
TTD homopolymer	NA	100	NA	NA	192
Hyflon® AD 60	40	60	NA	NA	125
Hyflon® AD 40	60	40	NA	NA	95
PDD homopolymer	NA	NA	100	NA	335
Teflon® AF 2400	13	NA	87	NA	240
Teflon® AF 1600	35	NA	65	NA	160
Cytop®	NA	NA	NA	100	108

NA, not available.

Teflon® AF is a copolymer of perfluoro-2,2 dimethyldioxole (PDD) with TFE, whereas Cytop® is homopolymer obtained by cyclopolymerization of perfluoro-butenylvinylether (BVE) characterized by a controlled alternating structure with a T_g equal to 108 °C.

The high solubilities in perfluorinated solvents associated with low solution viscosities make Hyflon® AD copolymers very attractive for solution processes membranes preparation [11]. Both features allow great flexibility in the selection of proper conditions for the preparation of membranes with different structures. Moreover, low solution viscosities imply greater ease of purification. This aspect is very important, since, in the polymer and polymeric solutions, it is often crucial to avoid the presence of both suspended and dissolved contaminants, such as dust, or dissolved organic molecules. In fact, this is of great importance for the preparation of composite membranes where the permselective layer is extremely thin and no defects are allowed.

Different procedures have been tuned to prepare various membrane typologies matching different application requirements. Examples of preparation methods and conditions for obtaining different membrane structures are presented in **Table 2**. In these examples, Galden® HT 110 and Galden® HT 55 are perfluoropolyether oils [12] with the following structure:

$$CF_3O\text{–}(CF_2\text{–}CF_2O)_n\text{–}(CF_2O)_m\text{–}CF_3$$

with normal boiling points equal to 110 and 55 °C, respectively.

Table 2 Examples of preparation procedures for different flat-sheet membrane types obtained from Hyflon® AD 60

Membrane type	*Symmetric*	*Asymmetric*	*Composite*
Method	Solution casting	Dry–wet phase inversion	Spin coating
Solvent	Galden® HT 110	Galden® HT 55	Perfluoroeptane
Solution concentration (by weight)	10%	10%	1%
Temperature for solvent elimination	50 °C	25 °C	25 °C
Nonsolvent	NA	*n*-perfluoropentane	NA
Temperature of coagulation bath	NA	12 °C	NA
Support	Glass	Glass	PVDF

NA, not available.

Flat-sheet porous and nonporous symmetric membranes can be obtained by following the evaporation method [13]. Flat-sheet symmetric membranes can be prepared by following the dry–wet phase-inversion method, with the Galden® HT as solvent and *n*-pentane as nonsolvent [13, 14]. Both the membranes can be prepared using a Braive Instruments knife to cast the polymeric film on glass plates at different initial thicknesses and coagulation bath temperatures. Flat-sheet laboratory porous and nonporous composite membranes of 1-μm-thick films on polyvinylidene fluoride (PVDF) inert supports were prepared by the spin-coating process [13, 14].

Hyflon® AD copolymers are characterized by good values of permeability and selectivity to gases and this makes them suitable for gas-separation processes. For example, asymmetric Hyflon® AD membranes, obtainable by dry–wet inversion phase, show selectivity values for O_2/N_2 and CO_2/N_2 around 3 and 8, respectively, in the pressure range of 5–7.5 bar in the steady state. The permeance values of these asymmetric membranes of N_2, CO_2, and O_2 are presented in **Table 3**.

Permeability and selectivity values obtained from composite Hyflon® AD membranes are in good agreement with values obtained from asymmetric membranes. Permeance values of N_2, CO_2, O_2, H_2, and CH_4 of composite membranes are presented in **Table 4** (1-μm-thick Hyflon® AD 60 on a PVDF support). Since the permselective Hyflon® AD layer is, in this case, 1 μm thick, these permeances expressed in graphics processing unit (GPU) coincide numerically with permeabilities expressed in Barrer. Permeability values for Teflon® AF are also presented for comparison in **Table 4** [9], together with the T_g values of the different polymers.

In addition, the permeation data for various gases for symmetric self-standing Hyflon® AD membranes are presented in **Table 5**.

Examination of these data indicates that, independently from the fluoropolymer type and gas, a linear correlation exists between permeability and the T_g [14]. In this respect, gas permeation is often attributed to the presence of voids at the molecular scale and to their size distribution. Amorphous perfluoropolymers show an experimental density lower than that theoretically expected [9, 14]. Considering the chemical structure of amorphous perfluoropolymers, the low values of the experimental density can be ascribed, at least qualitatively, to the different chain packing due to the low chain mobility and steric hindrance given by the large dioxole groups. In other words, the high chain stiffness leads to difficulties in the close packing of chain segments and thus to nanovoids. Since in amorphous perfluoropolymers their T_g is mainly related to the macromolecular chain stiffness, which controls the dimension of nanosize holes, it follows that increasing T_g increases gas permeation. The important effect of the dimension of nanosize holes on permeation is supported by the above permeation–T_g correlation.

Symmetric porous membranes with pore size between 30 and 80 nm have shown no permeation to water at pressures as high as 10 bar. On the other hand, high permeation to gases, such as O_2, N_2, and

Table 3 Gas permeances of Hyflon® AD 60 asymmetric membranes as a function of differential pressure (1 GPU = 10^{-6} cm^3 (STP) cm^{-2} s cmHg)

	Permeance (GPU)		
Δp (bar)	*N_2*	*CO_2*	*O_2*
1		15.3	6
5	1.7	14	5.3
7.5	1.7	14.7	5.3
10	1.8	15.3	NA

NA, not available.

Table 4 Gas permeability data (expressed in Barrer) of amorphous perfluoropolymers with different glass transition temperatures

Polymer	*T_g (°C)*	*P (N_2)*	*P (CO_2)*	*P (O_2)*	*P (H_2)*	*P (CH_4)*
Hyflon® AD 60	125	17	124	51	202	8
Hyflon® AD 40	95	8	64	26	NA	NA
Teflon® AF 2400	240	490	2800	990	2200	340
Teflon® AF 1600	160	NA	NA	340	NA	NA

NA, not available.

Table 5 Gas permeability for symmetric membranes of Hyflon® AD 40 and Hyflon® AD 60 at 35 °C and 50 psig

Gas	*Critical volume ($cm^3\,mol^{-1}$)*	*Permeability (10^{-10} cm^3(STP) cm cm^{-2} s cmHg) Hyflon® AD 40*	*Permeability (10^{-10} cm^3(STP) cm cm^{-2} s cmHg) Hyflon® AD 60*
He	57.3	211	387
H_2	65.0	83	182
O_2	73.4	25	57
Ar	74.6	15	33
N_2	88.6	8	20
CO_2	92.9	53	128
CH_4	99.4	4	10
NF_3	119.0	3	6
C_2H_4	129.1	3	6
CF_4	140.0	0.56	0.9
C_2H_6	146.7	2.5	3.3
C_3H_6	181.0	NA	4.3
C_3H_8	200.8	0.94	1.1

NA, not available.

CO_2, was observed. Composite membranes prepared by casting the polymeric solution (1% weight) on PVDF supports have shown unique combination of features:

- excellent organophobicity and hydrophobicity;
- gas fluxes higher than many commercial gas-separation membranes; and
- high chemical/wear resistance.

Contact angle measurement to distilled water compared with experimental results obtained on self-supported membranes and other commercial membranes are presented in **Table 6**. Contact angles of 120° and above for the amorphous perfluoropolymer membranes demonstrate the high hydrophobic character of these membranes.

To test the organophobic character of the membranes, contact angles to hexadecane was measured. In this case, the contact angle is around 65°, which is a high value compared to other values reported in the literature (see **Table 7**). This result confirms the strong organophobicity of the membranes, which corresponds to excellent fouling resistance and inertness.

Table 6 Contact angle to water for different membranes

Membrane polymer	*Contact angle to H_2O*
PMMA	76
PEEK-WC-NO_2	80
PES	82
PVDF	90
PE	96
PTFE	118
HYFLON® AD 60	120
HYFLON® AD 60 on PVDF	122

Table 7 Contact angle to hexadecane for different membranes

Membrane polymer	*Contact angle to $C_{16}H_{34}$*
PS	1
PTFE	39
CMS-7 on PP	57
HYFLON® AD 60	60
CMS-7 on PS	63
HYFLON® AD 60 on PVDF	65

Oxygen permeation data through Hyflon® AD porous composite membranes in comparison to other commercial gas-separation membranes are presented in **Table 8**.

Table 8 Oxygen permeation data through Hyflon® AD composite membranes in comparison to commercial gas separation membranes

Membrane polymer	*Permeance to O_2 (GPU)*
Generon polycarbonate	7
Permea polysulfone	15
Dow 4-methylpentene-1	90
Ethyl cellulose	100
Gore-TEX	350 (5 bar, 16 °C)
Silicone rubber	500
HYFLON® AD 60 on PVDF	700 (5 bar, 27 °C)

1.08.3 Hydrophylic Perfluoropolymer Membranes

Perfluorinated polymers with sulfonic pendant groups are the basic materials used for the preparation of hydrophilic membranes. These polymers are generally obtained in a three-step process:

1. free radical copolymerization of TFE and a sulfonyl fluoride vinyl ether (SFVE), whose general formula can be indicated as CF_2=CF-OR_f-SO_2F (where R_f is a perfluoroalkyl a perfluoro oxy alkyl unit);
2. reaction with an alkaline aqueous solutions at medium temperature (70–80 °C) to convert the $-SO_2F$ group into $-SO_3X$, where X is a metal cation; and
3. treatment with a strong acid solution to convert the $-SO_3X$ into $-SO_3H$ – the commonly used strong acids are H_2SO_4, HCl, and HNO_3.

In the second step, the transformation of the polymer into an ionomer, that is, an ion-containing polymer, leads to a dramatic change of the physicochemical properties of these materials due to the formation of ionic regions (generally referred to as clusters) [15]. As a consequence, ionomers consist of an amorphous phase, an ionic phase and, if the TFE content is relatively high, a crystalline phase.

Among the sulfonic perfluorinated polymers, Nafion® (Du Pont), a copolymer of TFE and an SFVE of formula CF_2=CF–$OCF_2CF(CF_3)OCF_2CF_2SO_2F$, is the most extensively studied and used. It was developed in the late 1960s as a polymer electrolyte for fuel cells designed for National Aeronautics and Space Administration (NASA) spacecraft missions. Since then, Nafion® and polymers of the same family (Aciplex® from Asahi Chemical and Flemion® from Asahi Glass) have found wide application in the chloro-alkali industry, due to their very high chemical inertness. They are also called long-side-chain (LSC) polymers[15–17] because they contain long pendant group carrying the ionic functionality.

Starting from the 1980s, increasing efforts were dedicated to the development of a short-side-chain (SSC) ionomer [18], obtained by copolymerization of TFE and CF_2=CF–$OCF_2CF_2SO_2F$, with the aim of improving the power output and the working temperature in the fuel cells. In particular, Solvay Solexis has applied its proprietary fluorovinylether process for the production of the SSC monomer at the industrial scale with a relatively simple process (**Figure 2**).

The polymerization of TFE and the SSC monomer is carried out by free radical polymerization taking advantage of the Solvay Solexis proprietary microemulsion polymerization process [19]. This technology, broadly applied to the polymerization of other Solvay Solexis fluoropolymers, is able to give very high polymerization kinetics and high-molecular-weight polymers with accurate control of the molecular structure. The polymer obtained is named as Hyflon® ion and its structure is shown in **Figure 3** both in the $-SO_2F$ and in the $-SO_3H$ form.

When the molar ratio TFE/SFVE in the polymer is approximately lower than 4, that is, when the SFVE molar content is higher than about 20%, the polymer is completely amorphous. On the contrary, at higher value of TFE/SFVE, a semicrystalline structure, due to the aggregation of the PTFE sequences, is observed.

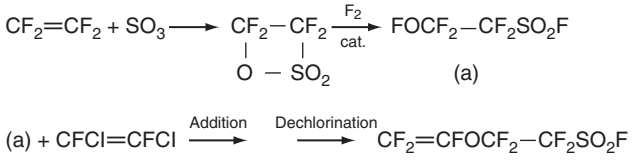

Figure 2 Solvay Solexis route for the synthesis of the SSC sulfonylfluoridevinylether monomer.

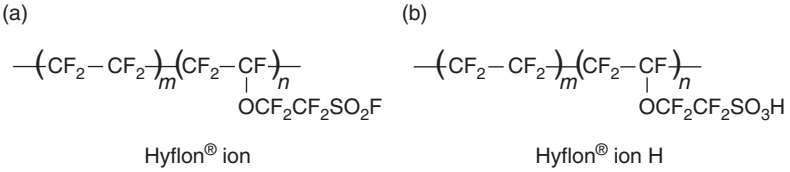

Figure 3 Structure of (a) Hyflon® ion and (b) Hyflon® ion H.

The glass transition temperature of Hyflon® ion is a function of polymer composition and decreases from about 50 to 5 °C for SFVE contents increasing from 10% to 30% (molar) when the polymer is in its precursor (i.e., SO_2F) form. Therefore, amorphous Hyflon® ion polymer precursors are rubbers at room temperature and can be dissolved in a variety of perfluorinated (such as Galden®) [12] or partially fluorinated solvents (such as H-Galden®) [20]. At high TFE content, when the crystalline phase appears, these copolymers become scarcely soluble in any solvent. In this case, films can be prepared by taking advantage of the melt processability of the polymer.

The thermal stability of Hyflon® ion polymers is very high due to its perfluorinated nature. Thermogravimetric analysis (TGA) shows 1% weight losses at temperatures as high as 420 °C (**Figure 4**).

Amorphous Hyflon® ion membranes are suitable for the use in separation processes [21], for example, in microfiltration, ultrafiltration, and iperfiltration of aqueous solutions, especially where aggressive reactants require a chemically inert membrane. High wettability required in these applications is guaranteed by the ionic nature of the polymer. These amorphous membranes can also find applications as proton exchangers in fuel cells or in membrane reactors [22]. Indeed, it is known that one of the most important problems for the good functioning of fuel cells is the membrane drying at the anode side and the excessive hydration from the cathode side. A better permeability of the membrane to water allows to limit these drawbacks and to obtain a lower resistance to proton transport and, as a result, a higher conductivity of the membrane in the cells. In all of these applications, semicrystalline ionomer membranes do not perform as well due to the lower water permeability.

More specifically, in applications such as pervaporation processes used to dehydrate wet gases, Hyflon® ion ionomers can be coated on microporous substrates to obtain ultrahigh wettability membranes which exhibit high water flux properties and low gas permeability, particularly when they are in the wet state. The microporous inert support is generally a fluorinated polymer, for example, bistretched PTFE. The technology described in the literature [21] can allow the incorporation of different amounts of ionomer to obtain membranes of different porosities. **Figure 5** shows the surface structure of a Hyflon® ion membrane obtained by this method starting from a bistretched PTFE substrate shown in **Figure 6**.

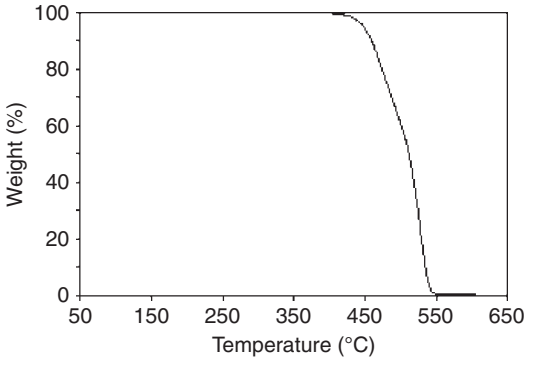

Figure 4 Dynamic TGA (in air at 10 °C min^{-1}) of a Hyflon® ion of EW = 900 g mol^{-1}.

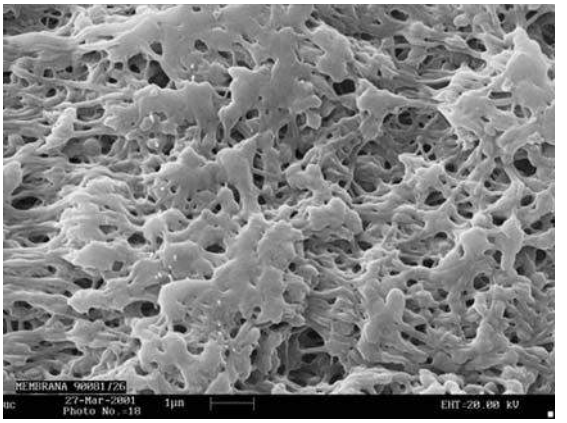

Figure 5 Hyflon® ion membrane deposited on a PTFE substrate.

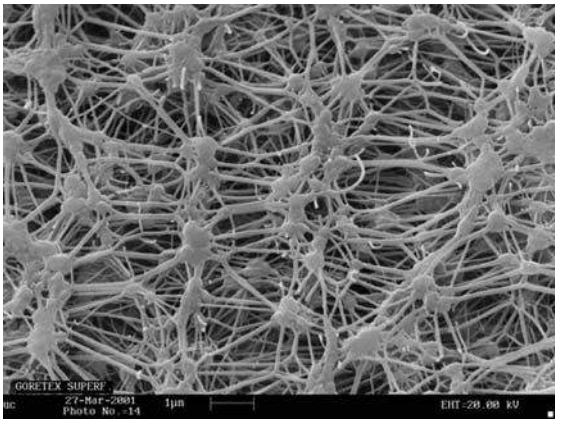

Figure 6 PTFE substrate used for the preparation of the membrane with Hyflon® ion.

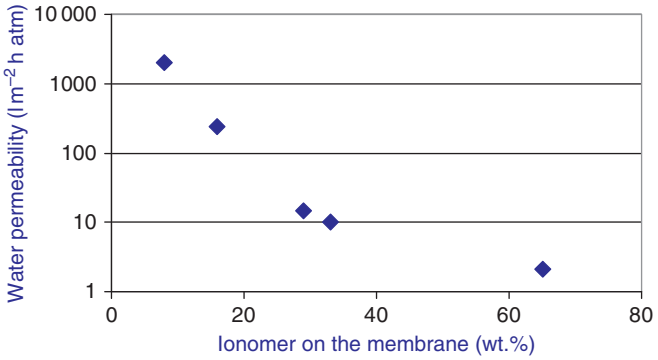

Figure 7 Permeability of water through an amorphous membrane of Hyflon® ion ($m/n = 3$).

Depending on the type of filtration, it is possible to control the membrane porosity by regulating the amount of ionomer deposited on the support. For example, membranes with a high permeability suitable for microfiltration are obtained with an amount of deposited ionomer from 0.5% to 10% by weight (referred to the system support and membrane). On the contrary, when the amount of ionomer is higher than 30% by weight, the pores are almost completely occluded and these membranes can be suitable for iperfiltration processes. Therefore, an entire range of hydrophilic membranes, particularly useful in water treatments, can be obtained.

In **Figure 7**, the permeability of water through the amorphous membrane (Hyflon® ion with TFE/SFVE = 3) is reported as a function of the ionomer content on the membrane.

The membrane porosity for liquid flow and the occlusion of gases can also be modified by cross-linking of the ionomer [21, 22]. This can be achieved either by an ionic or by a radical route, by introducing specific curing comonomers during the Hyflon® ion polymerization. Cross-linking is normally performed after the Hyflon® ion SO_2F precursor is deposited on the inert support and before the hydrolysis steps. The level of cross-linking allows to control the amount of ionomer on the membrane at the end of the fabrication process, and thus both the permeability and the stability of the ionomer coating on the membrane. If the ionomer is not cross-linked, high-temperature conditions or exposure to swelling chemicals (e.g., polar organic solvents) can lead to leaching out of the amorphous ionomer in time from the membrane in use. This can result in a loss of wettability of the membrane, eventually leading to local or diffuse dewetting, and possible pollution of the filtrate.

References

[1] Raupach, M. R., Marland, G., Ciais, P., Le Quere, C., Canadell, J. G.,Klepper, G., Field, C. B. Global and Regional Drivers of Accelerating CO_2 Emissions, 2007, http://www.pnas.org/cgi/reprint/0700609104v1 (accessed November 2009).
[2] Eisenberg, A., Yaeger, H. L., Eds. *Perfluorinated Ionomer Membranes*; ACS Symposium Series 180; ACS: Washington, DC, 1982.
[3] Trainham, J. A., III, *et al.*, inventors; E. I. Du Pont de Nemours and Company, assignee. 1995. Electrochemical Conversion of Anhydrous Hydrogen Halide to Halogen Gas Using a Cation-Transporting Membrane. US Pat. 5,411,641, 22 November 1993.
[4] Yeager, H. L., Gronowski, A. A. Membrane Applications. In *Ionomers: Synthesis, Structure, Properties and Applications*; Tant, M. R., Mauritz, K. A., Wilkes, G. L., Eds.; Blackie Academic and Professional: London, 1997; pp 333–164.
[5] Moya, W., inventor; Millipore Corporation, assignee. 2001. Surface Modified Polymeric Substrate and Process. US Pat. 6,179,132, 13 March 1998.
[6] Naylor, T. deV. *Rapra Rev. Rep.* **1996**, *8*(5), 39–45.
[7] Olah, G. A., Iyer, P. S., Prakash, G. K. S. *Synthesis* **1986**, *7*, 513–531.
[8] Navarrini, W., Tortelli, V., Colaianna, P., Abusleme, J., inventors; Ausimont S.p.A., assignee. 1997. Eur. Pat. Specificat. 0,633,257 B1, Date of application: 24 June 1994.
[9] Resnick, P. R., Buck, W. H. Teflon® AF Amorphous Fluoropolymers. In *Modern Fluoropolymers. High Performance Polymers for Diverse Applications*; Scheirs, J., Ed.; Wiley: Chichester, UK, 1997; pp 397–419.
[10] Sugiyama, N. Perfluoropolymers Obtained by Cyclopolymerization and Their Applications. In *Modern Fluoropolymers*. In *High Performance Polymers for Diverse Applications*; Scheirs, J., Ed.; Wiley: Chichester, UK, 1997; pp 541–556.
[11] Colaianna, P., Brinati, G, Arcella, V. inventors; Ausimont S.p.A., assignee. 1999. US Pat. 5,883,177, Date of application: 21 April 21 1997.
[12] Sianesi, D., Marchionni, G., De Pasquale, R. J. Perfluoropolyethers (PFPEs) from Perfluoroolefin Photooxidation: Fomblin® and Galden® Fluids. In *Organofluorine Chemistry, Principles and Commercial Applications*; Banks, R. E., Smart, B. E., Tatlow, J. C., Eds.; Plenum: New York, 1994; pp 431–461.
[13] Gordano, A., *et al. Korean Membr. J.* **1999**, *1*(1), 50–58.

[14] Arcella, V., Colaianna, P., Maccone, P., *et al. J. Membr. Sci.* **1999**, *163*, 203–209.
[15] Tant, M. R., Darst, K. P., Lee, K. D., Martin, C. W. Structure and Properties of Short-Side-Chain Perfluorosulfonate Ionomers. In *Multiphase Polymers: Blends and Ionomers*, Utracki, L. A., Weiss, R. A., Eds.; ACS Symposium Series 395; ACS: Washington, DC, 1989; pp 370–400.
[16] Fielding, H. C. Fluoropolymer Membranes. In *Fluoropolymers '92. Synthesis, Properties and Commercial Applications*: *Paper 5,* UMIST, Manchester, 6–8 January.
[17] Heitner-Wirguin, C. *J. Membr. Sci.* **1996**, *120*, 1–33.
[18] Prater, K. *J. Power Sources* **1990**, *29*, 239–250.
[19] Apostolo, M. Arcella, V. inventors; Ausimont S.p.A., assignee. 2002. Eur. Pat. Applicat. 1,172,382 A2, Date of application: 19 June 2001.
[20] Marchionni, G., Bassi, M., Fontana, G., Maccone, P., Ajroldi, G. *J. Fluor. Chem.* **1999**, *98*, 41–54.
[21] Arcella, V., Ghielmi, A. Porous Hydrophilic Membranes. US Pat. 6,902,676 B2, 7 June 2005.
[22] Arcella, V., Ghielmi, A. Porous Hydrophilic Membranes. US Pat. 6,896,777 B2, 24 May 2005.

Biographical Sketches

Vincenzo Arcella received his doctorate degree in chemical engineering from the University of Naples in 1977. During 1978–81, he did his research on fluid dynamics and polymerization engineering at the Donegani Research Institute of the Montedison Group. During 1982–86, he was responsible for the Fluoropolymers Process Development group at the Research Center of Montefluos S.p.A (Montedison Group).

During1987–92, he was responsible for the research and development of fluoroelastomers at Ausimont S.p.A. (Montedison Group). He worked on polymerization and posttreatment processes in 1990 and 1992 as a contract professor at Padua University.

During 1993–99, he was involved in the research and development of fluoroelastomers and melt-processable fluoropolymers at Ausimont S.p.A. Since January 2000, he has been engaged in doing the research on polytetrafluoroethylene (PTFE).

In 2001, he received a *Laurea honoris causa* in science conferred by the Saint Petersburg State Institute of Technology (Russia). He is currently the R&T director at Solvay Solexis S.p.A.

Paolo Toniolo graduated in chemical science from the University of Padua in 2000. From 2001 to 2004, he was a researcher in the Vibrational Spectroscopy Lab at the Research Center of Solvay Solexis S.p.A. Between 2004 and 2005, he was a researcher in the Nuclear Magnetic Resonance Lab. Since 2005, he has been working in the Innovative Fluoromaterials group as a project leader who deals with renewable energies and sustainable development.

Marco Avataneo graduated in 2000 in industrial chemistry from the University of Turin, with a specialization in macromolecular chemistry. Between 2001 and 2008, he worked as a researcher in the field of perfluoropolyethers and oxyradicals chemistry at the Research Center of Solvay Solexis S.p.A. Currently, he is involved in the Innovative Fluoromaterials group, whose research activities are focused on fluorinated and perfluorinated materials.

Alessandro Ghielmi graduated in 1995 in chemical engineering, with specialization in process design, from the Politechnical School of Milano. In 1999, he received his PhD in chemical engineering from ETH, Zurich, Switzerland, for a thesis pertaining to the field of polymer reaction engineering (modeling of polymerization processes) under the supervision of Prof. M. Morbidelli.

Since 1999, he has been working, at the Research Center of Solvay Solexis, on the development of perfluorinated ion-exchange polymers from polymerization to membranes and membrane electrode assemblies (MEAs), with special focus on fuel-cell application. He has contributed to the field of both polymerization modeling and fuel-cell ionomers with many scientific papers and patents.

He is currently responsible for the research and development of fuel-cell membranes in Solvay Solexis.

Giuseppe Marchionni graduated in industrial chemistry from the University of Bologna in 1979. From 1982, he worked at the Research Center of Montefluos S.p.A. (successively Solvay Solexis S.p.A) in the field of fluorinated products, focusing his activity on the industrial development of the new processes and products. Since 2008, he has been responsible for the Basic Inter-BU Research area, coordinating three research groups: oxyradical chemistry, monomers and intermediates, and innovative fluoromaterials. He is the author of nearly 60 scientific papers and holds 60 patents in the field of fluorine chemistry.

1.09 Plasma Membranes

S Roualdes, V Rouessac, and J Durand, Université Montpellier, Montpellier, France

Glossary

Cobb test A method for measuring the water absorption of sized paperboard, by determining the mass of water absorbed through one surface under a definite temperature, pressure, and time.

Corona discharge A type of localized discharge that results from high, nonuniform electric fields at atmospheric pressure, accompanied by ionization of surrounding atmosphere.

Debye length The scale over which mobile charge carriers (e.g., electrons) screen out electric fields in plasmas and other conductors. In other words, the Debye length is the distance over which significant charge separation can occur.

Duty cycle The ratio of run time to the total cycle time.

Electron cyclotron resonance The phenomenon involving electrons in a static and uniform magnetic

field moving in a circle due to the Lorentz force. The circular motion may be superimposed with a uniform axial motion, resulting in a helix, or with a uniform motion perpendicular to the field, for example, in the presence of an electrical or gravitational field, resulting in a cycloid.
Faraday cage A conductive enclosure that blocks out external static electromagnetic fields.
Free volume The ratio of empty space between molecular chains to the total volume of the material.
Ionization degree The ratio of density of ionized species to the total density of species in a gaseous phase.
Magnetron A diode vacuum tube in which the flow of electrons from a central cathode to a cylindrical anode is controlled by crossed magnetic and electric fields; used mainly in microwave oscillators.
Mean free path The average distance traveled by a particle between collisions with other particles.
Sputtering The physical process whereby atoms in a solid target material are ejected into the gas phase due to bombardment of the material by energetic ions (from a plasma). The ejected atoms then deposit onto a nearby substrate surface to form a coating.

1.09.1 Introduction

Plasma processes were initially developed for microelectronics in the 1950s. They represent a clean (producing few or no effluents) and also extremely flexible technology whose basic equipment, well adapted to automation, makes it possible to achieve goals as varied as possible in terms of their specific properties of use; their costs of operation are moreover relatively weak. Based on these advantages, they are used today in many fields of materials chemistry (particularly in the field of membranes) even if their industrialization is not very developed, because of the high cost of the equipment necessary for their implementation and due to a certain conservatism of the industrialists reticent to introduce this new technology, however promising.

The first part of this chapter presents basic aspects of plasma processes and transport phenomena in plasma membranes in relation to their structural properties. The parts following further deal with state of the art on plasma membranes in their main fields of application. Only the applications related to active membranes providing the transport of specific species are presented, that is, gas or liquid separation (particularly in environment matters), energy production devices, and sensors. Applications using membranes as barrier materials (especially packaging), for which the use of plasma processes is not so innovative, are not developed here. For each field of application, particular attention is paid to the specificities of plasma membranes in terms of structural and transport properties in comparison with more conventional membranes. The last part of this chapter is devoted to recent studies and prospects for innovating porous plasma membranes.

1.09.2 Basic Aspects of Plasma Processes and Related Materials

1.09.2.1 Fundamentals of Plasmas and Plasma Chemistry

Defined by Crookes in 1879 as the fourth state of matter, plasma is a partially ionized and overall neutral medium generated by the application of an electric field to a gas phase at low pressure (<10 Torr) [1–4]. The energy of the applied electric field is transferred to free electrons which collide with the gas molecules. Such inelastic impacts make the electrons gain enough energy (up to 50 eV) to induce the ionization of gas molecules. Such ionized species (acquiring energies typically in the range of 0–2 eV) initiate a large number of complex reactions (ionization, excitation, neutralization, recombination, de-excitation, etc.) constituting what is called a glow discharge. A glow discharge implies a large variety of species: electrons, negative and positive ions, radicals, neutral atoms and molecules, and also photons (emitted by radiative de-excitation) whose mixture constitutes the plasma state.

Plasma is essentially characterized by its energy and electronic density. Depending on the values of both the microscopic parameters, different kinds of natural or artificial plasmas can be distinguished and classified into two categories: hot plasmas and cold

plasmas. Hot plasmas are generated by an arc discharge at a pressure equal to or even higher than the atmospheric one. Highly widespread in nature (in the form of comets, galaxies, flashes, lightning), they are characterized by a high frequency of collision between electrons and gas molecules and a high gas temperature reaching many thousands of degrees. Artificial plasmas, generated by continued or alternating discharge at low frequency (25–450 kHz), radio frequency (RF) (1–500 MHz), or microwave frequency (500 MHz to some GHz) at rather low pressure (10^{-2}–10 Torr), are cold plasmas. Cold plasmas are characterized by energy and electronic density equal to 1–10 eV and 10^{10} cm^{-3}, respectively. Their ionization degree is lower than 10^{-3} so that the gas phase is mainly made up of neutral species in an excited state (radicals). A characteristic of these plasmas is the absence of thermodynamic balance between the electronic temperature (several thousands of degrees) and that of the gas (near to the ambient). Cold plasmas are generally achieved by means of two types of reactors: (1) a tubular-type reactor with an external coil or ring electrodes for excitation by RF discharge and (2) a bell-jar-type reactor with internal parallel-plate metallic electrodes. In the latter case, a low-frequency or RF voltage for discharge excitation is generally used. Microwave discharges have become widely used as well, with various methods of application of microwave energy (the most frequent is the multimode cavity also called microwave oven mode). Magnetic fields have also been employed to assist the plasma mode: electron cyclotron resonance discharge and planar or cylindrical magnetrons.

The interaction between cold plasma and a material placed within it (substrate) results in several types of effects occurring simultaneously or consecutively. Four major effects are generally distinguished:

1. *Etching*. This occurs by a combination of reactive species of the gas phase with atoms or groups of atoms of the substrate leading to the creation of active sites on the surface of the substrate (ablation of surface) and to the formation of volatile species which diffuse in the gas phase.
2. *Functionalization*. It occurs by the fixing of reactive species of the gas phase on active sites of the surface of the substrate.
3. *Crosslinking* (in the case of a polymeric substrate). This occurs due to the opening (under the action of the reactive species of plasma) of the bonds between atoms of the surface of the substrate allowing them to reorganize (by bridging between the macromolecular chains).
4. *Formation of a deposit on the surface of the substrate*. This occurs by a recombination of the reactive species adsorbed on the surface of the substrate.

The prevalence of one of these effects on the others is directly related to the nature of the gas subjected to the electric discharge. In the case of plasmas involving noncondensable gases (monoatomic or diatomic gases), the three principal effects are etching, functionalization, and crosslinking. The substrate undergoes only surface modifications; the related plasma processes are referred to as plasma treatments. In the case of plasmas involving condensable gases (organic, inorganic, or organometallic compounds), the dominating effect is the formation, on the surface of the substrate, of a deposit made up of a three-dimensional matrix formed from fragments of the reagent gas combined in a random way. The related plasma process is called plasma-enhanced chemical vapor deposition (PECVD) or plasma polymerization in the particular case of gases of organic compounds.

The nature of the gas subjected to the electric discharge is not the only plasma parameter. Many other parameters have a high influence on the effects undergone by the substrate:

1. *Geometrical nature*. The size and shape of the reactor chamber, location, nature, and morphology of the electrodes, localization of the gas(es) inlet(s), and pumping outlet;
2. *Phenomenological nature*. The frequency of the electric discharge (which controls the kinetic energy of the charged species), power of the electric discharge (which controls the degree of fragmentation of the species), gas(es) reactivity and flow rate(s) (controlling the residence time of the species in the plasma), ratio of different gases, working gas pressure (which controls the residence time as well as the average energy of the electrons, the mean free path of the species, and the density of the gas), and temperature of the substrate (controlling the mobility, the absorption, and the desorption of the reactive species on the surface of the substrate).

The manufacture of a tailor-made material requires the rigorous control of all these parameters.

1.09.2.2 Plasma Treatments

Plasma treatments are mainly used for the surface modification of polymers or metals. The predominant surface effect is directly related to the nature of the gas subjected to the electric discharge. Chemically reactive gases, such as ammonia (NH_3), nitrogen (N_2), oxygen (O_2), carbon dioxide (CO_2), water vapor (H_2O), tetrafluoromethane (CF_4), etc., especially, support the reactions of functionalization: grafting of amine-type or amide-type functional groups in the case of NH_3 or N_2, grafting of peroxide or hydroxide functions in the case of O_2 or H_2O, grafting of C=O, C–OH, and C(=O)OH functions in the case of CO_2, and grafting of CF_x functions in the case of CF_4. Hydrogen (H_2) gas primarily supports the phenomenon of crosslinking. Chemically inert gases, such as rare gases (argon (Ar) and helium (He)), mainly support the effect of etching.

In the field of membranes, the implementation of plasma treatments has grown rapidly in the last decade. Plasma treatments have been especially applied for improving the wettability, printability, adhesion, or biocompatibility of conventional polymer membranes, modulating their transport properties (by changing the hydrophilic/hydrophobic balance, providing the grafting of specific functional groups, or crosslinking the surface chains) or reinforcing their mechanical, thermal, and chemical stability (essentially under the effect of crosslinking). However, it is generally known that, in the case of some specific polymer membranes, the effect gained in such modifications may disappear or significantly diminish during storage. Moreover, plasma treatments can sometimes alter the physico-chemical properties of material, particularly polymer surfaces. An efficient way to overcome this limitation is the implementation of a process named plasma-induced graft polymerization or plasma grafting. In this process, plasma is used only to create on the polymer surface functionalities that are able to initiate conventional polymerization of monomers containing multiple bonds. The reaction may be carried out in two ways: in the vapor phase of monomer or in solution. Its principle is the following. Plasma treatments can induce radical formation on polymer surface through ion bombardment and ultraviolet (UV) radiation. The radicals formed on the surface of the treated polymers can be very stable in vacuum but react rapidly on exposure to a reactive gas. So if the vapor phase of an unsaturated monomer is introduced into a plasma reactor just after the surface treatment of a polymer substrate, the radicals formed on the surface of the polymer substrate immediately cause the polymerization of the monomer. The process can also be implemented in solution. In this case, the polymer substrate is released from the reactor after the plasma treatment and then exposed to atmosphere. In the presence of oxygen or air, peroxides and hydroperoxides are created on the polymer surface; such functions may initiate the polymerization of a desired monomer in solution. In both cases (vapor-phase route or solution route), grafting density and the length of grafted brush can be regulated to some extent by plasma and grafting parameters. One primary advantage of this technique is the ability to modify surface properties of the polymer substrates permanently without affecting the bulk mechanical and chemical properties.

1.09.2.3 PECVD or Plasma Polymerization

1.09.2.3.1 Deposition mechanism

The PECVD or plasma polymerization process is mainly used in the preparation of inorganic, hybrid, or polymer-like thin layers. In the field of membranes, most of the plasma deposits are prepared using organic precursors; in this case, the deposition process is referred to as plasma polymerization in preference to PECVD. Plasma polymerization has little in common with classic polymerization. Many side reactions occur during film deposition. This can be understood by the poor selectivity of the breaking up of chemical bonds in plasma. The mechanism of deposition is not yet well understood. This difficulty arises from the complexity and variety of active species, reaction steps, and the dependence on various plasma parameters. Several kinetic models of plasma polymerization have been proposed. The most popular ones are the models of Lam *et al.* [5], Poll *et al.,* [6], and Yasuda [1]. These models involve a competitive ablation and polymerization (CAP) mechanism which gives an account of the rather complicated and interrelated influences of fragmented elements in the deposition of plasma polymers (PPs). It is important to mention that chain-growth polymerization cannot occur in vacuum. This is simply because there are too many chain-carrying species but not enough monomers with a well-defined chemical structure capable of chain-growth polymerization. With the occurrence of fragmentation of the monomer structure, the situation becomes even worse. The way in which a PP is formed in plasma has been explained by the rapid step-growth

polymerization mechanism (**Figure 1**). The essential elementary reactions are the stepwise recombination of reactive species (free radicals) and stepwise addition or intrusion via hydrogen abstraction by impinging on free radicals. It is important to recognize that these elementary reactions are essentially oligomerization reactions that do not form polymers by themselves. To form a polymeric deposition, a certain number of steps must be repeated at the surface. As the plasma polymerization proceeds, the activated species may attack the growing polymer layer. This attack can decompose the polymer, extend the crosslinking of the polymer, or cause the elimination of deposited polymer (ablation process). These polymerization and ablation processes proceed competitively, and the overall plasma deposition rate is dependent on the plasma-polymerization parameters.

Among the numerous plasma-polymerization parameters, the ones having a direct effect on the fragmentation of the monomer are logically the most influent. Three parameters have a particularly pronounced effect: the nature of the precursor represented by its molecular weight M, the power of the electric discharge W, and the precursor flow rate F. The energy-input level manifested by W/FM (given in units of J kg^{-1}, or energy per mass of monomer), introduced by Yasuda [1], is the predominantly important factor determining the extent of fragmentation. Low W/FM values are related to operating conditions where the activated species have a far lower concentration than monomer molecules introduced into the plasma; in such a range of W/FM values, called the monomer-sufficient region, the number of activated species, and consequently the PP deposition rate, increases with W/FM. For medium W/FM values, corresponding to the competition region, the quantity of monomer molecules introduced into the plasma is exactly the quantity likely to be activated; in this case, the film deposition rate is invariable as a function of W/FM. For high values of W/FM, corresponding to the monomer-deficient region, the material deposition rate decreases with W/FM due to lack of monomer molecules likely to be activated (**Figure 2**).

For membrane applications, plasma polymerization is usually performed on a highly porous substrate whose only role is to mechanically support the thin PP. Nevertheless, plasma polymerization can also be applied on a dense or poorly porous substrate being already an active membrane; in this case, it could achieve the same effect as plasma treatment (in other words, modification of surface characteristics of the membrane substrate) with additional advantageous characteristic features of the nanometer film of PP. Moreover, a special kind of plasma polymerization that has received increased attention in recent years is the preparation of PPs by RF sputtering from polymeric targets. The maximum attention has been paid to fluorocarbon PP films sputtered from polytetrafluoroethylene (PTFE) using magnetrons [7]. The main advantage of this innovative process is that the deposition rate and the organization of the chains of the material structure are much higher than in the case of classical PPs. While the activation mechanism is very different from that of the classical plasma polymerization, the deposition mechanism is not.

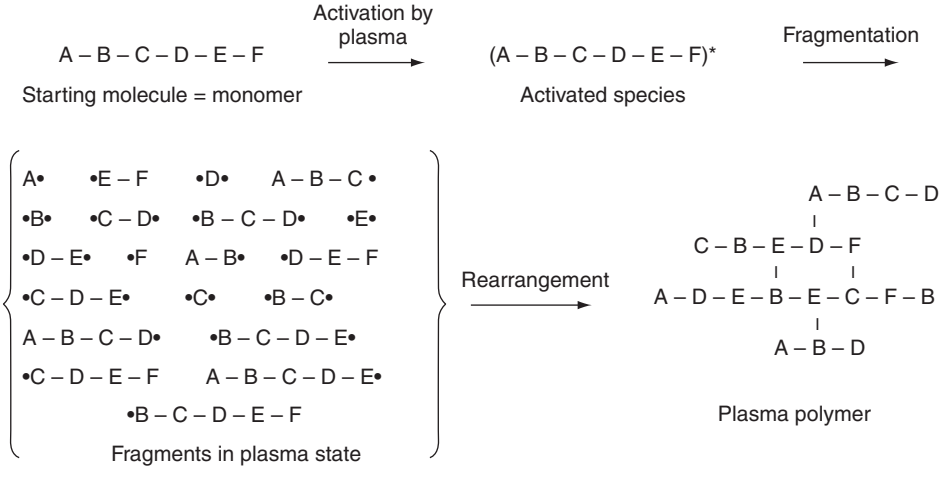

Figure 1 Schematic representation of plasma polymerization.

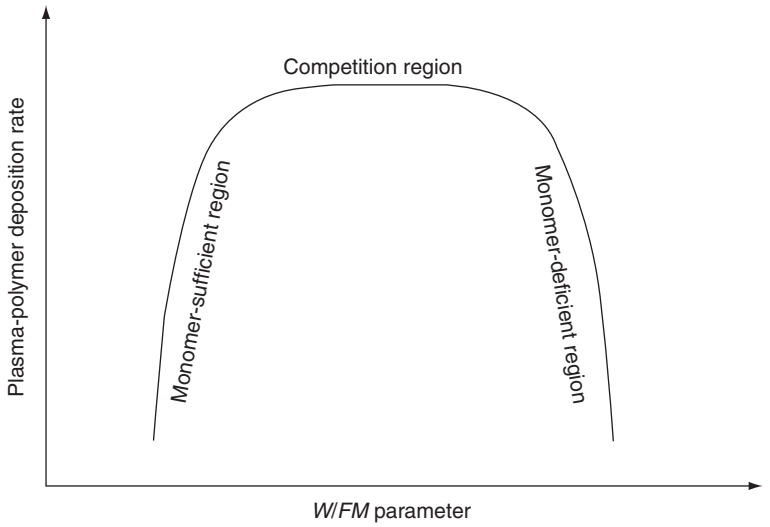

Figure 2 Domains of plasma-polymer deposition.

1.09.2.3.2 Structural properties of PPs

PPs, noted PP–X (X being the monomer), are not formed by the repetition of a monomer unit like classical polymers. They are disorganized thin films, with short and branched chains (randomly terminated with frequent crosslinks) often not reminders of the monomers they come from. In terms of material properties, PPs present a great number of advantages when compared to films synthesized, on the one hand, by other techniques of vacuum deposition and, on the other hand, by liquid-route synthesis methods:

1. Like all vacuum-deposition techniques, plasma polymerization makes it possible to produce very thin films with thicknesses of few nanometers to few microns (**Figure 3**), which is impossible with conventional polymerization. The deposition rate can be high (several $\mu m\ min^{-1}$) [8, 9], making the process ideal for industrial applications.
2. One of the major interests in this technique is the possibility of depositing materials at ambient temperature on substrates sensitive to heat such as conventional organic polymers (which is not possible with conventional chemical vapor deposition (CVD) – chemical plating in pyrolytic phase vapor). The polymeric supports constitute glasses, semiconductors, ceramics, and metal surfaces – the large variety of substrates on which plasma deposits have good adherence.
3. The materials deposited by plasma polymerization are generally dense, amorphous, strongly crosslinked, and present a low density of defects and holes compared with those obtained by other vacuum-deposition techniques such as evaporation or sputtering.
4. The three-dimensional and highly crosslinked structure of the plasma deposits is at the origin of a number of very specific properties of these materials, properties that one does not find in their counterparts worked out by conventional ways: chemical inertia, good thermal stability, anticorrosive character, and barrier properties with respect to oxygen and water vapor in particular.
5. Plasma polymerization makes it possible to adjust the chemical composition and the microstructure of deposited materials, and thus modify the

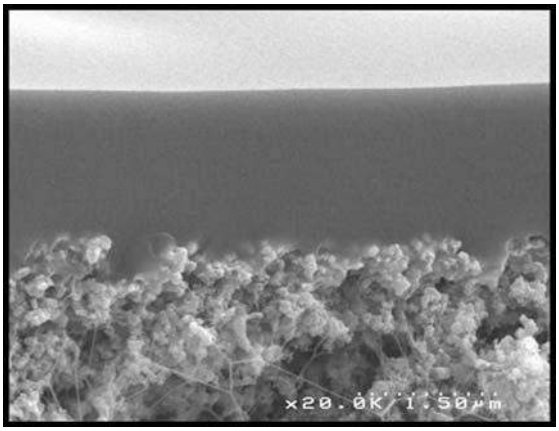

Figure 3 SEM micrography of a plasma polymer deposited onto a porous carbon substrate.

physical and chemical properties of these materials by a simple variation of the parameters of the process, and this is a field much broader than the other deposition techniques. If, from a technological point of view, this requires a rigorous control of the parameters of the process, the complexity and variety of active species and reaction steps directly related to the plasma parameters offer a high degree of flexibility in prepared materials properties.

The microstructural properties of deposits depend mostly on the parameters of plasma polymerization, particularly on the W/FM parameter. In the monomer-sufficient region (low W/FM values), monomer molecules are subjected to less fragmentation for plasma polymerization and PPs with less rearrangement and a small loss of some groups such as hydrogen, methyl, hydroxyl, and carbonyl groups are formed. Under such soft synthesis conditions, plasma polymerization retains more of the molecular structure of the monomer; PPs are more organic, less highly crosslinked, and thus resemble more conventional polymers – they are said to be polymer-like materials. In the monomer-deficient region (high W/FM values), monomer molecules are subjected to heavier fragmentation, and PPs with much more rearrangements and a larger loss of some groups (especially carbon-based ones) are formed. Under such drastic synthesis conditions, PPs are harder, more inorganic, and more highly crosslinked; they are said to be ceramic like. For intermediate values of W/FM, a wide range of hybrid materials can be manufactured. **Figure 4** [10] depicts the influence of the Yasuda parameter on the plasma materials structure in the case of hexamethyldisiloxane (HMDSO), widely used as monomer in plasma polymerization. For a single monomer, W/F can be used instead of W/FM as the main process-control parameter. In soft plasma conditions, the plasma film synthesized from HMDSO has a structure close to that of the HMDSO monomer and also polydimethylsiloxane (PDMS), which is the closest conventional polymer, as shown by Fourier transform infrared (FTIR) spectroscopy; this plasma film is thus called PDMS-like PP; its

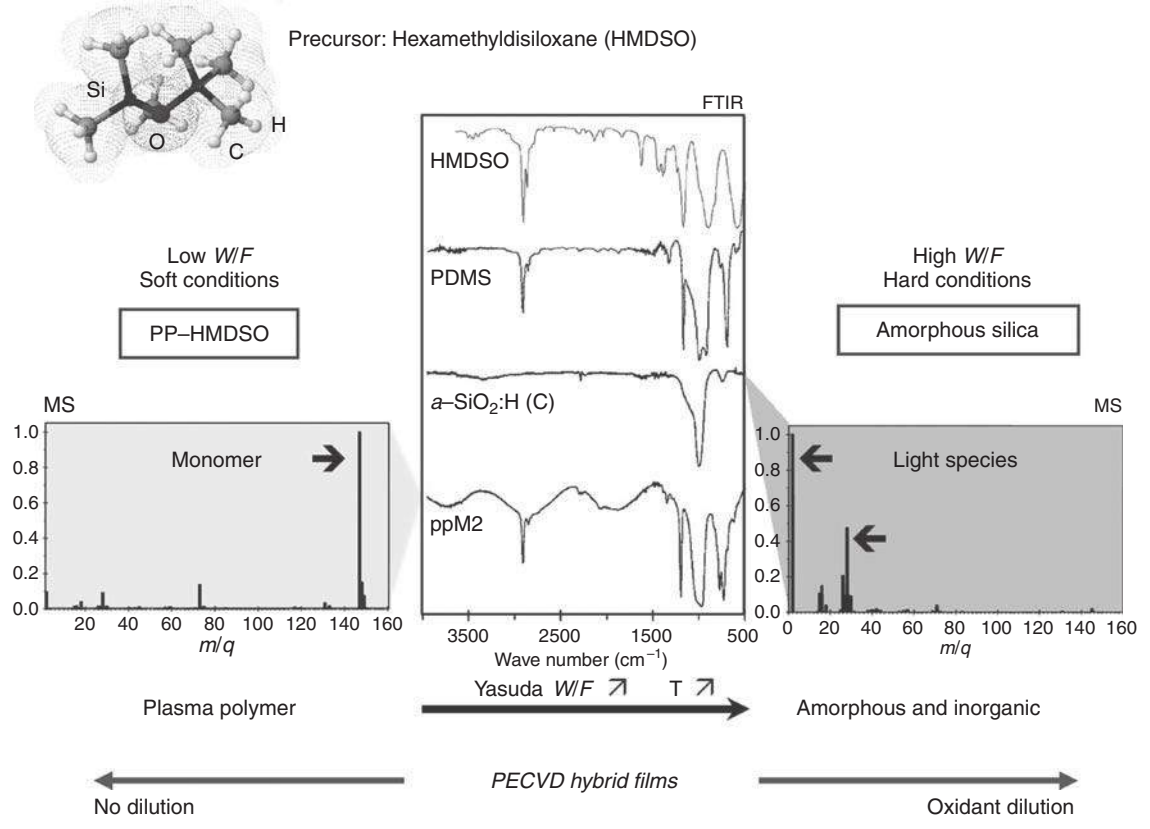

Figure 4 PECVD extreme conditions to obtain a polymer-like or an amorphous silica film from the same precursor HMDSO.

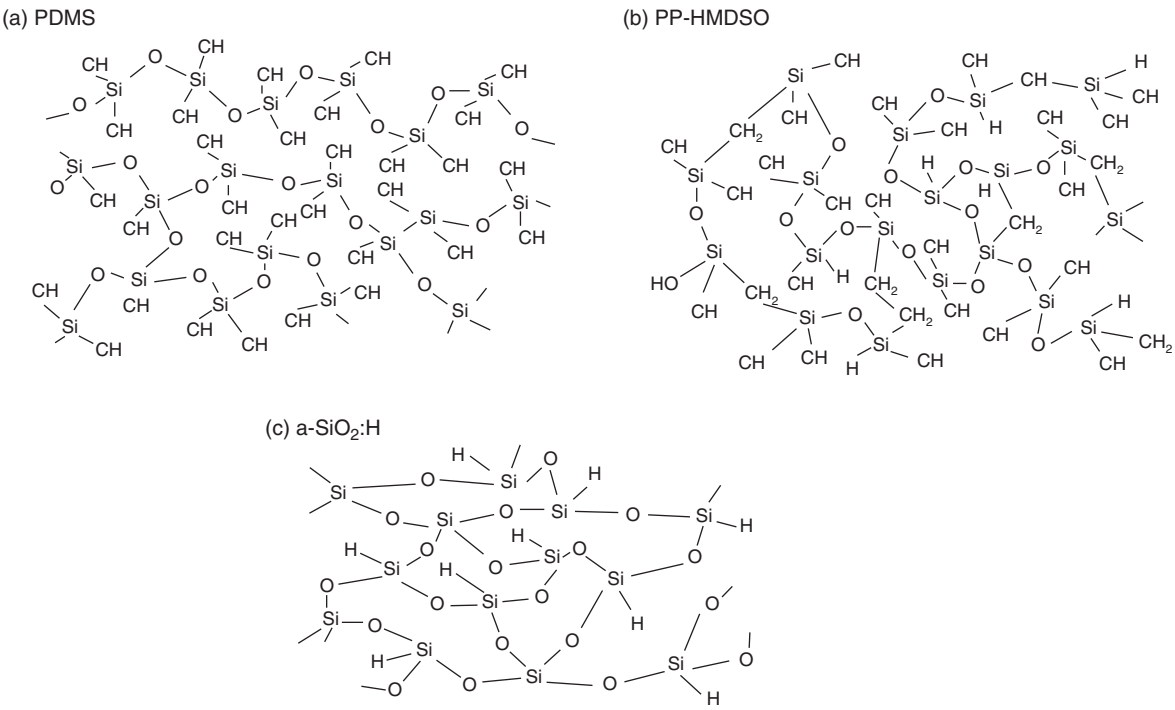

Figure 5 Schematic structures relative to a PDMS-like plasma polymer (b), a conventional PDMS polymer as reference (a) and an amorphous hydrogenated silica (c).

density is quite low, equal to 1.1. In hard plasma conditions, the obtained plasma film is similar to amorphous hydrogenated silica with a density of 2.2; it is denoted as a-SiO_2:H (a for amorphous, :H for hydrogenated); dilution with an oxidative gas such as O_2 or N_2O in the plasma reactor enables to achieve this silica structure at lower W/F values. Mass spectrometry (MS) is a very useful technique to reveal the low fragmentation of the monomer in soft plasma conditions, and in contrast, it also reveals the formation of many light species due to strong fragmentation in highly energetic plasmas. **Figure 5** shows the schematic structures relative to a PDMS-like PP (and a conventional PDMS polymer as reference) and an amorphous hydrogenated silica.

Although considered as dense materials, PPs are characterized by a free volume comparable to ultramicroporosity (spaces between chains lower than 0.7 nm). Changing the plasma parameters in the preparation of films enables the tuning of this free volume as well as the chain flexibility. The approaches that may achieve enhanced free volume and chain flexibility can be summarized as follows: (1) minimization of the W/FM parameter; (2) pulsing of the RF field to reduce the plasma-on time; (3) use of a Faraday cage around the substrate; (4) positioning the sample downstream from the plasma zone (postdischarge configuration); (5) use of monomers containing polymerizable double bonds; and (6) use of a cold substrate. It is possible to further increase free volume and change it into micro- (pore diameter between 0.7 and 2 nm) or meso- (pore diameter of some nanometers) porosity by adding a porogen in the plasma reactor as comonomer and then eliminating it from the prepared film by thermal or UV posttreatment [11, 12]. The porogen approach is mainly applied to polymer-like plasma films. Indeed, ceramic-like plasma materials are usually required for their highly dense structure; nevertheless, they sometimes contain some microporosity naturally due to chain breakage caused by very high degrees of crosslinking [13].

1.09.2.3.3 Transport properties of PPs

The high degree of flexibility in free volume and chemical structure of prepared materials makes them good candidates for use as membrane materials. PPs have been used as membrane materials since the 1980s; the first reported study was by Yasuda [14]. Their main advantages in such an application field

are their high degree of crosslinking giving them high separation efficiency as well as high chemical and thermal stabilities, and their small and easily tunable thickness enabling a modulation of their permeation ability. As PPs are not self-supportive, they must be deposited onto a symmetric or an asymmetric support with a surface pore size and a surface roughness that is in agreement with the deposited thickness. This support primarily acts as a mechanical support. The plasma polymerization technique cannot deposit thin films on the pore walls inside porous substrates as can be done by counterdiffusion CVD, but plasma polymerization is able to modify the mouth of the pores at the surface of substrates, especially if the latter are macroporous (pore diameter above 50 nm). In this case, the final membrane properties depend both on the PP and on the starting support as the duration of the applied plasma polymerization process is not enough to make a complete and homogeneous layer. In the case of a complete homogeneous layer, transport properties will be mainly governed by the intrinsic separation properties of the PP.

The first developed plasma membranes were intended for gas permeation or retention and also pervaporation; more recently, plasma membranes have been prepared for liquid-separation processes (nanofiltration and ultrafiltration, essentially). For gas or liquid separation, membranes providing high fluxes of penetrants are required. Polymer-like plasma films are more suitable in this case. If the plasma film does not totally plug the porosity of its support, the transport properties across the membrane will be controlled by the viscous flow. If the plasma film constitutes a complete homogeneous layer at the surface of its support, the transport properties of the membrane will be mainly governed by solution-diffusion, microporous surface diffusion, or molecular sieving mechanisms inherent to the PP. Being highly crosslinked in essence, polymer-like plasma materials are generally not as permeable as conventional membranes. In order to enhance their permeability, the easiest solution consists in reducing their thickness, to the detriment of their mechanical stability. Another solution is to increase their free volume and/or chain flexibility to make them resemble more conventional polymers. For gas retention (packaging application essentially), membranes providing low fluxes of penetrants are required. Ceramic-like plasma films are more suitable in this case; their transport properties are rather controlled by the molecular sieve mechanisms as in the case of classical crystallized ceramics.

The development of polymer-like plasma films has been more recently applied to fields using ion-conducting membranes such as electromembrane processes (electrodialysis in particular), electrochemical sensors, or, more broadly, energy-production devices (fuel cells, Li-ion batteries, etc.). Such applications require the use of materials having a good swelling in water and containing specific functions, often charged, distributed in an ordered manner in order to form effective channels of ionic conduction. Obtaining such materials by plasma polymerization is particularly challenging and requires delicate research in the choice of the precursor(s) and the adjustment of plasma parameters.

1.09.3 Plasma Membranes for Gas or Liquid Separation

1.09.3.1 Gas Permeation

Studies on permselective efficiency of gas-permeation membranes subjected to plasma treatment with a noncondensable gas, that is, without any deposition of new material, have been very few in the past 5–10 years. Recently, Kumasawa and coworkers studied the gas permselectivity of polyethylene [15] and polypropylene [16] membranes after a 5-min long N_2 or NH_3 plasma treatment. They found that nitrogen was not significantly incorporated into the polymer network and that CO_2 permeability coefficients slightly increased after plasma treatment whereas N_2 ones were not affected, which gives these plasma-treated polymer membranes an edge over classical glassy polymers like polyimides, in terms of CO_2 separation factor.

Most authors were interested in the preparation of PPs on porous substrates. Gas permeabilities of plasma membranes prepared, using HMDSO or octamethylcyclotetrasiloxane (OMCTSO) are presented in **Figure 6** according to their deposition conditions [13]. Gas-transport properties in such membranes were mainly controlled by the diffusion mechanism. Indeed, for soft plasma conditions, gas permeabilities increased with W/FM because the number of flexible siloxane bonds rose (as could be shown by chemical composition analysis not depicted here); for hard plasma conditions, gas permeabilities decreased with W/FM due to densification of the materials: chain crosslinking was the limiting factor in this region. Whatever the monomer might be, H_2 (the

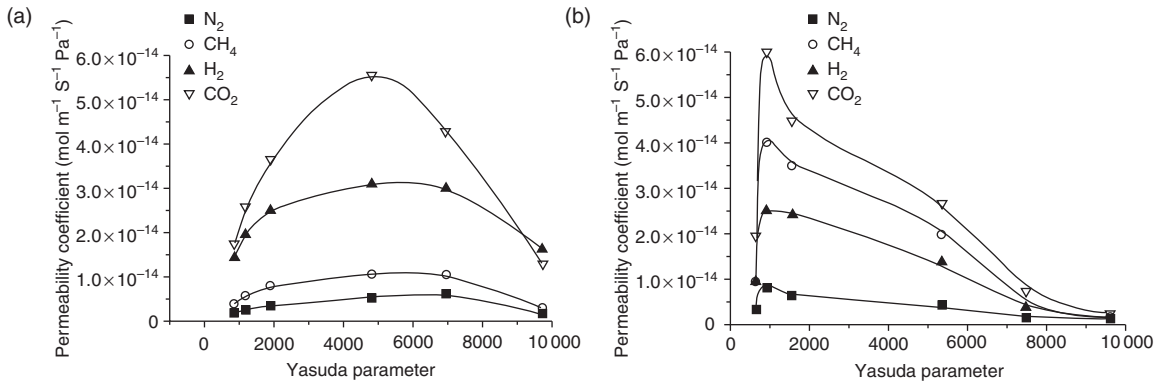

Figure 6 Permeability coefficients relative to different PECVD membranes (from polymer-like to amorphous silica a-SiO_2:H) synthesized from HMDSO (a) or OMCTSO (b).

lightest gas) should logically show the highest permeability. Nevertheless, the sorption phenomenon was also influential (particularly for PPs synthesized in soft plasma conditions) as shown by the high permeability coefficients of CO_2 in PP–HMDSO and CH_4 in PP–OMCTSO.

Inagaki and coworkers tested several hydrocarbon-based and fluorine-based precursors for the preparation of plasma-polymerized membranes intended for the separation of oxygen from nitrogen. An ideal selectivity up to $\alpha(O_2/N_2) = 5$ could be reached [17] and was strongly dependent on the C–CF_n concentration in materials [18] (**Figure 7**). In these 300–500-nm thick membranes, it was assumed that the less-fluorinated carbon units played an important role in the oxygen/nitrogen separation. Polymer-like plasma membranes could be further treated (by plasma-ion bombardment and pyrolysis) in order to increase the H_2/N_2 ideal selectivity up to 45 keeping a high hydrogen permeance: 2×10^{-6} mol m^{-2} s^{-1} Pa^{-1} at 150 °C [19].

In drastic plasma conditions and starting with a silazane vapor precursor, thin silicon carbonitride plasma membranes were deposited onto an asymmetric mesoporous alumina support whose average surface pore size was 5 nm [20]. Such membranes allowed separating light gases from heavier ones without a strong reduction in permeability due to their low thickness in the range 50–150 nm. Due to their high thermal stability, these membranes were especially adapted to hydrogen separation in the presence of water at intermediate temperatures. **Figure 8** presents the evolution of the nitrogen and helium permeability coefficients and the helium–nitrogen ideal selectivity as a function of the synthesis conditions. This selectivity was

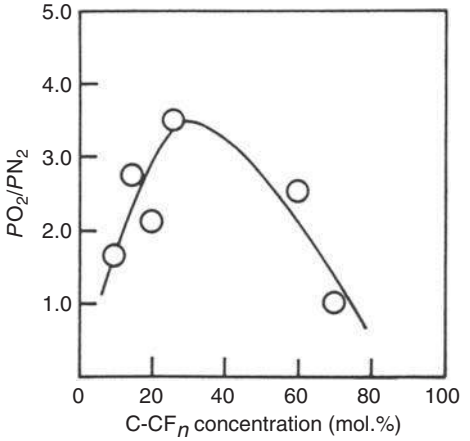

Figure 7 Ideal O_2/N_2 selectivity (calculated as the ratio of the O_2 permeability PO_2 to the N_2 permeability PN_2) for plasma polymers containing C–CF_n functions.

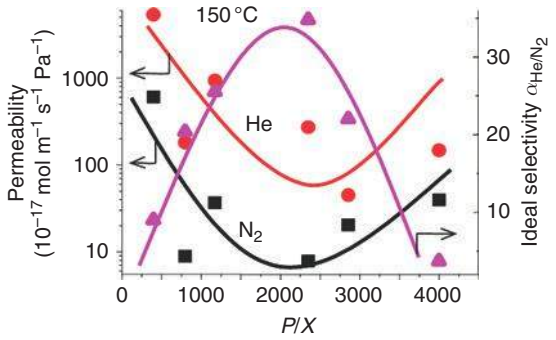

Figure 8 He and N_2 permeabilities and He/N_2 ideal selectivity as a function of *P/X* at 150 °C of *a*–SiN_XC_Y:H membrane deposited by PECVD on alumina (pore diameter: 5 nm).

strongly dependent on the plasma parameters. The x-axis in **Figure 8** corresponds to the dilution of hexamethyldisilazane (HMDSN) in ammonia to obtain silicon carbonitride layers: $X = [\text{HMDSN}]/([\text{HMDSN}]+[\text{NH}_3])$. At $X = 1$ (pure HMDSN), the material was flexible enough, allowing the heaviest gas to permeate. When increasing the ammonia dilution, the material became more rigid and selective. The ideal selectivity He/N_2 could be over 30. At low X, the growth of the inorganic-like plasma material became columnar with defects, which explained the increase in the permeability coefficients and the decrease in the ideal selectivity of He/N_2.

1.09.3.2 Pervaporation

Vilani and coworkers [21, 22] studied polyurethane membranes used to separate methanol from methyl-*t*-butyl ether by pervaporation after an acrylic acid vapor plasma treatment. They showed that a short time modification with a high plasma input power (100 W) allowed the increase of selectivity factor from 5 to 30 and also the permeate flux (**Figure 9**) [21]. They attributed these evolutions to an increase of C=C contribution and a loss of C–N content that might result in crosslinking at the surface due to decrease in surface free volume and chain flexibility.

Upadhyay and Bhat [23] proved the strong efficiency of a nitrogen plasma treatment (**Figure 10**) compared to oxygen or air plasma treatments of nonporous polyvinyl alcohol-based membranes. The extremely high selectivity of the nitrogen-treated membranes toward water molecules (over 1200 in isopropyl alcohol (IPA)–water mixture with IPA weight fraction below 0.8) could be attributed to surface crosslinking whereas air and oxygen plasma-etched amorphous regions decreased the swelling of the treated membranes and their selectivity to water.

Yamaguchi and coworkers [24] used the technique of plasma-induced graft polymerization to modify the surface of porous high-density polyethylene with acrylate for the removal of dissolved organics from water. The argon plasma power was 10 W, the pressure in the plasma reactor was 0.1 mbar, and the reaction time was 60 s. A series of acrylates (same concentration and same temperature) was used; the monomer which had the longest chain showed the lowest reaction rate. Pervaporation of dilute aqueous solution of 1,1,2-trichoroethane was very efficient. More recently, Li and coworkers [25] changed the surface of PTFE by plasma-induced grafting polymerization of acrylamide in order to increase the pervaporation performance for the dehydration of aqueous alcohol solutions (**Figure 11**). The water contact angle of such PTFE–g–PAAm membranes was 50° and their water permeation rate could go up to $373\,\text{g}\,\text{m}^{-2}\,\text{h}^{-1}$. An accurate argon plasma exposure time to polymerize the grafted AAm had to be applied to prevent any etching of the PTFE surface.

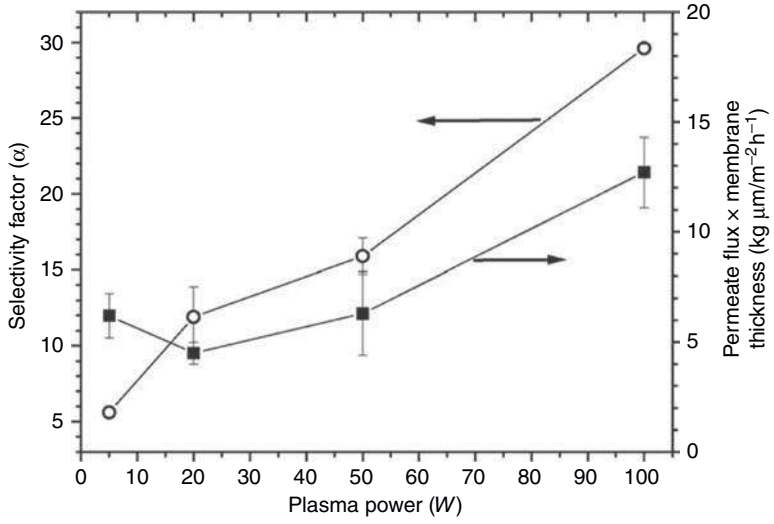

Figure 9 Effect of the acrylic acid plasma power on the permeate flux and selectivity factor in plasma-treated polyurethane membranes. Treatment time: 1 min.

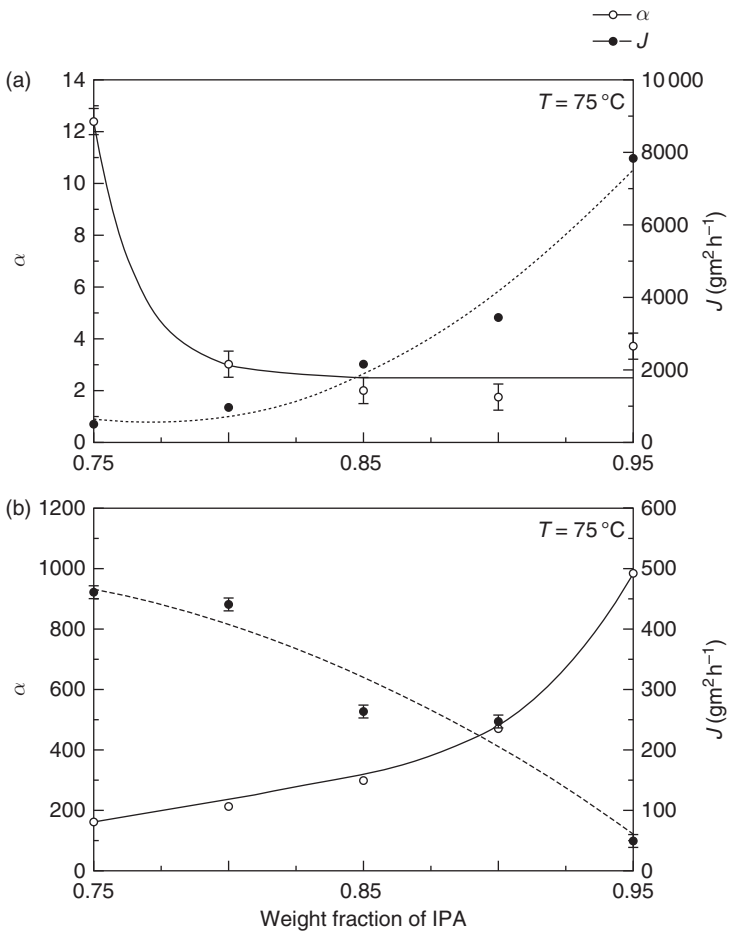

Figure 10 Flux (J) and selectivity (α) measured at 75 °C of polyvinyl alcohol membranes as a function of water–IPA mixture: untreated (a); treated in nitrogen plasma for 5 min (b).

In the experiment we conducted, thin plasma-polymerized films made by using HMDSO or OMCTSO were tested as pervaporation membranes for the recovery of organics (phenol, chloroform, pyridine, and methylisobutylketone) from aqueous streams [26]. More drastic conditions in the preparation of films induce an increase in the quantity of organics and water permeabilities, and therefore a decrease in selectivities, directly related to the densification of the membrane structure. In soft plasma conditions, selectivities are close to those of PDMS but permeabilities are three orders of magnitude lower. Yet, performances are comparable due to the small thickness of plasma-polymerized layers.

1.09.3.3 Liquid Separation

Membranes intended to cause liquid separation are porous membranes. Depending on their pore width, they are referred to as macroporous membranes (for pore diameter higher than 50 nm), mesoporous membranes (for pore diameter between 2 and 50 nm), or microporous membranes (for pore diameter lower than 2 nm). These are more suited for reverse osmosis (using micropores), electrodialysis (also using micropores), nanofiltration (using mesopores with pore diameter lower than 10 nm), ultrafiltration (using big mesopores or small macropores), or microfiltration (using macropores). Conventionally, various kinds of materials and structures are used depending on the aimed application.

The main conventional membrane materials used for filtration of noncharged species (reverse osmosis, nano-, ultra-, and microfiltrations) in aqueous solutions are polysulfone (PSU), polyethersulfone (PES), polyacrylonitrile (PAN), polypropylene, polyurethane, polyimide, PDMS, polyvinylidene fluoride (PVDF), PTFE, and

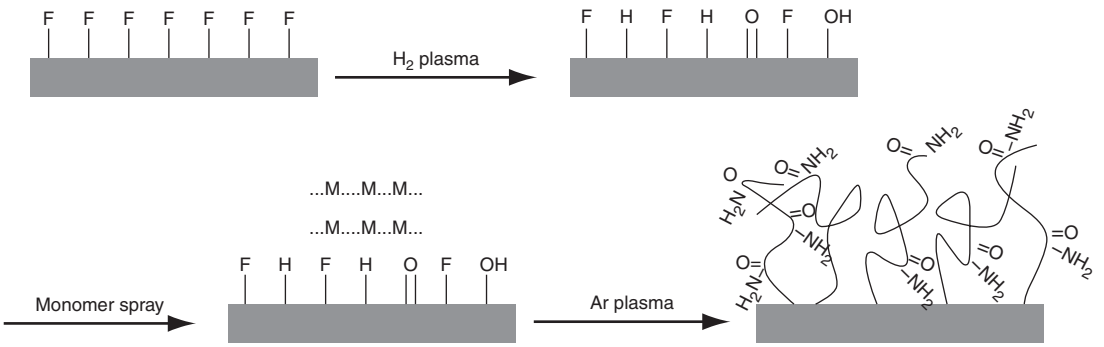

Figure 11 Schematic description of grafting of hydrophilic monomer onto PTFE membrane by plasma-induced graft polymerization process.

poly(ethylene)terephthalate. With regard to shapes, flat, in the form of a tube, or hollow fiber membranes can be envisaged. These membranes generally present good bulk properties such as thermal stability, mechanical strength, and solvent resistance. Nevertheless, their filtration properties are weak and some of them (especially microporous ones used for proteins separation) are likely to suffer from fouling due to their high hydrophobic nature. Plasma modification can provide a solution to these problems via plasma treatments using air, Ar, He, N_2, NH_3, CO_2, or water vapor, plasma-induced graft polymerization, or plasma polymerization. The aim of plasma modification is to obtain specific functionalities (acidic, amphoteric, or basic) at the surface of the membrane making it more hydrophilic. In the case of the separation of water from hydrophobic liquids (oil, diesel, etc.) by ultrafiltration, of great importance in petroleum, pharmaceutical, cosmetics, and nutritional oil industries, the surface of commonly used conventional membranes (porous materials such as filter paper or polyester textile) is, on the contrary, too hydrophilic. Plasma polymerization using fluorine-based or organosilicon monomers is a promising technique to make these membrane surfaces turn hydrophobic.

The membranes used for the separation of charged species by electrodialysis are ion-exchange polymer membranes. Such membranes can suffer from chemical instability in some aggressive acidic or alkaline media; moreover, their ion selectivity is not always very good. The deposition of a highly crosslinked PP on their surface can enhance their chemical stability as well as their ion selectivity.

1.09.3.3.1 Hydrophilic nature enhancement by plasma process for filtration applications

Plenty of work has been devoted to PSU membranes widely used in microfiltration or ultrafiltration processes, in particular for low protein adsorption in serums and plasma. There have been several reports on hydrophilization of PSU surfaces after plasma treatment by noncondensable gases, plasma-induced graft polymerization, or plasma polymerization. Some of them are as follows:

- *Plasma treatments*. PSU as well as PES have been widely treated by CO_2 plasmas. Wavhal and Fisher [27, 28] used a reactor equipped with an additional cylindrical glass membrane holder (**Figure 12**). The membrane, first cleaned in methanol, was then oriented perpendicular to the gas flow. This arrangement allowed the penetration of the plasma through the depth of the membrane. The pressure in the reactor was set to 150–160 mTorr, the RF power (13.56 MHz) was ignited at 5, 10, and 20 W (for PSU membranes) and in the range 20–35 W (for PES membranes). The treatment time varied from 10 to 300 s for PSU membranes and from 0.5 to 15 min for PES ones. Microstructural characterizations by FTIR and X-ray photoelectron spectroscopy (XPS) displayed the effect of CO_2 plasma treatments of PES films. After a 24-h exposure to air, the –OH stretching band (3200–3700 cm^{-1}) and the C=O absorption band (1700–1800 cm^{-1}) on FTIR spectra significantly changed. Thereafter, only small changes were observed. XPS elemental compositions of both sides of the PES membranes were determined before and after plasma treatment. For a plasma treatment of 30 s, both sides were equally modified: the oxygen concentration increased by 47%. For longer treatment times, the composition of both sides did not

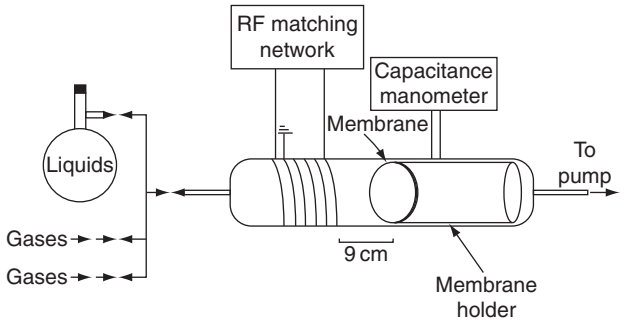

Figure 12 Plasma reactor equipped with an additional cylindrical glass membrane holder used by Wavhal and Fisher.

change even when both the plasma power and treatment time increased. High-resolution XPS C_{1s}, O_{1s}, and S_{2p} spectra are discussed in Reference 28. Contact-angle measurements were performed on both sides of PSU and PES membranes. The main conclusion was that the enhanced wettability of the treated membranes did not change even after storage in air for 6 months. The authors discussed the penetration of the reactive plasma species inside the depth of the membranes. Stacking up two membranes (open side 1–tight side 1/open side 2–tight side 2) allowed one to explore the depth of the plasma treatment through the membrane. As the treatment time increased, the four surfaces became more hydrophilic. This means that the plasma reactive species penetrated the depth of the membranes. The penetration depth was estimated to be approximately 150–300 μm which was consistent with the Debye length estimated to be 100–200 μm under the chosen plasma conditions. This was in accordance with previous results from the same authors concerning H_2O plasma treatment applied to PSU and PES membranes [29, 30].

Gancarz and coworkers worked on the modification of PSU membranes in a microwave(2.45 GHz)-pulsed CO_2 plasma discharge. The plasma conditions (gas flow rate, total pressure, power, duty cycle, and time of treatment) are described in Reference 31. Surface tension, dispersive, and polar components were determined. The results showed a rapid increase in hydrophilicity (polar and dispersive components were equal). The surface reactions occurred during the first minute of treatment and no change in the measured parameters was observed after 1 min of plasma treatment. The storage of the samples for 24 h in air caused a small decrease in the polar component but the total surface tension still remained relatively high. **Figure 13** shows the dependence of contact-angle measurements of PSU membranes before and after CO_2 plasma versus pH of water solution. Although the contact angle of the nonmodified PSU was independent of pH up to 13, that of the modified PSU decreased for pH > 7. These results confirmed the acidic character of the PSU surface after the CO_2 plasma modification which was as predicted by Shahidzadeh-Ahmedi and coworkers [32].

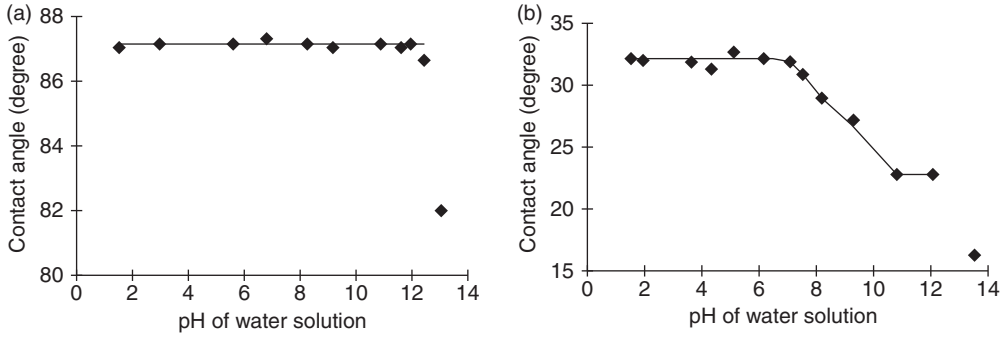

Figure 13 The pH of water as a function of (a) contact angle of untreated PSU membranes and (b) CO_2 plasma-modified PSU membranes.

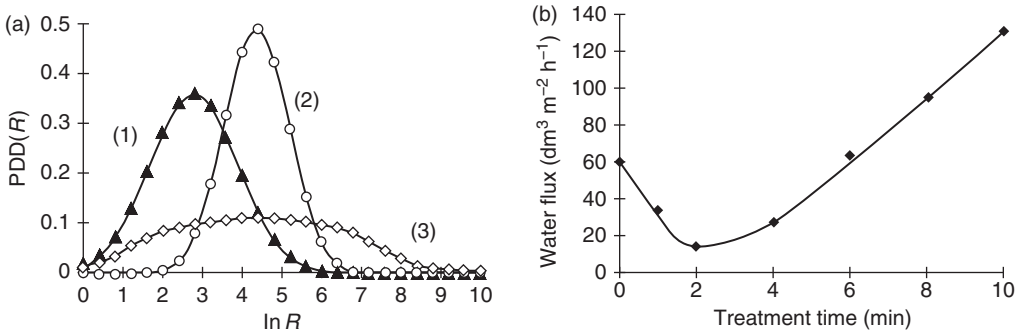

Figure 14 (a) Pore-size distribution of PSU membranes before treatment (1), after CO_2 plasma for 2 min (2), and for 10 min (3). PDD(*R*), pore diameter distribution; ln *R*, logarithm of the pore radius in nm; and (b) The water flux of CO_2 plasma-treated PSU membranes as a function of plasma treatment time.

In other papers, Gancarz and coworkers [31, 33] showed that plasma treatment had an influence on the pore size of the PSU membranes. They estimated the pore size with an assumption distribution using dextran standards. It was clearly seen that the pore size became larger after plasma modification due to ablation (**Figure 14(a)**). Consequently, the filtration properties of the PSU membranes changed: the water flux through them showed a minimum after 2 min of plasma treatment and then increased (**Figure 14(b)**). The water-flux decrease for plasma treatments shorter than 2 min could be ascribed to the preferential ablation of hydrophilic groups making the pore surface more hydrophobic, thereby inducing water retention; this effect produced an increase in the pore size. After a 2-min treatment, increase in the pore size became the main effect and the water flux increased.

In the same research group, nitrogen and ammonia plasma were also used to modify the surface of PSU membranes and improve their filtration properties. The effect of N_2 plasma was an increase in hydrophilicity during the first 2 min of treatment; the polar component was a little higher than the dispersive contribution [34]. For longer treatments, a slow increase in surface tension was observed. The storage of membranes in air for 1 day resulted in a decrease in the total surface tension and the polar component. This could be due to the mobility of surface functionalities or sorption of hydrophobic moieties of laboratory air. The treated membranes were kept in double-distilled water. The total surface tension decreased in the first week and was stable after that; at the same time, the dispersive contribution increased while the polar component decreased. Pore-size distribution of PSU membranes after 2- and 10-min N_2 plasma treatment is shown in **Figure 15**. The average pore size became slightly larger and the distribution wider, a proof of equilibrium between etching and grafting of nitrogen functions. NH_3 and NH_3/Ar plasma caused an increase in pore-size diameter and the effect was not dependent on treatment time [35].

CO2, N2 and NH3, and NH_3/Ar plasma-treated PSU membranes were tested for protein filtration. Fluxes of buffer ($\mathcal{J}_b^0$), bovine serum albumin (BSA) solution ($\mathcal{J}_p$), buffer after BSA filtration ($\mathcal{J}_b^f$), and buffer after cleaning ($\mathcal{J}_b^c$) for two different pH values (3 and 9) are shown in **Figure 16**. From these values, fouling index (FI), flux recovery after cleaning (FR), reduction of flux in filtration (RF), and protein retention (SR) are reported in Reference 36 (**Figure 17**). Considering the best results as corresponding to lowest FI and RF (less intensive fouling) and highest FR (best flux recovery), the best performances were obtained with CO_2 and N_2 plasma treatments. The indices for the membrane modified with NH_3/Ar plasma were not as good as those for NH_3. In all cases, there were no significant differences at various values of pH. This means that the modified membrane surface had an amphoretic character.

Unfortunately, plasma treatments can alter the physico-chemical properties of materials, particularly polymer surfaces. In the particular case of PSU membranes, plasma treatments can lead to photodegradation. Gesner and Kelleher [37] showed the most susceptible bonds for degradation (**Figure 18**); Poncin-Epaillard and coworkers [38] compared the degradation effects of plasma treatments to those of radical photooxidation. FTIR spectra of the surface were recorded using attenuated total reflectance (ATR) technique in order to obtain information about the structural change of the membranes after plasma treatment. Intensities

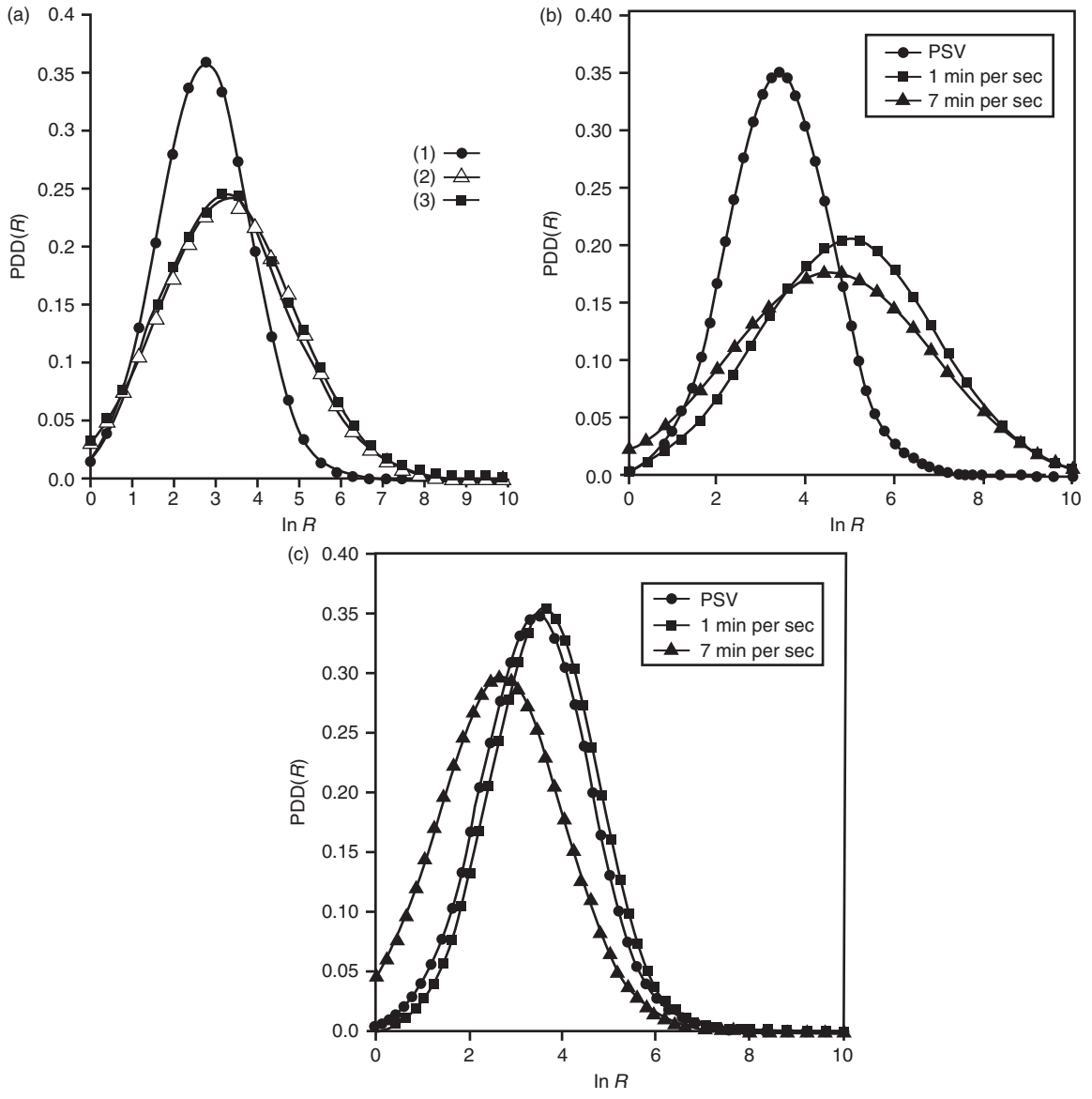

Figure 15 Pore-size distribution of PSU membranes treated with N_2 (a), NH_3 (b), and NH_3/Ar (c). In the case of N_2 (a), (1), (2), and (3) correspond to untreated, 2-min long-treated and 10-min long-treated membranes, respectively. PDD(*R*) refers to the pore diameter distribution and ln *R* the logarithm of the pore radius in nm.

of few bands characteristic of the membranes increased showing the reaction between the surface and the stable radicals created by the plasma. A large number of new absorption bands appeared in the spectra just after plasma treatment; subsequently, some of them decreased during the first 48-h storage in air. Photodegradation mechanism of membranes was deduced from FTIR observations. Scission takes place at every bond except the aromatic C–C and C–H bonds. Several steps may be distinguished: creation of free-radical sites due to surface bombardment by species in the plasma, chain cleavage with loss of volatile species, further gas-phase reactions of the primary volatile products in the plasma, reaction of the free-radical sites on the polymer, and reaction of the residual free radicals with oxygen and nitrogen after exposure to the air.

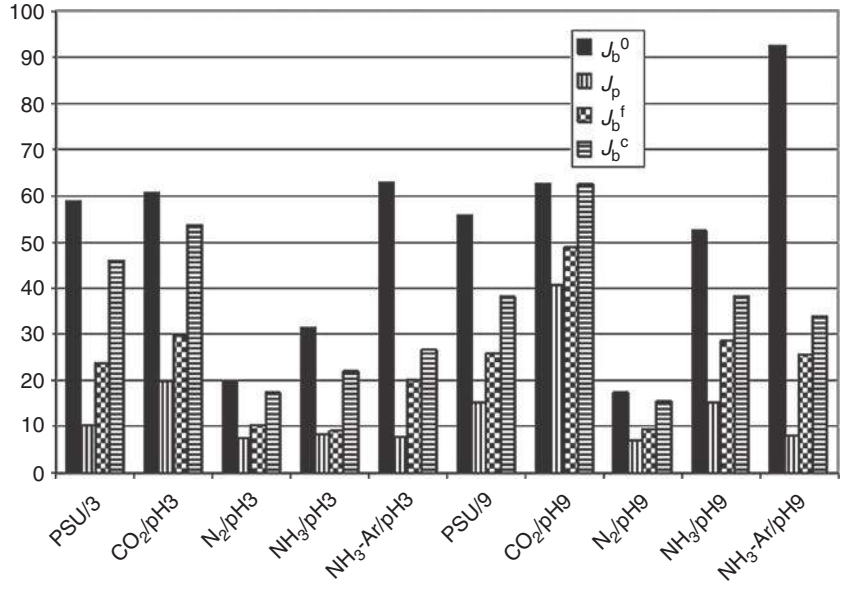

Figure 16 Fluxes of buffers and BSA solution through untreated and plasma-treated PSU membranes.

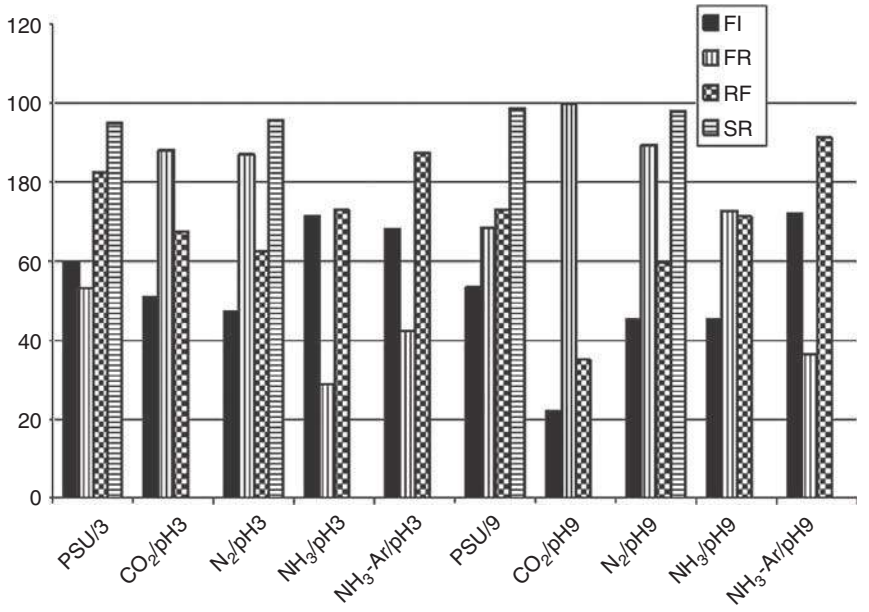

Figure 17 Filtration indexes for pristine and plasma-modified PSU membranes.

- *Plasma-induced graft polymerization.* Plasma treatment of membranes with gases such as CO_2, nitrogen, ammonia, or oxygen increases the hydrophilicity of the asymmetric ultrafiltration membranes but the hydrophilicity can decrease with aging in air; moreover, the etching effect of the plasma treatment can be detrimental for membrane integrity [39]. Plasma-induced graft polymerization can be a convenient technique for durable pore filling and hydrophilicity enhancement without alteration of the membranes. Some studies have been devoted to graft polymerization by immersion of the plasma-activated membranes in the monomer solution to be

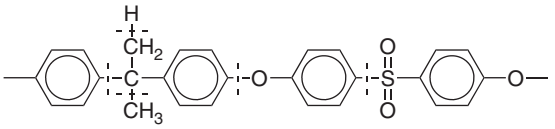

Figure 18 Formula of PSU and chemical bonds likely to break by photodegradation.

grafted; acrylic or methacrylic acids were grafted on PAN and PSU [40], and *N*-vinyl-2-pyrrolidone was grafted on PAN [41]. Graft polymerization was also implemented in vapor phase: acrylic and methacrylic acids on PAN and PSU [40, 42], styrene on PAN [43, 44], 2-hydroxy-ethyl methacrylate [40] or sodium vinyl-sulfonate on PTFE [45], *N*-vinyl-2-pyrrolidone on polypropylene [46], and allylamine or diaminocyclohexane on PVDF [47]. In all these studies, an equivalent plasma activation was used: the membrane was irradiated with an inert gas (He, Ar, N_2, O_2, etc.) in a plasma reactor for 10–300 s and then, either exposed to air for 5–10 min before grafting in the case of liquid-phase grafting, or put in contact with the monomer vapor to be grafted (in the plasma reactor) in the case of vapor-phase grafting. Generally, an RF generator (13.56 MHz) was used in a capacitively coupled reactor, and the input power varied between 20 and 100 W at a total pressure of 0.1–0.5 mbar. The postexposure to air, or/and the presence of water vapor in the plasma reactor, generated the formation of peroxides at the surface of the membranes. After grafting, membranes were finally rinsed in de-ionized water and dried.

We report here the results of Zhao and coworkers [42] related to grafting of acrylic acid on PAN membranes. XPS measurements proved the presence of acrylic acid grafted on the substrate. The field effect scanning electron microscopy (FESEM) photographs showed the smooth surface and the pore filling of the membranes. The pore size decreased with the irradiation time in the first step and then increased for plasma activation longer than 60 s (**Figure 19**). The effect of graft polymerization was a continuous decrease in the pore size and the enhancement of hydrophilicity. As a result of pore filling of PAN, the water-permeation flux through the membranes decreased with plasma input power and graft reaction time. Saccharose solution filtration versus graft reaction time was studied. The retention of saccharose reached about 75% after 15 min of plasma-induced graft polymerization. Similar results were obtained by the same team with plasma grafting of styrene [40, 42]. The pore-size distribution showed a decrease from 14 to 8 nm with an increase of plasma input power and graft reaction time. Such plasma-grafted polymerized PAN membranes were effective in de-waxing the lube oil stock by mixing a de-waxing solvent (methyl ethyl ketone or toluene). The membrane exhibited a rejection of oil up to 73% in de-waxing solvent. Flux and rejection increased with grafting time.

In the case of plasma amino-functionalization of PVDF, plasma-induced graft polymerization using allylamine or diaminocyclohexane as monomer to

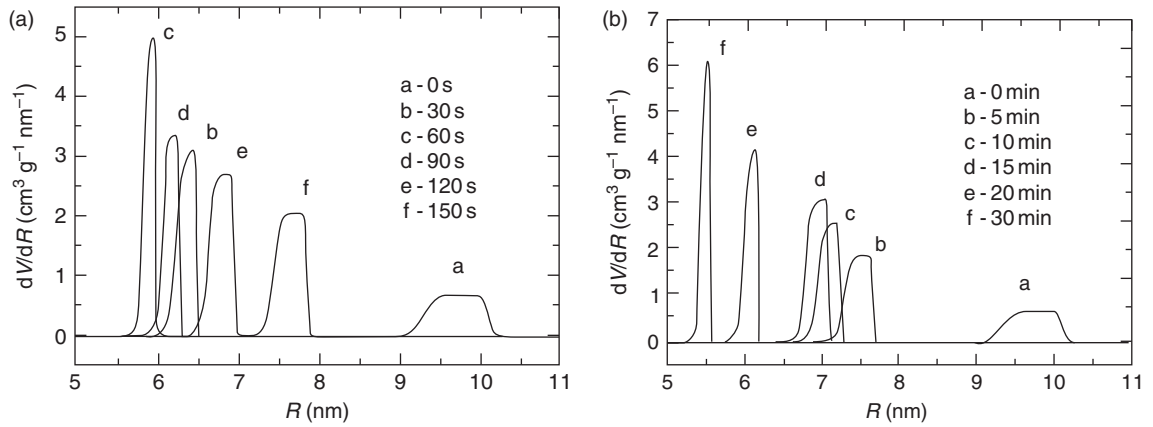

Figure 19 Pore-size distribution of acrylic acid-grafted PAN membranes. Effect of plasma graft-polymerization on (a) plasma time and (b) graft reaction time. d*v*/d*R*, the variation of the membrane specific volume (*v)* as a function of the pore radius (*R*).

be grafted was compared to continuous and pulsed plasma polymerization using nitrogen–hydrogen mixture or ammonia as plasma monomer [47]. A higher degree of functionalization with diaminocyclohexane was achieved when the grafting method was applied.

- *Plasma polymerization.* Acrylic acid deposited by plasma polymerization was compared to that which was plasma grafted on PSU membranes [48]. Plasma polymerization was performed with a microwave (2.45 GHz) plasma discharge. Pulsed plasma (pulse frequency of 125 Hz and 25% of duty cycle) and postdischarge techniques were applied. A low-powered plasma (30 W) resulted in a plasma-polymerized film very similar to conventional poly(acrylic acid). The polymerization yield was similar for both approaches: $34\,\mu g\,cm^{-2}$ for graft-polymerized (GP) and $20\,\mu g\,cm^{-2}$ for plasma-polymerized films. The pore-size distribution of plasma-polymerized membrane was a little wider than that of the GP one; however, the average pore size was smaller. A dramatic decrease of water flux through modified PSU membranes was observed with the degree of grafting in the case of GP-modified membranes, while plasma-polymerized-modified membranes showed a linear decrease of water flux (**Figure 20**).

Protein filtration used the same procedure as previously described in Section 1.09.2.2. Parameters FI, FR, RF, and SR were compared for GP and plasma-polymerized membranes for two pH values. The results are given in **Table 1**. Compared to untreated PSU membrane, modified membranes displayed better performances in basic solution than in the acidic solution of BSA: lower FI (fouling index) and RFF (reduction of flux in filtration), higher FR (flux recovery after cleaning) and comparable SR (protein retention). No significant differences appeared between GP-modified and plasma-polymerized-modified membranes.

1.09.3.3.2 Hydrophobic-nature enhancement by plasma polymerization for filtration applications

Selective membranes for the separation of water from hydrophobic liquids can be obtained by depositing a hydrophobic plasma-polymerized thin layer on porous materials such as filter paper or polyester textile. Organosilicon and fluorine-based compounds can be used as plasma monomers. Bankovic and coworkers [49] used HMDSN or HMDSN–*n*-hexane mixture as monomer. The contact-angle values obtained with water for the treated surface ranged from 135 to 155°. Aging did not affect the membrane performance. Water adsorption measured by Cobb test decreased from values ranging from 300 to $9000\,g\,m^{-2}$ for nontreated surfaces to values ranging from 0 to $20\,g\,m^{-2}$ for treated ones. These surface treatments were suitable for obtaining selective membranes to separate water from organic-polar (ethanol, 2-propanol, carbon tetrachloride, phenol, etc.) and nonpolar (*n*-hexane, cyclohexane, heptane, dodecane, benzene, etc.) compounds of different chain lengths.

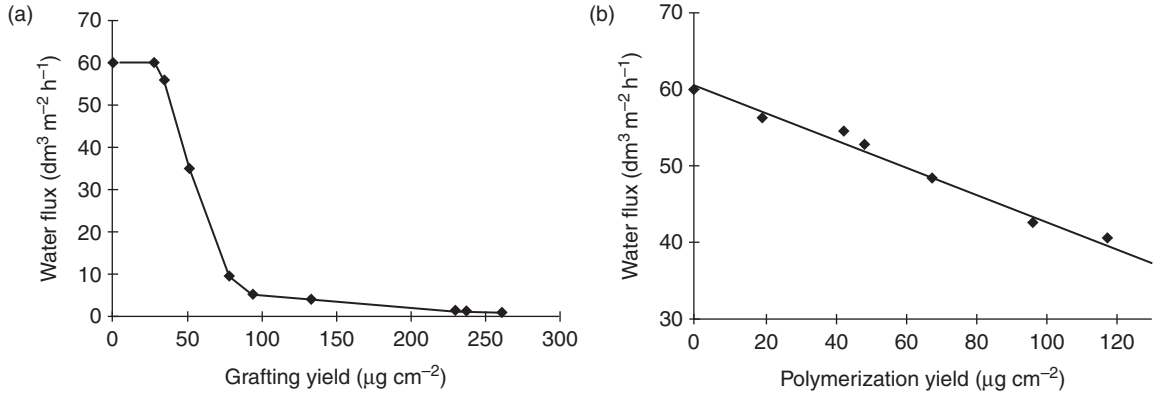

Figure 20 Water flux through treated PSU membranes as a function of the: (a) grafting yield in the case of acrylic acid grafting by plasma-induced graft polymerization and (b) polymerization yield in the case of plasma polymerization of acrylic acid.

Table 1 Comparison of parameters for graft-polymerized and plasma-polymerized membranes

	pH=3			*pH=9*		
	PSU	*GP*	*PP*	*PSU*	*GP*	*PP*
FI	59.9	66.1	65.7	53.5	40.7	41.6
FR	53.2	42.2	45.1	68.4	80.0	76.5
RFF	82.5	77.2	82.2	72.9	53.6	64.3
SR	95	76	93.6	98.6	92.6	97.1

1.09.3.3.3 Selectivity enhancement by plasma processes in electrodialysis application

The only study that reported selectivity enhancement of membranes in electrodialysis was by Vallois and coworkers [50]. To improve the ionic selectivity of cation-exchange Nafion® (perfluorosulfonated polymer commercialized by Du Pont de Nemours) and sulfonated polyimide (sPI) membranes for the recovery of acid from solutions containing metallic salts, a thin film of polyethylene imine (PEI) was deposited on the membrane surface by two techniques. The first one was a plasma preetching of membranes by a 50% O_2–50% Ar plasma discharge followed by a classical electrodeposition of PEI in solution. The second technique was plasma polymerization involving an ethylene–ammonia mixture. PEI-electrodeposited membranes led to a reduction in transport number of copper (in a solution containing protons and copper ions) by 65% and 26% when compared to pristine membranes, for Nafion® and sPI respectively. PEI-plasma polymerized membranes led to a greater reduction of 74% and 59%. So the plasma polymerization method appeared to be more effective than the conventional electrodeposition of a positively charged polyelectrolyte to increase the ionic selectivity of ion-exchange membranes.

1.09.4 Plasma Membranes for Energy-Production Devices

1.09.4.1 Rechargeable Batteries

Batteries are still irreplaceable and are used in a large variety of applications wherein their favorable electrical properties, excellent reliability, and low maintenance are of importance. In batteries, electrical energy is generated by conversion of chemical energy via redox reactions at the electrodes. In its elementary construction, a battery cell comprises two plates (anode and cathode), a battery separator, and an electrolyte. When a load is applied to the battery, electrons are generated at the anode (by its oxidation), pass through the load, and then return to the battery cell at the cathode, which is then reduced [51–53]. Separators play a key role in all batteries. They make a physical barrier between the positive and negative electrodes incorporated into most cells to prevent flow of any electric current between them. On the other hand, they have to allow for rapid transport of the ionic charge carriers that are needed to complete the circuit inside the battery during charging and discharging of an electrochemical cell. This means that the separator must be a good electric insulator and at the same time a good ionic conductor. Moreover, the separator is the smallest (by volume) and the weakest part of the battery and, as a rule, the cycle life of the cell and its performance are limited by failure of the separator. So, in addition to a minimal electrolytic resistance (good conductivity of ions) and electric insulation, the important requirements for a good separator include the following: good mechanical properties and chemical resistance to degradation by electrolyte or the active electrode materials. A manufacture at low cost would be another advantage. In most batteries, the separators are made of either woven and nonwoven fabrics or microporous polymeric films. As electric nonconductors with a high degree of porosity, such materials usually meet both requirements of electric insulation and good ionic conduction. Nevertheless, these materials are often not very mechanically and chemically resistant in aggressive media like the way batteries are. Plasma processes (treatment or deposition) can be promising for overcoming this problem.

1.09.4.1.1 Nickel–cadmium (Ni–Cd) batteries

One of the application fields for Ni–Cd batteries is military and civil aviation service. In addition to the general requirements presented before, Ni–Cd batteries must be very reliable and in some cases must exhibit high power factor; it means that all constituents of the unit cell, including the separator, must be of highest quality. Separators in sealed Ni–Cd (and also nickel metal-hydride) batteries have to be highly permeable to gas molecules for overcharge protection and act as an electrolyte reservoir. In these batteries, the separators are generally a bilayer system made of a polypropylene membrane with porosity of 50%, or more, and a nonwoven fabric mat. Separators in open or valve-regulated

high-power Ni–Cd cells should have very low thickness (in the current technology, 25.4 μm seems to be the standard thickness) with minimal electrolytic resistance. In these specific batteries, the separators used are made of either cellulose (Cellophane) or microporous polyolefine films. Unfortunately, all of these separator materials have some drawbacks. In particular, porous polypropylene membranes show very high electrolytic resistance and poor wettability by KOH solution. Several ways are described in the literature to overcome this disadvantage. The method most often used for this purpose includes the application of surfactants or priming of the membranes with certain solvents; unfortunately, such a method does not enable permanently stable surface hydrophilization and the achievement of minimum electrolytic resistance of the membrane. Other methods include treatments by flame, corona discharge, photons, electron beam, ion beam, X-rays and γ-rays, and above all plasma, which can provide the polymer with a new, stable, and monofunctional surface. The most noteworthy papers dealing with plasma processes concern poly(acrylic acid)-grafted or -deposited 25-μm polypropylene microporous films [54, 55]. The first method implemented by Ciszewski and coworkers [54] was plasma polymerization of acrylic acid in the presence of Ar giving rise to the deposition of a poly(acrylic acid)-like plasma polymer at the surface of the polypropylene membrane. The second method was plasma-induced graft polymerization with acrylic acid [54, 55]. An argon plasma (using a pulsed-microwave discharge) was first applied to the polypropylene film in order to generate activated sites on its surface, and then the film was put in contact with acrylic acid, either in vapor phase in the plasma chamber once the discharge was off or in liquid solution at elevated temperature or under UV irradiation. With both methods, presence of uniformly grafted poly(acrylic acid) on the polypropylene surface was confirmed by XPS, SEM, and FTIR–ATR methods. Polypropylene films grafted in solution under UV irradiation are those that exhibit the best performance. The electrolytic area resistance of such membranes is very low (around 60 $m\Omega\,cm^2$ at room temperature), stability is very good (100 cycles without any change), and the performance of real Ni–Cd cells with the separator (2000 $W\,dm^{-3}$ at 0.6 V) is comparable with cellulose membrane, considered to be the best commercial separator. Furthermore, the grafted polypropylene does not have the disadvantages of Cellophane. It is then a good candidate for an inexpensive and safe separator in rechargeable high-power Ni–Cd batteries.

1.09.4.1.2 Redox-flow batteries

Redox-flow batteries generally consist of two solutions divided by a separator. Each solution contains redox cations (e.g., Fe^{2+}/Fe^{3+}, Cr^{2+}/Cr^{3+}), protons, and anions. The overall performance of redox-flow batteries is strongly dependent on the separator permselectivity among ions of the same polarity. Indeed, the transport of the redox ions through the separator decreases the cell efficiency and cyclicity. Although an anion-exchange membrane might be suitable as a barrier against the redox cations, its electrical resistance is generally too high compared to that of conventional cation-exchange membranes. Furthermore, some anionic complex ions containing the redox species may permeate through anion-exchange membranes. Cation-exchange membranes, on the other hand, generally exhibit lower electrical resistance, but are readily permeated by the redox cations. Taking into account these considerations, the best separator would be a cation-exchange membrane (classically, Nafion®) having a high proton permselectivity. Unfortunately, the selectivity of Nafion® among different counterions is generally low. The deposition of an anion-exchange membrane on the surface of Nafion® can be the solution. The principle of the enhancement of monovalent cation permselectivity is given in **Figure 21**. Due to the electrostatic repulsion from the fixed anions in the cation-exchange membrane, the anion cannot permeate through the membrane. Similarly, the transport of monovalent cations and multivalent cations is also suppressed by the electrostatic repulsion from the fixed cations in the thin anion-exchange overlayer. However, since the repulsion exerted on monovalent cations from the fixed cations is weaker than that on multivalent cations, monovalent cations can be preferentially transported. A high fixed cation density in the thin anion-exchange overlayer will give rise to a high permselectivity of monovalent cations. This enhancement will be achieved, however, at the expense of membrane conductance. Plasma polymerization is a useful method for forming an ultrathin uniform layer which tightly adheres to Nafion®. A thin layer having groups containing nitrogen (e.g., pyridine rings or amines) is required so that it could behave as an anion-exchange layer once the groups containing nitrogen have been positively charged (or quaternized) in acidic or methyl halogenide solution.

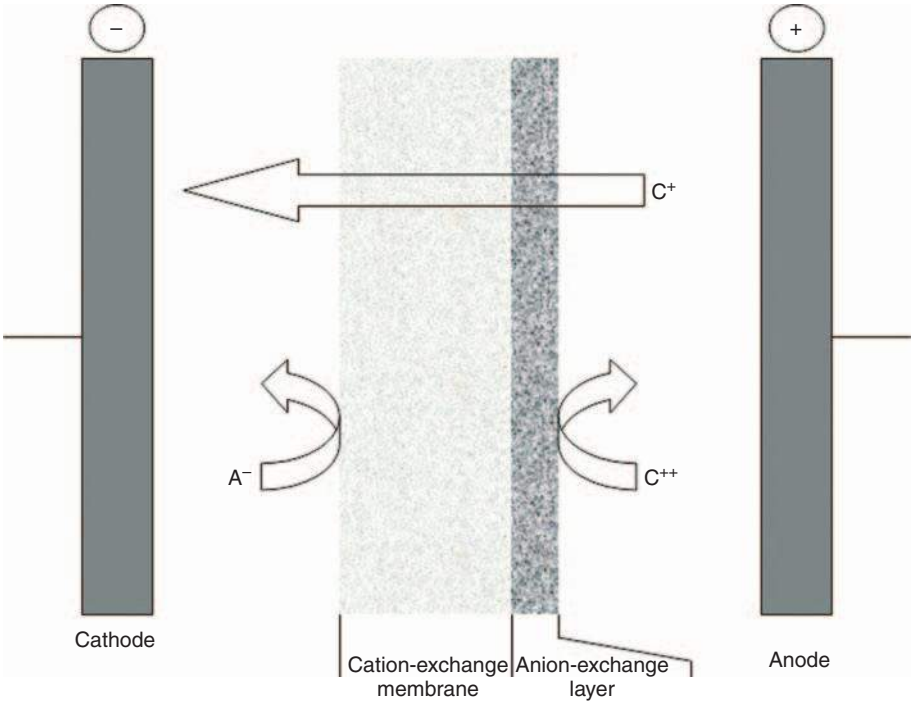

Figure 21 Principle of the enhancement of monovalent ion permselectivity through a cation-exchange membrane.

Ogumi and coworkers were the only researchers interested in using plasma polymerization in the field of redox-flow batteries (in the period 1989–95). First, they performed classical plasma polymerization; they used 4-vinylpyridine as monomer, with argon as diluting gas, in an RF plasma reactor with postdischarge configuration [56–59]. Nafion® 117, pretreated with oxygen plasma for the best adhesion of the 100–300-nm thick plasma polymer, was used as supporting cation-exchange membrane. Quaternization of the plasma polymer was performed by immersion of the bilayer membrane in 1-bromopropane–propylene carbonate solution. Microstructural characterizations showed that the plasma-polymer deposition rate was consistent with the CAP mechanism (highest value: $1000\,\mu g\,h^{-1}\,cm^{-2}$) for input powers and pressures in the range 5–10 W and 10–40 Pa, respectively. The preservation of the pyridine rings was favored at low input power and high pressure. The cation permselectivity of the bilayer membrane was evaluated measuring the Fe^{2+} transport number in $HCl/FeCl_2$ or LiCl, CH_3COOLi, and $CH_3COOH/FeCl_2$ solution. The lower the Fe^{2+} transport number, the higher the cation permselectivity. It could be observed that the lowest Fe^{2+} transport numbers were obtained for plasma polymers synthesized at high input power, low pressure, and high layer thickness; in the best synthesis conditions (50 W, 10 Pa, 300-nm thickness), it was as low as 10^{-2} (whereas it is equal to 0.6 for pristine Nafion®), but at the cost of high membrane resistance equal to $15\,\Omega\,cm^2$ (whereas it is equal to $0.5\,\Omega\,cm^2$ for pristine Nafion®). High resistance could be ascribed to the existence of an interfacial layer formed by penetrating nitrogen-containing species in Nafion®, that quaternized forming a tightly bonded ion pair between the sulfo group of Nafion® and the quaternized amino or the pyridil groups. Some years later, the same research team performed plasma-induced grafting polymerization of 4-vinylpyridine or 3-(2-aminoethyl)aminopropyltrimethoxysilane onto Ar or O_2 plasma-activated Nafion® 117 [60, 61]. Quaternization of the overlayer in the 1-bromopropane–propylene carbonate solution was the final step of the bilayer membrane preparation. The cation permselectivity of the bilayer membrane was evaluated measuring the Fe^{2+} transport number in a LiCl, CH_3COOLi, and $CH_3COOH/FeCl_2$ solution. The argon plasma activation was more beneficial to the cation permselectivity than the O_2 plasma activation, due to the fact that radicals formed by O_2 activation compete with amino radicals to fix on the surface of activated Nafion®. The use of 3-(2-aminoethyl)aminopropyltrimethoxysilane as grafting

compound was more beneficial to the cation permselectivity than the use of 4-vinylpyridine because the number of amino groups fixed from the first compound was higher than from the second. For the best plasma gas-grafting compound couple, Fe^{2+} transport number and membrane resistance as low as 7.5×10^{-3} and 6 $\Omega\,cm^2$ could be measured respectively. Here, the resistance is not too high as in the case of plasma-polymerized overlayers because nitrogen-containing cationic species was absent in the plasma and the interfacial layer between Nafion® and the overlayer did not form.

1.09.4.1.3 Lithium ion (Li-ion) batteries

In recent times, considerable attention has been focused on the preparation of solid-state Li-ion batteries utilizing solid polymer electrolytes, instead of traditional corrosive liquid electrolytes. Several Li-ion conducting polymer/salt complexes, especially polyethers with alkali metal salts, have been shown to be promising candidates as solid electrolytes owing to their relatively high ionic (Li^+) conductivity (10^{-6}–$10^{-8}\,S\,cm^{-1}$) at low or even room temperature. Since these solid polymer electrolytes generally have lower ionic conductivity than liquid electrolytes (10^{-4}–$10^{-6}\,S\,cm^{-1}$), ultrathin films are required to decrease actual film resistance. However, it is not easy to prepare an ultrathin film of solid polymer electrolyte because the thinner the film, the easier the generation of pinholes by conventional techniques. Plasma polymerization is an attractive method for providing an ultrathin uniform polymer layer strongly adhering to battery electrodes.

Among polyethers, those containing siloxane units are attractive because it is known that the introduction of siloxane units into the polymer leads to a low glass transition temperature, which favors the enhancement of the ionic conductivity of the solid polymer electrolyte. Ogumi and coworkers published many papers in this field during the period 1988–90. Their approach was based on the hybridization of a plasma polymer formed from an organosilicon compound with a lithium-based compound and eventually a third compound, polyethylene oxide (PEO) or polypropylene oxide (PPO), whose polarity increases the ionic conductivity. As a first strategy, they prepared a PDMS-like plasma film using an RF discharge, then soaked the plasma polymer in a lithium salt solution, and lastly dried it. First, they used OMCTSO as a single monomer and a mixture of PPO and $LiClO_4$ in butanol as the impregnation solution, and studied the influence of the RF input power and the lithium salt concentration on the microstructural and transport properties of the prepared films [62–64]. Whatever the input power may be, plasma films were thin (1–3 μm), very highly crosslinked (density: 1.45), and characterized by a uniform distribution of ClO_4^- and Li^+ species. In accordance with the CAP mechanism described earlier, the polymer deposition rate exhibited a maximum ($170\,\mu g\,h^{-1}\,m^{-2}$) for a medium value of input power (10 W); in such plasma conditions, plasma polymers were closed to conventional PDMS. For higher values of input power, methyl group elimination and Si–O–Si crosslinking reactions made the films resemble the structure of silica. Consequently, the film's lithium conductivity was all the more high as the input power in the preparation of materials became lower. Concerning the influence of the $LiClO_4$ concentration, two regions could be distinguished: in the low concentration range (<4 wt.%), an increase in salt concentration increased the number of ionic carriers inducing an increase in the conductivity; in the high concentration range (>4 wt.%), crystallized domains of $LiClO_4$ appeared on the films decreasing the conductivity with decrease in lithium salt concentration. Electrochemical measurements showed that the films were made up of a microheterogeneous structure (OMCTSO segments–PPO segments) in which the PPO segments were those mainly contributing to the ionic dissociation of $LiClO_4$. In best operating conditions, a rather good conductivity of $2.6 \times 10^{-6}\,S\,cm^{-1}$ (resistance: 40 $\Omega\,cm^2$) at 60 °C could be achieved. Tests on the cells revealed a fairly good rechargeability (cycling at 10–40 $\mu A\,cm^2$) but a large internal resistance, certainly due to lack of a close contact between the membrane and the electrodes due to the formation of a resistive layer at the interface. With the aim of having one single mobile species (only Li^+) on the films, more favorable to high ionic conduction than two mobile species, Ogumi and coworkers [65] added methyl methanesulfonate or methyl benzenesulfonate in the OMCTSO plasma discharge in order to obtain PDMS-like plasma polymers containing $-SO_3R$ groups. Such materials were successively soaked in LiI–propylene carbonate and butanol–PEO solutions to get hybridized PDMS-like (containing $-SO_3Li$)/PEO films. Microstructural characterizations showed a better efficiency of methyl benzenesulfonate rather than methyl methanesulfonate for the introduction of $-SO_3R$ groups into the polymer matrix. Uniform distribution of $-SO_3Li$ and good attachment of these groups on the polymer matrix were demonstrated. In best operating conditions, a rather good conductivity

of $1.3 \times 10^{-6}\,S\,cm^{-1}$ (resistance: 80 $\Omega\,cm^2$) at 60 °C could be achieved. As a second strategy, Ogumi and coworkers prepared a poly[tris(2-methoxyethoxy)-vinylsilane]-like plasma membrane using an RF discharge, then sprayed the plasma polymer with a lithium salt solution, deposited a second layer of plasma polymer on top of the sprayed solution, and lastly dried the multilayer structure so that the lithium salt solution could uniformly diffuse through both the polymer layers. First, they used tris(2-methoxyethoxy)vinylsilane (TMVS) as the only monomer and a methanol–$LiClO_4$ mixture as the sprayed solution whose uniform diffusion in materials was demonstrated [66, 67]. A good conductivity of $4.4 \times 0^{-5}\,S\,cm^{-1}$ (resistance: 2.3 $\Omega\,cm^2$) at 100 °C and a good rechargeability when integrated in a Li-ion battery were obtained. Nevertheless, the problem of large-cell internal resistance previously observed for PDMS-like plasma films was also observed for poly(TMVS)-like membranes. In order to overcome this problem, Ogumi and coworkers [68] added methylacrylate in the TMVS plasma discharge in order to obtain co-poly(TMVS)-poly(methylacrylate)-like plasma polymers containing –COOR groups, then sprayed LiI–propylene carbonate solution before a second deposition of plasma polymer, and a final drying. Microstructural characterizations showed a uniform distribution of –COOLi and a good attachment of these groups on the polymer matrix. Nevertheless, only a very low conductivity of $10^{-8}\,S\,cm^{-1}$ at room temperature could be achieved even for materials synthesized in best operating conditions, which may be ascribed to the weak acidity of carboxylic acid groups. A bit later, in the middle of the 1990s, Kwak and coworkers [69] reported for the first time the preparation of a lithium-conductive plasma membrane using the combination of plasma polymerization with plasma sputtering. The implementation of an RF discharge in a chamber containing C_2H_4 as hydrocarbon monomer (introduced with a diode gun), Ar and O_2 as diluting gases, and Li_3PO_4 target (placed on a magnetron) as lithium source enabled to obtain thin lithium-conductive composite plasma films. Such films were found to be randomly crosslinked alkanes with sporadic distribution of unsaturated C–C bonds. In addition, the films were found to contain various functional groups resulting from the reactions with the process gas species in the plasma: in particular, C–O–C, –OH, and C=O groups. The elements originating from Li_3PO_4 target were found to incorporate into both the polymeric backbone and the dispersed inorganic phase. The film deposition rate was consistent with the CAP mechanism; the amount of inorganic phase was tunable with the operating conditions. The ionic conductivity was found to increase with the amount of inorganic phase in films (highest value: $2.7 \times 10^{-9}\,S\,cm^{-1}$ at 40 °C), while the activation energy (0.8–0.9 eV) was found to depend on the crosslinking and coordination site densities in the polymer backbone. Authors pointed out that highest conductivities would have been obtained with single-phased macromolecules which could be produced using a pulsed discharge or a single monomer source containing all the desired elements (hydrocarbon groups and lithium). More recently, Choi and coworkers [70] were interested in electrospun PVDF nanofiber webs as base materials for ion-conductive membranes. The ion conductivity of the polymer electrolyte formed using these nanofiber webs and $LiN(CF_3SO_2)_2$ electrolyte solution embedding the porous polymer matrix was up to $2.0 \times 10^{-3}\,S\,cm^{-1}$ at room temperature. Despite being highly conductive, the clogging of pores of these membranes is necessary so that they could be used as a separator in Li-ion batteries. To serve this purpose, Choi and coworkers deposited a polyethylene-like plasma layer (from ethylene monomer subjected to a plasma discharge) onto the PVDF nanofiber webs before impregnating them with lithium salt. The ethylene plasma-treated mat performed the role of a shutter by melting the polyethylene-type layer grafted on the PVDF nanofibers. In our group, lithium-ion-conductive membranes made up of octamethylcyclotetrasiloxane-based plasma films impregnated with $LiPF_6$ were prepared. Satisfying conductivities of $10^{-6}\,S\,cm^{-1}$ were measured (nonpublished results).

1.09.4.2 Fuel Cells

A better control of natural resources needs the development of technologies for energy production that causes less potential environmental impacts. Fuel cells are often perceived as being one of the possible solutions to provide clean energy. Their operating principle is generally described as an electrochemical and controlled combustion of fuel (hydrogen, methanol, etc.) and oxygen with simultaneous production of electricity, water, and heat. This combustion takes place within a structure, usually called fuel-cell core, mainly composed of two catalyzed electrodes (the anode where the fuel is oxidized and the cathode where the oxygen is reduced) separated by an electrolyte. The electrolyte plays two key roles: on the

one hand, it forms a physical barrier between both electrodes preventing contact between the fuel and oxygen; on the other hand, it provides the transport of ions produced at one electrode and consumed at the other. Among the different kinds of fuel cells, the ones using a polymer membrane as an electrolyte are at present more widely studied. These fuel cells have numerous advantages: they are less sensitive to carbon dioxide than the others; they present a low working temperature (in the range 80–100 °C) enabling a quicker starting, a higher operating flexibility, and a better thermal management than other kinds of fuel cells; moreover, they are of multiple uses (stationary, transport, and portable applications), and cover a large power range (0.1 W–10 MW). For the specific market of portable electronic devices (mobile phones, microcomputers, cameras, small robots, etc.) requiring fuel cells in a microscale, polymer electrolyte fuel cells are particularly promising. Two different types of polymer electrolyte fuel cells can be distinguished depending on the acid or basic nature of the electrolyte. Those using an acidic polymer electrolyte are called proton exchange membrane fuel cell (PEMFC) (**Figure 22**(**a**)), or more generally, solid polymer fuel cell (SPFC) which includes direct methanol fuel cell (DMFC) and direct ethanol fuel cell (DEFC); their power density is up to 500 and 100 mW cm^{-2} for PEMFC and DMFC, respectively. Fuel cells using an alkaline polymer electrolyte, very recently conceptualized, are called solid alkaline membrane fuel cells (SAMFCs) (**Figure 22**(**b**)). Due to their simple handling, high safety, and high energy density, alcohols, especially methanol, are preferred to hydrogen to supply fuel cells on a microscale.

1.09.4.2.1 Acidic fuel cells

The electrolyte of PEMFC and DMFC is an acidic ion-exchange membrane, typically made up of a perfluorinated polymer matrix on which proton-exchange groups such as phosphonic acid ($-PO_3H$), carboxylic acid (–COOH), or more often sulfonic acid ($-SO_3H$) are grafted. The main role of this electrolyte is to provide the transport of protons from the anode where they are produced by the oxidation of fuel to the cathode where they are consumed by the reduction of oxygen into water (**Figure 22**(**a**)). Until now, research relative to the development of electrolyte membranes for PEMFCs or DMFCs has essentially focused on the Nafion® membrane known as a good proton-exchange material (proton conductivity: 0.01–0.1 S cm^{-1}) with quite high chemical stability. Nevertheless, the Nafion® membrane has many drawbacks which highly limit the competitiveness of acidic polymer electrolyte fuel cells, notably a high cost (800 € m^{-2}), a conduction ability highly dependent on its water content limiting its use at temperatures lower than 100 °C, and a high methanol permeability in DMFC ($(2.5–3) \times 10^{-6}$ cm^2 s^{-1}). The methanol permeability, which causes not only a mixed potential at the cathode but also a considerable amount of fuel loss [71, 72], is a very limiting feature. This methanol crossover phenomenon results from the large percolation size of the water-swollen Nafion® membranes. Although their large percolation size is the main

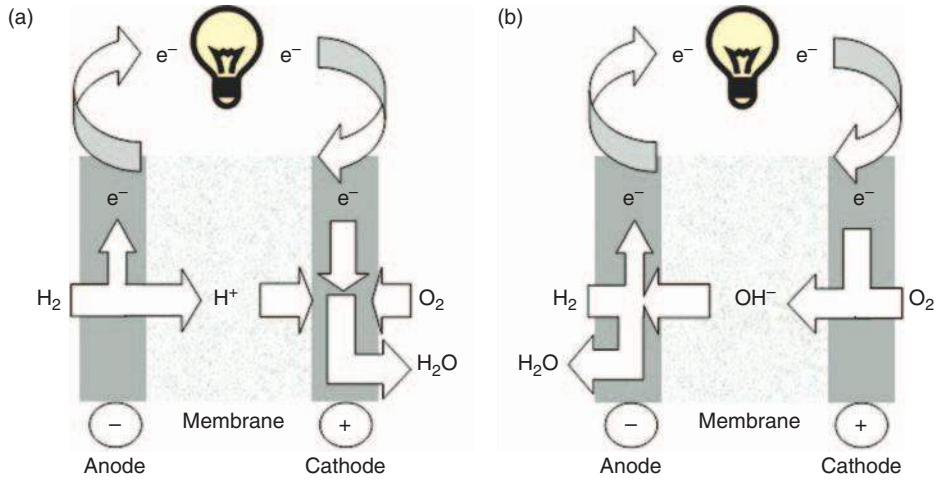

Figure 22 Schematic principle of PEMFC-type (a) and SAMFC-type (b) fuel cells.

reason for the high proton conductivity of Nafion®, membranes, it unfortunately allows the methanol molecules to penetrate through the membranes at the same time [73, 74]. As other handicaps, the low mechanical strength of Nafion®, due to the lack of intermolecular crosslinkage between the polymer skeletons, and the difficulty in reducing its thickness limit its use in micro-fuel cells. So, recent research efforts concentrate on the development of new kinds of membranes which could be advantageous alternatives to Nafion®. Main studies have been performed with the goal of developing alternative membranes, focusing on the reduction of methanol permeability. Studies were generally divided into two categories. The first was to modify the Nafion® membranes by blending them with other polymer/inorganic materials or by surface modification. The second was to develop new synthetic polymeric membranes that have ionic clusters with a small percolation size. Among many methods, plasma processes are promising techniques for contributing toward both approaches:

- *Surface modification of Nafion® by plasma processes.* Implementation of plasma processes on Nafion® aims at reducing the methanol crossover as a priority and also reinforcing the mechanical, thermal, and/or chemical resistance. A simple efficient approach consists in plugging the pores at the surface of Nafion® by palladium deposition using argon plasma combined with sputtering of a palladium target. The methanol permeability of Nafion® could be divided by a factor 1.5 [75, 76], but at the cost of proton-conductivity decrease (30% reduction) [76] leading to an unchanged or slightly improved fuel cell performance at low current density (where the effects of proton conductivity and methanol crossover on fuel cell performance are both important), and unfortunately, a worse fuel cell performance at high current density (where the effect of methanol crossover is generally quite negligible). Bae *et al.* [77] used the plasma-induced graft polymerization to deposit a sulfonated polystyrene layer on the surface of Nafion®. After activation of the surface by argon plasma, the Nafion® was soaked in a styrene or styrene–divinylbenzene (DVB) (as crosslinking agent) solution for grafting reaction, and then soaked in a acetic sulfate–1,2-dichloroethane mixture for sulfonation reaction. It was shown that increasing the DVB concentration in the grafting solution induced a reduction of the grafting reaction rate and consequently, a reduction of the thickness, degree of swelling, ionic cluster size, and water uptake of the grafted layer. The methanol permeability of the modified Nafion® decreased as the DVB concentration was increased up to 5 mol.% (due to reduction of the degree of swelling, ionic cluster size, and water uptake of the grafted layer) and then reached a plateau at about 2×10^{-6} $cm^2\,s^{-1}$ (83% of that of Nafion®) above 5 mol.% (under the tradeoff effects of the reduction of the grafted layer thickness and the reduction of the degree of swelling, ionic cluster size, and water uptake of the grafted layer). As the acidity of sulfonic acid groups attached to styrene is lower than that of sulfonic acid groups in Nafion®, the proton conductivity of the modified Nafion® was lower than that of pristine Nafion®. This proton conductivity showed an opposite trend toward methanol permeability; it increased as the DVB concentration was increased up to 5 mol.% (under the effect of the reduction of the grafted layer thickness) and then reached a plateau at about $0.03\,S\,cm^{-1}$ (90% of that of Nafion®) above 5 mol.% (under the tradeoff effects of all microstructural features).

Other authors were interested in the deposition of a plasma polymer onto the surface of Nafion®. Walker and coworkers [78–81] used a hexane–H_2 mixture or tetrafluoroethylene (TFE) as precursor(s) in a pulsed microwave discharge; polyethylene-type or PTFE-type plasma films with thicknesses in the range 200–300 nm were deposited on Nafion® 117, respectively. The methanol permeability could be reduced by a factor of 15 and 20, respectively, due to the low methanol sorption ability of plasma films. In return, the proton resistance increased by a factor of 7 in the case of the polyethylene-type plasma film (no published value in the case of the PTFE layer) [80]. Kim and coworkers [82] deposited a silica-like plasma layer on Nafion® 115 using tetraethoxysilane plasma. For plasma films with thickness lower than 10 nm, the methanol permeability was reduced by 40% without simultaneous decrease of proton conductivity, inducing a fuel cell performance increase of 20%. Finsterwalder and Hambitzer [7] deposited a 370-nm thick sulfonated PTFE-like plasma film on Nafion® 112 using the plasma sputtering of a PTFE target under the effect of an argon plasma combined with the plasma polymerization of a sulfonated monomer (SO_2, CF_3SO_3H, or $ClSO_3H$). The CF fragments stemming from the PTFE sputtering combined with the sulfur components coming from the sulfonated monomer fragmentation to form a coherent thin film.

In the case of SO_2, the sulfur components were smaller than for other sulfonated monomers; thus, the resulting monomer was made up of shorter chains and was consequently more highly crosslinked; so the reduction of the methanol permeability was more pronounced: by a factor of 10 when compared to the pristine Nafion®. In return, the proton resistance was multiplied by 20, due to the inability of SO_2 to form sulfonic acid groups in the plasma layer. In the case of CF_3SO_3H or $ClSO_3H$, giving rise to less-rigid plasma polymers containing sulfonic acid groups, not only was the reduction of the proton resistance less (factor 4) but methanol permeability was reduced as well (factor 5). Very recently, Prakash and coworkers [83] prepared phosphorus-doped silicate glass (PSG) films as a proton-conductive overlayer on Nafion®. Silicate glasses with adequate proton conductivity are ideal because they are inexpensive, reliable, easily fabricated by PECVD over a wide range of thicknesses, and can serve as a methanol barrier layer to lower the fuel crossover rate in DMFCs. The magnitude of the ionic conductivity in phosphorous-doped silica glasses depends on free volume and pore surface area (for ion transport), chemical structures in the glass (e.g., –Si–OH and –P–OH concentration), intermediate range order, and the local bonding environment in the glass network. A glow discharge of a mixture of SiH_4, PH_3, and N_2O gave rise to 2–3 μm thick films showing proton conductivity up to $2.5 \times 10^{-4}\,S\,cm^{-1}$ in the best synthesis conditions, that is, at low substrate temperature (100 °C) favorable for the incorporation of phosphorus and silanol into the films, at high input power increasing the silanol defect sites, and at moderate pressure enhancing the defect density of the films. Polarization experiments with pristine Nafion® and PSG-coated Nafion® indicated that the presence of the PSG film significantly improved cell performance (the open-circuit voltage was increased by approximately 65 mV and the current density at 0.4 V was nearly tripled).

- *New synthetic polymeric membranes mixing conventional and plasma materials.* The development of mixed conventional-plasma membranes aims at obtaining new synthetic polymeric membranes being cheaper than Nafion® and/or having ionic clusters with a smaller percolation size for a low methanol crossover and also high mechanical, thermal, and/or chemical stability. Won and coworkers [84] focused on cost reduction; they used sulfonated polystyrene-block-poly(ethylene-ran-butylene)-block-polystyrene (sSEBS), much cheaper than Nafion®, as the proton-conductive membrane. As sSEBS is less stable and more permeable to methanol than Nafion®, they deposited onto it a plasma-polymerized layer using maleic anhydride as precursor and then soaked it in two successive solutions: first a $NaOH–NaHCO_3–H_2O$ solution to change succinic anhydride groups into carboxylic acid salt groups and second in a HCl solution to get proton-conductive carboxylic acid groups. Increasing the flow rate of maleic anhydride monomer decreased the methanol permeability down to $1.4 \times 10^{-6}\,cm^2\,s^{-1}$ at the cost of reduction of proton conductivity (down to $6 \times 10^{-3}\,S\,cm^{-1}$) in spite of the presence of proton-conductive groups in the plasma layer. With the same aim, Lue and coworkers [85] used GEFC® as a proton-conductive membrane and deposited onto it a perfectly adherent and mechanically stable polyfluoroethylene-like plasma layer using perfluoroheptane diluted in Ar as monomer. A parametric study showed that the input power in the plasma discharge was the most dominant factor; at highest input power, it gives rise to the plasma layer with the highest hydrophobic nature and crosslinking degree together with the lowest water uptake and ionic exchange capacity, the methanol permeability was minimal, being $3.3 \times 10^{-8}\,cm^2\,s^{-1}$ (smaller by a factor of 73 when compared to that of GEFC®) at the cost of a minimal proton conductivity ($1.1 \times 10^{-4}\,S\,cm^{-1}$, smaller by a factor of 50 compared to that of GEFC®). Other authors implemented the concept of pore-filling electrolyte membrane which consisted in filling a porous polymer (chosen for its low cost, its mechanical, thermal, and chemical stability as well as for its rigidity unfavorable to methanol crossover) with an ion-conductive grafted polymer – grafting being performed via plasma activation. Using this technique, the grafted polymer can grow from the pore surface via covalent bonds and fill the entire substrate porosity; its mobility (in particular its ion conductivity) is high as it is a linear polymer. Yamaguchi and coworkers [86] implemented this technique using PTFE as porous substrate, argon plasma as grafting activation source, and acrylic acid as grafting monomer. The pore-filling electrolyte membrane showed low methanol permeability (10 times lower than that of Nafion® up to 130 °C) and high durability up to 180 °C. On the same principle, Bae and Kim [87] used polypropylene as porous substrate, argon plasma as grafting activation source, and styrene as grafting monomer; a post-sulfonation was realized soaking the membrane in a acetic sulfate–1,2-dichloroethane mixture. Small grafting and sulfonation times induced low methanol permeability (down to $8.6 \times 10^{-7}\,cm^2\ \ s^{-1}$) and also low ion-exchange

capacity (1–1.5 meq. g^{-1}) and low proton conductivity (3×10^{-3} S cm^{-1}), leading to the lowest fuel cell performance (16 mW cm^{-2} at best) when compared with Nafion® (21 mW cm^{-2}), ascribed to de-lamination between the membrane and catalyst layers. Finally, another strategy consisted in impregnating a porous stable polymer with Nafion® solution, the porous polymer being first fluorinated on the surface and in the pores by plasma treatment in order to increase the soaking amount of Nafion® and its interfacial stability with the porous polymer. Bae and coworkers [88] used this strategy with porous polypropylene as substrate and Freon-116 as plasma gas; methanol permeability ten times lower than Nafion® (at cost of proton conductivity 10^3 times lower) at room temperature could be measured.

- *Plasma ion-conductive membranes.* All studies previously described, used plasma as the grafting activation source or as the means of modulating the transport properties of conventional ion-conductive polymers. These studies showed that, because methanol transport and proton conductivity have a kind of tradeoff relationship in conventional polymers, it is difficult to selectively reduce one without affecting the other and vice versa. As the mass transport and especially the ionic transport mechanism is very different in plasma polymers, ion-conductive membranes made up of only plasma materials could overcome this limitation. Many research teams were interested in preparing plasma ion-conductive membranes. The main required criteria for a good ion-conductive membrane are: high water content when immersed in electrolytic solution, a large quantity of ionizable functional groups favorably distributed in the polymer matrix, and a small thickness. The manufacture of ion-conductive membranes by plasma polymerization is a real challenge. Indeed, high water content implies plasma polymers made up of sufficiently airy and flexible chains. Now plasma polymers are known to be naturally highly crosslinked. To overcome this lock, it is necessary, first, to choose a precursor with long and flexible chains or at best containing spacers in its structure (e.g., phenyl groups) and then initiate the synthesis process with a soft plasma discharge in order to preserve the constitutive elements of the precursor likely to constitute the skeleton of the final material. The second required criterion (large quantity of ionizable functional groups favorably distributed in the polymer matrix) is also very challenging. Indeed, plasma polymers are generally composed of nonionized and randomly distributed groups. The choice of a precursor containing the required ionizable functional group in its structure and the implementation of a soft plasma discharge may enable producing a material rich enough in ionizable groups. Nevertheless, control of the arrangement of these groups in the polymer matrix remains utopian.

Inagaki and coworkers [89–91] used a mixture of fluorocarbon compound (perfluorobenzene (PFB), pentafluorobenzene (PnFB), or tetrafluorobenzene (TFB)) and SO_2 (as source of sulfonic acid groups) or CO_2 (as source of carboxylic acid groups) as monomers in an RF plasma discharge. The highest deposition rate (14 μg cm^{-2} min^{-1}), ion-exchange capacity (1.3 meq. g^{-1}), and proton conductivity (4.3×10^{-5} S cm^{-1}) were obtained for the TFB–SO_2 (75 mol.%) mixture. Ogumi and coworkers implemented an RF- or low-frequency-plasma polymerization using methyl benzenesulfonate (MBS), benzenesulfonyl chloride (BSC), benzenesulfonyl fluoride (BSF), or trifluoromethanesulfonic acid (TFMS) as a source of sulfonic acid groups mixed with 1,3-butadiene, trifluorochloroethylene (TFCE), hexafluoropropene (HFP), or octafluorocyclobutane (OFCB) as monomer for the matrix edification; argon was used as the diluting gas. In the case of the MBS–butadiene mixture [92, 93], the 200-nm thick plasma polymers were soaked in a LiI–butanol solution to hydrolyze the sulfonic ester groups into lithium sulfonate ones. For low-input-power values (enabling the preservation of sulfonic ester groups during the plasma polymerization), synthesized plasma polymers showed the highest ion-exchange capacity (1.4 meq. g^{-1}), yet the lowest proton conductivity (1.8×10^{-4} S cm^{-1}) due to high crosslinking, but low proton resistance (0.04 Ω cm^2) when compared with Nafion® due to its very small thickness. In the case of the BSC– or BSF–butadiene mixture [94, 95], the plasma polymers were soaked in a NaOH–H_2O–methanol solution to hydrolyze the sulfonic halide groups into sodium sulfonate ones. For BSF, sulfonyl fluoride groups were introduced into the plasma polymers, whereas BSC tended to decompose during plasma polymerization. This difference was discussed based on results obtained by *in situ* mass spectrometry and molecular orbital calculations. For BSF, the parent ion ($[C_6H_5SO_2F]^{+\bullet}$ was the major species which introduced the sulfonic fluoride groups into the plasma polymers because S–F bond cleavage was difficult. However, the parent ion of BSC was unstable in the glow discharge plasma and cleavage of the S–Cl

bond was facile and produced Cl radicals. For low-input-power values, plasma polymers from BSF showed the highest ion-exchange capacity (1.5 meq. g^{-1}) when compared with Nafion®. In the case of the TFMS–TFCE mixture [96], plasma polymers containing sulfonic acid groups were directly obtained. Increasing the concentration of TFMS in the plasma reactor induced an increase of the sulfonic acid group content and consequently an increase of proton conductivity up to 5×10^{-5} S cm^{-1}. Although intrinsically less conductive than Nafion®, plasma polymers exhibited the same proton resistance (2 $\Omega\,cm^2$) due to their small thickness. From the same monomer mixture but using TFCE as carrier gas for TFMS instead of argon, Brumlik and coworkers [97] obtained conductivities ten times higher (6×10^{-4} S cm^{-1}) at room or at higher temperatures. Plasma polymers containing sulfonic acid groups could also be obtained from TFMS–HFP or TFMS–OFCB mixtures by Ogumi *et al.* Under the best plasma conditions (low input power, high pressure), HFP-based plasma polymers showed the lowest ion-exchange capacity (0.7 meq. G^{-1}) and the lowest proton conductivity (1.8×10^{-4} S cm^{-1}) when compared with Nafion® due to their highly crosslinked structure [98, 99]; OFCB-based plasma polymers exhibited the best proton conductivity (10^{-4} S cm^{-1}) when water vapor (more effective in preserving the sulfonic acid groups than argon) was added into the plasma discharge [100]. The sulfonated polytetrafluoroethylene-like plasma film deposited on Nafion® 112 by Finsterwalder and Hambitzer [7] (described previously) from PTFE and SO_2, CF_3SO_3H, or $ClSO_3H$ was also used as single plasma membrane. The highest ion conductivity (>10^{-4} S cm^{-1}), water uptake capacity (*c.* 8.5 mmol g^{-1}), and ion-exchange capacity (*c.* 0.15 mmol g^{-1}) exhibited membranes polymerized with $ClSO_3H$. Finsterwalder and Hambitzer proposed an explanation for the poor conductivity of plasma polymers containing sulfonic acid groups. This poor conductivity is probably attributed to its secondary structure. While in Nafion®, flexible backbone and side chains allow the sulfonic acid groups to agglomerate into a polar cluster, the mobility of sulfonic acid groups, and thus the extent of phase separation, was drastically reduced in the rigid crosslinked plasma polymers. The rigid matrix of the plasma polymers hampers an effective ionic-communication network via ion channels, and sulfonic acid groups remain isolated from each other, thereby not contributing to the proton transport. Water-uptake measurements indicate that the number of water molecules per sulfonic acid group is higher in the plasma polymers in Nafion®, so that the hydration water is more bulk like and Grotthus transport (the apparent jumping of protons from water to adjacent water molecules through the membrane) is favored. The effect of higher hydration could thus compensate for the little extent of phase separation. Nevertheless, this compensation is generally not important enough. The only compensation very profitable to plasma polymers is their low thickness which makes them as competitive as Nafion® in terms of ion conduction despite their low intrinsic conductivity.

Such observations could also be made in our group which has been working for some years on the preparation of sulfonated polystyrene-type plasma membranes from styrene/trifluoromethanesulfonic acid (CF_3–SO_3H) precursor mixture in an RF capacitively coupled plasma reactor [101–107]. Styrene was used as a polymerization agent giving rise to the formation of a carbonaceous matrix containing aromatic spacing groups (preventing too highly crosslinked structures), and trifluoromethanesulfonic acid as a sulfonation agent to promote protonic conductivity. The recent use of a pilot-scale reactor equipped with a pulsed power source and sophisticated monomer-injection devices [107] enabled the synthesis of very uniform plasma membranes with thicknesses of some tens of microns for a deposition duration of some hours (optimal growth rate: 160 nm min^{-1}) and a structural stability of up to 140 °C in air. In such optimized membranes, the proportion of sulfonic acid groups was much higher than in Nafion® and the protonic conductivity reached 1.7×10^{-3} S cm^{-1}. Although these conductivities were 40 times lower than that of Nafion® (7×10^{-2} S cm^{-1} measured in the same cell), the protonic transport ability of plasma membranes was not less competitive thanks to very small thicknesses. Low crossover to methanol (2.3×10^{-5} mol m^{-2} s^{-1}), 40 times lower than that of Nafion® (10^{-3} mol m^{-2} s^{-1}) was also demonstrated. Such plasma membranes were then integrated in a cell comprising two electrodes made up of commercial E-TEK on which Pt catalyst was deposited by plasma sputtering [108]; the obtained membrane–electrode assembly (**Figure 23**) showed perfect interfaces between all layers promising high cell performance (work in progress). In the future, the outcome of this work would be the development of such devices entirely

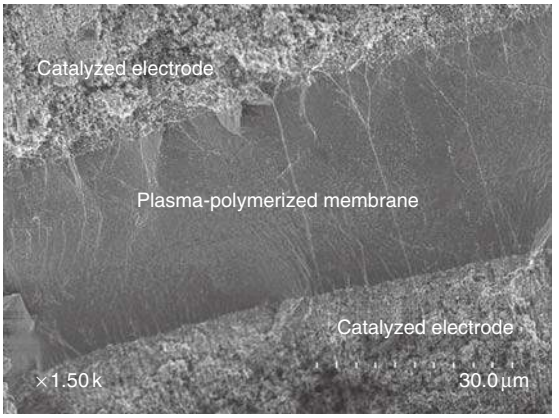

Figure 23 SEM micrography of a fuel cell core whose membrane and catalyst are synthesized using plasma processes.

composed of plasma materials (diffusion layers prepared by PECVD from a hydrocarbon-based monomer) in a single integrated plasma process.

Although less acidic than sulfonic acid groups, phosphonic acid ones ($-PO_3H$) present the advantage of higher chemical and thermal stability. Mex and coworkers [109, 110] worked on the preparation of highly thermally stable (up to 200 °C in air) proton-conductive plasma membranes containing phosphonic acid groups using a mixture of TFE and phosphonicvinyl acid (PhVA) as monomers. Both monomers exhibit π-bonds, which permitted plasma polymerization to be achieved without fragmentation of the phosphonic acid groups, and ensured a chemical binding of these groups into the polymeric backbone of the membrane. When prepared at low input power, plasma membranes showed very high proton conductivity (up to 0.56 $S\,cm^{-1}$ at 30 °C) and very promising fuel cell performance. Replacing PhVA by water vapor (intended to incorporate $-OH^-$ as proton exchanger groups) decreased the proton conductivity (0.14 $S\,cm^{-1}$ at 30 °C in the best synthesis conditions) but increased the cell performance, thanks to lower fuel permeability directly related to higher degree of crosslinking [111].

Lastly, a recent original study by Gruber and Müller [112] has to be mentioned; their work consisted in enhancing PEMFC performance by introducing additional thin layers to sputter-deposited Pt catalyst in order to improve accessibility of hydrogen to catalyst sites which are not directly adjacent to the micropores of the gas diffusion layer. The introduction of a H_2-permeable PDMS-like plasma membrane (prepared from HMDSO) underneath the anode catalyst layer improved the PEMFC performance by about 18%.

1.09.4.2.2 Alkaline fuel cells

The development of solid alkaline fuel cells (SAMFCs), as a new class of promising fuel cells in terms of performance and low cost, has very recently been investigated. The operating principle of SAMFCs is a hybrid concept between that of both DMFCs and classical alkaline fuel cells (AFCs) used in spatial applications (since Gemini programs in 1965) (**Figure 22(b)**). The electrolyte of SAMFCs is an alkaline ion-exchange membrane, typically made up of a hydrocarbon-based polymer matrix on which hydroxyl-exchange groups as quaternary amines ($-N(CH_3)_3^+$) are grafted. The main role of this electrolyte is to provide the transport of hydroxyl ions from the cathode where they are produced by the reduction of oxygen into water to the anode where they are consumed by the oxidation of fuel. The expected advantages of SAMFCs, when compared to classical AFCs, are the possibility of easy handling and stocking fuel (in this case, methanol) and the easy control of carbonation due to the solid nature of the electrolyte (in this case, a membrane instead of an alkaline solution in AFCs). When compared to DMFCs, the expected advantages of SAMFCs include decrease of methanol crossover due to the basic nature of the electrolyte and the possibility of using a less-expensive nonprecious metal catalyst. For such fuel cells, one of the main challenges is the development of hydroxyl-exchange membranes showing high anionic conductivity, low fuel permeability, and high chemical stability. The chemical stability of anion-exchange membranes in strong basic media is particularly problematic due to the well-known Hofmann degradation of quaternary amine groups in concentrated alkaline solutions [113, 114]. Very few studies have been devoted to the development of membranes for SAMFCs yet; these membranes are generally made up of a conventional polymer matrix (based on ethylene oxide, epichlorhydrin, hydrocarbon, or fluorocarbon chains) on which are grafted aliphatic or aromatic hydrocarbon side chains containing quaternary amine groups. To our knowledge, only two groups have been working on the development of such membranes by plasma polymerization: Ogumi's group and our team. Ogumi and coworkers [115] studied the plasma polymerization of 4-vinylpyridine post-quaternized with 1-bromopropane. In best synthesis conditions, the prepared plasma polymers had

a thickness of 10 μm, a hydroxyl conductivity of 5.4×10^{-4} S cm^{-1} and a related resistance of 1.9 Ω cm^2. When compared to commercial membranes (e.g., ADP Morgan® from Solvay, AHA from Tokuyama Co.), these plasma membranes were intrinsically ten times less conductive (due to their highly crosslinked structure) but as competitive due to their low thickness. Used as an interfacial layer between a commercial AHA membrane and an E-TEK anode, such a plasma-polymerized film led to an improvement of the anodic triple point; an increase of the anodic current by a factor 4.5 was measured. In our group, hydroxyl-conducting polyethylene-type plasma polymers containing amine groups were prepared by plasma polymerization of triallylamine (N-(CH_2–CH=CH_2)$_3$) in a pulsed RF discharge [104–106, 116]. The choice of triallylamine as precursor was related to the assumption that the implementation of a very soft plasma discharge should enable to the polymerization of triallylamine via its double bonds and therefore preserve the tertiary amine entities –NR_3 in the final materials. In order to get highly conductive materials, plasma polymers coming out of the plasma reactor were put in contact with a methylhalide compound (ICH_3, 30% in acetonitrile) with the aim of changing –NR_3 groups into quaternary amine functions –NR_4^+ well known to have very efficient anion-conductive functions. In fact, only amine functions at the upper surface of plasma films were really quaternized. Synthesized materials before or after methylation were uniform, very adherent on any substrate, and with thicknesses ranging between 10 nm and 10 μm. In best synthesis conditions (low input power and high pulse frequency), plasma-polymerized membranes before methylation showed a hydroxyl conductivity of 4×10^{-5} S cm^{-1} and a related resistance of 0.7 Ω cm^2 (close to that of conventional membranes). Conduction ability of plasma-polymerized membranes after methylation was not significantly higher as expected by the low impact of the quaternization reaction. The integration of these plasma membranes into fuel cells is now in progress.

1.09.5 Plasma Membranes for Sensors

Plasma polymerization is an attractive technique for providing novel, thin, highly crosslinked, strongly adherent, and active membrane materials for sensors. Two big families of sensors can be distinguished: ion-sensitive sensors such as electrochemical biosensors or ion-selective electrodes and gas sensors.

1.09.5.1 Ion-Sensitive Sensors

All studies presented in the part devoted to energy-production devices concern plasma membranes whose ionic conduction, strong adherence, and high stability properties make them also suitable for use in ion-sensitive sensors. In addition to these studies, others dealing specifically with membranes for sensors can be mentioned.

Some groups worked on the preparation of ion-selective electrodes. Kurosawa and coworkers [117] deposited a fluorinated membrane containing sulfonyl groups on a Millipore® filter by plasma polymerization, using a mixture of perfluorobenzene and SO_2. After impregnation with dioctylphthalate, the prepared plasma membrane showed an essentially Nernstian response for tetraphenylphosphonium, typical lipophilic cation, at a concentration in the range 10^{-2}–10^{-5} M (same range as for Nafion®) and had long life time. Zeng and coworkers [118] reported the deposition of an ultrathin anionic exchange layer on Nafion® by plasma polymerization of ethylene and ammonia. The proton-selectivity coefficient of the plasma-modified Nafion® membrane was measured and the results showed that a linear Nernst response was exhibited and the selectivity of proton was enhanced.

Other groups dealt with the manufacture of electrochemical biosensors. Such biosensors consist of ionic-conductive membranes (active layers) deposited onto electric conductive supports (electrodes). Phosphonic-acid-containing plasma polymers can be good candidates for active layers of biosensors, thanks to their ionic conductance, strong adherence, permselectivity, and biocompatibility. Danilich and coworkers succeeded in the preparation of plasma copolymers from perfluoroallylphosphonic acid (PAPA) alone or mixed with argon as carrier gas, pentafluoroallyldiethylphosphonate with or without argon as carrier gas, or a mixture of PAPA with chlorotrifluoroethylene. In all cases, lightly fluorinated, highly crosslinked materials containing phosphonic acid groups could be obtained in optimized synthesis conditions; such materials showed a strong adherence to gold electrodes in aqueous media and exhibited a good ionic conductivity up to 4.2×10^{-3} S cm^{-1} [119]. Highest deposition rates (up to 40 nm min^{-1}) could be obtained using PAPA diluted by argon [120].

1.09.5.2 Gas Sensors

Studies that present different integrated sensors produced using microelectronic fabrication techniques such as PECVD or plasma-etching techniques without dealing with the interaction between the active plasma material and the detected gas are not treated here. Two aspects, more related to gas transport or affinity, are presented in this part: first, some results on transducers to convert specific gas concentrations and traces into an electromagnetic signal using a plasma-polymerized active layer, and second, few results on plasma-polymerized membranes used to enhance the selectivity of gas sensors.

1.09.5.2.1 Resistive-type sensors

Inagaki [121] developed resistive-type humidity sensors from PECVD thin films synthesized using organosilicon precursors containing nitrogen (e.g., trimethylsilyldimethylamine (TMSDMA)) and then quaternized with methyl bromide. **Figure 24** shows the drastic decrease of electrical resistance of the quaternized PECVD thin film when humidity increases.

Another resistive-type sensor was studied by Dai [122] for trimethylamine (TMA) gas detection. The sensor consisted in a double layer of TiO_2 and Fe_2O_3 obtained in an inductive coupled reactor from $TiCl_4$ and $Fe(CO)_5$ gas precursors. **Figure 25** shows the sensitivity of such a sensor to different gas traces as a function of operating temperature.

1.09.5.2.2 Plasma materials combined with quartz crystal microbalance

Numerous groups have studied the combination of a mass-type sensor, quartz crystal microbalance (QCM), with a PECVD selective layer. The PECVD deposited layer is used as a preconcentrator for organic compounds. Plasma polymers of organosilicon compounds have been proved to strongly solubilize organic compounds. QCM analyses using such plasma polymers were carried out to characterize the solubility of simple gases [13] and hydrocarbon vapors [123] and diluted organic liquid-like chloroform in water [124]. **Figure 26(a)** presents the solubility of the first six saturated hydrocarbon vapors in two organosilicon composite membranes (synthesized using octamethyltrisiloxane (OMTSO) or hexamethylcyclotrisiloxane (HMCTSO)), measured by QCM. **Figure 26(b)** evidences the frequency shift due to the diluted chloroform when a PP–HMDSO film was deposited on the quartz compared to that of pristine quartz.

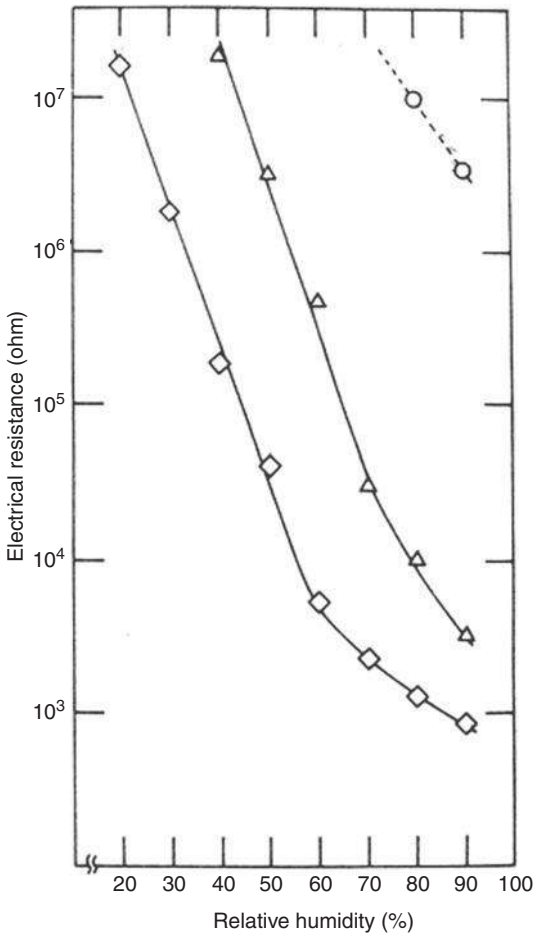

Figure 24 Electrical resistance as a function of relative humidity for plasma films prepared from TMSDMA: (○) unquaternized (0.45 μm tick); (◇) quaternized (0.45 μm thick); (△) quaternized (0.82 μm thick).

1.09.6 Recent Studies and Future for Innovating Porous Plasma Membranes

1.09.6.1 Tubular Plasma Membranes

The growth of a plasma-polymerized membrane by PECVD inside a long tubular support was recently possible with the setup shown in **Figure 27(a)** [125]. The setup consisted of a full concentric reactor with a noncondensable/reactive plasma top zone. The oxygen plasma was moved from this zone toward the inner surface of the support up to the deposition zone where the condensable (organosilicon) precursor exited from a capillary. The capillary diameter was small enough to avoid any deposition inside, even if the capillary was crossing the full plasma top zone. **Figure 27(b)** shows the local deposition profile of a plasma-polymerized film at the bottom

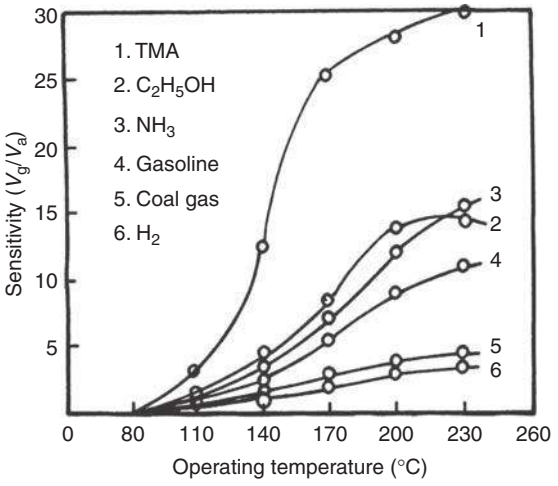

Figure 25 Gas sensitivity (V_g/V_a, V_g being the electric resistance in the case of air, V_a being the electric resistance in the case of air) of PECVD TiO_2–Fe_2O_3 deposits to different gases at the same concentration of 300 ppm as a function of operating temperature.

end of the capillary. To obtain a regular thin layer (**Figure 27(c)**) deposited on the inner side of a commercial macroporous alumina tube, the support was moved along its axis. **Figure 28** presents the hydrogen and nitrogen permeance evolutions as a function of $(T/M)^{0.5}$ (T being the temperature in kelvin, M being the gas molecular weight) for a plasma-polymerized tetramethylsilane membrane showing that, at low temperatures a possible effect of the adsorption on the PECVD micropore surface can not be totally neglected [126].

1.09.6.2 New Coupled Methods

New methods to produce porous silica or hybrid silica membranes by PECVD have been recently studied. They are based on the use of two vapor precursors: an organosilicon one to form the silica-based skeleton and the other one, generally a hydrocarbon compound with a low thermal stability (often called porogen), intended to form the porosity or initiate a high roughness leading to a porous film. As a first approach, the two precursors were codeposited by PECVD. A further thermal or UV treatment was applied to remove most of the organic part that issued from the porogen plasma polymerization [11]. Open mesoporosity was then created [12]. As a second approach, depositions of the two precursors were sequentially and cyclically applied, changing the energetic plasma conditions at each sequence: hard plasma conditions were chosen for the deposition of an inorganic a-SiO_2:H layer from the organosilicon precursor; soft plasma conditions were implemented for the deposition of a polymer-like a-C:H film from the porogen compound. During sequences under drastic conditions, both deposition of a-SiO_2:H and etching of a-C:H simultaneously took place. Porosity and pore size could be controlled by the PECVD deposition times during each cycle [127]. These hybrid and porous materials that have good thermal and chemical stabilities are promising for applications in liquid filtration in drastic conditions, where conventional polymers cannot be used.

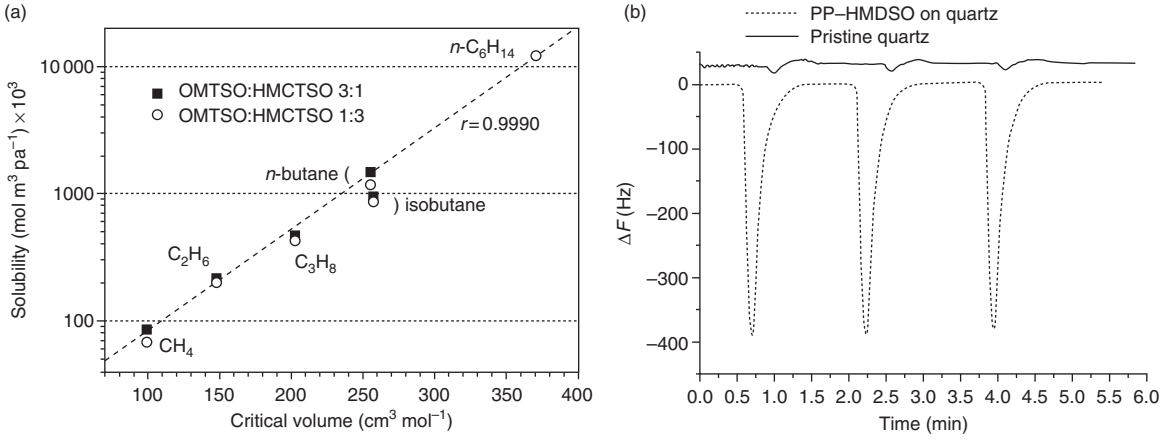

Figure 26 (a) Solubility of the first hydrocarbons as a function of their critical volume in composite PP–OMTSO/PP–HMCTSO membranes; (b) frequency variation of a quartz (ΔF) with a PP–HMDSO film under the effect of chloroform adsorption.

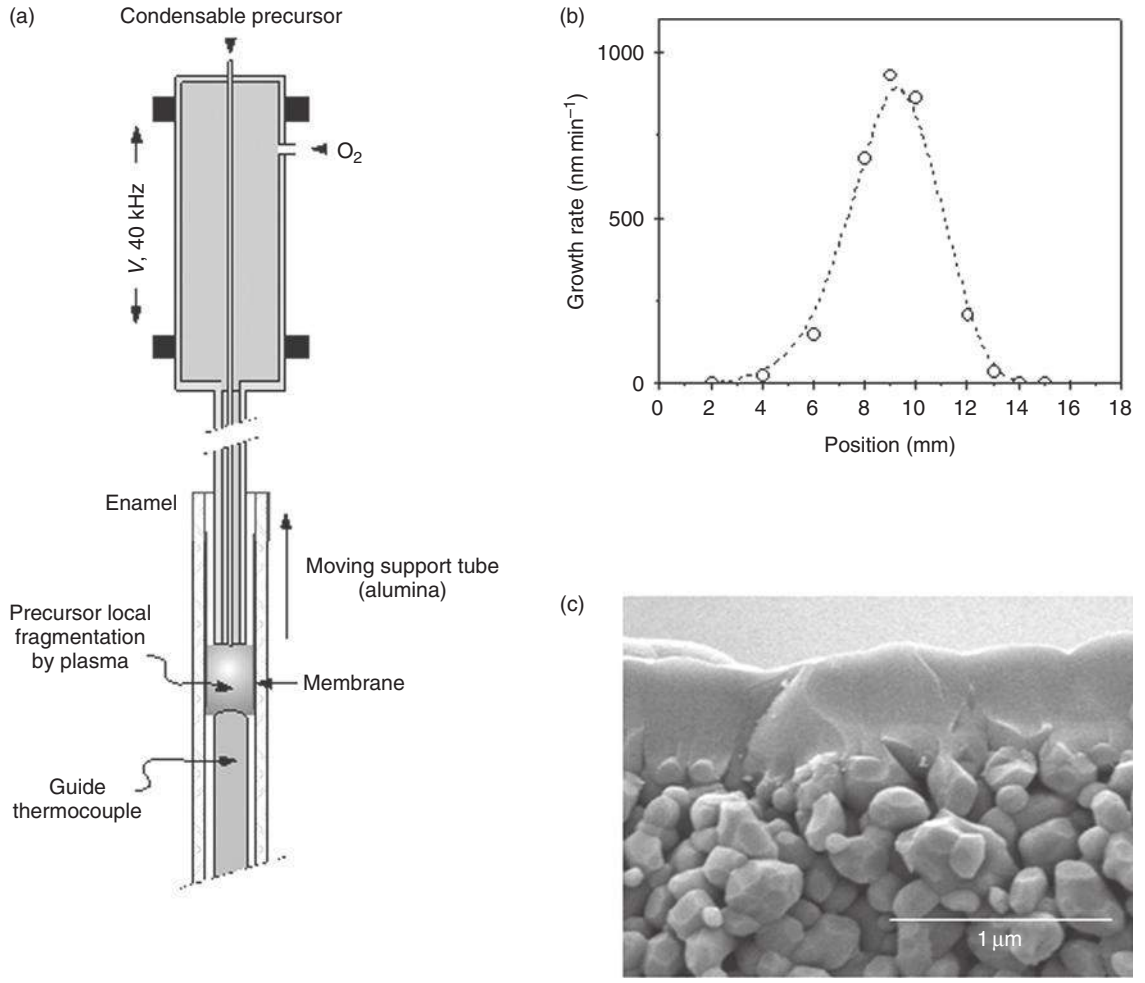

Figure 27 (a) PECVD setup to deposit thin films or membranes inside a tube. (b) Growth profile of a plasma-polymerized layer. (c) SEM picture of a plasma-polymerized layer deposited onto an alumina support; the tubular support was regularly moved to obtain an homogeneous membrane.

1.09.7 Conclusions

The potentialities of plasma processes in modifying or depositing thin layers on materials surface are exceptionally broad, hence their increasing interest in the membrane field since the 1980s.

Plasma treatments from noncondensable gas(es) are especially applied for improving the wettability, printability, adhesion, or biocompatibility of conventional polymer membranes, modulating their transport properties (by changing the hydrophilic/hydrophobic balance, providing the grafting of specific functional groups, or crosslinking the surface chains) or reinforcing their mechanical, thermal, and chemical stability (essentially under the effect of crosslinking).

PECVD or plasma polymerization using condensable precursors makes possible the deposition of thin layers whose physical and chemical properties can be largely tuned by the simple variation of the parameters of the process, and this is a field much broader than other deposition techniques. If, from a technological point of view, this requires a rigorous control of the parameters of the process, the complexity and variety of active species and reaction steps directly related to the plasma parameters offer a high degree of flexibility in prepared materials properties. This high degree of flexibility makes them good candidates as membrane materials. Their main advantages in such an application field are their high degree of crosslinking giving them high separation efficiency as well as high chemical and thermal stabilities, and

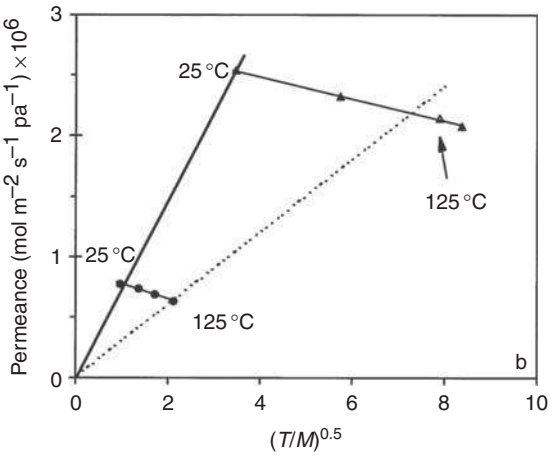

Figure 28 H_2 (▲) and N_2 (•) permeances of a PP–tetramethylsilane membrane as a function of $(T/M)^{0.5}$ (T being the temperature in kelvin, M being the gas molecular weight). Reproduced with permission from pagés, X., Rovessac, V., Cot, D., Nabias, G., Durand, J. *Sep. Purif. Technol.* **2001**, *25*, 399–406.

their small and easily tunable thickness enabling a modulation of their permeation ability.

The first developed plasma-modified or plasma-polymerized membranes were intended for gas permeation or retention and also pervaporation; more recently, since the 1990s, plasma membranes have been prepared for liquid-separation processes (nanofiltration and ultrafiltration, essentially). The development of polymer-like plasma films has been more recently applied to fields using ion-conducting membranes, such as electromembrane processes (electrodialysis in particular), electrochemical sensors, or, more broadly, energy-production devices (fuel cells, Li-ion batteries, etc.). For all these applications, plasma processes have enabled promising breakthroughs due to their high versatility in terms of prepared materials. In the current environmental context, plasma processes which represent a very clean technology are all the more promising. Owing to these advantages, industrialists should be convinced to introduce it and secure more markets in the future decade.

References

[1] Yasuda, H. *Plasma Polymerization*; Academic Press: Orlando, FL, 1985.
[2] d'Agostino, R. *Plasma Deposition, Treatment and Etching of Polymers*; Academic Press: New York, 1990.
[3] Biederman, H., Osada, Y. *Plasma Polymerization Processes*; Elsevier: Amsterdam, 1992.
[4] Inagaki, N. *Plasma Surface Modification and Plasma Polymerization*; Technomic Publishing: Lancaster, 1996.
[5] Lam, D. K., Baddour, R. F., Stancell, A. F. Fundamentals of Plasma Polymerization. In *Plasma Chemistry of Polymers*; Shen, M., Ed.; Marcel Dekker: New York, 1976.
[6] Poll, H. U., Arty, M., Wickleder, K. H. *Eur. Polym. J.* **1976**, *12*, 505–512.
[7] Finsterwalder, F., Hambitzer, G. *J. Membr. Sci.* **2001**, *185*, 105–124.
[8] Kim, Y., Cho, S., Lee, H., Yoon, H., Yoon, D. *Surf. Coat. Technol.* **2003**, *174–175*, 166–169.
[9] Storgaard-Larsen, T., Leistiko, O. *J. Electrochem. Soc.* **1997**, *144*, 1505–1513.
[10] Ayral, A., Julbe, A., Rouessac, V., Roualdes, S., Durand, J. Microporous Silica Membrane – Basic Principles and Recent Advances. In *Membrane Science and Technology*; Malada, R., Menendez, M., Eds.; Elsevier: Amsterdam, 2008; Vol. 13, Chapter 2, pp 33–79.
[11] Favennec, L., Jousseaume, V., Rouessac, V., Fusalba, F., Durand, J., Passemard, G. *Mater. Sci. Semicond. Process.* **2004**, *7*, 277–282.
[12] Rouessac, V., Puyrenier, W., Broussous, L., Rebiscoul, D., Ayral, A. *Proceedings of the 9th International Conference on Inorganic Membranes (ICIM9)*, Lillehammer, Norway, 25–29 June; Bredesen, R., Raeder, H., Eds.; 2006; pp 484–487.
[13] Roualdes, S., Sanchez, J., Durand, J. *J. Membr. Sci.* **2002**, *198* (2), 299–310.
[14] Yasuda, H. *J. Membr. Sci.* **1984**, *18*, 273–284.
[15] Nakata, M., Kumazawa, H. *J. Appl. Polym. Sci.* **2006**, *101*, 383–387.
[16] Teramae, T., Kumazawa, H. *J. Appl. Polym. Sci.* **2007**, *104*, 3236–3239.
[17] Inagaki, N., Tasaka, S., Park, M. S. *J. Appl. Polym. Sci.* **1990**, *40*, 143–153.
[18] Inagaki, N., Tsutsumi, D. *Polym. Bull.* **1986**, *16*, 131–136.
[19] Wang, L. J., Chau-Nan Hong, F. *Microporous Mesoporous Mater.* **2005**, *77*, 167–174.
[20] Julbe, A., Rouessac, V., Durand, J., Ayral, A. *J. Membr. Sci.* **2008**, *316*, 176–185.
[21] Vilani, C., Weibel, D. E., Zamora, R. R. M., Habert, A. C., Achete, C. A. *Appl. Surf. Sci.* **2007**, *254*, 131–134.
[22] Weibel, D. E., Vilani, C., Habert, A. C., Achete, C. A. *J. Membr. Sci.* **2007**, *293*, 124–132.
[23] Upadhyay, D. J., Bhat, N. V. *J. Membr. Sci.* **2004**, *239*, 255–263.
[24] Yamaguchi, T., Tominaga, A., Nakao, S. I., Kimura, S. *AIChE J.* **1996**, *42* (3), 892–895.
[25] Li, C.-L., Tu, C.-Y., Inagaki, N., Lee, K.-R., Lai, J.-Y. *J. Appl. Polym. Sci.* **2006**, *102*, 909–919.
[26] Roualdes, S., Durand, J., Field, R. W. *J. Membr. Sci.* **2003**, *211*, 113–126.
[27] Wavhal, D. S., Fisher, E. R. *J. Polym. Sci. Part B: Polym. Phys.* **2002**, *40*, 2473–2488.
[28] Wavhal, D. S., Fisher, E. R. *Desalination* **2005**, *172*, 189–205.
[29] Steen, M. L., Hymas, L., Harvey, E. D., Capps, N. E., Castner, D. G., Fisher, E. R. *J. Membr. Sci.* **2001**, *188*, 97–114.
[30] Steen, M. L., Jordan, A. C., Fisher, E. R. *J. Membr. Sci.* **2002**, *204*, 341–357.
[31] Gancarz, I., Pozniak, G., Bryjak, M. *Eur. Polym. J.* **1999**, *35*, 1419–1428.
[32] Shahidzadeh-Ahmedi, N., Arefi-Khonsari, F., Amouroux, J. *J. Mater. Chem.* **1995**, *5*, 229–236.
[33] Bryjak, M., Gancarz, I., Krajciewicz, A., Piglowski, J. *Angew. Makromol. Chem.* **1996**, *234*, 21–29.

[34] Gancarz, I., Pozniak, G., Bryjak, M. *Eur. Polym. J.* **2000**, *36*, 1563–4569.
[35] Bryjak, M., Gancarz, I., Pozniak, G., Tylus, W. *Eur. Polym. J.* **2002**, *38*, 717–726.
[36] Bryjak, M., Gancarz, I. *Angew. Makromol. Chem.* **1994**, *219*, 117–124.
[37] Gesner, B. D., Kelleher, P. G. *J. Appl. Polym. Sci.* **1968**, *12*, 1199–1208.
[38] Poncin-Epaillard, F., Chevet, B., Brosse, J. C. *Eur. Polym. J.* **1990**, *26*, 333–339.
[39] Vigo, F., Nicchia, M., Uliana, C. *J. Membr. Sci.* **1988**, *36*, 187–199.
[40] Ulbricht, M., Belfort, G. *J. Membr. Sci.* **1996**, *111*, 193–215.
[41] Zhao, Z. P., Li, J., Wang, D., Chen, C. X. *Desalination* **2005**, *184*, 37–44.
[42] Zhao, Z. P., Li, J., Zhang, D. X., Chen, C. X. *J. Membr. Sci.* **2004**, *232*, 1–8.
[43] Zhao, Z. P., Li, J., Chen, J., Chen, C. X. *J. Membr. Sci.* **2005**, *251*, 239–245.
[44] Chen, J., Li, J., Zhao, Z. P., Wang, D., Chen, C. X. *Surf. Coat. Technol.* **2007**, *201*, 6789–6792.
[45] Inagaki, N., Tasaka, S., Goto, Y. *J. Appl. Polym. Sci.* **1997**, *66*, 77–83.
[46] Liu, Z. M., Xu, K. Z., Wan, L. S., Wu, J., Ulbricht, M. *J. Membr. Sci.* **2005**, *249*, 21–31.
[47] Muller, M., Oehr, C. *Surf. Coat. Technol.* **1999**, *116–119*, 802–807.
[48] Gancarz, I., Pozniak, G., Bryjak, M., Frankiewicz, A. *Acta Polym.* **1999**, *50*, 317–326.
[49] Bankovic, P., Demarquette, N. R., da Silva, M. L. P. *Mater. Sci. Eng.* **2004**, *B112*, 165–170.
[50] Vallois, C., Sistat, P., Roualdes, S., Pourcelly, G. *J. Membr. Sci.* **2003**, *216*, 13–25.
[51] Falk, S. U., Salkind, A. J. *Alkaline Storage Batteries*; Wiley: New York, 1969.
[52] Barak, M. *Electrochemical Power Sources – Primary and Secondary Batteries*; Peter Peregrinus: Stevenage, 1980.
[53] Linden, D. *Handbook of Batteries*; McGraw-Hill: New York, 1995.
[54] Ciszewski, A., Gancarz, I., Kunicki, J., Bryjak, M. *Surf. Coat. Technol.* **2006**, *201*, 3676–3684.
[55] Ciszewski, A., Kunicki, J., Gancarz, I. *Electrochim. Acta* **2007**, *52*, 5207–5212.
[56] Ogumi, Z., Uchimoto, Y., Tsujikawa, M., Takehara, Z.-I. *J. Electrochem. Soc.* **1989**, *136* (4), 1247–1248.
[57] Ogumi, Z., Uchimoto, Y., Tsujikawa, M., Takehara, Z.-I., Foulkes, F. R. *J. Electrochem. Soc.* **1990**, *137* (5), 1430–1435.
[58] Ogumi, Z., Uchimoto, Y., Tsujikawa, M., Yasuda, K., Takehara, Z.-I. *Bull. Chem. Soc. Jpn.* **1990**, *63*, 2150–2153.
[59] Ogumi, Z., Uchimoto, Y., Tsujikawa, M., Yasuda, K., Takehara, Z.-I. *J. Membr. Sci.* **1990**, *54*, 163–174.
[60] Yasuda, K., Yoshida, T., Uchimoto, Y., Ogumi, Z., Takehara, Z.-I. *Chem. Lett.* **1992**, *21*, 2013–2016.
[61] Takehara, Z.-I., Ogumi, Z., Uchimoto, Y., Yasuda, K. *J. Adhes. Sci. Technol.* **1995**, *9* (5), 615–625.
[62] Ogumi, Z., Uchimoto, Y., Takehara, Z.-I. *J. Electrochem. Soc.* **1988**, *135* (10), 2649–2650.
[63] Ogumi, Z., Uchimoto, Y., Takehara, Z.-I. *J. Power Sources* **1989**, *26*, 457–460.
[64] Ogumi, Z., Uchimoto, Y., Takehara, Z.-I. *J. Electrochem. Soc.* **1989**, *136* (3), 625–630.
[65] Ogumi, Z., Uchimoto, Y., Takehara, Z.-I., Foulkes, F. R. *J. Electrochem. Soc.* **1990**, *137* (1), 29–34.
[66] Ogumi, Z., Uchimoto, Y., Takehara, Z.-I. *J. Chem. Soc., Chem. Commun.* **1989**, *6*, 358–359.
[67] Ogumi, Z., Uchimoto, Y., Takehara, Z.-I., Kanamori, Y. *J. Chem. Soc., Chem. Commun.* **1989**, *21*, 1673–1674.
[68] Uchimoto, Y., Ogumi, Z., Takehara, Z.-I. *Solid State Ion.* **1990**, *40/41*, 624–627.
[69] Kwak, B. S., Zuhr, R. A., Bates, J. B. *Thin Solid Films* **1995**, *269*, 6–13.
[70] Choi, S.-S., Lee, Y. S., Joo, C. W., Lee, S. G., Park, J. K., Han, K.-S. *Electrochim. Acta* **2004**, *50*, 339–343.
[71] Heinzel, A., Barragan, V. M. *J. Power Sources* **1999**, *84*, 70–74.
[72] Arico, A. S., Srinivasan, S., Antonucci, V. *Fuel Cells* **2001**, *1*, 133–161.
[73] Kreuer, K. D. *J. Membr. Sci.* **2001**, *185*, 29–39.
[74] Ren, X., Gottesfeld, S. *J. Electrochem. Soc.* **2001**, *148*, A87–A93.
[75] Choi, W. C., Kim, J. D., Woo, S. I. *J. Power Sources* **2001**, *96*, 411–414.
[76] Yoon, S. R., Hwang, G. H., Cho, W. I., Oh, I.-H., Hong, S.-A., Ha, H. Y. *J. Power Sources* **2002**, *106*, 215–223.
[77] Bae, B., Ha, H. Y., Kim, D. *J. Membr. Sci.* **2006**, *276*, 51–58.
[78] Walker, M., Baumgärtner, K.-M., Ruckh, M., Kaiser, M., Schock, H. W., Räuchle, E. *J. Appl. Polym. Sci.* **1997**, *64*, 717–722.
[79] Walker, M., Baumgärtner, K.-M., Kaiser, M., Kerres, J., Ullrich, A., Räuchle, E. *J. Appl. Polym. Sci.* **1999**, *74*, 67–73.
[80] Walker, M., Baumgärtner, K.-M., Feichtinger, J., Kaiser, M., Räuchle, E., Kerres, J. *Surf. Coat. Technol.* **1999**, *116–119*, 996–1000.
[81] Feichtinger, J., Galm, R., Walker, M., *et al. Surf. Coat. Technol.* **2001**, *142–144*, 181–186.
[82] Kim, D., Scibioh, M. A., Kwak, S., Oh, I.-H., Ha, H. Y. *Electrochem. Commun.* **2004**, *6*, 1069–1074.
[83] Prakash, S., Mustain, W. E., Park, S.-O., Kohl, P. A. *J. Power Sources* **2008**, *175*, 91–97.
[84] Won, J., Choi, S. W., Kang, Y. S., *et al. J. Membr. Sci.* **2003**, *214*, 245–257.
[85] Lue, S. J., Hsiaw, S.-Y., Wei, T.-C. *J. Membr. Sci.* **2007**, *305*, 226–237.
[86] Yamaguchi, T., Hayashi, H., Kasahara, S., Nakao, S.-I. *Electrochemistry* **2002**, *70* (12), 950–952.
[87] Bae, B., Kim, D. *J. Membr. Sci.* **2003**, *220*, 75–87.
[88] Bae, B., Chun, B.-H., Ha, H.-Y., Oh, I.-H., Kim, D. *J. Membr. Sci.* **2002**, *202*, 245–252.
[89] Inagaki, N., Tasaka, S., Horikawa, Y. *J. Polym. Sci. Part A: Polym. Chem.* **1989**, *27*, 3495–3501.
[90] Inagaki, N., Tasaka, S., Kurita, T. *Polym. Bull.* **1989**, *22*, 15–20.
[91] Inagaki, N., Tasaka, S., Chengfei, Z. *Polym. Bull.* **1991**, *26*, 187–191.
[92] Ogumi, Z., Uchimoto, Y., Yasuda, K., Takehara, Z.-I. *Chemi. Lett.* **1990**, *6*, 953–954.
[93] Uchimoto, Y., Yasuda, K., Ogumi, Z., Takehara, Z.-I. *J. Electrochem. Soc.* **1991**, *138* (11), 3190–3193.
[94] Uchimoto, Y., Yasuda, K., Ogumi, Z., Takehara, Z.-I., Tasaka, A., Imahigashi, T. *Ber. Bunsenges. Phys. Chem.* **1993**, *97* (4), 625–630.
[95] Uchimoto, Y., Endo, E., Yasuda, K., *et al. J. Electrochem. Soc.* **2000**, *147* (1), 111–118.
[96] Ogumi, Z., Uchimoto, Y., Takehara, Z.-I. *J. Electrochem. Soc.* **1990**, *137* (10), 3319–3320.
[97] Brumlik, C. J., Parthasarathy, A., Chen, W.-J., Martin, C. R. *J. Electrochem. Soc.* **1994**, *141* (9), 2273–2279.
[98] Yasuda, K., Uchimoto, Y., Ogumi, Z., Takehara, Z.-I. *Ber. Bunsenges. Phys. Chem.* **1994**, *98* (4), 631–635.
[99] Yasuda, K., Uchimoto, Y., Ogumi, Z., Takehara, Z.-I. *J. Electrochem. Soc.* **1994**, *141* (9), 2352–2355.
[100] Yoshimura, K., Minaguchi, T., Nakano, H., *et al. J. Photopolym. Sci. Technol.* **2000**, *13* (1), 13–20.

[101] Mahdjoub, H., Roualdes, S., Sistat, P., Pradeilles, N., Durand, J., Pourcelly, G. *Fuel Cells* **2005**, *5* (2), 277–286.
[102] Roualdes, S., Topala, I., Mahdjoub, H., Rouessac, V., Sistat, P., Durand, J. *J. Power Sources* **2006**, *158* (2), 1270–1281.
[103] Brault, P., Roualdes, S., Caillard, A., *et al. Eur. Phys. J. Appl. Phys.* **2006**, *34*, 151–156.
[104] Durand, J., Rouessac, V., Roualdes, S. *Ann. Chim. Sci. Mat.* **2007**, *32* (2), 145–158.
[105] Roualdes, S., Schieda, M., Durivault, L., Guesmi, I., Gerardin, E., Durand, J. *Chem. Vap. Depos.* **2007**, *13* (6–7), 361–363.
[106] Roualdes, S., Ennajdaoui, A., Schieda, M., Larrieu, J., Durand, J. *Membr. News* **2007**, *74*, 9–13.
[107] Ennajdaoui, A., Larrieu, J., Roualdes, S., Durand, J. *Eur. Phys. J. – Appl. Phys.* **2008**, *42* (1), 6–16.
[108] Caillard, A., Coutanceau, Ch., Brault, P., Mathias, J., Léger, J.-M. *J. Power Sources* **2006**, *162*, 66–73.
[109] Mex, L., Müller, J. *Membr. Technol.* **1999**, *115*, 5–9.
[110] Mex, L., Sussiek, M. *Chem. Eng. Commun.* **2003**, *190*, 1085–1095.
[111] Mex, L., Ponath, N., Müller, J. *Fuel Cells Bull.* **2001**, *39*, 9–12.
[112] Gruber, D., Müller, J. *J. Power Sources* **2007**, *171*, 294–301.
[113] Bauer, B., Strathmann, H., Effenberger, F. *Desalination* **1990**, *79*, 125–144.
[114] Sata, T., Tsujimoto, M., Yamaguchi, T., Matsusaki, K. *J. Membr. Sci.* **1996**, *112*, 161–170.
[115] Matsuoka, K., Chiba, S., Iriyama, Y., *et al. Thin Solid Films* **2008**, *516*, 3309–3313.
[116] Schieda, M., Roualdes, S., Durand, J., Martinent, A., Marsacq, D. *Desalination* **2006**, *199*, 286–288.
[117] Kurosawa, S., Kamo, N., Arimura, T., *et al. Jpn. Oil Chem. Soc.* **1994**, *43* (11), 1007–1010.
[118] Zeng, R., Pang, Z., Zhu, H. *J. Electroanal. Chem.* **2000**, *490*, 102–106.
[119] Danilich, M. J., Gervasio, D., Burton, D. J., Marchant, R. E. *Macromolecules* **1995**, *28*, 5567–5574.
[120] Danilich, M. J., Marchant, R. E. *Plasmas Polym.* **2002**, *7* (2), 127–149.
[121] Inagaki, N. *Thin Solid Films* **1984**, *118*, 225–230.
[122] Dai, G. *Sens. Actuat. B* **1998**, *53*, 8–12.
[123] Rouessac, V., Tuluc, P., Durand, J. *J. Membr. Sci.* **2004**, *230*, 49–59.
[124] da Silva, M. L. P., Tan, I. H., Nascimento Filho, A. P., Galeazzo, E., Jesus, D. P. *Sens. Actuat. B* **2003**, *91*, 362–369.
[125] Pagés, X., Rouessac, V., Cot, D., Nabias, G., Durand, J. *Sep. Purif. Technol.* **2001**, *25*, 399–406.
[126] Shindo, Y., Hakuta, T., Yoshitome, H., Inoue, H. *J. Chem. Eng. Jpn.* **1983**, *16*, 120–126.
[127] Barranco, A., Cotrino, J., Yubero, F., Espinos, J. P., Contreras, L., Gonzales-Elipe, A. R. *Chem. Vap. Depos.* **2004**, *10*, 17–20.

Biographical Sketches

Dr. Stéphanie Roualdes received her master's degree in chemical engineering from Institut National Polytechnique de Lorraine in 1997, and her PhD in materials chemistry from University of Montpellier in 2000. After spending a few months in the University of Bath as a lecturer, she worked again at the University of Montpellier where she secured a permanent position as a lecturer in 2002. Since then, she has been teaching physico-chemistry (electrochemistry, thermodynamics, and analytical chemistry) and materials science and leading a master formation on materials since 2005. As an academic researcher at the European Membrane Institute, she has worked on the synthesis of thin layers or modification of polymer membranes by plasma-enhanced chemical-vapor deposition for applications in membrane processes such as gas permeation or electrodialysis or in energy-production devices. Currently, she has been focusing on the development of ion-conductive plasma-polymerized membranes for microfuel cells. She has over 25 publications in refereed journals, 2 patents, and has also coauthored 2 chapters in books. Since 2001, she has been partner in 6 French or European projects, and advisor or coadvisor to over 20 masters, PhD, or postdoctoral students.

Dr. Vincent Rouessac (Phd in 1977) has an experience of 13 years in materials synthesis and characterization, with almost 9 years in research on plasmas. His focus at the European Membrane Institute has been on the surface modifications and PECVD materials. His current topics of interest are the synthesis and characterization of new hybrid and inorganic PECVD films for gas-separative membranes and for microelectronics and surface modifications by plasma. He has also specialized in the static and dynamic characterizations of deposited thin films: nanoporosity, swelling, and vapor affinity by coupled techniques (quartz crystal microbalance, ellipsometry, and X-ray reflectometry) with vapor adsorption, gas transfers, and permselectivities by permeance measurements. He is author or coauthor of 38 peer-reviewed articles, 2 book chapters, and 50 communications in national and international conferences. He has cosupervised four PhD students and is currently supervising two more.

Dr. Jean Durand joined the CNRS in 1977 after his PhD. He has been a senior researcher at European Membrane Institute (EMI) since 1977. His main focus has been on the study of C_{3v} symmetry compounds, the crystal growth of ABO_4 compounds, and the development of cold plasmas techniques for microelectronics and, since 1982, membrane applications. He was EMI deputy director during 1994–2002. Supervisor of the Plasma and Membrane team in EMI, he is the author of more than 170 papers and 50 proceedings. He has scientific responsibilities in the Chemical High School of Montpellier (ENSCM) and in the Carnot Institute.

This page intentionally left blank

1.10 Preparation of Membranes Using Supercritical Fluids

E Reverchon and S Cardea, University of Salerno, Fisciano, Italy

Glossary

Binodal curve Curve defining the region of composition and temperature in a phase diagram for a mixture across which a transition occurs from miscibility of the components to conditions where single-phase mixtures are metastable or unstable.

Interaction parameter It is employed in the Flory–Huggins theory, to account for the contribution of the noncombinatorial entropy of mixing and the enthalpy of mixing to the Gibbs energy of mixing.

Spinodal curve Curve defining the region of composition and temperature for a mixture across which a transition occurs from conditions where single-phase mixtures are metastable to conditions where single-phase mixtures are unstable and undergo phase separation by spinodal decomposition.

Nomenclature

χ interaction parameter

1.10.1 State of the Art

Polymeric membranes can be used for several industrial applications [1–3], such as gas separation, reverse osmosis, ultrafiltration, microfiltration, catalytic reactions, drug controlled release, and tissue engineering. Each application requires specific characteristics for membrane material and structure. In the case of microfiltration and ultrafiltration, the pore size and the porosity of the membrane determine the efficiency of the filtration. For gas separation, the permeability and the selectivity of the membrane determine the efficiency of the operation. For catalytic reactions and controlled release, the distribution of the catalyst (or of the drug) along the membrane structure and an appropriate porosity are fundamental.

Majority of membranes are prepared by controlled phase separation of polymeric solutions into a polymer-rich phase and a polymer-lean phase. Phase separation of polymer solutions can be induced in several ways; the two main techniques are

thermally induced phase separation (TIPS) and solvent-induced phase separation (SIPS) [4]. The performance of the membranes obtained by these processes strongly depends on the morphology obtained during phase separation and subsequent solidification.

To analyze the membrane formation mechanism, phase diagrams are frequently used and can indicate membrane morphologies that will be formed. Binary phase diagrams provide information for the TIPS process, whereas ternary isothermal phase diagrams are useful for the prediction of the phase transitions that can occur when phase separation is induced by a nonsolvent (i.e., SIPS). This type of analysis is also useful to describe supercritical-induced formation of membranes.

1.10.1.1 Solvent-Induced Phase Separation

This process presents many analogies with the one assisted by supercritical fluids (SCFs). In SIPS, a polymer solution is cast as a film on a support or extruded through a die, and is subsequently immersed in a nonsolvent bath. The second solvent (or antisolvent) is a good solvent for the solvent in the solution but the polymer is not soluble in it. Therefore, the solvent in the polymer solution is solubilized by the nonsolvent and a solid-phase precipitates. At least three components are involved and complex diffusion and convection processes can play an important role. The possible combinations of the three components can be plotted in a triangular phase diagram. The corners represent the pure components, the axes of the three binary compositions, and points in the triangle a ternary composition.

The phase diagram is, as a rule, divided into a homogeneous region and an area representing a liquid–liquid (L–L) demixing gap. The boundary of the L–L demixing gap is usually called the binodal curve; usually the L–L demixing is subdivided into a region of spinodal demixing, bounded by the spinodal curve, and two regions of nucleation and growth between the binodal and the spinodal curves [5, 6]. The point where the binodal and the spinodal coincide is called the critical point. A metastable area exists between the spinodal and the binodal curve at low polymer concentration, an unstable area is surrounded by the spinodal curve, and a second metastable area exists at higher polymer concentrations. The size and the location of the demixing gap depend on the molar volumes of the components, the polymer–solvent interaction parameter, the polymer–nonsolvent interaction parameter, and the solvent–nonsolvent interaction parameter [7].

All transitions, different from L–L demixing, are usually referred to as gel transitions in the literature. These include viscosity transitions and transitions due to solid–liquid demixing and vitrification. For amorphous polymers, membrane structures can be stabilized by vitrification, whereas semicrystalline polymers can exhibit crystallization (solid–liquid (S–L) demixing) concurrently with L–L demixing. At high polymer concentrations and low nonsolvent concentrations, the polymer crystallizes from solution; at moderate polymer concentrations and with moderate nonsolvent concentrations, L–L demixing occurs without the interference of S–L demixing; at higher nonsolvent concentrations, L–L demixing interferes with S–L demixing.

This process suffers various limitations that induced some researchers to find new preparation processes. In particular, it involves the use of two solvents that must be expensively removed from the membrane with posttreatments, since residual solvents can cause problems for the use in several applications. Moreover, relatively long formation times and a limited versatility characterize this process, due to the reduced possibility to modulate cell size and membrane structure once the polymer–solvent–nonsolvent system is fixed.

1.10.2 Preparation of Membranes by SCF-Induced Phase Separation

In this technique, a SCF replaces the liquid nonsolvent used in SIPS. A SCF is a substance at a temperature and pressure above its thermodynamic critical point (i.e., the highest temperature and pressure at which the substance can exist as a vapor and liquid in equilibrium). SCFs are suitable as substitutes for organic solvents since they can show liquid-like solvent power, gas-like diffusion, and zero surface tension. In addition, close to the critical point, small changes in pressure or temperature result in large changes in density, allowing many properties to be tuned. As a rule, CO_2 has been chosen as the SCF because it is safe, readily available, and has a low cost. It also allows supercritical operation at relatively low pressures and at near-room temperatures ($p_c = 7.21$ MPa, $T_c = 31.1\,^{\circ}C$).

Compared to the SIPS method, supercritical CO_2 phase-separation process can have several advantages:

1. SC-CO_2 can form and dry the polymer membrane rapidly, without the collapse of the structure due to the absence of a liquid–vapor interface when the supercritical mixture solvent–nonsolvent is formed. Moreover, the membrane can be obtained without additional posttreatments because the polymer solvent is completely extracted.
2. It is easy to recover the liquid solvent, since it dissolves in SC-CO_2 and can be removed from gaseous CO_2 by depressurization, in a separator located downstream of the membrane formation vessel.
3. SC-CO_2 allows one to modulate the membrane morphology, as well as cell and pore size by simply changing the pressure and temperature that produce different solvent powers and diffusivities.

1.10.2.1 Preparation of Membranes

In the majority of the published papers, polymeric membranes are prepared in a laboratory apparatus equipped with a high-pressure vessel, in which SC-CO_2 contacts the polymer solution in a single pass. An example of experimental apparatus is schematically reported in **Figure 1**.

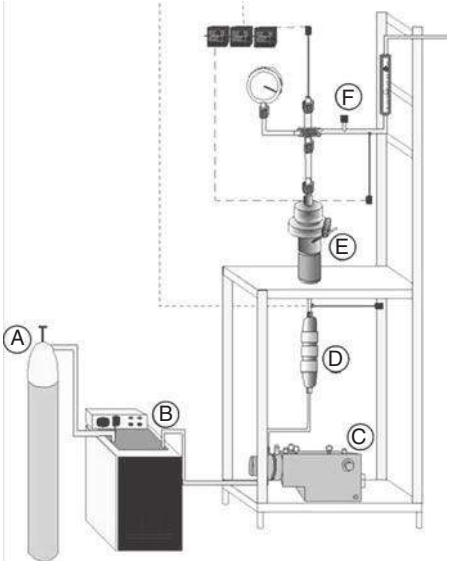

Figure 1 Schematic drawing of a typical SC-IPS apparatus: (A) CO_2 tank; (B) chiller; (C) high pressure pump for CO_2; (D) CO_2 preheater; (E) high pressure vessel; and (F) micrometric valve.

Membrane casting process is similar to the traditional procedure. Homogenous solutions of polymer are prepared by stirring the solution that is then placed in a membrane formation cell, on which it is spread to control the thickness of the film. The cell is rapidly placed inside the membrane preparation vessel (D) to avoid evaporation of the solvent. The vessel is then rapidly closed and filled with SC-CO_2, up to the desired pressure using a high-pressure pump (C).

CO_2 flows from a tank (A) and passes through a chiller (typically, a glycolic bath: B) to be sent to the pumping system as a subcooled liquid to avoid cavitation. After the pump, a preheater is usually placed to warm CO_2 above its critical temperature. Thereafter, SC-CO_2 flows into the vessel (E) and contacts the polymeric solution. Usually, the process can be divided in two parts: (1) the operation is performed in batch mode up to the final set pressure; and (2) a valve (F) is opened and the operation is performed in a continuous mode delivering a constant SC-CO_2 flow rate in the membrane formation vessel. Pressure and temperature are held constant and, during this step, the phase-separated membrane is also dried; then, the vessel is depressurized.

1.10.2.2 Characterization of Membranes

Various characterizations of membranes obtained by SC-CO_2-assisted process have been presented in literature. In particular, scanning electron microscopy (SEM), porosity, cell and pore size, differential scanning calorimetry (DSC), X-ray diffraction pattern (XRD), mechanical tests, solvent residue, N_2, and water flux analysis have been performed. A detailed description of the results is reported in the following section.

1.10.3 Experimental Results

A schematic representation of the results until now obtained in literature is reported in **Tables 1** and **2**. We summarized these results considering the polymer used, the parameters analyzed, the characterizations performed, the morphologies obtained, and the possible industrial applications. In the following, we analyze the results presented and the possible trends in the research on the formation of membranes by SC-CO_2-assisted phase inversion.

Table 1 Representation of the parameters analyzed in literature regarding the SC-IPS process

Polymer	*Analyzed parameters*	*Solvents*	*Polymer concentration (% (w/w))*	*Temp. range (°C)*	*Pressure range (MPa)*	*Depress. rate (min)*	*Addition of another compound (% (w/w))*	*Nonsolvent modification*	*Ref.*
Flat membranes									
Cellulose acetate	S, C, T, P	Acetone Methylacetate 1,3-dioxolane 2-butanone	5–40	45–65	10–20	-	-	-	[8, 9]
Nylon-6	C, P	TFE	15	-	10.4–17.3	-	-	-	[10]
PEEK-WC	C, P, T	NMP	10–20	45–65	8–20	-	-	-	[11]
PLLA	S, C, P, DR, N	Chloroform THF	20–25	-	13–16	2–30	-	THF-CO_2 0:100–2:98	[12, 13]
PMMA	C, S, P, T	DMSO Acetone THF	1–25	35–65	15–25	-	-	-	[14]
PolystyreneC, T, P	Toluene	15–30	25–70	8–16	-	-	-	[15]	
Polysulfone	C, T, P, S, DR, PCL Conc.	Chloroform NMP MP DMF DMA DMSO DMPA	2–30	35–65	10–20	1–60	PCL content 0–50	-	[16–18]
Polycarbonate	T, P, PEG Conc.	DCM	16	30–60	11–19	-	PEG content 0–30	-	[19]
PVA	C, T, P	DMSO	1–35	35–55	10–20	-	-	-	[20]
PVDF	C, T, P, PMMA Conc.	Acetone DMAC	1–20	35–65	8–20	-	PMMA Content 1.5–7.5	-	[21–23]
Loaded membranes									
PMMA/ amoxicillin	C, T, P, Drug Conc.	DMSO, acetone	10–40	35–65	15–25	-	Drug content 0–30	-	[24]
Membranes for scaffolding applications									
PLLA	C, T, P	DCM	10–30	35–65	10–23	-	-	-	[25, 26]

C, polymer concentration; P, pressure; T, temperature; S, solvent; DR, depressurization rate.

Table 2 Summary of the results obtained in literature regarding the SC-IPS process

Polymer	*Characterizations*	*Morphologies*	*Mechanisms*	*Possible applications*	*Ref.*
Flat membranes					
Cellulose acetate	SEM, WP	Cellular	L–L demixing	Microfiltration	[8]
Cellulose acetate	SEM, QTD	Cellular, bicontinuous, microparticles	L–L demixing	Filtration	[9]
Nylon-6	SEM, QTD	Cellular, sponge-like	L–L and S–L demixing	Filtration	[10]
PEEK-WC	SEM, N_2 flux	Dense, cellular, sponge-like	L–L and S–L demixing	Filtration	[11]
PLLA	SEM, X-ray, PM	Dense, cellular	L–L demixing	Gas separation Microfiltration	[12]
PLLASEM	Cellular	L–L demixing	Microfiltration	[13]	
PMMA	SEM, QTD	Cellular, bicontinuous, microparticles	L–L demixing	Filtration	[14]
Polystyrene	SEM	Cellular	L–L demixing	Filtration	[15]
Polysulfone	SEM, QTD	Cellular, bicontinuous, microparticles	L–L demixing	Filtration	[16]
Polysulfone	SEM, QTD, WP	Cellular	L–L demixing	Microfiltration	[17]
Polysulfone/PCL	CA, WP, MS	Cellular	L–L demixing	Microfiltration	[18]
PC	SEM, TS	Cellular	L–L demixing	Microfiltration	[19]
PVA	SEM, QTD, DSC, X-ray	Dense, cellular, bicontinuous, microparticles	L–L demixing	Filtration	[20]
PVDF	SEM, X-ray, DSC, TGA	Sponge-like	L–L and S–L demixing	Microfiltration	[21]
PVDF	SEM, QTD, DSC, X-ray	Sponge-like	L–L and S–L demixing	Microfiltration	[22]
PVDF	SEM, DSC	Sponge-like	L–L and S–L demixing	Microfiltration	[23]
Loaded membranes					
PMMA/amoxicillin	SEM, DSC, DR	Cellular	L–L demixing	Controlled release	[24]
Membranes for scaffolding applications					
PLLA	SEM	Cellular and sponge-like	L–L and S–L demixing	Tissue engineering	[25]
PLLA	SEM, SR, MS	Sponge-like	Gel drying	Tissue engineering	[26]

SEM, scanning electronic microscopy; WP, water permeability; QTD, qualitative ternary diagram; PM, polarized microscopy; TS, tearing stress analysis; DSC, differential scanning calorimetry; X-ray, X-ray analysis; TGA, thermogravimetry analysis; DR, dissolution rate; SR, solvent residue analysis; MS, mechanical stress analysis; CA, contact angle analysis.

1.10.3.1 Flat Membranes

1.10.3.1.1 Effect of the operative parameters

The effect of the operative parameters in the SC-induced phase-separation (SC-IPS) process has been investigated by several authors [8–23]. The most relevant parameters in the formation of membranes by SC-IPS include: polymer concentration, pressure, temperature, and type of solvent. In some cases, other process parameters have also been investigated such as the depressurization rate and the addition of another polymer in the starting solution. In the following, we report an organized summary of the results obtained.

•*Effect of polymer concentration.* Various ranges of concentration have been investigated depending on the polymer–solvent system used; polymer concentrations with a minimum of 1% w/w and a maximum of 40% w/w have been processed.

Depending on the process conditions and on the type of polymer used, four main morphologies were observed as a result of different polymer concentrations. Examples of SEM images of these morphologies are reported in **Figures 2(a)–2(d)**: a dense structure (**Figure 2(a)**–polyvinyl alcohol (PVA)), a cellular structure (**Figure 2(b)**–polymethyl methacrylate (PMMA)), a bicontinuous structure (**Figure 2(c)**–cellulose acetate), and a particulate structure (**Figure 2(d)**–PVA).

In the traditional phase inversion, the mass transfer of the nonsolvent in the cast solution and of the solvent in the coagulation bath is responsible for the modification in the composition of the polymer–solvent–nonsolvent system. The possible paths can be schematically reported in a ternary phase diagram

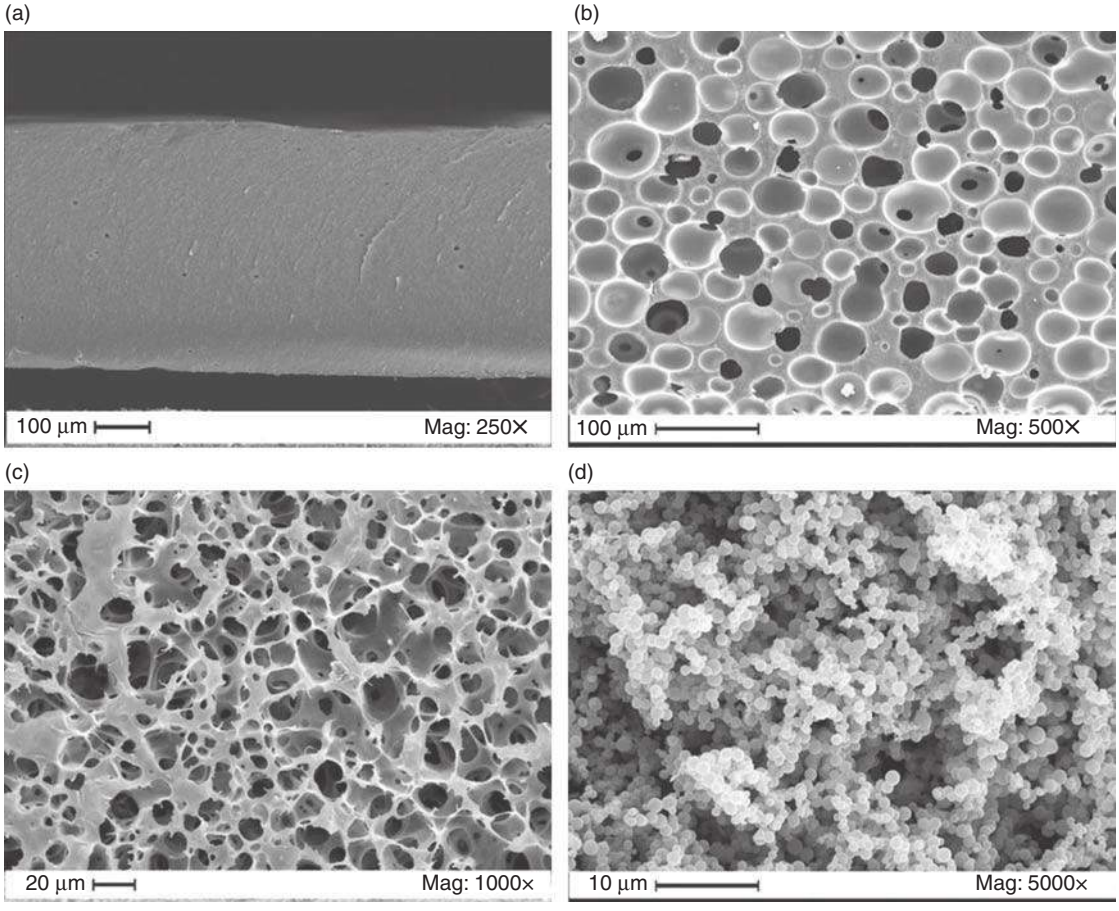

Figure 2 Different membrane morphologies obtained starting from a different polymer concentration: (a) dense structure (polyvinyl alcohol (PVA)), (b) cellular structure (polymethyl methacrylate (PMMA)), (c) bicontinuous structure (cellulose acetate), (d) particulate structure (PVA).

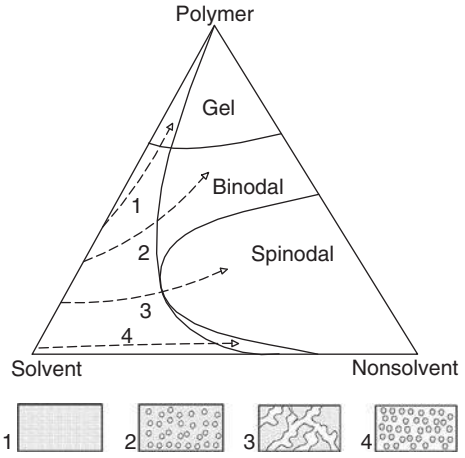

Figure 3 Ternary phase diagram of a generic polymer/solvent/nonsolvent system with various composition paths indicated by arrows and numbers; the typical membrane structures related to the composition paths are also reported.

indicating them as the composition paths. In **Figure 3**, a qualitative ternary phase diagram is presented in which an L–L demixing gap, divided into a region of spinodal demixing, two regions of nucleation and growth located between the binodal and the spinodal curve, and a gelation region are schematically reported.

The arrows numbered from 1 to 4 report the different composition paths that can occur during the formation of membranes:

1. The concentration of the polymer in the ternary system increases because the outflow of the solvent from the solution is faster than the inflow of the nonsolvent; the phase inversion does not occur and the polymer molecules solidify by gelation and/or crystallization into a dense structure (**Figure 2(a)**). This situation is also possible in the case of a supercritical nonsolvent, when the system is very concentrate and the diffusion of the nonsolvent is very reduced. The formation of dense structures has been observed, for example, for the system PVA/dimethyl sulfoxide (DMSO)/SC-CO_2 [20].
2. The ternary polymer solution becomes metastable; nucleation and growth of droplets of the polymer-lean phase occurs with solidification of the polymer-rich phase, leading to a cellular structure (**Figure 2(b)**); in this case, both porous or dense skins can be obtained depending on the polymer–solvent–nonsolvent system processed. This morphology has been frequently observed in the case of SC-CO_2-IPS, for example, for the system PMMA/DMSO/SC-CO_2 [14].
3. The ternary polymer solution becomes unstable; spinodal phase separation with the subsequent solidification of the polymer-rich phase takes place, leading to the formation of a bicontinuous structure (**Figure 2(c)**); in this case, porous skins are usually obtained. This morphology has also been observed in the case of SC-IPS, for example, for the cellulose acetate/acetone/SC-CO_2 system [8].
4. In this case, nucleation and growth of droplets of the polymer-rich phase is obtained, followed by solidification of the polymer-rich phase; a bead-like (particulate) structure is obtained (**Figure 2(d)**). Besides, this kind of morphology has been obtained by SC-IPS, as in the case of PMMA/DMSO/SC-CO_2 [14] system.

In the case of dense structure (**Figure 2(a)**), starting from the highest polymer concentration, the composition path can enter in the upper part of the ternary phase diagram (path 1) due to both the high concentration of the system and the slow diffusion of the SC-CO_2. In this manner, the accumulation of the polymer due to the outflow of the solvent occurs before the phase separation of the solution causing the dense layer formation.

In the region in which cellular structures are produced (path 2), as the polymer concentration in the starting solution is increased, the cell diameter usually decreases, as in the example reported in **Figure 4**. In the case of polysulfone membranes [16], increasing the polymer percentage from 15% to 30% w/w, the mean diameter of the cells

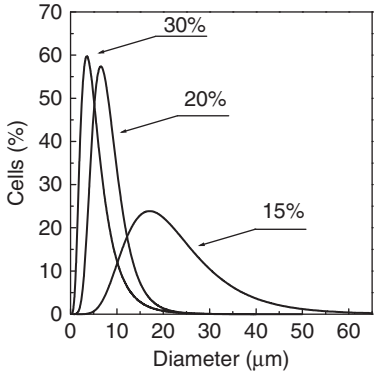

Figure 4 Cell size distribution at different polysulfone concentrations in *N*-methyl-2-pyrrolidone (NMP), obtained operating at 45 °C and 20 MPa.

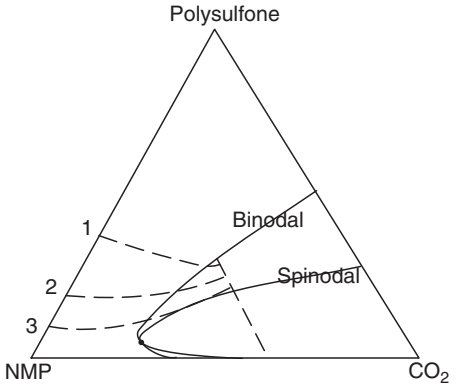

Figure 5 Hypothesized phase diagram for the ternary system polysulfone/*N*-methyl-2-pyrrolidone (NMP)/ supercritical CO_2. Composition paths: (1) 30% w/w, (2) 20% w/w, and (3) 15% w/w of polysulfone.

decreases and reduces from about 20 to 3 μm; correspondingly, the cell size distribution sharpens.

An explanation of this result has been presented in **Figure 5** considering again a qualitative ternary diagram. Three different compositions paths, starting at three different polymer concentrations (15%, 20%, and 30% w/w), show that the nucleation and growth of the droplets of the polymer-lean phase, with further solidification of the polymer-rich phase, can be the controlling mechanism. Increasing the polymer concentration in the starting solution, that is, passing from point 3 to point 1, the operative point (the intersection between the tie-line and the composition path) shifts toward the polymer-rich phase. Therefore, using the lever rule, we can observe that the quantity of the polymer- lean phase decreases. As a consequence, there will be a smaller amount of polymer-lean phase (smaller cells) inside a fixed volume of membrane.

Decreasing the polymer concentration, it is possible to fall in the spinodal decomposition region of **Figure 3** (path 3). In this case, a complete connection among the cells is obtained and high-porosity membranes are produced (**Figure 2(c)**) with porous skins.

Starting from dilute solutions, the operative point can lie in the region characterized by the fourth mass transport mechanism (path 4 in **Figure 3**) and, as a consequence, more or less networked microparticles can be produced (particulate structure). An explanation of this morphology is possible considering the existence of a second concurring mechanism of polymer precipitation under the action of SC-CO_2. At very low concentrations, the process driven by SC-CO_2 can be very fast and a part of polymer-rich phase can form microparticles. At lowest concentrations, this mechanism can become dominant and only microparticles can be obtained. These results agree well with those obtained in the case of cellulose acetate [8] and PVA [20] membranes. The process is substantially the same that it is obtained during batch supercritical antisolvent (GAS) experiments devoted at the production of microparticles [27]. In this type of experiments, a polymer solution at low concentration is placed inside a vessel and CO_2 is rapidly pumped to reach the final pressure and acts as a nonsolvent for the polymer. Therefore, it is possible to assume that, when the percentage of polymer in the solution is very low, the liquid solution is rapidly dried by SC-CO_2, the polymer precipitates as single or connected microparticles, and the continuous solid structure (membrane) is not formed. A contribution to the formation of these morphologies can also be attributed to the viscosity of the samples. When the viscosity of the sample increases (high percentage of polymer), a slower demixing is obtained and the polymer can rearrange to form the semisolid structure during the contact with SC-CO_2. On the contrary, at low viscosities (low amount of polymer), the process is very fast, the porous structure is not formed, and the polymer tends to form microparticles as in GAS experiments.

For crystallizable polymers, for example, polyvinylidene fluoride (PVDF) [21–23], S–L demixing can also take place during the phase-inversion process. In this case, the resulting membrane will exhibit characters from both types of phase demixing. The S–L demixing occurs in the crystallizable segments of the polymer to form membranes consisting of interlinked crystalline particles (leafy morphology). As crystallization is a slow process compared to L–L demixing, a crystallization-dominated membrane structure is difficult to prepare. An example of PVDF–hexafluoropropylene (HFP) membrane obtained by SC-CO_2 phase-separation process is reported in **Figure 6**. It is possible to observe that a cellular structure is obtained, but cell walls are not smooth; they are characterized by a leafy substructure.

In addition, in this case, it is possible to use as a reference the traditional phase-inversion process to explain these results; depending on the solvent and nonsolvent combination used, it is possible to obtain membranes with a structure either largely dominated by L–L demixing (cellular, bicontinuous, or bead-like morphology) or related to S–L demixing (leafy morphology). The application of these

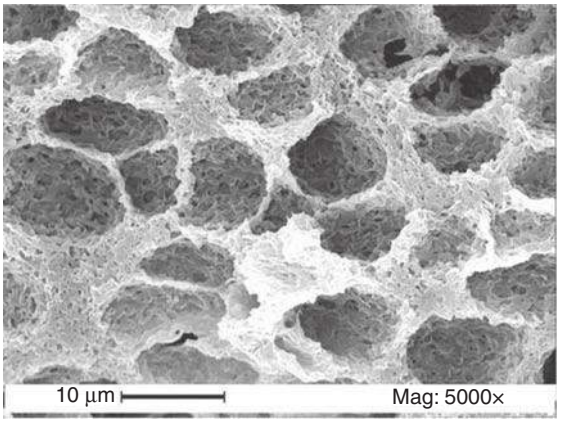

Figure 6 Leafy substructure of the cell walls of polyvinylidene fluoride–hexafluoropropylene (PVDF–HFP) membranes obtained at 20 MPa, 55 °C, and 20% w/w.

considerations to the phase-inversion method assisted by SC-CO_2 indicates that, in the case of PVDF–HFP membranes, L–L demixing is the dominant mechanism during the precipitation process; indeed, cellular structures have been obtained. On the other hand, the leafy morphology observed on the walls of cellular structures suggests that an S–L demixing (i.e., the crystallization process) occurs too. Therefore, both the demixing mechanisms (L–L and SL) concur to the formation of PVDF–HFP membranes and a competition between L–L and S–L demixing has to be taken into consideration.

The crystallization occurring during the formation of PVDF–HFP membranes process confirms the presence of a gelation region, delimited by a gelation line. The position of this line strongly depends on the nature of the solvent–nonsolvent system used [21]. Therefore, according to the results obtained and to the general knowledge on the formation of PVDF–HFP membranes, it is possible to hypothesize a qualitative ternary diagram for PVDF–HFP/solvent/SC-CO_2 system in which the gelation line is very close to the solvent apex [21]. As a consequence, the polymer solution contacts SC-CO_2 and its composition continuously changes by diffusion of SC-CO_2 in the liquid phase; at the beginning, the gelation line is crossed inducing an S–L demixing that causes the formation of the leafy morphology. Then, the composition pathway continues its trajectory inside the ternary diagram moving toward the pure polymer apex since it falls in a region characterized by one of the solidification mechanisms typical of L–L demixing. As a consequence, a solid structure caused by the superposition of the S–L and L–L phase-separation mechanisms is obtained.

•*Effect of SC-CO_2 density* (*pressure and temperature*). SC-CO_2 density depends on the process pressure and temperature and largely determines the solvent power of the antisolvent. Indeed, by increasing pressure and/or decreasing temperature it is possible to increase the SC-CO_2 solvent power and, as a consequence, to influence the phase-separation process.

An example of the effect on the final membrane morphologies is observable in the case of PVA membranes [20]. Experiments were performed starting from 1% w/w PVA–DMSO solutions. Various sets of process parameters from 10 MPa, 55 °C (329 kg m^{-3}) to 20 MPa, 35 °C (866 kg m^{-3}) were explored. As shown in **Figure 7**, for this system, the morphology completely changes by increasing SC-CO_2 density: at 10 MPa and 55 °C, a membrane with a cellular structure is obtained (**Figure 7(a)**); at 15 MPa and 45 °C, the structure becomes bicontinuous (**Figure 7(b)**) and is formed by filaments and crosslinked microparticles; and at 20 MPa and 35 °C, a membrane is not formed but well-defined spherical submicroparticles are generated with a diameter ranging between 0.2 and 0.7 μm (**Figure 7(c)**).

It is possible to explain these results considering the kinetic aspect of the SC-CO_2 phase-separation process [20]. When the pressure is high (20 MPa) and the temperature is low (35 °C) (i.e., high SC-CO_2 solvent power), the outflow of the solvent from the solution is limited and the trajectory of the pathways moves toward the pure antisolvent vertex, leading to the formation of microparticles (**Figure 7(c)**); by decreasing pressure (15 MPa) and increasing temperature (45 °C), the process becomes slower and the pathway enters in the central region of demixing gap (part of the solvent is lost by outflowing), leading to bicontinuous structures (**Figure 7(b)**). A further decrease of pressure (10 MPa) and increase of temperature (55 °C) produce an increase of the outflow of the solvent and the pathway enters inside the upper demixing gap (between spinodal and binodal curves), leading to a cellular structure (**Figure 7(a)**). Decreasing the SC-CO_2 solvent power again, the cell size decreases because the operative point shifts toward the polymer-rich phase.

Another example of the effect of pressure and temperature on membrane morphologies is reported in the case of polysulfone membranes [16]. In this case, the trend observed was the same; however, differently from PVA membranes [20], the thermodynamic aspects of the process were considered. Indeed, the

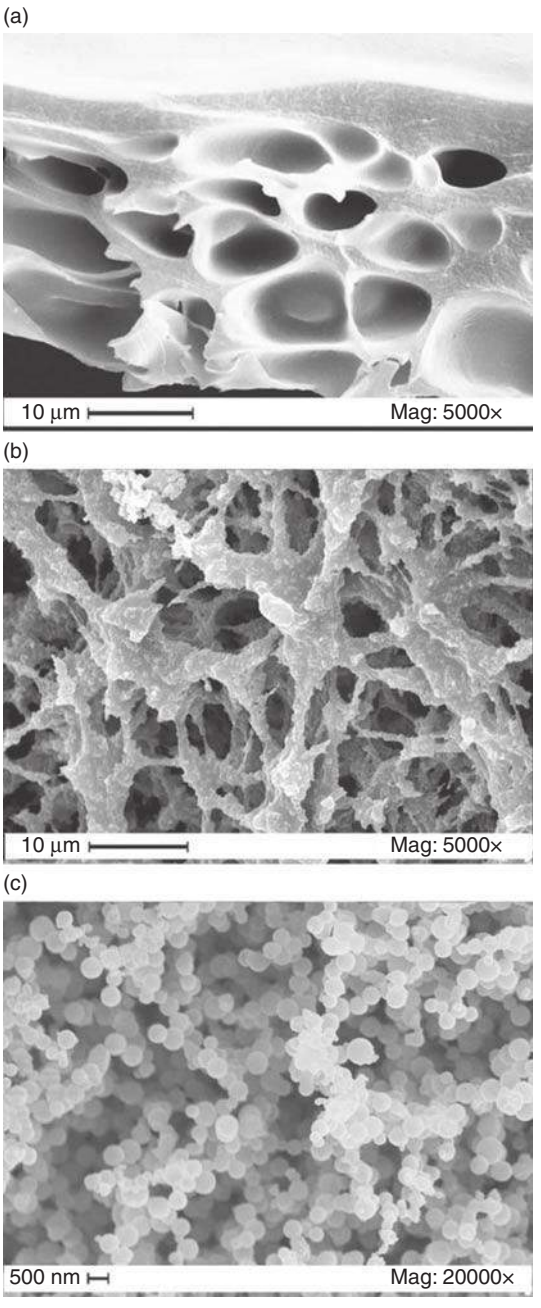

Figure 7 Effect of supercritical CO_2 density on membrane morphology and cell size at 1% w/w polyvinyl alcohol (PVA) in DMSO, operating at: (a) 10 MPa, 55 °C (329 kg m^{-3}); (b) 15 MPa, 45 °C (741 kg m^{-3}); and (c) 20 MPa, 35 °C (866 kg m^{-3}).

authors considered that the shape and size of the miscibility curve vary with pressure (and with temperature). Three possible binodal curves, related to the different pressures tested, were proposed [16]. The enlargement of the miscibility gap with a pressure reduction is in accordance with the studies on the fluid phase behavior in ternary systems containing dense CO_2 [28] which explains the results obtained (i.e., cellular structure is obtained and cell size decreases with the SC-CO_2 solvent power). Indeed, for a fixed polymer concentration, the enlargement of the binodal curve causes an increase of the polymer-lean phase/polymer-rich phase ratio generating a larger amount of polymer-lean phase (larger cells) inside a fixed volume of membrane. It is possible to suppose that an increase of temperature causes an effect similar to the decrease of pressure since in both cases a reduction of the SC-CO_2 density is obtained; as a consequence, the affinity between SC-CO_2 and the liquid solvent decreases and the cell size increases due to the formation of a larger quantity of the polymer-lean phase.

•*Effect of the liquid solvent.* The use of different solvents influences the demixing process that is related to the demixing gap in the phase diagram [29] and the diffusion kinetics such as the exchange rate between nonsolvent and solvent [30]. The position of the binodal curve is influenced by the nature of components in the mixture, particularly by the interaction parameters [4]. According to van de Witte *et al.* [4], it is possible to define three interaction parameters among polymer (1), solvent (2), and nonsolvent (3):

1. polymer/solvent (χ_{12}),
2. polymer/nonsolvent (χ_{13}), and
3. solvent/nonsolvent (χ_{23}).

χ_{13} is constant when the polymer and the nonsolvent are fixed, whereas χ_{23} and χ_{12} vary with the solvent used. A couple polymer/solvent with a low mutual affinity (i.e., high χ_{12}) produces an increase in the magnitude of the demixing gap, especially at very low values of χ_{23} (i.e., high solvent/nonsolvent affinity), whereas a low compatibility of the solvent–nonsolvent mixture (i.e., high χ_{23}) results in large differences in solvent/nonsolvent ratio at equilibrium. The determination of the interaction parameters is difficult, but a rapid indication for these values can be obtained by the solubility parameter approach [31–35]. Indeed, interaction parameters are inversely proportional to the difference between the solubility parameters of compounds. The solubility parameters represent the attractive strength between the molecules of the compounds and have been defined as the square root of the cohesive energy density $(J\ cm^{-3})^{1/2}$. Usually, the smaller is the difference of the solubility parameter value, the higher is the compounds miscibility (i.e., mutual affinity) [31].

When the casting solution is immersed in a coagulant bath, the exchange of solvent and nonsolvent across the interface of the polymer solution causes the phase inversion at a different exchange rate that depends on the solubility and diffusion parameters of the nonsolvent. In a process that uses SC-CO_2, the diffusion process is very fast and, consequently, the exchange rate is probably controlled by the difference between solubility parameters. When SC-CO_2 is used as the nonsolvent, it is also necessary to take in to account that its solubility parameter varies with the operative conditions; for example, an increase of the operating pressure produces an increase of miscibility between SC-CO_2 and the liquid solvent. The continuous variation of the affinity between solvent and nonsolvent is one of the key steps in the flexibility of the supercritical-assisted phase-inversion method. The solubility parameter for SC-CO_2 can be calculated, at different operative conditions, using the empirical equation of state (EOS) of Huang *et al.* [33]. The difference between solubility parameters of liquid solvents and SC-CO_2 modifies with a similar trend for all solvent–SC nonsolvent couples. Considering the case of PMMA membranes [14], the difference between solubility parameters of DMSO and SC-CO_2 is larger than between tetrahydrofuran (THF) and SC-CO_2; this indicates that, at the same operative conditions, THF has a higher miscibility with the nonsolvent than DMSO. Therefore, during membrane formation, SC-CO_2 can diffuse into PMMA–THF solutions quicker than into PMMA–DMSO solutions, making the solution faster to phase-separate, resulting in higher membrane porosity (high interconnectivity). It has been reported [36–38] that smaller membrane cells are associated with faster diffusion of the coagulant through the casting solution. To confirm this consideration, it is possible to observe in **Figure 8** that, at the same operating conditions, cells of PMMA membranes prepared using THF as solvent are smaller than those of the membranes prepared using DMSO.

The increase of cell size with the decrease of mutual affinity between solvent and nonsolvent can be explained considering that, when the mutual affinity is low, the outflow of the solvent into the SC-CO_2 phase is slow as well. This means that there is time enough for the polymer-lean phase, formed by the phase separation, to grow leading to the formation of larger pores. Another consequence is that, when experiments with low PMMA concentrations (3% and 5% w/w) were performed, membranes with cellular structure were obtained in DMSO (i.e., slow process), whereas, using acetone or THF (high affinity), the process was faster and PMMA precipitated as networked microparticles (particulate structure).

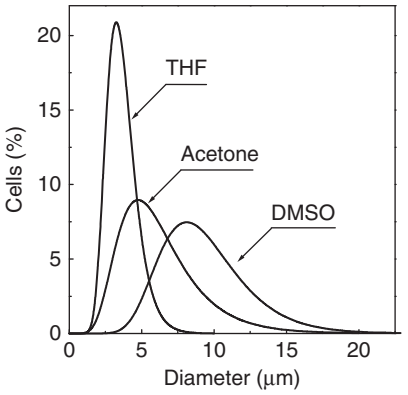

Figure 8 Polymethyl methacrylate (PMMA) cell size distributions obtained operating at 35 °C, 25 MPa, and 25% (w/w) and using different solvents.

• *Effect of the depressurization rate.* An example of the effect of depressurization rate on the membrane morphologies has been reported by Temtem *et al.* [17] for polysulfone membranes. They verified that higher depressurization rates produce larger pores. Similar trends were obtained with all solvents used. These observations are divergent from the results obtained by Xu *et al.* [13] in the preparation of poly-L-lactic acid (PLLA) membranes that found no changes in membrane structure with different depressurization rates. In any case, according to Temtem *et al.* [17], when the depressurization is performed, the polymer precipitation is already occurred due to the continuous extraction of the solvent. In a slow depressurization, the CO_2 diffuses slowly out of the polymer phase without affecting the polymer structure. A quick depressurization of the large amount of CO_2 dissolved in the polymer should result in a slight deformation of the existing pores and, consequently, in the increase of the mean diameter of the pores. The analysis of SEM images of the membrane surface produced by these authors confirms the above-mentioned explanation: fast depressurizations tend to increase surface porosity and promote the appearance of fissures in the membrane top layer. Water flux through the membranes increases by increasing the rate of the depressurization. These results have not found confirmations in other works; however, it is possible to suppose that for some polymers SC-CO_2 can also act as a foaming agent during the depressurization. Indeed, it is known from literature on SC-CO_2-assisted foaming

processes [39] that, if the depressurization temperature is above the actual glass transition temperature of the CO_2/polymer mixture, nucleation and growth of gas bubbles inside the polymer can occur. This phenomenon can also interfere with the final membrane morphologies adding some different peculiarities to the post-phase-separation structure.

• *Effect of the addition of another polymer*. Many studies in the traditional phase-inversion process assume that the incorporation of another polymer in the casting dope is an effective method to manipulate the morphology of the formed membrane and thereby to modify the membrane properties. An interesting example of investigation about this parameter for SC-IPS process is the one reported by Huang *et al.* [23] in the case of formation of PVDF membranes. They investigated the effect of PMMA content in the casting solution on the membrane structure. The casting solution was prepared by dissolution of polymer (PMMA and/or PVDF) in dimethylacetamide (DMAC) to form a solution containing 15% w/w of polymer.

By increasing the PMMA content in the starting solution, the cell shape ceases to be spherical and the cell wall structure changes significantly. For pure PVDF membranes, the cell wall is composed of uniform spherulite particles. When PMMA concentration in the solution is above 4.5% w/w, the cell wall is composed by a continuous matrix. The membranes generated at 1.5% w/w of PMMA are intermediate between these two cases; that is, the cell wall is composed of a continuous matrix in which many spherulite particles are embedded. Moreover, as the PMMA content in the dope increases, the cell size becomes less uniform. In addition, for the membrane produced from the solution containing 4.5% w/w of PMMA, both the cell size and the porosity are larger than those of the membranes formed at other PMMA concentrations. Although PVDF content in the casting dope decreases with the increase of PMMA content, crystallization still occurs in the late stage of the phase-inversion process. This is evident from the DSC thermograms of the membranes prepared from the casting dopes at different PMMA/PVDF mass ratios [23]. The melting point (T_m) of PVDF crystals decreases with increasing PMMA content in the dope. With the addition of PMMA at 7.5% w/w in the casting dope, the crystallinity decreases to 30%, indicating the inhibition of crystallization. Such a dramatic decrease in crystallinity is related to the good miscibility between PMMA and PVDF. These authors also found that when PMMA content is below 4.5% w/w, the crystallinity of PVDF in all the membranes is higher than that of original PVDF powder, indicating the occurrence of CO_2-induced crystallization.

Another example of incorporation of a second polymer in the starting solution is the one reported by Kim and Lee [19] for formation of polycarbonate (PC) membranes. They investigated the effect of polyethylene glycol (PEG) concentration on porosity and tearing stress of PC membranes. These authors found that porosity increases (from 65% to 72%) and the density of membranes decreases (from 1.19 to 1.14 $g\,cm^{-3}$) with an increase of the initial PEG concentration from 10% to 30% w/w.

1.10.3.1.2 Application of the SC-IPS to water-soluble polymers

The major drawback of the SC-CO_2-assisted phase-inversion technique is the very limited affinity between CO_2 and water at the ordinary process conditions; as a consequence, this process cannot be used to produce membranes of water-soluble polymers (i.e., the majority of biopolymers). To remove these limitations, Reverchon and Cardea [40] proposed the phase inversion of water-soluble polymers using liquids expanded by SC-CO_2. A SC-CO_2 expanded liquid is a mixture that shows intermediate physical properties between liquids and SCFs obtained operating at conditions above the CO_2 critical point but below the mixture critical point. This process has been applied to the production of PVA membranes using expanded ethanol. In this manner, it is possible to take advantage of the capability of the organic solvent to solubilize large quantities of water and of the presence of SC-CO_2 to confer near-critical properties to the solution, even operating at very low temperatures with respect to the critical temperature of the liquid solvent.

The feasibility of this process was demonstrated and the analysis regarding the effect of process parameters on formation of PVA membranes and morphology was performed. Several ethanol:CO_2 ratios (from 20:80 to 80:20 w/w), PVA concentrations (from 10% to 30% w/w), temperatures (from 35 to 65 °C), and pressures (from 15 to 25 MPa) were tested. The obtained PVA membranes were characterized by open cellular structures with cell size ranging between 0.5 and 4 μm; dense or porous skins were obtained at different process conditions. An example of a membrane section obtained is shown in the SEM images given in **Figure 9**. These results add further flexibility to the SC-IPS process, opening the process to the production of biopolymeric

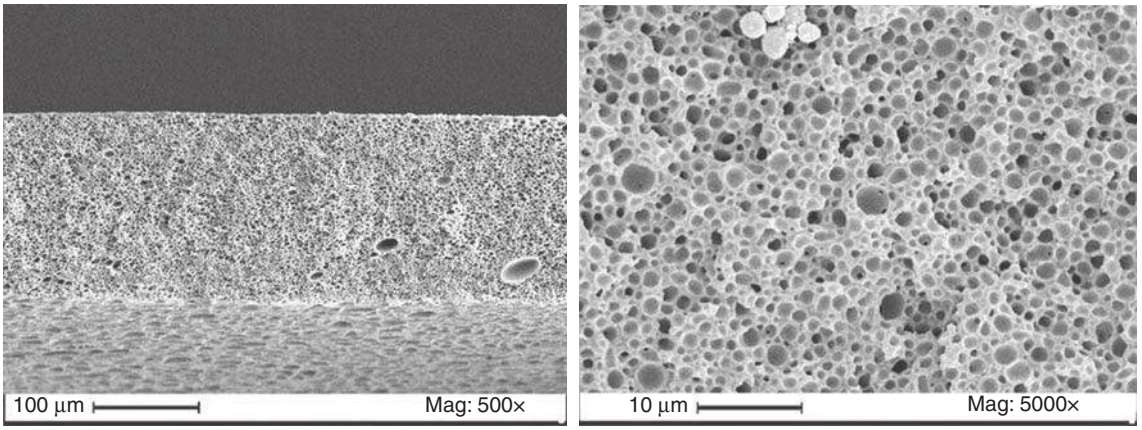

Figure 9 Cross section of a polyvinyl alcohol (PVA) membrane obtained at $P = 20$ MPa, $T = 45°C$, $C = 10\%$ w/w, and with an ethanol:CO_2 ratio of 60:40 w/w.

membranes. Moreover, the selection of solvent/CO_2 ratio as a process parameter gives one further possibility of modulating the membrane morphology.

1.10.3.2 Loaded Membranes

PMMA porous membranes have been prepared using the SC-IPS process and then they have been loaded with an antibiotic, amoxicillin, using two different techniques: dissolving it in the same organic solvent used to solubilize the polymer or suspending the drug in the organic solution formed by polymer and solvent [24]. The obtained porous membranes, produced at various drug loading, were characterized by SEM to study the morphology and cell size, and by DSC to analyze the interaction of drug–polymer in the structure.

The presence of the suspended drug does not interfere with the structure morphology (i.e., a cellular structure is obtained as in the case of pure PMMA [14]). Probably, it depends on the fact that amoxicillin dispersed in the solution does not influence the type of mass transport mechanism occurring during the phase separation. At larger drug percentages, a relevant increase of cell size is observed. This result can be related to two concurring effects: (1) the increase of drug percentage is accompanied by a decrease of the polymer percentage in the solution; therefore, the quantity of polymer-rich phase decreases (i.e., larger cells are obtained); (2) the presence of the drug influences the polymer-rich phase solidification acting as an obstacle in the organization of the solid phase.

The drug, initially dispersed, remains in this form during the membrane formation process, since the SC-IPS is an extremely fast process. SEM images of these membranes support this hypothesis (**Figure 10**).

Indeed, surfaces and cell walls present a distributed irregularity (roughness) that was not observed in pure PMMA structures. This result is due to the presence of the drug; that is, amoxicillin is encapsulated inside the polymeric structure. As the drug percentage increased, the surface roughness also increases.

Another important confirmation of the hypothesis of drug encapsulation is obtained by DSC analysis. Indeed, DSC can give qualitative and quantitative information about the physicochemical status of the drug in the polymeric structures. The thermograms

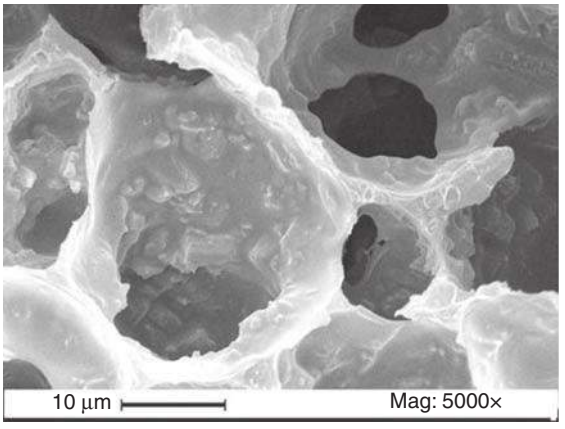

Figure 10 High magnification of a polymethyl methacrylate (PMMA) structure prepared using acetone, containing 30% w/w of amoxicillin, (20 MPa, 45 °C, and 80% (w/w) acetone); cell wall roughness is evident.

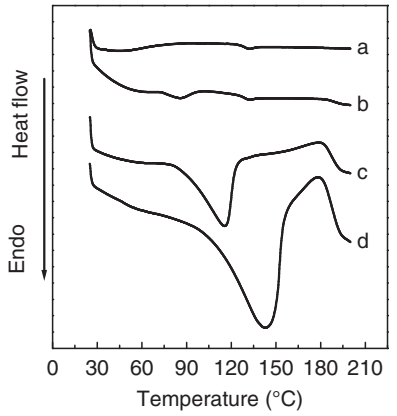

Figure 11 Thermograms of polymethyl methacrylate (PMMA) structures containing different percentages of suspended drug: (a) PMMA, (b) 10% amoxicillin, (c) 30% amoxicillin, and (d) amoxicillin.

of PMMA membranes obtained from acetone and containing percentages of amoxicillin varying from 0% to 30% w/w are shown in **Figure 11**. The DSC of pure amoxicillin is also reported for comparison. The lowering of the melting temperature and enthalpy of amoxicillin suggests an interaction due to the formation of a physical mixture.

DSC analysis suggests some interesting considerations: first, it confirms the encapsulation of amoxicillin inside the structure; second, it shows evidence that polymer and drug maintained their physical characteristics in the membranes; that is, the system behaves as a physical mixture of two components and substantially confirms the results of SEM analysis.

The same authors also prepared solutions with DMSO and a mixture formed by PMMA and amoxicillin. Moreover, in this case, PMMA-connected porous structures were successfully obtained. They show a uniform yellow color that is characteristic of amoxicillin, whereas, in the experiments with the amoxicillin suspension, the color of the membrane remained white. However, cell surfaces are smooth for all drug concentrations tested. The DSC analysis has been used again to compare the thermograms of the PMMA membranes obtained from DMSO and containing percentages of amoxicillin varying from 0% to 30% w/w. In this case, even at higher amoxicillin percentages, the characteristic peak of amoxicillin is not present in the thermograms.

The membrane characteristics observed (color, cell surface, and DSC analysis) show evidence that the two procedures lead to totally different interactions. In particular, when amoxicillin is dissolved together with PMMA in the starting solution, it is homogenously distributed inside the polymeric matrix, forming a solid solution. These authors also performed some drug release experiments to verify the efficiency of SC-CO_2-assisted encapsulation process and to study the effect of the collocation of drug in the structure on the release kinetics. They performed experiments using the PMMA porous membranes, obtained by starting from dissolved and dispersed amoxicillin with a content of 10% and 20% w/w of amoxicillin. Untreated amoxicillin dissolves completely in 10 min, whereas they observed an amoxicillin prolonged release of 20 h in the case of the dissolved drug PMMA membranes. No burst effect was observed; that is, no initial fast release of the drug has been verified, which means that no drug is present in the outer layer of the structure. These results agree with the previous considerations on SEM and DSC analysis confirming that amoxicillin forms a solid solution with PMMA.

In the case of dispersed drug, it dissolves completely in 3 h. Moreover, an initial burst release was observed (from 0 to 25 min) indicating that, probably, in this case, part of the drug molecules are exposed at the surface of polymer structure.

1.10.3.3 Membranes for Scaffolding Applications

Another possible application of polymeric membranes is related to tissue engineering. Indeed, several tissues show a membrane-like structure. However, the substitution of different biological materials requires different scaffold characteristics and they share a series of common peculiarities that have to be simultaneously obtained [41, 42]:

- A high regular and reproducible three-dimensional (3-D) structure (macrostructure) similar to the one of the tissue to be substituted.
- A porosity exceeding 90% and an open pore geometry that allows cell growth and reorganization; indeed, porosity and pore interconnectivity directly affect the diffusion of nutrients and the removal of metabolic wastes.
- A suitable cell size depending on the specific tissue to be replaced. For example, in the regeneration of bone tissues, cell sizes ranging between 200 and 400 μm and up to 500 μm are commonly indicated.
- High internal surface areas. The scaffold should be not only highly porous and interconnected but

should present nanostructural surface characteristics that allow cell adhesion, proliferation, and differentiation. The cells of different tissues, such as bones, tendon, cartilage, cardiac valves, and blood vessels, are submerged in a collagen matrix with a fibrous structure having diameters ranging between 50 and 500 nm. As a consequence, a fibrous structure should be formed on the walls of the scaffold to allow cell growth.

- Mechanical properties to maintain the predesigned tissue structure. The correct values depend on the organs to be repaired; for example, a bone temporary scaffold should present a compressive modulus of the order of 100 kPa.
- Biodegradability, biocompatibility, and a proper degradation rate to match the rate of the neotissue formation. For this reason, the choice of the polymer is very important because the biodegradability of the various polymers largely varies from one polymer to the other.

Porous structures of PLLA were prepared using the SC-IPS method by Tsiventzelis *et al.* [25]. The uniform cross sections and the cellular pores of the final samples indicated the occurrence of an L–L demixing process, followed by crystallization of the polymer-rich phase, as the dominant mechanism of the phase separation and pore production. The average pore size decreased with the increase of CO_2 density either by increasing the pressure or by decreasing the temperature, whereas the average pore diameter decreased with the increase of the initial polymer concentration.

The structures obtained using this approach have various limitations. Indeed, it is very difficult to obtain complex 3-D structures (i.e., usually films or hollow fiber membranes are generated) and the presence of the rough nanofibrous internal structure, which should mime the natural extracellular matrix necessary to obtain a good cell adhesion and growth (smooth cell walls are usually obtained).

For these reasons, Reverchon *et al.* [26] tested a new SCF-assisted technique for the formation of 3-D PLLA scaffolds, which consists of three subprocesses: the formation of a polymeric gel loaded with a solid porogen, the drying of the gel using SC-CO_2, and the washing with water to eliminate the porogen.

The PLLA scaffolds produced using this process have the following characteristics:

1. *Adequate internal structure.* These properties are conferred to the scaffold by the original fibrous nanometric substructure that is characteristic of the polymeric gel. The very porous structure obtained should also aid in the efficient removal of the porogen.
2. Accurate reproduction of the shape and 3-D structure of the tissue to be substituted.
3. Controlled and large porosity (> 90%).
4. Very large connectivity at micronic and nanometric levels.
5. Very short processing time.
6. Absence of solvent residues.

When PLLA gel drying is performed by SC-CO_2, the supercritical mixture formed during the process (solvent + CO_2) has no surface tension and can be easily eliminated in a single step by the continuous flow of SC-CO_2 in the drying vessel. The major problem in gel drying is the possibility of gel collapse. In this case, the absence of surface tension avoids this problem preserving the nanoporous structure. On the other hand, large interconnected cavities necessary to mime the tissue to be replaced are completely missing.

For this reason, the authors evaluated the possibility of superimposing a microporous structure in the aerogel to obtain a scaffold. They proposed a hybridization of the supercritical drying process with the particulate leaching. Indeed, it is possible to produce large cells inside a polymeric matrix using a porogen, an insoluble compound, which is introduced into the polymeric solution before the gelation. They successfully processed large and complex 3-D gel structures (i.e., bone-shaped gels), confirming the possibility of producing scaffolds with a specific geometry without size limitations and characterized by porosity of about 95%. Moreover, the overall process time is about 4 h, whereas the traditional process (i.e., freeze-drying) requires approximately 7 days.

Then, they optimized interconnection among the cells, increasing the pore connection by pressurizing at 1 MPa the suspension liquid polymer + porogen, before gelation. This pressure is sufficient to induce the contact among the porogen particles (i.e., fructose) that produces interconnection among the cells in the scaffold preserving the structure integrity. SEM images are reported in **Figure 12**. In these images, it is possible to observe the cellular structure (induced by porogen inclusion) and the nanofibrous substructure (produced by the polymeric gel) characterizing not only the polymeric network, but also the cells wall. In particular, fibers ranging between 50 and 400 nm add further porosity and interconnectivity and

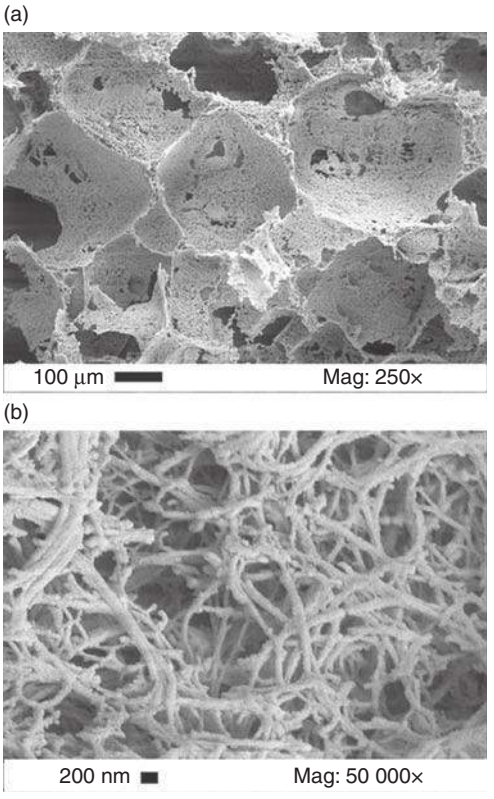

Figure 12 Scanning electron microscopy (SEM) images of the same part of a poly-L- lactic acid (PLLA) scaffold obtained at different magnifications: (a) image of cavities; (b) enlargement of part of a cavity.

produce the wall roughness that should be the key factor for cellular adhesion and growth.

Figure 12(b) is particularly significative in representing the structure of the cell walls. This image confirms that the presence of porogen particles during the gelation process did not influence the nanoporous structure formation also on the surfaces in contact with the porogen.

The solvent residue present in the produced scaffolds obtained after 4 h of drying was 263 ppm, which is lower than the limit of USP 467 Pharmacopea. By increasing the drying process time up to 8 h, as expected, solvent residue sensibly decreased down to a minimum of < 5 ppm.

The compressive modulus of some of the scaffolds obtained was measured to verify if mechanical resistance was compatible with the one required for bone scaffolding application. Stress–strain analysis indicated compressive modulus up to 81 kPa obtained for 15% w/w PLLA scaffolds.

The inclusion of hydroxyapatite particles inside the polymeric structure can modify the scaffold resistance and improve the formation of an environment suitable for bone cells growth; indeed, hydroxyapatite forms more than 30% of the natural bones and can behave as a support for the structure, increasing the compressive modulus. It also allows one to create an environment that better mimes the extracellular matrix. For this reason, the authors loaded hydroxyapatite nanoparticles inside the starting solution before the gelation.

As it is possible to observe from SEM image reported in **Figure 13**, a modification of the scaffold morphology is evident if compared to unloaded PLLA scaffold. Hydroxyapatite nanoparticles appear on the surface of polymeric fibers of cell wall, forming a hybrid particle–fiber cross-linked structure. Moreover, the scaffold compressive modulus, as expected, increases.

1.10.4 Conclusions and Perspectives

The SC-IPS process has substantially maintained the promises demonstrating to be fast and capable to produce membranes whose morphology can be tuned through the proper selection of the process parameters. Organic solvents used in the process have been rapidly and completely eliminated.

In the near future, we expect that SC-IPS will be extensively applied to hydrosoluble polymers and polymer blends that have, at present, only been demonstrated in terms of feasibility. Loaded membranes and scaffolds obtained by SCF-assisted processes are also promising applications that still require a large experimentation.

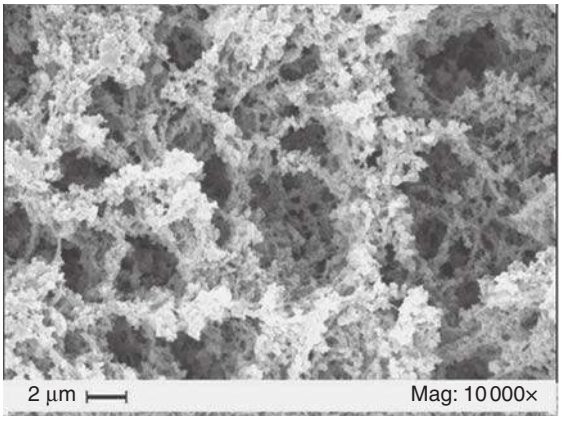

Figure 13 Scanning electron microscopy (SEM) image of a hydroxyapatite loaded scaffold cell wall.

Comprehensive characterization of SC-IPS membranes is also required together with the targeting of the various membranes toward specific industrial applications. The scale-up of the process should then be performed.

References

[1] Mulder, M. *Basic Principles of Membrane Technology*; Kluwer: Dordrecht, 1992.
[2] Lonsdale, H. K. *J. Membr. Sci.* **1982**, *10*, 81–91.
[3] Pusch, W., Walch, A. *Angew. Chem. Int. Ed. Engl.* **1982**, *21*, 660–685.
[4] van de Witte, P., Dijkstra, P. J., van der Berg, J. W. A., Feijen, J. *J. Membr. Sci.* **1996**, *117*, 1–31.
[5] Binder, K. *Materials Science and Technology, A Comprehensive Treatment*; VHC: New York, 1991; pp 405–472.
[6] Cahn, J. W. *Trans. Metal. Soc. AIME* **1968**, *242*, 166–195.
[7] Tompa, H. *Polymer Solutions*; Butterworths: London, 1956.
[8] Reverchon, E., Cardea, S. *J. Membr. Sci.* **2004**, *240*, 187–195.
[9] Matsuyama, H., Yamamoto, A., Yano, H., *et al. J. Membr. Sci.* **2002**, *204*, 81–87.
[10] Kho, Y. W., Kalika, D. S., Knutson, B. L. *Polymer* **2001**, *42*, 6119–6127.
[11] Cardea, S., Gugliuzza, A., Schiavo Rappo, E., Aceto, M., Drioli, E., Reverchon, E. *Desalination* **2006**, *200*, 58–60.
[12] Xu, Q., Pang, M., Peng, Q., Li, J., Jiang, Y. *J. Appl. Pol. Sci.* **2004**, *94*, 2158–2163.
[13] Xu, Q., Pang, M., Peng, Q., *et al. J. Appl. Pol. Sci.* **2005**, *98*, 831–837.
[14] Reverchon, E., Schiavo Rappo, E., Cardea, S. *Pol. Eng. Sci.* **2006**, *46*, 188–197.
[15] Matsuyama, H., Yamamoto, A., Yano, H., *et al. J. Membr. Sci.* **2001**, *194*, 157–163.
[16] Reverchon, E., Cardea, S. *J. Supercrit. Fluids* **2005**, *35*, 140–146.
[17] Temtem, M., Casimiro, T., Aguiar-Ricardo, A. *J. Membr. Sci.* **2006**, *283*, 244–252.
[18] Temtem, M., Casimiro, T., Aguiar-Ricardo, A., Mano, F. J. *J. Supercrit. Fluids* **2008**, *43*, 542–548.
[19] Kim, M. S., Lee, S. J. *J. Supercrit. Fluids* **2004**, *31*, 217–225.
[20] Reverchon, E., Cardea, S., Rapuano, C. *J. Appl. Pol. Sci.* **2007**, *104*, 3151–3160.
[21] Reverchon, E., Cardea, S. *Ind. Eng. Chem. Res.* **2006**, *45*, 8939–8945.
[22] Cao, J. H., Zhu, B. K., Ji, G. L., Xu, Y. Y. *J. Membr. Sci.* **2005**, *266*, 102–109.
[23] Huang, S., Wu, G., Chen, S. *J. Membr. Sci.* **2007**, *293*, 100–110.
[24] Reverchon, E., Cardea, S., Schiavo Rappo, E. *J. Membr. Sci.* **2006**, *273*, 97–105.
[25] Tsivintzelis, I., Pavlidou, E., Panayiotou, C. *J. Supercrit. Fluids* **2006**, *40*, 317–322.
[26] Reverchon, E., Cardea, S., Rapuano, C. *J. Supercrit. Fluids* **2008**, doi:10.1016/j.supflu.2008.01.005.
[27] Reverchon, E. *J. Supercrit. Fluids* **1999**, *15*, 1–22.
[28] Gauter, K. *Fluid Multiphase Behavior in Ternary Systems of Near-Critical CO_2. PhD Thesis,* Delft University, The Netherlands, 1998.
[29] Reuvers, A. J. *Membrane Formation: Diffusion Induced Demixing Processes in Ternary Systems. PhD Thesis,* Twente University of Technology, The Netherlands, 1987.
[30] Kang, Y. S., Kim, H. J., Kim, U. Y. *J. Membr. Sci.* **1991**, *60*, 219–232.
[31] Zhou, X. D., Zhang, S. C., Huebner, W., Ownby, P. D., Hongchen, G. *J. Mater. Sci.* **2001**, *36*, 3759–3768.
[32] Williams, L. L. Removal of Polymer Coating with Supercritical Carbon Dioxide. PhD Thesis, Colorado State University Fort Collins, CO, 2001.
[33] Huang, F., Li, M., Lee, L., Starling, K. *J. Chem. Eng. Japan* **1985**, *18*, 490–497.
[34] So, M. T., Eirich, F. R., Strathamann, H., Backer, R. W. *Polym. Lett.* **1973**, *11*, 201–215.
[35] Sedlacek, B., Kahovec, J., Eds. *Synthetic Polymeric Membranes*; Walter de Gruyter: Berlin–New York, 1987; pp 141–194.
[36] Yao, C. W., Budford, R. P., Fane, A. G. *J. Membr. Sci.* **1988**, *38*, 113–125.
[37] Radovanovic, P., Thiel, S. W., Hwang, S. T. *J. Membr. Sci.* **1992**, *65*, 231–246.
[38] Strathman, H., Kock, K., Aimar, P., Baker, R. W. T. *Desalination* **1975**, *16*, 179–203.
[39] Reverchon, E., Cardea, S. *J. Supercrit. Fluids* **2007**, *40*, 144–152.
[40] Reverchon, E., Cardea, S. *J. Supercrit. Fluids* **2008**, doi:10.1016/j.supflu.2008.01.017.
[41] Liu, X., Ma, P. X. *Ann. Biomed. Eng.* **2003**, *32*, 477–492.
[42] Ma, P. X. *Mater. Today* **2004**, *7*, 30–40.

Biographical Sketches

Ernesto Reverchon is a full professor and the head of the Supercritical Fluids Research Group operating at the University of Salerno. He is also the director of the Chemical and Food Engineering Department.

He developed several new processes (in some cases, up to the industrial scale) based on the use of supercritical fluids; his current research focuses mainly on new challenges in supercritical fluids, such as the engineering of nanoparticles and nanocomposites for a controlled drug delivery in the human body and the development of nanostructured scaffolds for tissue repairing.

He has more than 250 scientific publications on international journals and conferences; among them more than 210 are related to SCF. He has 15 patents on supercritical fluid products or processes. Furthermore, he has authored one book and six chapters in international scientific books.

Prof. Reverchon is currently a member of the editorial board of the *Journal of Supercritical Fluids* (Elsevier) and has been guest editor of some issues of this journal; he has been guest editor of an issue of IEC Res. (2006). He has been invited or plenary lecturer at many international congresses; he is a referee of the Australian Research Council for the evaluation of research based on SCF.

Dr. Stefano Cardea obtained his PhD degree in 2006. His activity, in collaboration with Prof. Reverchon at the University of Salerno, is devoted to different techniques assisted by SC-CO_2 for the formation of porous materials: (1) SC-CO_2 polymer foaming process; (2) SC-CO_2 phase-inversion processes for membranes formation starting from polymeric solutions; (3) SC-CO_2 gel drying process for membrane formation starting from polymeric gels; and (4) formation of nanostructured scaffolds for tissue repairing.

He has 12 scientific publications on international journals and he is also the co-author of one patent.

1.11 Basic Aspects in Inorganic Membrane Preparation

A Buekenhoudt, A Kovalevsky, Ir J Luyten, and F Snijkers, Flemish Institute for Technological Research (VITO), Mol, Belgium

Glossary

Calcination Thermal treatment of a green product at relatively low temperature (typically <600 °C) in order to remove the organic additives.

Critical thickness Maximum thickness limit to form a defect-free thin inorganic layer on top of a porous support. Above the critical thickness, tensile stresses cause defects in the layer.

Electroless plating A nongalvanic method to form a metal or metal alloy coating on a substrate (without the use of external electrical power). In the process, the substrate is submerged in an aqueous solution of metal ions. A reducing agent (typically hydrated sodium hypophosphite) is used to react with the metal ions and to deposit metal.

Extrusion A wet inorganic shaping technique in which a stiff plastic paste of an inorganic powder and suitable additives is forced by high pressure through an orifice or die, in order to form long tubular-type shapes (the cross section does not need to be circular).

Foam A sponge-like, very open porous structure with pores typically in the range of a few hundred micrometers up to a few millimeters.

Green product A dry article consisting of inorganic particles shaped in a certain form, with the aid of organic additives, before thermal treatments. The mechanical strength of the green shape is limited.

Phase inversion A wet shaping technique specific for polymer and inorganic membranes suitable for producing hollow fibers, capillaries, and flat sheets. In the phase inversion process, a viscous suspension consisting of a polymer powder, organic additives, and eventually an inorganic powder in a suitable solvent, is first shaped in the desired form, and subsequently contacted with a nonsolvent for the polymer. In the nonsolvent bath, polymer-rich and polymer-poor phases are formed, leading to a consolidation of the wet shape.

Replica technique A method in which an inorganic replica is made from a polymeric shape, by immersion of the polymeric shape into a concentrated inorganic suspension, and subsequent burning out of the polymer by a suitable thermal treatment.

Shaping The fabrication step in which powders are formed into useful shapes with the aid of organic additives.

Sintering Thermal treatment of a green product at relatively high temperature, leading to surface diffusion of solid matter and neck formation between the inorganic particles and to a partial or complete densification.

Slip casting A versatile inorganic shaping technique in which an aqueous slip of an inorganic powder is poured into a porous mold (mostly plaster), and left to dry.

Sol–gel process A process for forming mesoporous and microporous inorganic layers, converting a solution (sol) containing small inorganic particles (colloidal sol) or inorganic polymeric structures (polymeric sol) into a gel, by removal of the solvent in the solution through evaporation or through contact with a porous support. The sol is formed by hydrolysis and condensation of alkoxide or salt precursors in an organic solvent with an appropriate amount of water.

Solid-state reaction A reaction in which a mixture of solid inorganic reactants is heated in order to produce a new solid composition.

Tape casting A wet inorganic shaping technique in which a pseudo-plastic suspension of an inorganic powder and suitable additives is spread out over a moving carrier with the aid of a blade or a knife, in order to form thin flat shapes.

1.11.1 Introduction to Inorganic Membranes

Inorganic membrane science and technology is the latest developed field of membrane separation technology, which, until recently, was dominated by the earlier developed polymer membranes. As is common for recent developments, the field of inorganic membranes is still undergoing rapid change and innovation. The strong evolution and growth of the field account for the success of the dedicated International Conference on Inorganic Membranes (ICIMs), initiated in 1989 in Montpellier, France, organized biannually, and alternately in the US, Europe, and Asia. The proceedings of these conferences give a good overview of the field: the latest developments, innovative ideas, new potential applications, bottlenecks, state of commercialization, industrial interest, etc.

For most users, inorganic membranes are a relatively new product. However, in fact, their development started in the 1940s in order to enrich uranium for the Manhattan Project in World War II and for the subsequently constructed nuclear power plants [1]. This extensively used technology led to the first commercialization of inorganic membranes in the early 1980s and involved membranes with pores in the micrometer range, dedicated for microfiltration of liquids. Today, a wide variety of inorganic membranes exist in the market, covering not only the whole range of liquid filtrations, including pervaporation, but also a whole range of materials from different ceramics, over glass to metals. The latest commercializations are a titania nanofiltration membrane with pores just below 1 nm and a Linde type A (LTA) zeolite membrane with pores of 0.4 nm [2] (NF membranes commercialized by the German company HITK e.v. under the tradename Inopore®). Current research and development (R&D) efforts will lead to new membranes in the market, on both sides of the pore-size spectrum. On the one hand, there is a new R&D focusing on developing high-quality gas-separation membranes, mainly driven by the trend toward sustainable energy production. Among the potentially interesting membranes are dense ion-conducting or metal membranes, and zeolite and microporous carbon membranes. On the other hand, macroporous foams are developed intended for rough filtration applications, as bone scaffolds, or as efficient catalyst supports.

So far, commercialized membrane applications have been strongly (liquid separation) or exclusively (gas separation) dominated by polymer membranes. The share of inorganic membranes is currently estimated to be about 12% [3]. However, inorganic membranes will have their share of the future growth of membrane technology, if their strong points, being advantages over the polymeric alternatives, can be used:

- Their relatively high thermal stability, compatible with high-temperature operations, and suitable for real reaction–filtration integration, allowing therefore, for example, a shift of the reaction equilibrium as in membrane reactors.
- Their relatively high chemical stability and good corrosion resistance, compatible with highly aggressive media, allowing filtration in, for example, aprotic solvents that dissolve all currently existing polymeric membranes; in addition, allowing very aggressive cleaning, opening even economical implementation of ceramic membranes in drinking water production from difficult surface waters.
- Their biocompatibility facilitating their use in highly certified industries such as the pharmaceutical and food industry.
- Their noncompactability under high pressure, allowing application at more moderate pressures and without lengthy pretreatments.
- Their mechanical strength.
- Their long lifetime.

However, inorganic membrane production is intrinsically more expensive and complicated. Inorganic membrane applications will therefore mainly be found in those fields where polymer membranes cannot or do not perform well. It is also to be expected that the more aggressive situations (temperature and chemicals), in which inorganic membranes have great potential, will also call for clever solutions for suitable module construction (e.g., higher surface-to-volume ratio) and appropriate sealing (e.g., high-temperature gas-tight sealing).

1.11.2 General Principles of Inorganic Membrane Synthesis

Despite the wide pore-size range of all existing inorganic membranes, their synthesis shows some common aspects.

All synthesis starts from suitable powder preparation from precursor material. Subsequently, these powder particles are packed in a green product with a certain shape (flat or tubular). This can be done by wet or dry shaping techniques, facilitated by using one or more organic additives (in the role of binders, dispersants, and plasticizers). After shaping, the synthesis involves one or more heat treatments. A temperature treatment at relatively low temperature is required in order to remove the organic additives (calcination), and to consolidate the particle packing in the green product by initial neck formation between the particles (presintering). The pore size that can be obtained in this processing depends on the particle size of the starting powders, and is therefore limited to a minimum of about 0.1 μm. For denser membranes, a treatment at higher temperatures (sintering) follows, thereby causing serious material movements leading to a partial or complete densification of the green product. This sintering process gives the shaped article also its full mechanical strength.

As a result of these synthesis steps, in principle, membranes with a wide variety in pore sizes can be made. However, to make both porous and dense membranes suitable for real applications, all commercial and commercially interesting membranes always consist of a multilayer composition in which a coarse-porous support provides the necessary mechanical strength, and the porous or dense top layer is responsible for the separation aimed at. One or more intermediate layers between support and top layer take into account a gradual decrease of the pore size in the multilayer composition. **Figure 1** shows a scanning electron microscopy (SEM) picture revealing the typical multilayer structure of an inorganic membrane. In this manner, the membranes can combine a high flux and a high separation factor. The coarse-porous supports are fashioned as described above. The dense or fine-porous membrane layers coated on the porous supports are produced using other specific techniques. Layers with big mesopores can be produced from colloidal powder suspensions, whereas layers with meso- and micropores are produced by sol–gel techniques or chemical vapor deposition (CVD). Particular techniques exist for microporous carbon and zeolite layers. The dense or fine-porous membrane layers also require a temperature treatment similar to that of the coarse-porous supports in order to consolidate their microstructure.

In specific cases, the formed inorganic membranes are further functionalized by chemical modification of the membrane surface. This functionalization is used in order to either change the affinity of the membrane surface, or obtain catalytically active membranes.

This general scheme for inorganic membrane synthesis, which also clarifies the structure of this chapter, is shown in **Figure 2**.

This chapter gives a concise but broad overview of the different aspects of the state-of-the-art inorganic membrane synthesis. For more extended treatments in the literature, the reader is referred to three excellent books: *Inorganic Membranes Characterisation and Applications* [4], *Fundamentals of Inorganic Membrane Science and Technology* [5], and *Inorganic Membranes for Separation and Reaction* [3]. Other interesting references are provided as well. However, this chapter also focuses particularly on

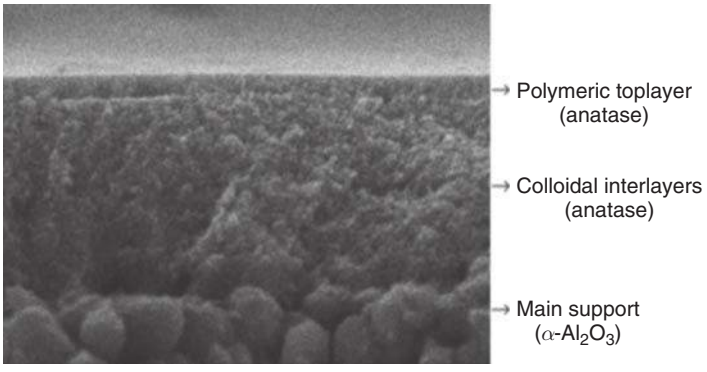

Figure 1 Scanning electron microscopy (SEM) picture of a titania nanofiltration membrane showing the typical multilayer structure of an inorganic membrane. Reproduced with permission from Van Gestel, T., Vandecasteele, C., Buekenhoudt, A., *et al*. *J. Membr. Sci.* **2002**, *207*, 73–89.

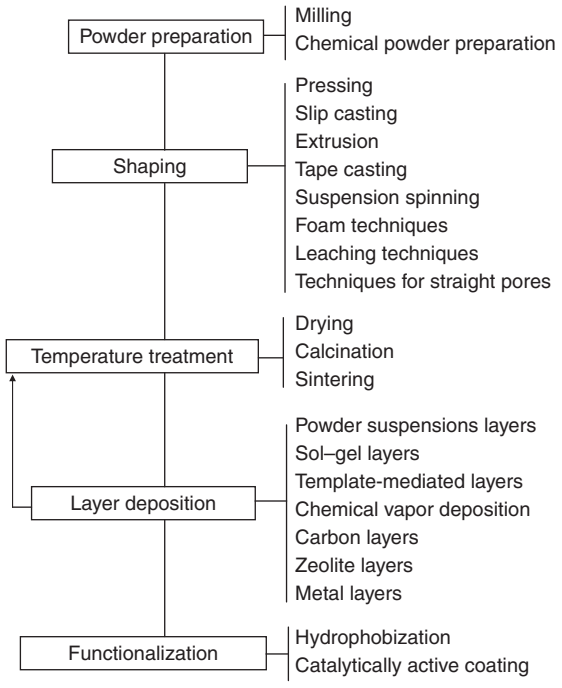

Figure 2 General scheme for the preparation of inorganic membranes.

the new trends, the recent developments, and the innovations related to membrane preparation in this highly evolving field.

1.11.3 Powder Preparation

1.11.3.1 Introduction

The starting powders for inorganic membranes are high-purity specialty chemicals. Powder preparation is a crucial step in the fabrication of inorganic membranes. High-purity, submicrometer powders with controlled physical characteristics, such as particle size, and, preferably, narrow particle-size distribution, are required for good membrane preparation. The characteristics of the inorganic powders used have a significant effect on the subsequent processing route and on the quality of the final membrane. Therefore, the proper choice of a powder synthesis method is an important task, especially for fine-porous or dense membranes.

The particle size (and, to some extent, the morphology) is an important parameter in membrane preparation, because it affects the porosity (or density) and the pore size of the final membrane. For porous membranes, when only neck formation between the packed particles takes place, the ratio of pore size to grain size is about 3 (the exact ratio depends on the particle shape). For dense membranes, small-size starting particles with an appropriate size distribution, which lead to a maximum packing density and final density, are essential to give complete densification in the sintering step. Moreover, as explained in Section 1.11.5, the required sintering temperatures to achieve complete densification in the case of small particles are much lower. Densification can also be improved by introducing sufficiently small-sized particles into a packing of large particles.

To obtain high-quality top layers, the particle size and particle-size distribution of the support are important as well. The pore size of the support must be adapted to the grain size of the layer to be deposited. The presence of large pores on the surface of the support could lead to penetration of the grains into the support and thus, to defects in the subsequent membrane layers. Defects can equally be formed by extra-large particles present on the surface of the support.

1.11.3.2 Milling

Good powder preparation commonly involves one or more mechanical milling steps in order to provide the breakdown of agglomerates and to adjust the particle size and particle-size distribution. Currently, a variety of mills can be used, including ball mills, roller mills, and attrition mills [6]. The most widely used are ball mills, utilizing the energy of balls which move in a jar and crush the agglomerates. Ball mills can, in turn, be categorized depending on the method used to impart the motion to the balls (e.g., vibration, tumbling, and agitation). The main advantages of this method include low cost and applicability to different kinds of membrane materials, whereas the main disadvantage is the incorporation of impurities from the mill and the milling medium into the powder. This can be avoided by the use of fluid-energy mills, where the powder is entrained in two impinging streams of high-velocity air so that particles are broken up by impact. Incorporation of impurities can also be reduced by lining the mill chamber with a plastic or ceramic material and by using ceramic stirrers and grinding medium.

In recent years, there has been growing interest in new techniques such as high-energy milling (also named mechano-chemical synthesis or mechanical

activation) [7]. It involves high-intensity vibratory milling for an extended period of time, leading to chemical interactions between the components and, as such, the formation of the final product having the desired composition and particle size at the same time. This method is most suitable for producing materials that are otherwise difficult to make (e.g., silicides and carbides). The incorporation of impurities is, however, much more severe than for conventional milling.

1.11.3.3 Chemical Powder Preparation

A variety of chemical methods is being used for the preparation of high-quality inorganic powders. Several reviews of the subject are available in the literature [6–8]. With respect to inorganic membranes, the solid-state reaction route and synthesis from liquid solutions (precipitation and sol–gel methods) are considered to be the most appropriate. The most important methods are described in the following subsections.

The production of inorganic membrane powders by vapor-phase reaction is less frequently used. In this process, reactant gases are mixed and heated to nucleate and grow particles from the gas phase. For the reaction, a number of different heat sources can be used, such as a direct-current or induction-coupled plasma, a laser, or a furnace.

1.11.3.3.1 Solid-state reaction

The solid-state reaction route involves chemical decomposition reactions, in which a mixture of solid reactants is heated to produce a new solid composition and gases. This method is commonly used for the production of complex oxides from simple oxides, carbonates, nitrates, hydroxides, oxalates, alkoxides, and other metal salts. Usually, the procedure includes several annealing steps with multiple intermediate milling steps to increase the homogeneity of the mixture, and to decrease the particle size of the powder. Extra milling also makes the powder more active in the subsequent heat-treatment steps (i.e., more sinter active). The solid-state route is relatively inexpensive and requires simple apparatus. Moreover, large volumes of powder can be prepared in a relatively simple manner. However, compared to the wet powder preparation routes described below, the obtained powder shows relatively high agglomeration, and, therefore, relatively large particle size as well as relatively limited homogeneity.

1.11.3.3.2 Wet powder preparation

The disadvantages of the solid-state reaction can be overcome by using liquid preparation methods, generating powders either by precipitation or by sol–gel processes. These methods offer a better control of the purity, chemical composition, and, in particular, the particle size. They involve a solvent removal step (e.g., filtration, centrifugation, and evaporation) and, eventually, a heating step to achieve the desired crystallinity. The production cost of these methods is, however, relatively high, and large-scale production is difficult.

Usually, the precipitation of metal cations is performed using oxalate, hydroxide, carbonate, citrate, acetate, or cyanide ions from aqueous solutions. The choice of the precipitating agent depends on the composition of the target material, taking into account the solubility of the precipitates. In addition to conventional precipitation, a number of other precipitation processes can be used, including precipitation under pressure (hydrothermal) and simultaneous precipitation of more than one cation (coprecipitation). Hydrothermal precipitation (often from hydroxides) can produce mixed cation precipitates and can precipitate oxides directly, whereas conventional precipitation usually produces hydroxides or salts, which must be heat treated to form oxides. Coprecipitation is used for many advanced multication powders to obtain more intimate mixing of the cations than can be achieved by mixing oxides or salts of the individual cations. Because of the intimate mixing produced by coprecipitation, the temperature required to produce the desired crystalline phase in the powder is usually lower than for mixtures of individual oxides.

In case fine particles and, especially, a good chemical homogeneity are required, a few methods utilize the formation of a gel or a high-viscosity resin from liquid precursors as an intermediate step in the synthesis of ceramic powder. Sol–gel processing may include the formation of a polymeric gel by the hydrolysis, condensation, and gelation of a metal alkoxide solution, followed by drying and grounding to produce the powder. In the Pechini method, from starting materials, the metal ions are complexed in an aqueous solution with carboxylic acids, such as citric acid; subsequently, they undergo polyesterification under heating with a polyhydroxy alcohol, and, after the removal of the excess liquid, form a resin. The resin is then heated to decompose the organic constituents, ground, and heat treated to produce the desired powder. The citrate gel method includes the

formation of a viscous liquid containing polybasic chelates between metal cations and citric acid, heating in vacuum to form an amorphous solid, and subsequent pyrolysis in air at elevated temperatures to produce a crystalline powder. The glycine–nitrate process is one of the general classes of combustion methods for the preparation of ceramic powders. A highly viscous mass formed by evaporation of a solution of metal nitrates and glycine is ignited to produce the powder. In this case, a short exposure to high temperatures during the ignition step provides the very fine size and crystalline nature of the powder.

Preparation of membrane materials in a fine particulate form can also be achieved by special thermal treatment of a precursor liquid solution, for example, spray drying or plasma spray drying [9] and spray pyrolysis [10] or freeze drying [11].

1.11.4 Shaping

1.11.4.1 Introduction

The fabrication step in which powders are formed into useful membrane shapes is called shaping or, alternatively, green forming. A wide variety of processes, wet and dry, can be used for shaping. Many of them are common techniques in the production of traditional or other advanced inorganic materials, and are useful for all different inorganic material types, namely, ceramics, metals, and glasses.

In all these techniques, organics, in large or small quantities, are added to the powder to facilitate the shaping process. In the wet-shaping techniques, a slip or paste is first formed by adding solvents (water or others) and other organic additives to the powder. The amount of organic additives is kept as low as possible. Additives are required to obtain the desired dispersity of the powder particles in the slip/paste, and the desired rheology of the slip/paste, and to avoid deflocculation. Binders are used to provide cohesion between the powder particles, to give adequate green strength, and to avoid crack formation. The pH of the slip/paste is often controlled in order to steer the degree of flocculation of the powder. Moreover, the slip/paste has to be mixed carefully, and subsequently degassed to remove any entrapped air before fabrication in order to avoid flaws formed on the surface of the final product. The slip/paste preparation is crucial for every shaping process and requires optimization of a number of factors, including viscosity, solid content, slip/paste stability, casting rate, drying rate, and drying shrinkage. All this involves an understanding of the surface chemistry of the particles in the slip. Since each powder reacts differently, good slip/paste preparation is a very empirical process. Moreover, it is important to notice that, although all the organic additives are removed in the subsequent thermal treatments and the powder of choice is the only remaining constituent in the final product, these organic ingredients, nevertheless, codetermine the final quality of the membrane formed. In order to optimize the final membrane material, a good characterization of the slip/paste can be of importance. Different techniques such as particle-size measurements, zeta potential measurements, and viscosity measurements can be used.

After shaping, the subsequent thermal treatments determine the final porosity of the membrane (see Section 1.11.5). In the case of low-temperature calcination and presintering, the particle size of the powder used determines the porosity. If the particles are packed densely and only necks are formed between the particles by the heat treatment, the pore size is typically about one-third to one-fifth of the particle size (the exact factor depends on the particle shape). Consequently, the pore size is typically limited to about 0.1 μm, although nanopowders, in principle, could lead to nanometer pores [12]. The formed coarse-porous bodies are commonly used as supports for further coatings and subsequent formation of finer-porous or dense membranes (Section 1.11.6). In case the temperature treatment involves a carefully performed high-temperature sintering, the green products can also be turned into fully dense membranes (see Section 1.11.5). However, as the so-formed dense membranes are, in most cases, relatively thick, these membranes are mainly used for laboratory tests and are of no commercial interest.

It has become very clear that the surface quality of the support is very important in order to be able to form high-quality multilayer membranes. This is due to the fact that defects or irregularities in the support usually produce defects in the layers coated on top of it. The necessity of a good-quality support is most important when microporous or dense membranes is the final product. Defects can be extra-large pores or broken out grains. Surface irregularities causing surface roughness are detrimental, although some roughness can be flattened by sufficiently thick layers.

In the following subsections, a short overview of the shaping techniques that are currently used for

membrane fabrication is given, the details of which can be found in References 3–5. For recent adaptations of the described methods and innovative approaches, the reader is referred to the published literature cited elsewhere in the text.

1.11.4.2 Pressing

Powder pressing (or die pressing or compaction, uniaxial pressing or compaction of powder or granules) is a cheap industrially important process, already used for a longtime, and used as a production step for many classes of materials. As such, powder pressing is a shaping technique that is also applied for the fabrication of ceramic and metallic membranes. It is believed that there is still scope for improvement, for example, by computer modeling of the powder-compaction process [13, 14].

Powder pressing uses a metal die (mostly hardened steel or eventually a more wear-resistant alloy) to compact dry or slightly humid powders. Disks, pellets, and cylinders are the most-used die geometries. The pressures applied strongly depend on the powder or mix to be compacted, and can vary from a few tens of MPa to several hundreds of MPa. The use of high pressure not only ensures the strength of the green body but also reduces shrinkage during the subsequent heat treatments. The presence of a few percent of water allows one to work with reduced pressures, compared to completely dry pressing. Often, a little amount of binder is added in order to reduce friction, minimize the wear of tooling, and give a more homogeneous density distribution as well as a higher quality of the green compact.

The maximum obtainable ratio of height to diameter of a compact is recognized to be a major limitation of standard powder die compaction. This is due to pressure differences and resulting inhomogeneous density distribution for relatively long die cavities. Uneven pressure distribution is also a regular cause of cracks in pressed bodies. One way to circumvent all these bottlenecks is by using cold isostatic pressing (CIP). In CIP, the loose powder is placed in a flexible rubber mold (with eventually a steel mandrel in its center in order to make tubular shapes). The rubber mold is submerged in the liquid in a thick-walled pressure vessel. Characteristic to applying the pressure through the fluid is that the forces applied to a submerged body is equal in all directions.

Powder pressing (standard pressing and CIP) is used in the fabrication of both fully dense membranes and porous membranes, depending on the subsequent temperature treatment (Section 1.11.5). The porous membranes can also be used as supports for further coating (Section 1.11.6). Porous membranes have also been made by compaction of a mixture of an inorganic powder and a pore former (e.g., graphite or starch). By applying a two-step process, pressing can also be used to form asymmetric membranes consisting of a dense top layer on a porous support that can be cosintered [15].

However, pressing has mainly been used to make membranes for laboratory coating and other laboratory tests; it has not been used for the fabrication of commercial membranes.

1.11.4.3 Slip Casting

Slip casting is a very economical and traditional shaping process for ceramics, in which the starting powders are suspended in water to form the slip. From the slip, green shapes are formed by pouring the slip into porous molds mostly made of plaster. The capillary action of the porous mold draws water from the slip and forms a solid layer on the inside of the mold. After pouring out the excess slip, the formed part is partially dried in the mold to cause it to shrink away from the mold and to develop adequate rigidity for further handling. The final strength and porosity are reached by subsequent thermal treatment (Section 1.11.5).

Although many complex shapes are possible with slip casting (e.g., main process to form sanitary ware), in the inorganic membrane synthesis, this process is mainly used to form flat or single tubular ceramic membranes (dense as well as porous, depending on the subsequent thermal treatment).

As mentioned before, in case the resulting green shape after thermal treatment is used as a support for further coating (Section 1.11.6), the quality of the surface is very important. Surface irregularities causing surface roughness can hinder the coating of a defect-free and thin top layer. In order to obtain better supports with smoother surfaces, the method of slip casting can be combined with centrifugation, specifically for tubular supports. The result of this centrifugal slip casting is a much better packing of the powder in the support layer [16]. In this method of centrifugal casting, a cylindrical mold is filled with the slip, and rotated around its central axis. The particles will then start to move toward the cylinder

wall and form a cast with increasing thickness. The centrifugal forces cause the largest particles to move to the mold wall first, followed by the smaller particles. The quality of the outside surface of the tube is determined by the surface quality of the mold, while the inside surface quality is determined by the slip quality and consists of the smallest particles in the slip. In order to combine the high surface quality of the tubes with good strength and high permeability, the particle size of the used powder and the temperature treatment is important. For further optimization, a multilayer centrifugal casting or the casting of a slip using a mixture of powders with different particle size can be used [17].

1.11.4.4 Extrusion

Extrusion is a green-forming technique used to form tubular shapes. It has been used for all inorganic materials (e.g., metals, ceramics, and glasses) and to form a wide variety of tubular shapes: single tubes, multichannel tubes, monolithic honeycomb tubes, and capillaries. Extrusion is a process in which a stiff plastic paste is forced by high pressure through a suitably shaped orifice or extrusion die. The plastic paste is strong enough to maintain its physical integrity after shaping by the die, even in the green state (before drying and thermal treatment). It is also possible to extrude a double-layer structure where the two layers are made of particles of different sizes in one step.

The final strength and porosity of the shaped tubes are again determined by the subsequent thermal treatments (Section 1.11.5). Likewise, both fully dense membranes and porous membranes or supports can be produced in this manner.

Extrusion is the common process used to make the supports of all commercially available tubular inorganic membranes. **Figure 3** gives an overview of some of the different tubular designs that are in use today. As regards materials, mainly α-alumina is used, and some cordierite ($2MgO{\cdot}2Al_2O_3{\cdot}5SiO_2$), mullite ($3Al_2O_3{\cdot}2SiO_2$), silicon carbide, silicon nitride, etc., as well as metals, such as stainless steel, are used. In the past decade, some titania supports also have become available [18, 19] due to their extra-high corrosion stability and high biocompatibility.

Extrusion can also be used to make tubes with small diameters: capillaries [20]. The term capillary is normally used for tubes with a diameter between 0.5 and 5 mm. Tubes with a inner diameter smaller than 0.5 mm are commonly called hollow fibers. However, both terms (hollow fibers and capillaries) are not always used as consequently as described here. With their small dimensions, the small-diameter tubular designs are also extra valuable for membranes, since they give the potential of high packing densities, or, in other words, they lead to very high surface-to-volume ratios ($>1000\,m^2\,m^{-3}$) of membrane installations, which is also the reason for the high success of capillary and hollow fiber polymer membranes. Capillaries can also be made by using suspension-spinning techniques, which are extensively used in polymer membrane synthesis as well. This technique is described briefly in Section 1.11.4.6, and the difference with the extrusion technique is also explained.

Figure 3 Overview of some of the different tubular designs for inorganic supports, in use today. (a) The tubular designs as produced by HITK e.v. (b) The tubular designs as produced by Tami Industries.

1.11.4.5 Tape Casting

Tape casting, also known as the doctor blading technique, has been advanced since the end of World War II as the best way to form thin, flat, large-area ceramic or metallic articles. Tape casting

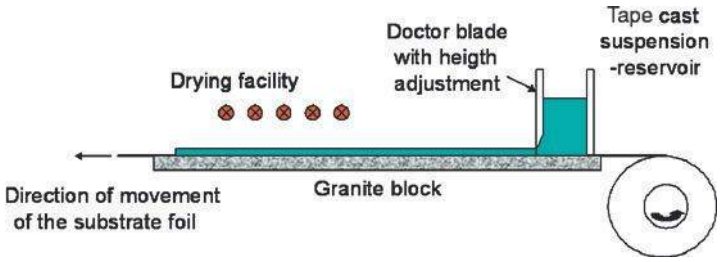

Figure 4 Schematic representation of a typical tape casting process.

is a well-established practice for making ceramic substrates in microelectronics [21]. The possible thicknesses are in the range of 0.01 to a few millimeters. Such parts can impossibly be obtained by pressing or extruding. It is a wet-shaping technique that uses a tape cast suspension with mostly pseudoplastic properties. The suspension is constituted from the inorganic powder chosen, several organic additives, and a liquid medium.

A typical tape casting process is depicted in **Figure 4**. The heart of the process is the so-called doctor blade that acts as a knife, spreading out the tape cast suspension over a moving carrier film. After spreading over the carrier film, a drying installation is foreseen. The drying rate can be crucial to the success of making a crack-free membrane. In the process, two major forces act upon the suspension. First, there is gravity-inducing pressure flow: the height of the liquid column in the reservoir behind the doctor blade forces the suspension to flow from the gap underneath the blade. This flow is also known as pressure flow. Second, and more importantly, the moving carrier film leads to drag flow. In typical conditions of tape casting, this force exceeds the pressure flow by one order of magnitude. Therefore, next to the suspension properties, the gap height under the doctor blade and the speed of the carrier relative to the doctor blade are important variables in a tape cast process.

Tape casting can be used not only to make self-supported thin shapes, but also to coat on top of a previously formed support. Again, both porous and dense supports and layers can be fabricated. For instance, tape casting is typically used to make both the dense electrolyte layer, and the porous anode for solid oxide fuel cells [22].

In the past decade, much effort has been made on developing water-based tape casting using water and natural products as alternatives for the frequently toxic solvents and binders, driven by environmental concerns. However, from the viewpoint of process control, solvent-based tape casting is often considered to be a better choice over water-based tape casting.

1.11.4.6 Suspension Techniques Coupled to Phase Inversion

As described in Section 1.11.4.4, tubes with a small diameter (<5 mm), commonly called capillaries and hollow fibers, can be fabricated by extrusion. However, there is another versatile technique to make these small-diameter tubes, that is, suspension spinning coupled to phase inversion. This method is a variant of the commonly used method to make polymer hollow fiber and capillary membranes (see Chapter 1.05). It has the potential of making tubes with much smaller diameter than extrusion: hollow fibers with outer diameters <0.5 mm can be easily produced. For making ceramic membranes, this method is useful for making porous membranes [23]. In order to make dense membranes, the technique was first used by our institute (Flemish Institute for Technological Research (VITO)), primarily to make high T_c superconducting wire [24], and, a few years later, to make ionic-conducting dense membranes [25, 26]. Currently, the method is used in many laboratories.

In spinning, a viscous suspension of the inorganic powder and organic additives (and not a stiff plastic pasted) as used for extrusion is shaped into a capillary or hollow fiber. Analogous to extrusion, the suspension is forced through a die, typically a tube-in-orifice called spinneret. **Figure 5** shows a scheme of a typical spinning apparatus, and a schematic representation of the spinning head. The spinning rate of the suspension is controlled by nitrogen pressure or a gear pump, commonly extra adjustable by a valve. Due to the relatively low viscosity of the suspension used, the green fiber after the shaping is very fragile and the shape is only properly consolidated in a nonsolvent

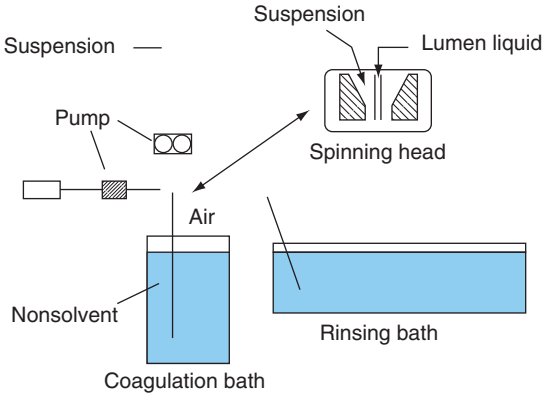

Figure 5 Scheme representing a typical spinning apparatus to make hollow fibers and capillaries using a phase-inversion technique.

coagulation bath by a phase-inversion process. This is in contrast to the standard extrusion process where the green extruded tape has substantial physical integrity by itself. Due to the inadequate strength of the green tubular shape, it is also necessary to run a liquid through the inside opening of the spinneret (bore liquid) while the small-diameter tubes are formed, in order to create a hydrostatic pressure on the inside of the tube and to prevent collapse of the tube. Usually, a coagulating liquid is used as bore liquid.

Because of the necessity of the phase-inversion process, the spinning suspension contains specific couples of polymer and solvents giving rise to a phase-inversion process in a specific nonsolvent. During the phase-inversion process, a solid polymer-rich phase forms the membrane structure and a liquid polymer-poor phase forms the pores. These are the typical polymer/solvent/nonsolvent trios used in polymer synthesis, which are used for producing inorganic membranes. One such very useful trio is the combination polysulfone/*N*-methyl-pyrrolidone/water. From this, it is clear that the organic additives typically used in extrusion are very different from the organic additives used in suspension spinning.

Another difference between suspension spinning and extrusion products is their morphology. The green shapes made by the extrusion process possess a homogeneous structure over the cross section of the hollow fiber or capillary. In contrast, the green shapes of the spinning process can show both a homogeneous structure or a very asymmetric structure containing large finger-shaped pores on the one side, and a thin dense layer on the other side, as can be seen in **Figure 6**. The exact microstructure depends on the details of the spinning process. The asymmetric structures are typical for the spinning process and are also commonly seen in polymeric hollow fibers. The possibility of producing asymmetric structures in one step can be a great advantage for membrane preparation. Indeed, in this manner, a multilayer structure is prepared in one step. Of course, for commercially interesting membranes, mechanical stability is also important, and the finger-shaped pores can be undesirable, in which case a more homogeneous structure will be preferred.

All aspects important in suspension spinning of inorganic membranes, that is, the preparation of good spinning suspension, the parameters important for the spinning process and the phase-inversion process, and possible pore structures of the final products, are extensively explained in Chapter 1.12.

This same method can also be used to make flat membranes [25, 26]. In this case, a doctor-blade shaping technique, as in tape casting (see Section 1.11.4.5), is used in combination with phase inversion in a coagulating bath. The same technique is also extensively

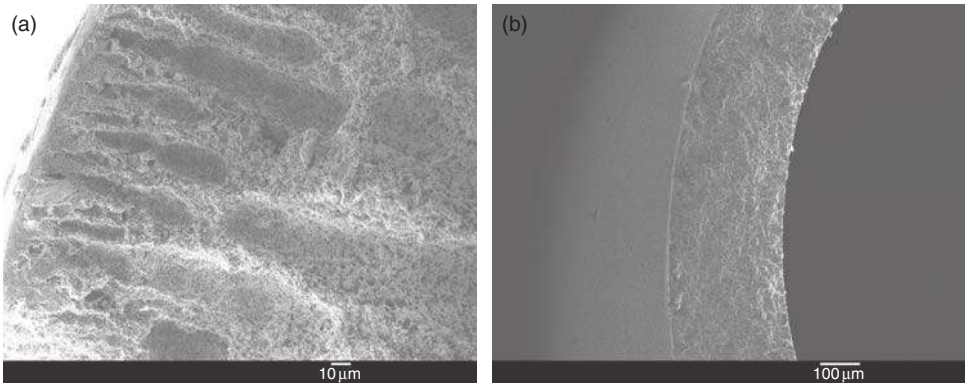

Figure 6 Scanning electron microscopy (SEM) pictures of inorganic hollow fibers made by suspension spinning coupled to phase inversion. (a) A microstructure with finger-shaped pores; (b) a homogeneous microstructure.

used to make flat polymer membranes on a commercial scale. The suspension is similar as for the shaping of hollow fibers and capillaries. This suspension is again different from the paste that is normally used for tape casting. The differences are similar to the differences between an extrusion paste and a spinning suspension, as previously described in this section.

1.11.4.7 Foam Techniques

Foams are very open porous structures with pores typically in the range of a few hundred micrometers up to a few millimeters. Foams can also be made of inorganic materials as ceramics. They are lightweight materials which can be described as a three-dimensional (3D) network of struts made of a ceramic material and hollow polygons with or without windows. Such a network of cellular structures is characterized by a number of parameters, such as cell size and morphology, strut thickness and length, and porosity and type of porosity (open vs. closed). As such, these materials combine properties related to their cellular structure and the ceramic material making up the struts. By choosing the proper ceramic materials and processing methods, the ceramic foams can combine their very high porosity with a relative high mechanical strength, and, being ceramics, have the additional advantage of chemical inertness and high-temperature resistance. Moreover, due to their low density, low thermal conductivity, thermal shock behavior, and large surface area, such materials are highly desirable for a wide range of other engineering applications next to membranes [27, 28].

Ceramic foams are rather recent membrane types. They have specific potential for filter applications in molten metals to filter out inclusions, as particle (e.g., soot) filter trapping the particles in the depth of the whole porous structure, and as support of catalysts with high and easily available specific surface [29–32].

As for other inorganic membranes, the synthesis of ceramic foams, in general, comprises three process steps: the appropriate powder preparation, shaping of a powder suspension, and temperature treatment. A wide range of specialized shaping routes has been developed. Basically, two main techniques are used with a series of variations on the basic theme: the replication of a polymeric template and direct foaming of a ceramic slurry. Some less spread techniques are summarized under Section 1.11.4.7.3.

1.11.4.7.1 The replication of a polymeric template

The replica technique (or polymeric sponge method) [33–36] consists of the immersion of a polymeric sponge in a ceramic or metallic suspension with a solid content usually between 50 and 70 wt.%. The impregnated polymer support is removed from the slurry and the excess material is squeezed out by means of a rolling mill. After drying and a thermal treatment that will burn out the polymer and other organic substances (at about 500 °C), the particles are sintered and the ceramic skeleton is obtained. The skeleton thus obtained will be a close replica of the polymeric template, considering the shrinkage linked to the firing step. A reticulated polyurethane (PU) foam is mostly used; however, other polymers, such as polyvinylchloride, polystyrene, and cellulose, can be used as well. **Figure 7** shows an example of a foam structure produced with this technique.

The main benefit of the PU replica technique is the wide variety in structural parameters of the ceramic foam, with pore-size distributions that vary between about 300 μm and up to several millimeters, as well as structural uniformity. Nevertheless, the relatively low mechanical strength of foams manufactured with the replication method is caused by the formation of hollow struts after calcinations of the polymeric substrate, and the presence of residual cracks. In order to overcome this intrinsic disadvantage, some strategies have been developed [37–39]: the use of a stronger ceramic material (e.g., reaction-bonded aluminum oxide (RBAO)), repeated coating, and infiltration of the struts with liquid metal.

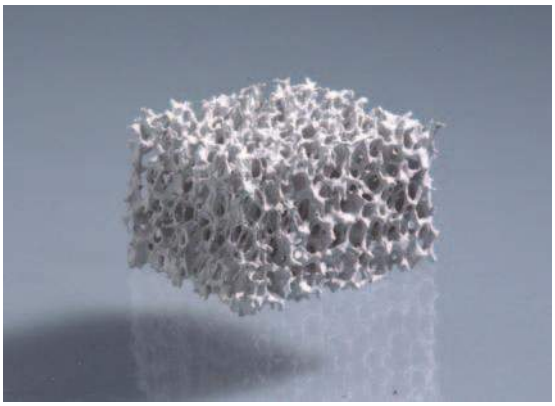

Figure 7 Picture of a typical ceramic foam prepared by the replication technique of a reticulated polyurethane. Reproduced with permission from Snijkers, F., Mullens, S., Buekenhoudt, A., Vandermeulen, W., Luyten, J., *Materials Science Forum* **2005**, *492–493*, 299–304.

A variation on the replication process is the pyrolysis and CVD coating of the polymer foam. In this technique, a resin-impregnated thermosetting foam is pyrolyzed to obtain a carbon skeleton. This reticulated carbon skeleton is then coated by a CVD process with the specific ceramic layer. In addition, the cellular structure of wood can, after pyrolysis, be used as a template to produce ceramic foams. Different types of porous ceramics can then be obtained by liquid or gas infiltration of the open biocarbon template [40].

An example of another template method is the so-called hollow beads method [41]. The basic idea is to prepare structures that are built up by ceramic hollow building blocks which are in the second stage of the procedure, connected together. The ceramic hollow beads are produced using a sacrificial coating technique. As cores, materials widely varying in origin and shape can be used, including styrene granules, seeds, peas, and nuts. After the beads are packed in a mold, they are joined together using a second slurry coating, then calcined and sintered. In this manner, lightweight materials, with densities as low as 10% of the theoretical density, can be obtained. **Figure 8** gives some examples of components processed by the hollow beads method.

1.11.4.7.2 Direct foaming of a ceramic slurry

This technique relies on the foaming of a stable ceramic slurry by mechanical agitation, injection, or *in situ* evolution of gases [42–46]. A surfactant is required to reduce the surface tension of the gas–liquid interface, and, further, a mechanism is required for the long-term stabilization (solidifying) of the foam, for example, gelling of the foamed suspension. This approach probably yields the widest range of cellular structures and, hence, properties; however, they are generally less open than the replicated foams.

Gel casting is one of the frequently used solidification processes. When heavily stirred, the suspension transforms into a foam structure and can be poured into a mold. The following step includes the gelling of the (liquid) foam, resulting in the creation of gel-like foam. Different gelling agents have been used: chemical monomers (mostly based on acrylamides) and several environment-friendly hydrocolloids (gelatin, agarose, etc.). Again, calcining and firing result in the final ceramic porous material.

Compared to the replica technique, gel casting produces foam structures with solid struts, greatly augmenting the mechanical strength. In addition, by using this method, it is feasible to obtain foams with smaller average cell sizes (<300 μm), which are more

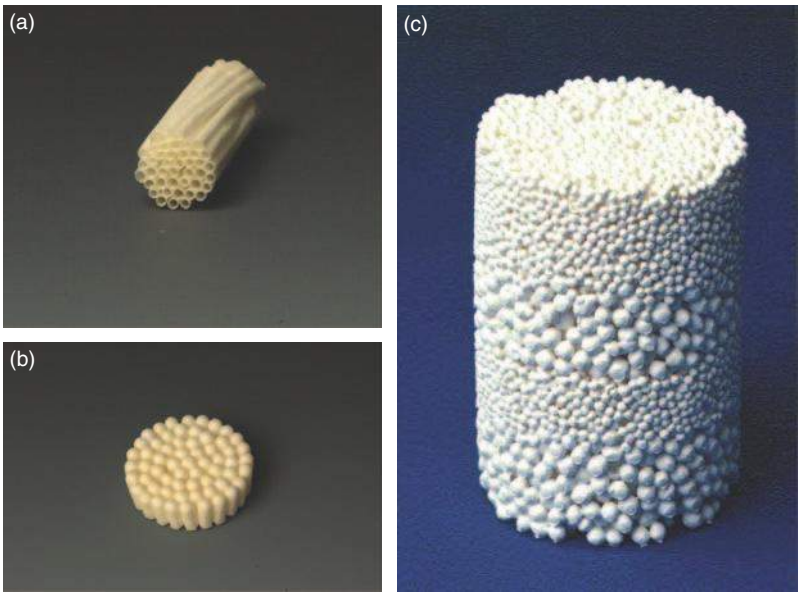

Figure 8 Some examples of ceramic foams processed by the hollow beads method. (a) Shows tubes, (b) elongated spheres, and (c) consecutive layers made from different spheres. Reproduced from Luyten, J., Mullens, S., Cooymans, J., De Wilde, A., Thijs, I. *Adv. Eng. Mater.* **2003**, *5*, 715–718.

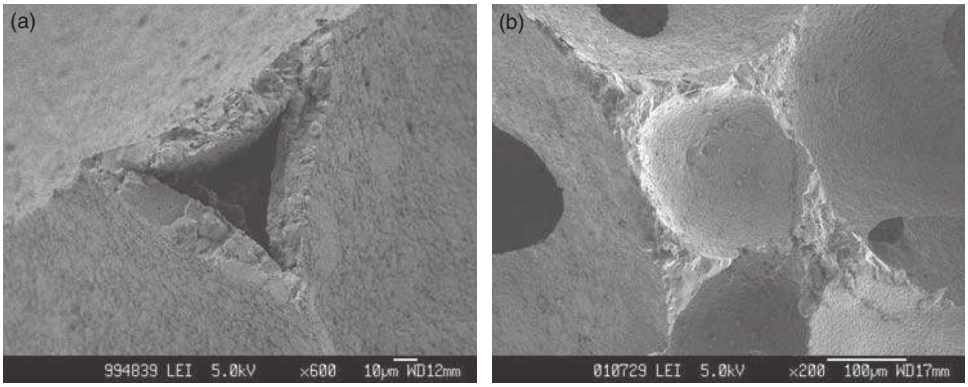

Figure 9 Picture comparing the hollow struts of a foam manufactured by the replica technique (a), and the dense struts of a foam produced by the gel-cast method (b). Reproduced with permission from Luyten, J., Cooymans, J., De Wilde, A., Thijs, I., *Key Eng. Mater.* **2002**, *206–213*, 1937–1940.

difficult to produce by the replica technique. The density ranges from 10% up to more than 50% of the theoretical density. These foams are mechanically stronger due to the dense struts, but are less flexible in the variation of the cell sizes. **Figure 9** shows the hollow struts of a foam manufactured by the replica technique and the dense ones of a foam produced by the gel-cast method [48].

1.11.4.7.3 Miscellaneous techniques

Another technique for the synthesis of ceramic foams uses the incorporation of pore formers or large grains [47]. This technique relies on the incorporation of sacrificial additives in the form of beads or related materials. Depending on the quantity added, the foams can be predominantly open or closed in nature. The structures produced by this method have limited pore-size distributions and porosity values. Another way to produce macroporous ceramic materials is to work with large grains, which are sintered together with a small fraction (5–10%) of fine, sinter-active powder. Again, there are limits for the porosity and pore sizes which can be obtained.

3D periodic porous structures as ceramic foams can also be manufactured by rapid prototyping methods that are currently developed, such as 3D printing, fused deposition, stereo lithography, robocasting, and laser sintering [48–51]. 3D fiber deposition (3DFD) is one of the very versatile rapid prototyping technologies that offers the ability to design and rapidly fabricate ceramic materials with complex 3D structures. The technique involves materials assembly through a layer-by-layer deposition of highly viscous ceramic pastes. The almost-unlimited freedom in design, the highly structural uniformity, the moldless manufacture, and the possibility to create graded functionality make this an emerging and promising topic in ceramic shaping technology.

1.11.4.8 Leaching Techniques

Besides ceramics and metals, glass is another material interesting for membranes. Two well-known glasses are Pyrex and Vycor, both containing SiO_2, B_2O_3, and Na_2O. In the ternary phase diagram of these three oxides, various miscibility gaps can be observed. When a homogeneous melt at high temperature (1300–1500 °C) is cooled down, phase separation occurs at certain compositions. One of these compositions, consisting of 70 wt.% SiO_2, 23 wt.% B_2O_3, and 7 wt.% Na_2O, is located in what is called the Vycor glass region. During cooling (at temperatures between 500 and 750 °C), demixing occurs into two phases: one phase consists mainly of SiO_2 and is not soluble in mineral acids; and the other phase is richer in B_2O_3 and can be leached out of the structure by a strong acid, resulting in a porous matrix with pores in the micrometer-to-nanometer range [52]. A careful control of the conditions used in the phase-separation process can reduce the pore size to approximately 0.5 nm [53, 54]. A disadvantage of these glass membranes is their poor mechanical stability and chemical resistance. The chemical instability is due to the very active silanol groups on the surface, which are very susceptible to reactions with different components that can be present in the feed solution, especially at high temperature.

This has been overcome partially by surface treatment (e.g., by means of chemical agents) of the internal pore structure which makes the surface hydrophobic. These easy modification possibilities of the glass membrane surface can also be used for other functionalization of the membrane (see Section 1.11.7). The advantage of glass membranes is that capillaries and hollow fibers can be easily formed. Hollow glass fiber technology is well established.

In a similar manner of heat treatment followed by leaching with a strong acid, base, or hydrogen peroxide, porous metal membranes can be synthesized.

1.11.4.9 Techniques for Making Straight Pores

To complete this section, two methods are described to produce membranes with straight pores: the track-etch technique and anodic oxidation. Membranes with nearly straight pores have been attractive to many researchers as a model system for fundamental transport studies. However, these membranes have remained merely a laboratory curiosity and have been of no commercial interest.

Pores with a very regular, linear shape can be produced by the track-etch method. Here, a thin layer of a material is bombarded with highly energetic particles from a radioactive source. The track left behind in the material is much more sensitive to an etchant in the direction of the track axis than perpendicular to it. Therefore, etching the material results in straight pores of uniform shape and size, with pore diameters ranging between 6 and 1200 nm. To avoid overlap of pores, only 2–5% of the surface can be occupied by the pores. This process has been applied on polymers and on some inorganic systems such as mica.

Pores with a linear form can also be produced by the so-called anodic oxidation process. Here, one side of a thin high-purity aluminum foil is anodically oxidized in an acid electrolyte. A regular pattern of pores is formed. The pore size is determined by the voltage used and by the type of acid. The process must be stopped before the foil is oxidized completely and also to avoid closure of pores. The unaffected part of the metal foil is subsequently etched away with a strong acid. The membranes so obtained consist of amorphous alumina and are not stable under long exposure to water, and are susceptible to acid and base attack. The stability can be improved by hydrothermal treatment in hot water or in a base, or by turning them into polycrystalline alumina by a careful calcination at temperatures above 850 °C. Alumina membranes with very narrow pore-size distributions in sheet and tubular form have been produced by this process. Pore diameters in the 10–250-nm range, pore densities between 10^{12} and $10^{15}\,m^{-2}$, and membrane thickness up to 100 μm have been obtained.

1.11.5 Temperature Treatment

1.11.5.1 Drying

Drying is, in most cases, an important first step in the temperature treatment of the green membrane shapes or the membrane layers. The drying temperature is mostly below 100 °C, and is often only room temperature. Since the organic additives used to shape the membranes have a much higher decomposition temperature, only water is eliminated during the drying stage. The first step corresponds to the elimination of interstitial water filling up the space between the particles. This leads to a first shrinkage of the green membrane. This shrinkage can be up to 10–20%, and is coupled to a weight loss of the same order of magnitude. The second step involves the removal of adsorbed water molecules (bonded via van der Waals forces). This happens without shrinkage but affects the pore structure. In the first step of the drying, when shrinkage occurs, the drying rate must be sufficiently low in order to avoid the formation of cracks and other defects, and enough time has to be reserved. Conversely, drying should be fast enough to prevent particles from settling out and, consequently, segregating in the green product. When the shrinkage is completed the drying rate can be increased without damaging the ceramic. In order to manufacture membranes reproducibly, the drying step should be carefully controlled.

In many cases, green membrane shapes are dried in normal air at room temperature.

1.11.5.2 Calcination

Calcining is, after drying of the wet membrane shape, the thermal treatment in which the organic constituents of the green product, such as binders, plasticizers, and dispersants, are combusted. The process is also called thermolysis. Calcining is mostly performed in air to make complete combustion of the organics possible, and to minimize the presence of residual carbon in the final product. In such cases,

complete combustion of organics is supported by calcining in pure oxygen.

Combustion of the organic additives typically takes place in the lower-temperature region situated between room temperature and 600 °C. In this region, commonly used binders are completely burned. In order to define the appropriate calcinations temperatures, investigation using thermogravimetric analysis (TGA) or differential thermal analysis (DTA) in a thermobalance, in most cases, combined with differential scanning calorimetry (DSC), delivers valuable information. Required calcination temperature and consequent weight loss of the sample can be deduced from these measurements.

Thermal analysis studies have shown that during the lower temperatures of the calcinations the remaining part of moisture, which was not removed during the drying step, will be removed. This remaining water includes water chemically bonded on the particle surface, and/or crystallization water in the formed inorganic phases. This highly bonded water may persist in the membrane up to a temperature exceeding 200 °C.

Calcination must be done sufficiently slowly, and with low heating rates, in order to remove the remaining moisture and the gases from the decomposition of the organic additives, without crack formation and damaging of the final product. In addition, this is the more important factor; the finer the inorganic particles, the higher the organic content in the green membrane shape. In the first case, this is due to the lower permeation rate for the formed gases out of the shape. In the second case, this is due to the higher amount of gases formed during calcination.

In the case of silicon or aluminum nitride and carbide ceramics, calcination is done in an inert atmosphere such as nitrogen. Due to the absence of oxygen, some residual carbon can be expected. This residual carbon usually removes the oxygen adsorbed on the surfaces of the inorganic particles and serves as a sintering aid in carbide and nitride ceramics.

Calcination is mostly carried out in a separate calcination furnace. Only if the amount of organics to be burned off is small, calcination is done as the first part of the temperature profile of a combined calcining–sintering treatment.

1.11.5.3 Sintering

Typical processing of inorganics includes a step during which the green shape can develop a stable microstructure and sufficient mechanical strength. This step involves heating at high temperatures and is characterized by firing or sintering. Sintering processes have been studied for longtime in order to understand the important changes that occur in the material during the process. These changes are due to the serious mass transport that is caused by the high-temperature treatment. This mass transport first leads to neck formation between neighboring particles. In the later steps of the sintering, grain growth occurs followed by real densification. The mass-transport phenomena that contribute are solid-state diffusion (i.e., surface, grain boundary, and bulk diffusion), viscous flow, plastic flow, and evaporation coupled to recondensation. In all cases, the driving force for these sintering phenomena is a decrease of the surface energy (Gibbs free energy) of the system with mass transport moving from areas with relatively high energy, that is, large convex curvature, to areas with relatively small energy, that is, small concave curvature.

In the first step of the sintering process (also called presintering), at relatively low temperatures, the surface of the particles in the calcined particle compact smoothens, grain boundaries are formed, and necks grow between the particles. This is mainly due to surface and grain boundary diffusion. In this process, a strong interconnected porous microstructure forms with enhanced mechanical stability.

At sufficiently high temperatures, grain growth will occur. In the grain-growth process, the larger grains will grow at the expense of the smaller grains: the smaller grains will be consumed by the bigger ones. This results in an increasing mean pore size, but a decreasing porosity since particle centers will approach each other. The temperatures required for grain growth are below, but close to the melting point of the metals or ceramics used (0.5–0.9 × the melting temperature). Consequently, they vary with the materials involved. However, the required temperatures also depend on the inorganic particle size. The smaller the particle size, the higher the driving forces for mass transport, and, therefore, the higher the sinter activity and sintering rate. The same effects are then visible at lower temperatures. This is the case when sintering fine-porous top layers. As a result, it is also possible to make dense top layers while leaving the supports sufficiently open-porous, even if they consist of the same inorganic material.

When the sintering is done at sufficiently high temperature and for sufficiently long duration, the grain growth continues, up to complete densification of the inorganic material. Only a small amount of closed porosity remains, of the order of a few percent. Dense ceramic membranes or dense membrane layers are thus produced.

It is clear from the above description that sintering determines the final pore structure of the membrane, and the sintering process is definitely important to make good, dense membranes. However, in commercially interesting porous membranes, where a high flux and, therefore, a high porosity are also important, serious grain growth and the related clear porosity decrease are avoided. In these porous membranes, the pores are mainly determined by the particle size of the inorganic powders used, or by the size of the inorganic structures used in the fine-porous layer deposition, and less by the sintering process.

Finally, the membrane system must be cooled down from the sintering temperature to room temperature. In the case of sintering of a multilayer system, this can result in stresses due to eventual mismatch of the thermal expansion coefficients between the layer(s) and the support. This enhances the risk of cracking or even delamination of the layer.

1.11.5.4 Thermal Stability of Membranes

Thermal treatment is the final step during the preparation of inorganic membranes. This affects the thermal stability of the final membranes. As mentioned above, calcination and sintering lead to a specific grain size and related pore size of the final membrane. When the material is kept long enough at the last thermal treatment temperature, it can be assumed that the material approaches an equilibrium structure. Therefore, the structure of the membrane will not vary when it is exposed to temperatures of 100–150 °C below its calcination/sintering temperature, since the reaction rates and driving forces for the sintering process will be too low at this point. However, when the material is heated to higher temperatures, it acts similar to any other inorganic material, indicating that sintering and grain-growth processes start afresh, leading to a new equilibrium. Therefore, in order to prevent the membrane from changing its pore structure during application, sintering has to be avoided or suppressed.

The thermal treatment process not only affects the pore size of the final membranes but also determines the final phase composition of the inorganic material. Indeed, for some materials, phase transitions occur during the heating up to the sintering temperature. These phase transformations are accompanied by an increase of the sintering activity, causing an extra-enhanced pore growth. For the thermal stability of an inorganic membrane, it is therefore very important that the material is in a thermodynamically stable phase and does not show any phase transformations below its working temperature. Here, it is important to state that phase transition temperatures depend on the exact preparation procedures of the inorganic powders or structures (in case of top-layer material) used. For granular material with sufficient grain size, the temperatures of the phase transitions are fixed. However, for fine-granular powders with grain sizes on the nanometer scale, transition temperatures generally decrease [55].

The thermal stability of the membrane and how to enhance this by specific doping of the inorganic membrane materials (e.g., La in γ-alumina or titania) are well described in Reference 56.

1.11.5.5 Thermal Treatment of Layers

The intermediate layers and top layers on top of the support also require a similar cycle of thermal treatments. In order to obtain the final microstructure, drying, calcination, and sintering are done. The same phenomena occur as for the thermal treatment of the support, as described in the previous subsections. However, in some cases, specific comments related to the thermal treatment of layers are important. They are compiled in this section.

After their formation, layers are first dried. This process should be controlled even more carefully than in the case of bulk green shapes. During the drying process, water is removed form the wet layer. The presence of the coarse-porous support or the porous asymmetric composition below the layer causes capillary forces. As a consequence, stresses occur due to shrinkage along the depth of the layer, which have to be released in some way. If a critical stress is exceeded, cracks are formed in the supported membranes. This occurs at a critical thickness. The exact value of the critical thickness depends on the support, the forming conditions of the layer, and on the morphology of the inorganic particles used. While shrinkage and, therefore, stresses are higher

for layers with smaller pore size, the critical thicknesses for these layers are relatively low; for instance, the critical thickness for sol–gel layers (Section 1.11.6.3) is typically on the order of 1–10 μm. Experiments have shown that the production of relatively thick defect-free membranes is easier for plate-shaped particles than for spheres, that is, their critical thickness is higher [57]. This explains the wide use of sol–gel γ-alumina intermediate layers (although its chemical stability is low), instead of sol–gel titania or zirconia intermediate layers, especially in the case of fine-porous or dense membranes.

The support has an important effect on the sintering process of a layer. It acts as a constraint and decreases the diffusion rate of the membrane-layer material and, therefore, retards the sintering process. As such, the support has a negative effect on the densification rate of the layer. This is consistent with the lower pore size of supported membrane layers compared to unsupported membrane layers (flakes made in the same manner as the membrane layer) [58]. For thick layers, the sintering stresses are relatively high (as the drying stresses), inducing tensile stresses in the film, which can result in cracks and even delamination of the layer from the support. When the membrane layers are thin enough, these tensile stresses lead to a decrease in the sintering rate.

Consideration should also be given to the calcination or sintering temperature when the layer material differs from the support material: the sintering temperature of the support should be higher than that of the layer. Moreover, it is essential that the thermal expansion coefficients of the layer and the support materials are closely matched in order to avoid delamination and cracking of the multilayer system during the fabrication, as well as during the application.

The support not only retards the sintering but can also increase the temperature of the phase transitions [58]. As the support clearly reduces the rate of sintering, and increases the temperature of the eventual phase transitions of the membrane material, it definitely increases the thermal stability for sufficiently thin layers.

1.11.6 Layer Deposition

1.11.6.1 The Multilayer Architecture

To make both porous and dense membranes suitable for real applications, all commercial and commercially interesting membranes always consist of an asymmetric multilayer configuration. A picture of such a multilayer membrane structure can be seen in **Figure 1**. The multilayer composition provides a convenient way to combine a high flux and high selectivity in the final membrane.

In the multilayer structure, a good support shows a high pore size and porosity, and, at the same time, can provide the necessary mechanical strength. The high porosity causes a negligible fluid resistance over the membrane support. Pore sizes of currently commercially used membrane supports are on the order of a few micrometers. In the early steps of membrane development, flat laboratory-made supports, generally prepared by slip-casting, are used. These supports have pores on the order of 50–100 nm. These supports have a much higher fluid resistance, but show a much lower surface roughness and a smaller amount of defects. Commonly used materials for the support are porous stainless steel, carbon, or ceramics.

The porous or dense top layers in the multilayer structure are responsible for the separation. They contain the desired pore size for the necessary separation and are of high quality (e.g., a minimum amount of defects and preferably none) in order to provide the desired selectivity. Good top layers are also sufficiently thin to provide a permeability that is as high as possible. The main challenge for high-quality top layers is to avoid defects in the layer. Indeed, these defects will decrease the final selectivity. It is obvious that this requirement is more stringent for microporous and dense membranes, than for more open-porous membranes.

One or more intermediate layers between the support and the top layer(s) take into account a gradual decrease of the pore size in the multilayer composition. Multiple interlayers are normally used, especially when a pore-size difference of micrometer to nanometer (or even no open pores) has to be bridged. The intermediate layers are also useful in a gradual reduction of the surface roughness of the membrane. Inevitable large surface irregularities and defects in the supports can be properly covered by the successive intermediate layers. Intermediate layers should be as thin as possible to maximize the flux of the final membrane, but, at the same time, sufficiently thick to smoothen the membrane surface enough for defect-free top-layer coating. The thickness of each layer is typically about 100–1000 times the pore diameter of the layer. The porosity of the intermediate layer is in many cases also designed so as to prevent any appreciable penetration of the finer particles or structures of the following intermediate

or top layer into the pores of the underlying support layer. In this manner, the fluid flux through the membrane will be maximal. It has recently been shown that making an intermediate layer by coating several identical thin layers on top of each other, instead of coating one thick intermediate layer, gives a significant improvement in the defect quality of the intermediate layer, and thus of the total membrane system [59].

Good supports are produced by the wet synthesis methods described in Section 1.11.4, followed by appropriate thermal treatments as described in Section 1.11.5. The intermediate layers and the fine-porous or dense top layers coated on the porous supports are produced using other specific techniques. These will be explained in this section. Layers with macropores or big mesopores can be produced from (colloidal) powder suspensions. Layers with meso- and micropores are produced by sol–gel techniques or CVD. Particular techniques exist for microporous carbon and zeolite layers. The dense or fine-porous membrane layers also require a temperature treatment similar to that of the coarse-porous supports, to consolidate their microstructure.

1.11.6.2 Powder Suspension Layers

1.11.6.2.1 Introduction

As mentioned in Section 1.11.4.2, the formation of a dense or porous layer on a support can be obtained by simply pressing a sufficiently fine powder on top of a precompacted green support, and cosintering the composition. However, the formation of layers from suspensions containing appropriate powders allows more freedom, since a variety of techniques become possible for layer formation. Moreover, powder suspension layers are more appropriate for large-scale production.

The use of powder suspensions is most appropriate for the first porous inorganic layers on a porous support. This technique is suitable to obtain (intermediate or top) layers with pore sizes of a few tens of micrometers. The wet suspension layer on the support will be further dried and treated thermally in order to consolidate its microstructure. The porosity of the formed layer depends primarily on the shape and particle size of the powder particles in the suspension. The pore size in the final layer is typically one-third of the particle size, and is therefore limited to a minimum of about 100 nm.

Powder suspensions generally contain more than one polymeric compound used as surfactant, binder, and plasticizer, as is the case in slips or pastes used for shaping of the support (see Section 1.11.4). The interaction between all these components determines the suspension behavior and the microstructural development during coating, drying, and heat treatment. Sufficient mixing, deaeration, and deagglomeration (e.g., chemically or by ultrasonification) of the suspension are important for the formation of high-quality layers (the same aspects that are also important for good slip or paste preparation in the shaping process, see Section 1.11.4).

1.11.6.2.2 Dip and spin coating

Different methods are available for applying the layer from the suspension onto the support. The most-applied methods are dip or spin coating. In both cases, some mechanical means (such as pumping and/or spinning) are provided to bring the suspension in direct contact with the support in a uniform manner. For example, the inner cavity of a porous support tube is filled with the suspension by dipping or pumping for a few seconds to a few minutes before being emptied. In spin coating, the suspension is spread over the support by a rotating head moving with a specific rotational speed. Rotation speeds up to about 1500 rotations per minute are commonly used. Centrifugal forces determine the distribution of the suspension over the support. Dip and spin coating can be applied to a broad range of materials, and are extensively used not only for metal oxides, but also for silicon carbide, silicon nitride, and glass compositions.

Dip coating is the dipping and subsequent withdrawal of the support from the powder suspension. When a porous support is withdrawn from a powder suspension, capillary forces cause the infiltration of the suspension liquid into the support pores. This drives the powder particles to the interface. If the support is not permeable for the particle, that is, if the particles are sufficiently large compared to the support pores, the particles concentrate at the surface and a compact layer is formed. However, in addition, drag forces exerted by the support during withdrawal from the suspension can be important. The relative importance of both capillary forces and drag forces depends on the contact time, the withdrawal speed, and the particle loading in the suspension. It determines the thickness of the formed layer (typically 20–100 μm). Moreover, the rheological properties of the powder suspension, determined by interactions of all particles in the suspension (e.g., van der Waals, electrostatic, and polymer–particle interactions),

play an important role in the dip-coating process. This is particularly true when the size of the particles involved is on the order of 1 μm or less. Powder suspensions are also called colloidal suspensions or sols, and colloid science comes into play. Stable suspensions give rise to more homogeneous and more densely packed layers. Although it has been studied extensively, the whole dip-coating process is not yet fully understood.

Normal dip coating is done with an empty membrane to provide for the necessary capillary forces, in which case, the capillary forces are dominant in the layer-formation process. However, in some cases, the capillary forces are reduced by filling the pores of the support with a liquid, with a small difference in surface tension compared to that of the used powder suspension. In other cases, the pores of the support are even rendered completely nonwettable for the suspension liquid. This can be obtained by forming a hydrophobic pore-wall surface on the support in the case of an aqueous coating suspension. The support surface is treated with, for example, organic silanes (see also Section 1.11.7). In this case, layer formation is dominated by the drag forces of the support in the withdrawal process, and layers can be made from suspensions with particles smaller than the pores of the support. The disadvantage of a decreased capillary action in the formation of a layer is the diminished adherence of the support and the layer.

1.11.6.2.3 Alternative coating methods

As an alternative for the dip-coating method, the first porous layers on an inorganic support can also be formed by filtration of the powder suspension, using the support as a filter. This can be done using an external pressure on top of the layer. Alternatively, a rough vacuum underneath the support can be used. This is called vacuum suspension (or alternatively slip or slurry) coating (or alternatively casting) [22].

Next to dip and spin coating and filtration of the suspension over the support, some other less-popular methods can be used to make the first layers on the support. A low-viscosity suspension can also be sprayed on a support through a nozzle from a pressurized container. Controlled movement of the spray gun enables the formation of a homogeneous powder layer. This is called spray coating or wet-powder spraying. Suspended particles with positive or negative charged surfaces can be deposited by electrophoretic deposition on either the anode or cathode by application of an electric field between the two electrodes. Electrically conducting materials are required for this method. Yet, powder particles can also be deposited on an electrical insulating material by positioning the insulator in between the electrically conducting electrodes. Screen-printing techniques require that the particles be dispersed in a highly viscous paste with a viscosity that is typically situated between 50 and 2000 Pa s. A paste is transferred to a screen and spread out by a metal blade or rubber squeegee. Screen printing is used abundantly in the preparation of the porous anode and cathode layers in the fuel cell technology [22].

1.11.6.3 Sol–Gel Layers

1.11.6.3.1 Colloidal and polymeric sols

In order to produce membrane layers with pore sizes smaller than 100 nm, suspension techniques are inappropriate and other methods need to be used. One of the most important methods used today in ceramic membrane preparation is the sol–gel process. One of the most used references in this respect is the book *Sol–Gel Science – The Physics and Chemistry of Sol–Gel Processing* [60]. Basically, sol–gel is a general process which converts a colloidal or polymeric solution called sol to a gelatinous substance called gel. It involves the hydrolysis and condensation of alkoxide or salt precursors in an organic solvent with an appropriate amount of water. Fine-porous membrane layers have been prepared by the sol–gel process with a variety of metal oxides and composite oxides. There are two main routes in the sol–gel preparation of membrane layers: the colloidal route and the polymeric route (see **Figure 10**).

In the colloidal sol–gel route, the alkoxide precursors are hydrolyzed and condensed (or peptized) in an excess of water. The water causes a fast hydrolysis and condensation. The rapid condensation causes the formation of medium-sized nanoparticles of the order of 20–100 nm in solution, that is, the colloidal sol. Reproducible and stable colloidal or particulate sols can be obtained by the precise control of the hydrolysis and condensation reaction conditions and/or by adding acids or bases as hydrolysis catalysts and/or as stabilizers. In order to form high-quality membrane layers, the colloidal sol is commonly mixed with typical binder materials such as polyvinyl alcohol or hydroxypropyl cellulose. The sol is subsequently dip- or spin-coated (see Section 1.11.6.2.2) on the already-formed multilayer structure with top layer pores in the order of the sol particles. It is the porosity of the support that leads to the removal of the sol solvent and to the gelling of the sol, similar to the forming of

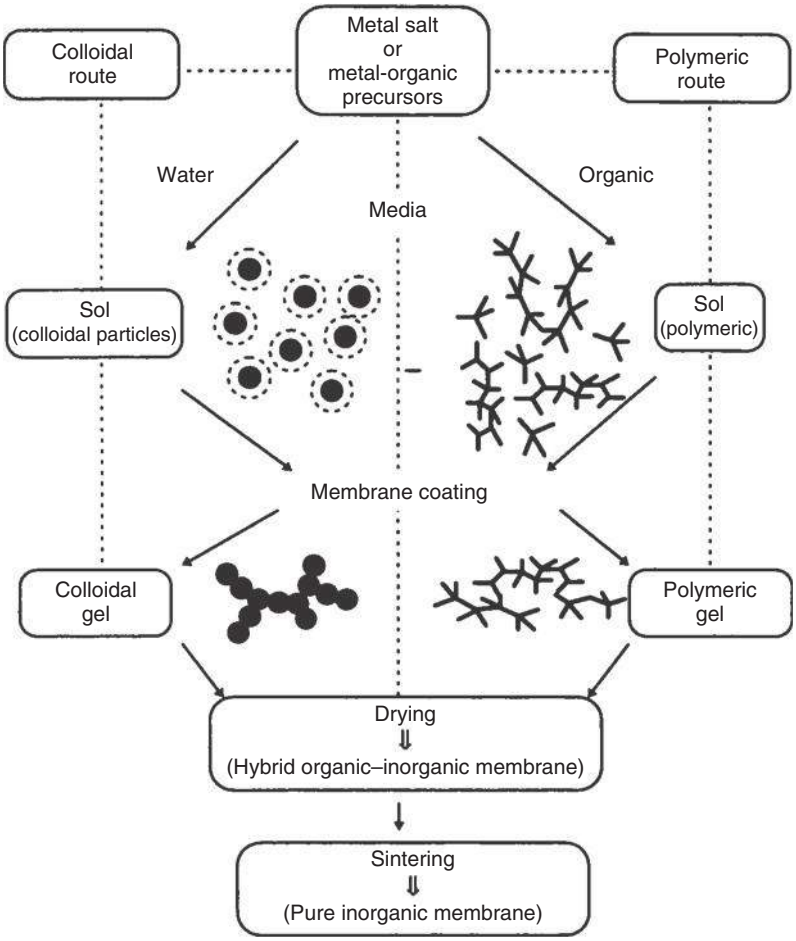

Figure 10 Schematic representation showing the two main sol–gel routes used in the preparation of fine-porous membrane layers. Reproduced with permission from figure 7.1 of Burggraaf, A. J., Cot, L., Eds. *Fundamentals of Inorganic Membrane Science and Technology*; Membrane Sciences and Technology Series 4; Elsevier: Amsterdam, 1996.

the powder suspension layers discussed in Section 1.11.6.2. All aspects of the previously mentioned dip-coating process are also relevant for sol–gel layers. The gel layer is then carefully dried and calcined at an appropriate temperature. The pore size of the formed layers depends on the details of the hydrolyzing/condensation process and of the calcination temperature. Pore sizes can be varied between a few nanometers up to about 50 nm.

The fine pores of microporous membrane layers can be obtained by the polymeric sol–gel route. A polymeric sol is produced starting from the common alkoxide precursors also used in the colloidal sol–gel route. However, in the polymeric route, the hydrolysis reaction is kept slower, and the precursors are now only partially hydrolyzed by using only less than the stoichiometric amount of water mixed in an organic solvent. This leads to a precipitate-free sol containing small nanometer-sized inorganic polymeric structures (fractals). Either weakly or highly branched inorganic structures can be obtained as a result of the conditions of hydrolysis and condensation (precursor concentration, and acid or, respectively, basic catalysis). The low branched structures can interpenetrate better during gel drying and lead to a more compacted layer with smaller pore size. For good microporous layers, the average fractal sizes need to be in the order of 5 nm. Due to these small structures, a good polymeric sol is transparent, in contrast to a colloidal sol. The polymeric sols are then used for dip or spin coating the support and interlayer system, in this case, without any addition of binder. Binders are not used since these compounds create very large voids in the coated layer after thermal treatment.

1.11.6.3.2 Drying and heat treatments

The gel layer formed during the spin or dip coating is subsequently carefully dried and heat treated. In order to avoid crack formation in this process, the layers need to be sufficiently thin, that is, below the critical thickness (see Section 1.11.5.5). In addition, the heat-treatment temperature is important. For microporous membranes, the heat-treatment temperature needs to be low enough, in order to avoid pore growth. Pore sizes between 0.5 and 2 nm are feasible. The heat-treatment temperature determines not only the final pore size of the top layer, but also the structural phase of the top layer material. For example, for temperatures as low as 200 °C, titania is in an amorphous state with very small pores in the order of 1 nm, whereas from 300 °C onward titania is in an anatase phase having somewhat larger pores in the order of 2.5 nm [61]. This has also a great influence on the chemical stability of the top layer: an amorphous phase is more easily attacked by corrosive liquids, and shows a lower acid and base stability than the crystalline phase [56].

The humidity control during coating and drying of sol–gel layers is also important and is essential for the quality of formed microporous layers. This is because it influences the hydrolysis and condensation of the gel network. For example, at a humidity higher than 50%, the hydrolysis in a polymeric titania gel is faster than the condensation, resulting in the formation of titania particles and finally, mesoporous interparticle pores [62]. To enhance the quality of final microporous membrane layers further, the dip- or spin-coating process is also often performed in a clean room [2, 63, 67].

1.11.6.3.3 Silica and other metal oxides

Since sols of very small particles or structures are prepared through hydrolysis and condensation of their corresponding alkoxides, the partial charges of the metal in the alkoxides influence the hydrolysis behavior. Transition metals such as Ti or Zr in the alkoxides carry much higher partial charges than Si in, for example, tetraethylorthosilicate (commonly called TEOS). Therefore, transition metal alkoxides hydrolyze much faster than Si alkoxides. In addition, the properties of the type of R ligands in the alkoxide, the degree of oligomerization of the starting alkoxide, the possibility of a coordination expansion of the metal during the hydrolysis, and the pH of the solution all influence the hydrolysis behavior.

In order to better control the hydrolysis, especially in the polymeric sol–gel route for nonsilica materials, chelating agents have been used to block the functional groups of the alkoxide. Typically used chelating agents are acetylacetone, alcohol amines, or carboxylic acids [64–67].

Mixed-oxide layers can also be prepared by the sol–gel process. The mixed-oxide sols are made by mixing of the individual sols, or by cohydrolysis and cocondensation of the respective alkoxide precursor mixtures.

The formation of microporous top layers of metal oxides or mixed metal oxides by the polymeric sol–gel route has made serious progress in the past decade. Previously, only high-quality microporous layers from amorphous silica were reported, mainly due to the relatively easy sol–gel process of this material [68–72]. Some of these silica membranes have been introduced in the market about a decade ago. A significant drawback of silica is, however, its limited hydrothermal stability, and its limited stability in alkaline pH's. In order to improve the stability, silica membranes with zirconia [73–76] or titania [77] added as a second component have been developed. Recently, however, also high-quality titania microporous membranes for nanofiltration have been prepared [2, 66, 78] and some have become commercially available [2]. The same quality of membranes has also been achieved on capillaries [20]. Recent efforts have been concentrated on zirconia or mixed zirconia/titania membranes [67, 79]. Microporous zirconia membranes are, however, not yet commercially available. Energy Research Centre of the Netherlands (ECN) has adapted another strategy to enhance the hydrothermal stability of silica: recently, they developed a new hybrid organic–inorganic membrane replacing the Si–O–Si bonds by the more stable Si–CH_2–CH_2–Si links [80].

Applications envisaged for all microporous materials are nanofiltration, pervaporation, and, eventually, gas separation also.

1.11.6.4 Template-Mediated Layers

1.11.6.4.1 Introduction

A more recent approach to prepare tailor-made porous ceramic layers is based on the incorporation of organic template agents in gel structures. These template agents can be organic groups chemically linked to the inorganic gel network (also called surfactants or amphiphilic molecules), or isolated molecules or clusters trapped in the inorganic gel matrix. The role of the organic template is to generate a uniform residual porosity after they are burned out by the

heat treatments: pores with a size based on the size of the organic template molecule are created. This porosity and pore size can be tailored by the nature and the size of the templates. Often, the pore structure of the template-mediated layers, as that of the related powder material, consists of two types of pores: the pores formed by the self-assembled templates (variable from micro- to macroporous) and the pores formed by the inorganic gel interacting with the template (usually microporous). The template method has, however, a limited ability to control the template pore alignment to the substrate surface.

1.11.6.4.2 Sharp pore-size distribution

The simplest way for forming a templated layer is based on the insertion in the gel matrix of passive template agents such as chemically fixed organic or inorganic entities or physically trapped polymer particles. In this case, the elimination of the templates leads to the formation of a porous structure in which the pore size and the dimension of the incorporated template is directly related, as shown in **Figure 11** [81, 82]. This method can be used for colloidal as well as for polymeric sols, and can lead to macro-, meso-, as well as microporosity. The resulting pore-size distribution is very sharp.

Another way obtaining narrow pore-size distributions in the micropore range makes use of the effect of nonionic surfactants. This has most extensively been studied for silica sols [83, 84]. Nonionic surfactants are susceptible to interacting with silica oligomers derived from TEOS by van der Waals forces or by interaction with OH groups. Due to these interactions, in the absence of polar solvents such as water, an organic shell made of surfactant molecules is formed around the inorganic structures (reversed micelle method). The resulting steric hindrance limits further condensation of the inorganic structures in the sol. After heat treatment, including the elimination of the surfactant shells, a homogeneous microporous membrane layer consisting of nanometric distinct silica particles is formed. The membrane with such a top layer shows strictly microporosity and gas-separation characteristics. The pore size can be varied by using surfactants with longer chain lengths, although the pore-size distribution then becomes wider.

1.11.6.4.3 Ordered porosity

Another efficient way of obtaining monodispersity of the pore-size distribution and control of the pore size is to develop materials with an ordered or textured

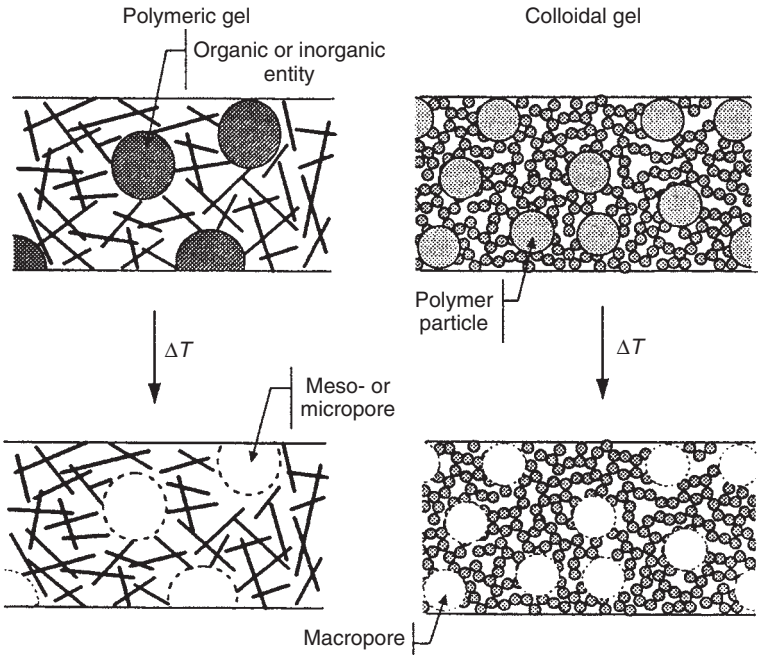

Figure 11 Schematic representation of the formation of a membrane layer using passive organic templates in a polymeric gel (left) and in a colloidal gel (right). Reproduced with permission from figure 7.13 of Burggraaf, A. J., Cot, L., Eds. *Fundamentals of Inorganic Membrane Science and Technology*; Membrane Sciences and Technology Series 4; Elsevier: Amsterdam, 1996.

porosity. This can be done by using mesoscopic templates such as lyotropic liquid-crystal mesophases as structure-directing agents. These ordered mesophases result from the self-assembly of surfactants or amphiphilic molecules. A successful process requires that both liquid crystal and inorganic network can form simultaneously in the sol and that the liquid-crystal mesophase must be carefully eliminated without the collapse of the solid part of the gel. The main lyotropic liquid-crystal mesophases are lamellar (surfactant bilayers separated by aqueous layers), hexagonal (hexagonal arrangement of cylindrical micelles), and cubic structures. **Figure 12** shows the example of a hexagonal packing of micellar cylinders surrounded by the inorganic polymers growing in the liquid phase near the surfactant head groups. The sols are initially very fluid and easy to deposit: the chemical composition of the sols corresponds to an isotropic region in the water-surfactant binary diagram. The ordered mesostructure develops only during the gelation process, and is induced by the formation of inorganic oligomers near the polar head of the surfactants [85]. After a careful thermal or chemical treatment to remove the surfactant, a stable ordered mesoporous texture can be formed.

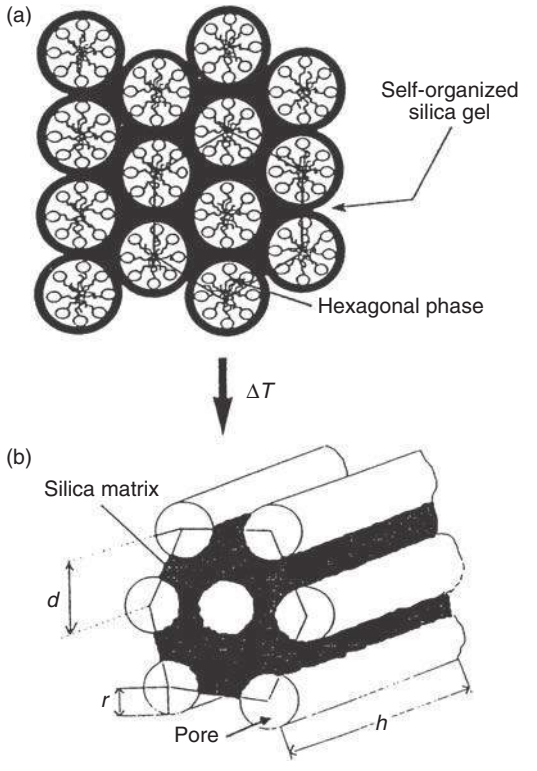

Figure 12 Schematic representation of the formation of a membrane layer using a hexagonal liquid-crystal phase as template. (a) The situation in the wet gel. (b) The pore formation in the heat-treated gel. Reproduced with permission from figure 7.11 of Burggraaf, A. J., Cot, L., Eds. *Fundamentals of Inorganic Membrane Science and Technology*; Membrane Sciences and Technology Series 4; Elsevier: Amsterdam, 1996.

Pioneering work on this subject was done on aluminosilicates using cationic surfactants as alkyltrimethylammonium halides in hydrothermal synthesis. Depending on the catalysts (base and, respectively, acid) and templates used, ordered mesoporous materials of the mobil catalytic material (MCM) or santa barbara acids (SBA) type can be formed [86, 87]. Recently, membrane layers of the MCM-48 type have been synthesized in a similar manner [88]. The layers clearly show that the mesoporosity of the mesophase and the separation characteristics are due to the ordered mesopores.

The group at the University of Montpellier, France, has done much work on mesophase templated silica. Cationic surfactants with relatively low hydrocarbon chains have been used to make hexagonal ordered structures [89, 90]. The specific surface area, pore volume, and porosity of the formed structures are very large and essentially microporous. The pore size depends on the length of the alkyl chain of the used templates (and is approximately half of the chain length). Supported membrane layers have been formed in this manner [91]. It has also been shown that the deposited layers are formed of submicron-size ordered domains [92].

The same group has also successfully synthesized 2D and 3D hexagonal mesoporous silica membrane layers using longer alkyltrimethylammonium bromide surfactants [93]. In the 2D mesoporous membrane layers, gas-separation measurements revealed that the mesopores are oriented parallel to the membrane surface, and that the different mesopores are only connected through the micropores in the inorganic walls. Seeding with amorphous silica nanoparticles promoted a more heterogeneous nucleation of the templating mesophase, giving rise to a more random orientation of the mesopore domains, with some domains nonparallel to the membrane surface. This leads to an increased assistance of the mesopores in the gas permeability, raising the permeability by about a factor 10. As a consequence, the separative properties of the membrane layers are determined only by the microporosity in the unseeded synthesis, and both by the templated mesoporosity and by the microporosity in the seeded synthesis.

Defect-free ordered mesostructured silica membrane layers were also formed using nonionic block copolymers as surfactants [94]. The formed membranes show Knudsen gas permeability due to the ordered mesopore structure. Block copolymers have also been used to produce mesostructured titania membrane layers [95–97]. The mesostructures are of 2D hexagonal and cubic types, and are clearly evidenced from transmission electron microscopy, as shown in **Figure 13**. The cutoff curves of these membranes show transport pores of about 1.5 nm, defined by the microporosity in the titania walls between the templated mesopores.

1.11.6.5 Chemical Vapor Deposition

CVD is a gas-phase layer deposition technique. In this process, a mixture of a carrier gas with reactive gases is brought into contact with the support in a reaction chamber at high temperature in order to form the desired membrane layer on the support by thermal decomposition, oxidation, hydrolysis, or reduction. For metal-oxide layers, one reactant is the metal source (e.g., organometallic compounds such as chlorosilanes) and the other is the oxidizing or reducing agent (e.g., oxygen, air, or hydrogen, carbon monoxide). The reactants are introduced in the reaction chamber on the same side of the support, or, more novel, on opposite sides (chemical vapor infiltration). The last technique has the advantage that the deposition location can be varied from the surface to the inside of the substrate. Once a pore is plugged, the vapor deposition process stops in that pore. If, however, the deposited material is oxygen permeable, such as yttria-stabilized zirconia, another type of deposition, electrochemical vapor deposition, starts: the oxygen source permeates through the pore plug and reacts with the organometallic vapor to continue deposition. In this manner, high-quality solid oxide electrolyte layers can be formed on a porous support. Deposition with both reactants introduced at the same side of the support, however, yields thinner and more permeable dense membranes, even though deposition always starts by partially plugging the pores with the deposit, before the deposition grows into an integral layer covering the surface of the support.

The CVD technique has the advantage of eliminating the need for drying and calcination required in the liquid-phase methods. In addition, the membranes produced in this manner are usually denser than those prepared by liquid-phase processes. The process offers the promise of being able to fine-tune the composition, growth, and uniformity of the deposited layers. Variations of the CVD process have yielded membranes with different morphologies.

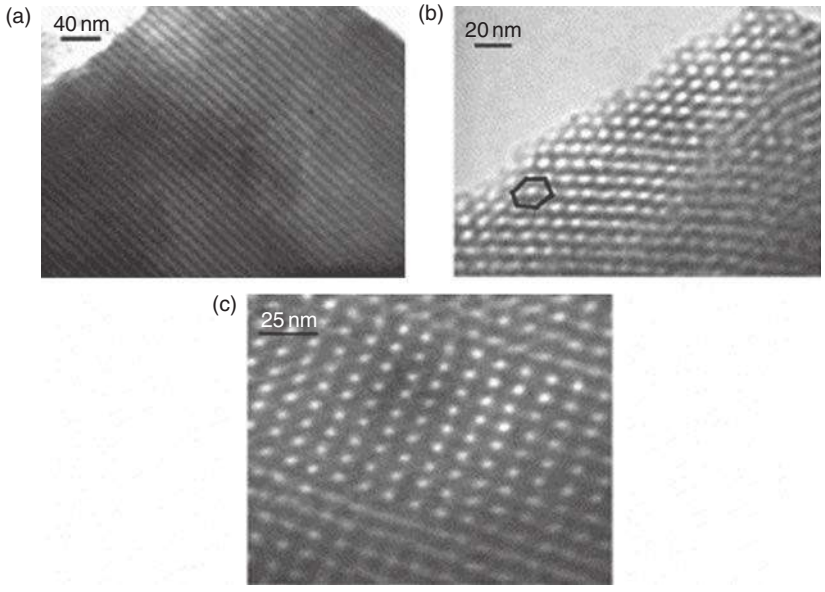

Figure 13 Transmission electron microscopy (TEM) images of mesostructured titania layers formed by using block copolymer templates. (a) The cylindrical pores of a two-dimensional (2D) hexagonally ordered pore structure along the axis of the pores. (b) The cross section of the same pore structure. (c) A cubic network of spherical pores. Reproduced with permission from Bosc, F., Ayral, A., Guizard, C. *J. Membr. Sci.* **2005**, *265*, 13–19.

With this technique, high-quality dense and microporous amorphous silica layers have been produced on different support types (e.g., Vycor glass and porous alumina with γ-alumina intermediate layer). The formed membranes show very high permselectivities combined with high permeabilities in gas separation, and are therefore interesting, for example, for H_2 separation. The method has also been used to narrow the pores of a microporous sol–gel silica membrane.

The CVD technique can also be used to form complex mixed metal-oxide membranes by using a mixture of their organometallic compounds as reaction gas.

1.11.6.6 Carbon Layers

The oldest microporous membranes were carbon membranes. The first carbon membranes in the 1960s were prepared by compressing high-surface-area microporous carbon powders at very high pressures. Nowadays, carbon membranes are made by pyrolysis of a polymer precursor. Typical precursors are thermosetting polymers as polyimide, polyvinylidene chloride, cellulose, polyacrylonitrile, and phenolic resin. The pyrolysis takes place in the absence of oxygen at high temperature typically in the range from 500 to 800 °C. The process is not only used to make the carbon layers, but also to make carbon supports. Depending on the degree of pyrolysis, the membrane material can be weakly hydrophilic (low temperature) or more hydrophobic (high temperature). The hydrophobic carbon is weaker and more brittle.

On top of the support, polymeric films are deposited (e.g., by dipping or spinning) using a solution of a common polymer precursor in an organic solution, followed by *in situ* polymerization and subsequent controlled pyrolysis to the desired pore shape. The membranes formed in this manner (sometimes multiple layer deposition is necessary) show clear molecular sieve properties. Depending on the polymer precursor, type and degree of pyrolysis, membrane surface properties (hydrophilicity or phobicity), pore size, and morphology can be adjusted. The same methods can also be used to make carbon layers on a metal-oxide support or a stainless steel support.

The pyrolysis process is also equipped to produce carbon hollow fibers by simply starting from the appropriate polymer hollow fiber membranes.

In the past decade, increasing interest has been shown in phenolic resins as polymer precursors. This reflects not only their ease of use and high carbon yield but also the well-defined pore structure that can be achieved [98]. Good carbon supports can be made from phenolic resin by controlled polymerization, milling to an appropriate pore size, and subsequent extrusion. Fine-porous membrane layers can be made as described above, directly on the dried extruded support, by using again phenolic resin as the polymer precursor. The complete resin membrane (support + layers) can then be pyrolyzed in one single step. The main drawback of this production route is that a significant top layer thickness ($\sim$10 μm) is required to generate a defect-free layer on the relatively coarse-porous support ($\sim$15 μm). In order to remediate this problem, phenolic-resin-based carbon membranes were also made on common alumina supports with an intermediate layer of about 100 nm [99]. A high-quality molecular sieving carbon top layer of about 1 μm could be produced directly on the two-layer support structure, without further intermediate layer deposition.

The carbon microporous membranes are more stable than the metal-oxide membranes, since they maintain their pore structure to about 1000 °C. However, these membranes are limited by reactivity to oxidizing gases such as steam (temperatures above $\sim$ 650 °C), carbon dioxide (up to $\sim$ 750 °C), and oxygen. In the case of oxygen, excessive oxidation will occur at around 300 °C, while at lower temperatures, chemisorption of oxygen on the carbon surface can modify the adsorption and transport properties even at room temperature.

More details on the synthesis and membrane properties of carbon membranes can be found in Chapter 1.13.

1.11.6.7 Zeolite Layers

Zeolite membranes form the most recent branch of inorganic membranes. Zeolites are porous crystalline silicates with a complex crystallographic structure giving rise to specific molecule-sized pores. They can have a wide variety of compositions with some of the silicon atoms replaced by other cations. The cations are also responsible for the catalytic properties of these materials.

Zeolites are typically prepared by a hydrothermal treatment of a caustic synthesis solution containing a silica source and an appropriate structure-directing agent as tetrapropylammonium (TPA) ions [100]. A calcination step is required to burn out the TPA, and free the zeolite pores. Zeolite layers can be made

similarly, by immersing a multilayered support in a zeolite synthesis solution in an autoclave and treating the whole hydrothermally. Subsequent calcination opens the zeolite pores. This processing leads to zeolite crystal formation and growth on the support surface, and is therefore called *in situ* direct crystallization. An alternative and more recent approach is a two-step process named seeding and secondary growth. First, some zeolite crystal seeds are deposited on the support system, and the whole is subsequently treated similarly as in the direct crystallization case. In both cases, the formed zeolite membrane layers are always polycrystalline, giving rise to intercrystalline pores that are generally somewhat bigger than the intracrystalline zeolite pores. Multiple layer deposition is generally required to reach high-quality membranes with molecular sieving properties. In the direct crystallization route, the zeolite layer is infiltrated in the support; in the seeding and secondary growth route, the zeolite layer is a thin top layer on top of the support. In the last case, the permeability of the final membrane is higher, and specific orientations of the zeolite crystals can be obtained. A recent promising new path in zeolite membrane synthesis is the use of microwave heating in the seeding and secondary growth process [101].

Multilayer alumina supports are frequently used for zeolite membrane synthesis. However, chemical leaching of the alumina occurs in the caustic media generally used for zeolite synthesis. As a consequence, the mechanical properties of the support alter, as well as the composition of the final membrane. Stainless-steel supports have also been successfully coated with zeolite layers.

To date, MFI (both silicalite and ZSM-5) and zeolite A (also called Na A or LTA) have been reported to be successfully manufactured, and are also currently commercially available. In the laboratory, however, membranes have been made of a wide variety of zeolite types [101].

Much more details on the synthesis, membrane properties, and recent progress of zeolite membranes can be found in the excellent recent review article of Caro and Noack [102].

1.11.6.8 Metal Layers

1.11.6.8.1 Introduction

Metals such as Pd or Pd alloys are interesting because of their high hydrogen permeation capacity. Defect-free dense Pd or Pd alloy membranes are therefore excellent hydrogen-selective membranes, with ideal infinite selectivity. They have great potential as a hydrogen-selective membrane in a membrane reactor (as a steam reformer or coal gasification reactor) for sustainable energy production [103]. In order to be commercially viable, the dense metallic layer should be as thin as possible (preferably $<10\,\mu m$), and deposited on an appropriate multilayer support system.

Dense metallic layers can be prepared by a number of processes: casting and rolling, vapor deposition, electroplating, and electroless plating. In the first process, a metal cast undergoes a sequence of alternate rolling and annealing steps to reach the required thickness. Dense metal layers can also be formed by physical (PVD) or chemical vapor deposition (CVD) (physical vapor deposition is also called sputtering). In electroplating, a support is coated with a metal or its alloy in a plating bath with the support as cathode. The bath is maintained at a constant temperature during plating. Electroless plating involves the autocatalyzed decomposition or reduction of a few selected metastable metallic salt complexes on a support surface. The reaction should be carefully controlled to avoid potential decomposition of the as-formed layer and to control the layer thickness. All techniques have their advantages and drawbacks [103]. However, in all cases, small thicknesses in the order of 10–20 μm are feasible (the rolling techniques leads obviously to the thickest membranes) and, with some creativity, Pd alloys can also be prepared.

1.11.6.8.2 Foil preparation and wrapping

Commercially interesting Pd or Pd alloy membranes can be made by mechanically assembling (by setting or wrapping) a thin metal film on a porous flat or tubular support. For instance, metal foils can be assembled with stainless-steel grids or nickel perforated sheets by pressing and subsequent heating in order to allow diffusion to occur at the contact points [104]. Tubes can also be made from this composite structure by wrapping it around an alumina bar and welding the seam line. The mechanical stability of the composite structure is, however, rather low. An alternative approach is the electrochemical thinning of rolled foils (e.g., by chemical or anodical etching) down to 10 μm [105]. The thinned foils can be made pinhole free, and are currently being commercialized as self-standing foils by mounting them between flat flanges.

Recently, another approach has been developed in order to make metal foil – support assemblies. First, a thin metal layer is formed (by sputtering or by

electrodeposition) on a high-quality smooth and dense support. This film is subsequently removed from that support, and wrapped around the appropriate porous support for the final membrane. In this manner, membranes were prepared with a 5-μm-thick Pd alloy layer on top of a perforated stainless steel sheet [106]. Very thin Pd alloy films with a thickness of 0.8–5 μm were prepared by Bredesen and Klette [107] by sputtering on a silicon wafer. The films, carefully removed from the wafer, were wrapped around porous stainless-steel tubes to form composite metallic membranes.

During the recent years, very thin (0.5–0.8 μm) composite Pd membranes have also been fabricated by microfabrication techniques [108, 109]. These membranes are very expensive and can hold only about 5 bar; however, due to their extremely high hydrogen fluxes they may have potential for portable applications.

1.11.6.8.3 Electroless plating

Electroless plating has been widely used for Pd membrane synthesis. A good overview of the current state of development and relevant references can be found in Reference 102. The fact that electroless deposition is so popular is due to the low cost, easy procedures, and simplicity of the required equipment. Supports do not have to be conductive and very complex shapes can be covered uniformly. The deposition of metal alloys, however, represents a challenge. In general, when a Pd alloy is desired, the two metals are deposited sequentially and heat treated at high temperatures to obtain the alloy. Prior to electroless deposition, supports need to be activated by sequential immersion in $SnCl_2$ and $PdCl_2$ solutions to deposit active Pd seeds on the surface.

Different supports have been used to form metal membranes by electroless plating. The most commonly used ones are glass, alumina, and porous metals supports. Metal supports are very suitable, since other supports give rise to easier delamination of the metal layer. Possible candidates are, for example, porous stainless steel, porous nickel, porous Hastelloy, and porous Inconel. A diffusion layer is, however, required in order to avoid the diffusion of the metallic elements of the support into the Pd layer. Mostly oxides (including thin ceramic layers) have been used as intermetallic diffusion barriers. The passive oxide film that naturally forms on most metals is usually too thin (about 50 nm) in order to protect against intermetallic diffusion at high temperatures. Therefore, a treatment of the metal support is necessary before Pd deposition. This treatment can consist of a high-temperature treatment, giving rise to a thick oxide protection layer of 5–7 μm. The γ-alumina sol–gel layers are also widely used as an intermetallic diffusion barrier. Other diffusion barriers used are TiN sputtered layers [110], or, more recently, porous PdAg layers prepared by electroless deposition [111]. **Figure 14** shows an SEM picture of a typical Pd membrane manufactured by electroless plating on a porous stainless steel support with a 0.5-μm grade and a metal-oxide diffusion layer prepared by a high-temperature treatment [112].

The maximum pore size on the surface of porous metal supports may be the most crucial parameter for preparing defect-free thin Pd films. The Pd thickness needed to obtain a leak-tight membrane was shown to be approximately 3 times the diameter of the largest pore of the support [113]. Therefore, in order to reach Pd membranes thinner than 10 μm, it is necessary to first narrow the pore-size distribution at the surface of the support. This can be done by shot peening with Fe particles, intermediate layer deposition, or grading with preactivated alumina powder [103].

In general, composite Pd membranes are prepared at temperatures and pressures that are different from the ones that will be used in the application. For instance, the electroless deposition temperature is typically about 60 °C, while the

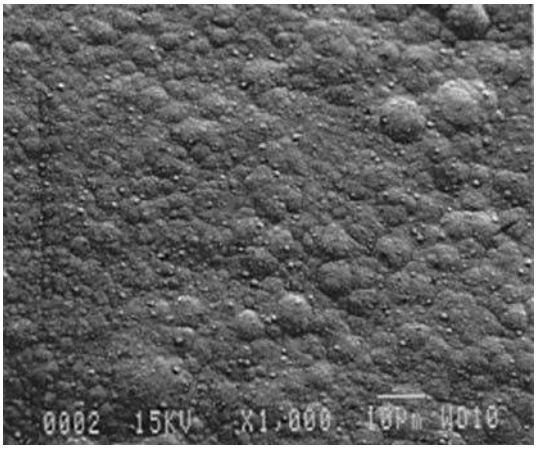

Figure 14 Scanning electron microscopy (SEM) picture of the surface of a Pd membrane manufactured by electroless plating on a porous stainless-steel support with a 0.5-μm grade and a metal-oxide diffusion layer prepared by a high-temperature treatment. Reproduced with permission from She, Y., Han, J., Ma, Y. H. *Catal. Today* **2001**, *67*, 43–53.

temperature of a steam reforming reactor is about 500 °C. Therefore, in use, composite Pd membranes undergo a series of structural transformations that lead to several problems such as permeance and selectivity loss over time. It has been shown that leak developments start only at about 500 °C [114]. This issue clearly needs more attention in future developments.

1.11.7 Functionalization

1.11.7.1 Hydrophobization

By surface modification of hydrophilic membranes, it is possible to obtain hydrophobic inorganic membranes. The objectives for this surface modification can be twofold. First, this modification changes the affinity of the pore surface of the membrane. This can be useful, for example, to obtain inorganic membranes appropriate for membrane distillation, or to obtain nanofiltration membranes that show high permeability for nonpolar solvents. Second, the modification allows a tailored decrease of the pore size of the membrane. The modification can be done by bonding specific organic compounds with varying hydrophobic tail lengths to the surface of a membrane. The most frequently used technique is a silane coupling treatment on the reactive OH groups of ceramic or glass materials (**Figure 15**). The technique is based on state-of-the-art modification processes used for silica in order to produce appropriate chromatography columns.

The silane-coupling method was first applied on macroporous and mesoporous membranes. This resulted in modified membranes with either a decreased pore size down to the micropore range [115, 116] or a modified hydrophilic/hydrophobic character [117]. The modification can be performed either in the liquid phase or in the vapor phase [118].

Modification of tight mesoporous membranes in order to enhance their performance in apolar solvents was first studied [119–121]. Tsuru *et al.* [119] modified mixed silica/zirconia membranes with the small trimethylchlorosilane in the gas phase. Van Gestel *et al.* modified a γ-alumina/anatase–TiO_2 multilayer membrane using bi-functional chlorosilanes, with two reactive chlorine groups, having a higher reactivity with the membrane surface [120]. However, these multifunctional chlorosilanes may also result in pore blocking due to polymerization reactions (hydrolysis and condensation between the silane molecules), having a negative influence on the solvent fluxes. That is the reason why Voigt *et al.* [121] worked with silanes with only one reactive group. All groups showed that in order to modify the complete specific surface of the membrane, the pore size has to be large enough for the specific silane to enter. In all the studies mentioned, hydrophobization of the inner membrane surface by the organochlorosilane reaction was clearly shown, that is, by permeation measurements of polar and apolar solvents.

However, the precise interaction between the chlorosilanes and the membrane surface is very complex and there is, in many cases, no evidence that it involves a chemical reaction rather than an adsorption reaction. It is shown that a chemical reaction of alkyltrichlorosilanes with a silica surface is not possible below 300 °C [123, 124]. At room temperature, the chlorosilane reacts only with water present in the solvent, or is adsorbed at the membrane surface. A polymeric chain is then formed that can adsorb or attach to the OH groups of the membrane surface by hydrogen bonding, without direct reaction with the

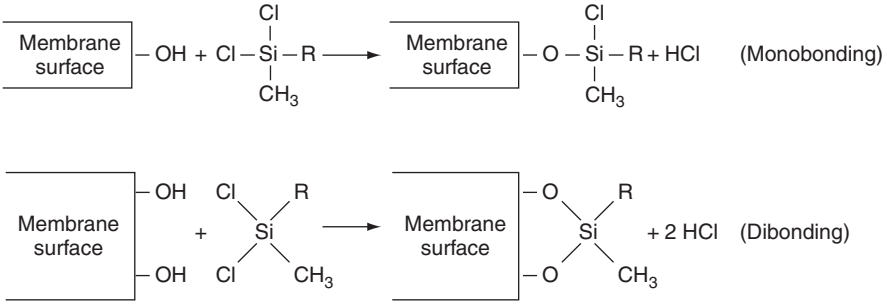

Figure 15 Schematic representation of the possible reactions between the OH groups on an inorganic membrane surface and a silane coupling reagent. Reproduced with permission from Van Gestel, T., Van der Bruggen, B., Buekenhoudt, A., Dotremont, C., Luyten, J., Vandecasteele, C., Maes, G. *J. Membr. Sci.* **2003**, *224*, 3–10.

membrane surface. However, a direct reaction with the membrane surface at room temperature is possible using a two-step procedure, involving an extra chemical agent as catalyst. In the first step, a strong base, such as triethylamine, is bound to hydroxyl groups on the surface. This creates a strongly nucleophilic oxygen atom on the hydroxyl site, which can react with the chlorosilane and then form a chemical bond.

It is also clear from the previous studies that the pretreatment temperature, determining the amount of reactive hydroxyl sites, and a curing process after the silanation can largely influence the final modified surface [123]. The nature of the metal oxide is also important for the reactivity and the success of the modification. It is clear from previous studies [125] and from our own recent work that silica is the easiest material to modify [126].

Besides chloroalkylsilanes, it is also possible to use phosphonic acids or fluoroalkylsilanes for the modification. Phosphonic acids were up to now only used to change ultrafiltration membranes to gas-separation membranes [125, 127]. Caro *et al.* [125] showed that there is a clear reaction between the γ-alumina surface and the phosphonic acids. Picard *et al.* [128] used fluoroalkylsilanes in order to make open zirconia ultrafiltration membranes more hydrophobic. Using proton nuclear magnetic resonance (NMR), they proved that for the fluoroalkylsilanes too, there is a real reaction between fluoroalkylsilanes and the membrane surface. These reagents were also successfully used by Voigt *et al.* [121] in order to make hydrophobic nanofiltration membranes, which are currently being commercialized.

Due to the lack of a real chemical reaction between organochlorosilanes and the membrane surface, the stability of the modification with these reactants is probably limited. Our own recent measurements [129] show that each exposure of the hydrophobic membrane to water systematically decreases the hydrophobicity of the membrane. This is most probably caused by a rehydroxylation of the surface. The stability of the modifications with phosphonic acids and fluoroalkylsilanes is expected to be better, thanks to the existing chemical bond between the membrane surface and the modifying agent.

1.11.7.2 Catalytic Functionalization

Membranes can have an extra advantage when the membrane surface is also catalytically active. This additional function is especially interesting in the field of membrane reactors [5, 130]. In a membrane reactor, a reaction is combined with a separation, in the same unit. This combination often creates synergy. For instance, the yield of equilibrium-limited reactions as dehydrogenation reactions can be enhanced by shifting the reaction equilibrium to the product by removing hydrogen from the reactor by the membrane. This has a direct consequence on the economics of such a membrane reactor: downstream separation of the product from hydrogen can be avoided, and the operating costs can be lowered, thanks to the decreased temperatures required for the reaction due to the yield enhancement. Extra synergy can be created in case the separative membrane contains also catalytic activity for the reaction. A typical example is a dense Pd or Pd alloy membrane. These membranes are not only hydrogen selective, but they act also as catalysts in the case of, for example, hydrogenation reactions. This has been shown to offer some interesting opportunities: when feeding the hydrogen to the reactor through the Pd membrane, it was demonstrated that the hydrogen, which permeates through the membrane, is a much more surface-active species (prior to recombination of the atoms to form H_2) than hydrogen that is adsorbed on a palladium-supported catalyst. Another possible function of a catalytic membrane in a membrane reactor is to improve the contact between the reactants and the catalyst. In this case, the membrane does not need to be permselective, but only catalytically active, with a thickness and a porous texture adapted to the reaction kinetics. Particularly, inorganic membranes have potential in membrane reactors, due to their higher-temperature resistance, compatible with the higher temperatures required for most reactions.

As mentioned above, inorganic membrane materials such as Pd or Pd alloys show catalytic activity by themselves. Other examples are zeolites, γ-alumina, LaOCl, and photocatalytic titania. Membrane layers of all these materials can be made by methods described in the previous section. Other membranes can be made catalytically active by incorporating catalytic particles, such as MgO, Ag, V, Pt, or Pd, in their porous structure. The method that is the most widely used for this incorporation is impregnation. The impregnation is done with an appropriate solution containing precursors for the desired catalyst. Some examples of this method are discussed in the following.

MgO and Ag loading of porous membranes has been done by impregnation with an aqueous mixture of the metal salt and urea [131]. Heating of the impregnated

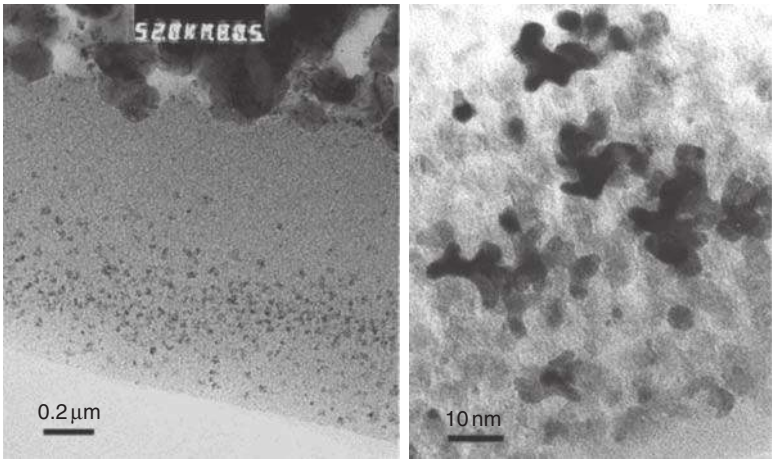

Figure 16 Transmission electron microscopy (TEM) picture revealing the dispersion of Pt nanoparticles in a mesoporous titania top layer, as obtained by impregnation. The dark spots are the catalyst particles. Reproduced with permission from Reader, H., Bredesen, R., Crehan, G., *et al*. *Sep. Purif. Technol.* **2003**, *32*, 349–355.

membrane at about 100 °C decomposes the urea, resulting in the formation of ammonia. This reacts with water and hydrolyzes the metal component. The so-formed metal hydroxide precipitates in the membrane pores. In a next step, the hydroxide is converted to the oxide form by a high-temperature treatment at 350–450 °C. When, after impregnation, the membrane is first dried in a controlled way, the solution can be concentrated in the top layer (the solvent is removed from the coarse-porous support and by capillary action concentrated in the fine-porous top layer), and the loading of the top layer with the metal or metal oxide can be greatly enhanced [132]. Using this procedure, it has been shown that the MgO and Ag particles formed are in the order of 10 nm and are homogeneously distributed across the thickness of the top layer.

Vanadia-modified membranes were synthesized by impregnation with a vanadium acetylacetonate (AcAc) solution [133]. The vanadium acetylacetonate reacts with the OH group of the membrane material to form a surface group –O–V–O (AcAc). After calcination at 450 °C, a surface vanadium oxide group is formed, which is structurally related to the catalytically active V_2O_5.

Dispersing Pt in a top layer can be done using impregnation of a precursor solution of hexachloroplatinic acid (H_2PtCl_6). The membranes are first saturated with deionized water by immersion accompanied by stirring. Then they are immersed in the Pt precursor solution, and dried in ambient air. Finally, the impregnated membranes are reduced under hydrogen at about 200 °C in order to form small Pt particles (5–10 nm) [134]. **Figure 16** shows a TEM picture of the dispersion of Pt particles in the membrane top layer.

An alternative for the impregnation process performed on the formed top layer is incorporation of catalyst particles during the preparation of the top layer. Particularly the sol–gel process offers good opportunities for this purpose. In this route, the active metal is incorporated in the sol used to make the top layer. This method has been used to make, for example, RuO_2–TiO_2 or RuO_2–SiO_2 membranes [135].

References

[1] Charpin, J., Rigny, P. *Proceedings of the 1st International Conference on Inorganic Membranes*, Montpellier, France, 3–6 July 1989; Cot, L., Ed.; 1989.
[2] Puhlfurss, P., Voigt, A., Weber, R., Morbé, M. *J. Membr. Sci.* **2000**, *174*, 123–133.
[3] Hsieh, H. P., Ed. *Inorganic Membranes for Separation and Reaction*; Membrane Science and Technology Series 3; Elsevier: Amsterdam, 1996.
[4] Bhave, R. R., Ed. *Inorganic Membranes: Synthesis, Characterization, and Applications*; Van Nostrand Reinhold: New York, 1991.
[5] Burggraaf, A. J., Cot, L., Eds. *Fundamentals of Inorganic Membrane Science and Technology*; Membrane Sciences and Technology Series 4. Elsevier: Amsterdam, 1996.
[6] Rahaman, M. N. *Ceramic Processing and Sintering*, 2nd edn.; CRC Press: Boca Raton, FL, 2003.
[7] Avvakumov, E., Senna, M., Kosova, N. *Soft Mechanochemical Synthesis: A Basis for New Chemical Technologies*; Kluwer: Boston, MA, 2002.
[8] Moulson, A. J., Herbert, J. M. *Electroceramics: Materials, Properties, Applications*, 2nd edn.; Wiley: Baltimore, MD, 2003.
[9] Masters, K. *Spray Drying Handbook*; Longman Scientific and Technical: New York, 1991.

[10] Messing, G. L., Shang, S. C., Jayanthi, G. V. *J. Am. Ceram. Soc.* **1993**, *76*, 2707–2726.
[11] Schnettler, F. J., Monforte, F. R., Rhodes, W. H. *Science of Ceramics*; Stewart, G. H., Ed.; The British Ceramic Society: Stoke-on-Trent, 1968.
[12] Sumitomo Electric Ind*ustries*. Method and Device for Incinerating Refuse. Jpn. Pat. 48,007,190, 1973.
[13] Kingery, W. D., Ed. *Introduction to Ceramics*; Wiley: New York, 1960.
[14] Brewin, P. R., Coube, O., Doremus, P., Tweed, J. H. *Modeling of Powder Die Compaction*; Springer: London, 2008.
[15] Kovalevsky, A. V., Kharton, V. V., Snijker, F. M. M., Cooymans, J. F. C., Luyten, J., Frade, J. R. *Solid State Ion.* **2008**, *179*, 61–65.
[16] Nijmeijer, A., Huiskes, C., Sibelt, N. G. M., Kruidhof, H., Verweij, H. *Amer. Ceram. Soc. Bull.* **1998**, *77*, 95–98.
[17] Steenkamp, G. C. Centrifugal Casting and Coating of Tubular Ceramic Membrane Supports. PhD Thesis, Potchefstroom University for Christian Higher Education, South Africa, 2000.
[18] Voigt, I., Fisher, G., Puhlfurss, P., Seifert, D. *Proceedings of the Fifth International Conference on Inorganic Membranes*, Nagoya, Japan, 22–26 July 1998; pp 42–45.
[19] Leschoche, P., Bergel, J.-Y. *Proceedings of the 8th International Conference on Inorganic Membranes*, Cincinnati, OH, USA, 18–22 July 2004; pp 430–433.
[20] Voigt, I., Fischer, G., Puhlfürss, P., Schleifenheimer, M., Stahn, M. *Sep. Purif. Technol.* **2003**, *32*, 87–91.
[21] Mistler, R. E., Twiname, E. R. *Tape Casting, Theory and Practice*; The American Ceramic Society: Westerville, OH, 2000.
[22] Tietz, F., Buchkremer, H. P., Stöver, D. *Solid State Ion.* **2002**, *152–153*, 373–381.
[23] Okubo T., Haruta, K., Kuksakabe, K., Morooka, S., Anzai, H., Akiyama, S. *J. Membr. Sci.* **1991**, *59*, 73–80.
[24] Weyten, H., Adriansens, W., Buekenhoudt, A., Leysen, R., Cornelis, R. *J. Alloys Compd.* **1993**, *195*, 31–34.
[25] Luyten, J., Buekenhoudt, A., Weyten, H., Adriansens, W., Cooymans, J., Leysen, R. *Proceedings of the Fifth International Conference on Inorganic Membranes*, Nagoya, Japan, 22–26 June 1998; pp 96–99.
[26] Gas-Separating Dense Ceramic Membrane. Eur. Pat. EP 0900587 B1, date of filing 1998.
[27] Colombo, P. *Key Eng. Mater.* **2002**, *206–213*, 1927–1930.
[28] Luyten, J., Mullens, S., Cooymans, J., De Wilde, A., Thijs, I. *Adv. Eng. Mater.* **2003**, *5*, 715–718.
[29] Le Brun, P., Krautlein, C., Rombach, G., Pouly, P., De Vries, P., Luyten, J. *Light Metals* **2007,** 657.
[30] Gauckler, L. J., Waeber, M. M., Conti, C., Jacob-Duliere, M. *Light Metals* **1985,** 1261–1283.
[31] Addler, J. *Int. J. Appl. Ceram. Technol.* **2005**, *2*, 429–439.
[32] Fino, D., Saracco, G. Gas Filtration, Cellular Ceramics. In *Cellular Ceramics: Structure, Manufacturing*; Scheffler, M., Colombo, P., Eds.; Wiley-VCH: Weinheim, 2005; Chapter 5.2, pp 416–438.
[33] Schwartzwalder, K., Somers, H., Somers, A. V. Method of Making Porous Ceramic Articles. US Pat. 3,090,094, May 1963.
[34] Saggio-Woyanski, J., Scott, C., Winnaer, W. P. *Am. Ceram. Soc. Bull.* **1992**, *71*, 1674–1682.
[35] Will, J. Porous Support Structures and Sintered Thin Film Electrolytes for Solid Oxide Fuel Cells. PhD Thesis, ETH Zürich, Switzerland, 1998.
[36] Luyten, J., Thijs, I., Vandermeulen, W., Mullens, S., Wallaeys, B., Mortelmans, R. *Adv. Appl. Ceram.* **2005**, *104*, 4–8.
[37] Luyten, J., Cooymans, J., De Wilde, A. *Adv. Eng. Mater.* **2002**, *4*, 925–927.
[38] Yoshihisa, K., Masashi, F. Ceramic Foam. Br. Pat. 2168337, 1986.
[39] Ortona, A., Molinary, M., Romelli, L. Open Cell Foam Ceramic Material. Eur. Pat. 1382590, 2004.
[40] Sieber, H., Kaindl, A., Greil, P. *Adv. Eng. Mater.* **2002**, *2*, 105–109.
[41] Thijs, I., Luyten, J., Mullens, S. *J. Am. Ceram. Soc.* **2003**, *87*, 170–172.
[42] Sepulveda, P. *Am. Ceram. Soc. Bull.* **1997**, *76*, 61–65.
[43] Binner, J. K., Sepulveda, P., Smith, R. *Ceram. Proc. Sci., Ceram. Trans.* **1998**, *83*, 273.
[44] Mullens, S., Cooymans, J., De Wilde, A., Beyens, F., Uytterhoeven, J., Luyten, J. *Proceedings of Shaping II*, Gent, Belgium, 24–26 October 2002; Luyten, J., Erauw, J. P., Eds.; pp 57–62.
[45] Janney, M., Omatete, O., Walls, C. *J. Am. Ceram. Soc.* **1998**, *81*, 581–591.
[46] Millan, A. J., Moreno, R., Nieto, M. I. *J. Eur. Cer. Soc.* **2000**, *20*, 2527–2533.
[47] Luyten, J., Buekenhoudt, A., de Barquin, F., Joiret, J. F. *Proceedings of Shaping II*, Gent, Belgium, 24–26 October 2002; Luyten, J., Erauw, J. P., Eds.; pp 219–224.
[48] Lewis, J. A. *J. Am. Ceram. Soc.* **2000**, *83*, 2341–2359.
[49] Gomes de Sousa, C., Evans, J. R. G. *J. Am. Ceram. Soc.* **2003**, *86*, 517–519.
[50] Chartier, T., Chaput, C., Doreau, F., Loiseau, M. *J. Mater. Sci.* **2002**, *27*, 1–7.
[51] Ping, J., Wijns, J. R., Van Blitterswijk, C. A., de Groot, K. *Biomaterials* **2006**, *27*, 1223–1235.
[52] Elmer, T. H. Porous and Reconstructed Glasses. In *Engineered Materials Handbooks*, Vol. 4: *Ceramics and Glasses*; Schneider, S. J., Ed.; ASM International: Metals Park, OH, 1992; p 427.
[53] Shelekhin, A. B., Dixon, A. G., Ma, Y. H. *AIChE J.* **1995**, *41*, 58–67.
[54] Kuraoka, K., Amakawa, R., Matsumoto, K., Yazawa, T. *J. Membr. Sci.* **2000**, *175*, 215–223.
[55] Hofman-Züter, J. M. Chemical and Thermal Stability of Mesoporous Ceramic Membranes. PhD Thesis, University of Twente, Enschede, The Netherlands, 1995.
[56] Buekenhoudt, A., Stability of Porous Ceramic Membranes. In *Inorganic Membranes: Synthesis, Characterization and Applications*; Mallada, R., Menendez, M. Eds.; Membrane Science and Technology Series 13; Elsevier: New York, **2008**.
[57] Van Praag, W., Zaspalis, V., Keizer, K., Van Ommen, J. G., Ross, J. R., Burggraaf, A. J. *Proceedings of the 1st International Conference of Inorganic Membranes*, Montpellier, France, 2–6 July 1989; pp 397–400.
[58] Kumar, K. N. P., Keizer, K., Burggraaf, A. J., Okubo, T., Nagamoto, H. *J. Mater. Chem.* **1993**, *3*, 1151–1159.
[59] Bonekamp, B. C., Horssen, A., Correia, L. A., Vente, J. F., Haije, W. G. *J. Membr. Sci.* **2006**, *278*, 349–356.
[60] Brinker, C. J., Scherer, G. W. *Sol–Gel Science – The Physics and Chemistry of Sol–Gel Processing*; Academic Press: New York, 1990.
[61] Van Gestel, T., Vandecasteele, C., Buekenhoudt, A., *et al. J. Membr. Sci.* **2002**, *207*, 73–89.
[62] Puhlfürss, P., Voigt, A., Weber, R., Morbé, M. *J. Membr. Sci.* **2000**, *174*, 123–133.
[63] De Vos, R. M., Verweij, H. *Science* **1998**, *279*, 1710–1711.
[64] Sanchez, C., Livage, J. *New J. Chem.* **1990**, *14*, 513–521.
[65] Vacassy, R., Guizard, C., Thoraval, V., Cot, L. *J. Membr. Sci.* **1997**, *132*, 109–118.
[66] Benfer, S., Popp, U., Richter, H., Siewert, C., Tomandl, G. *Sep. Purif. Technol.* **2001**, *22/23*, 231–237.
[67] Van Gestel, T., Kruidhof, H., Blank, D. H. A., Bouwmeester, H. J. M. *J. Membr. Sci.* **2006**, *284*, 128–136.

[68] Brinker, C. J., Ward, T. L., Sehgal, R., *et al. J. Membr. Sci.* **1993**, *77*, 165–179.
[69] Uhlhorn, R. J. R., Keizer, K., Burggraaf, A. J. *J. Membr. Sci.* **1992**, *66*, 271–287.
[70] de Lange, R. S. A., Hekkink, J. H. A., Keizer, K., Burggraaf, A. J. *J. Membr. Sci.* **1995**, *99*, 57–75.
[71] van Gemert, R. W., Cuperus, F. P. *J. Membr. Sci.* **1995**, *105*, 287–291.
[72] Van Veen, H. M., Van Delft, Y. C., Engelen, C. W. R. *Sep. Purif. Technol.* **2001**, *22/23*, 361–366.
[73] Yazawa, T., Tanaka, H., Nakamichi, H., Yokoyama, T. *J. Membr. Sci.* **1991**, *60*, 307–317.
[74] Tsuru, T., Wada, S., Izumi, S., Asaeda, M. *J. Membr. Sci.* **1998**, *149*, 127–135.
[75] Tsuru, T., Izumi, S., Yoshioka, T., Asaeda, M. *AICHE J.* **2000**, *46*, 565–574.
[76] Asaeda, M., Sakou, Y., Yang, J., Shimasaki, K. *J. Membr. Sci.* **2002**, *209*, 163–175.
[77] Sekulic, J., Luiten, W. J., ten Elshof, J. E., Benes, N. E., Keizer, K. *Desalination* **2005**, *148*, 1138–1156.
[78] Tsuru, T., Hironaka, D., Yoshioka, T., Asaeda, M. *Sep. Purif. Technol.* **2001**, *25*, 307–314.
[79] Van Gestel, T., Sebold, D., Kruidhof, H., Bouwmeester, H. J. M. *J. Membr. Sci.* **2008**, *318*, 413–421.
[80] Castricum, H. L., Sah, A., Kreiter, R., Blank, D. H. A., Vente, J. F., ten Elshof, J. E. *Chem. Commun.* **2008**, *9*, 1103–1105.
[81] Roger, C., Schaefer, D. W., Beaucage, G. B., Hampden-Smith, M. J. *J. Sol–Gel Sci. Technol.* **1994**, *2*, 67.
[82] Ayral, A., Guizard, C., Cot, L. *J. Mater. Sci. Lett.* **1994**, *13*, 1538–1539.
[83] Yamaki, T., Maeda, H., Kusakabe, K., Morooka, S. *J. Membr. Sci.* **1993**, *85*, 167.
[84] Julbe, A., Balzer, C., Barthez, J. M., Guizard, C., Cot, L. *J. Sol–Gel Sci. Technol.* **1995**, *4*, 89–97.
[85] Brinker, C. J., Lu, Y., Sellinger, A., Fan, A. *Adv. Mater.* **1999**, *11*, 579.
[86] Kresge, C. T., Leonowicz, M. E., Roth, W. J., Vartuli, J. C., Beck, J. S. *Nature* **1992**, *359*, 710–712.
[87] Soler-Illia, G. J. A. A., Sanchez, C., Lebeau, B., Patarin, J. *Chem. Rev.* **2002**, *102*, 4093.
[88] Kumar, P., Ida, J., Kim, S., Guliants, V. V., Lin, J. Y. S. *J. Membr. Sci.* **2006**, *279*, 539–547.
[89] Dabadie, T., Ayral, A., Guizard, C., *et al. Mater. Sci. Forum* **1994**, *152–153*, 267.
[90] Dabadie, T., Ayral, A., Guizard, C., Cot, L. *Mater. Res. Soc. Symp. Proc.* **1994**, *346*, 849.
[91] Dabadie, T., Ayral, A., Guizard, C., Cot, L., Robert J. C., Poncelet, O. *Proceedings of the Third International Conference on Inorganic Membranes*, Worcester, MA, USA,1994; p. 411.
[92] Klotz, M., Ayral, A., Guizard, C., Cot, L. *J. Mater. Chem.* **2000**, *10*, 663–669.
[93] Klotz, M., Ayral, A., Guizard, C., Cot, L. *Sep. Purif. Technol.* **2001**, *25*, 71–78.
[94] Higgens, S., Kennard, R., Hill, N., DiCarlo, J., DeSisto, W. J. *J. Membr. Sci.* **2006**, *279*, 669–674.
[95] Bosc, F., Ayral, A., Albouy, P. A., Guizard, C. *Chem. Mater.* **2003**, *15*, 2463–2468.
[96] Bosc, F., Ayral, A., Albouy, P. A., Datas, L., Guizard, C. *Chem. Mater.* **2004**, *16*, 2208–2214.
[97] Bosc, F., Ayral, A., Guizard, C. *J. Membr. Sci.* **2005**, *265*, 13–19.
[98] Lenghaus, K., Qiao, G. H., Solomon, D. H., *et al. Carbon* **2002**, *40*, 743–749.
[99] Tennison, S., Arnott, K., Richter, H. *Ann. Chim. Sci. Mat.* **2007**, *32*, 159–177.
[100] van Bekkum, H., Flanigan, E. M., Jansen, J. C. *Introduction to Zeolite Science and Practice. Studies in Surface Science and Catalysis*; Elsevier: Amsterdam, 1991; Vol. 58.
[101] Julbe, A., Ayral, A. *Ann. Chim. Sci. Mat.* **2007**, *32*, 213–229.
[102] Caro, J., Noack, M. *Microporous and Mesoporons Mater.* **2008**, *115*, 215–233.
[103] Ma, Y. H. Guazzone, F. *Ann. Chim. Sci. Mat.* **2007**, *32*, 179–195.
[104] Tosti, S. *Int. J. Hydrogen Energy* **2003**, *28*, 1445–1454.
[105] Judas, W., Krueger, C. W., Bombard, R. T. Method of Fabricating Thinned Free-Standing Metallic Hydrogen-Selective Palladium-Bearing Membranes and Novel Pin-Hole-Free Membranes Formed Thereby. US Pat. 6,103,028, 2000.
[106] Thornthon, P. H. Supported Membrane for Hydrogen Separation. US Pat. Appl. 20,020,078,827, 2002.
[107] Klette, H., Bredesen, R. *Membr. Technol.* **2005**, *5*, 7–9.
[108] Tong, H. D., Gielens, F. C., Gardeniers, J. G. E., *et al. Ind. Eng. Chem. Res.* **2004**, *43*, 4182–4187.
[109] Keurentjes, J. T. F., Gielens, F. C., Tong, H. D., van Rijn, C. J. M., Vorstman, M. A. G. *Ind. Eng. Chem. Res.* **2004**, *43*, 4768–4772.
[110] Shu, J., Adnot, A., Granjean, B. P. A., Kaliaguine, S. *Thin Solid Films* **1996**, *286*, 72–79.
[111] Ma, H. M., Mardilovich, I. P., Engwall, E. E. Composite Gas Separation Modules Having Intermediate Porous Metal Layers. US Pat. Appl. 20,040,237,779, 2004.
[112] She, Y., Han, J., Ma, Y. H. *Catal. Today* **2001**, *67*, 43–53.
[113] Ma, H. M., Mardilovich, I. P., Mardilovich, P. P. *Div. Pet. Chem.* **2001**, *46*, 154–156.
[114] Guazzone, F., Speakman, A. S., Payzant, E. A., Ma, Y. H. *Ind. Eng. Chem. Res.* **2006**, *45*, 8145–8153.
[115] Leger, C., De Lira, H., Paterson, R. *J. Membr. Sci.* **1996**, *120*, 187–195.
[116] Javaid, A., Hughey, M. P., Varutbangkul, V., Ford, D. M. *J. Membr. Sci.* **2001**, *187*, 141–150.
[117] Picard, C., Larbot, A., Guida-Pietrasanta, F., Boutevin, B., Ratsimihety, A. *Sep. Purif. Technol.* **2001**, *25*, 65–69.
[118] Miller, J. R., Koros, W. J. *Sep. Sci. Technol.* **1990**, *25*, 1257–1280.
[119] Tsuru, T., Miyawaki, M., Kondo, H., Yoshioka, T., Asaeda, M. *Sep. Purif. Technol.* **2003**, *32*, 105–109.
[120] Van Gestel, T., Van der Bruggen, B., Buekenhoudt, A., *et al. J. Membr. Sci.* **2003**, *224*, 3–10.
[121] Voigt, I., Phulfürss, P., Holborn, T. *Proceedings of the Aachener Membrane Colloquium*, Aachen, Germany, 2003.
[122] Sah, A., Casricum, H. L., Bliek, A., Blank, D. H. A., ten Elshof, J. E. *J. Membr. Sci.* **2004**, *243*, 125–132.
[123] Impens, N. R. E. N., Van der Voort, P., Vansant, E. F. *Microporous Mesoporous Mater.* **1999**, *28*, 217–232.
[124] Hair, M. L., Tripp, C. P. *Colloids Surf. A: Physicochem. Eng. Aspects* **1995**, *105*, 95–103.
[125] Caro, J., Noack, M., Kölsch, P. *Micorporous Mesoporous Mater.* **1998**, *22*, 321–332.
[126] Özen, M., Meynen, V., Buekenhoudt, A., Cool, P. *Innovations on Sustainable Production i-SUP 2008; Proceedings of the International Conference*, Brugge, Belgium, 22–25 April 2008.
[127] Randon, J., Paterson, R. *J. Membr. Sci.* **1997**, *134*, 219–223.
[128] Picard, C. Larbot, A., Tronel-Peyroz, E., Berjoan, R. *Solid State Sci.* **2004**, *6*, 605–612.
[129] Verrecht, B., Leysen, R., Buekenhoudt, A., Vandecasteele, C., Van der Bruggen, B. *Proceedings of the Ninth*

International Conference on Inorganic Membranes, Lillehammer, Norway, 25–29 June 2006; pp 135–138.
[130] Dalmon, J. A. Firoir-Fendler, A., Mirodatos, C. Mozzanega, H., Eds. Special Issue: Catalysis in Membrane Reactors. *Catal. Today* 1995, 25.
[131] Burggraaf, A. J., Keizer, K., van Hassel, B. A. *Solid State Ion.* **1989**, *32/33*, 771–782.
[132] Burggraaf, A. J. Modified Membrane. Eur. Pat. 0,395,184, 1990.
[133] van Praag, W., Zqpalis, V., Keizer, K., van Ommen, J. G., Ross, J. R., Burggraaf, A. J. *Proceedings of the 1st International Conference on Inorganic Membranes*, Montpellier, France, 3–6 July 1989; pp 397–400.
[134] Reader, H., Bredesen, R., Crehan, G., *et al. Sep. Purif. Technol.* **2003**, *32*, 349–355.
[135] Parvulescu, V., Parvulescu, V. I., Popescu, G., Julbe, A., Guizard, C., Cot, L. *Catal. Today* **1995**, *25*, 385–389.
[136] Snijkers, F., Mullens, S., Buekenhoudt, A., Vandermeulen, W., Luyten, J. *Materials Science Forum* **2005**, *492–493*, 299–304.
[137] Luyten, J., Cooymans, J., De Wilde, A., Thijs, I. *Key Eng. Mater.* **2002**, *206–213*, 1937–1940.

Biographical Sketches

Anita Buekenhoudt was born in Duffel, Belgium, in 1961. She studied physics at the University of Antwerp, Belgium, and graduated in 1983. In 1990, she obtained her PhD in solid-state physics at the Catholic University of Leuven. For 2 years, she worked at the K.U. Leuven as postdoc on nuclear magnetic resonance (NMR) studies in high-T_c superconductors. Since 1992 she has been working at the Flemish Institute for Technological Research in Mol, Belgium, as a project leader. Subsequently, her interest has shifted from high-T_c superconductors to ceramic ion-conducting materials for sensors. Since about 10 years, her work has involved the development and application studies of ceramic membranes for nanofiltration, pervaporation, and gas separation. Strong emphasis is also placed on the implementation of these and alternative membranes in industrial applications. She has authored or coauthored more than 50 papers and a few patents.

Andrei Vladislavovich Kovalevsky was awarded PhD in physical chemistry in 2002 by the Research Institute for Physical Chemical Problems, Belarusian State University, Minsk. In 1997, he received a BS degree in physical chemistry and, in 1998, an MS degree in chemistry from the Belarusian State University. A.V. Kovalevsky was employed as an engineer (1997–2001), junior researcher (2001–03), and executive chief of the Laboratory of Physical Chemistry of Solids (2003–04) at the Research Institute of Physical Chemical Problems, Belarusian State University. Between 2004 and the beginning of 2008, he had been a postdoctoral researcher at the University of Aveiro, supported by grants from Fundação para a Ciência ea Tecnologia (FCT, Portugal) and Centre for Research in Ceramics and Composite Materials (CICECO, University of Aveiro, Portugal). A.V. From the beginning of 2008 to the beginning of 2010 Kovalevsky was employed as a researcher in the Materials Department of Flemish Institute for Technological Research (VITO), Belgium. Currently his works again at the University of Aveiro Portugal. His scientific activities deal with physical chemistry of solids and high-temperature electrochemistry, being mainly focused on oxygen mixed-conducting membranes and solid oxide fuel cells. He has coauthored more than 60 papers that are published in international Science Citation Index (SCI) journals and various scientific volumes.

Jan Luyten was born in Diest, Belgium, in 1951. He received his master's degree in metallurgical engineering at the Catholic University of Leuven, Belgium. In 1979, he obtained his PhD in applied science at the same university. He stayed there for 1 year as a postdoctoral researcher. After 1 year of research and development at Union Miniere, he was a teacher at the Technical High School of Industrial Engineers in Leuven, Belgium (1982–87). During 1988–92, he worked as a project leader at the Nuclear Research Center (SCK) in Mol, Belgium. Since 1992 he has been working as a project leader at the Flemish Institute for Technological Research (VITO) in Mol, Belgium. He has about 30 years of experience in processing and characterization of metals and ceramics, and especially of ceramic membranes and sensors. His current research interests include ceramic foams. He is currently a member of several scientific committees on ceramic materials, including the Belgian and American Ceramic Society. He has authored or coauthored more than 150 articles and several patents.

Frans Snijkers was born in Kessenich, Belgium, in 1963. He studied chemistry at the University of Hasselt (the former Limburgs Universitair Centrum) and analytical and inorganic chemistry at the Catholic University of Leuven, where he obtained his MSc in 1985. For 5 years he worked at the Philips Research Laboratories in Eindhoven, the Netherlands, on the subject of thermionic cathodes for cathode ray tubes. In 1991, he joined the Innovation and Technology Center of Philips Display Components, NV Philips Electronics in Eindhoven, the Netherlands, as a project manager, dealing with product and process development in the area of thermionic cathodes and screen processing technology. Since 2001, he has been working at the Flemish Institute for Technological Research (VITO nv) in Mol, Belgium, as project manager. The projects involve research and development of ceramic components and processing of ceramic materials, including ceramic ion-conducting membranes for gas separation. He is currently a member of the Belgian, European, and American Ceramic Society. He has authored or coauthored more than 25 papers and over 10 patents.

1.12 Ceramic Hollow Fiber Membranes and Their Applications

K Li, Imperial College London, London, UK

1.12.1 Introduction

The combination of high chemical, thermal, and mechanical resistance has made ceramic membranes an attractive alternative to polymeric membranes [1, 2]. Due to the high surface area/volume ratios achieved by hollow fiber geometries, the compactness of the membrane systems made from ceramic hollow fiber membranes may greatly exceed that of other membrane systems. The ability to operate at high temperatures and pressures, and in corrosive environments, allows ceramic membranes to be used in a variety of applications including filtration for corrosive fluids [3], high-temperature membrane reactors [4–6], solid oxide fuel cells (SOFCs) [7], and membrane contactors [8, 9] besides robust membrane supports [10]. Although some attempts have been made in fabricating a silica glass hollow fiber membrane for gas separation [11], the membrane was too fragile to be used in large industrial scales. Recently, Tan *et al.* [12] and Liu and coworkers [13–16] successfully produced hollow fiber ceramic membranes using materials such as Al_2O_3 and perovskites by employing a phase inversion method which is a three-step process, including (1) preparation of a spinning suspension; (2) spinning of ceramic hollow fiber precursors; and (3) final sintering.

Preparation of ceramic hollow fiber membranes using the phase inversion method is a quite complex process. Many factors may affect the final membrane performance. Therefore, in the following sections, a detailed discussion on the preparation of ceramic

hollow fiber membrane is given first following the sequence of the three steps mentioned above. Subsequently, an example on fabrication of yittria-stabilized zirconia (YSZ) hollow fiber membranes will be given. Finally, potential applications of various ceramic hollow fiber membranes in separation and reaction are discussed.

1.12.2 Preparation of Spinning Suspension

Preparation of a spinning suspension may consist of a several steps in sequence: (1) mixing a dispersant and a solvent of choice; (2) adding preconditioned particles for deflocculant and dispersion; (3) adding polymer binders and plasticizers; and (4) degassing the suspension prior to the spinning of the membrane precursor. The deflocculation is a very important step, as soft agglomerates of the particles in the spinning suspension would have an effect on pore size and permeability of the final membrane product [17]. A more detailed preparation procedure will be given at the end of this section.

The main ingredients in the spinning suspension for the fabrication of hollow fiber ceramic membranes are the ceramic powders, additives, and solvents. In selection of the ceramic powders, one of the important factors is the particle sizes and its distribution as well as the shape of the particles. They effect the porosity, pore size, and pore-size distribution of the final membrane product [17].

Additives such as deflocculants/dispersants, binders, plasticizers, antifoaming agents, and pore formers are used to provide the spinning suspension with the required property. In preparing the ceramic hollow fiber membrane using the phase inversion technique, the requirement of the organic binders is that they should not only be invertible, but also must be burnt out without leaving ash and tar during the calcinations. The quantity of organic binders should be as low as possible, but without affecting the inversion capability.

The solvent(s) must dissolve the additives used and must show a high exchange rate with nonsolvent (coagulants). The rates of solvent outflow and coagulant inflow have an effect on the cross-sectional structures of the membrane precursor, hence the structures of the final membrane products [18].

As preparation of the spinning suspension is still in the development stage, the following few general rules are, so far, considered to be useful in the preparation of the spinning suspension:

1. The amount of dispersant must be maintained to ensure the stability of the suspension.
2. The amount of solvent must be fixed at a minimum to maintain a homogeneous suspension.
3. The ratio between organic components and ceramic powders must be as low as possible.
4. The plasticizer to binder ratio must be adjusted to make the membrane precursor flexible, resistant, and easy to release.

1.12.2.1 Particles and Packing of Particles

In ceramic membrane fabrication processes, the most important component in the spinning suspension is the ceramic powders. After binder removal and final sintering, the ceramic powders are the only component left and will determine the properties of the ceramic membrane produced. The other components in the spinning suspension such as solvents, plasticizers, binders, and dispersant are used simply to predesign the membrane morphology (i.e., pore size, pore-size distribution, porosity, cross-sectional structures, etc.) and to facilitate the spinning and phase inversion which is, in general, a process in obtaining and holding the powder particles in the hollow fiber configuration.

During the phase inversion (shape forming process), the particles in the spinning suspension undergo a process of particle packing. It is, therefore, possible to adjust the particles to attain high packing densities or to attain specific compact properties. The most widely used parameters of the particle packing are the packing density (or bulk density) and the coordination number. The bulk density (defined as weight of the particle bed/volume of the bed) is directly proportional to the density of the individual particles, and a high bulk density may be obtained simply because the particles have a high density rather than because the particles are closely packed. In order to avoid this difficulty an expression involving the ratio of the volume of particles composing the bed (V_p) to the volume of the bed (V_b) may be adopted. This ratio, that is, packing fraction (defined as bulk density/particle density), is usually referred to as the packing fraction or the fractional solids content. The fractional voidage ($\varepsilon = 1 - V_p/V_b$), expressed as a percentage, is often known as the volumetric porosity. The packing density can be improved by introducing smaller-sized

particles. Small particles are introduced into a packing of large particles, to fill its voids without increasing the overall volume of the bed. Several studies have been conducted to view the two-dimensional structure using disks and spheres [19–21]. Two dominant factors are the size ratio and composition of the mixture.

When two sizes of spheres are mixed, the smaller particles fill the unoccupied voids among the large particles. So as long as the proportion of the smaller sphere is sufficiently great, the proportion of large spheres could reach the stage at which they will touch each other. The resulting packing is optimal. When the quantity of small particles becomes too great since all of the voids are filled, further addition will force the large particles apart and no longer improve the packing density. The basic behavior for random dense packing is shown in **Figure 1**, which shows that the packing volume, termed the specific volume (volume to mass ratio), is a function of the composition for a mixture composed of large and small spheres. There is a composition of maximum packing density [22]. The relative improvement in packing density depends on the particle size ratio of the large and small particles. Detailed discussion on the packing of different particle sizes was given by Rahaman [23].

1.12.2.2 Dispersion of Particles

As mentioned above, in preparation of ceramic membranes, one of the problems to be tackled is the dispersion of each individual ceramic particle in a solvent. When individual primary particles are in proximity, they often have a tendency to form loosely bound groups usually known as soft agglomerates. In a fluid suspension of particles, particularly when the powder has little affinity for wetting, the soft agglomerates can form to lower the free energy of the suspension by reducing the solid–liquid interface area. There are many types of surface forces acting between particles: electrostatic forces, van der Waals forces, and steric forces are the most important ones. Descriptions of these three forces can be found elsewhere [23].

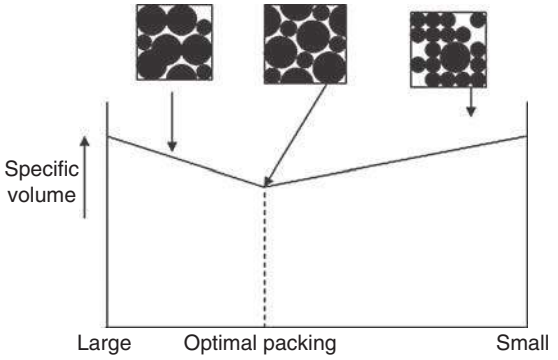

Figure 1 The reduction in specific volume for mixed large and small spheres, showing the condition of optimal packing where the small spheres fill all voids in the large sphere packing.

In order to deflocculate the soft agglomerate as well as to disperse the primary particles in a solvent, addition of a dispersant is usually required. The purpose of the dispersant is to disperse the primary particles and to hold them in a homogeneous suspension. As the dispersant separates primary particles and holds them in suspension, which allows the solvent to form a separating layer between particles, the suspension usually shows a lower viscosity due to the particle mobility offered by the solvent in the interparticle layer. There are basically two different mechanisms, that is, ionic repulsion and steric hindrance, in describing the deflocculation and dispersion. The term 'ionic repulsion' is used to describe the charging of particle surfaces so that they magnetically repel each other. In aqueous systems, this can be achieved by changing the pH. The surface charge of the particles can also be accomplished by introducing polyelectrolyte solutions, which coat the particle surfaces and provide the surface charge. The steric hindrance term is used to describe the separation of particles by coating a layer on one particle that would physically prohibit another particle to be in contact with it. Organic polymers are often used in both aqueous and nonaqueous systems to accomplish this particle–particle separation.

There are several reasons for a spinning suspension to be fully dispersed. First, the ceramic powders being added into the spinning suspension are usually in the form of soft agglomerates because they are normally produced through a sol/gel process and are high surface area powders. The soft agglomerates tend to trap air in the interstitial space between the primary particles. If the soft agglomerates are not broken up, the trapped air would produce bubbles in the membrane precursor, resulting in pinholes and unwanted surface porosity in the final sintered membranes. Second, when the polymeric binder is introduced, it will envelop the soft agglomerates instead of the individual (primary) particles. This

will make the soft agglomerates as a permanent group throughout the rest of the process, which produces less density membrane precursors, leading to high shrinkage during the final consolidation process.

The dispersion of particles in a solvent takes place in several stages. When the powder is first put in proximity to the solvent, the particle surfaces (or agglomerates) get coated with the solvent. Therefore, the stage 1 of suspension is the wetting of the particle surface. After the particle surface is wetted, soft agglomerates held together by electrostatic forces or by the van der Waals forces need to be separated, that is, the stage 2 of suspension is the mechanical separation of primary particles. After the completion of the stage 2, the particles are evenly distributed throughout the solvent. The final stage of suspension consists of protecting and stabilizing what has been accomplished, that is, prohibiting soft agglomerates from reforming in the spinning suspension.

Dispersion mechanisms have been fairly well studied in nonaqueous solvent systems, primarily with oxides. Although the main particle separation mechanism has been found to be steric hindrance, Lee and Rives [24] concluded that both steric and ionic mechanisms are active in the organic solvent-based suspension. The ionic repulsion dispersion mechanism may come into organic solvent systems with certain additives. However, since the spinning suspension generally contains a high solid loading and the particles are in close proximity to each other, the steric hindrance is still an important stabilization method [25].

One of the measurable effects of using a dispersant is a higher packed-bed density. This phenomenon has been used to determine the proper dispersant level. The level or extent of dispersion can be measured by a number of techniques such as microelectrophoresis, optical microscopy, and laser scattering. Targeted variables of these tests include zeta potential, isoelectric point, and equivalent spherical diameter. A settling experiment is perhaps another means for the characterization of the spinning suspension, as one of the main reasons for dispersing the solution is to form a densely packed bed of particles. It follows that a screening experiment should be performed with the densest packed bed as the goal. Therefore, an experiment in which different concentrations of dispersant are used to disperse identical suspensions of powder and solvent can be carried out. After a proper screening, the extent of dispersion in powder suspensions can be observed.

1.12.2.3 Summarized Preparation Procedure

Based on the each individual discussion discussed above, a general procedure in preparation of the spinning suspension can now be drawn. The first step is the dispersion of particles in the presence of a dispersant in the solvent(s). The usual procedure would be to dissolve a predetermined amount of dispersant in term of weight or volume by stirring or rolling. The powder(s) are then added.

Percentage of the solids loading during dispersion is dependent on the powder density, particle size, and dispersant effectiveness. It is beneficial to optimize the solids loading during this step, since any excess solvent will have to be removed during the phase inversion (shape forming step). The solid loading is often adjusted with experience, because the solvent volume also affects the final viscosity after the polymer binder and/or plasticizer(s) are added to the mixture. The viscosity of the dispersion is not a primary concern, as long as deagglomeration occurs. Viscosity of the dispersions at this stage is extremely low, but will increase when the binder is added.

The purpose of the dispersion procedure is to accomplish three goals: (1) to break apart any soft agglomerates, (2) to coat the primary particles with a dispersant, which (3) keeps the particles apart by steric effects, electrostatic effects, or both.

After the dispersion process is complete, the plasticizers (if any) are poured onto the top of the mixture, and followed by the weighed binder, either in powder form or dissolved in a solvent.

Once the plasticizer and binder are added, the mixture is stirred or rolled to make sure that the binder is not in large clumps. Usually, a few hours are required for the complete dissolution of the binder.

Usually, the suspension becomes more viscous with the addition of a long-chain polymeric binder. The only time that this does not occur is when the binder is a more powerful dispersant and replaces or overrides the chosen dispersant. This is also a good reason to use the suspension in the phase inversion process as soon as possible after the binder is mixed into the suspension. Rheological properties of the suspension can change with time. Once the plasticizer(s) and binder(s) have been mixed into the suspension formulation, it is ready for prespinning conditioning and characterization.

The next step is to de-gas the suspension to remove any air that may have been entrained during

the mixing process. Air bubbles cause defects in the membrane precursor. Pinholes (small holes left by air bubbles) are the most common defect, and these can lead to cracking which radiates from the pinhole during the sintering (consolidation step). It is therefore essential that entrained air be removed before the spinning. Several techniques are used for the de-gassing process. The simplest technique is the partial vacuum accompanied by gentle stirring or agitation. Once the spinning suspension is properly de-gassed, it is ready to be spun into hollow fiber precursors and this is discussed below.

1.12.3 Spinning of Ceramic Hollow Fiber Precursors

Spinning of ceramic hollow fiber precursors can be carried out in a spinning apparatus as shown in **Figure 2**. The hollow fiber precursors are spun through a tube-in-orifice spinneret as shown in the inset of the figure, typically with orifice diameter/inner diameter of the tube of 3.0/1.2 mm. The extrusion rate of the spinning suspension is controlled by the nitrogen pressure and an adjusting valve. The nonsolvent, usually water, is used at room temperature as the internal and external coagulants. The spinneret is arranged such that the nascent fiber precursor can be extruded vertically downward into the coagulation bath. After coagulation (immersion-induced phase inversion), the fiber precursor is guided through the wash bath, and then dried. **Figure 3** shows a typical fiber precursor spun from a suspension containing $La_{1-x}Sr_xCo_{1-y}Fe_yO_{3-\alpha}$ (LSCF) ceramic powders. It can be seen that the precursors are very flexible because of polymeric binders. In spinning of ceramic hollow fiber precursors, there are two important parameters, that is, spinnability and invertability of the powder suspension, which are discussed below.

1.12.3.1 Rheology and Spinnability

In any polymer solutions or particle suspensions, the rheological properties play a key role in controlling the shape-forming behavior [26]. A general observed

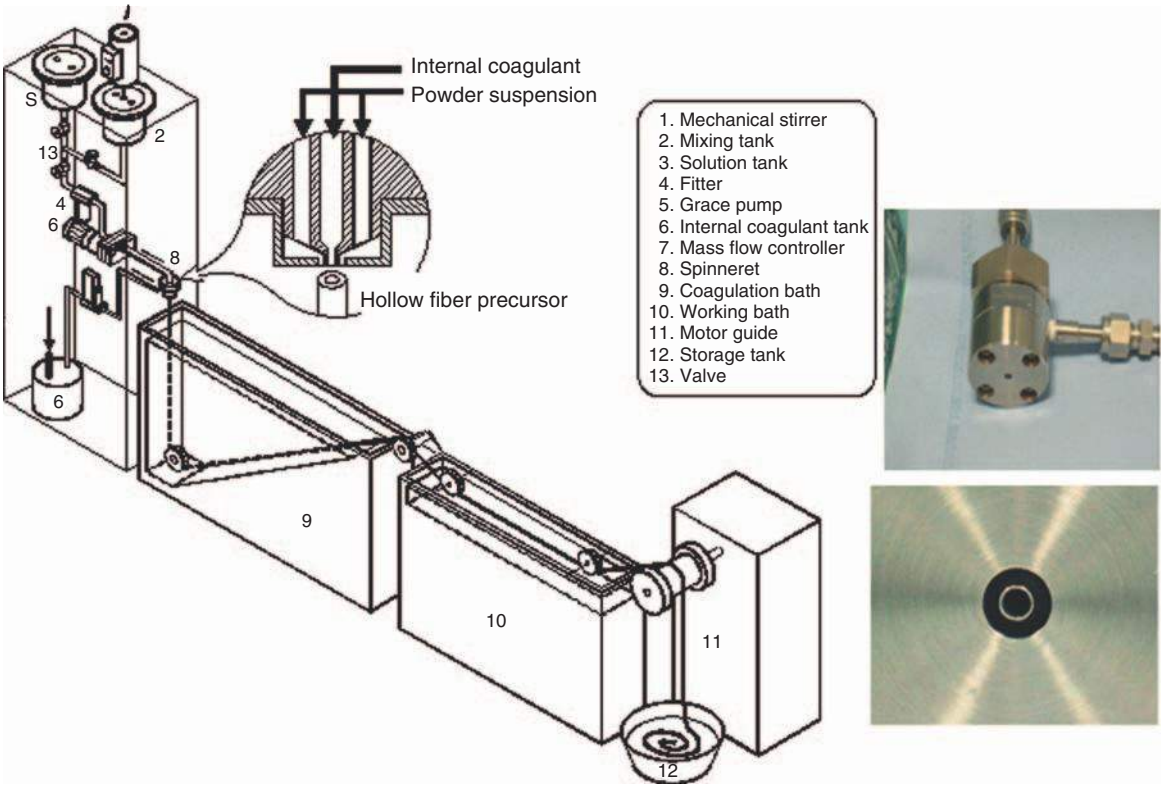

Figure 2 Hollow fiber ceramic membrane spinning apparatus (inset: photograph of a spinneret).

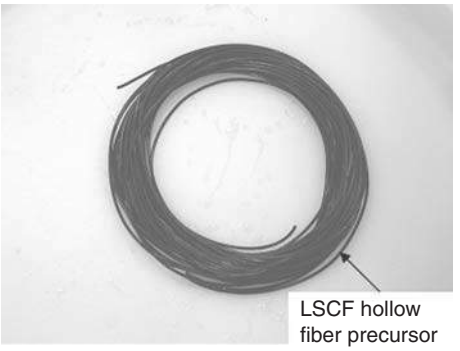

Figure 3 Ceramic hollow fiber precursors (prepared from LSCF).

phenomenon is that the viscosity increases with the increase of polymer contents in polymer solutions and increases with volume fraction of solids and finally ceases to flow at some critical maximum volume fraction of solids in particle suspensions. The rheological behavior of a concentrated suspension of ceramic particles is affected by a number of factors including the particle size distribution, particle shape, volume fraction of solids, and the range and magnitude of the interparticle forces [27–29].

When the viscosity reaches about 10 poise for a polymer solution, the solution becomes spinnable and fibers can be drawn through an orifice [30, 31]. For a suspension containing spherical particles, the relation between the reduced viscosity η_{sp}/c and the particles concentration c, where η_{sp} is the specific viscosity, can be examined. In principle, solutions containing spherical particles follow Einstein's formula [30]:

$$\eta_{sp}/c = k/\rho \tag{1}$$

where k is the constant and ρ the density of the particles.

For a concentrated particle suspension, the best spinnability should be observed when the viscosity behavior is highly shear-thinning but not thixotropic. A very high viscosity suspension is necessary to prevent the drawn fiber from breaking up into droplets. High viscosity is required for a stable fiber formation, which can generally be achieved by increasing the concentration of the suspension or adding some additives.

1.12.3.2 Phase Inversion

The immersion-induced phase inversion technique has been applied in production of polymeric membranes for many years and was first introduced by Loeb and Sourirajan [32]. The membranes produced by them [32] show an asymmetric structure: a dense and thin skin layer ($\sim$25 μm) integrated on a porous support of the same material. The dense skin layer shows a permselective property for separation of salt from sea water and is also thin enough for a high water flux. The porous substrate provides the mechanical stability for the membrane. Since then, this method has been one of the most common methods in the fabrication of polymeric membranes. Conceptually, membrane formation by phase inversion can be described in terms of a three-component system: nonsolvent, solvent, and polymer. After immersing a polymeric solution into a nonsolvent bath, the solvent diffuses out of the polymer solution, while nonsolvent diffuses into the solution. This exchange of solvent and nonsolvent, in general, leads to a change in the polymer solution from a thermodynamically stable state to a metastable or unstable state. Then, liquid–liquid demixing takes place in the solution. When a polymer solution is in contact with a nonsolvent, the solvent in the polymer solution will diffuse out, resulting in the increase of the polymer concentration at the surface. The highly concentrated polymer layer at the surface reduces the exchange speed of the solvent and nonsolvent. Hence, the polymer concentration in the sublayer is lower than the polymer concentration in the surface layer. The further replacement of solvent by nonsolvent results in solidification of the polymer rich phase, and the asymmetric structure of the membrane is thus obtained. For a suspension system containing ceramic particles and polymer binders, the situation may be different. When a high viscous suspension is in contact with a low viscous hydrophilic nonsolvent (normally water), hydrodynamically unstable viscous fingering takes place, resulting in finger-like structures of the membrane substrate. Due to the hydrophilic nature of particles with different sizes, it is logical to postulate that the smaller particles move faster than the larger particles toward the surface during the phase inversion when water is used as a coagulant and the ceramic membranes with a graded structure can be formed using the phase inversion technique as long as the particles with different sizes are used. A similar phenomenon has been observed by Chung *et al.* [33] when preparing mixed-matrix membranes. It, thus, follows that a good control of the ratio of small and large particles in the suspension and the exchange rate of the solvent and nonsolvent may tailor the membrane

structure, which can only be prepared by multiple steps if conventional techniques are used.

1.12.4 Sintering

Sintering processes have been studied for long time and considerable breakthrough in understanding the fundamental aspects of the basic mechanism of sintering of ceramics has been achieved [34, 35]. In sintering the hollow fiber membrane precursors mentioned above, three main steps including presintering, thermolysis, and final sintering are required and are described separately in the following sections.

1.12.4.1 Presintering

Sintering does not commonly begin until the temperature exceeds one-half to two-thirds of the melting temperature of the material. This temperature will be sufficient to cause a significant atomic diffusion for solid-state sintering or a significant diffusion and viscous flow when a liquid phase is present or produced by a chemical reaction. In presintering process, the material changes due to heating prior to sintering mainly include vaporization of chemically combined water from the surface of particles or formed within inorganic phases containing water of crystallization. Therefore, care must be taken to prevent the precursor from cracks or fractures because of the stresses from the pressure of the vapor evolved or from differential thermal expansion of phases. The initial heating may remove any liquid remaining after forming and drying the membrane precursor and any moisture adsorbed from the atmosphere during transporting and setting. The adsorbed moisture may persist in the membrane precursor up to a temperature exceeding 200 °C.

1.12.4.2 Thermolysis

Thermolysis is a process of burning out the organic components such as binder and dispersant. It is an important step prior to the densification on sintering. Incomplete binder removal and uncontrolled thermolysis may introduce membrane defects. These defects may impair the performance of the membrane. With the proper choice of binders for the membrane and controlled heating in an appropriate atmosphere, the membrane precursors should survive thermolysis without deformation, distortion, formation of cracks, or expanded pores. Binder burn-out is very dependent on the composition of the binder material and the composition and flow of the gas surrounding the precursor. It is also highly dependent on the microstructure of the organic, powder, and porosity phases, and dynamic changes in the microstructure as the binder are eliminated. The thermochemistry of the binder and additives, binder concentration, precursor dimension, precursor's configuration, heating rate, and furnace atmosphere may influence the thermolysis behavior. Precursors containing low amounts of a binder will open pore channels sufficiently to allow the transport of vapors and gases between the reaction zone and the membrane surface. The time for thermolysis is controlled by the diffusion length of vapor-phase transport rather than the characteristic dimension of the binder phase. Decomposition and vaporization of the organics will cause an internal gas pressure, which depends on the gas evolution rate, gas permeability, and the precursor size. The gas permeation rate is much lower in dense precursors of very fine particles. In precursors containing a higher organic content, the weight loss is much higher and the time for thermolysis without bubbling is relatively long. Thermolysis of an organic binder in an inert atmosphere such as nitrogen, as it is used when calcining silicon nitride and aluminum nitride ceramics, proceeds differently. Some residual carbon may be expected in the absence of oxygen. The residual carbon commonly removes adsorbed oxygen from surfaces of particles and serves as a sintering aid in carbide nitride ceramics.

1.12.4.3 Final Sintering

Sintering is normally thought to occur in three stages: (1) the initial stage, (2) the intermediate stage, and (3) the final stage [36]. The movements of particles have different features at each stage and attributed to full density, grain coarsening, and pores closing. The temperature program of sintering process would be different for different materials. Rapid densification with limited grain growth occurs at lower temperature followed by rapid grain growth with little densification at higher temperature as shown in **Figure 4**.

There are at least six different mechanisms for mass transport during sintering as listed in **Table 1**. All of these will lead to growth of necks between particles. As shown in **Figure 5**, the neck growth produces bonding between the particles, so the strength of the consolidated powders increases during sintering. Only certain mechanisms, however, lead to shrinkage and densification. Surface diffusion

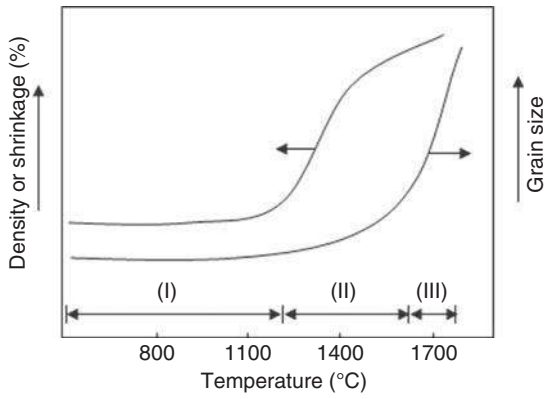

Figure 4 Density or shrinkage and grain size of powder compact as a function of the sintering temperature.

Table 1 Mass transport mechanisms in sintering

Mechanism	*Densification*
Surface diffusion	No
Evaporation–condensation	No
Grain boundary diffusion	Yes
Lattice diffusion	Yes
Viscous flow	Yes
Plastic flow	Yes

is a general transport mechanism that can produce surface smoothing, particle joining, and pore rounding, but it does not produce volume shrinkage. In materials where the vapor pressure is relatively high, sublimation and vapor transport to surfaces of lower vapor pressure also produce these effects. Diffusion along the grain boundaries and diffusion through the lattice of the grains produce both neck growth and volume shrinkage. The mechanisms of bulk viscous flow and plastic deformation may be effective when a wetting liquid is present and when a mechanical pressure is applied, respectively.

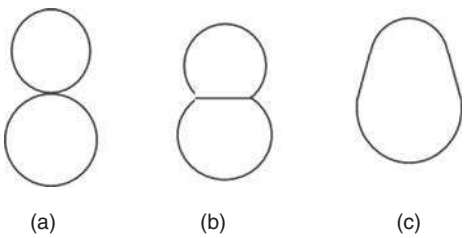

Figure 5 A two-sphere sintering model for a qualitative mechanism for grain growth in porous powder compacts: (a) particles of slightly different size in contact; (b) neck growth by surface diffusion between particles; and (c) grain growth.

1.12.4.4 Grain Growth

The properties of ceramic membrane are strongly dependent on its microstructure. The important microstructural features are the size and shape of the grains, the porosity, the pore size, and the distribution of the pores in the structure. In order to achieve the desired properties during the fabrication of ceramic membranes, the microstructural features must be controlled. For most applications, microstructural control usually means the achievement of maximum possible high density, smallest grain size, and as homogeneous microstructure as possible. There are a few factors that should be understood such as how the grains grow, the interaction between the pores and the moving grain boundaries, and the coarsening process.

Grain growth is the term used to describe the increase in the grain size of a single-phase solid or in the matrix grain size of a solid containing second-phase particles at a sufficiently high temperature. For the conservation of matter, the sum of the individual grain sizes must remain constant; therefore, the increase in the average size of the grains is always accompanied by the disappearance of some grains, usually the smaller ones. In porous solids, both the grains and the pores normally increase in size while decreasing in number. Frequently, the term 'coarsening' is used to describe the progress by which grains and pores grow. The driving force for grain growth is the decrease in grain boundary energy that results from a decrease on the grain boundary area. Grain growth in ceramic membranes is generally divided into two types: normal and abnormal. In the normal grain growth, the grain sizes and shapes fall within a fairly narrow range and the distribution in grain sizes at a later time is fairly similar to that at an early time. In abnormal grain growth, a few large grains develop and grow fairly rapidly at the expense of the smaller ones. The grain size distribution may change significantly.

For stable structures, the grain boundary energy of all grain boundaries should be the same. The edges must meet at an angle of 120°. Taking N as the number of edges, when $N = 6$, grain boundaries are straight. Gains with $N > 6$ have concave boundaries, and those with $N < 6$ have convex boundaries. Since the boundaries migrate toward their center of curvature, grains with $N > 6$ tend to grow while those with $N < 6$ tend to shrink.

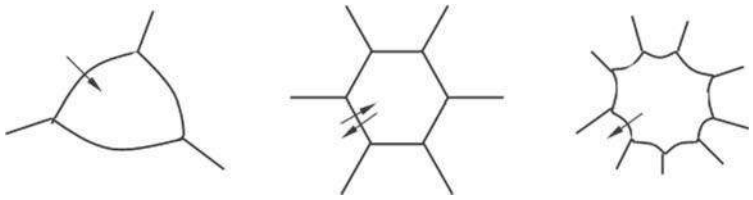

Figure 6 Pore stability in two dimensions for a dihedral of 120°: (a) pore shrinks; (b) metastable; and (c) pore grows.

Following the above description of the grain growth, pore changing in the sintering should be discussed, because it is the direct reflection of membrane performance. For the case of a grain surrounded by other grains, a pore is surrounded by N number of grains. The N is normally called the pore coordination number. The pore has straight sides if $N = 6$, convex sides for $N < 6$, and concave sides for $N > 6$ as shown in **Figure 6**. Since the surface of the pore moves toward its center of curvature, the pore with $N < 6$ will shrink, whereas the one with $N > 6$ will grow. The pore is metastable for $N = 6$, and this number is called the critical pore coordination number N_c. For making a dense membrane, the shrinkable pores are favorable. This pore can be obtained by careful control of the particle packing and the grain growth in the sintering process.

1.12.5 Examples: Preparation of Ceramic Hollow Fiber Membranes

Both dense (nonporous) and porous (ultrafiltration-type) ceramic hollow fiber membranes can be prepared using the method mentioned above. The dense membranes have been prepared using membrane materials of $La_{1-x}Sr_xCo_{1-y}Fe_yO_{3-\alpha}$ (LSCF), $SrCe_{0.95}Yb_{0.05}O_{3-\alpha}$ (SCYb), and YSZ [37–41], while the porous membranes have been prepared using Al_2O_3 [12] and YSZ [42]. Detailed studies in development of these ceramic hollow fiber membranes can be found in literature [37–41], while following example is focused on the YSZ only.

Materials used in the preparation of YSZ hollow fiber membranes were obtained commercially. The powders of 8 mol.% YSZ with particle diameters (d_{50}) of 0.1 and 0.02 μm were purchased from NexTech Materials Ltd., Ohio. Polyethersulfone (PESf) (Radel A300, Ameco Performance, USA) and 1-methyl-2-pyrrolidinone (NMP) (HPLC grade, Sigma-Aldrich) were used as the polymer binder and solvent, respectively. Polyvinyl pyrrolidone (PVP) (Acros Organics) and/or Solsperse 3000 (Noveon Inc., Ohio) were used as the additives. Tap water was used as external coagulant and deionized water was used as internal coagulant. The compositions of the suspensions for the preparation of the YSZ hollow fiber precursors are given in **Table 2**.

1.12.5.1 Morphology

Figure 7 shows the scanning electron microscopy (SEM) photographs of the asymmetric structure of the YSZ hollow fiber membranes prepared from starting suspension S1. As can been seen from **Figures 7(a)** and **7(A)**, the outer and inner diameters (OD/ID) of the hollow fiber precursor and sintered fiber were measured to be 2.0/1.2 mm and 1.3/0.8 mm, respectively. **Figures 7(b)** and **7(B)**, **7(c)** and **7(C)**, and **7(d)** and **7(D)** show the cross-sectional structures, inner surfaces, and outer surfaces of precursor and sintered fiber, respectively. As can be seen, a finger-like structure is formed in the inner

Table 2 Composition of YSZ starting suspensions for spinning precursors

	Composition (wt.%)				
Starting suspension	*YSZ (0.1μm)*	*YSZ (20nm)*	*NMP*	*PESf*	*Additive*
S1	55		38.5	6.0	0.5
S2	45	10	38.5	6.0	0.5
S3	45		47.1	7.3	0.6

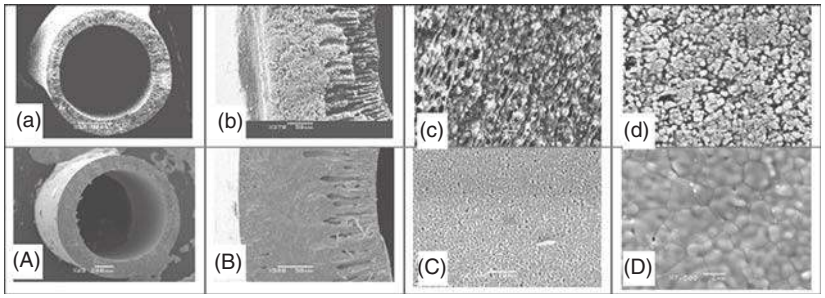

Figure 7 Structures of YSZ hollow fiber membranes prepared using starting suspension of S1: (a–d) before sintering, (A–D) after sintering at 1500 °C for 4 h; (a, A) whole fiber; (b, B) cross section; (c, C) inter surface; and (d, D) outer surface.

surface and is then gradually transformed to a denser sponge-like structure toward outer surface. Such a structure was formed due to the several factors such as viscous fingering phenomenon and movement of particles. During the spinning of the ceramic membrane precursors, pure water was used as the internal coagulant and was immediately in contact with the high viscous suspension. Therefore, the hydrodynamically unstable viscous fingering takes place, resulting in finger-like structures in the inner surface as long as the rate of viscous fingering is greater than that of phase inversion. **Figure 7** also illustrates that the finger-like structure in outer surface of the hollow fiber is much suppressed. This is because during the spinning of the fiber precursors, an air gap longer than 15 cm was used so that the external surface of the nascent fiber experienced solvent evaporation and absorption of water moisture from air, both of which would induce the phase inversion of the polymer binder. Therefore, the viscous fingering may not be possible to establish, as solidification of the outer surface takes place before immersing the nascent fiber into the external coagulation bath.

Figure 7 further illustrates that the asymmetric structure is generally maintained after high temperature sintering. Compared to the inner porous surface of the fiber as shown in **Figure 7(C), Figure 7(D)** depicts the outer surface of the sintered fiber, which is dense and smooth and consists of tightly connected grains with clear boundaries formed during sintering. The size of grains is in the range between 1 and 3 μm, which is grown compared to the initial particle size used in the starting suspension.

The effect of sintering conditions on the membrane surface morphology was further investigated. **Figure 8** illustrates evolution of the surface morphologies at different sintering temperatures between 1000 and 1500 °C, with the sintering time of 4 and 8 h, respectively. It can be seen that porosities of the membrane surface are reduced greatly when the sintering temperature is increased for both the sintering time of 4 and 8 h. At the sintering temperature of 1000 °C, the membrane surface almost remains unchanged as the original morphology formed by the raw particles as shown in **Figure 8(A)**. Obvious changes in the surface morphology take place at about 1200 °C, and the interconnected pores are observed from the membrane surface as shown in **Figures 8(b)** and **8(B)** for both the sintering time of 4 and 8 h. At sintering temperature of 1300 °C, the interconnected pores are still observed from the membrane surface as shown in **Figures 8(c)** and **8(C)**, although their porosities are much reduced compared to those sintered at 1200 °C. When the sintering temperature is increased to 1400 °C, the membrane surface becomes almost fully dense as shown in **Figures 8(d)** and **8(D)**. On further increasing the sintering temperature up to 1500 °C, no obvious pores can be observed; the grain size is increased considerably as shown in **Figures 8(e)** and **8(E)**. Compared to the membrane surfaces sintered at temperatures of 1200 and 1300 °C for 4 h (as shown in **Figures 8(b)** and **8(c)**), the porosity of the membrane surfaces sintered at the same temperatures for 8 h is much smaller (as shown in **Figures 8(B)** and **8(C)**). The above observation indicates that both sintering temperature and sintering duration play important roles for pore elimination of the YSZ hollow fiber membranes. The SEM photographs shown above provide useful information on the sintering behavior of the prepared YSZ hollow fiber membranes.

Based on the particle packing principle, the voids (pores) formed between the particles can be reduced by filling the voids with smaller particles [23]. The effect of smaller particles on the surface morphology

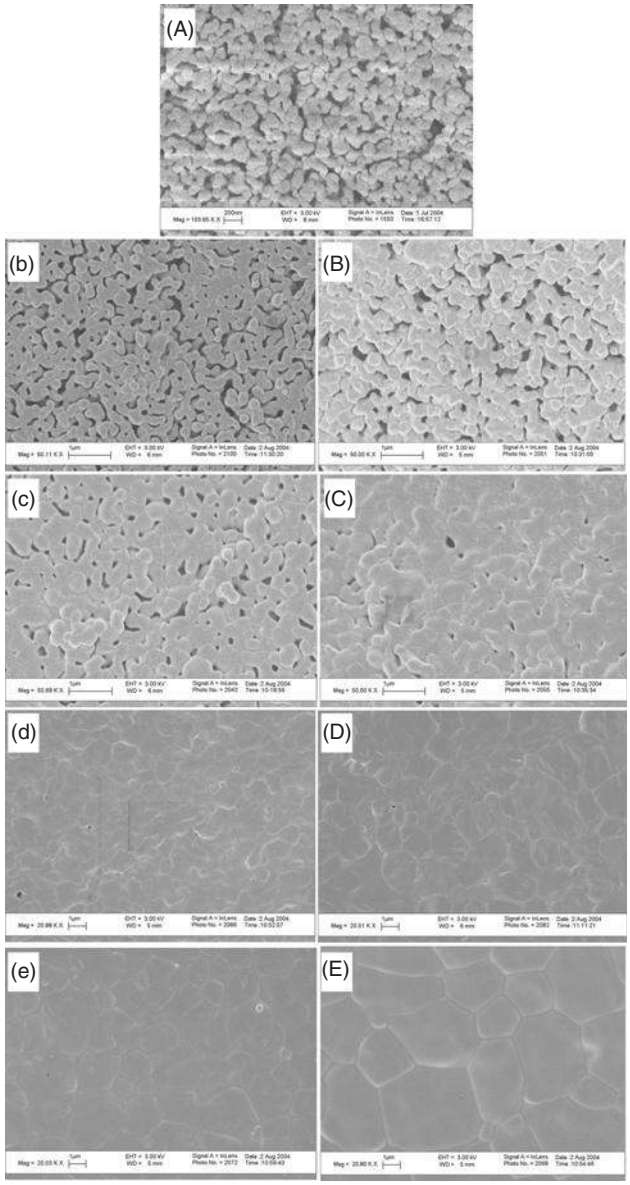

Figure 8 Surface morphology of the YSZ membranes prepared using S1 and sintered at different temperatures for 4 (b–e) and 8 (A–E) h, respectively; (A) 1000 °C, (b, B) 1200 °C, (c, C) 1300 °C, (d, D) 1400 °C, and (e, E) 1500 °C.

of the membranes was investigated using the starting suspension of S2 where 10% of 0.1 μm was replaced by 20 nm particles. SEM observation of the resultant membrane is given in **Figure 9** together with the SEM of the membrane prepared from S3 at the identical sintering condition for comparison purpose. It can be seen that the membrane surface obtained using low powder contents of S3 (45% of 0.1 μm powders) and sintered at 1200 °C is still very porous (**Figure 9**(**a**)). However, the porosity of the YSZ hollow fiber membrane is considerably reduced if a 10% of 20 nm particles is added in the starting suspension as shown in **Figure 9**(**b**). It follows that addition of smaller particles would enhance the densification of the membrane, which would be particularly important if the prepared YSZ membrane is used as a membrane electrolyte for SOFCs.

Figure 10 shows the atomic force microscopy (AFM) images of the outer surface of the prepared YSZ hollow fiber membranes, which are presented in (5 μm × 5 μm) scanning area. It can be seen that the surface of the membranes is not smooth but consists

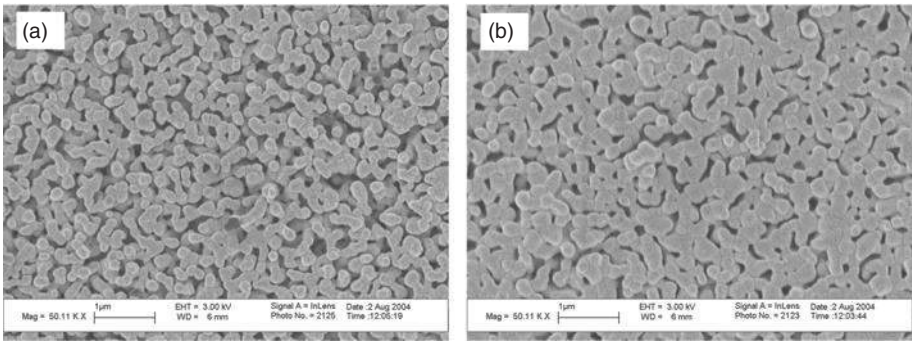

Figure 9 Surface morphology of the YSZ membranes sintered at 1200 °C and prepared from (a) S3 and (b) S2.

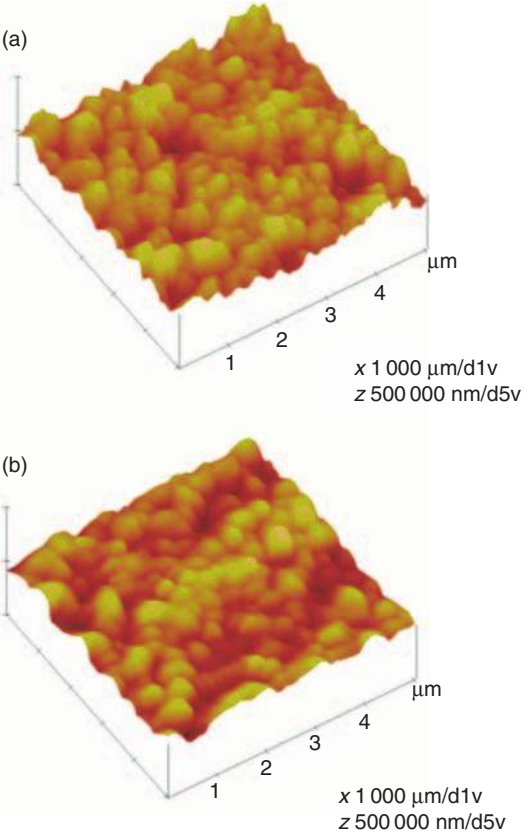

Figure 10 AFM images of the YSZ membranes. S1 sintered at: (a) 1200 °C and (b) 1300 °C.

of a mass of peaks (bright region) and valleys (dark region). Roughness of the membranes (in terms of the mean roughness, Ra) and the root mean square roughness, Rq, are obtained from the AFM images and are summarized in **Table 3**. Obviously, the membrane's roughness may reflect the surface porosity of the membrane because the valleys may probably be the membrane's pores on the surface.

Table 3 Surface roughness data

	Roughness (scan size = 5 µm × 5 µm)	
Membranes of S1 sintered at: °C	*Ra (nm)*	*Rq (nm)*
1200	42.41	54.40
1300	34.06	41.88

1.12.5.2 Permeation Characteristics

A gas permeation test using purified nitrogen as a test gas was carried out to determine the permeation characteristics of the YSZ hollow fiber membrane prepared [42]. Since the membranes prepared using the staring suspension of S3 are very porous and showed remarkable high gas permeance, only the effect of sintering temperature on the gas permeance for the membranes prepared using staring suspensions of S1 and S2 was studied and the results are illustrated in **Figure 11**. As can be seen, the gas permeance for both membranes decreases as sintering temperature is increased. The gas-tight property for the membrane prepared using S1 could be achieved at sintering temperature of 1400 °C, whereas the membrane prepared using S2 still showed a nitrogen permeance of 10.6×10^{-7} mol m^{-2} Pa^{-1} s^{-1} at same sintering condition and could not be gas-tight unless the sintering temperature is increased to 1500 °C. It should be noted that the gas-tight property for the membrane of S1 was further determined using a method developed by Tan *et al.* [43]. The obtained nitrogen permeance is less than 2.0×10^{-10}mol m^{-2}Pa^{-1}s^{-1}, further confirming that the membrane is nonporous and is gas tight.

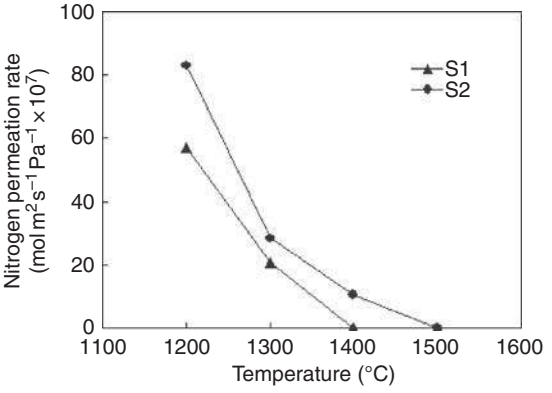

Figure 11 Gas permeance of the YSZ hollow fiber membranes prepared using starting suspensions of S1 and S2 at different sintering temperatures for 8 h.

It should be noted that although similar result to the above was also obtained by Tan *et al.* [12], it is contrary to the analysis conducted by Lu [44] who showed theoretically that the porosity (hence permeance) of a ceramic powder compact reduces when smaller particles are used alone for the preparation of the powder compact. In general, addition of smaller particles would enhance the densification, that is, reduce the volumetric pores. However, it may not be true for the surface pores (through pores for permeation). In this study, an immersion-induced phase-inversion process was employed for spinning of the hollow fiber. As pore formers were added into the spinning suspension, asymmetric structure and surface pores of the fiber precursor were formed during the coagulation process and were altered after the sintering. In view of the complicity of the combined spinning and sintering processes, the relationship between the particle size and the structure of the final resultant membrane remains unclear and needs to be further explored. The presence of the 20 nm particles, however, enhances significantly the mechanical strength of the hollow fibers as shown in Section 1.12.5.3.

Based on the gas permeation data plotted in **Figure 11**, the membranes sintered at temperature less than 1400 °C are porous. Thus, the data were used to calculate the pore-size distribution of the membranes using a method developed by Kong and Li [45]. The purpose of this analysis is obviously to investigate the behavior of surface porosity in the membranes, as it is impossible to obtain membranes with absolutely uniform pore size using the method described above. In fact, the membrane pore size varies according to a pore-size distribution function. Comparison between S1 and S2 at sintering temperatures of 1200 and 1400 °C for 4 h was carried out. The behaviors of the pore-size distribution are shown in **Figure 12** where the x-axis represents the membrane pore radius, r (μm), and the y-axis represents the log–normal distribution function, $g(r)$, as follows [45]:

$$g(r) = \frac{1}{\sqrt{2\pi}r}[\ln(1+\sigma^2)]^{-0.5} \times \exp\left[-\frac{(\ln(r/r_m)(1+\sigma^2)^{0.5})^2}{2\ln(1+\sigma^2)}\right] \quad (2)$$

where r_m is the mean pore radius and σ is the dimensionless standard deviation of the membrane pore

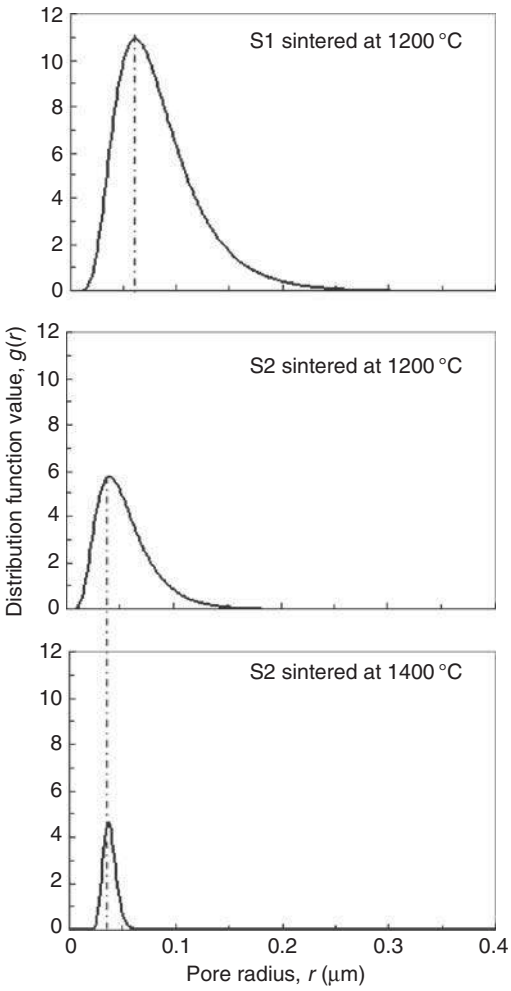

Figure 12 Pore-size distributions of S1 and S2 (sintering time: 4 h).

size. It can be seen that at sintering temperature of 1200 °C, both S1 and S2 show similar distribution profiles with the mean pore radius of 0.07 and 0.03 μm, respectively. When the sintering temperature was increased to 1400 °C, the membrane from S1 achieved gas-tight, suggesting that surface pores were eliminated at this temperature as shown in **Figure 11**, while the membrane prepared from S2 still showed a nitrogen permeance of 10.6×10^{-7} mol m^{-2} Pa^{-1} s^{-1} with a narrow distribution as shown in **Figure 12** compared to that sintered at 1200 °C, although the mean pore size remained unchanged at 0.03 μm. It should be noted that the results on the narrow distribution with increased sintering temperature are uncommon, as the reduction in porosity should normally be at the expense of smaller pores. The reason for such contrary results may be due to the fact that the pores measured using the gas permeation technique are through pores only. Large pores growing due to the increase of sintering temperatures may be dead-end pores and cannot be detected by the gas permeation technique.

The above gas-permeation analysis suggests that both porous and nonporous YSZ hollow fiber membranes can be prepared, depending on the sintering conditions. Pore sizes of the YSZ membrane prepared fall into the pore-size range of untrafiltration membranes. However, the surface porosities of the membranes prepared from S2 and sintered at 1200 and 1400 °C are around 5000 and 300 m^{-1}, respectively. The former is comparable to the polymeric PVDF membranes, whereas the latter is an order of magnitude smaller [46].

1.12.5.3 Mechanical Strength

The effects of particle size on the mechanical strength of YSZ hollow fiber membranes were studied using the suspension containing uniform-sized particles (S1 and S3) and mixed-sized particles (S2). The bending strength of YSZ hollow fiber membranes is plotted against the various sintering temperatures (from 1200 to 1500 °C) and sintering duration (30 min, 4 h, and 8 h). The effects of sintering temperature on the fiber mechanical strength are illustrated in **Figure 13**. A mild improvement in the membrane mechanical strength was observed for the membrane prepared using uniform-sized particle following a short sintering time of 0.5 h (S1 and S3) (**Figure 13(a)**). With increase in the sintering duration, two distinctive membrane strength profiles were unveiled, as shown in **Figures 13(b)** and **13(c)**. Mechanical strength for membrane prepared using the starting suspension of S3 showed little variation despite the increase in sintering duration (**Figures 13(b)** and **13(c)**). On the other hand, the membrane prepared using starting solution S1 exhibited a maximum bending strength at midway sintering temperature for 4 and 8 h sintering duration. An improved mechanical strength was noted for the membrane prepared using mixed-sized particles (S2) following the increase in sintering temperatures for all of the sintering duration studied (**Figures 13(a)–13(c)**).

1.12.5.4 Conclusion

The above experimental results and analyses suggest that both porous and nonporous asymmetric YSZ hollow fiber membranes can be prepared depending on phase inversion parameters and the sintering conditions. A well-designed phase inversion/sintering process coupled with an optimal condition of a starting suspension is the key in obtaining asymmetric hollow fiber membranes with desired permeation characteristics as well as excellent mechanical strength.

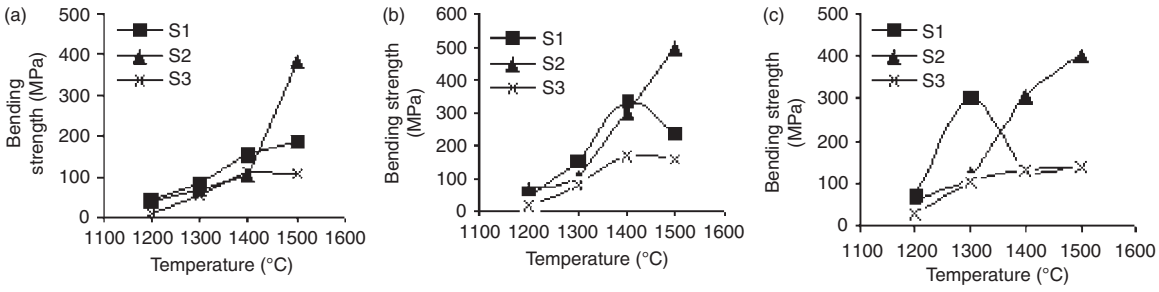

Figure 13 Mechanical strength of the YSZ hollow fiber membranes prepared using different starting suspensions for: (a) 0.5 h; (b) 4 h; and (c) 8 h.

1.12.6 Possible Applications

As illustrated above, both dense (nonporous) or porous (ultrafiltration-type) hollow fiber ceramic membranes have been prepared using a phase inversion technique. The dense membranes prepared using membrane materials of LSCF, SCYb, and YSZ have been used in applications in air separation, oxidative and nonoxidative methane coupling reactions, and SOFCs [6, 7, 43, 47], while the porous membrane prepared from Al_2O_3 has been employed in solvent distillation [8]. Detailed studies can be found elsewhere [6–8, 43, 47] and some key data on these applications are discussed below.

1.12.6.1 LSCF for Oxygen Separation

LSCF is a mixed oxygen conducting ceramic showing an appreciable oxygen permeation at high temperatures (>800 °C). **Figure 14** shows the results for air separation using asymmetric LSCF membranes prepared. As expected, the oxygen permeation rate increases with increase the argon or the air feed flow rate because the driving force for oxygen permeation is increased. The figure also indicates that the experimental results are better than the theoretical ones except for the operating temperature of 900 °C. This difference resulted from the membrane's porous inner surface, which provides more areas for the surface exchange reactions [43]. As the temperature increases, the bulk diffusion plays an increasingly important role in oxygen permeation and gradually becomes the controlling step. As a result, the enhancement of oxygen permeation due to the better membrane surface structure is diminished as the operating temperature increases; hence, the experimental results are close to the theoretical ones (900 °C), which were developed assuming bulk diffusion is the rate-limiting step [48]. **Figure 15** compares the results between the lumen-feed operation and the shell-feed operation at 850 °C. As can be seen, the experimental data for the lumen-feed operation are much inferior than those obtained from the shell-feed operation, further confirming that the downstream surface exchange kinetics play the important role in oxygen permeation at low operating temperatures.

1.12.6.2 LSCF for Oxidative Coupling of Methane

Figure 16 illustrates the experimental results of oxidative coupling of methane (OCM) [6] in an asymmetric LSCF module at different temperatures. As shown, the methane conversion rate increases with increasing operating temperature. The C_2 yield increases with temperature, but remains relatively constant at temperature above 925 °C because the C_2 selectivity is decreased noticeably. Nevertheless, it is still much higher than that obtained in the disk-shaped membrane reactor (only 1–2%). On the other hand, the observed maximum C_2 selectivity in the membrane reactor is only 22.4% (70% in the disk membrane reactor) [49]. This may be attributed to the better structures of the hollow fiber membranes as described above, which favors oxygen permeation. As can be seen from **Figure 16(b)**, the oxygen concentration in the methane stream is always above 3% in the whole temperature range, indicating that the oxygen permeated from the air stream is more than that required for the OCM reaction. It, thus, follows that the OCM reaction in the membrane reactor is not controlled by the oxygen permeation, but by the reaction activity of the LSCF membranes.

Effect of methane feed flow rate on the OCM in the membrane reactor is shown in **Figure 17**. It can

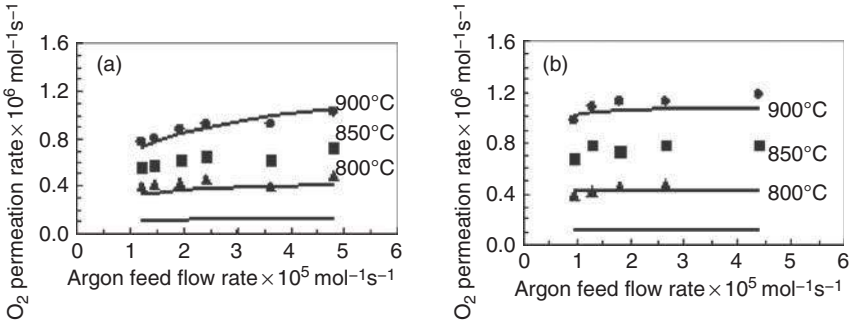

Figure 14 Oxygen permeation rate as a function of the gas flow rate for the shell-feed and cocurrent operating mode: (a) air feed flow rate is constant and (b) argon feed flow rate is constant (experimental data: ▲, 800 °C; ■, 850 °C; ●, 900 °C).

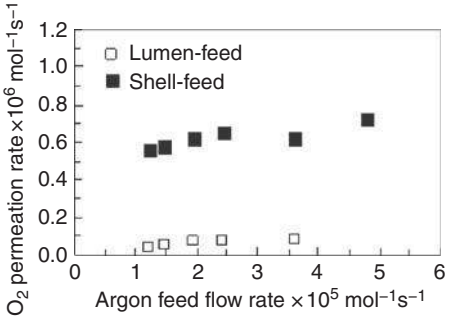

Figure 15 Comparison between lumen- and shell-feed modes.

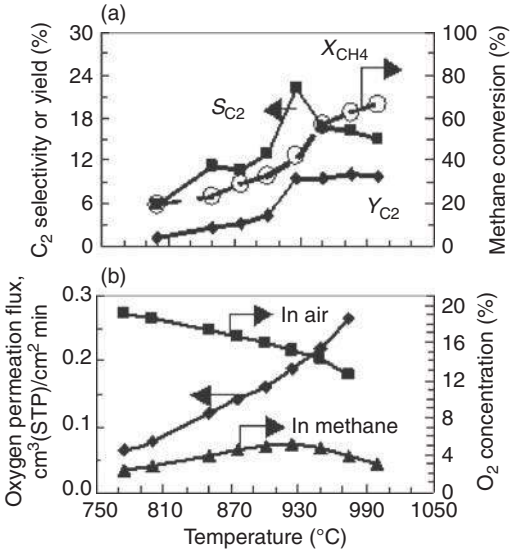

Figure 16 Effect of temperature on OCM in the LSCF (Air feed = 22.96 and methane feed = 17.2 cm^3(STP)min^{-1}).

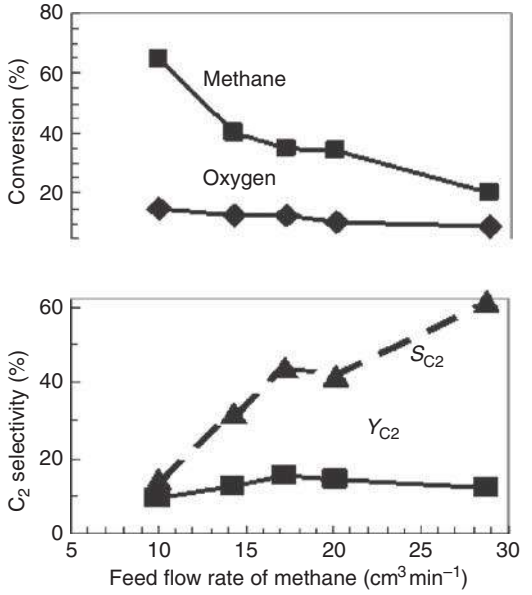

Figure 17 Effect of methane feed flow rate on OCM in the LSCF (air feed = 32.9 cm^3(STP) min^{-1}, T = 950 °C.

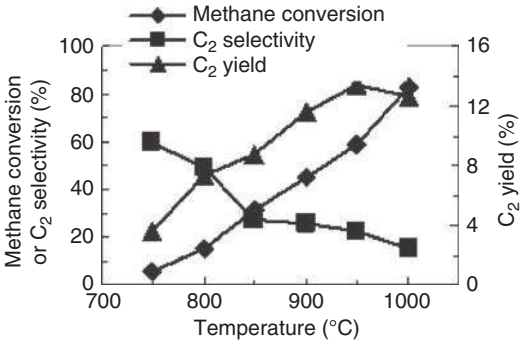

Figure 18 Methane coupling in the SCYb.

be seen that both the methane and oxygen conversions decrease with increasing the methane feed flow rate. This suggests that more oxygen reacts with methane into C_2 instead of carbon oxides as the flow rate of CH_4–Ar is increased. The C_2 selectivity increases with the methane feed flow rate due to the decrease in the local oxygen concentration. The maximum C_2 yield in the membrane reactor can reach 15.3%, which is much higher than the fixed bed reactor and the disk-shaped membrane reactor.

1.12.6.3 SCYb for Non-OCM

SCYb is a proton-hole conducting ceramics and its asymmetric hollow fiber membranes prepared can be used for nonoxidative methane coupling reactions [47]. The results from the SCYb membrane reactor are shown in **Figure 18**. As shown, the methane conversion increases with increasing temperature until it reaches 82.7% at 1000 °C. However, the C_2 selectivity is gradually decreased as the temperature increases, the maximum of which is only about 60% at 750 °C. This value is much less than that expected for no oxygen taking part in the methane compartment. The reasons for this include the further conversion of C_2 products into higher hydrocarbons, as shown in **Figure 19**. Furthermore, SCYb also exhibits some oxygen ion conduction at a very high temperature, leading to oxygen permeation into the methane side that reduces the C_2 selectivity. As a result, only 15.3% of the C_2 selectivity is achieved at

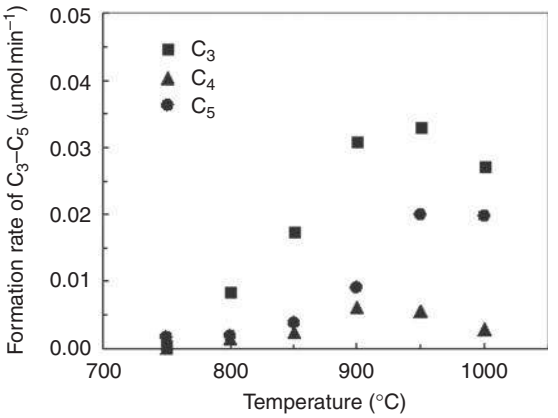

Figure 19 C_3–C_5 formation rates as a function of temperature (feed flow rate of methane stream = 4.3 cm^3 (STP) min^{-1}, methane feed concentration = 9.22%, air feed flow rate = 40 cm^3 (STP) min^{-1}).

the temperature of 1000 °C. Nevertheless, the C_2 yield still increases from 3.6% to 13.4% as the temperature increases from 750 to 950 °C, but then is decreased with further increasing temperature. Although the obtained C_2 yield is still much lower than the desired industrially expected value, which was usually considered to be above 30%, it is much higher than most literature values obtained in disk-shaped membranes.

1.12.6.4 Solvent Distillation

Distillation is considered as a workhorse in petrochemical industries for decades [8]. The process consumes a large amount of energy and is one of the major costs in oil production [50]. Distillation is usually carried out in conventional tray columns, whereas the use of packed columns has been increasing recently because they hold many advantages, such as lower pressure drop, lower liquid hold-up, and higher efficiency. [51]. The improvement of the distillation column efficiency largely resulted from continuous development in column packings. So far, the fourth generation of random packings and the improved structured packings are considered to be the state-of-the-art ones, giving a height of transfer unit (HTU) as low as 0.3 m [52].

Recently, a new concept of column packings has been proposed by Zhang and Cussler [53] who first explored the feasibility of distillation using a hollow fibers membrane contactor. Such a device is very similar to a conventional packed column but the only difference is that the column is packed with a large number of hollow fibers. In the operation, the vapor flows on the shell side of the hollow fibers, whereas the liquid flows on the tube side. The mass transfer then takes place through the membranes without any mixing of the two phases, driven by the concentration gradient of the components. Since there is no direct contact between vapor and liquid, almost all hydrodynamic problems, normally found in conventional devices, such as flooding, loading, weeping, and foaming, are eliminated. In addition, one of the most important advantages is the large surface area per unit volume, provided by small diameter hollow fibers, which can improve the efficiency of the column. Many more advantages of hollow fiber membrane contactors have been elaborated in details by Gabelman and Hwang [54].

A few binary solvent pairs have been used in the studies of distillation by a hollow fiber membrane contactor. Zhang and Cussler [53] employed a contactor packed with polyether membranes coated with polydimethylsiloxane to distil the mixture of isopropanol and water. The module was able to operate above the flooding limit of conventional columns with the HTU as low as 11 cm. A similar work to separate methanol from deionized water was carried out by Zhang *et al.* [55] who showed even a smaller HTU of 8 cm, implying the high efficiency of the system. The distillation of methanol and ethanol was studied by Chung *et al.* [56] using different types of coated and porous membranes. The results showed no significant difference in the separation by different membranes used. This new distillation concept was also applied to the olefin/paraffin separation, operated at room temperature. High capacity and excellent mass transfer efficiency were reported [57].

Although the above studies [53–57] have been carried out to prove the concept of distillation in hollow fiber-packed columns, the investigators have realized that this new type of packing is still far from practical applications. The main problem is the limited stability of the polymeric membranes which obviously cannot withstand high temperature and harsh chemical conditions usually found in industrial distillation. So, the distillation columns developed are limited to the operation at low temperature and to separate weak solvents only. Koonaphapdeelert *et al.* [8] recently attempted in developing hollow fiber membranes from alumina, which is the same material used to produce commercial random packings for the solvent distillation. It is expected that the novel ceramic hollow fiber can provide better

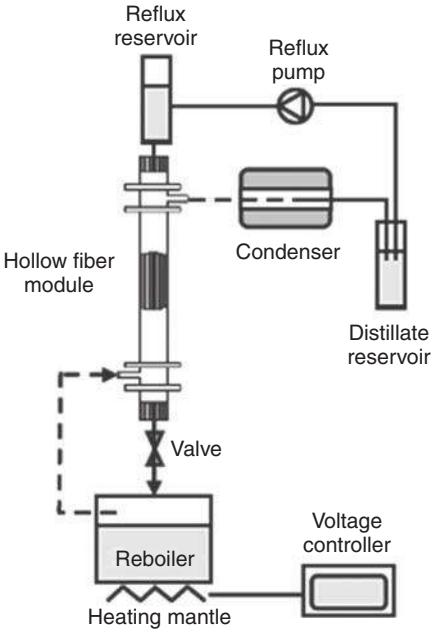

Figure 20 Schematic setup of a hollow fiber membrane contactor of solvent distillation.

thermal and chemical stability compared to the polymeric ones and, thus, has been tested in distillation of a strong solvent pair of the benzene–toluene system. The distillation experiment was conducted in an apparatus shown in **Figure 20**. The experimental results indicated that the system has high capacity which allows the distillation to be operated many times above the flooding limit of conventional equipments. This feature is the function of the hollow fiber membranes that separate the vapor from the liquid phases. Therefore, there is no hydrodynamic problem such as flooding and loading, commonly found in conventional distillation columns. Moreover, the efficiency of separation, measured by the HTU, is very high compared to conventional equipments. The lowest HTU found is as small as 10.1 cm. This means the membrane contactor is not only more productive, but also more efficient [8].

1.12.6.5 Solid Oxide Fuel Cells

SOFCs, known for their high (up to 80%) chemical to electrical conversion efficiencies, their versatility in fuel intake (hydrogen, natural gas, methanol and other petroleum products, etc.), and their relatively environmentally benign operation, have a high market potential, but are not yet mass produced, because of outstanding technological and economic issues. Wei and Li [7] addressed these problems by establishing the feasibility of, and developing, a novel design of SOFC, fabricated using hollow fibers, thereby increasing the specific surface area of electrodes, increasing the power output per unit volume/mass, facilitating sealing at high temperatures, and decreasing costs. The electrolyte in the hollow fiber configuration was fabricated primarily by a combined phase inversion/sintering technique; it consists of a thin dense layer, with integrated porous sublayers on one side. The porous sublayers were deposited with anode and cathode materials, to produce a single hollow fiber SOFC, bundles of which can be assembled subsequently into an SOFC stack.

Figure 21 shows a SEM and a digital photo of a single hollow fiber SOFC based on YSZ electrolyte membrane [7]. The porous inner surface provides a higher surface area for Ni loading and the dense layer at outer wall provides good ionic conductivity. The YSZ hollow fiber electrolyte membrane displayed a good mechanical strength and excellent gas-tight property. After coating with cathode (LSCF/YSZ) and anode (Ni) as shown in **Figure 21(b)**, the hollow fiber SOFC was tested for its electrochemical performance and the results are given in **Figure 22**. As can be seen, in most tests, the relation between power densities and current densities tends to be parabolic, but these densities take different time to reach their maximum value. The maximum power density was about $0.018\,W\,cm^{-2}$ at 800 °C with an effective operating length of 4 cm (constant temperature zone of the furnace). The power densities of electrolyte supported SOFCs are relatively lower than other types of supported SOFCs. Although the thicker electrolyte would provide good mechanical strength, one of the disadvantages of the electrolyte-supported SOFCs is the higher electrolyte ohmic loss which causes a lower power density. Therefore, it is important to minimize the thickness of electrolyte and, at the same time, to maintain sufficient mechanical strength. Apart from minimizing the ohmic loss, Hatchwell *et al.* [58] demonstrated that improvement of interconnection between electrode and electrolyte could also enhance power densities. It is, therefore, envisaged that the power density can be considerably improved once the structure of the electrolyte supported is optimally designed.

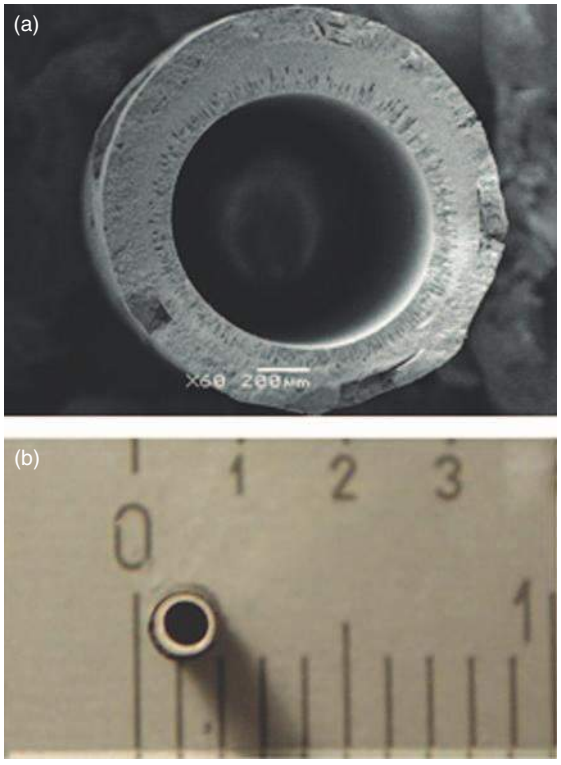

Figure 21 Overall views: (a) SEM image of hollow fiber SOFC and (b) digital picture of hollow fiber SOFC.

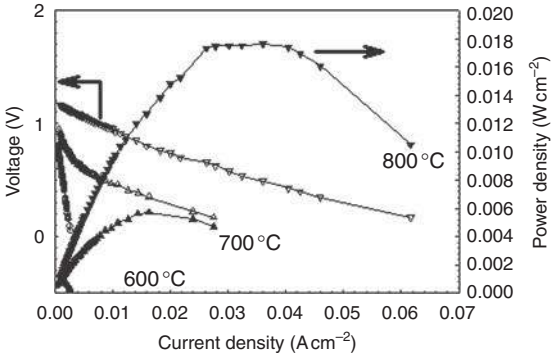

Figure 22 The performance of hollow fiber solid oxide fuel cell showing voltage and power density as function of current density and temperature. The cell consisted of air, (LSCF+YSZ)/YSZ/Ni, H_2 at a constant gas flow rate of 20 cm^3 (STP) min^{-1}.

1.12.7 Conclusions

The recent development on ceramic hollow fiber membranes and its applications in separations and catalytic chemical reactions have been presented. These membranes have shown promising applications in oxygen separation, methane coupling reation, solvent distillation, and solid oxide fuel cells. Although some progresses have been achieved, there is still a long way to go before the successful applications of these ceramic hollow fiber membranes in separation and reaction can be achieved in industrial scales. Significant achievements in this new research area would become feasible if joint efforts were established from both material scientists and chemical engineers.

References

[1] Guizard, C., Ayral, A., Julbe, A. *Desalination* **2002**, *147*(1–3), 275–280.
[2] Lee, S., Cho, J. *Desalination* **2004**, *160*(3), 223–232.
[3] Weber, R., Chmiel, H., Mavrov, V. *Desalination* **2003**, *157*(1–3), 113–125.
[4] Terry, P. A., Anderson, M., Tejedor, I. *J. Porous Mater.* **1999**, *6*(4), 267–274.
[5] Takehira, K., Sakai, N., Shimomura, J., *et al. Appl. Catal. A: Gen.* **2004**, *277*(1–2), 209–217.
[6] Tan, X. Y., Li, K. *Ind. Eng. Chem. Res.* **2006**, *45*(1), 142–149.
[7] Wei, C. C., Li, K. *Ind. Eng. Chem. Res.* **2008**, *47*(5), 1506–1512.

[8] Koonaphapdeelert, S., Tan, X., Wu, Z., Li, K. *J. Membr. Sci.* **2008**, *314*(1–2), 58–66.
[9] Koonaphapdeelert, S., Li, K. *Desalination* **2006**, *200*(1–3), 581–583.
[10] Julbe, A., Farrusseng, D., Guizard, C. *J. Membr. Sci.* **2001**, *181*(1), 3–20.
[11] Way, J. D., Roberts, D. L. *Sep. Sci. Technol.* **1992**, *27*(1), 29–41.
[12] Tan, X., Liu, S., Li, K. *J. Membr. Sci.* **2001**, *188*(1), 87–95.
[13] Liu, S. M., Li, K., Hughes, R. *Mater. Res. Bull.* **2004**, *39*(1), 119–133.
[14] Liu, S. M., Li, K., Hughes, R. *Ceram. Int.* **2003**, *29*(8), 875–881.
[15] Liu, S. M., Li, K. *J. Membr. Sci.* **2003**, *218*(1–2), 269–277.
[16] Liu, S. M., Tan, X. Y., Li, K., Hughes, R. *J. Membr. Sci.* **2001**, *193*(2), 249–260.
[17] Hsieh, H. P. *Inorganic Membranes for Separation and Reaction*; Elsevier: Amsterdam, 1996; pp 23–86.
[18] Tan, X. Y., Liu, S. M., Li, K. *J. Membr. Sci.* **2001**, *188*(1), 87–95.
[19] Bideau, D., Troadec, J. P. *J. Phys. C: Solid State Phys.* **1984**, *17*(28), L731–L735.
[20] Visscher, W. M., Bolsterl, M. *Nature* **1972**, *239*(5374), 504–507.
[21] Kausch, H. H., Fesko, D. G., Tschoegl, N. W. *J. Colloid Interface Sci.* **1971**, *37*(3), 603–611.
[22] Starr, T. L. *Am. Ceram. Soc. Bull.* **1986**, *65*(9), 1293–1296.
[23] Rahaman, M. N. *Ceramic Processing and Sintering*; Marcel Dekker: New York, 1995; pp 265–279.
[24] Lee, B. I., Rives, J. P. *Colloids Surf.* **1991**, *56*, 25–43.
[25] Mikeska, K. R., Cannon, W. R. Dispersants for Tape Casting Barium Titanate. In *Advances in Ceramics*; Mangels, J. A., Messing, G. L. Eds.; The American Ceramic Society: Westerville, 1984; pp 164–183.
[26] Bergstrom, L. *J. Am. Ceram. Soc.* **1996**, *79*(12), 3033–3040.
[27] Bergstrom, L. Rheology of Concentrated Suspensions. In *Surface and Colloid Chemistry in Advanced Ceramics Processing*; Pugh, R. J., Bergstorm, L., Eds.; Marcel Dekker: New York, 1994; pp 193–244.
[28] Bergstrom, L. Surface and Colloid Chemistry. In *Advanced Ceramic Processing*; Pugh, P. J., Bergstrom, L., Eds.; Marcel Dekker: New York, 1994; pp 193–224.
[29] Kitano, T., Kataoka, T., Shirota, T. *Rheol. Acta* **1981**, *20*(2), 207–209.
[30] Sakka, S. Rheology of Sols in Sol–Gel Processing. In *Sol–Gel Science and Technology*; Aegerter, M. A., Jafelicci, M., Souza, D. F., Zanotto, E. D.; Eds.; World Scientific Publisher: Singapore, 1989; pp 76–103.
[31] Deshmukh, S. P., Li, K. *J. Membr. Sci.* **1998**, *150*(1), 75–85.
[32] Loeb, S., Sourirajan, S. Sea Water Demineralization by Means of an Osmotic Membrane. In *Saline Water Conversion – II, Advances in Chemistry*; Gould, R. F., Ed.; American Chemical Society: Washington, DC, 1963; pp 117–132.
[33] Chung, T. S., Jiang, L. Y., Li, Y., Tin, P. S., Kulprathipanja, S. *NAMS 2006,* 2006; Chicago, IL, USA.
[34] Richardson, D. W. *Morden Ceramic Engineering*; Marcel Dekker: New York, 1992.
[35] Binner, J. G. P. *Advanced Ceramic Processing and Technology*; Noyes Publications: Park Ridge, NJ, 1990.
[36] Reed, J. S. *Principles of Ceramic Processing*, 2nd edn.; Wiley: New York, 1995.
[37] Tan, X. Y., Liu, Y. T., Li, K. *Ind. Eng. Chem. Res.* **2005**, *44*(1), 61–66.
[38] Liu, L. H., Tan, X. Y., Liu, S. M. *J. Am. Ceram. Soc.* **2006**, *89*(3), 1156–1159.
[39] Liu, Y., Tan, X., Li, K. *J. Membr. Sci.* **2006**, *283*(1–2), 380–385.
[40] Liu, Y. T., Tan, X. Y., Li, K. *AIChE J.* **2006**, *52*(4), 1577–1585.
[41] Liu, Y., Chen, O. Y., Wei, C. C., Li, K. *Desalination* **2006**, *199*(1–3), 360–362.
[42] Wei, C. C., Chen, O. Y., Liu, Y., Li, K. *J. Membr. Sci.* **2008**, *320*(1–2), 191–197.
[43] Tan, X., Liu, Y., Li, K. *AIChE J.* **2005**, *51*(7), 1991–2000.
[44] Lu, G. Q. M. *J. Mater. Process. Technol.* **1996**, *59*(4), 297–302.
[45] Kong, J., Li, K. *J. Membr. Sci.* **2001**, *182*(1–2), 271–281.
[46] Li, K., Kong, J., Tan, X. *Chem. Eng. Sci.* **2000**, *55*(23), 5579–5588.
[47] Liu, Y. T., Tan, X. Y., Li, K. *Ind. Eng. Chem. Res.* **2006**, *45*(11), 3782–3790.
[48] Xu, S. J., Thomson, W. J. *Chem. Eng. Sci.* **1999**, *54*(17), 3839–3850.
[49] ten Elshof, J. E., Bouwmeester, H. J. M., Verweij, H. *Appl. Catal. A: Gen.* **1995**, *130*, 195–212.
[50] Mix, T. W., Dweck, J. S., Weinberg, M., Armstrong, R. C. *Chem. Eng. Prog.* **1978**, *74*(4), 49–55.
[51] Sinnott, R. K. *Coulson & Richardson's Chemical Engineering*; Pergamon: Oxford, 1993.
[52] Schultes, M. *Trans. IChemE A* **2003**, *81*(A1), 48–57.
[53] Zhang, G., Cussler, E. L. *AIChE J.* **2003**, *49*(9), 2344–2351.
[54] Gabelman, A., Hwang, S.-T. *J. Membr. Sci.* **1999**, *159*(1–2), 61–106.
[55] Zhang, G., Lin, L., Meng, Q., Xu, Y. *Sep. Purif. Technol.* **2007**, *56*(2), 143–149.
[56] Chung, J. B., DeRocher, J. P., Cussler, E. L. *J. Membr. Sci.* **2005**, *257*(1–2), 3–10.
[57] Yang, D., Barbero, R. S., Devlin, D. J., Cussler, E. L., Colling, C. W., Carrera, M. E. *J. Membr. Sci.* **2006**, *279*(1–2), 61–69.
[58] Hatchwell, C. E., Sammes, N. M., Kendall, K. *J. Power Source* **1998**, *70*(1), 85–90.

Biographical Sketch

Kang Li is currently a professor of chemical engineering at Imperial College London. His present research interests are in preparation and characterization of polymeric and inorganic hollow fiber membranes, fluid separations using membranes, and membrane reactors for energy application and CO_2 capture. Professor Li serves as an editor of *Thermopedia* for the Separation Technologies Subject Area and as an editorial board member of Advances in Environmental Research and Development (AERD). He is a chartered engineer and a fellow of the Institution of Chemical Engineers and is a council member of European Membrane Society.

This page intentionally left blank

1.13 Preparation of Carbon Membranes for Gas Separation

A F Ismail, Universiti Teknologi Malaysia, Johor, Malaysia

Glossary

Membrane physical aging Change in the transport properties of a membrane over a period of time due to physical–chemical–structural alterations.

Membrane posttreatment Process carried out on a membrane after its essential structure has been formed but prior to its exposure to an actual feed stream.

Membrane pretreatment Process carried out on a membrane after the completion of its preparation and prior to its use in a separation application.

Precursor A substance from which another substance is formed.

Pyrolisis The chemical decomposition or transformation of a compound caused by heat that occurs spontaneously at high enough temperatures.

Sintering A method where the material is heated in a sintering furnace below its melting point until particles adhere to each other.

Thermosetting polymer Polymer material that irreversibly cures.

Turbostratic structure Structure consisting of sheets of carbon atoms that are haphazardly folded or crumpled together.

1.13.1 Introduction

Polymeric membrane materials were recognized as a promising tool for gas separation. However, these polymer membranes are deficient to meet the requirements of membrane technology, especially operation at high temperature and harsh environment. In the recent decades, membrane materials based on carbon material have served as an alternative candidate for various types of gas separations. Carbon membrane is an inorganic membrane, which can be fabricated by using thermosetting polymer. The concept of carbon membrane or film for gas separation can be traced back to the early 1970s. These membranes were prepared by compressed nonporous graphited carbon into a plug (hence the name 'carbon membrane') [1]. Carbon membranes have excellent thermal and chemical stability, compared to polymeric membranes commercially available in the industry. Besides, they can also attain

high selectivity without losing the productivity and thus surpass the upper bound limit of polymeric membranes [2–5]. At present, carbon membrane materials have become more important in the new era of membrane technology for gas separation and liquid–liquid phase separation due to their higher selectivity and permeability, stability and high-temperature operations, and well-defined stable pore structure. In addition, unlike polymeric membranes, carbon membranes are usually durable and capable of withstanding adverse and rigorous environment because of their high thermal and chemical resistance.

Carbon membranes demonstrate attractive characteristics among molecular sieving materials such as excellent shape selectivity for planar molecule and high hydrophobicity. It is, however, more feasible to form carbon molecular sieve membranes (CMSMs) [6–8]. These characteristics have stimulated interest among researchers in the early 1980s to further investigate the separation characteristics of these membranes. Recently, carbon membranes have also been found to be very useful materials in the preparation of nanofiltration [9], pervaporation [10], and microfiltration membrane [11]. This chapter addresses the important aspects of carbon membrane fabrication in view of preparing a good-quality carbon membrane for gas separation processes.

1.13.2 Preparation and Characterization of Carbon Membrane

As shown in **Figure 1**, carbon membranes can be generally classified into two groups: unsupported membrane (flat, hollow fiber, and capillary tube) and supported membrane (flat and tubular). However, it has proved to be difficult to prepare these membranes in a defect-free, continuous form. The preparation of carbon membranes is not an easy task because it involves a number of important steps that must be carefully controlled and optimized. The success of preparing carbon membranes depends on the experience and knowledge during, in particular, the preparation of polymeric precursor or membranes, because good-quality membranes in turn ensure good-quality carbon membranes. The preparation of carbon membranes can be divided into five steps: precursor material selection, polymeric membrane preparation, pretreatment of the precursor, pyrolysis process, and posttreatment of pyrolyzed membranes. The understanding and manipulation of the preparation conditions and variables will provide an opportunity to further enhance the performance of carbon membranes. In this section, the general steps for carbon membrane preparation are outlined and some guidelines in the preparation of high-performance carbon membrane are discussed in detail. The typical characterization of the carbon membrane for gas separation, including gas permeation measurement, structural and morphological characterization using Fourier transform infrared spectroscopy (FTIR), X-ray diffraction (XRD), and scanning electron microscopy (SEM), is also addressed briefly.

The synthesis of a membrane should be cheap and simple in order to establish an economically viable separation unit. Another demand is that the membrane should have a long-time stable flux, that is, no significant aging. Furthermore, it should have sufficient mechanical strength to overcome fabrication as well as oscillating process conditions, such as variations in pressure and temperature. **Figure 2** shows the flow diagram of the general carbon membrane fabrication process. Discussion of the individual steps is given in the following section.

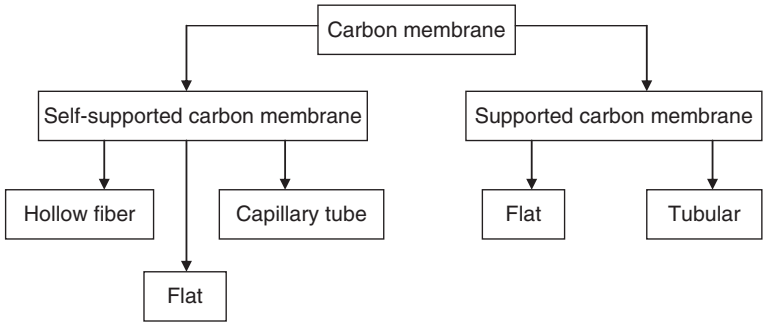

Figure 1 Classification and configuration of carbon membrane [12].

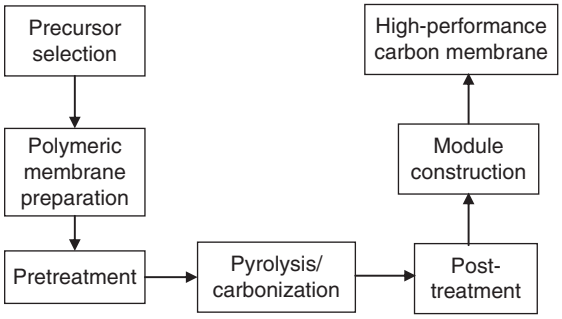

Figure 2 The fabrication steps of carbon membranes [12].

1.13.2.1 Selection of Precursors

The properties of the polymeric precursor are probably one of the most important factors to be considered in order to produce a good-quality carbon membrane. Because of the variety of polymeric precursors available for carbon membrane preparation, the most suitable characteristics for carbon membrane must be first identified for preparing successful carbon membranes as pyrolysis of different precursors may result in different types of carbon membranes. Through practical experience and knowledge gained during carbon membrane preparation exercises, two most dominant characteristics have been identified: thermoresistance and good polymer molecular distribution at molecular levels. These characteristics allow further fine-tuning of membrane morphology as well as separation performance optimization. In addition to high-temperature resistance, a thermosetting polymer neither liquefies nor softens during any stage of pyrolysis [13]. Suitable precursor materials for carbon membrane preparation will not cause any pore holes or cracks to appear following pyrolysis [14]. Based on practical experience, another important reason why polymer precursor is preferred is because of the resultant membrane prepared with fewer impurities as compared to activated carbon precursor [15].

Recently, different polymeric materials, such as polyimides (PIs) and the PI-like polymers [16–24], phenolic resins [25–27], polyfurfuryl alcohol (PFA) [28], phenol formaldehyde [29, 30], and cellulose [31], have been considered for polymeric precursors. **Figure 3** shows the chemical structure of precursor PIs that is normally used for the preparation of carbon membranes. These polymeric precursors demonstrated thermosetting property so that they do not melt when heated and thus retain the structure shape during heating and pyrolysis. Among the possible polymeric precursors, PIs are considered as

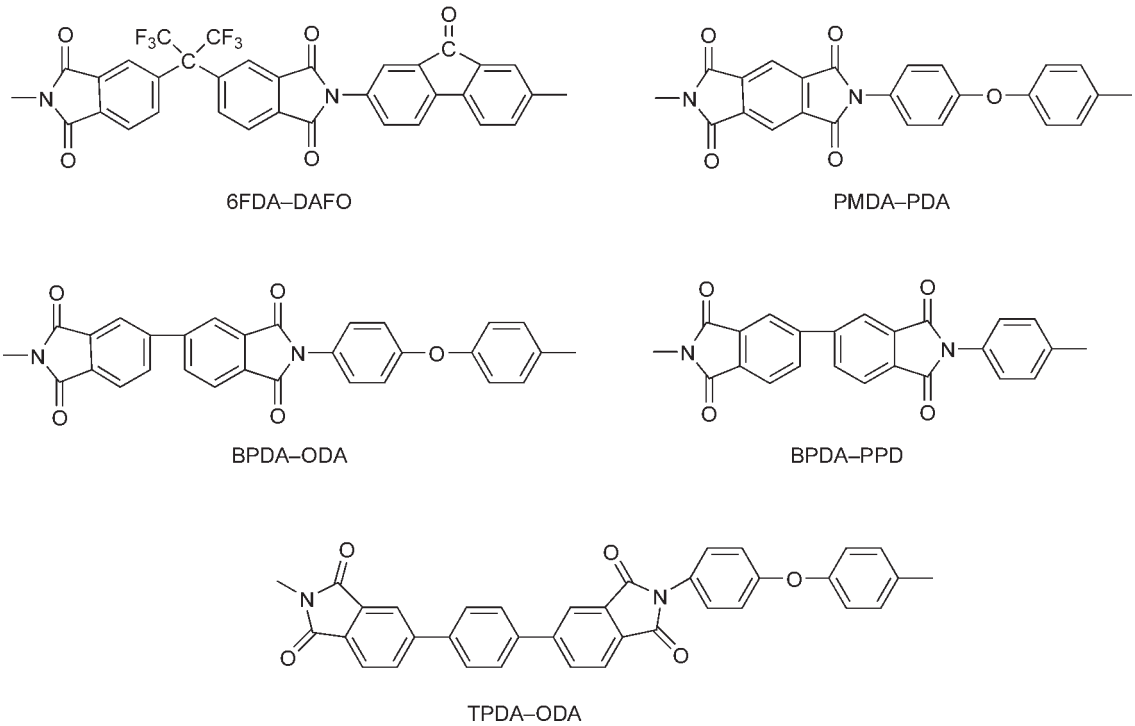

Figure 3 Chemical structure of some polyimide (PI) precursors.

one of the most intensive precursors that have been studied for carbon membranes, due to their excellent physical properties and the tunable chemical composition utilizing different molecular structures composed of dianhydride and diamine monomers. The most common commercial PI used for preparing carbon membrane is Kapton (DuPont^{TM}) PI. Carbon molecular sieve (CMS) film with homogeneous fine pores and without cracks or large pores normally can be achieved by carbonizing Kapton film at 800 °C [32] Kapton PI was also carbonized in the form of a capillary membrane which can retain high gas selectivity even at high temperatures [33]. The membrane exhibited a selectivity of 2000 for He/N_2 at 0 °C and 170 at 250 °C. Recently obtained Kapton-PI-based carbon membranes have shown that the selectivity for O_2/N_2, CO_2/CH_4, and CO_2/N_2 is 4, 16, and 9, respectively, at 25 °C [34].

1.13.2.2 Pretreatment of Precursor Membranes

Prior to the pyrolysis, the polymeric membranes are often subjected to pretreatments in order to ensure the stability and the preservation of the precursor structure during pyrolysis. In fact, carbon membrane of good quality, in terms of stability and separation performance, can be produced using specific pretreatments. In general, pretreatment methods are divided into physical and chemical methods. Physical pretreatment consists of stretching of the precursor, whereas chemical pretreatments involve the treatment of the polymeric precursor with some chemical reagents. Sometimes, the precursor is subjected to more than one pretreatment method to achieve desired properties in a carbon membrane.

Oxidation is considered very important as it has substantial influence on the performance of the resulting carbon membrane. Oxidation pretreatment can be applied at very different ranges of thermal soak times, depending largely on the precursor uses. In all cases, the treatment contributes to the stabilization of the asymmetric structure of the precursor and provides sufficient dimensional stability to withstand the high temperatures of the pyrolysis steps. Stretching is a pretreatment that is usually applied to the hollow fiber precursor. This technique is adapted from the fabrication of carbon fiber and is sometimes referred to as post-spinning. An ideal post-spinning modification scheme would allow the removal of surface defects, attenuation of variations in filament diameter, and an enhanced retention of molecular orientation prior to the heat treatment [32].

Pretreatment of the membrane with certain chemicals can provide enhanced uniformity of the pore system formed during pyrolysis. Hydrazine, dimethylformamide (DMF), hydrochloric acid, and ammonium chloride are commonly used for chemical pretreatment [2]. During the chemical pretreatment, the membrane is fully immersed in the appropriate solution and followed by washing and drying before it is subjected to heat treatment. In certain cases, it has also been proved that it may be advantageous to evacuate the pores of the membrane by applying a low air pressure, and subsequently fill them with nitrogen gas at normal pressure prior to pretreatment with a chemical reagent. In this manner, the membranes with higher carbon content can be obtained [33].

1.13.2.3 Pyrolysis of Carbon Membrane

One of the distinctive features of CMSMs is the pyrolysis conditions of a polymeric precursor. When a given precursor and its pyrolysis conditions are properly selected, a desirable micropore size and shape can be tailored. Tailoring of correct pore size is important for the fabrication of high-performance carbon membranes with optimal balance between selectivity and permeability that is suitable for various gas separations. It demands a good understanding of the optimum production conduction with respect to the pyrolysis condition. Through the rigorous control of the pyrolysis conditions, such as temperature, heating rate, atmosphere and thermal soaking time, gas flow rate, pressure and concentration, and pre/posttreatment conditions, the pore aperture can be nearly continuously tuned, so that a membrane module can be specifically designed for gas separation and reaction [34].

Carbon membranes are prepared by the pyrolysis of polymeric precursors. Pyrolysis is usually carried out at temperatures of 500–1000 °C under vacuum or inert atmosphere. This process removes most of the heteroatoms originally present in the polymeric macromolecules, leaving behind a stiff and cross-linked carbon matrix with an amorphous porous structure created by the evolution of gaseous products and the rearrangement of the molecular structure of the starting polymeric precursor during the pyrolysis. **Figures 4** and **5** show the typical hollow fiber membranes with the substructure and skin layer morphology produced under different pyrolysis temperatures.

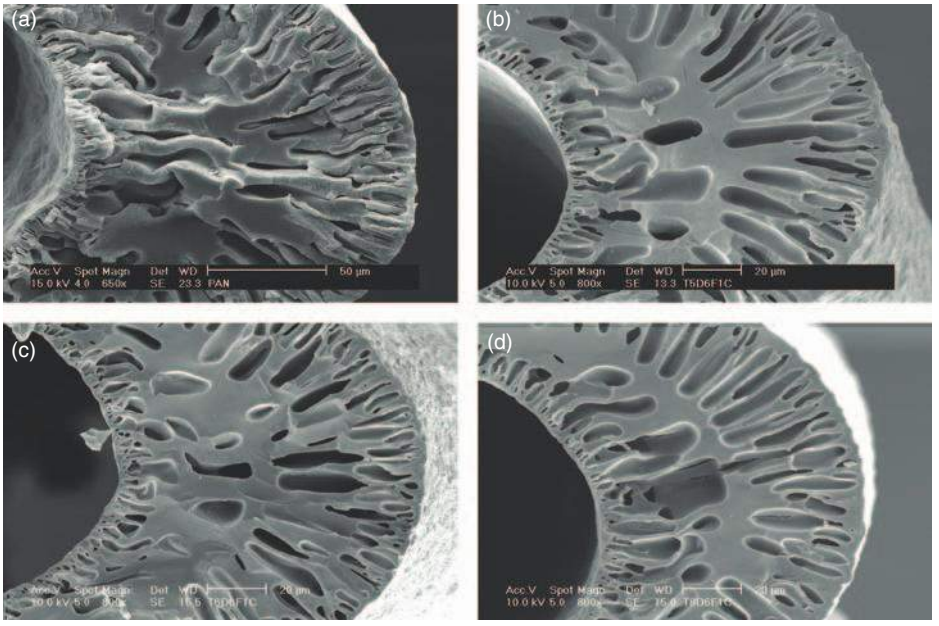

Figure 4 Structural change of the typical hollow fiber membrane substructure at different pyrolysis temperatures: (a) polyacrylonitrile (PAN) membrane; (b) $T_{pyrolysis} = 500\,^{\circ}C$; (c) $T_{pyrolysis} = 600\,^{\circ}C$; and (d) $T_{pyrolysis} = 800\,^{\circ}C$ [35].

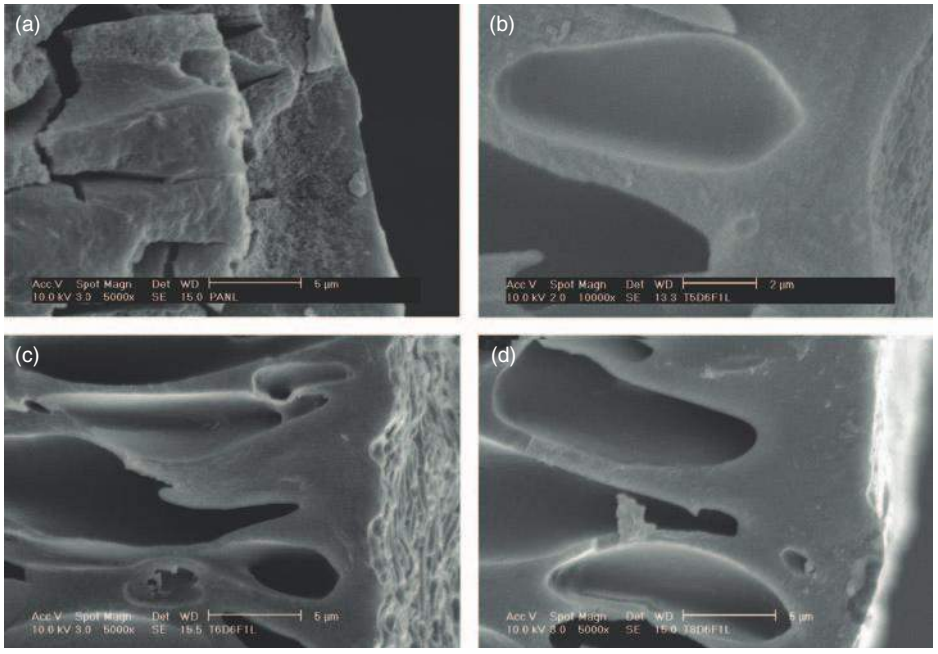

Figure 5 Structural changes of the typical hollow fiber membrane skin layer at different pyrolysis temperatures: (a) polyacrylonitrile (PAN) membrane; (b) $T_{pyrolysis} = 500\,^{\circ}C$; (c) $T_{pyrolysis} = 600\,^{\circ}C$; and (d) $T_{pyrolysis} = 800\,^{\circ}C$ [35].

The transport properties of the carbon membrane are dependent on its porous structure and pore-size distribution [16]. During pyrolysis, amorphous carbon material is created and exhibits a distribution of micropore dimensions with only a short-range order of specific pore sizes and also pores larger than the ultramicropores. These larger pores that connect the ultramicropores are required to exhibit molecular sieving properties and therefore allow high gas separation productivities. The pore system of carbon

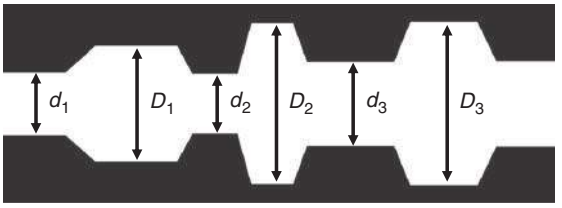

Figure 6 Idealized structure of a pore in a carbon material [37]. Reproduced with permission from Ismail, A. F., Li, K. From Polymeric Precursors to Hollow Fiber Carbon and Ceramic Membranes. In *Inorganic Membranes: Synthesis, Characterization and Applications*; Mallada, R., Menéndez, M., Eds.; Membrane Science and Technology Series; Elsevier: Amsterdam, 2008; Vol. 13, pp 81–119.

membranes is generally nonhomogeneous, as it is comprised of relatively wide openings with a few constrictions [36]. The pores may vary in size, shape, and degree of connectivity, strongly depending on the nature of the polymeric precursor and the conditions of pyrolysis. **Figure 6** depicts an idealized structure of a pore in a carbon material. The pore mouth *d* often referred as an ultramicropore (<10 Å) that allows molecular sieving of the penetrating molecules, meanwhile the larger micropores, *D* of the material (6–20 Å), may allow the diffusion of gas molecules to occur through the carbon material [18, 25, 35, 37]. Therefore, it is believed that a properly prepared carbon material is able to simultaneously demonstrate the ability to perform molecular sieving and also allow a considerably high flux of the penetrating molecules through the material [38].

Pyrolysis temperature has a remarkable influence on the carbon membrane properties in terms of the membrane structure, separation performance (permeability and selectivity), and the transport mechanism for gas separation [23]. The increase in pyrolysis temperature will normally lead to a carbon membrane with higher compactness, a more turbostratic structure, higher crystallinity and density, and smaller average interplanar spacing between the graphite layers of the carbon [39]. In general, an increase in the pyrolysis temperature will give rise to a decrease in gas permeability and an increase in selectivity.

1.13.2.4 Posttreatment of Carbon Membrane

Upon pyrolysis, polymeric membranes are transformed into carbon membranes with varying degrees of porosity, structure, and separation properties that depend to an extent on the pyrolysis conditions. In some cases, it is found to be an advantage that the pore dimensions and distribution in a carbon membrane can be finely adjusted by a simple thermochemical treatment to meet different separation needs and objectives [3]. Therefore, various posttreatment methods have been applied to meet the desired pore structure and separation properties of carbon membranes, and, at the same time, repair the defects and cracks that exist in the carbon membrane.

Post-oxidation or activation is one of the commonly used posttreatments to alter the pore structure of carbon membranes. Typically, when a membrane is exposed to an oxidizing atmosphere after the pyrolysis, the pore size and micropore volume are increased [13, 33, 40, 41], but the pore-size distribution is not broadened. Different activation temperatures and residence times have been applied to obtain desired pore structures in different materials [14, 42, 47].

The selectivity of a carbon membrane may be increased through the introduction of organic species into the pore system of the carbon membrane and their pyrolytic decomposition, that is, chemical vapor deposition (CVD) [40, 41, 48, 49]. In general, to manufacture CMSs, the inherent pore structure of the carbonaceous precursor is initially tailored into a suitable pore size range by controlling the thermal pretreatment, followed by a final adjustment of the pore apertures by CVD. Commonly, the CVD of carbon onto a carbon membrane may bring about three distinct results: homogeneous deposition, adlayer deposition, and in-layer deposition.

Aside from CVD, post-pyrolysis is another treatment that can be used to decrease membrane pore size. Typically, post-pyrolysis is applied after post-oxidation in order to recover from an excessive pore enlargement. Sometimes post-oxidation and post-pyrolysis are repeated several times until the desired pore size distribution is achieved. However, this treatment is rarely used, because the first pyrolysis step at high temperature produces small pores efficiently due to the shrinkage of the carbon structure.

1.13.3 Preparation of Self-Supported Carbon Membrane

1.13.3.1 Flat-Sheet Membrane

In general, the properties of porous carbon structures and the gas permeation properties of CMS membranes based on aromatic PI depend upon the

thermal decomposition profile of this organic precursor. During pyrolysis, the various gases evolved originate from the polymer precursors, and are produced over a wide temperature range. The initial microporous carbon structures are converted into ordered selective turbostratic carbon structures depending on the pyrolysis temperature. Kim *et al.* [23] studied the effect of pyrolysis condition, that is, pyrolysis temperature and dwell time toward the structure of precursor and the resulting porous CMSM using benzophenone tetracarboxylic dianhydride (BTDA)–4,4′-oxydianiline (ODA) PI as precursor. The pyrolysis temperature was increased from 300 to 550, 700, and 800 °C using a heating rate of 3 °C min^{-1}, and then the samples were kept at their respective final temperatures for a period of 30 min. When compared with the FTIR spectra of the CMSMs pyrolyzed at temperatures of 550, 700, and 800 °C, the intensities of the characteristic absorption bands (C═O and aromatic C═C) existed in PI precursor disappeared at higher pyrolysis temperature due to their evolution during the pyrolysis as shown is **Figure 7**.

Thermogravimetric analysis (TGA) showed that PI was thermally stable up to a temperature of 500 °C, and showed rapid thermal decomposition in the temperature range of 550–700 °C. The weight loss due to the evolution of a large volume of gas (e.g., CH_4, CO_2, or CO) in the temperature range 500–600 °C resulted in a cleavage of the benzene ring present in PI precursor. On the other hand, the lower weight loss in the temperature range of 700–1000 °C is mostly caused by the evolution of a small volume of gas (e.g., CH_4, H_2, or N_2), which leads to an incremental densification of the porous CMSMs. Wide-angle X-ray diffraction (WAXD) spectra with different pyrolysis temperatures provided comparative values of the degree of packing of the microporous carbon structures, meanwhile the average *d*-spacing values are extensively used as a relative comparison of the amorphous materials and infer some information of the interplanar distance on microstructure. As illustrated in **Figure 8**, the shift of the broad peak with the increasing pyrolysis temperature to the higher diffraction angle indicated that the interlayer spacings between neighboring planes decreased with increasing pyrolysis temperature. Consequently, a reduction in average *d*-spacing values of the microporous carbon structures was observed, which in turn suggested the formation of an increased degree of packing of the microporous carbon domains in the carbon matrices.

1.13.3.2 Hollow Fiber Membrane

Barbosa-Coutinho *et al.* [50] prepared hollow fiber membranes by wet spinning of polyetherimide

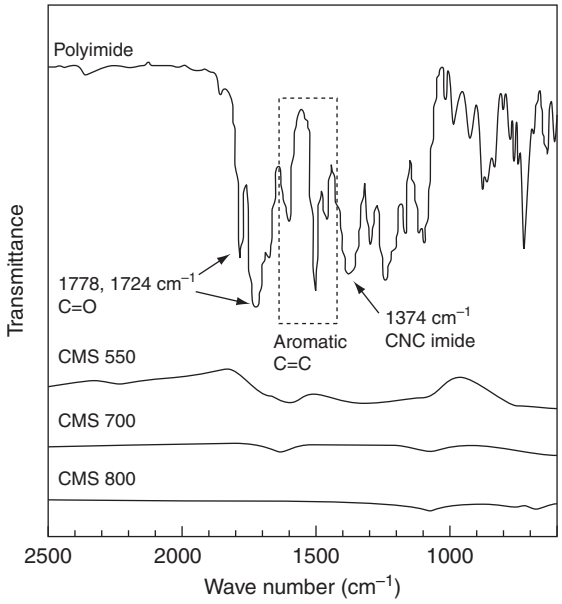

Figure 7 Fourier transform infrared spectroscopy (FTIR) spectra of polyimide precursor and carbon molecular sieve (CMS) membranes pyrolyzed at 550, 700, and 800 °C [23].

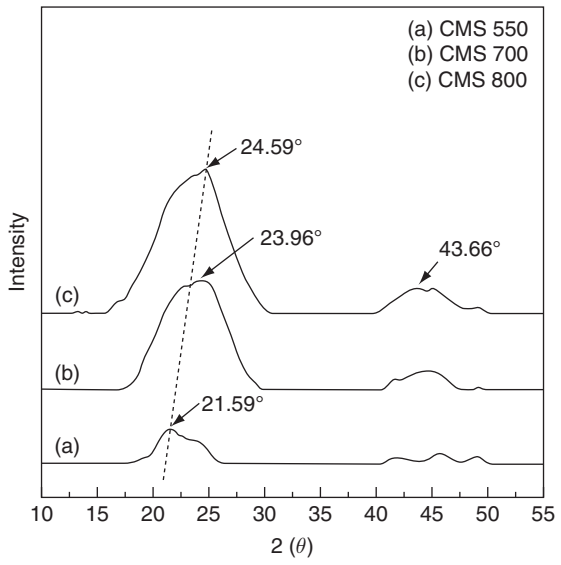

Figure 8 Wide-angle X-ray diffraction (WAXD) of carbon molecular sieve (CMS) membranes pyrolyzed by the incremental pyrolysis temperatures [23].

(PEI) and polyvinylpyrrolidone (PVP) solution in *N*-methyl-2-pyrrolidone (NMP) solution. Prior to the pyrolysis under inert atmosphere, the polymeric membrane is first subjected to treatment at mild temperature under an oxidizing atmosphere forming chemical groups, such as hydroxyl and carbonyl that promote stabilization of the membrane for further high-temperature treatment. During this thermostabilization process, oxygenated groups are incorporated in the polymeric chain. Therefore, the overall weight change during stabilization is small due to the introduction of these groups. During stabilization up to 400 °C, few volatile compounds were observed, mainly CO_2 and H_2O, which indicated the degradation of polymer and oxidation of the polymer chain. The investigation of pyrolysis conditions pointed to a notable influence exerted by the oxidation with an optimum temperature (400 °C) where the oxidation is more effective, as observed by less deformation and irregularities of the fibers. An extended oxidation period with a heating rate of 3 °C min^{-1} or lower contributed to the completion of the oxidation reaction and it was more effective in obtaining stabilized fibers. However, the prolonged pyrolysis reduced the mechanical stability of the hollow fibers, evidenced by the morphology analysis. During pyrolysis at a temperature above 400 °C, there was large volatile evolution. First, CO, CO_2, and H_2O were released, between 420 and 680 °C, evidencing cross-linking reactions and some degradation reactions. At higher temperatures (450–800 °C), hydrogen exit was detected, indicating the forming of a graphite-like structure.

The pyrolysis atmosphere has a strong influence on the carbon membrane properties and must be properly tailored in order to prevent undesired burn-off and chemical damage of the membrane precursor during pyrolysis. In a recent research, Favvas *et al.* [51] reported the effects of the pyrolysis atmosphere on the structure and properties of the membranes produced in both inert and reactive conditions by using carbon hollow fiber membranes based on commercially available Matrimid 5218 precursor. Pyrolysis was carried out in three different gas atmospheres to produce three different types of carbon fibers: in N_2, in N_2 saturated with H_2O, and in CO_2 as pyrolysis media. Upon heating up to 650 °C, higher mass loss was observed for the membranes pyrolyzed in reactive atmosphere (water saturated N_2 and CO_2) within the pyrolysis oven compared to that in the inert atmosphere. The results suggested that higher degree of polymer decomposition and subsequent carbon oxidation have taken place. After the pyrolysis process, a number of macrovoids can still be observed on the fiber wall, which can be attributed to the effect of the pyrolysis procedure on the polymeric hollow fiber precursor. Conversely, the nitrogen adsorption properties of the membranes implied that the environment of the pyrolysis process is important to the micropore volume. It is noticed that oxidized agents reduce the resistance of the skin surface to thermal degradation, resulting in an increase in micropore volume. Carbon dioxide is a more effective oxidizing agent than water, possibly due to the increased hydrophobicity of the carbon surface during the high-temperature treatment. **Figure 9** demonstrates the SEM micrographs of the polymer precursor and the resulting hollow fiber structure pyrolyzed under CO_2 atmosphere.

1.13.4 Preparation of Supported Membrane

Supported carbon membranes for gas separation are commonly prepared by coating a suitable polymeric

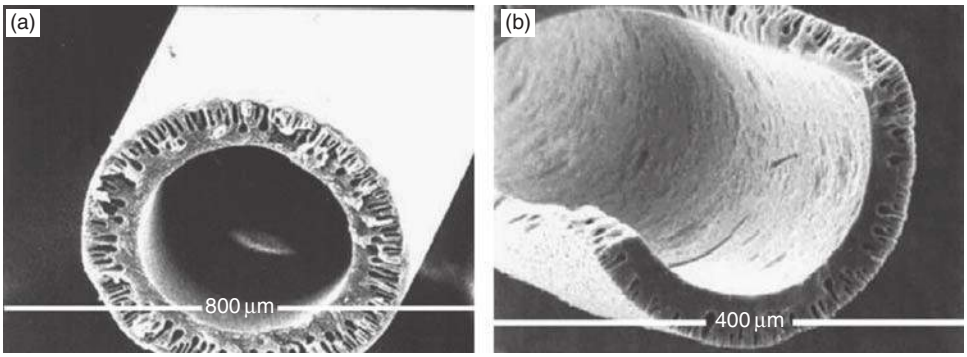

Figure 9 Scanning electron microscopy (SEM) micrographs of (a) polymer precursor and (b) the resulting hollow fiber structure pyrolyzed under CO_2 atmosphere [51].

solution on porous carbon, ceramic, or metal supports and subsequent carbonization under controlled conditions. Supported membranes are known to be suitable for large-scale industrial application. One limit to incorporating carbon membranes into actual application is the preparation process. In order to obtain a defect-free carbon membrane, the coating–pyrolysis cycle must be repeated several times, which needs time and special care.

In a very recent study, Lee *et al.* [52] studied the effect of the post-oxidation conditions, such as oxidation temperature and time, on the gas permeation properties of poly(2,6-dimethyl-1,4-phenylene oxide) (PPO)-derived carbon membranes. The carbon membranes were prepared by coating a thin film on a macroporous tubular ceramic support. The supported membrane was pyrolyzed at 700 °C in argon atmosphere and then followed by the air oxidation of carbon membranes at different oxidation conditions. In the weight loss of the air oxidation of the pyrolyzed carbon membrane, the total weight loss measured to 4% even when the temperature increased up to 400 °C during the air oxidation of the pyrolyzed carbon material. The small weight loss indicates that this supported pyrolyzed PPO carbon membrane has a good thermal stability even in the air oxidation. Characterization of the pore properties in the nitrogen adsorption measurement showed that the pore characteristic values (**Table 1**), such as pore size, pore volume, and surface area, were increased by the post-oxidation, and hence contributed to the enhancement of gas separation performance, particularly for gas species with a large molecular size.

For selection of membrane support, criteria such as the cost, flexibility for large-scale applications, and adherence between the substrate and the top membrane layer need to be considered. In order to prepare a low-cost supported membrane that shows high gas separation performance, coal-based carbon tubes can serve as a suitable candidate [28]. C/CMS composite membranes from PFA were prepared, in which porous coal-based carbon tubes were used as support. The pyrolysis temperature has substantial effect on the gas separation performance of C/CMS composite membranes. It has been identified that higher final pyrolysis temperature leads to carbon membranes having an amorphous carbon structure with ultramicropores. These are more compact and more selective and also show a decreased *d*-spacing of the interlayers of graphitic carbon planes as observed in XRD patterns. These structural changes in turn reduce the permeability but at the same time greatly enhance the selectivity of gas molecules.

1.13.4.1 Fabrication of Membrane Module

To ensure the efficiency of a membrane process in a given application, the geometry of the membrane and the manner it is installed in a suitable device are important [53]. The selection of a membrane module is mainly determined by economic considerations. However, the cheapest configuration is not always the best choice because the type of application, and thus the functionality of a module, is also an important factor to be taken into account [54]. Many researchers have proposed a wide variety of modules for carbon membrane production. The most challenging task that must be considered while fabricating these modules is the poor mechanical stability of carbon membranes [55].

For commercial applications of membranes, it is preferable to fabricate a module with an asymmetric structure and capillary or hollow fiber configurations in order to increase the rate of permeation of the products [55]. As summarized in **Table 2**, the characteristics of modules, in terms of production, cost, maintenance, and efficiency, must be considered in all system designs [53, 57, 58]. **Figures 10** and **11** illustrate the modules for hollow fiber configuration fabricated by Ismail and David [59, 60] and Koros and coworkers [61], respectively.

Table 1 Pore properties of carbon materials based on the nitrogen adsorption

Carbon material	*Pore volume (BET) ($cm^3 g^{-1}$)*	*Surface area (BET) ($m^2 g^{-1}$)*	*Representative pore diameter (HK method) (nm)*
M700	26.82	116.8	0.43
M700-MOx-400	80.35	349.7	0.54

Reproduced with permission from Lee, H. J., Suda, H., Haraya, K. *Sep. Purif. Technol*. **2008**, *59*, 190–196.

Table 2 Important considerations for the preparation of membrane module

Category	*Characteristic*
Production	High surface area (i.e., packing density – the ability of a material to form stable membranes) The ease of formation of a given configuration and structure Nature of polymer/membrane
Cost Low investment cost	Low operating cost Low fouling tendency
MaintenanceEase to clean	
	Membrane replacement is possible
Efficiency	The extent of use The nature of the desired separation Structural strength

Reproduced with permission from Saufi, S. M., Ismail, A. F. *Carbon* **2004**, *42*, 241–259.

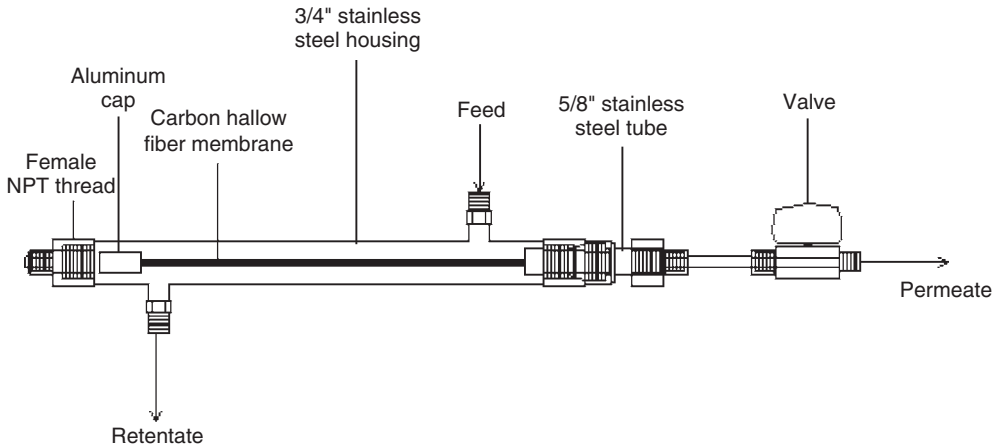

Figure 10 Module constructed by Ismail and David [50]. Reproduced with permission from David, L. I. B., Ismail, A. F. *J. Membr. Sci.* **2003**, *213*, 285–291.

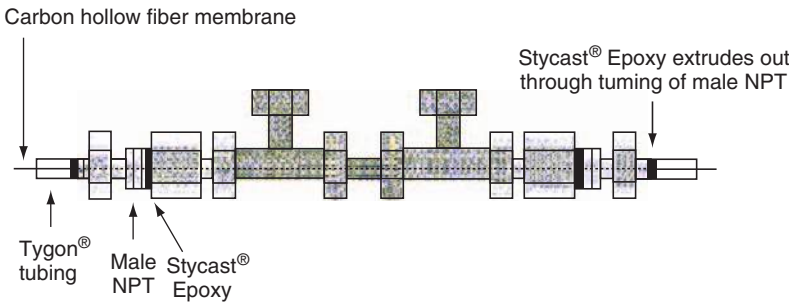

Figure 11 Module constructed by Koros and coworkers. Reproduced with permission from Vu, D. Q., Koros, W. J., Miller, S. J. Ind. Eng. Chem. Res. **2002**, *41*, 367–380.

1.13.5 Gas Transport and Separation through Carbon Membrane

As gas separation applications become commercially attractive, there is a need for novel membranes that can withstand high operating temperatures and harsh environments, and could at the same time boost the viability of processes such as natural gas purification. In general, the gas transport properties of a carbon membrane strongly depend on the pyrolysis temperature. The pyrolysis temperature around 800 °C leads to the formation and the enlargement of pore

structure; meanwhile, higher temperatures cause pore shrinkage and destruction of the pore system [62]. The heating rate may also affect the gas separation performance of the membrane. In addition, the choice of pyrolysis atmosphere may also influence the changes in pore size and geometry or even the nature of the surface by sintering (pore closure) or activation (pore opening by removal of surface groups or by burn-off) effects, which in turn give rise to different gas transport properties [24].

For gas separation through a porous membrane, four separation mechanisms of transport are considered: Knudsen diffusion, surface diffusion, capillary condensation, and molecular sieving. The contribution of these four mechanisms to the total transport strongly depends on the experimental conditions [8, 45]. The transport mechanism owned by most of the carbon membrane is molecular sieving mechanism as shown in **Figure 12**. The carbon membranes contain constrictions in the carbon matrix, which approach the molecular dimensions of the absorbing species [8]. In this manner, they are able to effectively separate the gas molecules with similar size. According to this mechanism, the separation is caused by the passage of smaller molecules of a gas mixture through the pores while the larger molecules are retained.

In the study of gas transport, permeability is considered as a function of the diffusivity of solutes within the membrane material and it is often expressed in Barrer, while selectivity is defined as the ratio of single gas permeabilities. It is known that the permeability and selectivity of the different components of a multicomponent gas mixture are the result of a complex equilibrium governed by factors such as the concentration of the different species, their potential of adsorption, and interactions between species [63]. There is a general relationship reported in the literature that as the permeability of a respective gas increases, its selectivity decreases.

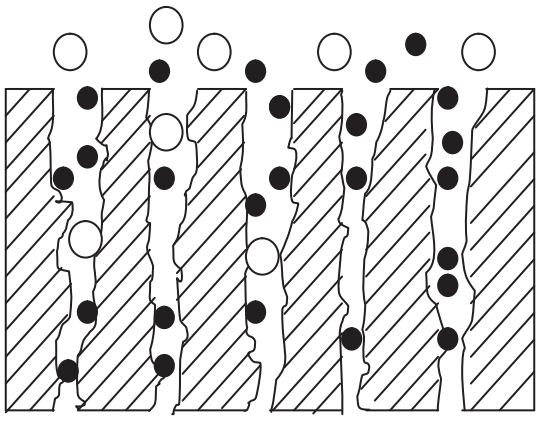

Figure 12 Typical molecular sieving transport mechanism. Reproduced with permission from Ismail, A. F., David, L. I. B. *J. Membr. Sci*. **2001**, *193*, 1–18.

One of the key factors that affects gas diffusivity is the changes of the amount of free volume in the membrane matrixes. The diffusivity can be enhanced by creating a channeling effect and facilitating the diffusion of the gas molecules through the membrane. For the binary gaseous mixtures of high industrial interest, such as CO_2/CH_4, the increase in selectivity values is very crucial for natural gas purification. The permeation measurements can be carried out for single gases as well as for the gas mixtures. Previous research done by Peterson *et al.* [54] using carbon membrane showed that each component in gas mixtures exhibited nearly identical permeation behavior with that of the single gas. The selectivity of the mixed gas consisting of light and heavy components did not show the decrease caused by sorption effects of the heavy components. Therefore, using data of single gas experiments, the selectivity of these carbon membranes can be approximately estimated.

Table 3 shows a comparison of the gas separation performances among various configurations of carbon membranes produced by the previous researches. As expected, in most of the cases, the increase in the permeability of the gases has led to a decrease in selectivity between those gases. For instance, Zhang *et al.* [31] have reported that the gas permeability of the composite carbon membranes decreases along with the selectivity increasing when the pyrolysis temperature is elevated from 650 to 800 °C. At higher temperature, both the permeability and selectivity for the composite carbon membranes decrease except for CO_2/N_2 selectivity. The reduction of gas permeability is due to the rearrangement of turbostratic carbon structure at high pyrolysis temperature, while the decrease of selectivity is probably ascribed to the enlargement of interfacial gap additive and the carbon matrix.

However, this general inversely proportional relationship between selectivity and permeability of the desired gases can be minimized by proper formulation of the membrane dope, which may enable the production of much better performing carbon membranes.

Table 3 The gas transport and separation properties of the carbon membranes produced by the researchers

			Permeability (barrer)						*Selectivity*			
Configuration	*Test temp. (°C)*	*Test pressure (atm)*	N_2	O_2	H_2	CO_2	CH_4	O_2/N_2	H_2/N_2	CO_2/N_2	CO_2/CH_4	*Ref*
Tube/PPO	150	-	16	-	-	219	7	-	-	13.69	31.29	[52]
Flat/MMM	30	1.5	1.08	6.52	-	-	-	6.04	-	-	-	[64]
Flat/CZ650	30	1	19.4	199.7	758.1	791.5	-	10.29	39.08	40.80	-	[65]
Flat/MMM-	-	0.23	1.23	-	5.19	0.28	5.35	-	22.57	18.54	[66]	
Flat/composite membrane25	0.7	4.3	-	-	123	-	-	-	28.60	-	[67]	
Hollow fiber/CMSM	25	1	12.5	125	-	529	5.19	10.00	-	42.32	101.93	[68]
Flat/MMM	35	4	14.42	36.57	79.62	190.67	34.16	2.54	5.52	13.22	5.58	[17]
Flat/CMSM	30	2	4.2	54	9400	1900	4.6	12.86	2238.1	452.38	413.04	[31]
Flat/CMSM	35	6.8	2.1	24	-	94	0.77	11.43	-	44.76	122.08	[18]
Flat/CMSM	25	-	0.6	19.3	-	26	-	32.17	-	43.33	-	[19]
Flat/CMSM	35	10	17	168	-	465	6	9.88	-	27.35	77.50	[20]
Flat/CMSM	25	-	83	707	-	2863	-	8.52	-	34.49	-	[69]
Flat/CMSM	35	10	15.8	138	-	423	4.8	8.73	-	26.77	88.13	[70]
Flat/Na-CMSM	25	0.3	1.1	5.3	-	-	-	4.82	-	-	-	[71]
Flat/Ag-CMSM	-	-	19.9	170	-	619	-	8.54	-	31.11	-	[43]
Flat/CMSM	35	-	0.18	1.3	-	9.0	0.27	7.22	-	50.00	33.33	[63]

1.13.6 Aging Phenomenon of Membrane

The main challenge faced by current membrane technology is to achieve the high separation properties, such as high permeability and high selectivity Therefore, a better understanding of the sorption and transport of gases in these membranes enables the choice of materials and preparation of membranes for the enhanced separation properties.

Recently, the study of membrane aging has been the area of interest due to its effects toward the structure, as well as the gas separation properties of the identified membrane. However, at present, the effects of membrane aging toward the membrane performance have been scarcely discussed in the open literature. Basically, aging of membrane can be defined in two ways: the physical aging, which is commonly suffered by polymeric membrane [72, 73], and carbon aging, which can be normally found in carbon membrane [74, 75].

Physical aging is the observed change in properties of the polymer as a function of storage time, at constant temperature, at zero stress, and under no influence from any other external condition [72]. Conversely, carbon aging takes place along with the formation of surface oxygen groups with the active sites on the carbon surfaces as a consequence of the oxygen–carbon interaction when the carbon materials are exposed to air, even at room temperature. These chemisorbed oxygen species will eventually reduce the open porosity toward gas transport, resulting in the additional restriction in diffusion [74].

Physical aging of polymeric membranes is usually defined in terms of free volume, the main structural feature involved in the diffusion mechanism. Previous studies of Hu *et al.* [73] performed on various types of membranes demonstrated that this physical aging reduced the permeation rate of the polymers, as a result of the decrease in free volume [73]. They observed that the permeability of poly(methyl methacrylate) (PMMA) membrane decreased with the aging time which can be attributed to the first-stage collapse of the membrane, which in turn gives rise to the decrease in diffusion coefficients. Besides, they also suggested that the decrease of free volume affects the permeability coefficient of larger gas molecules more significantly than that of the smaller ones [73].

Lagorsse *et al.* [74] and Menendez and Fuertes [75] studied the aging behavior of carbon membrane under different atmospheres. When CMSM was exposed to both humid and dry air, a rapid loss of permeability was observed. In other words, prolonged storage of carbon membrane in air caused serious damage to the membrane's separation capacity. The effect is more notable for penetrants with critical dimensions close to the critical pore size. At room temperature, exposure to air increases the number of constrictions of the pore structure, hence resulting in the diffusion restriction through the microporous space. Menendez and Fuertes [75]

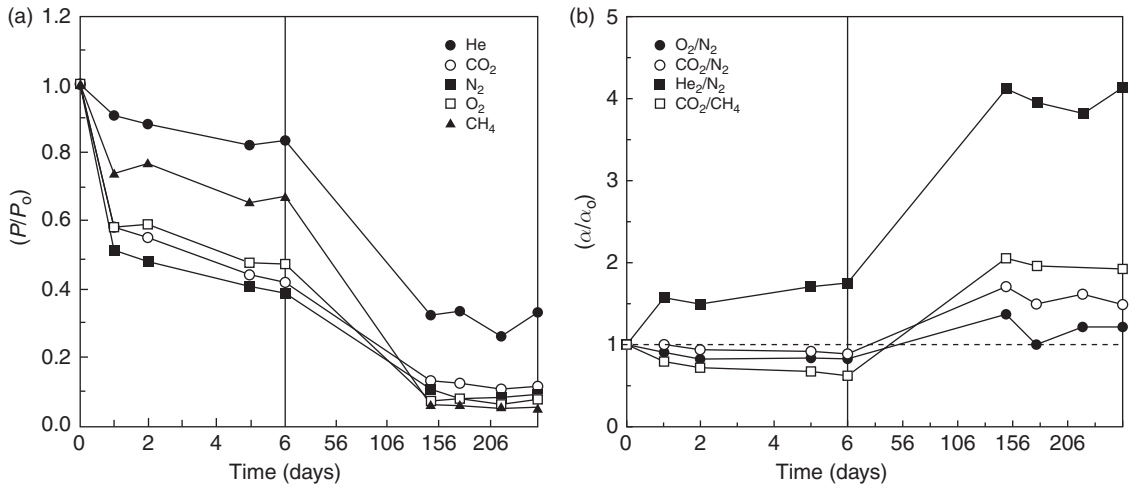

Figure 13 Modification with time of (a) the normalized permeability (P/P_0) and (b) the normalized selectivity (α/α_0) of a carbon membrane stored under ambient conditions. Reproduced with permission from Menendez, I., Fuertes, A. B. *Carbon* **2001**, *39*, 733–740.

compared the transport properties of the fresh and the aged carbon membrane. They observed that the excellent gas separation properties of fresh membrane toward the separation of gas pair such as O_2/N_2 demonstrated rapid loss after storage under ambient conditions. As illustrated in **Figure 13**, the O_2 permeability of 136×10^{-10} mol m^{-2} s^{-1} Pa^{-1} and N_2 permeability of 15×10^{-10} mol m^{-2} s^{-1} Pa^{-1} decreased to 2.5×10^{-10} mol m^{-2} s^{-1} Pa^{-1} and 0.31×10^{-10} mol m^{-2} s^{-1} Pa^{-1}, respectively. Surprisingly, the selectivity increased with the increasing storage time for all the systems tested, but the reason for this phenomenon was unexplained. However, it was observed that both permeability and selectivity reach a constant value after long storage duration.

The gas transport and separation properties of the aged carbon membrane can be recovered through the removal of the water molecule that previously adsorbed onto the membrane during the aging period [74]. Upon heating up to 600 °C under vacuum, the properties of the membrane can be partially regenerated. Under such conditions, the stability of the surface could be increased; however, the left surface, containing reactive carbon sites, is still capable of readsorbing oxygen at room temperature. In order to completely eliminate the surface-attached groups, high-temperature heating is required. However, the severe heat treatment could change the microporosity of the membranes through either annealing or carbon gasification.

Lie and Hagg [76] carried out the electrothermal process to regenerate the aged carbon membrane. At low voltage, operating direct current is applied on an iron-doped carbon, and the permeation rate of the regenerated membrane can be enhanced. This simple, energy-effective, rapid regeneration method is capable of fully restoring the initial permeability of the carbon membrane. Besides, it can be used not only for batchwise regeneration, but also in a continuous way.

1.13.7 Conclusion and Future Direction in Carbon Membrane Research

Carbon membranes provide potentially higher selectivity as well as thermal and chemical stabilities when compared to conventional polymeric membranes. These membranes can normally surpass upper-bound curves in the tradeoff relationship between the permeability and selectivity. Carbon membranes offer the best candidates for the development of new membrane technologies, because of their stability and molecular sieving capabilities.

The most popular precursor currently used for manufacturing carbon membranes is PI. Although PI offers the best separation potential for carbon membranes, its cost is too high and its commercial availability is sometimes very limited. Therefore, in order to reduce the overall cost and production time during carbon membrane fabrication, an alternative polymer must be selected or synthesized. Optimization of fabrication parameters during the pyrolysis process is arguably the best way to fabricate carbon membranes that achieve a superior performance in order to compensate for their higher cost. Pyrolysis condition as well as the pretreatments and posttreatments during the membrane fabrication process should also be extensively examined as these steps provide a great opportunity for tailoring the separation properties of a given carbon membrane.

Once a carbon membrane of high performance is produced, the effect of membrane aging must be considered. The humidity found in the ambient atmosphere has an adverse effect on carbon membrane performance, which greatly decreases the permeability of the gases. Therefore, the study of storage conditions or the regeneration of aged carbon membranes is an important consideration for carbon membrane research in the future.

References

[1] Ash, R., Barrer, R. M., Lowson, R. T. *J. Chem. Soc., Faraday Trans. I* **1973**, *69*, 2166.
[2] Itoh, N., Haraya, K. *Catal. Today* **2000**, *56*, 103–111.
[3] Liang, C., Sha, G., Guo, S. *Carbon* **1999**, *37*, 1391–1397.
[4] Koros, W. J., Mahajan, R. *J. Membr. Sci.* **2000**, *17*, 181–196.
[5] Park, H. B., Lee, Y. M. *J. Membr. Sci.* **2003**, *213*, 263–272.
[6] Hayashi, J., Mizuta, H., Yamamoto, M., Kusakabe, K., Morooka, S. *J. Membr. Sci.* **1997**, *124*, 243–251.
[7] Kyotani, T. *Carbon* **2000**, *38*, 269–286.
[8] Jones, C. W., Koros, W. J. *Ind. Eng. Chem. Res.* **1995**, *34*, 158–163.
[9] Kishore, N., Sachan, S., Rai, K. N., Kumar, A. *Carbon* **2003**, *41*(15), 2961–2972.
[10] Sakata, Y. Muto, A., Uddin, M. A., Suga, H. *Sep. Purif. Technol.* **1999**, *17*(2), 97–100.
[11] Song, C., Wang, T., Pan, Y., Qiu, J. *Sep. Purif. Technol.* **2006**, *51*(1), 80–84.
[12] Ismail, A. F., David, L. I. B. *J. Membr. Sci.* **2001**, *193*, 1–18.

[13] Morthon-Jones, D. H. *Polymer Processing*; Chapman and Hall: London, 1989.
[14] Soffer, A., Rosen, D., Saguee, S., Koresh, J. Carbon Membrane. GB Pat. 2,207,666, 1989.
[15] Laszlo, K., Bota, A., Nagy, L. G. *Carbon* **2000**, *38*, 1965–1976.
[16] Lua, A. C., Su, J. *Carbon* **2006**, *44*, 2964–2972.
[17] Kim, S., Pechar, T. W., Marand, E. *Desalination* **2006**, *192*, 330–339.
[18] Steel, K. M., Koros, W. J. *Carbon* **2005**, *43*, 1843–1856.
[19] Park, H. B., Lee, S. Y., Lee, Y. M. *J. Mol. Struct.* **2005**, *739*, 179–190.
[20] Shao, L., Chung, T. S., Wensley, G., Goh, S. H., Pramodac, K. P. *J. Membr. Sci.* **2004**, *244*, 77–87.
[21] Park, H. B., Jung, C. H., Kim, Y. K., Nam, S. Y., Lee, S. Y., Lee, Y. M. *J. Membr. Sci.* **2004**, *235*, 87–98.
[22] Kim, Y. K., Park, H. B., Lee, Y. M. *J. Membr. Sci.* **2005**, *251*, 159–167.
[23] Kim, Y. K., Park, H. B., Lee, Y. M. *J. Membr. Sci.* **2005**, *255*, 265–273.
[24] Centeno, T. A., Fuertes, A. B. *J. Membr. Sci.* **1999**, *160*, 201–211.
[25] Centeno, T. A., Fuertes, A. B. *Sep. Purif. Technol.* **2001**, *25*, 379–384.
[26] Fuertes, A. B., Menendez, I. *Sep. Purif. Technol.* **2002**, *28*, 29–41.
[27] Wei, W., Hua, H., You, L., Chen, G. *Carbon* **2002**, *40*, 445–467.
[28] Song, C., Wang, T., Wang, X., Qiu, J., Cao, Y. *Sep. Purif. Technol.* **2008**, *58*, 412–418.
[29] Zhang, X., Hua, H., Zhua, Y., Zhua, S. *J. Membr. Sci.* **2007**, *289*, 86–91.
[30] Wei, W., Qin, G., Hu, H., You, L., Chen, G. *J. Membr. Sci.* **2007**, *303*, 80–85.
[31] Lie, J. A., Hagg, M. B. *Carbon* **2005**, *43*, 2600–2607.
[32] Chen, J. C. Modification of Polyacrylonitrile (PAN) Precursor Fiber via Post-Spinning Plasticization and Stretching. PhD Thesis, The Pennsylvania State University, 1998.
[33] Schindler, E., Maier, F. Manufacture of Porous Carbon Membranes. US Pat. 4,919,860, 1990.
[34] Lagorsse, S., Magalhaes, F. D., Mendes, A. *J. Membr. Sci.* **2007**, *301*, 29–38.
[35] Ismail, A. F., Li, K. From Polymeric Precursors to Hollow Fiber Carbon and Ceramic Membranes. In *Inorganic Membranes: Synthesis, Characterization and Applications*; Mallada, R., Menéndez, M., Eds.; Membrane Science and Technology Series; Elsevier: Amsterdam, 2008; Vol. 13, pp 81–119.
[36] Koresh, J. E., Soffer, A. *J. Chem. Soc., Faraday Trans. I* **1980**, *76*, 2457–2471.
[37] Donnet, J. B., Bansal, R. C. *Carbon Fibre.* Marcel Dekker: New York, 1984.
[38] Steel, K. M. Carbon Membranes for Challenging Gas Separations. PhD Thesis, University of Texas, 2000.
[39] Tanihara, N., Shimazaki, H., Hirayama, Y., Nakanishi, S., Yoshinaga, T., Kusuki, Y. *J. Membr. Sci.* **1999**, *160*, 179–186.
[40] Soffer, A., Azariah, A., Amar, A., *et al.* Method of Improving the Selectivity of Carbon Membranes by Chemical Vapor Deposition. US Pat. 5,695,818, 1997.
[41] Soffer, A., Koresh, J., Saggy, S. Separation Device. US Pat. 4,685,940, 1987.
[42] Katsaros, F. K., Steriotis, T. A., Stefanopoulos, K. L., *et al.*, *Physica B* **2000**, *276–278*, 901–902.
[43] Wang, S., Zeng, M., Wang, Z. *J. Membr. Sci.* **1996**, *109*, 267–270.
[44] Steriotis, T. H., Beltsios, K., Mitropoulos, A. Ch., *et al. J. Appl. Polym. Sci.* **1997**, *64*, 2323–2345.
[45] Fuertes, A. B. *Carbon* **2001**, *39*, 697–706.
[46] Kusakabe, K., Yamamoto, M., Morooka, S. *J. Membr. Sci.* **1998**, *149*, 59–67.
[47] Yoshinaga, T., Shimazaki, H., Kusuki, Y., Sumiyama, Y. Asymmetric Hollow Filamentary Carbon Membrane and Process for Producing the Same. EP Pat. 0,459,623, 1991.
[48] Yamamoto, M., Kusakabe, K., Hayashi, J., Morooka, S. *J. Membr. Sci.* **1997**, *133*, 195–205.
[49] Cabrera, A. L., Zehner, J. E., Coe, C. G., Gaffney, T. R., Farris, T. S. *Carbon* **1993**, *31*, 969–976.
[50] Barbosa-Coutinho, E., Salim, V. M. M., Borges. C. P. *Carbon* **2003**, *41*, 1707–1714.
[51] Favvas, E. P., Kapantaidakis, G. C., Nolan, J. W., Mitropoulos, A. Ch., Kanellopoulos, N. K. *J. Mater. Process. Technol.* **2007**, *186*, 102–110.
[52] Lee, H. J., Suda, H., Haraya, K. *Sep. Purif. Technol.* **2008**, *59*, 190–196.
[53] Strathmann, H. *Membr. Technol.* **1999**, *113*, 9–11.
[54] Yoneyama, H., Nishihara, Y. Carbon Based Porous Hollow Fiber Membrane and Method for Producing Same. US Pat. 5,089,135, 1992.
[55] Saufi, S. M., Ismail, A. F. *Carbon* **2004**, *42*, 241–259.
[56] Petersen, J., Matsuda, M., Haraya, K. *J. Membr. Sci.* **1997**, *131*, 85–94.
[57] Smith, S. P. J., Linkov, V. M., Sanderson, R. D., Petrik, L. F., O'Connor, C. T., Keiser, K. *Micro. Mat.* **1995**, *4*, 385–390.
[58] Baker, R. *Membr. Technol.* **2001**, *138*, 5–10.
[59] David, L. I. B., Ismail, A. F. *J. Membr. Sci.* **2003**, *213*, 285–291.
[60] David, L. I. B. Development of Asymmetric Polyacrylonitrile Carbon Hollow Fiber Membrane for Oxygen/Nitrogen Gas Separation. MSc Thesis, Universiti Teknologi Malaysia, 2001.
[61] Vu, D. Q., Koros, W. J., Miller, S. J. *Ind. Eng. Chem. Res.* **2002**, *41*, 367–380.
[62] Katsaros, F. K., Steriotis, Th. A., Romanos, G. E., Konstantakou, M., Stubos, A. K., Kanellopoulus, N. K. *Microporous Mesoporous Mater.* **2007**, *99*, 181–189.
[63] Fuertes, A. B. *J. Membr. Sci.* **2000**, *177*, 9–16.
[64] Rafizah, W. A. W., Ismail, A. F. *J. Membr. Sci.* **2008**, *307*, 53–61.
[65] Zhang, B., Wang, T., Wu, Y., *et al. Sep. Purif. Technol.* **2008**, *60*, 259–263.
[66] Kim, S., Chen, L., Johnson, J. K., Marand, E. *J. Membr. Sci.* **2007**, *294*, 147–158.
[67] Cong, H., Zhang, J., Radosz, M., Shen, Y. *J. Membr. Sci.* **2007**, *294*, 178–185.
[68] Yoshimune, M., Fujiwara, I., Haraya, K. *Carbon* **2007**, *45*, 553–560.
[69] Kim, Y. K., Lee, J. M., Park, H. B., Lee, Y. M. *J. Membr. Sci.* **2004**, *235*, 139–146.
[70] Tin, P. S., Chung, T. S., Kawi, S., Guiver, M. D. *Microporous Mesoporous Mater.* **2004**, *73*, 151–160.
[71] Suda, H., Haraya, K. *J. Phys. Chem. B* **1997**, *10*, 3988–3994.
[72] Kim, J. H., Koros, W. J., Paul, D. R. *Polymer* **2006**, *47*, 3094–3101.
[73] Hu, C. C., Fu, Y. J., Hsiao, S. W., Lee, K. R., Lai, J. Y. *J. Membr. Sci.* **2007**, *303*, 29–36.
[74] Lagorsse, S., Magalhaes, F. D., Mendes, A. *J. Membr. Sci.* **2008**, *310*, 494–502.
[75] Menendez, I., Fuertes, A. B. *Carbon* **2001**, *39*, 733–740.
[76] Lie, J. A., Hagg, M. B. *J. Membr. Sci.* **2006**, *284*, 79–86.

Biographical Sketch

Born in 1966, Ahmad Fauzi Ismail obtained his bachelor's degree in petroleum engineering and his master's degree in chemical engineering from Universiti Teknologi Malaysia (UTM). In 1994, he was awarded an Association of Commonwealth University Scholarship to continue his doctoral studies and, in 1997, he was awarded a PhD for a dissertation which proposed and confirmed that molecular orientation in a synthetic polymeric membrane is the factor to be considered for super-selective hollow fiber membranes in gas separation. As a result, a US and European patent were granted to him for his groundbreaking findings. He is currently a professor of membrane technology in the Faculty of Chemical and Natural Resources Engineering at UTM, Malaysia, and Director of Advanced Membrane Technology Research Center (AMTEC), UTM. He is particularly interested in gas separation processes, especially CO_2 removal from natural gas, O_2/N_2 separation, N_2CH_4 separation, H_2 recovery, H_2/N_2 separation using polymer and inorganic materials, as well as hybrid or composite materials. In addition, he also has special interest in developing reverse osmosis, and nanofiltration and ultrafiltration membrane for water and wastewater treatment and for biotechnology applications. Recently, he has developed an interest in the preparation of composite materials from carbon fibers and carbon nanotube for energy storage.

1.14 Carbon Nanotube Membranes: A New Frontier in Membrane Science

M Majumder, Monash University, Clayton, VIC, Australia

P M Ajayan, Rice University, Houston, TX, USA

1.14.1 Introduction

Iijima, in 1991, [1] reported the first detailed transmission electron microscope images of arc-grown multiwalled carbon nanotube (MWCNT). The single-walled carbon nanotubes (SWCNTs) were reported later on [2]. There have been other reports, predating these, for the observation of filamentous forms of carbon, some of them resembling the well-formed tubular structures of nanotubes [3]. However, the proper characterization of the real structure of nanotubes has kindled the imagination of the nanoscience community and impacted the field in many ways. Research efforts over the past 17 years have been focused on the electrical, optical, and mechanical properties of this material [4–6]. Although several early experiments [7–10] had shown the ability to open up carbon nanotubes (CNTs) to serve as nanoscale containers, it is in the past 4–5 years that experimental molecular transport through CNTs, or the interstice between vertically oriented CNTs, has become a subject of intense interest. This interest has been generated by the discovery of the fascinating mass-transport properties of this nanoscale material. For example, the transport rate of water is almost four to five orders of magnitude higher than that of other porous materials of comparable size, and is very close to that of biological membrane channels, such as aquaporin [11]. An artist's rendition of this novel phenomenon is shown in **Figure 1**, while transport properties of liquids through the inner core of ~7-nm-diameter nanotubes are shown in **Table 1**. Although molecular dynamic (MD) simulation studies indicate extremely fast mass transport of gases and liquids through the inner core of CNTs [12, 13], membranes fabricated from crystalline as-formed CNTs have experimentally verified these enticing mass-transport predictions through the smooth, hydrophobic, and crystalline interior of the nanotubes. Owing to this significant advantage, there has been a major interest in nanotube membranes as a technological alternative even to mature processes such as reverse osmosis for desalination [14]. Therefore, a review showcasing the major milestones in CNT membrane research and their application is pertinent.

While the CNTs are grown by bottom-up approaches, such as chemical vapor deposition (CVD), fabrication of macroscopically useful membranes from these nanoscale materials is often a combination of several top-down components, such as electrochemical anodization of a metal film, polymer processing, chemical etching, and plasma etching. We discuss the state-of-the-art approaches for processing the CNT membranes and critically evaluate the advantages and/or drawbacks of these

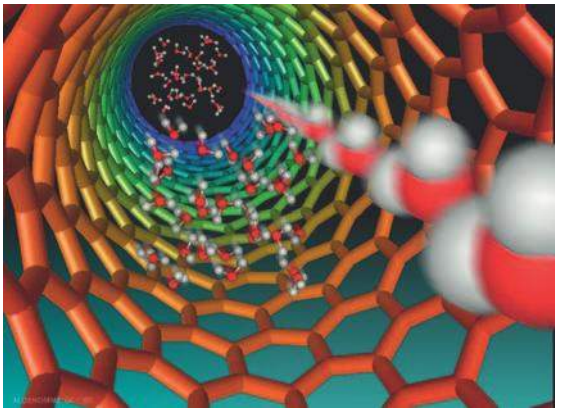

Figure 1 Artist's rendition of water molecules zipping through the inner core of carbon nanotube (CNT). Courtesy of Mark Denomme from the University of Kentucky. This chapter examines the state of the art in membranes based on CNTs.

approaches. The potential of these novel membrane materials for liquid separation, gas/vapor separations, and membrane reactor applications is elaborated. Membranes have traditionally been used for large-scale applications. However, there is considerable interest in integrating nanoporous membranes to microfluidic devices as they can integrate multiple functionalities in a device [15] – how nanotube membranes could be seamlessly integrated with microfluidic devices is also discussed. Apart from the extremely fast mass-transport properties, additional benefits of membranes based on CNTs are their ability to be functionalized – allowing them to be chemically tuned to suit applications. Furthermore, CNTs have inherent properties, such as super-compressibility and electrical conductivity, which can be exploited for designing active membrane structures. Finally, the chapter touches upon the future directions in CNT membrane research from a technology-enabling point of view.

1.14.2 CNT Membranes

Primarily, there are four approaches to the synthesis of membranes based on CNTs:

1. deposition of carbonaceous materials inside preexisting ordered porous membranes, such as anodized alumina, also known as the template-synthesized CNT membranes [16];
2. membranes based on the interstice between nanotubes in a vertical array of CNTs, subsequently referred to as the dense-array outer-wall CNT membrane [17];
3. encapsulation of as-grown vertically aligned CNTs by a space-filling inert polymer or ceramic matrix followed by opening up the CNT tips using plasma chemistry, or the open-ended CNT membrane [18, 19]; and
4. membranes composed of nanotubes as fillers in a polymer matrix, also known as mixed-matrix membranes.

1.14.2.1 Template-Synthesized CNT Membrane

In the template synthesis approach, a preexisting ordered porous membrane serves as a template for deposition of carbonaceous materials, usually using CVD [16, 20] at elevated temperatures, resulting in pore structure with reduced dimensions. The template is usually a ceramic membrane formed by the electrochemical anodization of metal films. The anodized membranes have extremely small

Table 1 Summary of pressure driven liquid flow measurements in CNT membranes. The permeable pore density is estimated from salt diffusion experiments

Liquid	*Permeable pore density (# per m^2)*	*Membrane thickness (m)*	*Flow velocity normalized at 1 bar (ms^{-1})*	*Viscosity (cP)*	*Enhancement factor*
Hexane	3.4×10^{13}	126×10^{-6}	5.6×10^{-2}	0.3	1.09×10^{4}
Decane	3.4×10^{13}	126×10^{-6}	0.67×10^{-2}	0.9	3.9×10^{4}
Water	$1\text{-}3.4 \times 10^{13}$	$34\text{-}126 \times 10^{-6}$	$26.1\ (\pm 17.2) \times 10^{-2}$	1.0	$6\ (\pm 1.6) \times 10^{4}$
EtOH	3.4×10^{13}	126×10^{-6}	4.5×10^{-2}	1.1	3.2×10^{4}
IPA	3.4×10^{13}	126×10^{-6}	1.12×10^{-2}	2	1.4×10^{4}

Note that the enhancement factor, that is, the ratio of the observed flow velocity to the Hagen–Poiseuille flow velocity for ~7-nm pipes, is ~10 000–100 000, suggesting strong deviation from no-slip hydrodynamic flow. Adapted with permission from Majumder, M., Chopra, N., Andrews, R., Hinds, B.J. *Nature* **2005**, *438*, 44.

(<10%) porosity, are mechanically very brittle, and fabrication of anodized membranes with small pore size (<5 nm) is often irreproducible. However, anodization of metals is an interesting approach to synthesize ordered membrane structures with controlled pore-size distribution and small tortuosity. Although these membranes have found applications in size-based separations [21] and as catalytic membrane reactors [22], further modification by carbonaceous material deposition provides many possibilities.

The synthesis and characterization of template-synthesized membranes have been pioneered by Charles Martin's group at the University of Florida. A schematic and scanning electron microscopy (SEM) image of the template-synthesized CNT membrane is shown in **Figure 2**(**a**). In the schematic, the dark-gray intrusions are the

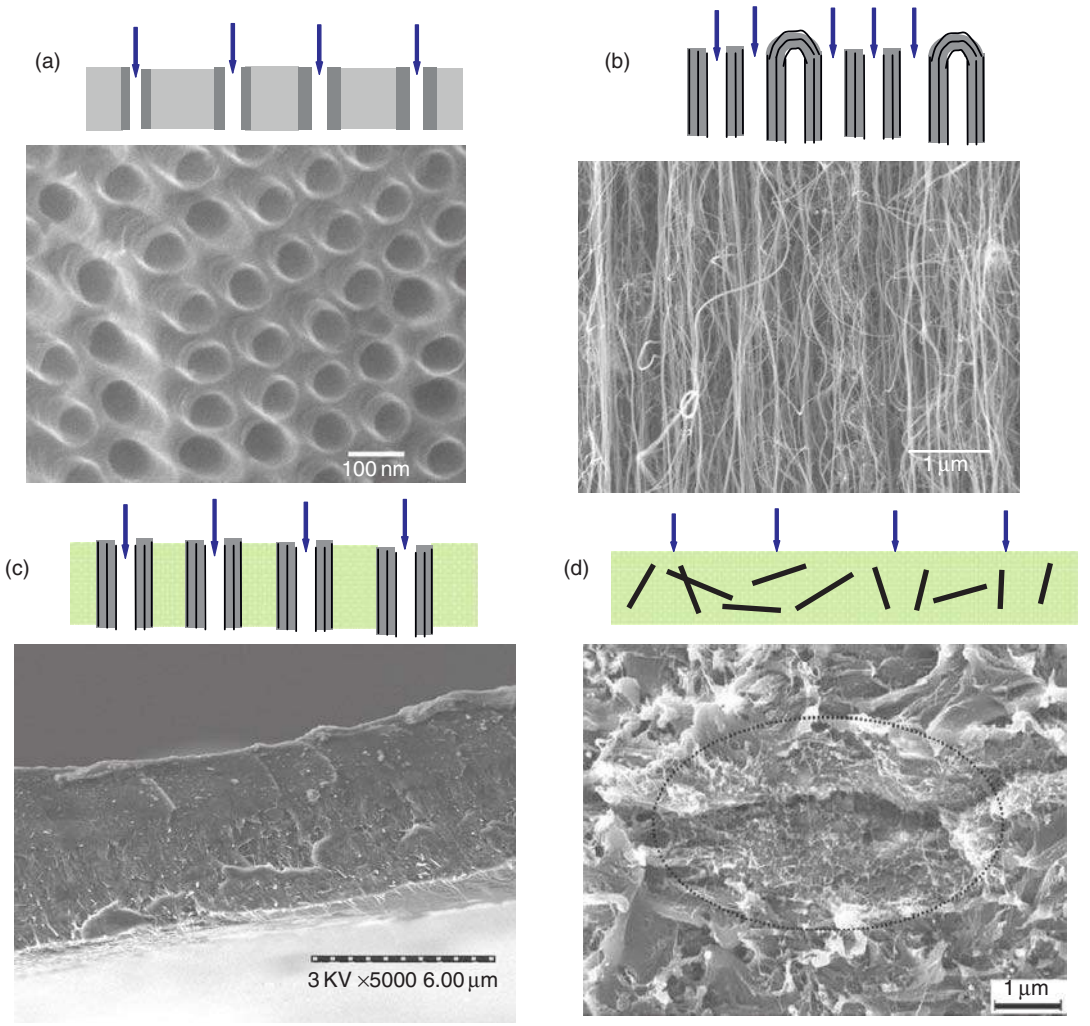

Figure 2 Different approaches to carbon nanotube (CNT) membrane synthesis. (a) Template synthesis approach-carbonaceous material deposited inside anodized alumina template; (below) scanning electron micrograph (SEM) micrograph of the nanotubes after dissolution of the template. (b) Dense-array outer-wall CNT membrane; SEM image demonstrating the dense array of CNTs. The fluid transport is through the interstice between the nanotubes, although some transport can occur through some open-ended tubes [17]. (c) Open-ended CNT membrane; (below) SEM image showing the cross section of the membrane with aligned CNTs in an impervious polymer matrix; transport in this membrane structure occurs through the inner core of the CNT [18]. Image taken with permission from Majumder, M., Zhan, X., Andrews, R., Hinds, B. J. *Langmuir* **2007**, *23*, 8624–8631. (d) Mixed-matrix membrane composed of CNTs in a polymer matrix; (below) SEM image of the composite-membrane structure. Image taken with permission from Geng, H.-Z., Kim, K. So, K., Lee, Y., Chang, Y., Lee, Y. *J. Am. Chem. Soc.* **2007**, *129*, 7758–7759.

carbonaceous material deposited inside the light-gray (anodized alumina) template. The deposition of carbonaceous materials inside template membranes by CVD of ethylene can reduce the pore size from ~300 to ~200 nm, but further reduction was not observed [23]. It is likely that faster kinetics of this deposition process is less controllable for obtaining smaller dimension of pores, and is the reason for much of Martin's later work devoted to the use of a more-controlled solution-based electroless deposition technique for steric separation of small molecules [24]. This conjecture is further supported by the work of Alsyouri *et al.* [20], in which CVD, using trimethyl ammonium and water, resulted in the reduction of porosity of ~20-nm templates and not their pore size. The CNT membranes synthesized by this method also contain amorphous or partially graphitized CNTs and are chemically different from the membranes based on the highly ordered graphitic CNTs. They can, however, be graphitized by heat treatment at higher temperature. This was shown in template-synthesized partially graphitic nanotubes, which can be annealed at a higher temperature (>2000 °C) to form graphitic nanotubes, as evidenced by electrical conductivity, transmission electron microscopy, and contact angle measurements [25]. It should, therefore, be possible to convert template CNT membranes to partially graphitized CNT membranes by heat treatment, although such treatments are likely to increase the cost of the membranes.

In this vein, it is worthwhile to point readers to the fabrication of well-controllable, hierarchically branched, and crystallized CNT architectures by Ajayan and coworkers [26] using this template approach. The well-branched porous architecture has smaller pore dimensions at one end and larger pore structure at the other end – similar to the asymmetric membranes commonly used for filtration purposes [26]. Fluid flow or permeability of these novel nanoscale architectures will verify its applicability in nanofluidic applications. A major advantage of the template synthesis approach is that the modular components of thin-film deposition, electrochemical treatment, and CVD can be integrated to microfluidic device fabrication platforms. However, other approaches using as-formed graphitic CNTs seem to be more realistic for producing CNT membrane for large-scale applications. In the subsequent sections, we discuss membranes based on as-formed CNTs.

1.14.2.2 Dense-Array Outer-Wall CNT Membrane

Aligned arrays of CNTs can be used as membranes, where transport occurs primarily through the interstice between the CNTs, although some of the nanotubes might be open – as shown schematically in **Figure 2(b)**. The CNTs, in this membrane structure, are held together by van der Waals bonding between tubes and carbonaceous materials formed during the CVD process. The pore size of this membrane is usually in the range of 40–100 nm – suitable for ultrafiltration applications.

In some cases of CNT synthesis, such as by high-pressure CO conversion (HiPco) or laser oven processes, the nanotubes are produced as an entangled mesh held together by van der Waals forces [27]. Alignment of CNTs, from such an entangled mesh, can be achieved by the application of some externally applied forces. Partial alignment of CNTs (~50%) inside a polymer matrix can be attained by mechanical stretching during extrusion of a polymer–nanotube composite melt [28, 29] – although the degree of alignment would be limited by the high viscosity of the melt, especially for samples with large volume fraction of CNTs. Researchers at Rice University were able to align purified SWCNT bundles, in plane, using a magnetic field (~7 T) during filtration of a nanotube suspension [30, 31], which is contrary to out-of-plane alignment requirements for filtration application. Therefore, a particular emphasis in the fabrication of CNT membranes is formation of macrostructures with CNTs aligned perpendicular to the substrate. CVD from carbon-containing source and a metal catalyst can readily produce aligned CNT arrays over a substrate, such as Si and SiO_2.

In the early 1990s, primarily after the discovery of fullerene, research efforts were directed to synthesize carbon nanostructures in large-scale capabilities. There was also a concerted effort to produce controlled nanostructures composed of aligned CNTs, with the goal of investigating the anisotropic properties of CNTs applicable in field-emission devices. The earliest report of aligned MWCNT films was by deHeer *et al.* in 1995 [32] using the arc evaporation process. Subsequently, other methods, such as CVD, a scalable and industrially viable process, became popular [33]. Aligned MWCNTs were also grown on nickel-coated glass substrates by plasma-enhanced hot-filament CVD from a mixture of acetylene and ammonia below 666 °C [34]; however, the CNTs produced by this method had significant bamboo-type structures

making them unsuitable for flow-through applications. Among others, efforts at the Center for Applied Energy Research (CAER) at the University of Kentucky were focused on perfecting and scaling up production of MWCNT arrays from a continuous source of ferrocene and xylene at ~650 °C [35].

The overall geometry of the aligned CNT structure depends on the shape of the substrate on which the CNTs are deposited. Srivastava and coworkers succeeded in materializing this concept and formed hollow cylinders of aligned MWCNT (up to few centimeters long) along the walls of a tubular quartz reactor. The cylinders are composed of radially oriented MWCNTs of about 300–500-μm length and have been utilized for liquid and gas filtration application [17]. More importantly, the mechanical strength of the CNT filter is high enough to allow liquid filtration by tangential cross flow, which is widely used in industrial membrane filtration. Molecular transport in these membranes occurred, primarily, through the interface between nanotubes, although transport through the inner core of the open nanotubes cannot be overruled. Inter-nanotube distance in the MWCNT arrays is in the range of 40–100 nm, which sets the pore size of the membranes. A potential drawback of this membrane structure is the considerable variation in the size distribution of the filtration pores – although these dimensions could be tuned with closer packing of nanotubes or with nanotubes of smaller outer diameter [36].

1.14.2.3 Open-Ended CNT Membrane

A contemporary approach in CNT membrane research is the use of open-ended CNT channels as conduits for molecular transport. A composite film is synthesized from an aligned array of the CNT by a space-filling polymer [18] or ceramic matrix [19]; however, maintaining the alignment of the CNTs during this processing step is critical. Subsequently, the tips of the CNTs are oxidized by plasma chemistry to form open-ended and conducting CNT channels. A schematic and SEM image of a typical nanotube membrane fabricated by such a process is depicted in **Figure 2(c)**.

The open-ended CNT membranes, with space-filling polymers, have been primarily based on poly(styrene) [18]. The choice of poly(styrene) in this work is dictated by its high wettability [37] with CNTs allowing easy penetration into the MWCNT array ($\sim 10^{10}$ tubes cm^{-2}) by a simple film fabrication process. However, other mechanically robust polymers and conformal deposition techniques can substitute polystyrene. The CNT–polymer film is released from the quartz substrate, on which the CNTs grow, by hydrofluoric acid (HF) etch. The vertically oriented CNTs in the polymer matrix often have a graphitic end cap (which have larger concentration of defects and are easily oxidized compared to the side walls) or a catalyst metal particle sealing the graphitic interiors, which are etched away using mild plasma oxidation without destroying the mechanical structure of the CNTs [38]. High-temperature oxidative [39] or acidic oxidation treatments can compromise the mechanical integrity of the membrane and are not suitable for the membrane fabrication process. The elegance of the plasma-oxidation process stems from its controllable oxidation kinetics, and the ability to fabricate a macroscopic CNT array device. This plasma-oxidation process, inherent to the membrane fabrication process, performs three very important functions:

1. It removes excess polymers by oxidative trimming, since the oxidation kinetics of the polymer (CNT) is faster than that of the CNTs. This results in the exposure of the CNTs out of the polymer matrix, making the membrane electrically conducting.
2. The plasma-oxidation process also removes amorphous carbon and Fe impurities, aided by HCl treatment. Note that the permeable pore densities ($\sim 10^{9}\ cm^{-2}$) of membranes in **Table 1**, estimated from salt-diffusion experiments, are almost a magnitude smaller than the density of the CNTs in the arrays ($\sim 10^{10}\ cm^{-2}$) estimated from microscopy experiments. This is attributed to the incomplete removal of the iron nanocrystals from the interiors of the CNTs.
3. The plasma-oxidation process introduces functional groups (mainly –COOH) at the CNT tips, which makes the tips amenable to facile functionalization-chemistry approaches.

The CNT membrane structure after the plasma-oxidation process showed a pore-size distribution of $\sim 6 \pm 2$ nm, which is consistent with TEM observations of the inner core of ~7 nm.

In a similar work, aligned CNTs (with sub-2-nm diameter) were grown on a Si chip patterned with metal catalyst using a CVD process. A conformal deposition of a ceramic material, Si_3N_4, filled up the space between the nanotubes. Standard etching

procedures were adopted to create openings on the Si chip; subsequently, excess Si_3N_4 and catalyst nanoparticles were removed by Ar-ion milling, while the CNTs were uncapped by reactive ion etching [19]. In both these works, the production of the CNT membranes relied on standard lithography tools commonly associated with microelectronic industry.

More traditional inorganic membrane fabrication research groups have focused on making robust and cost-efficient CNT membranes by using macroporous membrane support layer and avoiding the use of lithographic tools. In this effort, aligned CNT arrays were grown over macroporous alumina supports and the interstitial space between the CNTs was filled by poly(styrene); however, the viscosity of the polymer was high enough to preclude its entry into the macroporous alumina support. Mechanical polishing and acid treatment were adopted to remove the polymer overlayer and to open up the CNTs [40].

The methodologies for fabrication of the first-generation CNT membranes were aimed at understanding the fundamental transport behavior. They suffer from several drawbacks, for example, the porosity of these membranes and the overall permeability is uncertain, due to the presence of considerable amount of Fe nanocrystals from the vapor deposition process and the overall yield is painstakingly small. The research approaches discussed earlier [18, 19, 40] have utilized as-formed aligned CNTs for the fabrication of membranes; an alternative route is to adapt colloidal processing approaches. In this regard, Kim *et al.* [41] claim to have developed a scalable process for the fabrication of open-ended nanotube membranes by filtering a CNT suspension through a hydrophobic porous polytetrafluoroethylene (PTFE, 0.2-μm pore diameter). Quite surprisingly, a substantial number ($\sim 10^{10}\,cm^{-2}$) of CNTs were observed to stick out of the filter surface, most likely due to the hydrophobic–hydrophobic interaction between the nanotubes and the filter surface. A thin polymer binder filled up the interstice between the nanotubes, leading to the formation of the membrane. The key advantage of this approach lies in the ability to use purified nanotubes (lower amount of Fe catalyst) with larger through porosity and to use diameter-sorted CNT suspensions. Scalability and the overall simplicity of the colloidal approach have the potential to lower the cost of CNT membrane fabrication.

In sum, the fabrication of the open-ended CNT membranes is complex, but it offers tighter control over pore size as the transport occurs through the inner core of CNTs.

1.14.2.4 Mixed-Matrix CNT Membranes

Polymeric membrane materials are intrinsically limited by a tradeoff between their permeability and their selectivity, yet they have been the basis for high-performance gas-separation applications. Virtually, all gas separations in polymeric membranes are limited by an upper boundary in a log–log plot of gas selectivity and permeability [42]. One approach to increase the selectivity is to include dispersions of inorganic nanoparticles, such as zeolites, carbon molecular sieves, or CNTs, into the polymeric membranes – these membranes are classified as mixed-matrix membranes. In these membranes, the choice of both these components is a problem of materials selection, and also involves several fundamental issues, such as polymer-chain rigidity, free volume, and the altered interface – all of which influence transport through the membrane [43]. Several research groups are investigating the effects of incorporation of CNTs to develop mixed-matrix membranes. Schematic and SEM image of mixed-matrix CNT membranes are shown in **Figure 2(d)**. In the dense-array or open-ended CNT membranes, transport is through the pores of CNTs and interparticle pores in CNT array – a mechanism quite similar to porous ultrafiltration or nanofiltration membranes, whereas transport through the mixed-matrix membranes is predominantly by a solution–diffusion mechanism. Eva Marand and coworkers have incorporated open-ended and amine-functionalized CNTs (with ~13.6-Å pore diameter) into poly(sulfone) [44] and poly(imide-siloxane) copolymer [45]. Incorporation of CNTs increases the permeability of most gases by up to 60%, but the selectivity does not improve compared to the polymeric membranes. However, appropriate manipulation of the interface can significantly improve the separation performance. Considering the plethora of polymeric materials at the disposal, the combinatorial selection of components for membrane formulation may pose a problem of plenty. Therefore, modeling and simulations are needed for predicting the transport properties of the mixed-matrix membranes *a priori*. Further, rational design of experiments for optimization of materials processing and property relationships can pave the way for the development of high-performance CNT-based mixed-matrix membranes.

1.14.3 Properties and Application of CNT Membranes

In this section, we discuss the properties of the CNT membrane with particular emphasis on their potential applications.

1.14.3.1 Functionalization of CNT Membranes

Selective chemical transport through porous membranes can be affected by steric, electrostatic, or chemical interactions – often a combination of these mechanisms results in the desired selectivity. For example, membranes can be engineered with polyelectrolytes containing charged amino and carboxyl groups to achieve separation of ions by electrostatic adsorption [46], or proteins by an affinity-based separation [47]. CNTs are composed of rolled-up grapheme sheets consisting of sp^2-hybridized carbon; however, liquid-phase (acid) and gas-phase (air and plasma) treatments introduce surface functional groups. Experimental results indicate that liquid-phase treatments tend to introduce carboxylic acid groups, whereas gas-phase treatments introduce less-oxidized groups such as hydroxyl and carbonyl [48]. Water plasma treatment for opening the CNTs is most likely to introduce the carboxyl groups on the tips of the CNT membrane, because the high reactivity of the plasma precludes its entrance deep into the pores, limiting the functionalization to the surface[49]. These functional groups, particularly carboxylic acids can then be further modified by covalently attaching molecules of interest to these anchor points, using carbodiimide-mediated coupling of the carboxylic acid groups with amine groups of the desired molecule. Modulation of ionic transport through the CNT membrane, by selective chemical functionalization at the CNT tips, has been demonstrated [50]. Transport through the membrane of two different-sized, but equally charged, molecules (ruthenium–bipyridine $[Ru-(bipy)_3{}^{2+}]$ and methyl viologen $[MV^{2+}]$) was quantified to understand the effect of the functionalization chemistry. The selectivity of the permeating molecules varied from 1.7 to 3.6 and a hindered diffusion model to explain the observed selectivity was consistent with a geometry of functionalization concentrated at the CNT tip and not along the length of the CNT core. Furthermore, it is possible to increase the density of functional molecules by using electrochemical approaches, such as diazonium grafting chemistry. Such chemistries enhanced the electrostatic interactions between the membrane and the permeating species [51]. Molecular transport through membranes can also be driven by an electric field. This process, known as electro-osmosis, arises from the drag exerted by counterions on solvent molecules and provides a means to manipulate liquids by an electric field, particularly in microfluidic devices. The direction of overall molecular transport is in the direction of counterion migration, and is directly related to the bound surface charge. Researchers have shown that template-synthesized CNT membrane functionalized with charged groups demonstrate controlled electro-osmotic transport [16]. In general, readers should be aware that a wide range of literature for electrochemical (or chemical) functionalization of the CNTs exists [52]; however, selection of appropriate chemistry compatible with the mechanical integrity of the CNT membranes and pertinent application is critical. Nevertheless, these experiments (**Figure 3**) indicate the feasibility of functionalizing CNT membranes and should offer avenues for imparting antifouling, biocompatible, molecular recognition or selective adsorption properties, whenever desired.

1.14.3.2 CNT Membranes for Gas/Vapor Transport Applications

Gas transport through the hollow interiors of CNTs has been the fancy of many scientists. Preliminary answers to how gaseous molecules are transported through these nanoscale and highly smooth conduits came through MD simulations. Several research groups in the US and UK studied the transport properties of CNTs. Prominent among them are David Sholl and Karl Johnson at the Carnegie Mellon University. They investigated the transport of small gas molecules, such as N_2, Ar, and CH_4, through nanoporous materials, including CNTs, with the overarching goal of screening inorganic materials for potential gas-separation applications. In 2003, they reported that the transport diffusivities of Ar through CNTs were almost three to four orders of magnitude larger than through zeolitic pores of comparable dimensions [13]. Arguments based on specular reflection of the gases along the smooth and frictionless graphitic interface were forwarded. Some work on MD simulations on gas transport was also conducted by the Susan Sinnot group at the University of Kentucky and their simulations

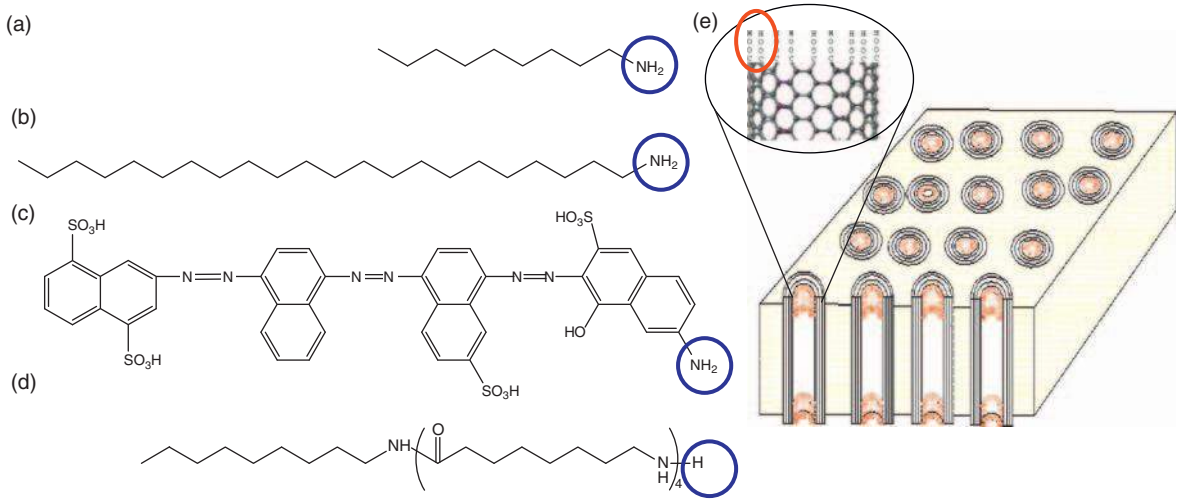

Figure 3 Functionalization of the CNT membrane via coupling chemistry between amine groups (in blue circle) of the functional molecule and the carboxylic acid (in red) with (a) short (C9)-chain amine, (b) long (C22)-chain amine, (c) charged dye molecule with SO_3^{2-} groups, and (d) long-chain polypeptide resulted in change of transport properties through the CNT membrane (e) Figures (a) through (e) adapted with permission from Majumder, M., Chopra, N., Hinds, B. J. *J. Am. Chem. Soc.* **2005,** *127*, 9062–9070. These experiments indicate the feasibility of functionalizing CNT membranes and should offer avenues for imparting antifouling, biocompatible, molecular recognition or selective adsorption properties, whenever desired.

also predicted extremely fast transport of gases through CNTs [53]. Nick Quirke's group at Imperial College investigated hydrodynamics of low-Knudsen-number fluid flow through graphitic pores. Their simulation results indicated the presence of large slip lengths for such flows [54]. In 2002, they proposed for the first time the presence of slip-boundary conditions in Poiseuille flow of fluids, such as CH_4 on smooth CNT surfaces [55]. In summary, several research groups computationally predicted the extremely fast mass-transport characteristics through the inner core of the hydrophobic, and smooth CNTs.

From an experimentalist's viewpoint, gas transport through mesoporous materials is generally a combination of (1) viscous or Poiseuille flow, (2) Knudsen diffusion, and (3) surface diffusion [56, 57]. While the Poiseuille permeation scales inversely with the viscosity, the characteristics of Knudsen-type transport are an inverse scaling with the square root of molecular weight of the gases – paralleling arguments for the kinetic theory of gases. Knudsen diffusion becomes prominent when the mean free path of the diffusing species is larger than the pore diameter. In some cases of porous membranes, a surface-adsorption-based preferential diffusion may lead to highly selective transport, especially in carbon membranes with extremely small pore dimensions (<1 nm) [58, 59].

Careful control experiments, such as retention of Au nanoparticles and size-dependent separation of molecules, have validated the membrane structure consisting of open-ended CNTs inserted inside an impermeable polymer matrix [11, 19]. Pore density (number of pores/m^2) in these membranes can be estimated with reasonable accuracy by direct visualization using SEM or by diffusive transport measurements. Often, a large number of CNTs, which are visible by electron microscopy, can have their cores blocked by the catalyst particles (especially in the case of membranes composed of large-diameter MWCNTs), so the microscopy experiments can provide a higher estimate to the number of open-ended nanotubes. Nonetheless, this estimation is crucial for understanding the molecular transport properties through the CNT membranes, as it allows the macroscopic transport measurements to be converted to that for single nanotubes. It is also worthwhile to recollect that the mean free path for gases (~600 Å for air) is significantly larger than the pore diameter of the CNT membrane (~12–70 Å) – therefore, Knudsen diffusion is the likely gas-transport mechanism. For gas transport through smooth pores, such as CNTs, it is worth commenting that Knudsen diffusivity can exceed the diffusivities predicted from the kinetic theory of gases because of specular reflection along the CNT walls [60]. Indications that such behavior can be true is provided

by gas-transport measurements in a template-synthesized CNT membrane (~20–30 nm thick and 200-nm pore diameter) – the authors concluded that ~50% of the gas collisions were specular [61]. However, for more comprehensive assessments, gas-transport measurements through the open-ended CNTs are critical. Indeed, the observed permeability of gases in these CNT membranes scales inversely with the molecular weight by an exponent ~0.4 (for ideal Knudsen diffusion this is 0.5); however, the diffusivities are around one to two orders of magnitude larger than Knudsen diffusivity predictions [19, 62]. Thus, a Knudsen-type diffusive transport, but with a highly specular reflection along the CNT walls, is the dominant gas-transport mechanism for open-ended CNT membranes. The next obvious question is how can we utilize these amazing mass-transport properties for real-life gas-separation applications. We must recognize that in such applications one is interested not only in the throughput, but also in the selectivity; here is the caveat. The smoothness of the graphitic interiors, which is the reason for fast transport, is actually responsible for the lack of selectivity – the selectivity will be limited by the Knudsen-type selectivity. For all practical applications, it would, therefore, be necessary to impart selectivities based on either functional molecules or surface adsorption–diffusion in CNTs with much smaller diameter (<1 nm) [63].

A school of thought is to include these nanoscale materials in conventional membranes to augment vapor/gas-transport efficiencies. For example, let us consider membrane distillation, a thermal-membrane process for desalination of seawater. In this process, water vapor is preferentially transported through the hydrophobic pores of membranes over saline water to affect the separation. The advantage of the membranes, here, is to lower the thermal requirements due to convective mass-transport effects. Open-ended CNTs, where the kinetics of gas transport is much larger than Knudsen-type diffusion, could be a potentially interesting additive to the conventional microporous and hydrophobic membranes. Indication about the validity of such concepts comes from pervaporative separation of benzene/cyclohexane using membranes based on polyvinyl alcohol–CNT–chitosan mixed-matrix membranes [64]. Pervaporation is a process by which a component in a liquid mixture is preferentially vaporized through the membranes. It was observed that the incorporation of CNTs increased not only the permeability of benzene but also its selectivity compared to similar membranes without the CNTs.

Let us now address, from the perspective of gas separations, where membranes based on CNTs stand. Zeolites have been the basis of the chemical industry from selective adsorptive separations for several decades. However, synthesis of defect-free zeolite membranes is yet to reach commercial success, mainly because their irregular grain and pore structure is incompatible to large-area synthesis of membranes. If CNTs, with their crystalline pore and small pore dimensions (<1 nm), could achieve the selectivity of zeolites, the recent developments in the synthesis of defect-free CNT membranes would be important in several gas-separation applications. However, the smallest dimensions (1–2 nm) of the CNT membranes made till date are not suitable for such sieving purposes and the gas-separation properties of open-ended CNT membranes are, at best, modest. Mixed-matrix CNT membranes seem to be potentially more attractive toward gas-separation applications [65].

1.14.3.3 CNT Membranes for Stimuli-Responsive Applications

CNTs have several unique properties, including high electrical conductivity and elasticity, which have been exploited in creating stimuli-responsive membranes. An account of such demonstrations and how it might influence some technologies is presented in this section.

Researchers have demonstrated that superhydrophobic CNT arrays can be rendered hydrophilic by application of an electric potential. These membranes are analogous to dense outer-wall membranes, but are superhydrophobic; water transport through the CNT arrays can be controlled by the application of an electrical bias to the membrane (see **Figures 4(a)** and **4(b)**) [66]. Although this potential-dependent wicking behavior through the CNT membrane is analogous to the well-known phenomenon of electrowetting, the ability to control water transport through a membrane structure by an external stimulus can be useful in applications where controlled transport of water droplets is necessary, for example, in lab-in-a-chip devices.

Another example of controlled molecular transport through CNT membranes is an effort to mimic the complex functionality of biological voltage-gated membrane channels in artificial systems. In simplified terms, biologists have shown that charged

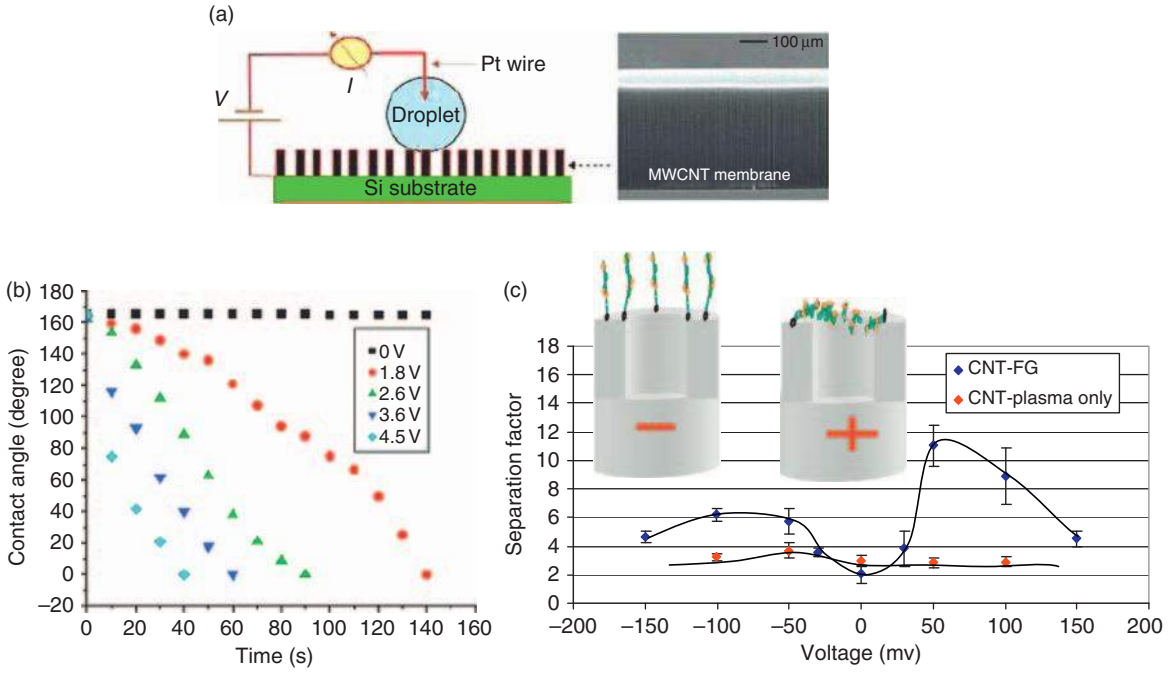

Figure 4 Voltage-controlled transport through carbon nanotube (CNT) membranes. (a) Contact angle measurements on dense-array outer-wall CNT membrane as a function of applied electrical potential. (b) Variation of contact angle with applied potential. Change of contact angle allows control of transport of water droplets for drop-in-demand-type applications. Figures (a) and (b) used with permission Wang, Z. K., Ci, L. J., Chen, L., Nayak, S., Ajayan, P. M., Koratkar, N. *Nano Lett.* **2007**, *7*, 697–702. (c) Voltage-gated membrane channels, in which large macromolecules tethered to the conducting pores of CNTs can be actuated to selectively occlude the pores. Figure used with permission from Majumder, M., Zhan, X., Andrews, R., Hinds, B. J. *Langmuir* **2007**, *23*, 8624–8631. This results in a voltage-controlled transport, mimicking biological membranes, for transdermal drug delivery-type applications.

protein segments in the membrane channels induce paddle-like conformational changes, in response to an external stimuli, such as voltage, thereby changing the transport through the channel [67]. Molecules attached to the walls and entrances of CNT membranes can be actuated electrostatically, thereby selectively occluding the pores and altering transport of molecules through the pores [68]. In these experiments, the electrically conducting CNT membrane is the electrode in a three-electrode electrochemical cell, and demonstrates the ability of these membranes to mimic voltage-gated channels found in nature (see **Figure 4(c)**). Such electrostatically actuated molecular transport is being considered as the enabling principle in transdermal drug delivery devices.

From voltage-controlled transport properties to mechanically regulated transport, CNT membranes can exhibit them all. Membranes that change pore size in response to compressive forces are found in the kidney. Li *et al.* [69] have utilized the super-compressible property of CNTs to mimic such behavior. Super-compressibility is a spring-like property of vertically oriented CNTs in which the arrays can be compressed to a zigzag configuration, but retain their original texture when the force is released [70]. Application of compressive force to the vertically oriented dense outer-wall membrane flattens the nanotubes and decreases the pore size between them, resulting in the concomitant increase in steric selectivity and decrease in water permeability (see **Figure 5**).

The concept of stimuli-responsive membranes is pertinent to biological membrane channels and mimicking them in artificial systems to create functional membranes can be fundamentally elegant, as well as useful in practical applications, such as in microfluidics and lab-on-a-chip devices.

1.14.3.4 CNT Membrane in Liquid Transport Applications

There had been several early experiments demonstrating the ability of the tubular interior of the CNTs to be used as nanoscale containers or conduits

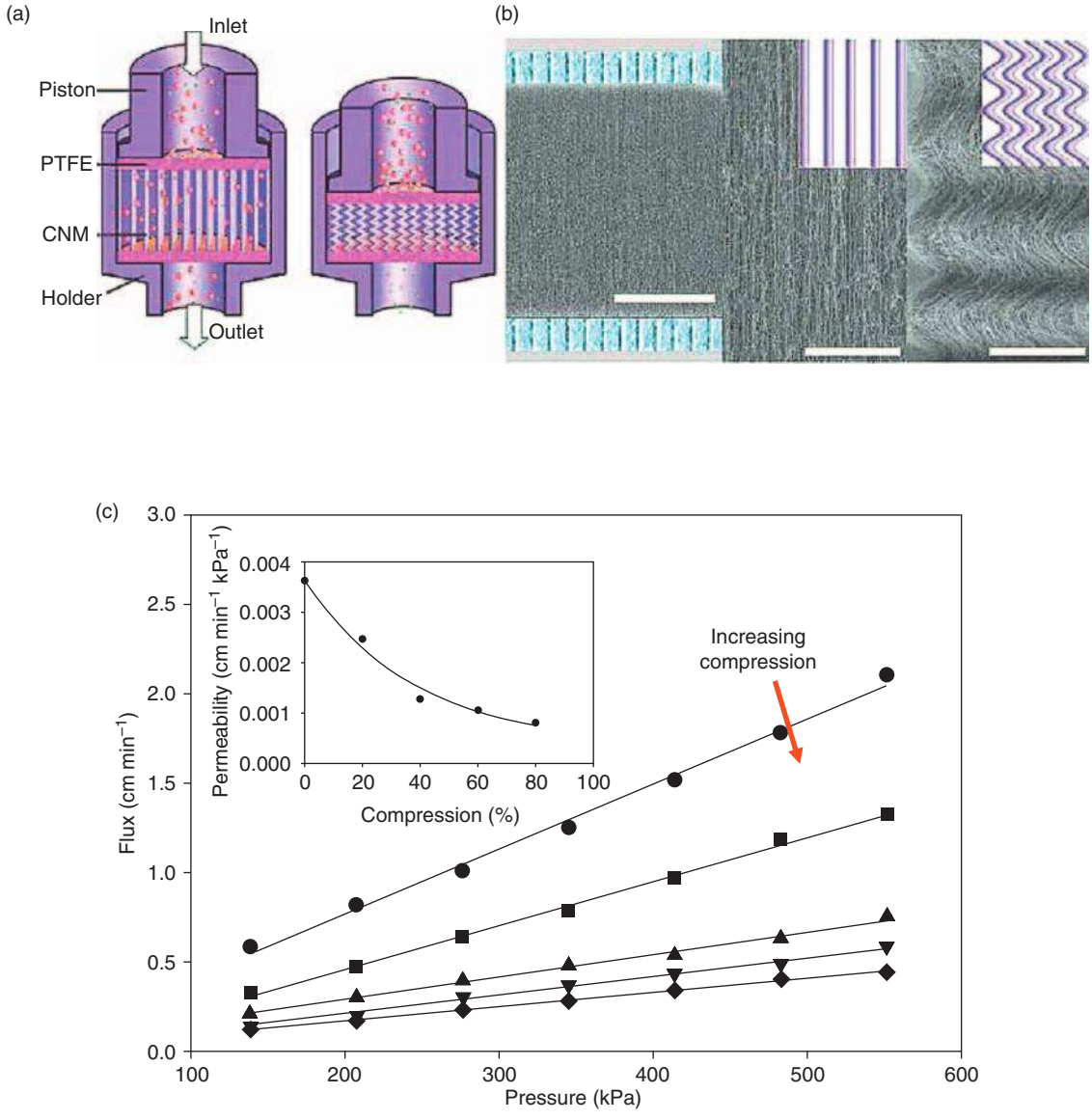

Figure 5 Compression-modulated transport through carbon nanotube (CNT) membrane. (a) The experimental apparatus for water transport studies in the dense-array outer-wall CNT membrane, simultaneously with applied compressive force (b). SEM images showing that the compressive force causes the membranes to shrink the inter-nanotube distance with a concomitant decrease in liquid permeability (c). This is yet another demonstration that transport through membranes composed of CNTs can be tuned by an external stimuli such as pressure. All pictures obtained with permission from Li, X., Zhu, G,. Dordick, J. S., Ajayan, P. M. *Small* **2007**, *3*, 595–599.

for mass transport. The earliest experiments demonstrating the feasibility of infiltration of liquid molten metal, such as lead, inside the inner cores of CNTs were conducted by Ajayan and Ijima in 1993 [7]. In a subsequent publication in the same year, the group reported that inorganic materials, such as lead oxide, were more difficult to incorporate inside open-ended CNTs than molten metals [8]. Dujardin *et al.* [9, 10] also studied the wetting behavior of CNTs by infiltration of molten metals in bulk MWCNT samples with diameters of 2–20 nm. It was concluded that liquids with surface tension less than $\sim$80 mN m^{-1} will wet the MWCNTs. Hence, liquids such as water ($\sim$80 mN m^{-1} at 20 °C) and organics (e.g., ethanol has a surface tension of $\sim$20 mN m^{-1} at 20 °C), which have significantly less surface tension, could

easily wet MWCNTs. Nevertheless, the important conclusion from these early reports was the feasibility of opening the CNTs using gas-phase oxidation such that the CNTs would act as nanoscale containers for host materials [71].

However, the initial foray into the transport behavior of liquids, such as water, through the CNTs, as in the case of gases, was through computer simulations. At the National Institutes of Health in Maryland, Gerard Hummer's interest in water transport through CNTs was primarily derived from their hydrophobic nature and similarity to protein channels. CNTs perhaps provided the possibility of a much simpler model for MD simulations compared to complex protein channels. Their seminal publication in 2001 suggested that hydrophobic CNT channels, aided by the frictionless and smooth graphitic walls along with a cooperative behavior of a single-file hydrogen-bonded network, allow water to be transported at extraordinary speed [12]. Kalra *et al.* [72] studied the osmotically driven transport of water through CNTs, and the simulated water-flow velocities were very close to those found in natural water channels such as aquaporin. More esoterically, Klaus Schulten's group at the University of Illinois Urbana-Champaign studied water and proton transport behavior through CNTs. In their simulations, the water dipoles were found to be aligned unidirectionally in pristine nanotubes, but somewhat disturbed in CNTs containing charged groups, indicating a structural change in the water structure inside defective CNTs [73]. Nick Quirke's group at Imperial College reported extremely rapid wicking kinetics of oil in CNTs and that the kinetics were not explainable by the conventional Washburn equation [74]. Overall, the simulation studies by all these scientists indicated that the physics of the interaction of liquids, particularly water, with CNTs is something special and needs efforts from their experimental counterparts.

Yuri Gogotsi and coworkers of Drexel University have experimentally studied the behavior of water inside hydrothermally synthesized CNTs by *in situ* microscopy techniques. In 2002 [75], the group reported that the flow velocities of water is $\sim 0.5 \times 10^{-6}$ m s^{-1} in 50-nm inner-diameter nanotubes. Although this study conclusively proved the presence of water in equilibrium with a gas inside the CNTs, uncertainty remained as to the driving force of this transport measurement. In a subsequent work, MWCNTs were hydrothermally filled with water, frozen at –80 °C, and examined by high-resolution transmission electron microscopy and electron emission loss spectrometry [76]. Two key observations emerged from this study. The first one indicated that the CNTs with larger pore diameter (20–100 nm) had water segments interspersed with intermittent air pockets, while a rather continuous cylinder of water existed in CNTs with smaller pore diameter in the range of 5–10 nm. In the other case, an air gap of ~4 Å between the graphitic walls and frozen water was also observed, especially in the case of smoother graphitic nanotubes [77]. This observation of an air gap between the graphitic surface and the proximal layer of water is remarkable and can be explained by drying transitions of water in nanoscale hydrophobic objects [78].

The earliest experimental mass-transport measurements through CNTs were undertaken on single-pore CNT membranes of ~120-nm pore diameter by the Crooks group, formerly at Texas A&M University [79]. The large-diameter single-pore nanotubes did not exhibit any unusual transport properties and were suited as Coulter counting devices. A Coulter counter is a device that can count biological cells or colloidal particles based on the measurement of ion current through the pores [80]. Based on this approach, there is potential for the development of single-pore membranes of (1–2-nm diameter) for stochastic ion-channel sensing of DNA/RNA translocation [81].

For more macroscopic measurements, flow velocity of liquids ($\mathcal{J}$) through porous membranes can be predicted using the Hagen–Poiseuille equation and is given by

$$\mathcal{J} = \frac{\varepsilon_p . \mu . r^2 . \Delta P}{8 . \mu . \tau . L}$$

where ε_p is the relative porosity, r_0 the pore radius, P the applied pressure, μ the dynamic viscosity, τ the tortuosity, and L the pore length. The basic assumptions behind this equation are laminar flow and no slip at the boundary layer (i.e., the velocity of the fluid at the CNT wall is zero) and is available in any standard fluid mechanics text.

Pressure-induced transport of a variety of liquids, including water, ethanol, isopropyl alcohol, hexane, and decane, was studied through the inner core of open-ended CNT membrane structure. Enhancement factors for different liquids, shown in **Table 1**, are calculated from the equation

$$\text{Enhancement factor} = \frac{\text{Experimentally observed flow velocity}}{\text{Hagen–Poiseuille flow velocity}}$$

The flow velocities were found to exceed predictions of liquid flow with no-slip boundary condition by 10 000–100 000-fold, suggesting frictionless flow through the CNT cores [11]. The observed flow velocities were consistent with MD simulation predictions by Hummer *et al.*, and have also been confirmed in sub-2-nm CNTs by another independent research group [19]. Interestingly, progressive functionalization of the CNT tips and cores by bulk macromolecules slowed down the flow of liquids through the membrane, confirming the hypothesis that the enhanced flow velocities are due to the noninteracting nature of the graphitic cores [62]. However, the mechanism of fast water transport through CNTs is still unclear. Hummer's MD simulations [12] were obtained for very small nanotubes (~0.8 nm) and suggested a hydrogen-bonded single-file transport of water molecules. It is possible that these simulation results are not applicable to larger nanotubes, such as those in the recent experimental observations in nanotubes with ~1.6- or ~7-nm diameters. More applicable for these dimensions of nanotubes is the concept of slip boundary conditions. Theoretically, the existence of micron-scale slip lengths has been explained by the presence of a gas–liquid or a depletion interface, which provides a nonzero velocity at the walls [82, 83]. Recent MD simulations have attempted to understand the water structure at the depletion region of a smooth nanotube interface and relate it to the water-transport properties [84]. Although water transport in tubular nanoscale channels made from, for example, boron nitride, Si, or CNTs with rough surfaces behaved in a usual manner, the enhancement factors on 1.6-nm-diameter CNT showed excellent agreement with prior experimental data. These simulations underline the direct relationship between the noninteracting graphitic interface and their unique mass-transport properties. Despite these developments, there remain several unresolved questions regarding the structure and properties of liquids in the hydrophobic cores of CNTs. It is likely that the experimental scaffolds made from CNTs, using methods as discussed earlier, can shed light on some of these nanoscale transport phenomena.

Transiting to the more worldly applications of these membranes–liquid filtration studies on dense outer-wall membranes made from CNTs can separate bacteria such as *Escherichia coli* and *Staphylococcus aureus* and even polio virus in the size range of ~25–30 nm. A competitive advantage of these membranes over polymeric counterparts is the ability to use autoclave processes at ~121 °C for steam cleaning [17]. These membranes could be an alternative to commercial ultrafiltration membranes for separation of bacteria, virus, and proteins. One must also recognize another unique advantage of these membranes – the high electrical conductivity can enable several flux regeneration strategies using principles of electrochemistry.

The concept of membrane reactors, which combine reaction and separation to increase efficiency based on laws of mass action, is well established [85]. The development of electrochemical membrane reactors has been stymied by the lack of electrical conductivity of the membrane materials used to date. As discussed earlier, the high electrical conductivity, chemical inertness of the dense-array outer-wall CNT membranes make them a candidate for simultaneous electrochemical reaction and separation, particularly for destruction of hazardous organic compounds [86]. The concept of such a membrane reactor is shown in **Figure 6**, which could possibly oxidize phenol to benign compounds such as carbon dioxide, water, and aliphatic compounds such as oxalic acid, along with CO_2 and H_2O [87].

The fast water transport through the inner core of CNTs along with the steric and electrostatic selectivity offered by the pores of the nanotubes will have competitive advantage over traditional liquid filtration membranes. In this vein, researchers are considering the use of CNT membranes for developing compact and energy-efficient desalination systems – all stemming from the exceptional mass-transport properties of the CNTs. The inspiration for CNT-membrane-based desalination comes from biological protein channels known as aquaporin, which can transport water at extraordinary speed and selectivity [88] (see **Figure 7**).

Although the ability of CNTs to transport water at speeds close to that of aquaporin has been shown by several research groups, rejection of monovalent ions (in the range of 80–90%) by nanotubes has not been demonstrated. The book-chapter was written in late 2008. However, recently, Donnan-type exclusion has been realized in CNT membranes. Please see the article by Fornasiero *et al.* for more details. Therefore, it remains one of the grand challenges in CNT membrane research – the possibilities being

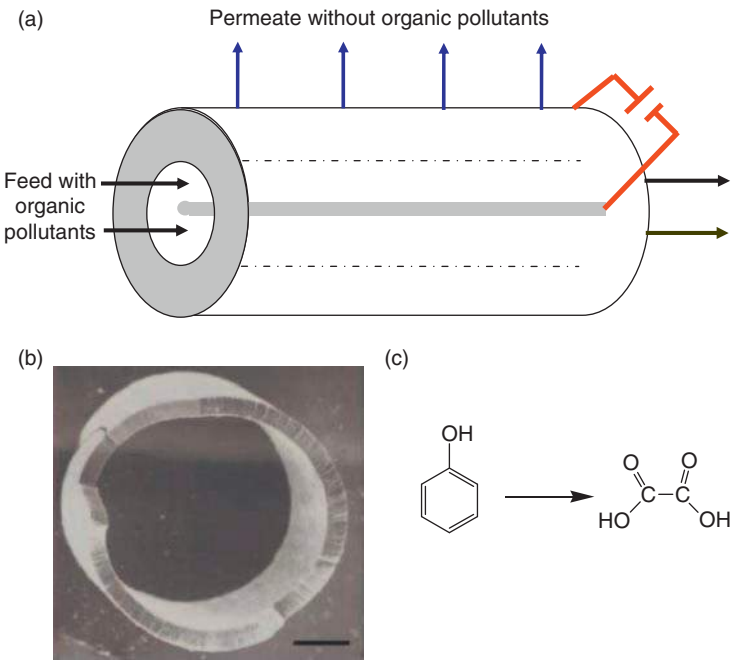

Figure 6 (a) Illustration of a cross-flow electrochemical membrane reactor based on carbon nanotube (CNT) membranes. (b) Scanning electron microscopy (SEM) of a cylindrical-shaped dense-array CNT membrane. Adapted with permission from Srivastava, A., Srivastava, O. N., Talapatra, S., Vajtai, R., Ajayan, P. M. *Nat. Mater*. **2004**, *3*, 610–614. (c) Example of electrochemical oxidation of an organic compound, phenol, at the CNT membrane electrode. The removal of the products can aid in increased conversion efficiency based on Le Chatelier's principle and could be accomplished either by the CNT electrode alone or with functional nanoscale catalysts. Although the reaction shown here is representative of the concept of conversion of a hazardous material such as phenol to a benign compound such as oxalic acid, this general concept could be extended to other hazardous organic compounds.

rejection of ions by nanotubes through electrostatic rejection by charged groups on the CNTs via a Donnan exclusion mechanism or by an energy-barrier-based exclusion mechanism [89] in smaller-diameter (~1 nm or smaller) CNTs. There have been reports for synthesis of CNTs with ~0.8 nm [90], and even smaller diameter of ~0.3 nm [91], providing credence to the concept of nanotube membranes for desalination. While the Donnan-type separation is likely to produce ~50–60% salt rejections [92] – similar to nanofiltration membranes – the presence of functional groups will decrease the permeability. A mechanism based on smaller-diameter CNTs, although a significant technical challenge, can obtain both selectivity and permeability not observed in conventional membrane materials. It is estimated that CNT membranes with ion-rejection capabilities, similar to those in reverse-osmosis membranes, can reduce the cost of desalination by as much as 75% [93]. Owing to this significant advantage, Shanon *et al.* [14] have identified desalination by nanotube membranes as the technology for the coming decade.

Another potential application of these membranes is as solvent-resistant nanofiltration membranes for recovery and reuse of transition-metal catalysts in the size range of 1–3 nm [94]. The current state-of-the-art membranes based on polymers, such as poly-dimethyl siloxane or poly-imides, are lacking in chemical stability, selectivity, and flux [95]; CNT membranes, with their chemical stability, high solvent transport characteristics, and steric selectivity based on the inner core of the CNTs, can be a dramatic improvement over the conventional membrane materials.

Finally, we move from the larger to smaller scale applications, that is, interfacing nanofluidic materials, particularly CNTs, with microfluidic devices [15]. Although assembly and hierarchical synthesis strategies for seamlessly integrating the nanofluid channels with microfluidic devices constitute a significant challenge for the scientific community (**Figure 8**),

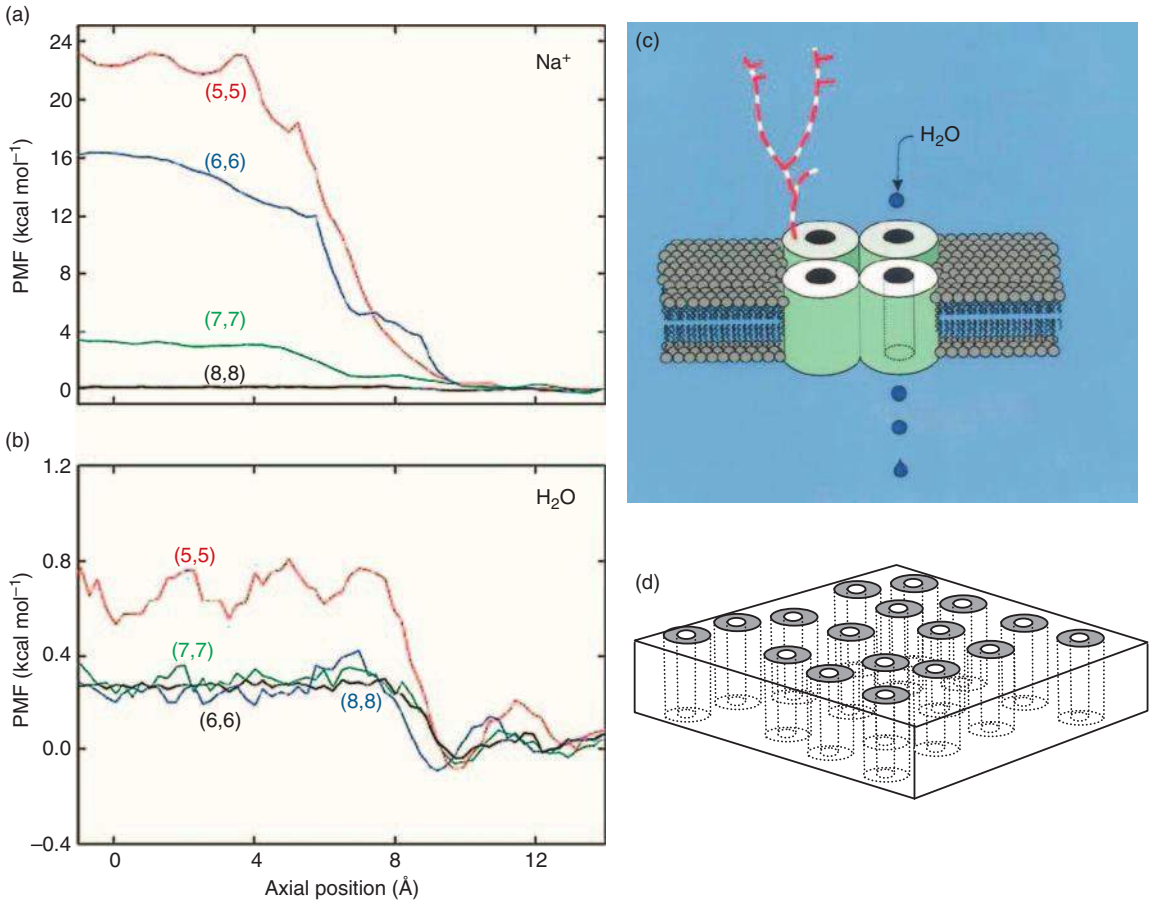

Figure 7 Molecular dynamic studies of ion (a) and water (b) permeation through an open-ended carbon nanotube (CNT) membrane composed of (5,5), (6,6), (7,7), and (8,8) CNTs. Potential of mean force (PMF) is the force for pulling an ion (a) or water molecule (b) from the bulk solution ($z = 14$) to the center of the pore ($z = 0$). Note the considerably large energy barrier for penetration of Na^+ for small-diameter nanotubes. Figures (a) and (b) used with permission from Corry, B. *J. Phys. Chem. B* **2007**, *112*, 1427–1434. The recent enthusiasm of CNTs for salt removal is inspired by protein channels such as aquaporin (c), which can transport water very selectively and with extraordinary speed. Figure used with permission Nielsen, S., Frokiar, J., Marples, D., Kwon, T.-H., Agre, P., Knepper, M. A. *Physiol. Rev.* **2002**, *82*, 205–244. This forms the inspiration for developing CNT membranes (d) for desalination. Figure (d) used with permission from Majumder, M., Zhan, X., Andrews, R., Hinds, B. J. *Langmuir* **2007**, *23*, 8624–8631.

CNTs can provide multifunctional properties, such as frictionless flow, voltage-controlled transport, and electrokinetic mixing at the nanoscale. Therefore, such themes are emerging areas of research in CNT membranes.

1.14.4 Directions of Future Research

CNT membranes represent an emerging branch of membrane science with myriad opportunities in materials science and engineering, which can spawn applications in diverse areas concerning our environment and energy. Researchers may be inspired by the fact that a concerted effort in the United States, presently, is considering CNT membranes as alternatives to mature materials, such as thin-film composite membranes, for desalination of seawater. At this point, it may be worthwhile to reiterate that this novel class of membranes can provide several competitive advantages, such as:

1. very fast liquid- and gas-transport properties;
2. tighter control over the pore-size distribution;
3. chemically tuned mass-transport properties;
4. stimuli-responsive behavior; and
5. well-defined nanofluidic scaffolds for understanding molecular transport at the nanoscale.

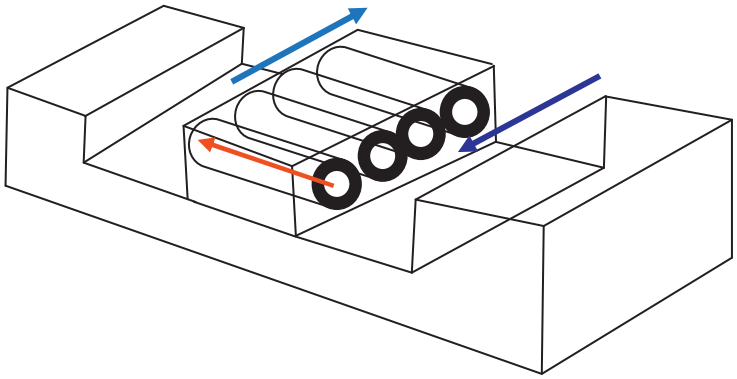

Figure 8 Illustration of carbon nanotubes (CNTs) as an interface between two microfluidic channels. The CNTs could act as filtration channels, control transport of molecules through external stimuli, such as voltage, or aid in mixing via electrokinetic phenomena at the nanoscale. While some of these application potentials have been demonstrated in voltage-controlled transport experiments in macroscopic membranes [66, 68], the template synthesis allows seamless integration of these nanoscale transport channels into microfluidic platforms.

It is not surprising that a wide range of applications in controlled-release devices, sensors, membrane reactors, and nanoscale fluidic interconnects in microfluidic devices along with traditional membrane separations (which we will discuss later) can be easily conjured. Such a wide range of properties, not obvious with traditional membrane material, is why CNT-based membranes are a new frontier in membrane science. In this chapter, we have discussed different approaches for the fabrication of these membranes and showcased their novel transport properties. To further aid our readers, a summary of the demonstrated and future applications (as thought by the authors) of membranes based on CNTs is presented in **Table 2**. For example, the dense-array outer-wall CNT membranes are potentially attractive for ultrafiltration applications such as protein separations. Their electrical conductivity could be useful for flux regeneration and environmental remediation applications as electrochemical membrane reactors. Open-ended CNT membranes are being considered for desalination applications, while mixed-matrix membranes could provide materials with novel transport properties for conventional membrane processes, such as membrane distillation, pervaporation, or gas separation.

Table 2 Current status and future applications of CNT membrane

Type of CNT membrane	*Pore size*	*Applications demonstrated*	*Future applications*
Template-synthesized CNT membrane	20 nm [20] 200 nm [23]	Water-vapor/oxygen separation [20] Electro-osmotic transport [23]	Nanofluidic interconnects in microfluidic platforms
Dense-array outer-wall CNT membrane	20–100 nm [17]	Heavy hydrocarbon (liquid) separation [17]	Ultra filtration membranes
		Bacteria separation [17]	Electrochemical membrane reactors
		Voltage-controlled transport [66]	
		Protein separation [69]	
		Compression-modulated transport [69]	
Open-ended CNT membrane	1–2 nm [19] ~7 nm [18]	Nanoparticle separation [50] Small-molecule separation [50]	Desalination [14] Recovery of homogenous catalysts
		Voltage-gated transport for transdermal drug delivery [68]	Dialysis Stochastic sensing [81]
Mixed-matrix CNT membranes	Nonporous	Gas separation [44] Pervaporation [64]	Gas separation Pervaporation

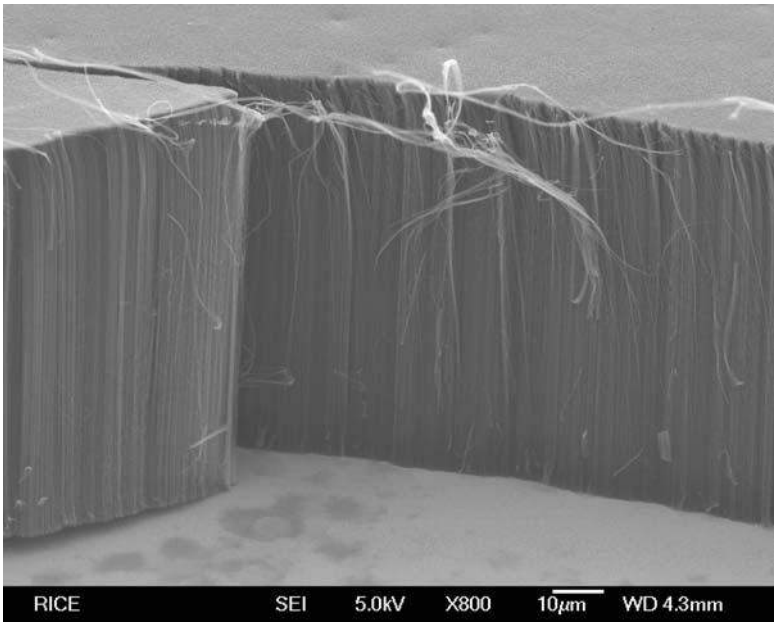

Figure 9 Future research has to be focused on tuning the growth of CNTs with closer packing, finer (1–2 nm) pores, and less spread in pore sizes. Several critical applications, such as desalination and separation of homogenous catalysts, require uniformity of the dimensions of the nanotube in large areas. Shown here is a scanning electron microscopy (SEM) image of an array of SWCNT, in which the theoretical inner diameter can be as small as 0.4 nm. Courtesy of Dr. Robert Hauge, Chemistry, Rice University.

Despite this euphoria, challenges remain to synthesize these membranes reproducibly, cost effectively, and with minimum spread of diameters over large areas. For example, desalination membranes for >95% salt rejection (a very modest number for desalination purposes) would require less than 1 in 100 tubes above 1-nm diameter [89]. These approaches could be controlled at the formation stage, that is, understanding and fine-tuning the growth of nanotubes. An array of SWCNT (with inner diameter ~3 nm) grown by hot-filament CVD technique at Rice University is shown in **Figure 9**.

The alternative approach would require utilization of diameter-controlled sorting of CNTs from SWCNT suspensions [96], followed by alignment of CNTs based on self/electric-field-based assembly. To sum, research on CNT membranes is at its nascent stage of evolution – several real-life applications can emerge in the near future – however, several fundamental and engineering questions still remain unaddressed. Therefore, this highly rewarding and crosscutting multidisciplinary research area needs synergistic contributions from nanoscale materials science, composite materials engineering, and transport phenomena to bring paradigms to several conventional technologies.

References

[1] Iijima, S. *Nature* **1991**, *354*, 56–58.
[2] Iijima, S., Ichihashi, T. *Nature* **1993**, *363*, 603–605.
[3] Monthioux, M., Kuznetsov, V. L. *Carbon* **2006**, *44*, 1621–1623.
[4] Fischer, J. E., Dai, H., Thess, A., *et al. Phys. Rev. B* **1997**, *55*, R4921.
[5] Frank, S., Poncharal, P., Wang, Z. L., Heer, W. A. *Science* **1998**, *280*, 1744–1746.
[6] Dai, H., Wong, E. W., Lieber, C. M. *Science* **1996**, *272*, 523–526.
[7] Ajayan, P. M., Iijima, S. *Nature* **1993**, *361*, 333–334.
[8] Ajayan, P. M., Ebbesen, T. W., Ichihashi, T., Iijima, S., Tanigaki, K., Hiura, H. *Nature* **1993**, *362*, 522–525.
[9] Dujardin, E., Ebbesen, T. W., Hiura, H., Tanigaki, K. *Science* **1994**, *265*, 1850–1852.
[10] Dujardin, E., Ebbesen, T. W., Krishnan, A., Treacy, M. M. J. *Adv. Mater.* **1998**, *10*, 1472–1475.
[11] Majumder, M., Chopra, N., Andrews, R., Hinds, B. J. *Nature* **2005**, *438*, 44.
[12] Hummer, G., Rasaiah, J. C., Noworyta, J. P. *Nature* **2001**, *414*, 188–190.
[13] Ackerman, D. M., Skoulidas, A. I., Sholl, D. S., Johnson, J. K. *Mol. Simul.* **2003**, *29*, 677–684.
[14] Shannon, M. A., Bohn, P. W., Elimelech, M., Georgiadis, J. G., Marinas, B. J., Mayes, A. M. *Nature* **2008**, *452*, 301–310.
[15] Whitby, M., Quirke, N. *Nat. Nanotechnol.* **2007**, *2*, 87–94.
[16] Miller, S. A., Young, V. Y., Martin, C. R. *J. Am. Chem. Soc.* **2001**, *123*, 12335–12342.
[17] Srivastava, A., Srivastava, O. N., Talapatra, S., Vajtai, R., Ajayan, P. M. *Nat. Mater.* **2004**, *3*, 610–614.

[18] Hinds, B. J., Chopra, N., Rantell, T., Andrews, R., Gavalas, V., Bachas, L. G. *Science* **2004**, *303*, 62–65.
[19] Holt, J. K., Park, H. G., Wang, Y., *et al. Science* **2006**, *312*, 1034–1037.
[20] Alsyouri, H. M., Langheinrich, C., Lin, Y. S., Ye, Z., Zhu, S. *Langmuir* **2003**, *19*, 7307–7314.
[21] Sano, T., Iguchi, N., Iida, K., Sakamoto, T., Baba, M., Kawaura, H. *Appl. Phys. Lett.* **2003**, *83*, 4438–4440.
[22] Cho, S.-H., Walther, N. D., Nguyen, S. T., Hupp, J. T. *Chem. Commun.* **2005** 5331–5333.
[23] Miller, S. A., Young, V. Y., Martin, C. R. *J. Am. Chem. Soc.* **2001**, *123*, 12335–12342.
[24] Jirage, K. B., Hulteen, J. C., Martin, C. R. *Science* **1997**, *278*, 655–658.
[25] Mattia, D., Rossi, M. P., Kim, B. M., Korneva, G., Bau, H. H., Gogotsi, Y. *J. Phys. Chem. B* **2006**, *110*, 9850–9855.
[26] Meng, G., Jung, Y. J., Cao, A., Vajtai, R., Ajayan, P. M. *Proc. Natl. Acad. Sci. U.S.A.* **2005**, *102*, 7074–7078.
[27] Bronikowski, M. J., Willis, P. A., Colbert, D. T., Smith, K. A., Smalley, R. E. Vacuum, Thin Films, Surfaces/Interfaces, and Processing NAN06. In *The 47th International Symposium*, Boston, MA, 2001; pp 1800–1805.
[28] Jin, L., Bower, C., Zhou, O. *Appl. Phys. Lett.* **1998**, *73*, 1197–1199.
[29] Thostenson, E. T., Chou, T.-W. *J. Phys. D: Appl. Phys.* **2002**, *35*, L77–L80.
[30] Smith, B. W., Benes, Z., Luzzi, D. E., *et al. Appl. Phys. Lett.* **2000**, *77*, 663–665.
[31] Casavant, M. J., Walters, D. A., Schmidt, J. J., Smalley, R. E. *J. Appl. Phys.* **2003**, *93*, 2153–2156.
[32] deHeer, W. A., Bacsa, W. S., Chatelain, A., *et al. Science* **1995**, *268*, 845–847.
[33] Li, W. Z., Xie, S. S., Qian, L. X., *et al. Science* **1996**, *274*, 1701–1703.
[34] Ren, Z. F., Huang, Z. P., Xu, J. W., *et al. Science* **1998**, *282*, 1105–1107.
[35] Andrews, R., Jacques, D., Rao, A. M., *et al. Chem. Phys. Lett.* **1999**, *303*, 467–474.
[36] Raravikar, N. R., Schadler, L. S., Vijayaraghavan, A., Zhao, Y., Wei, B., Ajayan, P. M. *Chem. Mater.* **2005**, *17*, 974–983.
[37] Safadi, B., Andrews, R., Grulke, E. A. *J. Appl. Polym. Sci.* **2002**, *84*, 2660–2669.
[38] Huang, S., Dai, L. *J. Phys. Chem. B* **2002**, *106*, 3543–3545.
[39] Chiang, I. W., Brinson, B. E., Smalley, R. E., Margrave, J. L., Hauge, R. H. *J. Phys. Chem. B* **2001**, *105*, 1157–1161.
[40] Mi, W. L., Lin, Y. S., Li, Y. D. *J. Membr. Sci.* **2007**, *304*, 1–7.
[41] Kim, S., Jinschek, J. R., Chen, H., Sholl, D. S., Marand, E. *Nano Lett.* **2007**, *7*, 2806–2811.
[42] Robeson, L. M. *J. Membr. Sci.* **1991**, *62*, 165–185.
[43] Mahajan, R., Koros, W. J. *Ind. Eng. Chem. Res.* **2000**, *39*, 2692–2696.
[44] Geng, H.-Z., Kim, K. So, K., Lee, Y., Chang, Y., Lee, Y. *J. Am. Chem. Soc.* **2007**, *129*, 7758–7759.
[45] Kim, S., Pechar, T. W., Marand, E. *Desalination* **2006**, *192*, 330–339.
[46] Hollman, A. M., Bhattacharyya, D. *Langmuir* **2004**, *20*, 5418–5424.
[47] Hollman, A. M., Christian, D. A., Ray, P. D., *et al. Biotechnol. Prog.* **2005**, *21*, 451–459.
[48] Ago, H., Kugler, T., Cacialli, F., *et al. J. Phys. Chem. B* **1999**, *103*, 8116–8121.
[49] Domingo-Garcia, M., Lopez-Garzon, F. J., Perez-Mendoza, M. *J. Colloid Interface Sci.* **2000**, *222*, 233–240.
[50] Majumder, M., Chopra, N., Hinds, B. J. *J. Am. Chem. Soc.* **2005**, *127*, 9062–9070.
[51] Majumder, M., Keis, K., Zhan, X., Meadows, C., Cole, J., Hinds, B. J. *J. Membr. Sci.* **2008**, *316*, 89–96.
[52] Alison, J. D. *Electroanalysis* **2000**, *12*, 1085–1096.
[53] Mao, Z., Sinnott, S. B. *J. Phys. Chem. B* **2000**, *104*, 4618–4624.
[54] Sokhan, V. P., Nicholson, D., Quirke, N. *J. Chem. Phys.* **2001**, *115*, 3878–3887.
[55] Sokhan, V. P., Nicholson, D., Quirke, N. *J. Chem. Phys.* **2002**, *117*, 8531–8539.
[56] de Lange, R. S. A., Keizer, K., Burggraaf, A. J. *J. Membr. Sci.* **1995**, *104*, 81–100.
[57] Cussler, E. L. *Diffusion: Mass Transfer in Fluid Systems*, 2nd edn.; Cambridge University Press: London, 2003.
[58] Rao, M. B., Sircar, S. *J. Membr. Sci.* **1993**, *85*, 253–264.
[59] Fuertes, A. B. *J. Membr. Sci.* **2000**, *177*, 9–16.
[60] Arya, G., Chang, H.-C., Maginn, E. J. *Phys. Rev. Lett.* **2003**, *91*, 026102.
[61] Cooper, S. M., Cruden, B. A., Meyyappan, M., Raju, R., Roy, S. *Nano Lett.* **2004**, *4*, 377–381.
[62] Majumder, M. PhD Dissertation, University of Kentucky, 2007, 43–66.
[63] Wei, B.-Y., Hsu, M.-C., Yang, Y.-S., Chien, S.-H., Lin, H.-M. *Mater. Chem. Phys.* **2003**, *81*, 126–133.
[64] Peng, F., Pan, F., Sun, H., Lu, L., Jiang, Z. *J. Membr. Sci.* **2007**, *300*, 13–19.
[65] Cong, H., Zhang, J., Radosz, M., Shen, Y. *J. Membr. Sci.* **2007**, *294*, 178–185.
[66] Wang, Z. K., Ci, L. J., Chen, L., Nayak, S., Ajayan, P. M., Koratkar, N. *Nano Lett.* **2007**, *7*, 697–702.
[67] Jiang, Y., Lee, A., Chen, J., *et al. Nature* **2003**, *423*, 33–41.
[68] Majumder, M., Zhan, X., Andrews, R., Hinds, B. J. *Langmuir* **2007**, *23*, 8624–8631.
[69] Li, X., Zhu, G,. Dordick, J. S., Ajayan, P. M. *Small* **2007**, *3*, 595–599.
[70] Cao, A., Dickrell, P. L., Sawyer, W. G., Ghasemi-Nejhad, M. N., Ajayan, P. M. *Science* **2005**, *310*, 1307–1310.
[71] Ajayan, P. M., Stephan, O., Redlich, P., Colliex, C. *Nature* **1995**, *375*, 564–567.
[72] Kalra, A., Garde, S., Hummer, G., *Proc. Natl. Acad. Sci. U.S.A.* **2003**, *100*, 10175–1080.
[73] Zhu, F., Schulten, K. *Biophys. J.* **2003**, *85*, 236–244.
[74] Supple, S., Quirke, N. *Phys. Rev. Lett.* **2003**, *90*, 214501.
[75] Megaridis, C. M., Yazicioglu, A. G., Libera, J. A., Gogotsi, Y. *Phys. Fluids* **2002**, *14*, L5–L8.
[76] Rossi, M. P., Ye, H. H., Gogotsi, Y., Babu, S., Ndungu, P., Bradley, J. C. *Nano Lett.* **2004**, *4*, 989–993.
[77] Naguib, N., Ye, H. H., Gogotsi, Y., Yazicioglu, A. G., Megaridis, C. M., Yoshimura, M. *Nano Lett.* **2004**, *4*, 2237–2243.
[78] Lum, K., Chandler, D., Weeks, J. D. *J. Phys. Chem. B* **1999**, *103*, 4570–4577.
[79] Sun, L., Crooks, R. M. *J. Am. Chem. Soc.* **2000**, *122*, 12340–12345.
[80] Ito, T., Sun, L., Crooks, R. M. *Anal. Chem.* **2003**, *75*, 2399–2406.
[81] Bayley, H., Cremer, P. S. *Nature* **2001**, *413*, 226–230.
[82] Lauga, E., Brenner, M. P. *Phys. Rev. E (Stat., Nonlinear, Soft Mat. Phys.)* **2004**, *70*, 026311-1–026311-7.
[83] de Gennes, P. G. *Langmuir* **2002**, *18*, 3413–3414.
[84] Joseph, S., Aluru, N. R. *Nano Lett.* **2008**, *8*, 452–458.
[85] Denbigh, K. G., Turner, J. C. R. *Chemical Reactor Theory: An Introduction*, 3rd edn.; Cambridge University Press: London, 1984.
[86] Martinez-Huitle, C. A., Ferro, S. *Chem. Soc. Rev.* **2006**, *35*, 1324–1340.
[87] Maluleke, M. A., Linkov, V. M. *Sep. Purif. Technol.* **2003**, *32*, 377–385.

[88] Nielsen, S., Frokiar, J., Marples, D., Kwon, T.-H., Agre, P., Knepper, M. A. *Physiol. Rev.* **2002**, *82*, 205–244.
[89] Corry, B. *J. Phys. Chem. B* **2007**, *112*, 1427–1434.
[90] Marn, C., Serrano, M. D., Yao, N., Ostrogorsky, A. G. *Nanotechnology* **2002**, *13*, 218–220.
[91] Zhao, X., Liu, Y., Inoue, S., Suzuki, T., Jones, R. O., Ando, Y. *Phys. Rev. Lett.* **2004**, *92*, 125502.
[92] Fornasiero, F., Park, H. G., Holt, J. K., *et al. Proc. Natl. Acad. Sci. U.S.A.* **2008**, *105*, 17250–17255.
[93] Lamont, A. Some Results Bearing on the Value of Improvements of Membranes for Reverse Osmosis; UCRL-TR-219746, Lawrence Livermore National Laboratory, 2006.
[94] Cole-Hamilton, D. J. *Science* **2003**, *299*, 1702–1706.
[95] Wong, H.-T., See-Toh, Y. H., Ferreira, F. C., Crook, R., Livingston, A. G. *Chem. Commun.* **2006,** 2063–2065.
[96] Arnold, M. S., Green, A. A., Hulvat, J. F., Stupp, S. I., Hersam, M. C. *Nat. Nano.* **2006**, *1*, 60–65.

Biographical Sketches

Dr. Mainak Majumder received his undergraduate degree from the Calcutta University in 1999 and a master's degree from the Banaras Hindu University in 2001. He then served as a staff scientist for 2 years at the Central Glass and Ceramic Research Institute (CGCRI), a national laboratory in India, with a focus on membrane technologies for water purification. He received his PhD from the University of Kentucky in 2007, where he studied the molecular transport properties through carbon nanotube membranes. At present, he is pursuing research at Rice University on colloidal processing of carbon nanotubes. His research focus is the interface of materials science and chemical engineering, particularly how nanoscale materials can be applied to develop novel materials for energy and environmental applications. Presently he is an academic staff member at the Department of Mechanical and Aerospace Engineering, Monash University, Australia.

Professor Pulickel M. Ajayan received his undergraduate degree from the Banaras Hindu University in 1985, and doctoral degree from Northwestern University in 1989. A pioneer in the area of carbon nanotubes, Prof. Ajayan has been one of the key figures in the development of carbon nanotube technologies. After 10 years at the Rensselaer Polytechnic Institute (RPI), including as director of the RPI Interconnect Focus Center, New York, he joined Rice University as the Benjamin M. and Mary Greenwood Anderson Professor of Engineering in Mechanical Engineering and Materials Science Department. His research goals are oriented toward developing multifunctional nanostructures and hybrid platforms that would have applications in diverse fields, such as alternative energy storage, structural composites, sensors, electronic devices, and biomedical applications. Prof. Ajayan has authored or coauthored about 320 publications, two books, and his work has received more than 25 000 citations and h-index of 72. He has won several awards such as the MRS medal and the Burton medal from the Microscopy Society of America. He was selected as one of 2006 Scientific American 50 by the Scientific American Magazine and has also been selected as Nano50^{TM} Innovator by Nanotech Briefs (2007).

1.15 Characterization of Filtration Membranes

C Causserand and P Aimar, Université de Toulouse, Toulouse, France, CNRS, Toulouse, France

> I often say that when you can measure what you are speaking about, and express it in numbers, you know something about it; but when you cannot express it in numbers, your knowledge is of a meagre and unsatisfactory kind; it may be the beginning of knowledge, but you have scarcely, in your thoughts, advanced to the stage of Science, whatever the matter may be.
>
> Lord Kelvin

1.15.1 Introduction

The characterization of membrane properties helps not only to choose the right membrane for a given application but also to gain a better understanding of their preparation methods and on the selectivity and fouling mechanisms. The methods used give access to macroscopic or microscopic quantities, characteristic of the membrane structure and the chemistry of

the material. Some of these techniques are proper to membrane or separation processes, others are drawn from polymer science or are much more general.

The structural and transfer characteristics (hydraulic permeability and selectivity curve) are the most important for the choice of a membrane as they provide information on how the membrane will perform in the intended separation process: the permeate flow that can be expected and the size of molecules likely to be rejected by the membrane.

Also involved in the choice of a membrane are its surface physicochemical and chemical properties (charge, hydrophilic–hydrophobic nature, and chemical composition), which allow fouling and interactions among the different types of molecules at the membrane surface to be predicted to some extent. They may also play a role in the transport mechanisms.

In this chapter we focus on two categories of characterization methods: those which characterize the chemical and structural properties of the membrane, and those which characterize the functional properties, such as selectivity or permeability. It should be mentioned that some of these methods might be useful as well for membranes designed for purposes other than filtration, as, for example, for gas separation or for contactors.

1.15.2 Structural Characteristics

A variety of characterization methods have been developed for obtaining information on the structure of membranes, in particular on the pore size. They can be divided into three types: microscopy techniques, liquid intrusion or displacement techniques, and techniques that measure tracer molecule retention, although the latter provide information on the structural properties of the membrane via assumptions on the shapes of pores and mass transport phenomena through such porous media.

1.15.2.1 Microscopy Techniques

These techniques provide information on surface topology, roughness, and pore size. Several microscopic observation methods are used, which differ by their implementation and their resolution.

1.15.2.1.1 Electron microscopy

The first generation of microscopic techniques used scanning electron microscopy (SEM) and transmission electron microscopy (TEM), with resolutions of the order of 10 and 5 nm, respectively (for a membrane sample and in ideal experimental conditions for the instrument).

Electron microscopy is based on interactions between electrons and a sample of material. A very thin monochromatic beam of electrons is produced by focusing (using magnetic lenses) the electrons produced by sources such as a tungsten filament in a deep vacuum. The beam scans the surface of the specimen causing interactions that lead to the emission of waves. Two microscopic analyses are then possible, one by transmission and the other by reflection also named 'scanning electron microscope' (**Figure 1**).

Transmission electron microscopy. In the TEM, the incident electrons coming from the source are either completely stopped or deviated and slowed down or transmitted by the specimen. An objective diaphragm eliminates the deviated electrons. The image is produced by a fluorescent screen and consists of dark zones corresponding to electrons that are stopped and light zones where the electrons are transmitted. Specimen must be very thin layers to allow the beam through. The resolution is a few tens of nanometers, and the magnification can be up to 600 000.

Scanning electron microscopy. In SEM, the incident electrons excite the surface layer of the sample, causing the emission of secondary and backscattered electrons.

The secondary electrons are emitted by the atoms from the specimen surface. These electrons, which produce bright zones on the image, are more frequently emitted by the upper parts of the sample, making the hollows appear darker. An image of the specimen surface is thus built up, in which the contrast is determined by the morphology of the zone analyzed.

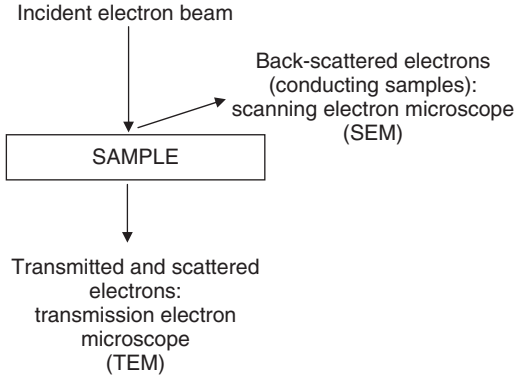

Figure 1 Principles of electronic microscopes.

The backscattered electrons are primary electrons that are reflected by the atoms in the sample. The image contrast is determined by the atomic number of the elements making up the specimen. However, the quality of the images obtained using backscattered electrons is not as good as the quality obtained with secondary electrons. SEM microscopy is therefore mainly carried out using secondary electrons. If the sample does not emit enough secondary electrons and/or is not a conductor (the case for polymer), it is necessary to consider sputtering a thin layer of metal such as gold. The magnification obtained is the ratio of the dimensions scanned on the specimen to the dimensions on the screen. It can reach 400 000 in recent instruments and its resolution is a few nanometers.

Constraints. Electrons are slowed down by the gas molecules they encounter, which explains the need for a high vacuum in the microscope column. This vacuum in the instrument makes it impossible to observe hydrated objects at room temperature. Therefore, electron microscopy imposes specific techniques of sample preparation, notably when polymer membranes are to be observed. These include:

1. dehydration of the specimens or immobilization of their water by freezing and preparation of ultrafine sections of the frozen material;
2. metallization of the membrane surface (after dehydration) in the case of SEM, such that the secondary electrons can be emitted and the charges can drain away. Gold, platinum, palladium, or their alloys are used for this purpose,
3. inclusion of resins in the case of TEM so that ultrafine sections, 50–100 nm thick, can be cut.

One of the limitations of any imaging technique when analyzing the porous structure of materials is that any single information provides a 2D information, whereas the porous structure is 3D in nature. Therefore, and except if series of micro-cuts are obtained using a micro-knife, the information obtained from such images does not discriminate between through pores and superficial cavities, neither they inform on the shape of the channels [55].

Some attempts at using image analysis routines help at offering a more quantitative and statistically meaningful picture of the membrane pore-size distribution, as exemplified by Torras and Garcia Vals [45].

Applications of SEM. SEM is often used to study the morphology of membranes (**Figure 2**). It is proved to be an effective method for:

1. characterizing flat membranes;
2. assessing the effect of preparation conditions on the structure of hollow fiber membranes [31];
3. observing the evolution of membrane morphology after contact with washing solutions; works have concerned the analysis of cellulose acetate (Qin and Wong, 2002) and polyvinylpyrrolidone-modified polysulfone (Qin *et al.*, 2003) membranes after treatment with sodium hypochlorite; and
4. measuring the thickness of deposits (0.2–0.4 μm) formed during membrane fouling [39].

A few studies have been published in this field [17, 28] but many authors agree that, although scanning electron microscopy is a very powerful tool for analyzing the structure of membranes, it is not suitable for measuring the sizes of membrane pores, particularly in ultrafiltration membranes. In this case, where the pores have diameters between 1 and 30 nm, the resolution of SEM proves to be insufficient. The fact that the specimen has to be dried and metallized reduces the interest of this technique for observing membrane pores as a change in the apparent characteristics of the pores may be expected as a consequence of the sample preparation.

Environmental low-pressure SEM is a technique that can be envisaged. It has the advantage of requiring much less vacuum (*c.* 20 kPa) than conventional SEM, and the electronic conductivity of the specimen surface is not a requirement as in conventional SEM. This is an interesting alternative for membranes as they can be characterized in a natural working environment. However, the resolution obtained is not as good as in traditional SEM.

1.15.2.1.2 Near Field Microscopy

Another generation of microscopic methods was ushered in by near field microscopes such as the scanning electron tunneling microscopy (STM, applicable only to conducting surfaces) and the atomic force microscopy (AFM, for observing all types of surfaces, even insulating ones). The latter has the advantage of requiring no specimen preparation and being usable in an aqueous medium. Also, it gives 3D information on the surface of the membrane. These microscopes have high potential for observing ultrafiltration membranes where the pore diameters are between 1 and 30 nm. Nevertheless, great caution is to be exercised when interpreting the images as the topographical readings obtained depend not only on the shape of the objects observed but also on the size and shape of the microscope probes used.

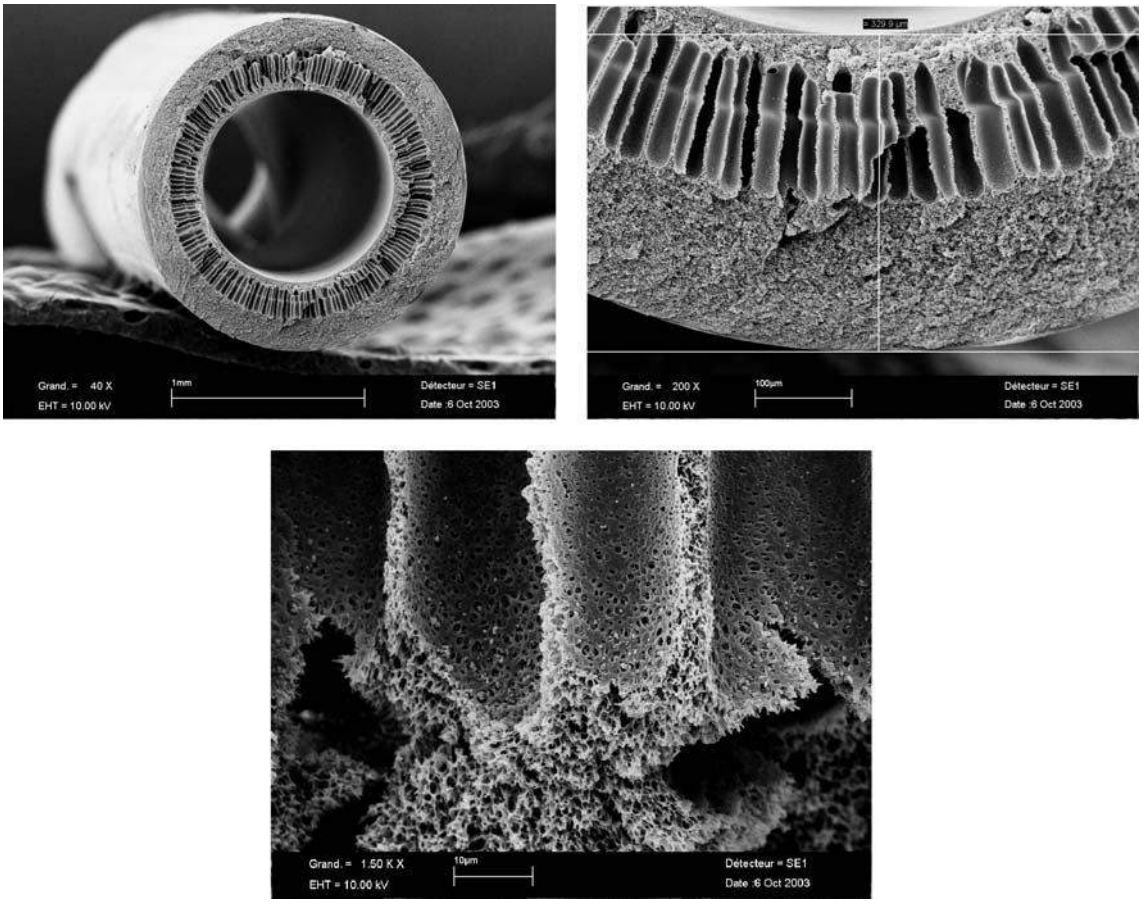

Figure 2 Example of an image of a polysulfone hollow fiber membrane (MWCO: 40 kD[a]) obtained by scanning electron microscopy (SEM).

Scanning tunneling microscopy. The operating principle of a tunneling microscope is based on measuring a current of electrons crossing an insulating zone by the tunneling effect. The key elements of the device are the two electrodes between which the tunnel current is measured. One electrode is composed of a tip, assumed to be monoatomic, of a probe that can move in the three spatial directions (piezoelectric ceramic system). The surface to be analyzed constitutes the other electrode. The tip and the surface are a distance d apart (**Figure 3**).

The tunnel current measured depends on both the probe–surface distance and the electronic structure of the specimen surface. This type of microscope thus reveals the topography (**Figure 4**) and the electronic structure of a material at the same time.

One of the limitations of tunneling microscopy, however, is the need to deposit a thin conducting film on nonconducting samples. This enables the surface topography to be observed but lowers the resolution.

Atomic force microscopy. The main feature of this type of microscopy is a very thin, and therefore very flexible, cantilever with a monoatomic tip at the end. When the atoms of the tip are sufficiently close to the surface to be analyzed, inter-atomic forces (of between 10^{-6} and 10^{-9} N) come into play and the cantilever is bent slightly according to the topology as it scans the surface. The deflections of the cantilever are monitored using a laser beam shed on its upper face. The beam is reflected by a mirror and falls on photodetectors that record the light signal. Transcribing the movements of the cantilever thus traces the topography of the sample even if it is an insulator.

The images obtained by AFM depend mainly on the specimen's topography [23], whereas those obtained by STM also reflect its conductivity

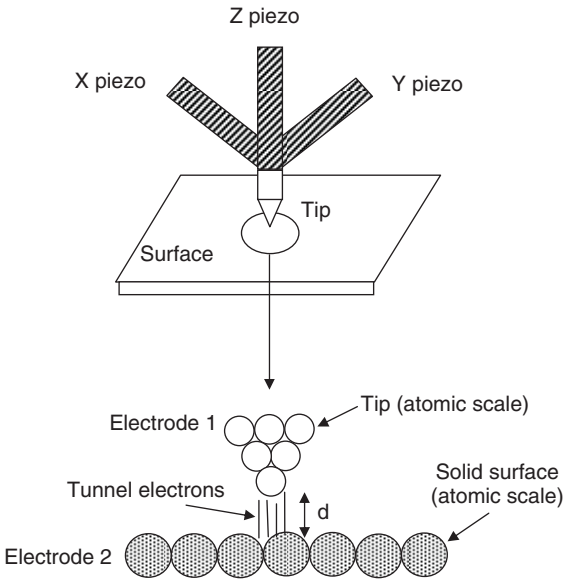

Figure 3 Schematic description of a scanning tunneling microscope (STM).

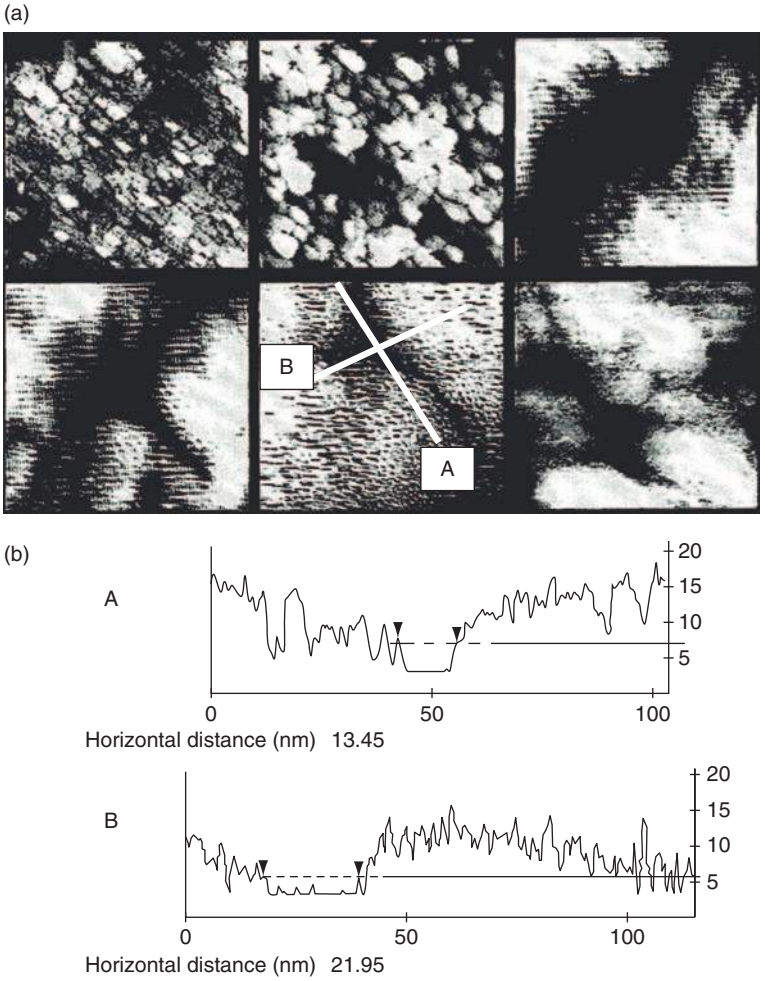

Figure 4 (a) Image of a 100 kD[a] polysulfone membrane obtained by scanning tunneling microscopy (STM); (b) Cross sections corresponding to the lines drawn in the picture 5 (middle-bottom). From Bessieres, A., Meireles, M., Coratger, R., Beauvillain, J., Sanchez, V. *J. Membr. Sci.* **1996**, *109*, 271–284.

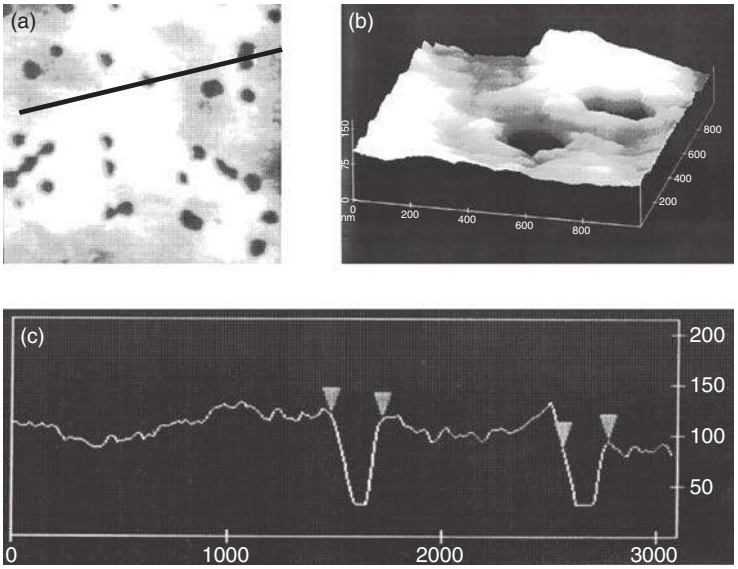

Figure 5 (a) Example of an image of a tracked etched polycarbonate membrane (Nuclepore) – nominal pore size : 0.2 μm; (b) same sample – blow-up (1000 × 1000) nm^2; and (c) cross section along the line drawn in picture (a).

variations. It is impossible to observe thick, nonconducting specimens by STM while this poses no problem with AFM.

AFM has been used to determine the sizes of membrane pores (**Figure 5**). Some authors have shown that, for microfiltration [7] and ultrafiltration membranes, the measured dimensions of the pores are in agreement with those provided by the manufacturer or calculated from hydraulic permeability. By contrast, analyses performed on hollow, dialysis fibers [26] or nanofiltration membranes [8] overestimate the pore sizes for the former and underestimate them for the latter.

The uncertainty of the AFM measurements of pore sizes may be due to:

1. the fact that the tip (5–10 nm in size) could not probe the depth of the smallest pores and thus did not detect the outline accurately;
2. convolution between the tip and the pore walls; and
3. the fact that some pores can have their maximum opening at the membrane surface.

Another application of the AFM is to capture the surface roughness (**Figure 6**). For instance, the roughness of new, clean membranes can be studied together with the variations in the surface structure after membrane fouling.

An example of data collected by imaging various membranes by STM and AFM was exploited to produce the results presented in **Table 1**.

1.15.2.1.3 X-ray synchrotron micro-tomography

The use of synchrotron X-ray radiation source provides new possibilities to characterize membrane morphology. Since their discovery, X-rays have been used to image the bulk of materials that are not transparent for visible light by taking advantage of their inhomogeneous absorption. From the many 2D images (radiographs) recorded at various angular positions of the objects and via appropriate algorithms (described, for instance, by Baruchel *et al.* [2]) and the derived software, 3D data volume, projections, or perspective renditions of the objects can be obtained at will. Micro-tomography with spatial resolution better than 20 μm has recently emerged with bench scale X-ray tomographic instruments. X-ray micro-tomography allows then reconstructions of the 3D internal structure of objects nondestructively without any prior preparation (cutting, coating, or vacuum treatment).

Remigy *et al.* [36] report the new possibilities associated with the availability of third-generation sources of synchrotron radiation to characterize the 3D morphology of a polyvinylidene fluoride (PVDF)

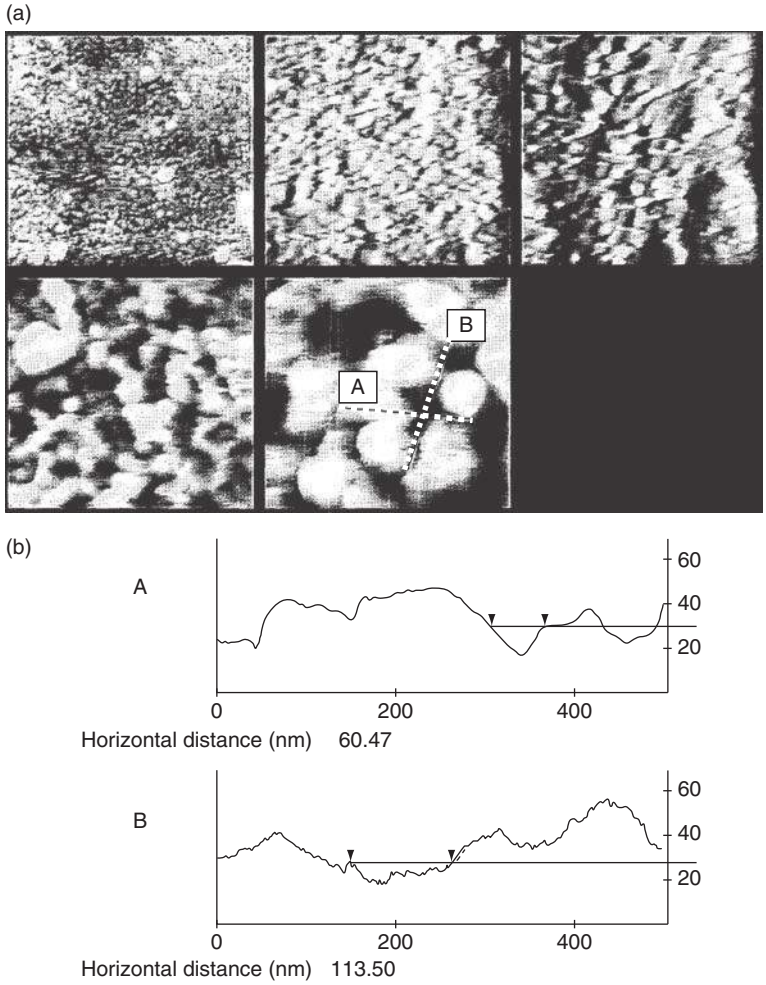

Figure 6 (a) Image by atomic force microscopy (AFM) of the surface of a sulfonated polysulfone membrane, and (b) cross sections along the lines drawn in picture 5 (midlle-bottom row). From Bessieres, A., Meireles, M., Coratger, R., Beauvillain, J., Sanchez, V. *J. Membr. Sci.* **1996**, *109*, 271–284.

hollow fiber microfiltration membrane prepared by phase inversion (**Figure 7**). The membrane actually appears as a complex 3D bi-continuum of interconnected pores. An interesting feature of this kind of characterization method is that it provides a 3D numerical mesh of the membranes which can be further used for flow simulation, for example, using a Boltzmann lattice method. The lower limit of the resolution of such a technique is today at the micrometer range.

Table 1 Membrane characteristics derived from STM and AFM images

	100 kD[a] PSS		*200 kD[a] PSS*		*0.1 μm PVDF*	
	STM	*AFM*	*STM*	*AFM*	*STM*	*AFM*
d_p (nm)	16	31	28	38	82	96
D_p (nm)	31	69	94	114	170	185
η_{pore} (pores/m^2)	1.23×10^{14}	7×10^{13}	1.4×10^{13}	2×10^{13}	1.4×10^{13}	7×10^{13}
ε (%)	4.8	11.8	2.9	6.8	1.5	9.8

d_p: smallest pore dimension (or clack width) (nm); D_p: largest pore dimension (or crack length) (nm).
From Bessieres, A., Meireles, M., Coratger, R., Beauvillain, J., Sanchez, V. *J. Membr. Sci.* **1996**, *109*, 271–284.

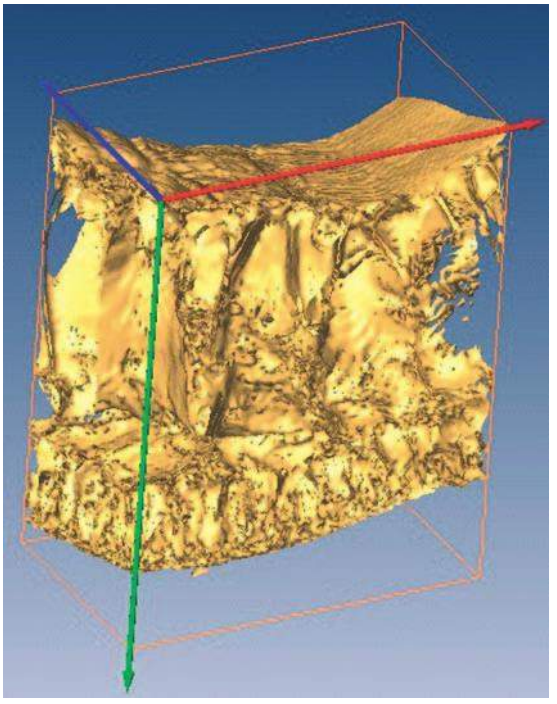

Figure 7 Three-dimensional (3D) reconstruction volume of a part of polyvinylidine fluoride (PVDF) hollow fibber microfiltration membrane from SR μCT. Dimensions of the observed volume (i.e., the box) are 595 × 456 × 268 voxels or 420 μm × 320 μM ×190 μm. From Remigy, J.C., Meireles, M., Thibault, X. *J. Membr. Sci.* **2007**, *305*, 27–35.

1.15.2.1.4 General remarks on microscopic methods

The resolution of microscopic techniques has been much improved over the last decade. Equipment maintenance and sample have been simplified and this allows quite an extensive use of these techniques to visualize the internal and external structure of membranes. This is definitely of great help for assessing the membrane preparation procedures, for example, for an evaluation of fouling conditions. Quantitative analysis of these images should be considered carefully when the sample preparation can modify the sample. One should also make sure that the information taken from very small samples, such those accessible by AFM, are statistically significant.

1.15.2.2 Displacement Techniques

These methods (bubble point, liquid/gas displacement, and liquid–liquid porometry) consist of wetting the membrane with a wetting agent (phase 1) of known surface tension, γ, and contact angle, θ, with the membrane, then expelling it from the membrane pores by displacing it with a second phase (phase 2), which is generally air or an immiscible liquid. The pressure difference ΔP across the membrane is gradually increased from zero and the value from which phase 2 forms drops extruded out of the membrane is measured. This value can then be linked through physical laws to the maximum pore radius of the membrane, the mean pore radius, or a pore-size distribution based on the technique used.

1.15.2.2.1 Bubble point

In the bubble point method, the pores of the membrane are completely wet with a liquid (phase 1) which is then displaced with air (phase 2). The Young–Laplace equation allows the maximum pore radius $r_{p,max}$ (m) to be calculated from the value of the transmembrane pressure ΔP (Pa) measured when the first bubbles are detected in the permeate compartment:

$$\Delta P = \frac{4\gamma_L \cos\theta}{2r_{p,max}} \qquad (1)$$

where γ_L is the surface tension of liquid ($N\,m^{-1}$) and θ the contact angle between liquid and membrane surface (°).

1.15.2.2.2 Mercury intrusion

Mercury intrusion is a variant of the bubble point method, in which phase 1 is air and phase 2 is mercury that is gradually forced into the membrane pores. Mercury has a very small contact angle with most materials and a surface tension of $6.48\,J\,m^{-2}\,cm^{-1}$ at 25 °C.

Both the methods discussed above have the drawback: they require very high pressures (from 1 to several kilobars) to analyze pores of the order of 10 nm like those found in ultrafiltration membranes.

1.15.2.2.3 Liquid–liquid porometry

This method consists of wetting the membrane with a wetting liquid (phase 1) then expelling the liquid from the membrane pores by displacing it with another liquid (phase 2) that is immiscible with the former. The pressure that has to be applied depends directly on the interfacial tension between the two liquids. Thus, by a appropriate choice of the liquid 1–liquid 2 pair (based on a water–isobutanol–methanol combination), the pressures to be applied for the analysis of small-radius pores need not exceed 10 bar or so.

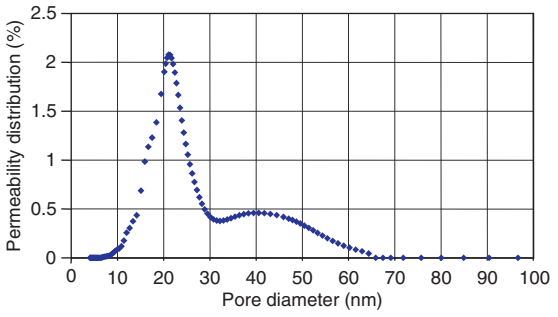

Figure 8 Example of a bi-modal pore-size distribution obtained on an ultrafiltration membrane by bi-liquid porometry (liquid mixture: methanol, isobutanol, butanol 1 and water; interfacial tension between organic phase and aqueous phase: 0.35 $mN^{-1}m$).

When samples having a distribution of pore sizes are to be analyzed, the pressure is step wisely incremented from the value of ΔP that is sufficient to wet the pores having the largest radius. The flow corresponding to each transmembrane pressure is recorded until all pores are wetted (flux is then proportional to the applied pressure difference). A pore radius distribution can then be deduced from these measurements (**Figure 8**).

1.15.2.3 Water Permeability

In the presence of a pure solvent, any increase in transmembrane pressure leads to a proportional increase in the permeate volume flux density which allows the membrane to be considered as an ideal porous medium. The coefficient of proportionality, Lp (assuming μ constant), is called the hydraulic permeability of the membrane and depends on its intrinsic characteristics: porosity, pore-size distribution, thickness, and hydrophilic nature. This parameter (Lp) thus represents the volume of solvent that passes through the membrane per unit of pressure, filtering area, and time.

From tests with pure water, the permeability of the membrane can be determined by means of Darcy's law, which links the flux with the transmembrane pressure:

$$\mathcal{J} = \frac{Q}{A} = \frac{Lp}{\mu}.\Delta P = \frac{\Delta P}{\mu.\Re_m} \qquad (2)$$

with $\mathcal{J}$ being the flux density ($m\,s^{-1}$), Q the pure solvent filtration rate ($m^3\,s^{-1}$), A the filtering surface area (m^2), Lp the hydraulic permeability of membrane (m), μ the dynamic viscosity of pure solvent (Pa s), ΔP the transmembrane pressure (Pa), and $\Re_m$ the hydraulic resistance of membrane (m^{-1}).

The determination of the membrane permeability coefficient or of the membrane resistance requires that the flux density for pure solvent is measured over a range of pressure differences which correspond to the specifications of the membrane manufacturer. The plot of this measured flux versus the applied pressure must be a straight line, and its extrapolation to a zero pressure must meet the flux origin. If these two conditions are not respected, any value of the slope of this curve does not correspond to a Darcy permeability or to a membrane resistance. Deviations from linearity may arise from the compressibility of the membrane, or from the retention of some impurities remaining in the retentate compartment.

From this law, one can deduce the hydraulic permeability and the resistance of the membrane (the resistance of the membrane is defined as the reciprocal of the hydraulic permeability).

Because the viscosity varies with temperature, it has to be measured throughout the experiment. In the case of water, the viscosity can be calculated using the following equation:

$$\mu(T) = 1.73e^{-0.0268T} \qquad (3)$$

where T is the temperature (°C). This equation is valid for $0\,°C < T \leq 30\,°C$.

Monitoring the permeability allows membrane fouling to be quantified in terms of additional resistance (e.g., Reference 52). Conversely, the permeability can be used to evaluate the efficiency of chemical or mechanical cleaning [25, 33].

1.15.2.4 Tracer Retention Techniques

The information collected by microscopy or by displacement techniques does not give a direct indication of the selectivity that can be expected for a membrane used in normal conditions (hydration, swelling of the polymer in an aqueous medium). Yet for the user, one of the main aims of characterizing a membrane is to know its efficiency for a chosen separation operation.

Tracer retention techniques measure the transfer of macromolecules (ultrafiltration) or calibrated

particles called tracers, and these measurements are then compared with a transport model. The principle is to measure the retention of a series of tracers of different sizes so as to obtain a curve of selectivity versus molar mass (or size) of the molecules. For this, an initial phase is necessary to define the choice of tracers and the operating conditions required to obtain the data. In a second phase, a model linking the selectivity to the sizes of the tracer and the pores can be used to convert the selectivity curve into a pore-size distribution.

1.15.2.4.1 Choice of tracers

The tracers used must fulfill several criteria:

1. have few specific interactions with the membrane material or the macromolecules that may be absorbed on to the membrane to account for its intrinsic characteristics;
2. have molar masses (or sizes) that cover the broadest retention range possible, especially in the region close to 100%; and
3. be detectable even at very low concentrations in the collected permeate.

From the first criterion, the use of proteins (**Table 2**) or bio-colloids as tracers may make it difficult to interpret the results since most of them have strong interactions with membrane materials. This leads to fouling and thus modifies the medium under study. The information collected, although very dependent on the molecules used in this case, may nevertheless be of interest to users in a particular application sector as the extrapolation of characterization data to the filtration of real fluids will be easier in this domain.

Certain manufacturers and users often use synthetic soluble polymers (**Table 2**) such as dextran, polyethylene glycol, or polyvinylpyrrolidone, which, although not totally inert with respect to the membrane materials, still have far fewer interactions than bio-colloids and perturb the measurements to a lesser extent. These molecules are often available in a variety of molar mass (or size) ranges, which allows selectivity curves to be plotted for a given family of tracers. This method, very suitable for ultrafiltration membranes, is difficult to extend to microfiltration membranes, for which there are few standard molecules of sufficient size (poly(ethylene oxide), high-molecular-weight dextrans). For this type of membrane, the most widely used method remains bubble point measurement, described above for the evaluation of maximum pore radius and the retention of bacteria (*Escherichia coli, Pseudominas diminuta*), which will be dealt with later in this chapter. The latter method involves checking whether the pores of the membrane have a nominal radius smaller than the dimensions of the bacterium being filtered. Bubble point measurement and bacterial retention techniques can enable the integrity of modules, or even a complete plant, to be tested.

On the other hand, tracer retention measurement is applicable to nanofiltration membranes, for which the tracer molecules can be small poly(ethylene glycol)s, sugars (glucose, sucrose, dextrose), or inorganic salts. However, in nanofiltration, steric effects are not the only phenomena responsible for retention by the membrane and it is necessary to complete the characterization by measuring the retention of ions in various physicochemical conditions so as to evaluate the effects of charges. In particular, the comparison of the retention of mono-valent and divalent cations and anions is an interesting information as nanofiltration membranes are popular for their selectivity with regard to multivalent ions.

For reverse osmosis, the most widely used tracer is sodium chloride NaCl. Reverse osmosis

Table 2 Proteins and polymers frequently used as tracers for the characterization of membrane sieving properties

	Molar mass (kD[a])	*Polydispersity*	*Stokes radius (nm)*	*Hydrodynamic radius (nm)*
α-Lactalbumin	14 000	–	2.1	2.5
β-Lactoglobulin	35 000	–	2.7	4.0
Serum albumin	67 000	–	3.6	4.8
PEG	10 000	–	2.6	4.6
	35 000	–	4.5	9.2
	100 000	–	7.1	16.4
Dextranes T10	9 300	1.94	2.3	3.3
T40	37200	1.34	4.3	6.7
T70	66 300	1.97	5.6	8.5

membranes intended for water desalination have a NaCl rejection rate of about 99%, and those developed for brackish water have a NaCl rejection rate of 96%, under predetermined operating conditions (pressure, temperature, conversion rate, etc.).

The capacity of nanofiltration or reverse osmosis membranes to retain small chemical molecules, namely the micro-pollutants, often present in waters nowadays is sometimes characterized via the challenge with standard micro-pollutants such as atrazin, bisphenol A, or similar molecules. Not only the size, but also the hydrophobic nature of such molecules can have strong influence on their retention. Therefore, there is today no standard for the characterization of the retention of this class of molecules [21]. A peculiarity that has to be taken into account for such characterizations is the strong adsorption of such molecules, often used at very low concentrations (pg l^{-1} or mg l^{-1}).

Regarding synthetic polymers frequently used for characterizing ultrafiltration membranes, some are only available in the form of polydisperse fractions (dextrans). It is then necessary to resort to gel permeation chromatography to determine the concentrations of each fraction in the various samples. In this case, a calibration, elution volume $= f$(molar mass), is performed so that the molar masses can be read from the chromatograms.

Finally, it should be noted that these synthetic polymers often have the disadvantage of being flexible, that is, likely to change their apparent size depending on the shearing conditions at the pore openings.

However, in spite of the drawbacks mentioned above and in the absence of other molecules satisfying all the criteria stated at the beginning of this section, dextrans and PEGs remain, along with proteins, the tracers that are most used in ultrafiltration.

1.15.2.4.2 Obtaining the selectivity curve and molecular weight cutoff

The selectivity of a membrane is usually represented by its molecular weigh cutoff. This is defined as the minimum molar mass of a test solute that is 90% retained (or 95% depending on the manufacturer) by the membrane. It is thus determined experimentally from a plot of the variation of the retention rate for tracer molecules according to their molar mass: the selectivity (or sieving) curve (**Figure 9**).

Choice of ordinates. With the aim of determining a cut-off threshold that is an intrinsic characteristic of the membrane only, it is essential that the operating conditions (transmembrane pressure, tangential circulation speed, etc.) should not affect the retention data. For this reason, it is not advisable to directly use the values of R_{obs} obtained experimentally as they are very dependent on the operating conditions.

The film model (Equation (4)) links the membrane retention coefficient R_m with the observed retention coefficient R_{obs}:

$$\ln\left(\frac{1-R_{obs}}{R_{obs}}\right) = \ln\left(\frac{1-R_m}{R_m}\right) + \left(\frac{\mathcal{J}}{k_{bl}}\right) \qquad (4)$$

where R_{obs} is the observed retention coefficient, R_m the membrane retention coefficient, $\mathcal{J}$ the filtration

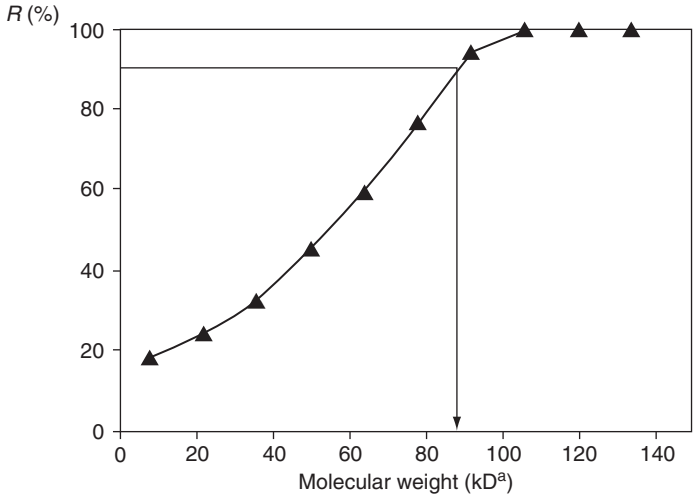

Figure 9 Example of a selectivity curve for dextran molecules. The molecular weight cut-off, i.e., the molecular weight of a molecule rejected at 90% by the membrane is 85 kD[a].

flux density (m s^{-1}), and k_{bl} the transfer coefficient in the boundary layer (m s^{-1}).

This equation shows that it is possible, for each molecule, to graphically determine R_m, the membrane retention rate, and k_{bl}, the mass transfer coefficient for the solute in the boundary layer, from the experimental data (R_{obs} and $\mathcal{J}$) in conditions where a straight line is obtained for the plot (**Figure 10**) of

$$\ln\left(\frac{1-R_{obs}}{R_{obs}}\right) = f(J) \tag{5}$$

This method thus frees retention measurements from the effects of concentration polarization. It should be noted that the retention rate R_m thus obtained remains dependent on the operating conditions through the concentration at the membrane C_m.

A more advanced level of description of the transfer mechanisms enables the observed retention rate R_{obs} to be expressed as a function of the transfer of solute not only in the boundary layer but also via the porous structure:

$$R_{obs} = \frac{1}{\left[1 + \frac{(1-R_{inf})\exp(Pe_{bl})}{R_{inf}\left(1-\exp\left(-Pe_{pore}\right)\right)}\right]} \tag{6}$$

with

$$Pe_{bl} = \frac{\mathcal{J}}{k_{cl}} \tag{7}$$

$$Pe_{pore} = \frac{\mathcal{J}}{k_{pore}} \tag{8}$$

and

$$k_{bl} = \frac{D}{\delta} \tag{9}$$

$$k_{pore} = D_\infty \frac{\varepsilon}{L}\frac{K_d}{K_c} \tag{10}$$

where Pe_{bl} is the Peclet number in the boundary layer, K_{pore} the mass transfer coefficient in the pore

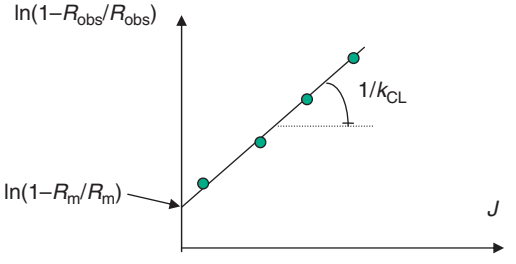

Figure 10 Plot of Equation (4). R_m and the mass transfer coefficient can be calculated from the intercept at origin and from the slope of the line.

(m s^{-1}), Pe_{pore} the Peclet number relating to the pore, D_∞ the diffusion coefficient at infinite dilution (m^2 s^{-1}), D the mean diffusion coefficient of the solute in the boundary layer (m^2 s^{-1}) (often taken equal to the coefficient of diffusion at infinite dilution D_∞), ϵ the membrane porosity, L the length of pores (m) (often taken to be equal to the thickness of the membrane skin), K_c the steric factor reducing transfer by convection [12], and K_d the steric factor reducing transfer by diffusion [12].

The use of Equation (6) gives access to more pertinent values of the transfer coefficients and retention rates through R_{inf}, a value independent of the operating conditions, to which the membrane retention rate R_m tends when the Peclet number relating to the pore Pe_{pore} increases [10]. This approach however requires quite an intensive experimental work, and for a purpose of comparison between membranes or for a same membrane between various operating conditions, one may prefer to compare values of Robs, obtained in conditions for which $\mathcal{J}/k_{bl}$ is constant (cf. Equation (4)).

Choice of abscissae. Some works have shown that, when different types of tracers are used, a selectivity curve $R = f$(molar mass) is obtained per family of standard molecules. However, if the selectivity curve is not expressed as a function of the molar mass of the solute but rather as a function of its radius, a single curve $R = f$(radius) is obtained whatever the type of tracer used [30]. For this, it is advisable to use the hydrodynamic radius of the molecule, which gives a good description of the volume actually occupied by the molecule crossing the pore by convection.

The hydrodynamic radius r_{hyd} of a molecule of known molar mass can be calculated by means of the following equation [30]:

$$r_{hyd} = \left(\frac{3.\eta.MM}{4\pi\,\xi\,N}\right)^{\frac{1}{3}} \tag{11}$$

where r_{hyd} is the hydrodynamic radius of the molecule (m), η the intrinsic viscosity of the solution (m^3 g^{-1}), MM the molar mass (g mol^{-1}), (ηMM) the hydrodynamic volume (m^3 mol^{-1}), ξ the constant of proportionality between the radius of the equivalent sphere and the radius of gyration of the molecule of solute, and N the Avogadro's number (mol^{-1}).

The following equations can be used to calculate η [30]:
For dextrans

$$\eta = 2.43 \times 10^{-7} \times MM^{0.42} \tag{12}$$

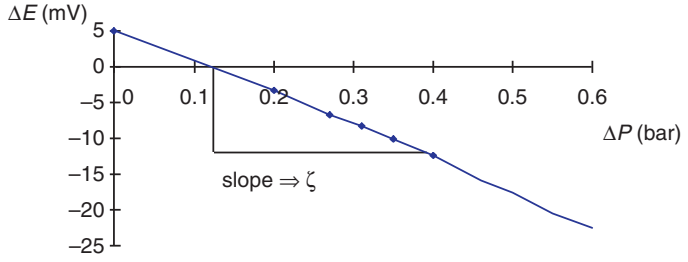

Figure 11 Example of a plot of Equation (16). The zeta potential is derived from the slope.

For PEG

$$\eta = 4.9 \times 10^{-8} \times \mathrm{MM}^{0.672} \tag{13}$$

1.15.2.4.3 Conversion into pore-size distribution

Using (R, r_{hyd}) pairs with an appropriate transfer law gives access to the pore-size distribution of the membrane under study. It is possible to consider either that the membrane is homoporous (all the pores have the same size and shape) or that there is a pore-size and shape distribution. The most frequently chosen hypothesis is a log normal distribution with a dissymmetry toward larger-sized pores. The experimental data can then also be used to evaluate the mean pore radius and the width of the pore-size distribution at mid-height [29]. In the absence of any assumption on the shape of the pore-size distribution requires more sophisticated approaches. Baltus [1] applies the moment theory to derive a pore-size distribution out of the sieving curves. Zhao *et al.* [56] describe a method for the determination of the pore-size distribution out of sieving curves. In their method, the friction of tracer molecules through the pores is experimentally measured via chromatography experiments, according to an approach initially developed by Matsuura and Sourirajan.

1.15.2.4.4 Microbiological tracers

Microbiological tracers have been used to characterize filters from the early times of membrane technology. The obvious reason for this is that, from the beginning, membranes have been considered as potential screens against microbiological contamination of waters or air.

Bacteria. The ground of this work has been established in the 1960s for the discrimination between filters rated 0.2 and 0.45 μm, by using *Brenvenuta diminuta*. Since then, this bacteria has been used as a tracer to qualify filters, microfiltration, and ultrafiltration membranes. In **Table 3** the characteristics of some of the bacteria which can be used for membrane characterization are provided.

Lebleu *et al.* [22] show, using tracked etched membranes, that for a given pore size and given operating conditions, the retention of microorganisms depends on their Gram character, and in particular that Gram-negative bacteria have a flexible envelope which can deform and help the transfer of such bacteria, when filtered through pores that are smaller than their smallest dimension.

In general, filtration reduces the content in microorganisms, but does not guarantee their complete elimination. The reduction in microorganisms is often measured by the log removal value (LRV), defined as

$$LRV = \log\left[\frac{C_b}{C_p}\right] \tag{14}$$

with

$$LRV = \log\left[\frac{1}{1 - R_{obs}}\right] \tag{15}$$

Table 3

Name	*Shape*	*Size*	*Adhesion to hexadecane (%)*[a]	*Potential (mV)*	*Gram +/−*
E. coli	Rod	2 × 1 μm	13	−16.2	−
C. xerosis	Rod	2 × 1 μm	100	−16.5	+
P. aeruginosa	Rod	1.5 × 1 μm	58	−17.4	−
M. luteus	Sphere	1 μm	8	−32.9	+
S. aureus	Sphere	0.8 μm	75	−21.5	+
B. diminuta	Rod	0.4 × 0.8 μm	81	−3.8	−

[a] Bellon-Fontaine, M.-N., Rault, J., Van Oss, C. J. *Colloids Surf. B* **1996**, 7(1–2), 47–53.

The retentate and permeate concentration are in general measured by counting the colony forming units (cfu) grown on agarose gels. The maximum LRV that can be claimed depends on the concentration of bacteria in the challenging suspension. For example, if the concentration is 10^6 cfu ml^{-1} in the retentate and zero in the permeate, one counts 1 cfu ml^{-1} in the latter and the LRV is then 6. On the other hand, increasing the concentration in bacteria in the retentate increases the risk of membrane fouling: membrane fouling has in general a positive effect on retention, but from the point of view of membrane characterization, this masks the plain membrane capacity, and therefore should be avoided. A tradeoff has then to be found for the bulk concentration, which has to be high enough to allow enough sensitivity, and not too high to avoid membrane fouling and particle aggregation during the test: in general, concentrations between 10^6 and 10^8 cfu ml^{-1} have been found to be a good compromise.

For instance, the US Environment Protection Agency recommends that membranes used for the production of drinking water show a minimum LRV of 4 for *Cryptosporidium*.

Viruses. The characterization of membrane retention with respect to viruses, although in the biocontaminants area, differs from the one of bacteria. As a matter of facts, most viruses are two orders of magnitude smaller than bacteria: this difference has its importance regarding their diffusivity, and the role of surface interactions in their behavior. In particular, viruses have a strong tendency to adsorb onto surfaces whether on the equipment walls (tanks, pipes, glassware, etc.) or on particles which may be present in the tests or process solutions. For this reason, the apparent retention of viruses by membranes may be much higher than the actual filter capacity and this has to be considered with great care, in the perspective of the true membrane characterization.

The main objective of membrane characterization with respect to the retention of viruses is to run the experimentation in the worst-case conditions, conditions that the viruses have the highest chances to pass through the membranes: this will guarantee that when in operation, the membrane will show either the same or a better retention of the viruses. Recent works help define the conditions for which viruses such a MS2 and Q-β are stable in a suspension, which type of materials should be used for the test rigs so as to avoid adsorption [24].

Given the small size of the viruses, not only the membrane but also the systems should be tested for integrity, since micro-leaks through potting, gaskets, and fittings may allow the contamination of the permeate, even though the membrane itself offers an efficient barrier.

Surrogates. The characterization of membrane modules may require large volumes of suspension, as well as of rinsing solutions afterward, so as to eliminate any trace of the microorganisms used for the test. For this reason, researchers have thought of developing surrogates of the microorganisms, which would mimic their behavior and allow simpler and faster membrane characterization. Latex or silica particles, and gold sols have therefore been used. Thus far, two major drawbacks have been pointed out:

- the much lower sensitivity of the particle detection methods, which limitates the range of LRV that can be explored and
- the difference in surface properties (charge, stiffness, hydrophilic character, etc..) between such surrogates and bioparticles, which induces a difference in retention, as, for example, by charge exclusion, by adsorption on or in the membrane material.

Recently Guo *et al.* [16] have proposed to use ferromagnetic nanoparticles, to be used as surrogates. They report quite a high sensitivity to the breakage of fibers in a hollow fiber ultrafiltration module. Although the behavior of such surrogates has not been compared to that of a virus, they offer very interesting perspectives in terms of integrity testing of membranes and modules.

1.15.3 Characterization of Membrane Charge

Most porous membrane carries charges; electrostatic interactions also play a part in the transfer and selectivity both in ultrafiltration (e.g., Reference 13) and of course in nanofiltration [40]. More and more researchers and industrialists therefore feel the need to characterize properties other than the pore-size distribution, such as the zeta potential, which is the subject of this section.

1.15.3.1 Definitions

The presence of charged groups on the membrane surface partly conditions the level of fouling reached during a filtration operation. From another point of view, if we wish to analyze the transfer of a solute through a porous membrane, the charges of the material that need to be taken into consideration are those

present along the walls of the pores through which the molecules move.

The measuring methods must thus be adapted according to whether the charges to be accounted for on the surface or inside the pores. In the latter case, it is also necessary to take the membrane specificities into account, in particular for ultrafiltration membranes in which the pore radius (~10 nm) and the mean flux are small.

The techniques used are electrokinetic and consist of measuring:

1. electro-osmotic fluxes for microfiltration membranes: flux of solvent through the membrane pores as a result of the application of an electrical potential difference; and
2. streaming potentials for ultrafiltration or microfiltration membranes: because of the formation of a double electric layer, when an electrolyte solution is set in motion with respect to the membrane or pore surface, a flux of ions is created, giving rise to the streaming potential [43, 44].

Each of the methods mentioned above can lead to the determination of the same quantity, known as the zeta potential (ζ). This purely experimental potential can be theoretically defined as the potential on the hydrodynamic shearing surface at which the fluid phase moves relative to the layer of ions immobilized in the vicinity of the charged surface.

1.15.3.2 Relation between Streaming Potential and Zeta Potential

When the chosen technique is the measurement of the streaming potential, plotting the curve $\Delta E = f(\Delta P)$ leads to a straight line (**Figure 12**), the slope of which allows the zeta potential to be calculated using the Helmholtz–Smoluchowski equation:

$$\frac{\Delta E}{\Delta P} = \frac{\varepsilon_0 \varepsilon_r \zeta}{\mu \chi} \qquad (16)$$

where ΔP the transmembrane pressure if the measurement is made inside the pores, charge loss in the streaming channel if the measurement is made at the membrane surface (Pa), ΔE the streaming potential (V), ε_0 the vacuum permittivity ($C^2\,J^{-1}\,m^{-1}$), ε_r the dielectric constant relative to solvent (−), ε the zeta potential (V), μ the dynamic viscosity of electrolyte solution (Pa s), and χ the conductivity of electrolyte solution ($S\,m^{-1}$).

It is theoretically possible to connect the values of the zeta potential with the charge density on the surface under study. For this calculation, it is necessary to know the exact number of ions present in the electrolyte solution. However, the determination of this value becomes approximate when there is a change of pH, making the charge density calculation imprecise.

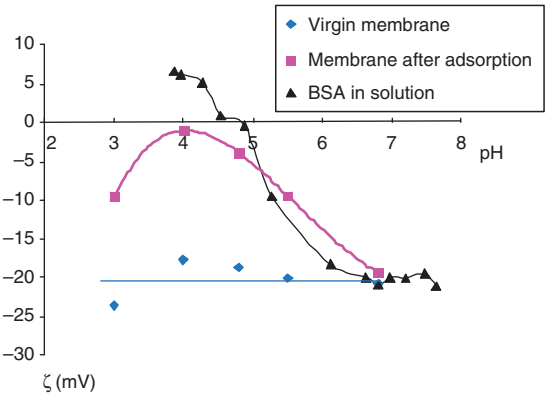

Figure 12 pH influence on the zeta potential measured at the surface of an ultrafiltration membrane before and after adsorption of bovine serum albumin (BSA).

1.15.3.3 Examples of Results

Zeta potential measurements indicate the variation of charge on the membrane surface due to the presence of a fouling agent.

Figure 12 reports the results obtained with a cell measuring the streaming potential across the pores of a 100 kDa sulfonated polysulfone membrane. The objective here is to compare the zeta potential values obtained before and after the membrane is put in contact with a bovine serum albumin (BSA) solution having an isoelectric point of about 4.8.

The results lead to the conclusion that the membrane pores that allow protein access have their walls at least partially covered by adsorption of these proteins. Some of the amphoteric properties of serum albumin are thus transferred to the membrane [9].

The difference in the isoelectric point pI before and after fouling has also been observed for inorganic zircon microfiltration membranes fouled by silica (pI of new membrane = 8, pI of fouled membrane = 5.2) [18].

In the second example presented in **Table 4**, a study was made on the effects of various cleaning solutions, acid, base, or detergent, on the electrical properties of the surface of a sulfonated polysulfone membrane. In membrane processes, industrial formulations are used for cleaning (Ultrasil®). They are composed of soda, surfactants, phosphates, and

Table 4 Example of the changes in zeta potential along with two different cleaning protocols: Sulfonated polysulfone membrane

	1st cycle			*2nd cycle*			
Cleaning procedure	*Packing then ultrasil cleaning*	*NaOH*	*HNO_3*	*Ultrasil*	*HNO_3*	*NaOH*	*Ultrasil*
ζ (en mV)	−14	−15	−3	−14	−3	−8	−12

carbonates, and successfully clean membranes fouled by proteins. Acids are used to solubilize the fouling layers containing mineral salts. HNO_3 also has an oxidizing action on proteins. The soda saponifies grease and hydrolyzes the proteins.

The solutions indicated in **Table 4** were filtered one after the other through a new membrane in two cycles. The results show that, to preserve and/or restore the electrical properties of the membrane surface, the washing cycle needs to be chosen judiciously.

1.15.4 Determination of Hydrophilic/Hydrophobic Nature of Membranes

The hydrophilic nature of a material is a very important parameter as it conditions the solute–membrane and solvent–membrane interactions. In many applications, hydrophilic membranes are more efficient than hydrophobic ones, the latter being confronted with more serious fouling whenever hydrophobic molecules or particles (proteins, colloids, etc.) are present in the fluid to be filtered [11]. The same is true for surfactants, the adsorption of which is more pronounced on hydrophobic materials [19].

Also, the energy of interaction between hydrophobic molecules and a hydrophilic surface is lower than for a hydrophobic–hydrophobic system, so it is easier to regenerate the surface by washing in the former case [34].

The hydrophilic/hydrophobic nature of a membrane is determined by measuring the contact angle or by using the capillary elevation balance. The liquid normally used for this purpose is water.

1.15.4.1 Contact Angle Measurement by Drop Profile Analysis

1.15.4.1.1 Sessile drop method

This method consists of placing a drop of liquid (generally water) on the surface of the membrane. The wettability of the surface is then characterized by the contact angle θ between the solid surface and the tangent to the liquid surface at the contact point. By convention, this angle is measured inside the liquid (**Figure 13**) [53].

The volume of the drop placed on the surface must be such that wetting effects predominate over gravitational effects. In other words, the radius r_e corresponding to the volume of the sessile drop must be such that

$$r_e \ll \sqrt{\frac{\gamma_L}{\rho_L \cdot g}} \tag{17}$$

where r_e is the radius of the liquid drop (m), γ_L the surface tension of the liquid ($N\,m^{-1}$), ρ_L the density of the liquid ($kg\,m^{-3}$), and g the acceleration due to gravity ($m\,s^{-2}$).

For example, a 2-μl drop of water has a radius of 0.8 mm (assuming the drop to be spherical), which should be compared with

$$\sqrt{\frac{\gamma_L}{\rho_L \cdot g}} \cong 2.7mm \tag{18}$$

These conditions thus satisfy the above-mentioned criterion.

The contact angle is directly obtained from a video image of the drop sitting on the solid. Measuring the geometrical parameters of the drop – h (height of the drop at the apex) and r_e (radius of the drop) – enables the cosine of the angle θ to be found from the following relationship:

$$\cos\theta = \frac{1-\left(\frac{h}{r_e}\right)^2}{1+\left(\frac{h}{r_e}\right)^2} \tag{19}$$

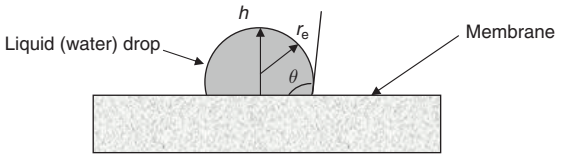

Figure 13 Diagram of the sessile drop method to measure the contact angle.

where h is the height of the drop at the apex (m) and θ the contact angle formed by the membrane surface and the tangent to the liquid surface at the contact point (°).

The solid is considered to be perfectly wettable by the liquid (hydrophilic if the liquid is water) if $\theta = 0$, more or less wettable if $\theta < \pi/2$, and more or less not wettable (hydrophobic if the liquid is water) if $\theta > \pi/2$.

This method requires the sample to be dried beforehand as the presence of water in the structure modifies the value of the contact angle. This preconditioning can have the disadvantage of inducing changes in the surface properties of the membrane which may affect the angle measured.

A distinction is also made between the advancing contact angle, which corresponds to the angle formed between a dry material and water, and the receding contact angle, which corresponds to the angle obtained after wetting with water. The difference between the advancing and receding angle is a hysteresis, which is enhanced on rough surfaces. In general, model equations, such as Equation (16), consider the advancing angle.

1.15.4.1.2 Captive bubble method

When membrane properties do not allow the contact angle to be measured by placing a drop on the surface (surface too porous or too hydrophilic) or if it is undesirable to dry the sample, the captive bubble method may be used (Zhang *et al.*, 1990).

As shown in **Figure 14**, the membrane is immersed in water with the surface to be analyzed facing downward. A micro-syringe is then used to trap an air bubble on the lower surface of the membrane. As before, the contact angle is calculated by determining the geometrical parameters of the air bubble.

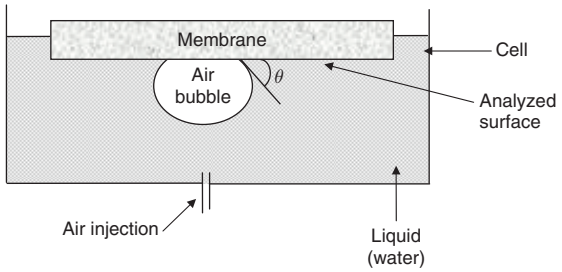

Figure 14 Diagram showing the captive bubble method to measure the contact angle between a liquid (water) and a membrane.

The captive bubble method does not require the sample to be preconditioned (no membrane drying). Nevertheless, the method remains sensitive to the roughness, porosity, and heterogeneity of the surface.

According to the literature, it is possible to find a classification [53] established using this method (captive air bubble in an aqueous medium) giving advancing contact angles in decreasing order (1st value, followed by the receding contact angle): polyolefin (83°–54°) > polysulphone (73°–42°) > cellulose acetate (60°–47°) > sulfonated polysulfone (54°–16°) > polyacrylonitrile (53°–34°).

1.15.4.2 Capillary Elevation Balance

The two methods presented above are suitable for analyzing plane surfaces at sample scale. For membranes with nonplanar geometry, such as hollow fibers, another method can be envisaged. It consists of measuring the weight gained by a material placed in contact with a liquid as a function of time. The speed at which a given liquid spontaneously penetrates a porous solid by capillarity depends directly on the porous structure of the material and the affinity of the liquid for the material. In Washburn's differential equation, the weight gain (m) is given as a function of time (t) by

$$\frac{\mathrm{d}m}{\mathrm{d}t} = \frac{1}{m} \cdot \left[\frac{\gamma_L . R . \rho_L^2 \cdot \cos\theta}{4 . \mu} \right] \tag{20}$$

where γ_L is the surface tension of the liquid (N m^{-1}), ρ_L the density of the liquid (kg m^{-3}), μ the viscosity of the liquid (Pa s), θ the advancing contact angle between the liquid and the solid (°), and R the geometrical parameter characteristic of the porous structure of the material.

By integration, we obtain

$$m^2 = \frac{\gamma_L . R . \rho_L^2 . \cos\theta}{2 . \mu} . t \tag{21}$$

This method is theoretically applicable only if $\theta < 90°$, that is, if the liquid wets the solid.

The plot of

$$\frac{2 . m^2 . \mu}{t . \rho_L^2} = f(\gamma_L) \tag{22}$$

allows cos θ to be found and hence the contact angle the liquid makes with the surface of the membrane. This method has been used by some authors [46] to determine the surface tension of membranes made of poly(tetrafluoroethylene), poly(ethylene), and

poly(propylene) using several organic liquids (hexane, toluene, cyclohexane, to mention but a few). The results obtained are in agreement with the values obtained from other methods.

It should be stressed here that the values obtained for contact angles depend on the measuring technique used. Moreover, they also depend on many factors connected with how the sample is prepared and the characteristics of the zone analyzed (local roughness, porosity, heterogeneity in the surface chemical composition, etc.). It has been shown that the more porous a membrane is, the more hydrophilic it appears to be. It also seems necessary to correlate the membrane surface charge with the values measured for the contact angles. Bearing this in mind, it is preferable to use these methods to establish a comparative classification of membranes, all other things being equal.

As for the zeta potential, a change in contact angle can have many origins. Hence, it is an interesting parameter for monitoring well-controlled modifications, achieved in lab conditions. On the other hand, finding the cause of a change in contact angle, for a membrane used in field conditions, is often a needle in a haystack type of problem.

1.15.5 Analysis of Chemical Composition

Various techniques are available for determining the chemical functions present at the surfaces of membranes: infrared attenuated total reflectance (IR-ATR) spectroscopy, secondary ion mass spectrometry (SIMS), and X-ray photoelectron spectroscopy (XPS), also known as electron spectroscopy for chemical analysis (ESCA). Some of these techniques can also serve for in-depth chemical analysis.

1.15.5.1 Fourier Transform Infrared – Attenuated Total Reflectance Spectroscopy

Fourier transform infrared spectroscopy (FTIR) is a powerful analysis tool for characterizing and identifying organic molecules. It is the spectroscopic technique that is the most widely used for determining the characteristics of new membranes. In attenuated total reflectance mode, this type of spectroscopy enables functional groups present over a depth of about 1 μm to be identified.

During ATR analysis, the sample is kept in contact with a crystal allowing total internal reflection. An infrared ray arrives at the crystal where the material under study has been placed. The internal reflection of the ray in the crystal gives rise to an evanescent wave which, at each reflection, continues beyond the surface of the crystal and penetrates the sample over about 1 μm. The penetration depth depends on the wavelength, the angle of incidence of the beam on the crystal, and the nature of the crystal.

Spectra are thus obtained (curves of absorbance vs. wavelength) that have absorption peaks characteristic of the functions present at the membrane surface.

FTIR-ATR is a sensitive, nondestructive method that can be used qualitatively and quantitatively. However, it requires prior drying of the membrane sample.

One of the applications of FTIR-ATR is the characterization of modified surfaces. In this case, the spectra show bands characteristic of the basic membrane with, in most cases, bands characteristic of the new functional groups related to the modification. FTIR-ATR also enables the efficiency of membrane cleaning to be assessed [57].

This method can also be used to analyze the adsorption of macromolecules at the membrane surface [27] and to check whether the conformation of the adsorbed compounds (e.g., proteins) has been modified by comparing the spectra of the adsorbed product with those of the same product in solution [4]. When the deposits are very small, however, it is difficult to determine the presence of fouling agents; this necessitates the use of elaborate data-processing methods that eliminate the contributions of the membrane and water from the raw spectra [3, 35]. **Figures 15–17** show a few examples of spectra obtained for new or fouled polyethersulfone membranes.

A first analysis performed on the PES membrane is shown in **Figure 15**. The contribution of water to the raw spectrum of a PES membrane has been eliminated and it is possible to identify the main adsorption bands of polyethersulfone (**Table 5**), for which the structural formula is

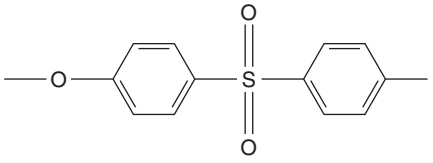

The same PES membrane was analyzed by FTIR-ATR after fouling by skimmed milk.

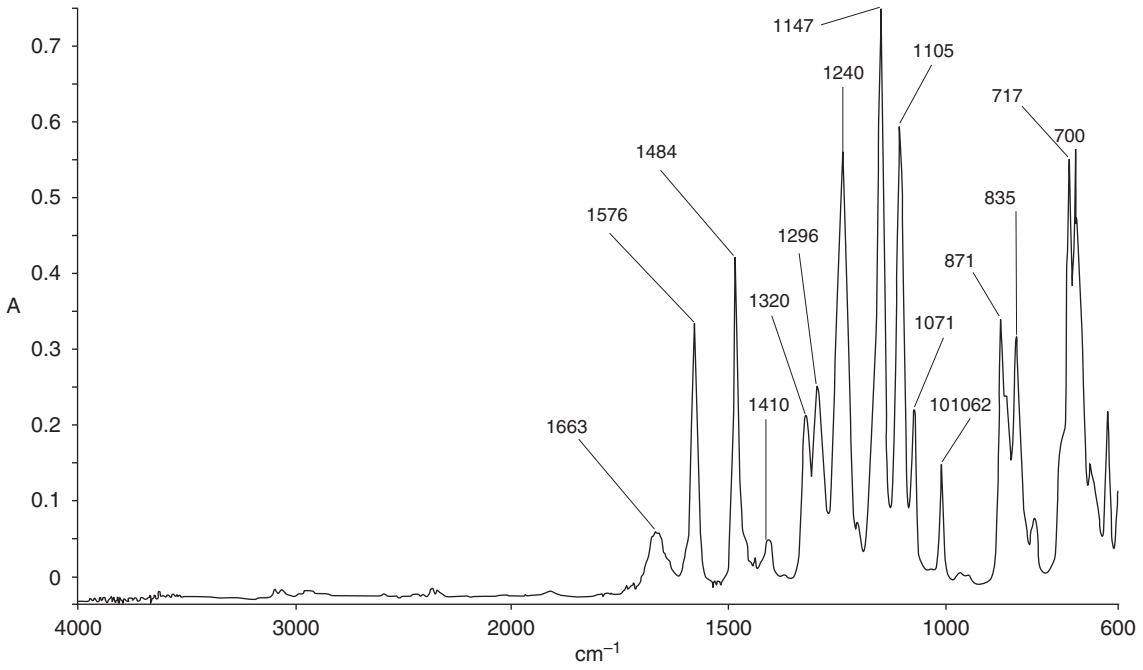

Figure 15 Infra-red spectrum of a polyethersulfone membrane (after removal of the residual water signal). From Begoin, L. Analyse de modules spirales industriels d'ultrafiltration de fluides laitiers. Physico-chimie du nettoyage de membranes en polyethersulfone d'ultrafiltration de lait écrémé. PhD Thesis, University of Rennes I, 2004.

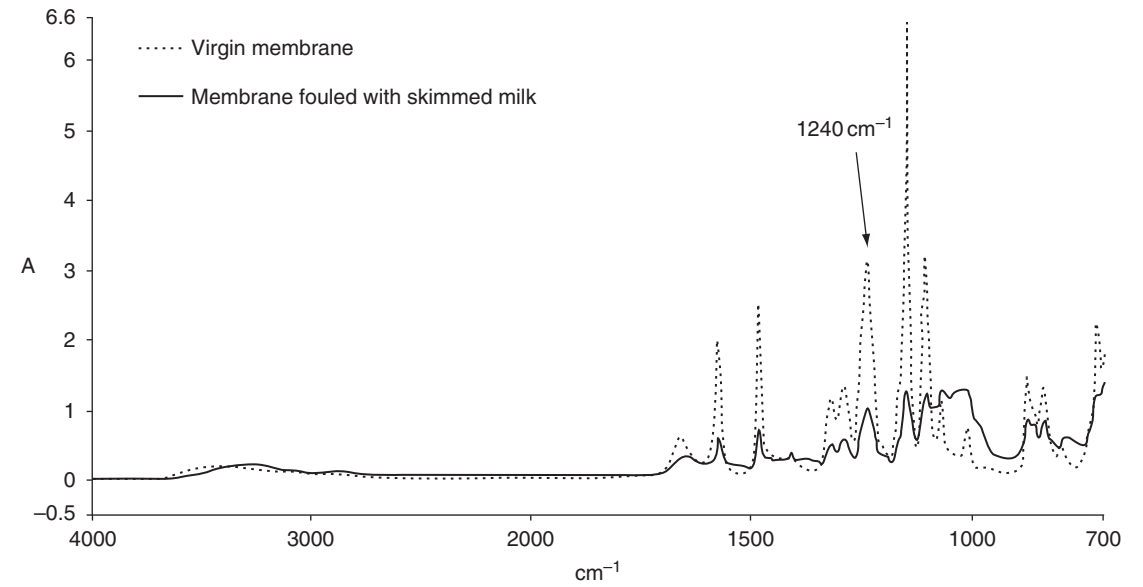

Figure 16 Infra Red spectra of a clean and a fouled with skimmed milk ultrafiltration membrane (polyethersulfone). From Begoin, L. Analyse de modules spirales industriels d'ultrafiltration de fluides laitiers. Physico-chimie du nettoyage de membranes en polyethersulfone d'ultrafiltration de lait écrémé. PhD Thesis, University of Rennes I, 2004.

The raw spectrum obtained for the fouled membrane (**Figure 16**) was processed by double difference, which consists of firstly removing the water contribution (difference 1), and secondly removing the contribution of the PES membrane (difference 2). The new spectrum thus obtained (**Figure 17**(**a**)) was comparable to the difference 1 spectrum of the fouling agent in solution, skimmed milk in this case (**Figure 17**(**b**)).

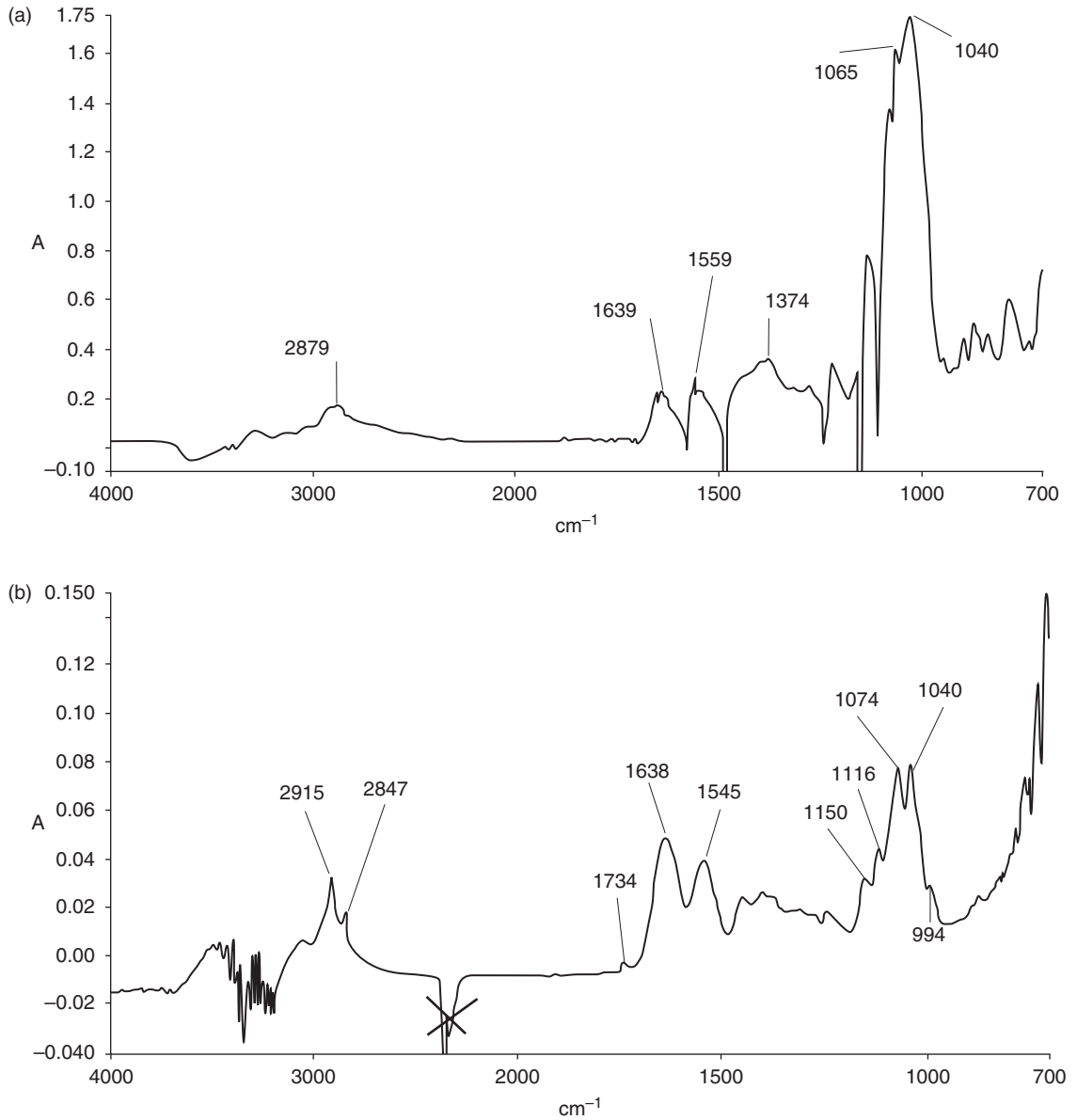

Figure 17 Comparison of the IR spectra of a membrane fouled with skimmed milk (a), and of skimmed milk (b). From Rabiller-Baudry, M., Le Maux, M., Chaufer, B., Begoin, L. *Desalination* **2002**, *146*, 123–128.

Table 5 Some IR adsorption bands and their connection to chemical functions

Wave number (cm^{-1})	*Intensity*	*Vibration*	*Chemical group*
1576	Strong	C = C	Benzene ring
1484	Strong	Aromatic ring	
1320	Moyenne	O = S = O	Sulfonic group
1296	Moyenne	Antisymetric stretching	
1240	Strong	C–O–C stretching	Ether group
1147	Strong	Symetric stretching	Sulfonic group
1105	Strong	Aromatic ring vibration	

1.15.5.2 Secondary Ion Mass Spectrometry

SIMS enables the identification of elements, and possibly other chemical species, present in a material, not only on the surface but also in the thickness of the sample.

Primary ions (Ar^+, O_2^+, Cs^+, Ga^+) with incident kinetic energies of a few keV (0.1–50 keV) penetrate the target solid, where a series of collisions occur. Some of the particles emitted by the target are ionized. SIMS analyzes the secondary ions by mass spectrometry. The emission of secondary ions by the surface of a solid excited by an ion beam provides information on the molecular and isotopic composition of the solid, and concentration profiles across the sample can be established [41].

It should, however, be noted that this technique is destructive. Moreover, obtaining the true concentrations in a material from the secondary ion emission signals is generally one of the weak points of the method because of the complexity of the processes involved, in particular, the variations in the ionization yield of the species depending on the chemical nature of the phases where they occur.

This method is widely used because of its great sensitivity for all elements, from hydrogen to uranium. It can detect an impurity in a sample (detection limit below 0.1 ppb), and allows the adsorption, adhesion, corrosion, contamination, and biocompatibility of materials to be studied. SIMS is thus used for studying the grafting of polymers on to the surfaces of various membranes or for comparing different samples having the same reference state (e.g., in studies of membrane aging).

An example of analysis is presented in **Figure 18** for the case of a polyvinylpyrrolidone (PVP)-modified polysulfone membrane. To overcome the problems of quantification, a comparative study was made of the various samples by following the analyzed element content relative to a reference element. In the case presented here, the reference chosen was sulfur as it is the main element present in the main polymer, polysulfone. **Figure 18** shows the variation of the nitrogen content (element specific to PVP) over an analyzed depth of 60 μm, on both the selective skin side of the native membrane and the support side. While PVP was not detected on the support side, the results revealed the presence of PVP on the skin side, at a concentration becoming weaker with deeper penetration into the structure. These results are in agreement with the protocol used in the manufacture of the membrane, which leads to a greater modification by PVP on the surface of the skin.

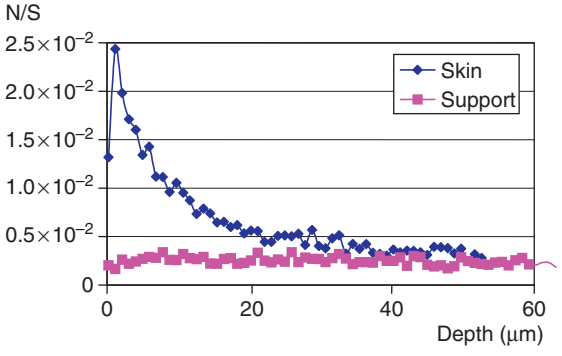

Figure 18 Example of a nitrogen concentration profile (normalized by the sulfur concentration) through the skin and through the support obtained by secondary ion mass spectrometry (SIMS), in a PVP/PS membrane. PVP, polyvinylpyrrolidone.

1.15.5.3 XPS or ESCA

This technique allows the chemical composition to be determined on the surface and down to a depth of ~1 nm for various materials.

The sample is irradiated with X-rays in order to excite its atoms which emit electrons from different atomic levels. The electrons emitted generally have low energies and are strongly absorbed. Those that arrive at the surface with sufficient energy thus come from a layer having a depth of the order of the mean free path [37].

The electrons are collected, analyzed, and classified according to their identity. The important information they contain is the bond energy, the energy they had before they left the atom. The spectrum of the binding energy of the photoelectrons is specific to an atom, which can be identified and its amount in a given compound determined. The analyzer counts the electrons according to their bond energy, and spectra like the one shown in **Figure 19** are built up.

ESCA, often considered as the easiest technique to carry out and interpret, can be adapted for a wide variety of surfaces and (unlike SIMS) provides a quantitative analysis of the chemical information.

The atomic composition of the surface of a grafted membrane [20] and a membrane treated by plasma [42] can be determined by ESCA.

This method is complementary to SIMS and FTIR-ATR. Some authors have performed studies with the three techniques in parallel in order to confirm their conclusions [14]. In addition, these authors note that ESCA, with its short analysis times, damages the samples to a small extent.

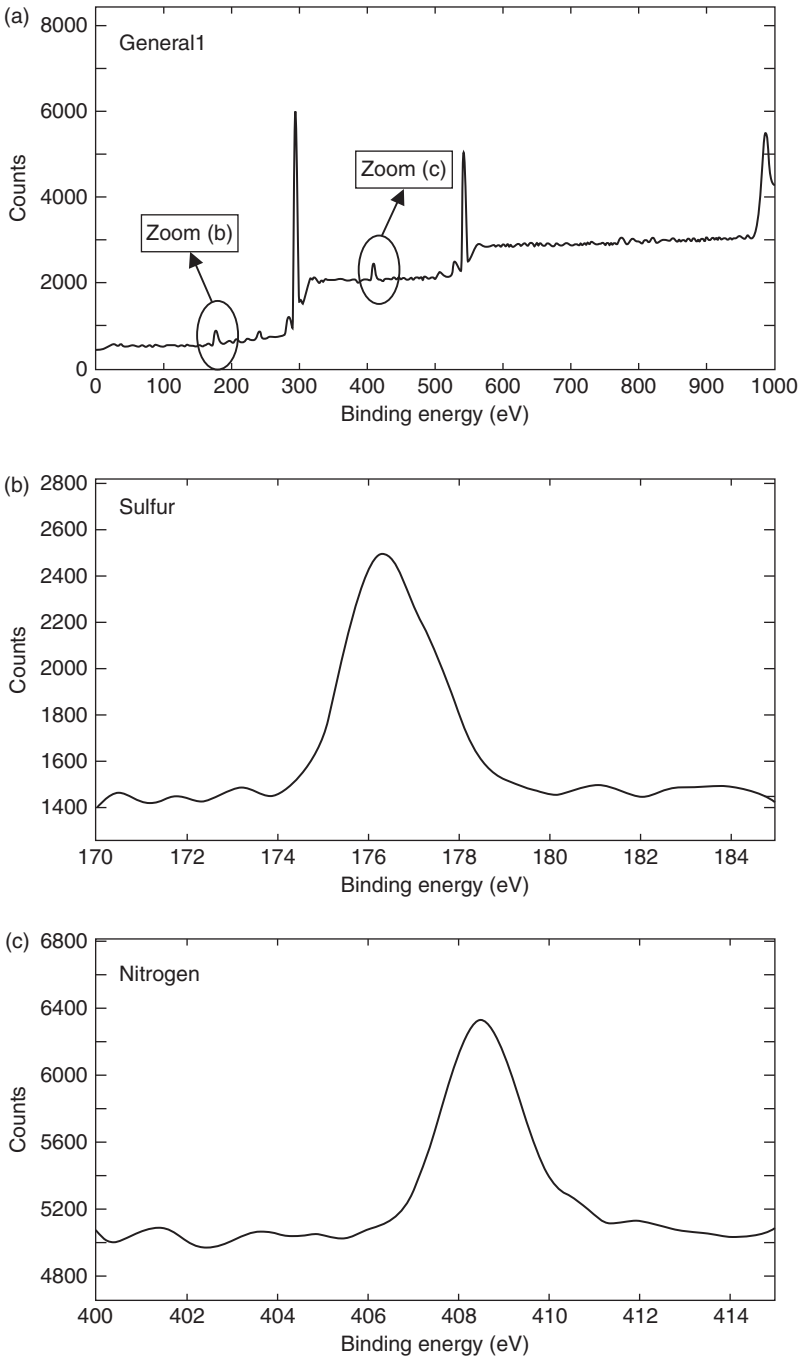

Figure 19 ESCA spectra of a PS/PVP membrane: (a) general spectrum, (b) zoom on the sulfur band, and (c) zoom on the nitrogen band (PVP specific). PVP, polyvinylpyrrolidone.

1.15.6 Mechanical Characterization

Local movements of polymers underlie the elementary processes of many physical (glass transition and secondary transitions, diffusion and flow) and mechanical (viscoelasticity, plastic deformation, etc.) phenomena. These movements are very closely connected with the chemical structure of the polymers, and their storage or utilization conditions.

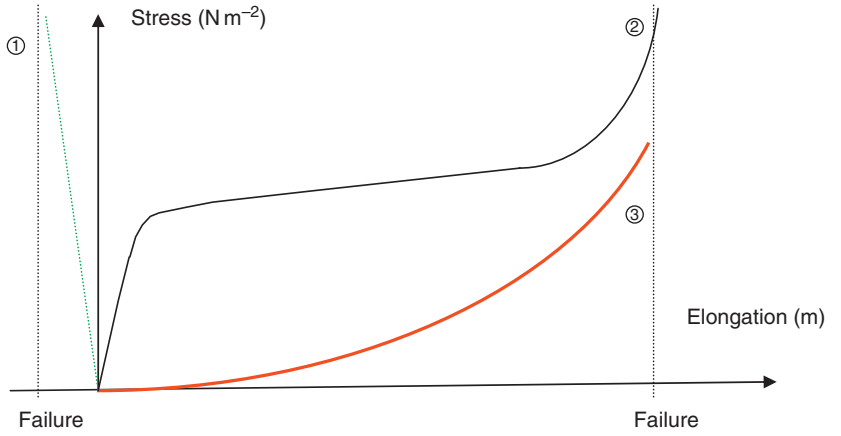

Figure 20 Mechanical characteristic curves obtained with polymers: case ①: rigid plastic polymer: it can undergo small compressions for high stresses; case ②: flexible plastic polymer: small strains for high stresses up to a plateau, after which rupture occurs; and case ③: elastomer: large strains for small stresses.

A study of the mechanical properties can thus be used to characterize the structure of a polymer membrane and, in particular, to follow its evolution with time as discussed in more detail below. Polymers can be classified in three families according to the strain they show (e.g., elongation) when stressed (e.g., tensile stress): elastomers, flexible plastics, and rigid plastics.

An example of a tensile test (stress-strain curve) is given in **Figure 20**.

Curves of stress versus deformation are obtained in tension (or compression) tests, in which the sample is drawn out at constant speed until it breaks (**Figure 21**). Knowing the pulling speed, the initial distance between the grips, and the geometrical characteristics of the sample, we have access to various mechanical characteristics:

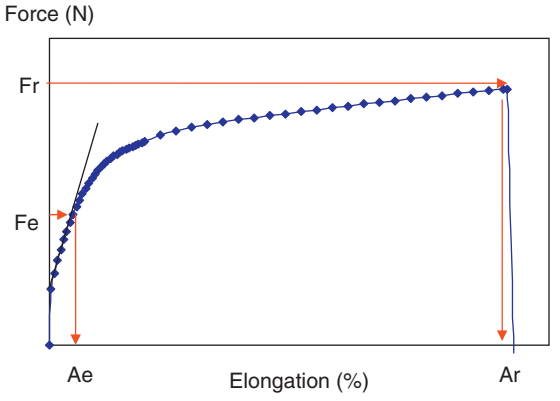

Figure 21 Elongation curve for a flexible plastic polymer (see **Figure 22**).

- the force, extension, and stress at break (F_b, A_r and σ_r);
- the force, elongation, and elastic stress (F_e, A_e, and σ_e); and
- the Young's modulus (E in Pa).

Figure 21 shows how these various parameters are determined graphically.

A tensile force F applied at the end of a cylinder of cross-sectional area S induces a stress σ in the cylinder, which leads to the following relationship:

$$\sigma = \frac{F}{S} \tag{23}$$

with F being the force (N), S the cross-sectional area (m^2), and σ the stress (N m^{-2}).

The modulus of elasticity, or Young's modulus, E, is the elastic constant which, for a uniform, isotropic material, links the stress with the strain and thus characterizes the stiffness of the material or the resistance to elastic strain [15]. For a given stress, a material having a high modulus of elasticity will be deformed less than a material with a low modulus of elasticity, as depicted by Equation (24):

$$\sigma = \frac{\Delta A}{A} E \tag{24}$$

where $\frac{\Delta A}{A}$ is the deformation (–).

The rheological properties of polymers depend on the temperature and also on the deformation speed. The faster the deformation takes place, the greater the mechanical resistance of the polymer will be,

even at high temperatures. Moreover, for the same chemical type, the molecular mass of the polymer under consideration has a marked influence on the rheological properties. High molecular masses favor the elongation of the product.

The possible variation of the mechanical properties of polymers during aging provides us with information on the damage of membranes. The behavior at low strains (modulus of elasticity and flow threshold) should be little affected by aging, which essentially acts on the rupture properties.

1.15.6.1 Failure Envelopes

Mechanical tests enable failure envelopes to be plotted (Nitta *et al.*, 2004). By definition, these concern the time variation of the stress–strain behavior.

In the case of aged materials, these envelopes comprise the tension curve of the reference material (not aged) on which is superimposed the variation of the breaking stress versus the elongation at rupture for samples with different aging times (**Figure 22**). These envelopes allow us to know whether a material has been damaged or not and, if it has, whether there is one aging mechanism or several.

In the case of damage in the material properties, if the data points tend toward low stresses at break along the tension curve of the reference material, the damage is due to a single, polymer-chain-breaking mechanism.

The technique of studying mechanical properties has been used to characterize the epoxidation of polyurethane-based membranes [51] and has shown that the longer the epoxidation time, the higher the breaking force and the smaller the elongation. Xu *et al.* [49] used the mechanical properties of membranes to characterize the action of a hypochlorite treatment on polyvinylpyrrolidone-modified polyetherimide membranes. They show that, after 2 days of immersion in a 4000-ppm sodium hypochlorite solution, the Young's moduli were the same as those of membranes that had not received post-treatment with sodium hypochlorite.

Rouaix *et al.* (2006) show that a long exposure of hollow fiber polysulfone membranes to sodium hypochlorite produces polysulfone chain rupture which is closely related to changes in the mechanical properties of the membrane. A few chain scissions have a very high impact on elongation and tensile strength at break point of the membrane (loss of 80% in elongation at break point for a percentage of chain scissions lower than 2.8%).

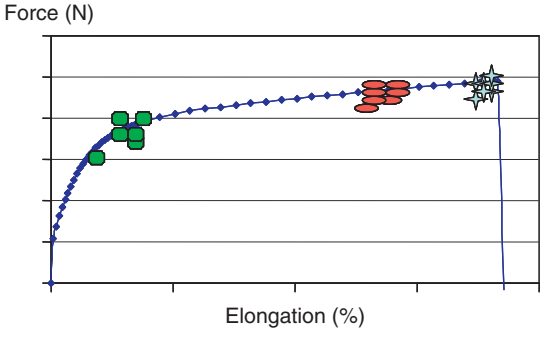

Figure 22 Rupture envelopes of various materials: (✦): not degraded; (⬭): slightly degraded; (■): seriously degraded; (◆): tension curve of reference material).

References

[1] Baltus, R. E. *J. Membr. Sci.* **1997**, *130* (1–2), 157–172.
[2] Baruchel, J., Buffiere, J. Y., Maire, E., Merle, P., Peix, G. *X-Ray Tomography*; Hermes Science Publications: Paris, 2000.
[3] Begoin, L. Analyse de modules spirales industriels d'ultrafiltration de fluides laitiers. Physico-chimie du nettoyage de membranes en polyethersulfone d'ultrafiltration de lait écrémé. PhD Thesis, University of Rennes I, 2004.
[4] Belfer, S., Fainchtain, R., Purinson, Y., Kedem, O. *J. Membr. Sci.* **2000**, *172*, 113–124.
[5] Bellon-Fontaine, M.-N., Rault, J., Van Oss, C. J. *Colloids Surf. B* **1996**, *7* (1–2), 47–53.
[6] Bessieres, A., Meireles, M., Coratger, R., Beauvillain, J., Sanchez, V. *J. Membr. Sci.* **1996**, *109*, 271–284.
[7] Bowen, R. W., Hilal, N., Lovitt, R. W., Williams, P. M. *J. Membr. Sci.* **1996**, *110*, 233–238.
[8] Bowen, W. R., Mohammad, A. W., Hilal, N. *J. Membr. Sci.* **1997**, *126*, 91–105.
[9] Causserand, C., Nystrom, M., Aimar, P. *J. Membr. Sci.* **1994**, *88*, 211–222.
[10] Causserand, C., Rouaix, S., Akbari, A., Aimar, P. *J. Membr. Sci.* **2004**, *238*, 177–190.
[11] Choo, K. H., Lee, C. H. *J. Colloid Interface Sci.* **2000**, *226*, 367–370.
[12] Deen, W. M., Bohrer, M. P., Epstein, N. B. *AIChE J.* **1981**, *27*(6), 952–959.
[13] Ebersold, M. F., Zydney, A. L. *Biotechnol. Bioeng.* **2004**, *85*(2), 166–176.
[14] Flosch, D., Lehmann, H.-D., Reichl, R., Inacker, O., Gopel, W. *J. Membr. Sci.* **1992**, *70*, 53–63.
[15] Gijsbertsen-Abrahamse, A. J., Cornelissen, E. R., Hofman, J. A. M. H. *Desalination* **2006**, *194* (1–3), 251–258.
[16] Guo, H., Wyart, Y., Perot, J., Nauleau, F., Moulin, P. *J. Membr. Sci.* **2010** (in press).
[17] Huisman, I. H., Pradanos, P., Hernandez, A. *J. Membr. Sci.* **2000**, *179*, 79–90.
[18] Huisman, I. H., Tragardh, G., Tragardh, C., Pihlajamaki, A. *J. Membr. Sci.* **1998**, *147*, 187–194.
[19] Jonsson, A. S. E., Jonsson, B. *J. Membr. Sci.* **1991**, *56*, 49–76.
[20] Kim, J. H., Ha, S. Y., Nam, S. Y., Rhim, J. W., Baek, K. H., Lee, Y. M. *J. Membr. Sci.* **2001**, *186*, 97–107.

[21] Kiso, Y., Sugiura, Y., Kitao, T., Nishimura, K. *J. Membr. Sci.* **2001**, *192*(1–2), 1–10.
[22] Lebleu, N., Roques, C., Aimar, P., Causserand, C. *J. Membr. Sci.* **2009**, *326*(1), 178–185.
[23] Koyuncu, I., Brant, J., Luttge, A., Wiesner, M. R. *J. Membr. Sci.* **2006**, *278*(1–2), 410–417.
[24] Langlet, J., Ogorzaly, L., Schrotter, J. C., *et al. J. Membr. Sci.* **2009**, *326*(1), 111–116.
[25] Liikanen, R., Yli-Kuivila, J., Laukkanen, R. *J. Membr. Sci.* **2002**, *195*, 265–276.
[26] Lindau, J., Jonsson, A. S., Wimmerstedt, R. *J. Membr. Sci.* **1995**, *106*, 9–16.
[27] Maruyama, T., Katoh, S., Nakajima, M., *et al. J. Membr. Sci.* **2001**, *192*, 201–207.
[28] Masselin, I., Durand-Bourlier, L., Laine, J.-M., Sizaret, P.-Y., Chasseray, X., Lemordant, D. *J. Membr. Sci.* **2001**, *186*, 85–96.
[29] Meireles, M., Aimar, P., Sanchez, V. *J. Membr. Sci.* **1991**, *56*, 13–28.
[30] Meireles, M., Bessieres, A., Rogissart, I., Aimar, P., Sanchez, V. *J. Membr. Sci.* **1995**, *103*, 105–115.
[31] Mok, S., Worsfold, D. J., Fouda, A. E., Matsuura, T., Wang, S., Chan, K. *J. Membr. Sci.* **1995**, *100*, 183–192.
[32] Nitta, K.-H., Ishiburo, T. *Macromol. Symp.* **2004**, *214*, 251–259.
[33] Nyström, M., Zhu, H. *J. Membr. Sci.* **1997**, *131*, 195–205.
[34] Pasmore, M., Todd, P., Smith, S., *et al. J. Membr. Sci.* **2001**, *194*, 15–32.
[35] Rabiller-Baudry, M., Le Maux, M., Chaufer, B., Begoin, L. *Desalination* **2002**, *146*, 123–128.
[36] Remigy, J. C., Meireles, M., Thibault, X. *J. Membr. Sci.* **2007**, *305*, 27–35.
[37] Robinson, J. W. *Practical Handbook of Spectroscopy*; CRC Press: Boca-Raton, FL, 1991.
[38] Rouaix, S., Causserand, C., Aimar, P. *J. Membr. Sci.* **1996**, *114*, 93–104.
[39] Sayed Razavi, S. K., Harris, J. L., Sherkat, F. *J. Membr. Sci.* **1996**, *114*, 93–104.
[40] Schaep, J., Vandecasteele, C. *J. Membr. Sci.* **2001**, *188* (1), 129–136.
[41] Skoog, D. A., Holler, F. J., Nieman, T. A. *Principles of Instrumental Analysis*, Vth edn.; Harcourt Brace Publishers: Philadelphia, PA, 1998.
[42] Steen, M. L., Hymas, L., Havey, E. D., Capps, N. E., Castner, D. G., Fisher, E. R. *J. Membr. Sci.* **2001**, *188*, 97–114.
[43] Szymczyk, A., Fatin-Rouge, N., Fievet, P. *J. Colloid Interface Sci.* **2007**, *309* (2), 245–252.
[44] Sung, J. H., Chun, M.-S., Choi, H. J. *J. Colloid Interface Sci.* **2003**, *264* (1), 195–202.
[45] Torras, C., Garcia-Valls, R. *J. Membr. Sci.* **2004**, *233*(1–2), 119–127.
[46] Troger, J., Lunkwitz, K., Grundke, K., Burger, W. *Colloid Surf. A* **1998**, *134*, 299–304.
[47] Weast, R. *Handbook of Chemistry and Physics*, 58th edn.; CRC Press: Boca Raton, FL, 1977–1978.
[48] Wienk, I. M., Meuleman, E. E. B., Borneman, Z., Van den Boomgaard, Th., Smolders, C. A. *J. Polym. Sci., Part A: Polym. Chem.* **1995**, *33*, 49–54.
[49] Xu, Z.-L., Chung, T.-S., Huang, Y. *J. Appl. Polym. Sci.* **1999**, *74*, 2220–2233.
[50] Xu, J., Xu, Z. L. *J. Membr. Sci.* **2002**, *V208*, 203–212.
[51] Yang, J. M., Lai, W. C., Lin, H. T. *J. Membr. Sci.* **2001**, *183*, 37–47.
[52] Yeh, H. M., Wu, H. P., Dong, J. F. *J. Membr. Sci.* **2003**, *213*, 33–44.
[53] Zhang, W., Wahlgren, M., Sivik, B. *Desalination* **1989**, *72*, 263–273.
[54] Zhang, W. Hallström, B. *Desalination* **1990**, *79* (1), 1–12.
[55] Ziel, R., Haus, A., Tulke, A. *J. Membr. Sci.* **2008**, *323* (2), 241–246.
[56] Zhao, C., Zhou, X., Yue, Y. *Desalination* **2000**, *129* (2), 107–123.
[57] Zhu, H. Nyström, M. *Colloid Surf. A* **1998**, *138*, 309–321.

This page intentionally left blank

1.16 The Use of Atomic Force Microscopy in Membrane Characterization

N Hilal and D Johnson, Swansea University, Swansea, UK

Glossary

Colloid probe An AFM probe where the sharp imaging tip has been replaced with a colloidal particle. This allows the measurement of interactions between particles and surfaces. This is useful for measuring colloid–membrane interactions, of interest when considering the fouling of membranes by particulates.

Contact mode AFM imaging mode where the probe maintains constant contact with the sample surface. A feedback mechanism is employed to maintain a constant deflection of the cantilever allowing the topography of the sample to be recorded. This is the most basic mode of operation of the AFM.

Degree of modification (DM) The extent to which a membrane surface has been chemically modified to improve its surface properties. This is commonly expressed as mass of modifying chemical divided by unit surface area (e.g., $\mu g\,cm^{-1}$).

Hooke's law This law relates the deflection of the cantilever to the forces applied by the probe tip via the stiffness of the lever.

Intermittent contact (tapping) mode Mode of AFM imaging where the cantilever is allowed to oscillate, causing the probe tip to intermittently come into contact with the sample surface. This reduces artifacts due to lateral or frictional forces and can achieve better image results than with contact mode, especially for soft sample surfaces.

Noncontact mode In this AFM mode the probe tip does not make hard contact with the sample surface, but instead probes repulsive forces close to the surface. The minimal forces applied to the sample cause little deformation of the sample and thus very high resolution images are obtainable. In practice, however, true noncontact imaging is difficult to achieve under many conditions.

R_q (rms roughness) A common measure of the roughness of a surface. Essentially, it is the standard deviation of the heights of all the pixels in a topographic image from the mean height.

Quaternary 2-dimethyl-aminoethylmethacrylate (qDMAEMA) Chemical used in the studies described here to improve the fouling properties of various membranes.

1.16.1 Introduction

Over the past two decades, atomic force microscopy (AFM) has proven itself to be a powerful and versatile tool for the physical characterization of surfaces. As an imaging technique, it is capable of resolving features from a few micrometers down to the subnanometer scale. Unlike many other high-resolution imaging techniques, it can image both conducting and nonconducting surfaces, it does not require hard vacuum to function, and is capable of visualizing samples in air as well as in liquids. This is of great use to researchers interested in studying membranes and other surfaces, which are routinely exposed to aqueous solutions as it means that they may be imaged in their operational media. The basic operation of the AFM uses a probe with a sharp tip to physically feel the surface of interest, generating a three-dimensional (3-D) topography, allowing quantification of physical properties, such as roughness, step heights, and pore sizes. This mechanical nature of the AFM also allows it to be used as a direct force sensor. Replacing the sharp tip with a particle of colloidal size or single cell allows the characterization of adhesive and long-range surface forces in different environmental conditions. This can provide insight into the fouling properties of membranes, without recourse to using full-scale membrane filtration rigs.

In this chapter, we outline the operation of the AFM, giving specific examples of the use of the AFM to characterize a range of properties of filtration membranes.

1.16.2 Principles of AFM

In **Figure 1**, the basic setup of a typical AFM is shown. A cantilever, which may commonly be either V-shaped, as shown, or a rectangular diving-board-shaped cantilever, attached to a chip, has mounted close to its free end a sharp tip which acts as the probe of interaction forces. The probe is brought into and out of contact with the sample surface by the use of a piezocrystal, upon which either the cantilever chip or the surface itself is mounted, depending upon the particular system being used. Movement in this direction is conventionally referred to as the z-axis. A

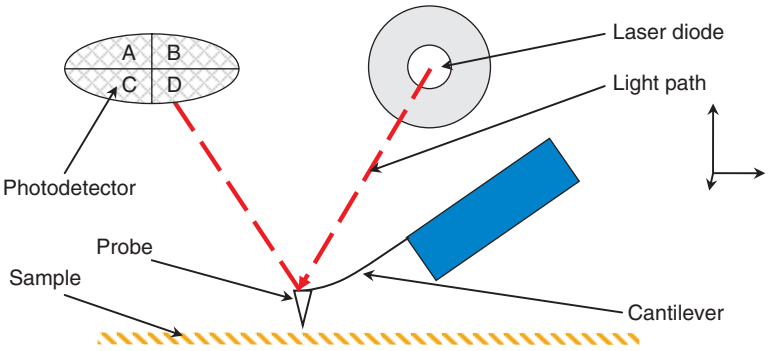

Figure 1 Basic setup of the atomic force microscopy (AFM). A probe is mounted at the apex of a flexible Si or Si_3N_4 cantilever. The tip of the probe is moved in relation to the sample surface by the use of piezo crystals. Deflection of the cantilever is monitored by the change in the path of a beam of laser light deflected from the upper side of the end of the cantilever by a photodetector. As the tip is brought into contact with the sample surface, by movement of the piezo, its deflection is monitored. This deflection can then be used to calculate interaction forces between probe and sample.

laser beam is reflected from the reverse (uppermost) side of the cantilever onto a position-sensitive photodetector. Any deflection of the cantilever will produce a change in the position of the laser spot on the photodetector, allowing changes to the deflection to be monitored. The most common configuration for the photodetector is that of a quadrant photodiode divided into four parts with a horizontal and a vertical dividing line. If each section of the detector is labeled A–D as shown in **Figure 1**, then the deflection signal is calculated by the difference in signal detected by the A + B versus C + D quadrants. Comparison of the signal strength detected by A + C versus B + D will allow detection of lateral or torsional bending of the lever. Once the probe is in contact with the surface, it can then be raster-scanned across the surface to build up relative height information of topographic features of the sample.

Scanners are available in different configurations, depending upon the particular AFM employed, or the purpose for which it is required. Tube scanners consist of a hollow tube made of piezoceramic material. Depending on how electrical current is applied, the tube may extend in the *z*-direction, or be caused to flex in either the *x*- or *y*-direction to facilitate scanning. Alternatively, scanners may consist of separate piezo crystals for each movement direction. Such a configuration removes certain nonlinearity problems which may occur in the simpler tube scanners. In many commercially available AFMs, especially in older models, the movement in the *x*- and *y*-direction may be achieved by the movement of the sample rather than by the movement of the probe.

1.16.2.1 Imaging Modes

There are many different imaging modes available for the AFM, providing a range of different information about the sample surfaces being examined. However, for simplicity the most common modes are considered here. In **Figure 2**, the force regimes under which the main imaging modes occur are illustrated schematically. In the figure, the interaction forces are sketched as the probe approaches and contacts the surface, with separation distance increasing to the right. At large separations, there are no net forces acting between the probe and the sample surface. As the probe and surface approach each other, attractive van der Waals interactions begin to pull the probe toward the surface. As contact is made, the net interaction becomes repulsive as electron shells in atoms in the opposing surfaces repel each other. In **Figure 2**, the repulsive forces are shown as being positive and attractive forces negative.

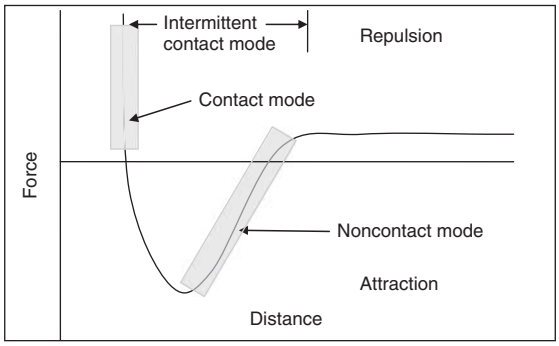

Figure 2 Diagram illustrating the force regimes under which each of the three most common atomic force microscopy (AFM) imaging modes operate. Contact mode operation is in the repulsive force regime, where the probe is pressed against the sample surface, causing an upward deflection of the cantilever. Noncontact mode interrogates the long-range forces experienced prior to actual contact with the surface. With intermittent contact, or tapping mode, the probe is oscillated close to the surface where it repeatedly comes into and out of contact with the surface.

1.16.2.1.1 Contact mode imaging

Contact mode imaging is so called because the probe remains in contact with the sample at all times. As a result, the probe–sample interaction occurs in the repulsive regime as illustrated in **Figure 2**. This is the simplest mode of AFM operation and was that originally used to scan surfaces in early instruments. There are two variations in this technique: constant force and variable force. With constant force mode, a feedback mechanism is utilized to keep the deflection, and hence force, of the cantilever constant. As the cantilever is deflected, the *z* height is altered to cause a return to the original deflection or set point. The change in *z*-position is monitored and this information as a function of the *x*,*y* position is used to create a topographical image of the sample surface. For variable force imaging, the feedback mechanisms are switched off so that *z* height remains constant and the deflection is monitored to produce a topographic image. This mode can be only used on samples which are relatively smooth with low-lying surface features, but for surfaces where it is applicable it can provide images with a sharper resolution than constant force mode.

Contact mode is often the mode of choice when imaging a hard and relatively flat surface due to its relative simplicity of operation. However, there are several drawbacks. Lateral forces can occur when the probe traverses steep edges on the sample, which may cause damage to the probe or the sample, or also result from adhesive or frictional forces between the probe and the sample. This can also lead to a decrease in the resolution of images due to the stick-slip movement of the probe tip over the surface. In addition, the relatively high forces with which the probe interacts with the sample can cause not only a deformation of the sample, leading to an underestimation of the height of surface features, but also an increase in the area of contact between the probe and the surface. The area of contact between the probe and the surface sets a limit to the resolution which can be achieved. Where a soft, and therefore easily deformable and easily damaged, sample is to be imaged, dynamic modes of imaging, such as intermittent contact or noncontact modes, are usually preferable.

1.16.2.1.2 Intermittent contact (tapping) mode

In order to overcome the limitations of contact mode imaging as mentioned above, the intermittent, or tapping, mode of imaging was developed [1–3]. Here, the cantilever is allowed to oscillate at a value close to its resonant frequency. When the oscillations occur close to a sample surface, the probe will repeatedly engage and disengage with the surface, restricting the amplitude of oscillation. As the surface is scanned, the oscillatory amplitude of the cantilever will change as it encounters differing topography. By using a feedback mechanism to alter the z height of the piezo and maintain constant amplitude, an image of the surface topography may be obtained in a similar manner as with contact mode imaging. In this manner, lateral forces, as the probe is scanned across the surface, are greatly reduced, compared with the contact mode.

When using tapping mode in air, capillary forces due to thin layers of adsorbed water on surfaces, particularly with very hydrophilic surfaces, have to be overcome, as well as any other adhesive forces which may be present. If the restoring force of the cantilever due to its deflection is insufficient to overcome adhesion between the probe and the surface, then the probe will be dragged along the surface in an inadvertent contact mode. As a result, for this mode in air, the spring constants of AFM cantilevers are by necessity several orders of magnitude greater than those used for either tapping mode in liquid or contact mode (typically in the range of 0.01–2 $\mathrm{N\,m^{-1}}$ for contact mode to 20–75 $\mathrm{N\,m^{-1}}$ for tapping in air).

As surfaces with different mechanical and adhesive properties are scanned, the frequency of oscillation will change causing a shift in the phase signal between the drive frequency and the frequency with which the cantilever is actually oscillating [4, 5]. This phenomenon has been used to produce phase images alongside topographic images, which are able to show changes in the material properties of the surfaces being investigated. However, while the qualitative data this provides are useful, it is difficult to extract quantitative information from the phase images due to the phenomenon being a complex result of a number of parameters, including adhesion, scan speed, load force, topography, and the material, especially elastic, properties of the sample and probe [5, 6].

1.16.2.1.3 Noncontact mode

In noncontact mode, imaging the cantilever is again oscillated, as in intermittent contact mode, but at much smaller amplitude. As the probe approaches the sample surface, long-range interactions, such as van der Waals and electrostatic forces, occur between atoms in the probe and the sample. This causes a detectable shift in the frequency of the cantilever oscillations. Detection of the shift in phase between the driving and oscillating frequencies allows the z positioning of the cantilever to be adjusted to allow the cantilever to remain out of contact with the surface by the operation of a feedback loop [7]. As the probe does not contact the surface in the repulsive regime, the area of interaction between the tip and the surface is minimized, allowing potentially for greater surface resolution. As a result, it is imaging in this mode which is best able to achieve true atomic resolution, when examining a suitable surface under suitable conditions with a tip of requisite asperity. However, in practice, obtaining high-quality images is a more daunting prospect than for intermittent contact mode. When imaging in air, all but the most hydrophobic of surfaces will have a significant water layer, which may be thicker than the range of the van der Waals forces being probed. This combined with the low oscillation amplitude will mean that the probe will be unable to detach from the water layer easily, degrading imaging resolution.

1.16.2.2 The AFM as a Force Sensor

One of the major applications of the AFM is in the quantitative measurement of interaction forces between either the probe tip, or an attached particle replacing the tip, and a sample surface. This technique has been employed to examine a wide variety of systems, including the mechanical properties of materials on the micro- and nanoscale [8–13], of interest for characterizing nanoengineered materials; adhesion between surfaces [13–18]; attractive and repulsive surface forces, such as van der Waals and electrostatic double-layer forces [19–22], both of interest when studying the properties of colloidal particles; and to probe the mechanical properties and kinetics of bond strength of biomolecules [23–26].

As the tip of the cantilever is brought into and out of contact with a surface, a force curve is generated, describing the cantilever deflection (or force) as a function of distance. A typical force curve is illustrated in **Figure 3**. Raw data are plotted as displacement of the *z* piezo on the abscissa, while cantilever deflection is plotted as the signal on the photodetector

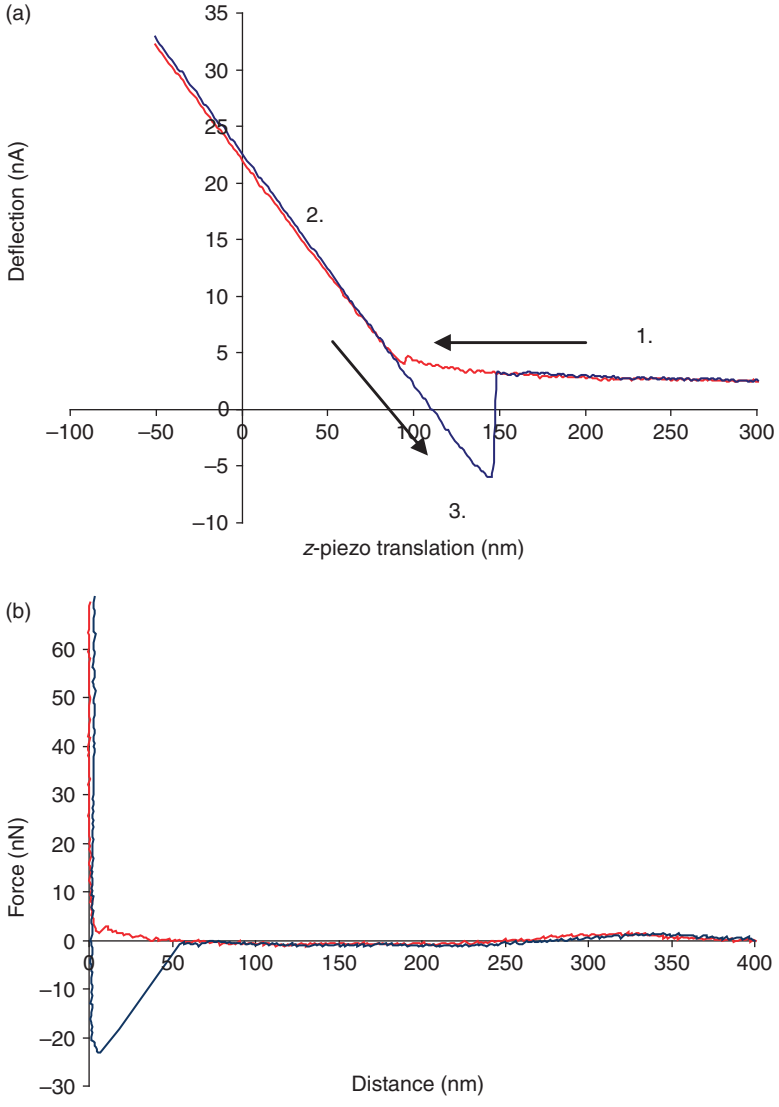

Figure 3 An example force curve. Raw data are shown in (a) plotted as displacement of the *z*-piezo vs. deflection as measured on the photosensitive detector. Calculation of the cantilever stiffness and sensitivity of the optical lever setup allows the raw data to be converted into probe–sample separation distance vs. the force, with converted force curve shown in (b). By convention, for atomic force microscopy (AFM) force curves attractive forces are portrayed as negative and repulsive forces as positive.

(commonly either as voltage, V, or also sometimes as current, A) on the ordinate. As the cantilever begins its approach (described by the red trace), it is away from the surface and hence there is no change in force detected (point 1 in **Figure 3**) – the cantilever is said to be at its free level, that is, at this point there are no net forces acting on it (assuming that the probe is not traveling fast enough for hydrodynamic drag forces to have a significant effect). As the probe comes into close proximity with the cantilever, long-range forces may begin to interact between the probe and the objective surface. Repulsive forces will cause the lever to deflect upward and away from the surface, while attractive forces will deflect the lever downward, toward the surface. If the gradient of attractive forces is less than the stiffness of the lever, then the probe will remain at its free level due to the restoring force stored in the lever. If the probe reaches a point where the gradient of attractive forces exceeds the stiffness of the cantilever, then the cantilever will be rapidly deflected downward allowing the probe to touch the surface in a snap-in or jump-to-contact. In the absence of attractive surface forces, this jump-to-contact will not be seen. When the cantilever makes hard contact with the surface, it is deflected upward due to repulsion between electron shells of atoms in the opposing material surfaces and a positive force is observed (point 2). The cantilever is then retracted (blue trace) and initially follows the path of the approach trace in the contact region. The cantilever often remains attached to the surface by adhesive forces which results in a downward deflection of the cantilever as the probe retracts away from the surface, causing a hysteresis between the trace and retrace. Eventually, the separation force becomes sufficient to overcome the adhesion between the probe tip and the surface and the cantilever snaps back to its initial free-level position (point 3).

This behavior results in a curve of deflection (measured as raw signal) versus the displacement of the piezo in the z direction. When the surface being pressed against is hard and does not undergo significant deformation, the z movement will be equal to the deflection of the cantilever. As a consequence, the slope obtained from contact with an unyielding surface provides the sensitivity of the optical lever system. By dividing the raw deflection data by this sensitivity value, it can be converted into an actual deflection distance. This sensitivity value is essential for the calculation of force values from raw deflection data. This deflection value (distance) can also then be subtracted from the z piezo displacement to give the actual distance traveled by the probe. An alternative method of finding the optical lever sensitivity without requiring to make hard contact with the surface was suggested by Higgins *et al.* [27].

Within operational limits the AFM cantilever behaves as a linear, or Hookean, spring. As a result, the magnitude of the deflection of the cantilever can be used to calculate the force being exerted on the cantilever using Hooke's law:

$$F = -kx \tag{1}$$

where F is force (N), x is the deflection of the cantilever (m), and k is the spring (or force) constant of the cantilever ($\mathrm{N\,m^{-1}}$), which essentially represents the stiffness of the cantilever.

1.16.2.3 Colloid Probes

By attaching a microsphere to the end of a tipless cantilever, the geometry of interactions between the probe and the surface can be greatly simplified, allowing the AFM to be used to probe surface forces, much akin to the surface force apparatus (SFA). Microparticles can also be used as probes that allow particle-to-particle adhesion forces to be measured. An example of a colloid probe is illustrated in **Figure 4**. Here, a scanning electron microscope (SEM) image shows a 5-μm-diameter silica bead attached with glue close to the apex of a standard AFM microcantilever.

The first reported use of an AFM as a colloidal probe was by Ducker and coworkers [28, 29] who attached a 3.5-μm silica sphere to an AFM cantilever

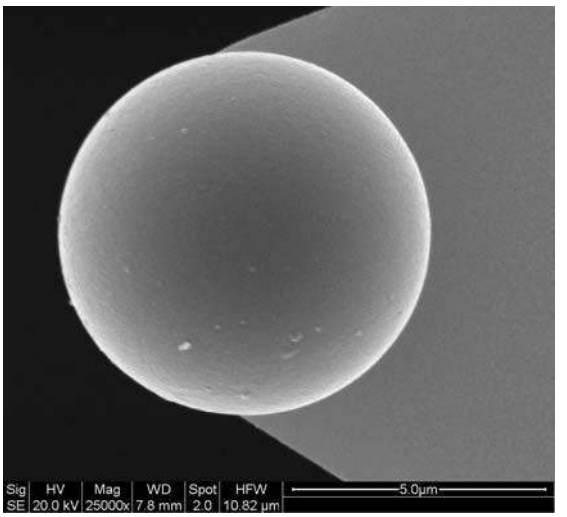

Figure 4 A colloid probe prepared by attaching a glass microsphere to the apex of an atomic force microscopy (AFM) cantilever.

and used it to measure forces between the sphere and a silica surface as a function of electrolyte concentration and pH. Since then this technique has been used to probe the interaction forces between a variety of materials and surfaces, including silicates and other inorganic materials [13, 16, 29, 30]; protein and polymer-coated beads and surfaces [31–34]; membrane-fouling materials and membranes [35]; biological cells and surfaces [36, 37]; between drug particles, important in powder formulations [14, 17, 20]; and for probing the rheological properties of liquids [38, 39].

1.16.3 Visualization of Membrane Surfaces

The primary use of AFM for the characterization of filtration membranes is the 3-D imaging of surface topography, which can yield quantitative parameters such as the surface roughness and the pore-size distribution. As the images obtained are actually arrays of height information, the roughness parameters are easy to extract. The most commonly used roughness parameter is the root mean squared (rms) roughness (R_q), essentially the standard deviation of the heights of all the image pixels from the mean height:

$$R_q = \sqrt{\frac{\sum (Z_i - Z_{ave})^2}{N}} \qquad (2)$$

where Z_i is the height information contained in each pixel, Z_{ave} is the mean height, and N is the total number of pixels in the image.

If a suitable number of pores are clearly obtained on an image, the pore-size distribution and average pore-size parameters can be obtained. **Figure 5** shows a Cyclopore microfiltration membrane which has been imaged using an AFM in air under ambient conditions [40]. Here, the membrane surface is presented in a 3-D view, which allows the eye to become drawn to the undulations in the surface, as well as making the locations of the pores appear clearer. By convention, the images are shaded so that higher areas appear light, with the lowest areas appearing darker. This allows the pores to be seen as localized dark patches. A number of pores are visible in the image with approximately 200 nm in diameter. Instrument software on commercial AFMs routinely allows the measurement of surface features in the *x*- and *y*-direction, allowing the measurement of the size of each pore in at least two dimensions, and with a sufficient number of pores measured in this way the distribution of pore sizes can be ascertained. Occasionally, features of interest may be serendipitously recorded on the membrane surface; **Figure 6** shows a 0.3-μm colloidal particle blocking an entrance of a pore on the surface of a microfiltration membrane. This image shows a membrane in the early stages of being fouled by particulate matter, inhibiting flow through the membrane.

For the example shown above, the pores are relatively large and thus easily imaged. The imaging of membrane pores much smaller in size, such as those found in nanofiltration membranes, is much more challenging. **Figure 7** shows an image of a single pore from a XP117 membrane (PCI Membranes) alongside the pore-size distribution for this particular membrane [41]. As can be seen, the mean pore size is ~1 nm in diameter, which is typical for this type of nanofiltration membrane. It must be noted here that

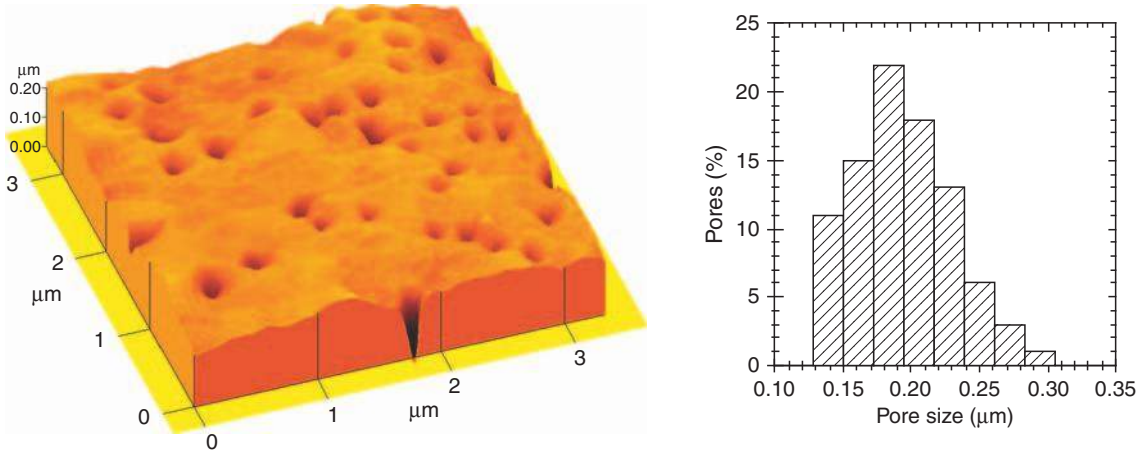

Figure 5 Atomic force microscopy (AFM) image of a Cyclopore microfiltration membrane and pore-size distribution [40].

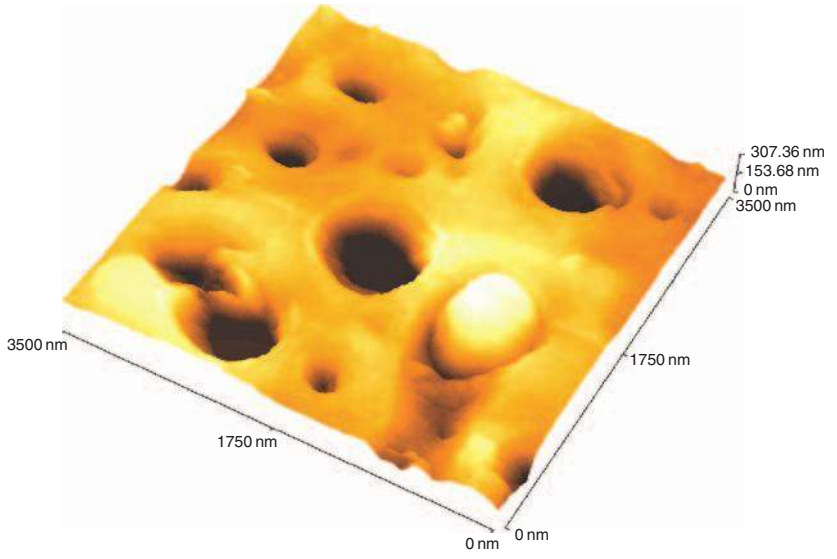

Figure 6 Biocolloid of 0.3 mm blocking membrane pore.

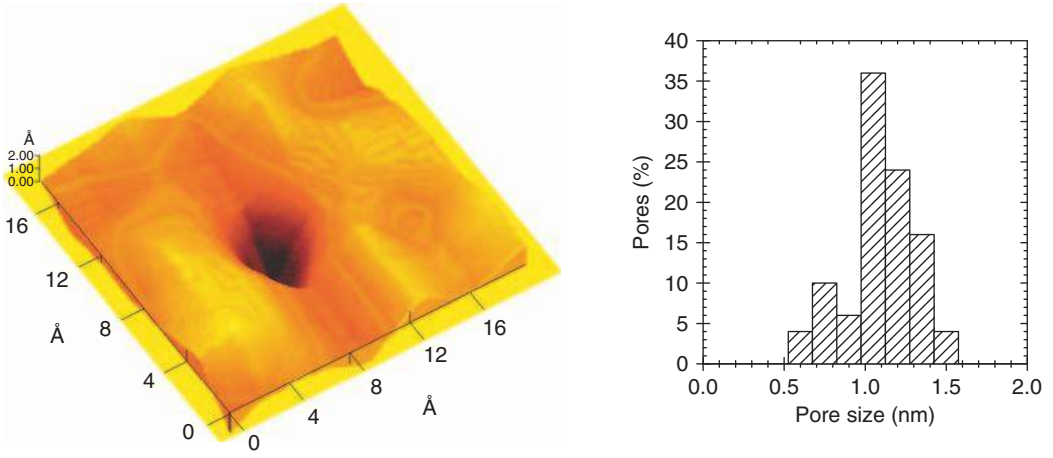

Figure 7 Image of a single pore from an XP117 nanofiltration membrane alongside the pore-size distribution for this membrane.

when imaging features of this scale, the operator must be very careful to ensure that pores are actually being imaged, and that the images do not contain other artifacts which may be mistaken for pores.

For the purposes of modifying the fouling behavior of filtration membranes, much interest is currently being placed on the chemical modification of membrane surfaces. In such cases, it can be useful to quantify the changes in physical characteristics of a treated membrane. **Figure 8** shows a series of topographies of a polyethersulfone (PES) membrane, both unmodified and treated with different degrees of modification (DM) of quaternary 2-dimethyl-aminoethylmethacrylate (qDMAEMA).

Pore size and pore-size distribution of each membrane were determined from surface topography. The lognormal distribution was chosen to represent the pore-size data for each of the membranes. This was found to give a good fit to the pore-size distribution. All these distributions were fitted to lognormal distributions given by frequencies ($\%f$):

$$\%f = \%f_{\max} \exp\left[-\frac{1}{2\sigma^2}\ln\left(\frac{d_p}{X_0}\right)^2\right] \qquad (3)$$

where d_p is the measured pore size, σ is the standard deviation of the measurements, $\%f_{\max}$ is the maximum frequency, and X_0 is the modal value of d_p.

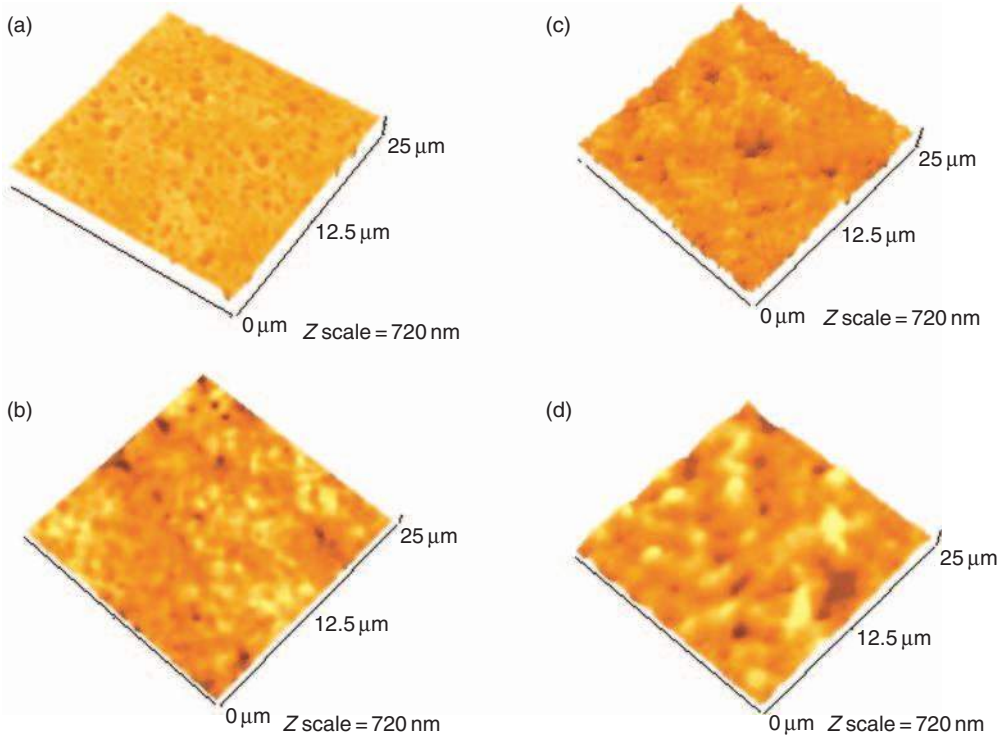

Figure 8 Atomic force microscopy (AFM) images of polyethersulfone (PES) membranes: (a) unmodified; (b–d) modified with quaternary 2-dimethyl-aminoethylmethacrylate (qDMAEMA) with respective degrees of modification (DM) of 202, 367, and 510 $\mu g\,cm^{-2}$.

Mean pore sizes and pore-size distributions of initial membranes determined from AFM images are shown in **Figure 9** and **Table 1**. The table shows that with a mean pore size of $0.535 \pm 0.082\,\mu m$, the polyvinylidene fluoride (PVDF) membrane has slightly larger pores than the PES membrane (mean pore size $0.470 \pm 0.188\,\mu m$). Pore-size distributions are detailed in **Figure 9**, along with fits described by Equation (3). The measured pore sizes are larger than the nominal pore size of $0.22\,\mu m$ as specified by the manufacturers. The AFM data confirm that the pore sizes of studied membranes are of approximately the same size. The topographical images give a clear perception of a notable difference in the surface morphology of the membranes used for the modification. A quantification of the surface parameters (see **Table 1**) provides an insight into morphological features of the membrane which influence both separating properties of the membrane and the process of modification by graft copolymerization.

According to **Figure 9(a)**, the initial PES membrane has a very wide postsynaptic density (PSD) with a σ value of $0.56\,\mu m$. However, grafting of poly-qDMAEMA resulted in narrowing PSD and shifting the whole curve toward smaller pore sizes. As a result, the mean pore size gradually decreased with the increase in the amount of poly-qDMAEMA grafted to the membrane surface. Significant improvement of the PSD was observed even for the modified PES membranes with the smallest degree of modification.

Narrowing of the PSD occurred mostly due to the disappearance of large pores (greater in diameter than $0.6\,\mu m$). Taking into consideration that substantial narrowing of large pores demands higher quantities of grafted polymer compared to smaller pores, it can be assumed that higher rates of polymer growth were initiated at the walls of the larger pores. At the entrance of narrower pores, a higher density of free radicals results in chain termination and, consequently, a lower rate of polymer grafting. With time, when the PSD becomes more uniform, free radicals are eventually distributed across the membrane surface. This leads to a gradual decrease of all surface pores with the PSD shifting to smaller sizes. With $DM > 202\,\mu m\,cm^{-2}$, a slight fluctuation in the width of PSD (σ) was observed.

Using the topography data, surface analysis was carried out to obtain the surface roughness parameters, as shown in **Table 2**. The formation of a graft polymer layer

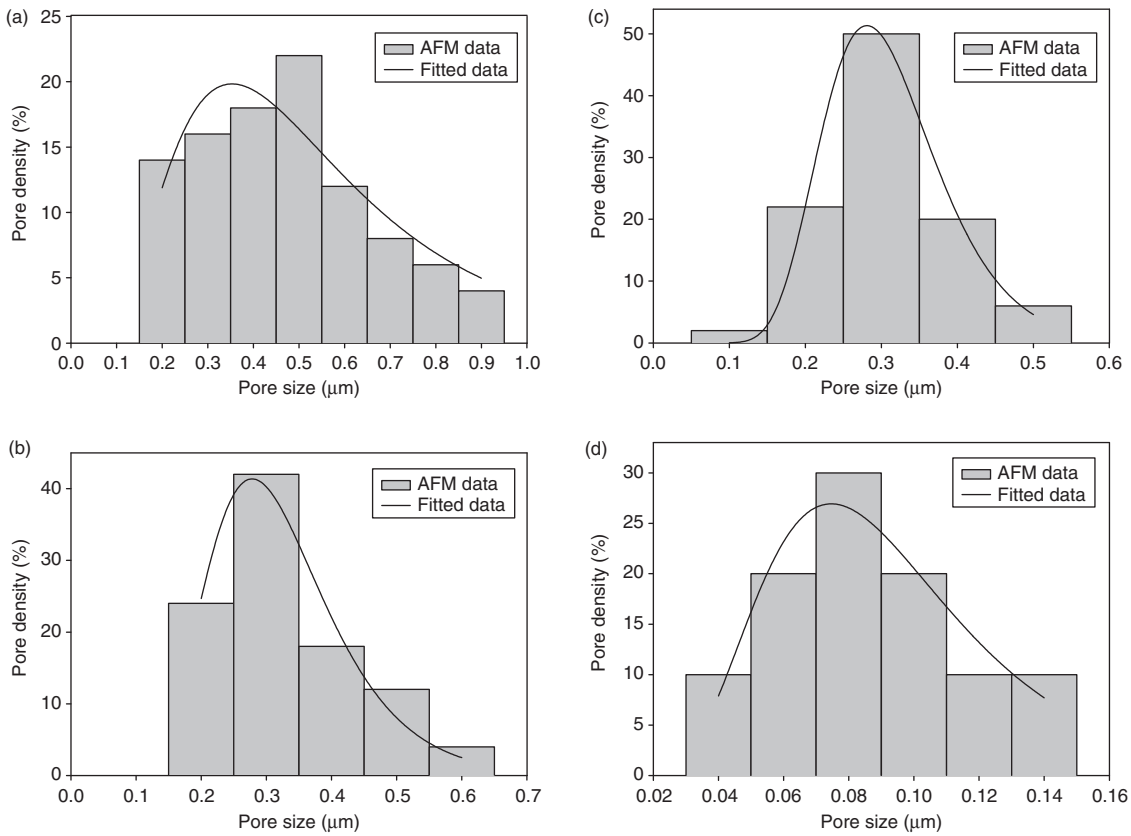

Figure 9 Pore-size distributions obtained from surface topography for unmodified (a) and modified with (b) 202 μg cm^{-2}, (c) 367 μg cm^{-2}, and (d) 510 μg cm^{-2} of quaternary 2-dimethyl-aminoethylmethacrylate (qDMAEMA).

Table 1 AFM measurements of mean pore size and pore-size distribution for PES membranes modified with qDMAEMA

		PSD parameters		
DM (μg cm^{-2})	*Mean pore size (μm)*	*X_0 (μm)*	*%f_{max}*	*σ*
0	0.470 ± 0.188	0.353 ± 0.028	19.8 ± 2.2	0.56 ± 0.08
202	0.337 ± 0.098	0.278 ± 0.010	41.4 ± 4.4	0.32 ± 0.04
367	0.293 ± 0.072	0.281 ± 0.003	51.3 ± 2.0	0.26 ± 0.01
510	0.100 ± 0.083	0.075 ± 0.004	26.9 ± 2.9	0.40 ± 0.05

Table 2 AFM measurements of membrane surface morphology for membranes modified with qDMAEMA

DM (μg cm^{-2})	*Ra (nm)*	*Rq (nm)*	*Mean height (nm)*	*Max range (nm)*
0	27.93	36.43	161.77	275.46
202	32.26	42.91	250.09	378.4
367	67.37	85.28	329.46	537.27
510	81.64	103.82	357.5	3000.5

on the membrane surface resulted in significant changes in the surface morphology. Structural modifications became more pronounced with increasing DM [42].

A slight increase in the membrane roughness, compared with the unmodified membrane, was observed for membranes modified with the lowest degree of grafted polymer ($202\,\mu g\,cm^{-2}$). At such a degree of modification, grafted chains would most likely be able to be accommodated within the pores. Further increases in DM led to a significant increase in surface roughness with a layer of grafted polymer forming its own porous structure.

1.16.4 Imaging of Membrane Surfaces in Liquid

In aqueous solution, membrane surfaces commonly carry electrical charge, with the sign and magnitude of the charge dependent upon the state of the surrounding solvent, with the pH and ionic strength being especially important. On approach of an AFM probe tip to a membrane surface, the long-range forces experienced will be a combination of electrical double-layer forces and van der Waals forces. The net forces experienced by the probe tip may be either repulsive or attractive, depending upon the particular interaction being observed. In addition, when imaging in the noncontact mode, the finest resolution may be achieved when the forces between the probe tip and the membrane are repulsive. This allows the interactions between the apex of the probe tip and the membrane to be minimized, leading to the maximum possible resolution.

Figure 10 shows force measurements taken between a silicon nitride AFM tip and a Cyclopore membrane at various concentrations of NaCl [43]. All the measurements shown are the forces measured as the tip first approaches the membrane. As can be seen at all concentrations of salt, the tip–surface interactions are repulsive at all separation distances. For these measurements, the pH was maintained at a constant value (6.5). As the ionic strength is increased, the range of the repulsive forces decreases, as would be expected from conventional Derjaguin–Landau–Verwey–Overbeek (DLVO) theory, from a maximum of approximately 35 nm down to about 2–3 nm. This suggests that the electrical double-layer interaction between the tip and the surface is dominant in all cases. Under these conditions, both the probe tip and the membrane would be expected to carry a negative charge.

With information such as that shown in **Figure 10**, it is now possible to image at a specified imaging force corresponding to any point on the force curves using noncontact mode imaging. **Figure 11** shows two series of images obtained: first with varying imaging force at a constant solution ionic strength and second at a constant force at various ionic strengths, along with the pore-size

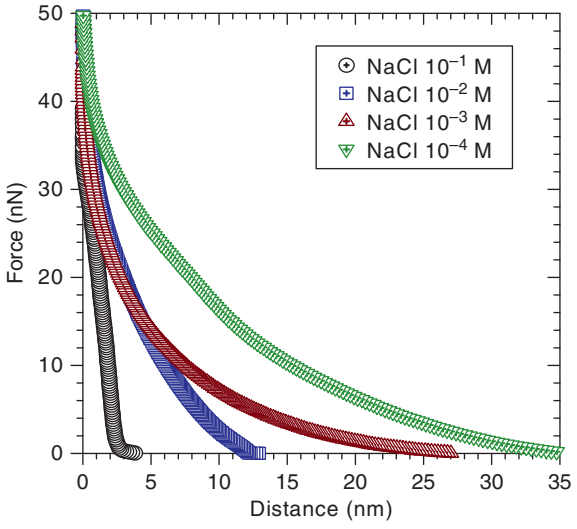

Figure 10 Force vs. distance curves for the approach of an atomic force microscopy (AFM) tip to a Cyclopore microfiltration membrane in NaCl solutions of various ionic strengths.

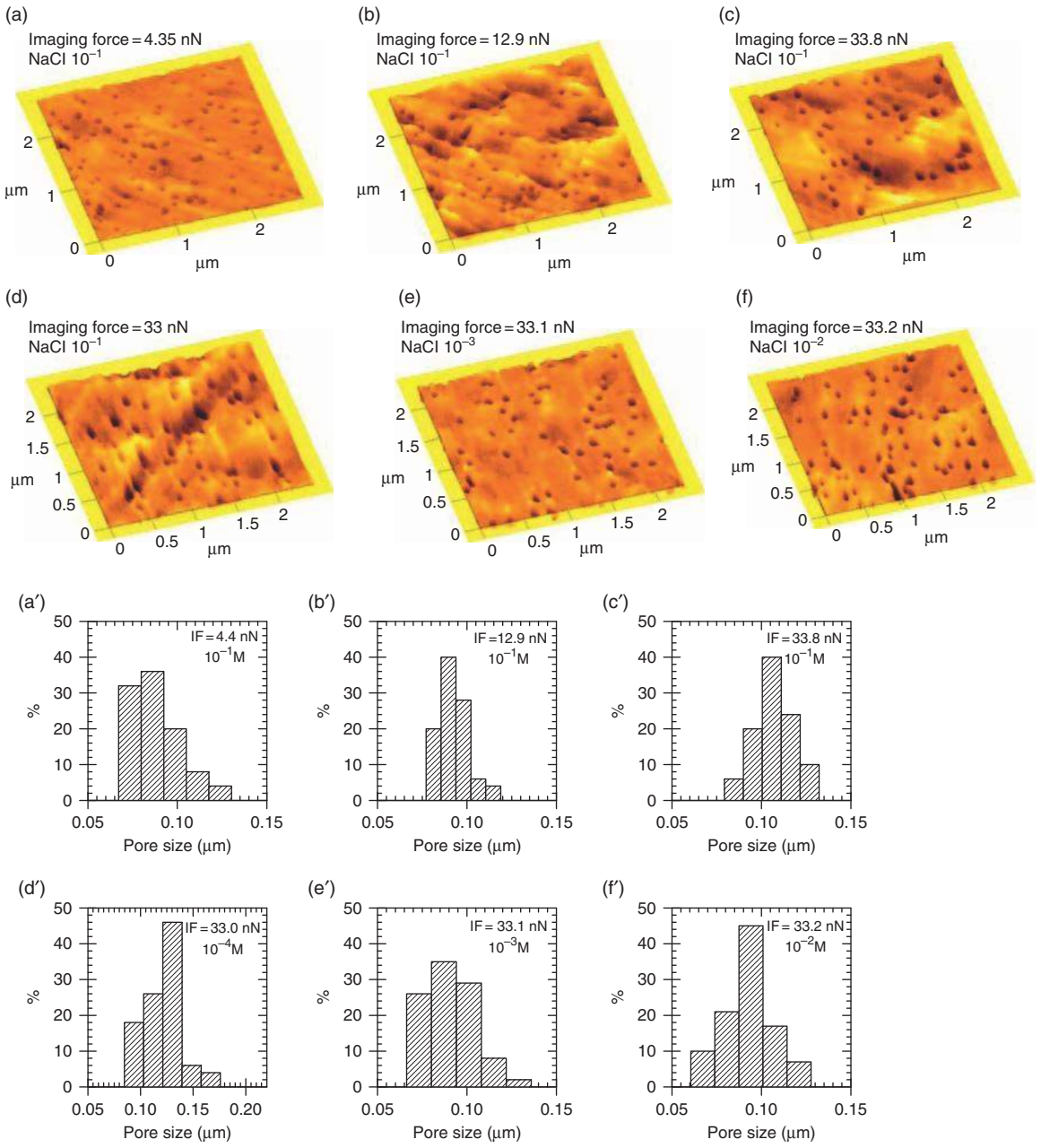

Figure 11 Atomic force microscopy (AFM) images of a Cyclopore membrane in electrolyte solutions. (a–c) and (a′–c′) at various forces in 10^{-1} M NaCl solution; (c, c′), (d–f), and (d′–f′) at approximately constant force at various ionic strengths. All data at pH 6.5. IF, imaging force.

distributions obtained from the same images [43]. As the imaging force or ionic strength is increased, the image quality is improved. In addition, the pore-size distributions also vary, with a greater mean pore diameter being obtained at the higher force and ionic strengths. This does illustrate a limitation of the values for pore sizes obtained from AFM images: the accuracy of the sizes obtained is in part dependent upon the quality of the images obtained. Whenever imaging any surface, using AFM is of great importance to obtain as sharp an image as is possible.

1.16.5 Measurement of Adhesion of Colloidal Articles and Cells to Membrane Surfaces

Using a colloidal probe mounted on an AFM cantilever, it is possible to measure the adhesion between a range of materials and membranes under a number of different conditions. These adhesive forces are important determinants in the fouling properties of any membrane. The process testing of new membranes to determine their fouling properties can be costly in terms of both money and time. Development of use of the AFM to directly quantify the adhesion of particulates of different types to membranes has a great potential role in predicting and optimizing the fouling properties of filtration membranes. In this section, we describe a series of measurements to measure the changes in adhesion between a model biocolloid and PES membranes under different environmental conditions. This was then repeated with the same membrane, but grafted with a polymer (qDMAEM) to hopefully decrease its tendency to become fouled. As a probe, silica spheres were coated with a layer of the globular protein bovine serum albumin (BSA). BSA is a protein which has been utilized in a number of applications due to its high degree of nonspecific binding [44].

Examples of retraction curves measured at three different loading forces for a BSA-modified microsphere interacting with PES membrane grafted with qDMAEMA, shown in **Figure 12**, demonstrate that the adhesion force (pull-off force) increased with the force applied by the colloid [44]. Similar findings have been observed in previous studies [45–49].

The increase in the adhesion force is most likely to result from an increase in the number of chemical bonds formed between the biopolymers when the surfaces are forced into closer contact using higher loading forces [49]. In addition, the deformation of the membrane surface at high loading forces may increase the area of contact between the probe and the membrane surfaces. In order to exclude the influence of loading force in comparison of interactions force, the experimental results will be presented by plotting the adhesion force versus the loading force. For purposes of comparison, the adhesion force at loading force equal to $80\,\mathrm{mN\,m^{-1}}$ was measured, interpolated or extrapolated from the obtained experimental data.

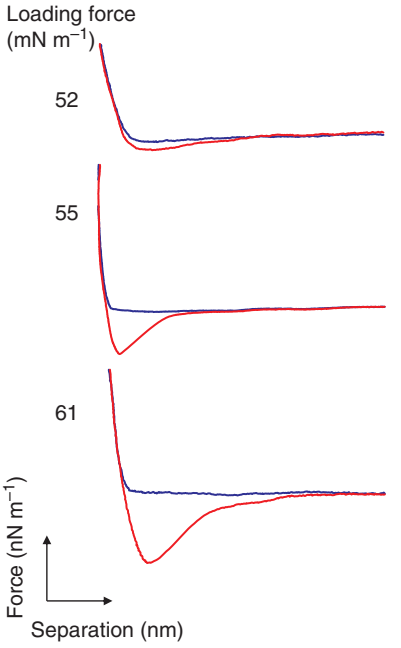

Figure 12 Representative force curves (approach = blue, retract = red) showing interactions between a bovine serum albumin (BSA)-coated silica probe and quaternary 2-dimethyl-aminoethylmethacrylate (qDMAEMA)-modified polyethersulfone (PES) membrane at different loading forces.

1.16.5.1 Interactions Forces between Unmodified PES Membranes and BSA-Coated Colloid probes

1.16.5.1.1 Effect of pH on measured adhesion

Figure 13 shows the normalized adhesion force measurements against the normalized loading force applied to the cantilever between a BSA-modified probe and initial PES membrane at different pH values [44]. It can be seen that the adhesive force is highest at pH 5, followed by moderate values at pH 3, and the lowest at pH 7.

At pH 7, both the BSA and the membrane surface are negatively charged [49], which provoke increases in the repulsive electrostatic interaction leading to a reduction in adhesion. BSA is more hydrophobic at pH 5 than at 7, which would be expected to increase adhesion. Second, the protein has a more expanded structure at pH values away from its isoelectric point (pI). Thus, a steric repulsive interaction between the interacting surfaces will be higher at pH 3 than at pH 5, leading to reduced adhesion at pH 3. Finally, PES possesses a slight positive charge at pH 3 [49], provoking an electrostatic repulsive force between the membrane and colloidal probe.

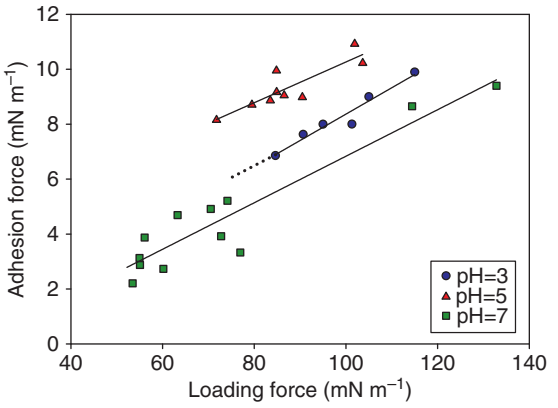

Figure 13 Relationship between the loading force and adhesion measured for unmodified polyethersulfone (PES) membrane at a range of pH values.

1.16.5.1.2 Effect of ionic strength on adhesion forces

The effect of the solution ionic strength on the measured adhesion force is shown in **Figure 14** [44]. Increased NaCl concentration leads to an increase in the adhesion force between the BSA probe and the PES membrane surface. The adhesion of the BSA probe to initial unmodified PES increased by a factor of ~2.4 across the concentration range 1–100 mM NaCl. This behavior is qualitatively consistent with the DLVO theory [50], as increasing the ionic strength compresses the thickness of the electrostatic double layer and should therefore reduce the repulsion force between the two surfaces resulting in an increase in measured adhesion force.

1.16.5.2 Interaction Forces between PES Membranes Modified with qDMAEMA and BSA-Coated Colloid Probes

1.16.5.2.1 Effect of pH

The effect of solution pH on adhesion force for PES membranes modified with qDMAEMA is shown in **Figure 15**. An increase in adhesion force with increasing pH is observed for modified membranes with three different DMs and is approximately threefold at a loading force of 80 mN m^{-1} [44].

The dominant contribution in the increase in adhesion force with increasing pH can be attributed to the electrostatic force between the positively charged modified membranes and the BSA probe. At pH 3, both surfaces (membrane and BSA probe) possess a positive charge resulting in greater repulsion at this pH and, hence, a lower adhesion than seen at other pH values. At pH 7, the modified PES membranes remain positively charged, while BSA carries a negative charge. This change in the nature of the electrostatic interaction leads to a greater observed adhesive force at pH 7.

Taking into consideration the amphoteric behavior of BSA, which leads to a change in protein charge with changing pH, the BSA possesses a positive charge at pH below the pI and negative charge at pH above the isoelectric point. This fact explains the high adhesion at pH 7 where both the BSA and the membrane surface are oppositely charged. Thus, an attractive electrostatic force between the interacting surfaces results in higher adhesion.

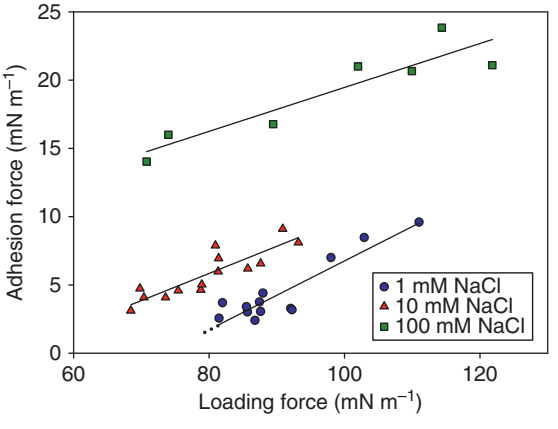

Figure 14 Dependency of adhesion force on loading force for interactions between a bovine serum albumin (BSA)-coated silica probe and unmodified polyethersulfone (PES) membrane measured in solutions of increasing ionic strength.

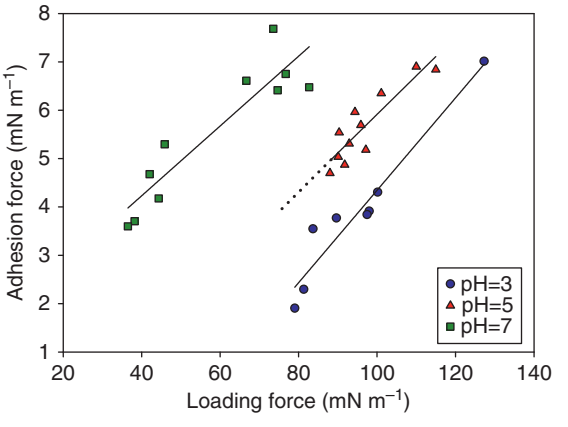

Figure 15 Measured adhesion force vs. loading force between a bovine serum albumin (BSA)-coated probe and a quaternary 2-dimethyl-aminoethylmethacrylate (qDMAEMA)-modified polyethersulfone (PES) membrane (DM = 510 μg cm^{-2}).

Steric interaction could be another factor which plays a role in reducing the adhesion force observed with both membranes at pH 3. The overlap of the expanded protein layer and the modification polymer chain of qDMAEMA, which is fully dissociated at this pH, enhance the repulsive interactions between the colloid probe and the surface of the modified membrane. In addition, at pH 5, there is practically no electrostatic interaction because this pH is close to the isoelectric point of the protein (the net charge is around zero) and, therefore, the electrostatic repulsion is negligible. As at pH 5 the protein has no net charge so the structure of the protein is more compact and it has hydrophobic properties, such interaction may be lead to high adhesion at pH 5 than at pH 3.

1.16.5.2.2 Effect of ionic strength

Normalized adhesion forces versus normalized loading forces for interactions involving the modified PES membrane are shown in **Figure 16** at different solution ionic strengths. An increase in adhesion force with increased ionic strength is evident.

1.16.5.2.3 Comparison of (bio)adhesion force measurements between unmodified membranes and membranes modified with qDMAEMA

The normalized adhesion forces at the same loading force (loading force = 80 mN m^{-1}) for initial and modified PES membranes with qDMAEMA are shown in **Figure 17**. It is clear that the unmodified membrane has a higher adhesion force than the modified membranes at pH 3 and pH 5, while the lowest adhesion was observed at pH 7. In addition, at pH 3, modified membrane with the lowest DM exhibits the lowest adhesion. At pH 5, modified membrane with DM of 510 μg cm^{-2} showed the lowest adhesion force, while both membranes show almost the same adhesion at pH 7 [44].

The BSA-functionalized probe and both modified and unmodified membranes all possess a positive surface charge at pH 3. However, the qDMAEMA-functionalized membrane possesses a markedly greater charge than the unmodified PES membrane. The resulting greater electrostatic repulsion accounts for the greater adhesive forces observed with the initial unmodified PES membrane than with the modified membrane. When the surrounding solution is at pH 7, both the initial PES membrane and BSA possess negative surface charges, with the qDMAEMA membrane still carrying a positive charge. This accounts for the modified membrane having a greater adhesive force with the BSA-coated probe than the unmodified membrane.

The adhesion force measured between BSA-coated colloid and modified PES membranes is shown in **Figure 18**. The adhesion force for all the investigated membranes was found to increase with increasing solution ionic strength.

The modified membrane with DM 367 μg cm^{-2} demonstrated the lowest adhesion force followed by

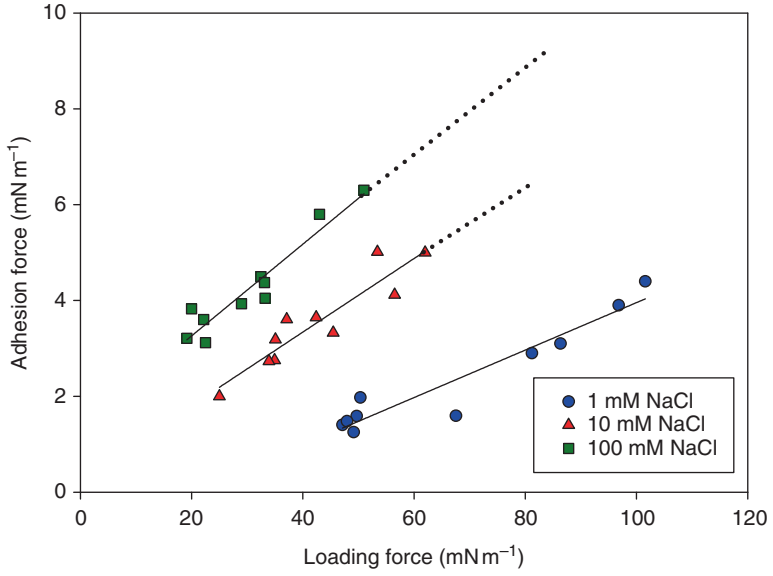

Figure 16 Adhesion and loading forces between bovine serum albumin (BSA)-coated silica probe and quaternary 2-dimethyl-aminoethylmethacrylate (qDMAEMA)-modified PES membrane in solutions of differing ionic strengths.

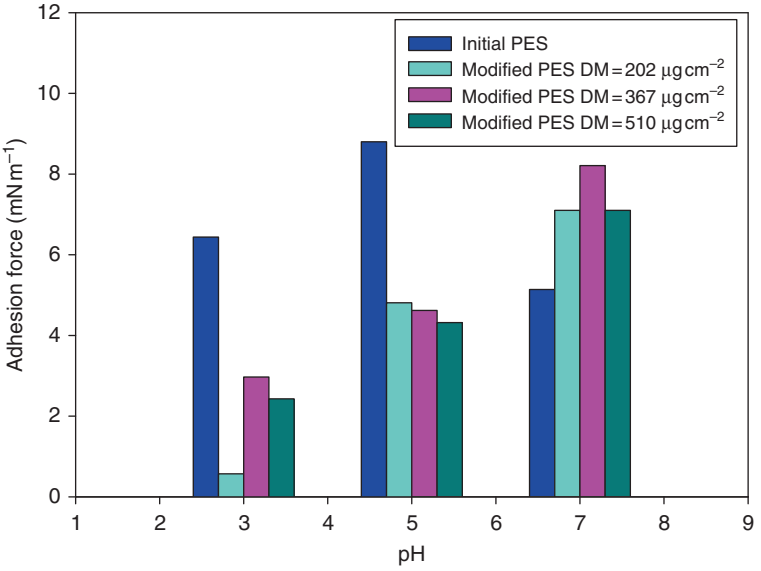

Figure 17 Comparison of measured adhesion forces of bovine serum albumin (BSA)-modified silica probes to unmodified and modified membranes at different environmental pH values.

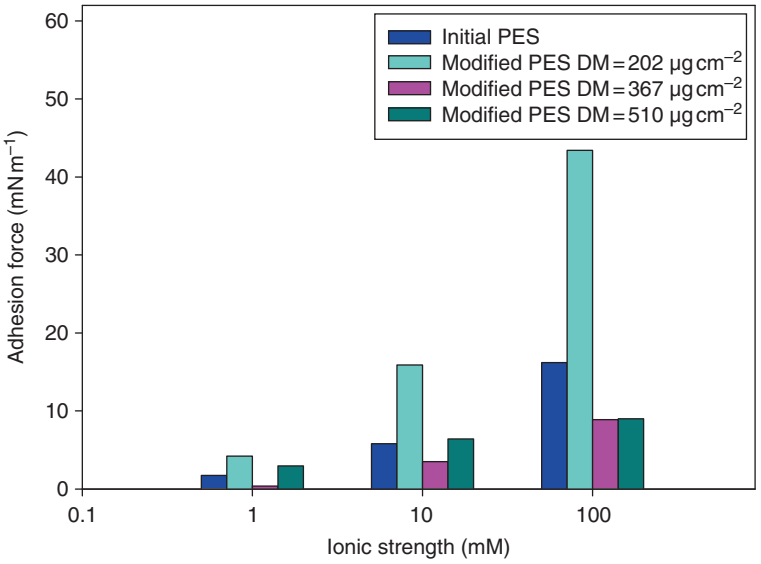

Figure 18 Comparison of adhesion forces measured between a bovine serum albumin (BSA)-coated silicon probe and modified and unmodified membrane surfaces as a function of ionic strength.

the initial membrane which shows an increase in adhesion force compared to modified membrane with medium DM.

References

[1] Hansma, H. G., Sinsheimer, R. L., Groppe, J., *et al. Scanning* **1993**, *15*(5), 296–299.
[2] Hansma, H. G., Cleveland, J. P., Radmacher, M., *et al. Appl. Phys. Lett.* **1994**, *64*(13), 1738–1740.
[3] Zhong, Q., Inniss, D., Kjoller, K., Elings, V. *Surf. Sci. Lett.* **1993**, *290*(1–2), L688–L692.
[4] Schmitz, I., Schreiner, M., Friedbacher, G., Grasserbauer, M. *Appl. Surf. Sci.* **1997**, *115*, 190–198.
[5] McLean, R. S., Sauer, B. B. *Macromolecules* **1997**, *30*, 8314–8317.
[6] Loos, J. *Adv. Mater.* **2005**, *17*, 1821–1833.
[7] Lüthi, R., Meyer, E., Howald, L., *et al. J. Vac. Sci. Technol. B* **1994**, *12*(3), 1673–1676.
[8] Kaliapan, S. K., Capella, B. *Polymer* **2005**, *46*, 11416–11423.
[9] Domke, J., Radmach, M. *Langmuir* **1998**, *14*, 3320–3325.

[10] Plassard, C., Lesniewska, E., Pochard, I., Nonat, A. *Ultramicroscopy* **2004**, *100*, 331–338.
[11] Vinckier, A., Heyvaert, I., D'Hoore, A., *et al. Ultramicroscopy* **1995**, *57*, 337–343.
[12] Dulinska, I., Targosz, M., Strojny, W., *et al. J. Biochem. Biophys. Methods* **2006**, *66*, 1–11.
[13] Weisenhorn, A. L., Maivald, P., Butt, H.-J., Hansma, P. K. *Phys. Rev. B* **1992**, *45*(19), 11226–11233.
[14] Roberts, C. J. *Eur. J. Pharm. Sci.* **2005**, *24*, 153–157.
[15] Kapple, M., Butt, H.-J. *Part. Part. Syst. Charact.* **2002**, *19*, 129–143.
[16] Bowen, W. R., Hilal, N., Lovitt, R. W., Wright, C. J. *Colloids Surf. A* **1999**, *157*, 117–125.
[17] Eve, J. K., Patel, N., Luk, S. Y., Ebbens, S. J., Roberts, C. J. *Int. J. Pharm.* **2002**, *238*, 17–27.
[18] Xu, L., Logan, B. E. *Langmuir* **2004**, *20*, 8817–8822.
[19] Burnham, N. A., Dominguez, D. D., Mowery, R. L., Colton, R. J. *Phys. Rev. Lett.* **1990**, *64*(16), 1931–1934.
[20] Davies, M., Brindley, A., Chen, X., *et al. Pharm. Res.* **2005**, *22*(7), 1158–1166.
[21] Gillies, G., Kapple, M., Butt, H.-J. *Langmuir* **2005**, *21*, 5882–5886.
[22] Hartley, P. G., Grieser, F., Mulvaney, P., Stevens, G. W. *Langmuir* **1999**, *15*, 7282–7289.
[23] Allen, S., Chen, X., Davies, J., *et al. Biochemistry* **1997**, *36*, 7457–7463.
[24] Best, R. B., Brockwell, D. J., Toca-Herrerra, J. L., *et al. Anal. Chim. Acta* **2003**, *479*, 87–105.
[25] Clarke, J., Williams, P. M. Unfolding Induced by Mechanical Force. In *Protein Folding Handbook. Part 1*; Buchner, J., Kiefhaber, T., Eds.; Wiley-VCH: Weinheim, 2005; pp 1111–1142.
[26] Rief, M., Gautel, M., Oesterhelt, F., Fernandez, J. M., Gaub, H. E. *Science* **1997**, *276*, 1109–1113.
[27] Higgins, M. J., Proksch, R., Sader, J. E., *et al. Rev. Sci. Inst.* **2006**, *77*, 013701.
[28] Ducker, W. A., Senden, T. J., Pashley, R. M. *Nature* **1991**, *353*, 239–241.
[29] Ducker, W. A., Senden, T. J. *Langmuir* **1992**, *8*(7), 1831–1836.
[30] Götzinger, M., Peukert, W. *Powder Technol.* **2003**, *130*, 102–103.
[31] Li-Chong, X., Logan, B. E. *Environ. Sci. Technol.* **2005**, *39*, 3592–3600.
[32] Gillies, G., Prestidge, C. A. *Langmuir* **2005**, *21*, 12342–12347.
[33] Reitsma, M., Craig, V., Biggs, S. *Int. J. Adhes. Adhes.* **2000**, *20*, 445–448.
[34] Castro, L. B. R., Kapple, M., Petri, D. F. S. *Langmuir* **2006**, *22*, 3757–3762.
[35] Hilal, N., Bowen, W. R. *Desalination* **2002**, *150*, 289–295.
[36] Bowen, W. R., Hilal, N., Lovitt, R. W., Wright, C. J. *Colloids Surf. A* **1998**, *136*, 231–234.
[37] Li, X., Logan, B. E. *Langmuir* **2004**, *20*, 8817–8822.
[38] Barrow, M. S., Bowen, W. S., Hilal, N., *et al. Proc. R. Soc. Lond. Ser. A* **2003**, *459*, 2885–2908.
[39] Notley, S. M., Biggs, S., Craig, V. S. J. *Rev. Sci. Inst.* **2003**, *74*(9), 4026–4032.
[40] Bowen, W. R., Hilal, N., Lovitt, R. W., Williams, P. M. *J. Membr. Sci.* **1996**, *110*, 233–238.
[41] Bowen, W. R., Hilal, N., Lovitt, R. W., Williams, P. M. *J. Membr. Sci.* **1996**, *110*(2), 229–232.
[42] Hilal, N., Al-Khatib, L., Al-Zoubi, H., Nigmatullin, R. *Desalination* **2005**, *185*, 1025–1035.
[43] Bowen, W. R., Hilal, N., Lovitt, R. W., Sharif, A. O., Williams, P. M. Atomic Force Microscope Studies of MF, UF and NF Membranes: Force Measurement and Imaging in Electrolyte Solutions. In *Euromembrane 97: Progress in Membrane Science and Technology*; Kemperman, A. J. B., Koops, G. H., Eds.; University of Twente: Enschede, The Netherlands, 1997, p 281.
[44] Al-Khatib, L. Development of (Bio)Fouling Resistant Membranes for Water Treatment Applications. PhD Thesis, School of Chemical, Environmental and Mining Engineering, University of Nottingham, UK, 2006.
[45] Toikka, G., Hayes, R. A., Ralston, J. *J. Colloid Interface Sci.* **1996**, *180*, 239–248.
[46] Bowen, W. R., Hilal, N., Lovitt, R. W., Wright, C. J. *J. Membr. Sci.* **1998**, *139*(2), 269–274.
[47] Bowen, W. R., Hilal, N., Lovitt, R. W., Wright, C. J. *Colloids Surf. A* **1998**, *136*(1–2), 231–234.
[48] Xu, L.-C., Vadillo-Rodriguez, V., Logan, B. E. *Langmuir* **2005**, *21*, 7491–7500.
[49] Kuzmenko, D., Arkhangelsky, E., Belfer, S., Freger, V., Gitis, V. *Desalination* **2005**, *179*(1–3), 323–333.
[50] Brant, J. A. *Environ. Eng. Sci.* **2002**, *19*(6), 413–427.

Biographical Sketches

Professor Nidal Hilal is currently the director of the Centre for Clean Water Technologies at the University of Nottingham in the United Kingdom. He obtained his PhD in chemical engineering from the University of Wales in 1988. In addition to 3 years of industrial experience, he has worked continuously in academia since graduation in 1981. Over the years, he has made a major contribution becoming an internationally leading expert in the application of atomic force microscopy to chemical and process engineering, particularly in membrane separation. In recognition of this, he has been awarded a DSc degree from the University of Wales in 2005. The world-leading reputation for research that Professor Hilal has earned in the fields of membrane technology and water treatment has been formally recognized by the award of the Kuwait Prize of Applied Science for Water Resources Development in the Arab World for the year 2005. He is also a member of the editorial board for desalination and desalination and water treatment journals, on the advisory board of Lifeboat Foundation, a member of the project advisory board of the Middle East Desalination Centre, on the panel of referees for the research councils in the UK, Canada, Finland, and Norway and has published articles in more than 59 international journals. Professor Hilal has authored over 300 refereed publications, 4 textbooks, and 11 invited chapters in international handbooks. He is a registered European Engineer – Paris, a chartered engineer in the United Kingdom, and fellow of the Institution of Chemical Engineers – London.

Dr. Daniel Johnson is currently a postdoctoral researcher at the Centre for Clean Water Technologies at the University of Nottingham. He studied for his PhD in the Laboratory of Biophysics and Surface Analysis in the School of Pharmacy at the University of Nottingham. He currently undertakes research into interaction forces between colloidal particles and surfaces and in the characterization of water treatment membranes using atomic force microscopy.

Index to Volume 1

The index is in letter-by-letter order, whereby hyphens and spaces within index headings are ignored in the alphabetization, and it is arranged in set-out style, with a maximum of four levels of heading. Page numbers suffixed by *f* or *t* refer to figures or tables respectively.

B

C

D

E

F

G

H

I

K

L

M

N

O

P

Q

R

S

T

U

V

W

X

Y

Z